LOCKHEED MARTIN

LOCKHEED MARTIN ASTRONAUTICS

GPHS - RTGs

In Support of the

Cassini RTG Program

Final Technical Report

Document No. RR18

**11 January 1991
through
30 April 1998**

August 1998
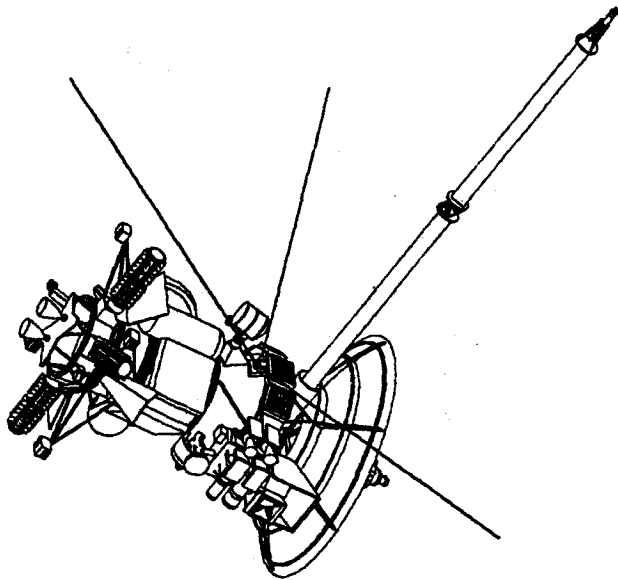
MASTER

Space Power Programs

DISCLAIMER

DISCLAIMER

Portions of this document may be illegible
in electronic image products. Images are
produced from the best available original
document.

Final Technical Report

Contract No.
DE-AC03-91SF18852

GPHS-RTGs in Support of the Cassini Mission

Document No. RR18

11 January 1991
through
30 April 1998

Prepared for:

U.S. Department of Energy
Oakland Operations Office
1301 Clay Street
Oakland, CA 94612-5208

Prepared by:

Lockheed Martin Astronautics
Valley Forge Operations
P.O. Box 8555
Philadelphia, PA 19101

LOCKHEED MARTIN

August 1998

Space Power Programs

Final Technical Progress Report

Table of Contents

Final Technical Progress Report

Table of Contents (Cont'd)

Final Technical Progress Report

Table of Contents (Cont'd)

Final Technical Progress Report

Table of Contents (Cont'd)

Final Technical Progress Report

Table of Contents (Cont'd)

Final Technical Progress Report

Table of Contents (Cont'd)

Final Technical Progress Report

Table of Contents (Cont'd)

Final Technical Progress Report

Table of Contents (Cont'd)

Final Technical Progress Report

Table of Contents (Cont'd)

Final Technical Progress Report

List of Illustrations

Final Technical Progress Report

List of Illustrations (Cont'd)

Final Technical Progress Report

List of Illustrations (Cont'd)

Final Technical Progress Report

List of Illustrations (Cont'd)

Final Technical Progress Report

List of Illustrations (Cont'd)

Final Technical Progress Report

List of Illustrations (Cont'd)

Final Technical Report

Acronyms

Final Technical Report

Acronym List

3DMP	Three Degree-of-Freedom Trajectory Prediction Tool
3DOF	Three Degree-of-Freedom
6DOF	Six Degree-of-Freedom
ACS	Active Cooling System
ADS	Automatic Destruct System
AIC	Accident Initiating Condition
AMAD	Activity Media Aerodynamic Diameter
AOC	Accident Outcome Condition
ASI	Italian Space Agency
BCI	Bare Clad Impact
BCL	Battelle Columbus Lab
BIE	Basic Initiating Event
BOM	Beginning of Mission
BPCA	Base and Protective Cover Assembly
BRV	Ballistic Reentry Vehicle
CBCF	Carbon Bonded Carbon Fiber
CCAS	Cape Canaveral Air Station
CPD	Cumulative Probability Distribution
CET	Component Engineering Test
CFM	Cubic Feet per Minute
CRAF	Comet Rendezvous Asteroid Flyby
CSC	Converter Shipping Container
CSDS	Command Shutdown and Destruct System
CSR	Converter Support Ring
CVS	Clad Vent Set
DAS	Data Acquisition System
DCF	Dose Conversion Factor
DFSAR	Draft Final Safety Analysis Report

Final Technical Report
Acronym List (Cont'd)

DMM	Digital Multimeter
DMP	Degrees of Motion Prediction
DOE	Department of Energy
DOF	Degrees-of-Freedom
DR	Defect Report
ECN	Engineering Change Notice
EDST	Eastern Daylight Savings Time
EHS	Electric Heat Source
EIS	Environmental Impact Statement
EMQ	Engineering, Manufacturing, Quality
EOM	End of Mission
ESA	Early Safety Assessment
ET	Engineering Test
ETG	Electrically Heated Thermoelectric Generator
ETG-SC	ETG Shipping Container
FA	Flight Acceptance
FC	Fueled Clad
FE	Final Environment
FEM	Finite Element Model
FOS	Face-on-Stable
FRB	Failure Review Board
FSAR	Final Safety Analysis Report
FSII	Full Stack Intact Impact
FTS	Flight Termination System
FWPF	Fine Weave Pierced Fabric
GE	General Electric
GESP	General Electric Space Power
GFE	Government Furnished Equipment

Final Technical Report

Acronym List (Cont'd)

GIS	Graphite Impact Shell
GMV	Gas Management Valve
GPHS	General Purpose Heat Source
GPHSA	General Purpose Heat Source Assembly
GPV	Gas Processing Valve
GSC	Gas Service Cart
GSE	Ground Support Equipment
HOVI	Hydrogen Oxygen Vertical Impact
HSA	Heat Source Assembly
IAAC	Inert Atmosphere Assembly Chamber
IBSA	Inboard Heat Source Support Assembly
ICD	Interface Control Drawing
IHS	Isotope Heat Source
IIP	Instantaneous Impact Point
INSRP	Interagency Nuclear Safety Review Panel
JPL	Jet Propulsion Laboratory
KSC	Kennedy Space Center
LANL	Los Alamos National Laboratory
LAS	Loading and Assembly Station
LC	Launch Complex
LeRC	Lewis Research Center
LES	Lincoln Experimental Satellites
LHS	Latin Hypercube Sampling
LM	Lockheed Martin
LMMS	Lockheed Martin Missiles & Space
LV	Launch Vehicle
LVA	Launch Vehicle Adapter
MECO	Main Engine Cut-Off

Final Technical Report
Acronym List (Cont'd)

MES	Main Engine Start
MET	Mission Elapsed Time
MHW	Multihundred Watt
MRA	Mid-Ring Assembly
MRB	Material Review Board
MRMF	Module Reduction and Monitoring Facility
MSA	Midspan Support Assembly
NASA	National Aeronautics and Space Administration
NASDA	National Space Development Agency of Japan
NR	Non-Conformance Report
OBSA	Outboard Heat Source Support Assembly
OR	Oak Ridge
OSA	Office of Special Applications
OSC	Orbital Sciences Corporation
OSTP	Office of Science and Technology Policy
PDF	Probability Distribution Function
P/FR	Problem/Failure Report
PHSF	Payload Hazardous Servicing Facility
PLF	Payload Fairing
POF	Probability of Failure
POR	Probability Of Release
PRA	Probabilistic Risk Assessment
PRD	Pressure Relief Device
QAP	Quality Assurance Program
QAPP	Quality Assurance Program Plan
RAS	Representative Accident Scenario
RGA	Residual Gas Analyzer
ROC	Readout Console

Final Technical Report
Acronym List (Cont'd)

RSA	RTG Safety Assessment
RTD	Resistance Temperature Device
RTG	Radioisotope Thermoelectric Generator
RTGF	Radioisotope Thermoelectric Generator Facility
SEIS	Supplemental Environmental Impact Statement
SEM/EDS	Scanning Electron Microscope/Energy Dispersive Spectroscopy
SER	Safety Evaluation Report
SMB	Steady Misdirected Burn
SNL	Sandia National Laboratory
SOI	Saturn Orbit Insertion
SRESP	SRMU Propellant Fallback Response Model
SRM	Solid Rocket Motor
SRMU	Solid Rocket Motor Upgrade
SRP	Savannah River Plant
SVII	Space Vehicle Intact Impact
SVT	Safety Verification Test
TA	Type Acceptance
TBVD	Total Boost Vehicle Destruct
TGA	Thermogravimetric Analysis
TMP	Turbo-Molecular Pump
TSP	Transportation System Package
USAR	Updated Safety Analysis Report
VCA	Vent Chamber Assembly
VEEGA	Venus-Earth-Earth-Gravity-Assist
VVEJGA	Venus-Venus-Earth-Jupiter-Gravity-Assist

Section 1

Introduction

SECTION 1

INTRODUCTION

This document is the Final Report for the GPHS-RTGs (General Purpose Heat Source-Radioisotope Thermoelectric Generators) in support of the Cassini RTG Program. This program spans the period 11 January 1991 to 31 December 1998. As noted in the following historical summary, this program encountered a number of changes in direction, schedule, and scope over that period. The report provides a comprehensive summary of all the varied aspects of the program over its seven and a quarter years, and highlights those aspects that provide information beneficial to future radioisotope programs.

In addition to summarizing the scope of the Cassini GPHS-RTG Program provided as background, this introduction includes a discussion of the scope of the final report and offers reference sources for information on those topics not covered.

Much of the design heritage of the GPHS-RTG comes from the Multi-Hundred Watt (MHW) RTGs used on the Lincoln Experimental Satellites (LES) 8/9 and Voyager spacecraft. The design utilized for the Cassini program was developed, in large part, under the GPHS-RTG program which produced the Galileo and Ulysses RTGs. Reports from those programs included detailed documentation of the design, development, and testing of converter components and full converters that were identical to, or similar to, components used in the Cassini program. Where such information is available in previous reports, it is not repeated here.

1.1 SCOPE OF CASSINI GPHS-RTG PROGRAM

The Cassini GPHS-RTG program was initiated by the General Electric Company (GE) in 1991 under Department of Energy (DOE) contract DE-AC03-91SF18852, entitled "General Purpose Heat Source Radioisotope Thermoelectric Generator (GPHS-RTG) for the CRAF/Cassini RTG Program". As a result of business transactions during the period of this contract, in 1993 GE Aerospace became Martin Marietta Aerospace, and in 1995 Martin Marietta became part of Lockheed Martin. GE/Martin Marietta documents and equipment were transferred to Lockheed Martin.

The program was sponsored by the DOE Office of Special Applications and administered by the Oakland Operations Office. Initially, this was a 74 month program consisting of the following scope:

1. Serve as System Integrator working with NASA and DOE to establish system specifications and interface definitions for the CRAF (Comet Rendezvous-Asteroid Flyby) and Cassini (the Saturn Orbiter/Titan Probe) missions and to update the GPHS-RTG design to meet mission requirements.

2. Establish and qualify manufacturing, testing, and inspection facilities for unicouples and ETGs (Electrically Heated Thermoelectric Generators).

3. Manufacture, assemble, test, and deliver three ETGs.

4. Provide technical support for the fueling of RTGs and launch/field support for launch-site activities.

5. Conduct an appropriate RTG safety program and prepare safety assessments.

6. Fabricate, but not assemble, a fourth ETG.

7. Provide an option to assemble and to support fueling of a fourth RTG.

The schedule for accomplishing this scope was based on providing two RTGs for each mission and a common spare (one unfueled ETG and one fueled RTG remained from the Galileo/Ulysses program) for launch in August 1995 (CRAF) and April 1996 (Cassini). The program was to end in October 1996, five months after the Cassini launch. It was stipulated that the RTGs for these missions would be fabricated with few, if any, changes from existing converter and heat source designs.

In 1992 NASA canceled the CRAF mission and delayed the launch of Cassini. The GPHS-RTG program was subsequently redirected to provide two (2) new ETGs for conversion to RTGs and to fabricate but not to assemble a third ETG. The latter was to be assembled in part and packaged for long term storage. The tasks which resulted from the redirected program were:

Task 1   Spacecraft Integration and Liaison
Establish the two top level specifications for the missions: a) GPHS-RTG Systems Specification and b) Environmental Criteria and Test Requirements Specification for the

GPHS-RTG. This was to be done via liaison with the user (NASA/JPL) and the DOE Office of Special Applications (OSA).

Task 2 Engineering Support

Establish engineering documentation for the Cassini GPHS-ETGs, GPHS-RTGs, and ground support equipment. Convert all GPHS-RTG project engineering documentation (i.e. engineering drawings, specifications, procedures, etc.) to the current contractor engineering documentation system. Incorporate design changes required to accommodate unique Cassini mission/spacecraft requirements with approval of DOE OSA.

Establish acceptance criteria for the following Electrically-Heated Thermoelectric Generator (ETG) and RTG units which will be transferred from the Galileo/Ulysses Project to the Cassini RTG project: a) the spare F-5 GPHS-RTG, and b) the spare E-2 ETG and associated components.

Perform structural, thermal, and thermoelectric design analyses of the GPHS-RTG in order to support definitive design bases in such areas as system response to launch dynamic loads, heat source support and preload, thermal interface definition, radiation properties, and cooling requirements during and prior to launch. Develop power predictions for specified mission profiles.

Provide technical review and oversight of ETG/RTG handling, fueling, acceptance testing, qualification of the ETG to RTG conversion process, and hardware acceptance and operations at the Government Fueling Agency facility as defined in the Contractor/Fueling Agency Interface Working Agreement. The contractor shall also interface with various Government Heat Source Production facilities as defined in the Encapsulated Fuel Form Interface Working Agreement.

Task 3 Safety

Prepare safety assessments of the GPHS-RTGs based upon use on the Mariner Mark II spacecraft with Titan IV/Centaur launch vehicles. Prepare a Safety Test Plan, provide engineering and/or quality oversight for safety tests conducted at Government laboratories, perform response analysis, prepare the Safety Analysis Reports, and participate in the

Interagency Nuclear Safety Review Panel (INSRP) reviews with DOE and NASA to obtain launch approvals.

Task 4 Qualified Unicouple Production

Re-establish a unicouple manufacturing facility which meets existing Government furnished specifications and procedures for manufacture of thermoelectric materials and fabrication of unicouple devices. Provide for the training and qualifying of operators, supervisors and inspectors. Qualify the production facility and procedures by the manufacture of qualification lots of unicouples and by the fabrication and test of three qualification 18 couple module assemblies. Two 18 couple module assemblies are to be tested at accelerated life test conditions and one at normal operating conditions.

Task 5 ETG Fabrication, Assembly, and Test

Manufacture, assemble, acceptance test and deliver to the Government Fueling Agency two (2) ETGs and deliver to DOE parts and sub-assemblies for a third ETG. Adhere to national, state, and local safety, health, and environmental laws in the manufacture of ETGs. Maintain in place, to the end of the contract, the manufacturing line for unicouple fabrication after all unicouples are completed.

Task 6 Ground Support Equipment (GSE)

Determine and implement the necessary work required to refurbish and/or upgrade existing Government Furnished Equipment (GFE).

Task 7 RTG Shipping and Launch Support

Participate in the design and development effort of another contractor fabricating a new RTG transportation system. Provide launch site support for the receiving, shipping, storage, maintenance, and flight preparation of RTGs, including spacecraft integration, support activities, and testing of the RTGs.

Task 8 Designs, Reviews, Mission Applications

Participate in RTG application and improvement studies for the Department of Energy as authorized by DOE OSA.

Task 9 Program Management, Quality Assurance and Reliability

Establish and implement project management/control, quality assurance, environmental, and reliability activities required for the contract with the focus on providing three RTGs for the Cassini mission to be launched in October 1997. The program period of performance was extended to April 1998. Task 5 was further modified to maintain the unicouple fabrication facility by providing periodic maintenance. Because a new launch vehicle (Titan IV-B) was to be used to launch the Cassini spacecraft, together with two Venus swingbys followed by an Earth swingby, the safety program was considerably expanded to include effects of an inadvertent Earth reentry during the swingby at velocities much greater than previously analyzed.

1.2 SCOPE OF FINAL REPORT

This report focuses on the GPHS-RTG, as provided for use on the Cassini mission. The report is organized to begin with the requirements summary, excerpted from the appropriate system and product specifications. This is followed by a description of the flight RTGs, the ETGs insofar as they differ from the RTGs, and the principal refurbishments incorporated into the GSE. The principal difference between the Cassini RTGs and the previous RTGs, namely the PRD (Pressure Relief Device) is discussed. A discussion of the work which went into the re-establishment of the unicouple production, together with improvements in the processes and their requalification, are also presented. The database of thermoelectric performance provided by 18 couple module and other unicouple testing is introduced as part of the supporting data discussion. This approach addresses the principal activities defined in the statement of work.

The RTG performance is addressed as a separate topic. This section of the report provides summaries of the results of the electrical performance tests, power projections and comparisons with flight data. The latter is limited to the time from launch to 1 April 1998. This section also includes a summary of the qualification program and RTG flight performance data from the Galileo and Ulysses missions. Other topics of special interest, advanced thermoelectric material developments, multicouple tests, a solid rivet attachment study, a small RTG study, and residual hardware are treated separately.

1.3 REFERENCE DOCUMENTATION

All drawings and specifications referenced in this report are Lockheed Martin documents unless otherwise specified. Much of the documentation for the GPHS-RTG activities for the Cassini mission is contained in previously released reports. It is beyond the scope of this report to duplicate that information. The following is a listing of significant documents, along with a discussion of the information they provide.

Design Review Report for Updated GPHS-RTG

CDRL A.2, dated 31 March 1992, presents the design changes, rationale, and approach for the Cassini set of modifications e.g., the Pressure Relief Device which was modified in order to accommodate launch on the Titan IV-B to be barometrically operated similar to the design used on the MHW RTG.

GPHS-RTG Interface Working Agreement for the Cassini RTG Program

GESP-7231, dated 8 February 1996, depicts the responsibilities of Lockheed Martin, Mound EG&G, and DOE relative to heat source assembly and the RTG.

Product Specification for the General Purpose Heat Source for Cassini

Specification PS23009146, dated 14 June 1995, updates the specification for the GPHS previously developed under the Ulysses and Galileo programs to reflect the Cassini changes. The changes include an increase in the fuel load and modification of the fuel capsule weld shield.

Product Specification for the GPHS-ETG for Cassini

ETG specification PS23009147, dated 2 May 1995, updates the specification to the Cassini requirements. These changes were the result of changes in requirements due to launch vehicle environments, etc.

Product Specification for the GPHS-RTG for Cassini

Specification PS23009148, dated 31 January 1996, incorporates and updates the RTG product specification to the requirements for the Cassini mission. These changes were the result of changes in requirements due to launch vehicle environments, etc.

System Specification for the GPHS-RTG for Cassini

Specification SS23009149, dated 5 March 1996, incorporates changes and updates the system requirements, consistent with the Cassini mission. These changes were the result of changes in requirements due to launch vehicle environments, etc.

Environmental Criteria and Test Requirements for the GPHS-RTG

Specification PS2300150, dated 6 March 1996, incorporates and updates the environmental criteria to which the Cassini RTG could be subjected and updates the acceptance test requirements.

Final Reliability Assessment Report for the Cassini Mission

GESP-7252, dated 14 March 1997, provides a summary assessment of the reliability of the GPHS-RTG in meeting the end of mission power requirements for the Cassini mission.

RTG Design Qualification Report

GESP-7242, dated 11 August 1995, summarizes the results of analyses, inspections, and tests performed to demonstrate that the General Purpose Heat Source - Radioisotope Thermoelectric Generator (GPHS-RTG) is qualified for the Cassini mission in accordance with the requirements of specification PS23009148.

RTG Safety Assessment Report

This report, dated 5/7/93, gives an early assessment of the safety of the RTG design relative to its performing its mission.

Final Safety Analysis Report (Including Addendum)

CDRL C.3, dated November 1996 through May 1997. This is the final in a series of reports which analyze RTG safety relative to fuel release throughout all phases of flight. Launch environments for the Titan IV-B are used in assessing the impact of a series of launch accident scenarios, reentry of the GPHS due to failure to attain the proper trajectory, and the effect of an inadvertent reentry during the Earth swingby.

Monthly Technical Progress Reports

Monthly reports were issued for the duration of the program. These reports provide technical detail on activities occurring during the reporting period as they occurred.

Plans, procedures, and topical/engineering reports were issued during the program's period of performance (some in the GESP series) and are specifically applicable to the GPHS-RTG for the Cassini program. These are listed in the appropriate sections.

Section 2

Requirements

SECTION 2
REQUIREMENTS

Requirements for the GPHS and GPHS-RTG are defined in the following Lockheed Martin specifications:

PS23009146B   Product Specification, General Purpose Heat Source for Cassini

PS23009148E   Product Specification, GPHS-RTG for Cassini

In addition, the physical interface requirements for the GPHS-RTGs with the Cassini spacecraft are defined in the following JPL (Jet Propulsion Laboratory) drawing:

10135938B   Radioisotope Thermoelectric Generator Interface Control Drawing

Following in this section is a discussion of the GPHS and GPHS-RTG requirements and physical characteristics excerpted from the above documents. The specification paragraph numbers do not coincide with the paragraph numbers of this report. The specification paragraph number is listed herein in parentheses following the paragraph title.

2.1   GPHS REQUIREMENTS

The following requirements for the GPHS are excerpted from PS23009146B, "Product Specification, General Purpose Heat Source for Cassini." The specification should be referenced for a full description of detailed requirements. Further, in some instances, individual requirements have remained unchanged from those of the previous program documented in report GESP-7209. Both the specification and report are useful supplements to the information contained herein. As noted above, numbers in parenthesis following paragraph titles are specification section numbers.

2.1.1   Operating Life (3.2.1.1)

The required period of operation for the GPHS Assembly (GPHSA) shall be 18 years, including two years storage and test in the RTG and 16 years mission operation.

2.1.2 Storage Life (3.2.1.2)

The GPHSA shall perform satisfactorily after two years storage and test in the RTG. Storage and test time are defined as commencing with installation of the heat source assembly into the converter and ending at Beginning of Mission (BOM). Storage of fuel pellets or fueled modules in their respective storage containers shall be consistent with satisfying the requirements for the GPHSA as specified herein.

2.1.3 Fuel (3.2.1.3)

The fuel form shall be plutonium dioxide. The ^{238}Pu content of the total plutonium isotopes (including ^{236}Pu, ^{238}Pu, ^{239}Pu, ^{240}Pu, ^{241}Pu, and ^{242}Pu) in the fuel powder shall not be less than 82.0 percent, as of the date of precipitation. The ^{236}Pu present in the fuel powder shall not exceed 2 micrograms/gram of the total plutonium content, as of the date of precipitation. Detailed requirements for fuel feed powder shall be as defined in LANL Specification 26Y-318180.

2.1.4 Thermal Power (3.2.1.4)

2.1.4.1 Fuel Pellet

No thermal inventory requirements are specified for the fuel pellet. However, in order to meet the thermal output requirement of the fueled clad, each fuel pellet shall be pressed to contain 151.0 +.7/-.5g of fuel. Detailed requirements for the fuel pellet shall be as defined in LANL specification 26Y-318181.

2.1.4.2 Fueled Clad

The thermal output of a fueled clad shall be 62.5 + 2.0/-1.5 watts thermal. Detailed requirements for the fueled clad shall be in accordance with LANL specification 26Y-318182.

2.1.4.3 Module

As of Cassini BOM (October 1997), the variation of thermal output from GIS to GIS within a module shall be less than 10%. Also when referenced to BOM, the total thermal output of each module shall be 236 to 240 watts, however, module thermal outputs which are less

than or greater than these values are acceptable, provided the thermal output requirements of the GPHSA are satisfied.

2.1.4.4 Heat Source Assembly (18 Modules)

- The difference between the total thermal output of adjacent groups of three stacked modules shall not be more than 20 thermal watts.

- The difference between the total thermal output of the two nine packs of modules within the RTG shall not be more than 20 thermal watts.

- The total heat source thermal output per RTG at BOM shall be a minimum of 4258 watts. This requirement shall be met after accounting for all measurement uncertainties, e.g., calorimetry uncertainty.

  Note: The F-5 RTG is calculated to have a heat source thermal output of 4029 watts at BOM. This information is provided for reference only.

2.1.5 Mission Temperature

The GPHSA shall be capable of operating in the converter in a space vacuum of 1×10^{-10} torr for a period of 16 years at an exterior surface temperature of 1100°C or less.

2.1.6 Neutron Emission Rate (3.2.1.8)

The specific neutron emission rate from the unshielded GPHSA shall not exceed 7.0×10^3 neutron/second/gram of plutonium-238, exclusive of any neutron multiplication obtained from the configuration of the fueled clads in the assembled heat source or attenuation within the RTG.

2.1.7 Weight (3.2.2.2)

The unit weight of a fueled module, exclusive of lock members, shall not exceed 3.20 lbs. The weight of the GPHSA, including lock members but excluding the midspan support plate, shall not exceed 57.70 lbs.

2.1.8 Coatings (3.3.1.6)

Thermal control and material protective coatings, if required, shall be stable for a period of 10.75 years at mission operating conditions and two years storage environment.

2.1.9 Cleanliness (3.3.7.1)

All fabrication and assembly operations shall be done in a manner that will prevent the inclusion of foreign substances that would degrade the performance of individual components or assemblies. As a minimum, all parts shall be visually clean. Additional requirements with respect to cleanliness level and/or procedures shall be defined on the individual drawings and specifications. Just prior to installation in the converter, each module shall be cleaned by vacuuming on each of its six external faces. The cleaning process shall be repeated and the module visually inspected for damage due to the vacuum process. The module shall then be vacuum cleaned a third time with a tool containing an in-line filter. The filter shall be inspected for conductive particles using a 16X stereoscope. Acceptable criteria for graphite felt particles are:

Allowable Quality	Linear Dimension
None	>30 mils
1	10 to 30 mils
5	5 to 10 mils
no criteria	<5 mils

- No metal particles greater than 5 mils are acceptable.

- Any metal particles detected within 0.235 inches of the outer edge of the circular filter paper may be artifacts of the filter installation and are not applicable to acceptance or rejection of the part.

- There are no criteria for material protruding from the Fine Weave Pierced Fabric (FWPF), i.e., pieces of z rods.

2.2 RTG REQUIREMENTS

The following RTG requirements are excerpted from PS23009148E, "Product Specification, GPHS-RTG for Cassini." The specification should be referenced for a full description of detailed requirements. Further, in some instances, individual requirements have remained unchanged from those of the previous program documented in report GESP-7209. Both the specification and report are useful supplements to the information contained herein. As noted earlier, numbers in parentheses following paragraph titles are section numbers in Cassini specification PS23009148E.

2.2.1 Operating Life (3.2.1.1)

The required period of operation for the RTG shall be 18 years, including two years in test and storage, and 16 years mission operation. For the F-5 RTG only, the required period of operation shall be 28 years, including twelve years in test and storage, and 16 years mission operation.

2.2.2 Storage Life (3.2.1.2)

RTGs, except the F-5 unit, shall be capable of satisfactory performance after a maximum storage period of two years. F-5 shall be capable of satisfactory performance after a maximum storage period of twelve years. RTGs shall be pressurized with inert gas during storage, maintained in a short-circuited condition, and stored in a facility that maintains an inert, temperature-controlled environment.

2.2.3 Electrical Requirements (3.2.1.3)

2.2.3.1 Voltage (3.2.1.3.1)

The RTG shall supply power as specified below when operated at 30 +0.7/-0.5 volts DC, as measured at the output power connector.

2.2.3.2 Acceptance Power (3.2.1.3.2)

The RTG shall produce no less than the indicated electrical power under the conditions listed in Table 2-1, as determined at the output power connector. Power shall be normalized for a fuel loading of 4410 watts for F-2, F-6 and F-7 and to 4100 watts for F-5, based on the actual GPHS thermal output at the time of acceptance testing.

2.2.3.3 Launch Power (3.2.1.3.3)

The RTG electrical power, with a xenon cover gas, in October 1997 and within 30 days of the xenon gas exchange, shall be a minimum of 172 watts for F-2, 155 watts for F-5, and 174 watts for F-6 and F-7.

Table 2-1. RTG Acceptance Power Requirements

Test Conditions	
Voltage	30 vDC
Chamber Pressure .	$<1 \times 10^{-5}$ Torr
Chamber Equivalent Sink Temperature	+32°C
RTG Internal Pressure	Vented to Chamber
Acceptance Power	
F-2 (Fuel loading 4410 watts)	291W
F-5 (Fuel loading 4100 watts)	255 W
F-6, F-7 (Fuel loading 4410 watts)	293 W

2.2.3.4 Mission Power (3.2.1.3.4)

The RTG steady state electrical power during October 1997, when operating in space vacuum and after complete venting of the cover gas, constitutes BOM power. Mission power shall be no less than the following when based on the heat source thermal power listed in Section 2.2.3.13 of this report.

	BOM (October 1997)	Sixteen Years Later (October 2013)
F-2	274 W	198 W
F-5	249 W	182 W
F-6, F-7	276 W	199 W

2.2.3.5 Circuit Condition (3.2.1.3.5)

The RTG shall be capable of operating open-circuited with cover gas for a period of 12 hours during testing operations plus 2 hours at the launch site with no permanent damage or degradation. When the RTG is evacuated it shall not be open-circuited for more than 3 minutes. Short circuit shall be possible without time restriction.

2.2.3.6 Dynamic Capability (3.2.1.4)

The RTG shall be designed to withstand the effects of vibration, acoustic noise, acceleration, and shock environments that it will experience during ground testing, transportation, launch, and subsequent mission maneuvers. These environments are defined in the Environmental Criteria and Test Requirements, GPHS-RTG for Cassini: specification 23009150.

2.2.3.7 Thermal Requirements (3.2.1.5)

2.2.3.7.1 RTG Case Temperature

The RTG case temperature shall be no greater than 260°C as measured by the average of the RTG case resistance temperature devices (RTDs) under normal conditions of ground test and pre-launch activities. The inboard mounting flange and electrical connectors shall not exceed 240°C.

However, some transient temperature excursions are permitted above 260°C for assembly/test operations. The total excursions shall not exceed: (1) 350 hours to a maximum temperature of 265°C, (2) 92 hours to a maximum temperature of 270°C, (3) 11 hours to a maximum temperature of 280°C, and (4) 80 minutes to a maximum temperature of 295°C.

During launch and space operations, temperatures on the RTGs shall not exceed the following allowable temperature excursions, which were also defined for the Galileo mission: (1) 146 days to a maximum temperature of 280°C, and (2) 41 days to a maximum temperature of 290°C. Temperature excursions for the Cassini mission will be enveloped by these temperature excursions.

2.2.3.7.2 External Cooling Connections

An Active Cooling System (ACS) shall be provided on the RTG to meet the requirements listed in Table 2-2. The ACS shall meet the proof pressure, pressure drop, and leak requirements defined per drawing 47J306130, even though the ACS will not be utilized on the Cassini mission.

2.2.3.8 Magnetics (3.2.1.6)

With the RTG operating at rated current, the total dipolar magnetic field vector shall not exceed 78 nT at 1 m from the geometric center of the RTG, with or without compensating magnets. Compensating magnets, if required to meet this requirement, shall be provided and installed by JPL.

The RTG shall be equipped with holders for compensating magnets to be used on the external portion of the RTG, identical to those used for the Ulysses mission as defined by drawing 47D306809.

Table 2-2. RTG Cooling Requirements*

Coolant	Water/28 ± 2% ethyl alcohol	
Flow Rate	450 ± 22 lb./hr	
Maximum coolant pressure	90 psia in shuttle loop	
	250 psia during GSE start-up	
Allowable pressure drop	12 psig	
Coolant inlet temperature (°F)	Minimum	Maximum
Pre-launch	35	100
Ascent (First 2-5 minutes)	35	85
Ascent (On orbit, doors closed)	70	120
On orbit, doors open	35	110
Orbit entry	35	85
Active cooling heat transfer	Greater than or equal to 3500 watts	
(In vacuum with average radiant sink temperature of 25°C and coolant inlet temperature of 30°C)		

* These requirements apply to each individual RTG.

2.2.3.9 Instrumentation (3.2.1.7)

The RTG shall be equipped with four (4) resistance temperature measurement devices (RTDs). The RTDs shall be capable of measuring over the temperature range of -9 to +300°C. The capacitance between RTD and RTG case shall be less than 400 picofarads. The detailed requirements for the RTDs are defined in specification NS0010-13-20.

2.2.3.10 Multiple Heat Source Criticality (3.2.1.8)

For the Cassini mission, the total number of isotope heat sources, either in their as-designed and assembled shape and configuration, or in possible configurations resulting from credible accidents, aborts, and post abort environments, shall not be capable of a self-sustaining fission reaction in any arrangement and/or combination with reflecting materials, as verified by analysis.

2.2.3.11 Pressurization (3.2.1.9)

The RTG shall be capable of withstanding an internal nominal gas pressure, argon or xenon, of 25 psia (maximum of 30 psia), with an external vacuum at an outer case temperature not to exceed 260°C. The gas pressure decay rate shall be such that a minimum positive pressure of 0.5 psi exists in the RTG relative to room ambient pressure (14.7 psia) after a period of 30 days from initial pressurization of 25 ± 0.5 psia.

2.2.3.12   Venting of Cover Gas (3.2.1.10)

The PRD shall be designed integral with the RTG to enable venting of the RTG and it shall be activated by a decrease in the barometric pressure during launch. The design shall also incorporate provisions for ensuring that the PRD will not prematurely activate during ground handling and pre-launch operations. Adequate assurance shall be demonstrated through test and/or analysis to show that RTG venting (caused by the malfunctioning of any of the elements on the RTG/PRD side of the interface with the spacecraft) will not take place during launch prior to the PRD being exposed to a pressure within the payload fairing of less than or equal to 13.0 psia. Detail requirements of the PRD are defined in specification PS23003753.

2.2.3.13   General Purpose Heat Source (3.2.1.11)

The RTG shall be fueled with 18 General Purpose Heat Source modules containing Pu^{238} oxide as the thermal power source. Thermal inventory of the GPHS, extrapolated to BOM, shall be as a minimum, as follows:

F-2	4258 watts
F-5	4029 watts
F-6, F-7	4258 watts

2.2.3.14   Insulation Resistance (3.2.1.12)

The insulation resistance, as measured between the thermoelectric circuit and the outer case multifoil insulation, shall be equal to or greater than 1000 ohms under all conditions.

2.2.3.15   Electrostatic Cleanliness Requirements (3.2.1.13)

General

The potential difference between any point on the outer surface of the RTG and ground structure shall not exceed 10 volts when subjected to an electron irradiation charging current of 5×10^{-10} A/cm^2. Verification of compliance with this requirement can be accomplished either by test and/or by using the requirements as specified below.

RTG Surface Materials

The exterior (exposed to space) RTG surfaces shall be electrically connected and shall be capable of being grounded to the spacecraft structure through the case ground. The resistance to ground of RTG surface materials for both conductive and partially conductive materials is given as follows:

Conductive Material Ground Resistance

Conductive (metallic) surfaces will be grounded through a resistance, r, as follows.

$$r < 2 \times 10^{10}/A \ \text{ohm}$$

where A = exposed surface area of the material (cm^2)

This requirement will be used for each connector outer shell to the RTG case, and any other metallic protuberance on the RTG.

Partially Conductive Material Ground Resistance

Partially conductive materials which are in contact with a grounded substrate shall satisfy the following relation. This can be used for the anodized PRD attachment bolt heads.

$$\rho t \leq 2 \times 10^{10} \ \text{ohm-cm}^2$$

where ρ = anodized material resistivity (ohm-cm)
                      t = thickness of anodized coating (cm)

2.2.3.16 Internal Charging

All metallic elements greater than 3 cm^2 in surface area or longer than 25 cm shall have a conductive path to ground with a resistance of $< 10^8$ ohms when measured in air and $< 10^{12}$ ohms when measured in a vacuum. This requirement does not apply to elements of the RTG electrical power circuit, for which isolation requirements are defined separately. No further testing is required to demonstrate compliance with this requirement, since verification has been adequately demonstrated for previous models of the RTG.

2.2.3.17 Electrostatic Discharge Susceptibility

The ETG shall not be damaged by a 3 mJ arc discharge (13 KV from a 35 pF capacitor or equivalent) at a distance of 25 cm (10 in.) from the RTG exterior surface. This requirement includes all associated instrumentation.

2.2.3.18 Miscellaneous

- Teflon on an exterior surface is not permitted.

- Non-conductive surfaces which can be shown to store not more than 3 mJ of electric charge are permitted.

- Conductive external surfaces < 0.5 cm^2 need not be grounded.

- Dielectric parts of disconnected electrical connectors exposed to space shall be covered with a grounded metallic surface. This requirement is not applicable since both RTG connectors will have mating connectors attached.

- The temperature instrumentation leads shall be covered with a conductive wrap or shield. The wrap shall be grounded to the case.

- Coatings used on the RTG must not outgas in excess of limits specified in NASA SP-R-0022A while in the operating environments in space.

- A molydisulfide nickel fused coating is acceptable for use on the inside of the PRD housing.

2.2.3.19 Physical Characteristics (3.2.2)

2.2.3.19.1 Envelope (3.2.2.1)

The overall dimensions of the RTG shall be capable of meeting the envelope requirements as defined in JPL ICD 10135938.

2.2.3.19.2 Mass (3.2.2.2)

The flight mass of each RTG, excluding gas fill, shall not exceed 56.7 kg (125.0 lb.). All delivered units shall be within 1.0% of one another. The mass measurement error shall be less than or equal to 0.1 kg.

2.2.3.19.3 Center of Mass (3.2.2.3)

The RTG shall be designed to have its center of mass on the longitudinal axis of the RTG and as near its midpoint as practical. The center of mass of all the units shall be within a

right circular cylinder, 0.64 cm. in diameter by 1.27 cm long with its axis along the longitudinal axis of the RTG. The actual location of the center of mass of each RTG shall be known to lie within a 1.5 mm diameter sphere. The center of mass location shall not change more than ±0.0025 cm over any 4 week period of transverse accelerations (normal to the RTG longitudinal axis) of 0.01g due to spacecraft precision maneuvers while the spacecraft is spinning at 5 RPM. Such a requirement may be met by demonstrating analytically that the cg shift, under cruise conditions, is within these limits.

2.2.3.19.4 Moments and Products of Inertia (3.2.2.4)

The moments and products of inertia of the RTG about its three orthogonal axes shall be calculated. The calculated moments of inertia of each RTG shall be determined to an accuracy of 0.05 kg-m^2. The calculated products of inertia of each RTG shall be known to an accuracy of 0.012 kg-m^2 in the spacecraft X-Z and Y-Z planes.

2.2.3.19.5 Mounting and Lifting Provisions (3.2.2.5)

The RTG mechanical design shall incorporate features for mounting to the spacecraft as shown in the JPL ICD 10135938. The design for the Cassini spacecraft shall incorporate a single mounting location on the RTG with four mounting points. Attachment bolt and alignment pin holes in the interface flanges shall be drilled from a template as defined by drawing 47D305773. Lifting features shall be incorporated to allow lifting of the RTG by ground handling equipment as identified on the JPL ICD 10135938.

2.2.3.20   Connections (3.2.2.6)

2.2.3.20.1 Pressurization and Venting

The RTG shall be equipped with two separate vent systems: one to permit pressurization and venting of the RTG during ground testing and the other to permit venting of the RTG automatically after launch.

The gas management valve, as shown in drawing 47D305293, shall be used for ground testing. This vent system shall include a manual valve that shall be used to control flow during venting and pressurization, and shall be designed to indicate clearly the open position. The RTG shall be vented after launch by a Pressure Relief Device (PRD) per drawing 23003764.

2.2.3.20.2 Electrical Power Connectors

The electrical output of each RTG shall be delivered at the electrical power connector. The power connector shall be a five (5) pin, hermetically sealed connector as defined by drawing 47C305095. Both positive and negative power pins in the connector shall be redundant and shall be separated by a distance adequate to prevent shorting of the RTG power output. One pin shall be used for case ground.

2.2.3.20.3 Instrumentation Connector

The outputs from the RTD temperature transducers shall be terminated in a separate instrumentation connector as defined by drawing 23008081. The physical location of this connector shall be in close proximity to the power connector.

2.2.3.20.4 Thermoelectric Couple Interconnectors

The thermoelectric couples shall be in a series-parallel, cross-strapped configuration to provide high reliability as shown on drawing 47J305306.

2.2.3.20.5 Electrical Isolation

The thermoelectric power circuit shall be electrically isolated from the RTG housing and from the temperature instrumentation circuits. At time of acceptance, the dc resistance measured from the electrical power circuit to RTG case with the generator operating at nominal operating voltage and temperature, shall be no less than 1000 ohms. The dc resistance between the RTD instrumentation circuit and the case shall be at least 1 megohm at 10 volts, measured at room temperature and at 300°C.

2.2.3.20.6 Case Ground

The RTG outer case shall incorporate a ground conductor to carry the case ground to the spacecraft structure through a separate pin in the power connector. This shall be in addition to structural grounds provided by the case. Resistance between the connector grounding pin and RTG outer case shall be less than 20 milliohms.

2.2.3.20.7 External Cooling Connections

Location of the input and output connections for the ACS shall be as shown on JPL ICD 10135938. These provisions were not utilized on the Cassini mission.

2.2.3.20.8 Electrical Cabling (3.2.2.7)

Each RTG shall be provided with two separate GSE electrical cables, one for power and one for instrumentation, for use during ground operations. Power connectors and receptacles on these cables shall comply with National Fire Code, Electrical, Vol. 5, AIA File No. 40-E-7.

2.3 PHYSICAL REQUIREMENTS

The physical requirements for the Cassini RTGs are primarily defined in JPL ICD 10135938B. (Other physical requirements are included in the RTG Product Specification PS23009148E, previously discussed in Section 2.2.) The following physical requirements are excerpted from the ICD.

2.3.1 Static Envelope Dimensions

Each Cassini RTG must be enveloped by a right cylinder 18.00 inches in diameter and no more than 45.50 inches long axially.

2.3.2 Mounting

The inboard flange must have provision for four holes equally spaced on a 9.520 + 0.020/-0.005 inch mounting circle as shown in the ICD (drilled per Lockheed Martin drawing 47D305773).

2.3.3 Electrical Power Connector

The electrical power receptacle shall mate with connector MS3106A18-11S.

2.3.4 Instrumentation Connector

The RTG instrumentation receptacle shall mate with connector MS3106A18-1S.

2.3.5 Handling Attachment Points

Ground handling attachment points shall be as specified in ICD 10135938B.

2.3.6 PRD Safety Pin

The PRD safety pin shall be removed before flight.

2.4 VERIFICATION OF REQUIREMENTS

Verification that the RTG design meets requirements is documented in "RTG Design Qualification Report," GESP-7242. The General Purpose Heat Source was previously qualified on the Galileo/Ulysses programs with documentation provided in GESP-7191.

Section 3

Cassini RTG Design Description

SECTION 3

CASSINI RTG DESIGN DESCRIPTION

3.1 FLIGHT UNIT DESCRIPTION

This section provides a general description of the GPHS-RTG. A more detailed design description of each of the RTG subassemblies is provided in Section 4.

The GPHS-RTG, shown in Figure 3.1-1, consists of three basic parts: the heat source, the thermopile, and the converter shell. The heat source produces a nominal 4400 watts of thermal energy by the radioactive decay of its Pu^{238} isotope fuel. The thermopile converts some of the thermal energy of the heat source into a nominal 300 watts of direct current electrical power by means of the thermoelectric process. The outer shell provides containment and structural support for the heat source and thermopile, rejecting surplus heat by means of its radiating fins.
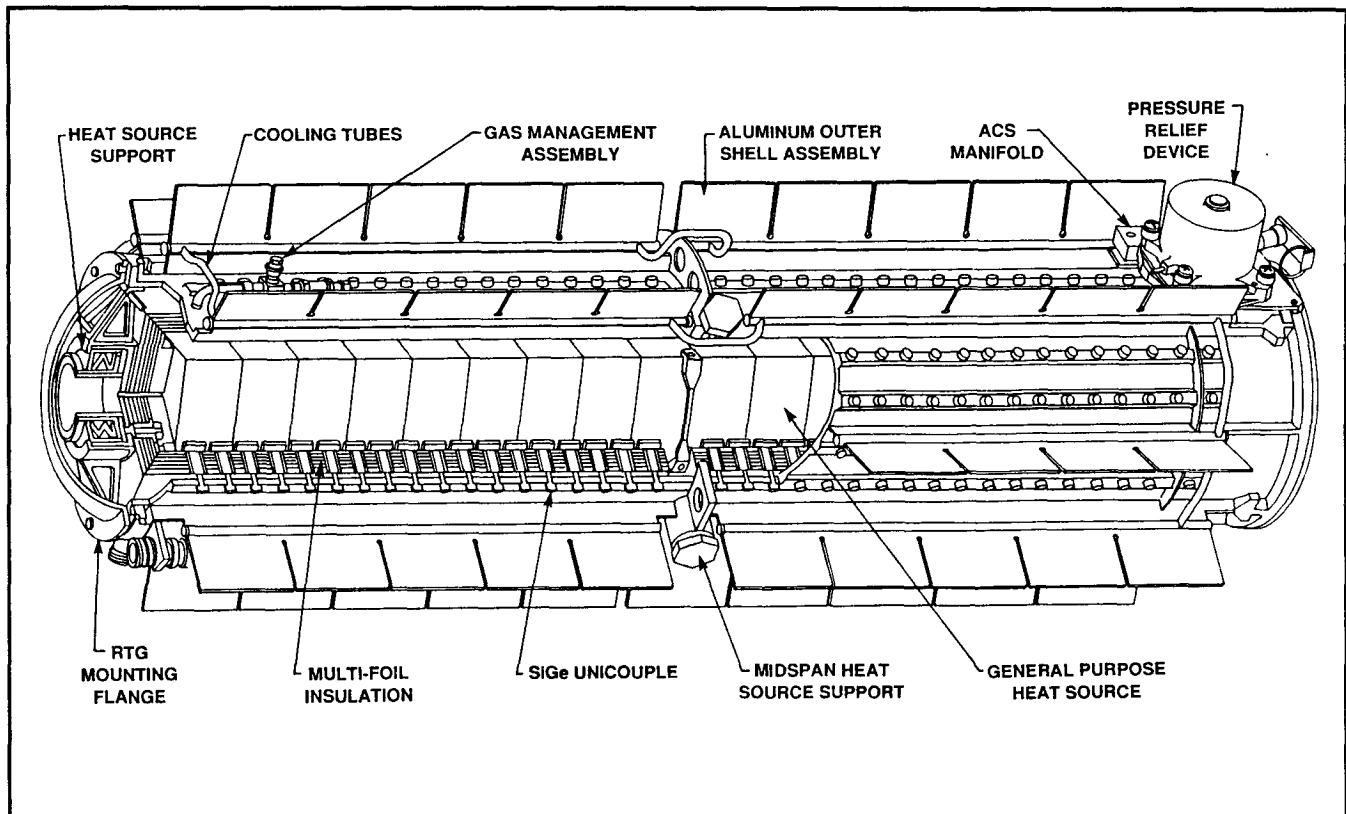
Figure 3.1-1. General Purpose Heat Source - Radioisotope Thermoelectric Generator (GPHS-RTG)

3.1.1 General Purpose Heat Source

The General Purpose Heat Source (GPHS) is comprised of 18 modules, in two stacks of 9 modules each separated by a midspan plate. A cut-away view of a single GPHS module is shown in Figure 3.1.1-1. The modules are composed of five main elements: the fuel, the fuel cladding, the graphite impact shell, the carbon insulation, and the aeroshell. Each module contains four plutonium dioxide (PuO_2) fuel pellets, with a thermal inventory of
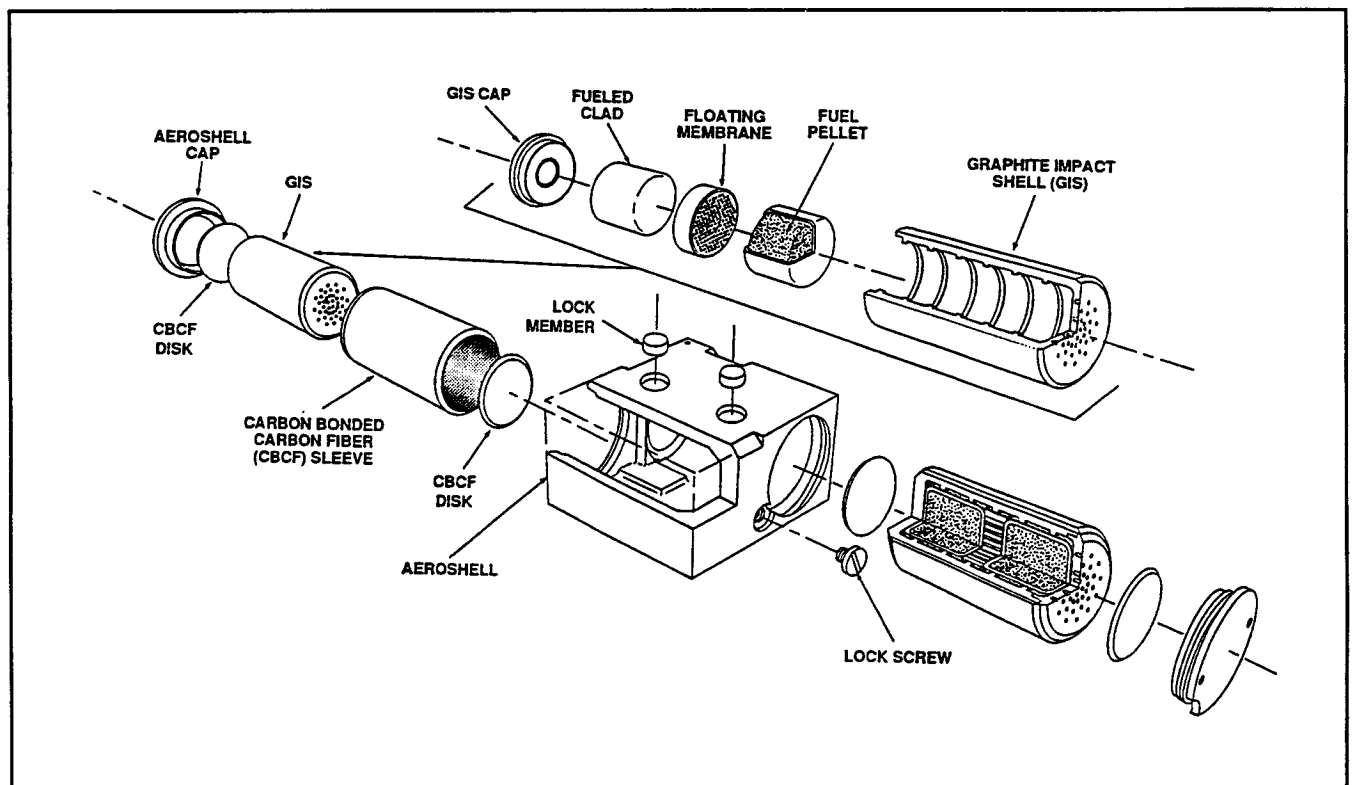
Figure 3.1.1-1. General Purpose Heat Source Module

approximately 62.5 watts per pellet. Each pellet is encapsulated within a vented iridium cladding, which functions as the primary fuel containment. The encapsulated pellet is called a Fueled Clad (FC). Each GPHS module contains four FCs encapsulated within two cylindrical Fine Weave Pierced Fabric (FWPF) containers, known as Graphite Impact Shells (GISs). Thermal insulators made from Carbon Bonded Carbon Fiber (CBCF) surround each GIS. These insulators are designed to provide acceptable iridium temperatures during normal operation, during possible reentry, and at possible impact. Two GISs with thermal

insulator disks and sleeves are placed in a rectangular FWPF aeroshell to form a GPHS module. The aeroshell is the primary heat source structure that provides reentry protection for the FCs. Eighteen GPHS modules provide the total thermal inventory required for the GPHS-RTG. FWPF lock members are used to facilitate stacking and to resist shear loads due to lateral loading.

3.1.1.1 Radioisotope Fuel

The radioisotope fuel is an isotopic mixture of plutonium in the form of the dioxide, PuO_2. The ^{238}Pu content is 82.2 weight percent of the total plutonium, based on the assay data for the fuel used in the F-2, F-6, and F-7 heat sources (References 3.1.1-1 to 3.1.1.-3). Specific details regarding the fuel feed powder may be found in Reference 3.1.1-4. The physical form of the fuel is a cylindrical, solid ceramic pellet, chamfered at each end. The pellets have a diameter of 2.76 ± 0.02 cm and a length of 2.76 ± 0.04 cm. The average geometric density of the fuel is 9.89 g/cm^3 and the average specific thermal power of the fuel at BOM is 0.404 Wt/g, based on the assay data for the fuel used in the F-2, F-6 and F-7 heat sources (References 3.1.1-1 to 3.1.1.-3). The resultant calculated average power density based on the average density and specific power is 4.0 W/cm^3. The half life of the ^{238}Pu isotope is 87.75 years.

Each pellet contains approximately 151 grams of fuel and provides a thermal inventory of approximately 62.5 watts at the time of FC calorimetry. The 72 pellets within the F-2, F-6 and F-7 GPHSs provide a projected thermal power of 4368, 4413, and 4404 watts, respectively, at launch. A total of 10.9 kg of PuO_2 fuel per RTG (with 82.2 wt % ^{238}Pu) is required to meet mission power requirements. A thermal power reduction of approximately 0.8 percent per year will occur due to alpha decay. Table 3.1.1-1 summarizes the average fuel composition and characteristics of the flight units at BOM as provided in References 3.1.1-1 through 3.1.1-3.

Table 3.1.1-1. Flight GPHS Fuel Composition and Characteristics at BOM*

	F-2 RTG	F-6 RTG	F-7 RTG
^{238}Pu Weight (g)	7,693.695	7,774.060	7,756.398
^{239}Pu Weight (g)	1,426.545	1,447.791	1,441.775
^{240}Pu Weight (g)	199.873	212.380	202.623
^{241}Pu Weight (g)	20.236	20.754	20.540
^{242}Pu Weight (g)	11.836	14.134	12.534
^{236}Pu Weight (g)	1.07×10^{-4}	1.14×10^{-4}	1.13×10^{-4}
Total Pu Weight (g)	9,352.185	9,469.119	9,433.869
Other Actinides (g)	235.073	166.955	184.739
Impurities (g)	14.456	15.538	14.263
Oxygen (g)	1,275.940	1,243.133	1,263.327
Total Fuel (g)	10,877.654	10,894.745	10,896.198
Pu-238/Total Pu (%)	82.266	82.099	82.219
Avg. Pellet Weight (g)	151.078	151.316	151.336
Heat Output (Wt)	4,368.06	4,413.78	4,403.68
Avg. Pellet Heat (Wt)	60.668	61.302	61.162
Avg. Pellet Density (g/cc)	9.832	9.936	9.895
Activity (Curies)	133,934	135,368	135,040

*BOM - Beginning of Mission, Launch date of 15 October 1997

3.1.1.2   Fueled Clad (FC)

Each fuel pellet within a GPHS module is individually encapsulated in a welded iridium alloy (DOP-26) clad which has a minimum wall thickness of 0.055 cm. The clad consists of an iridium alloy shield cup and an iridium alloy vent cup. The DOP-26 alloy is capable of resisting oxidation in a post-impact environment while also being chemically compatible with the fuel and graphitic components during high temperature operation and postulated accident environments.

The fueled clad is designed with an iridium frit vent that permits release of helium gas produced by the decay of the Pu-238 fuel without releasing fuel particulates. The FC also contains a decontamination cover which is welded over the FC vent hole to permit decontamination after encapsulation welding. A weld shield is located inside the FC to

provide thermal protection to the fuel during closure welding and to prevent contamination of the weld by the fuel. The decontamination cover is removed from the FC prior to installing the FCs into the heat source assembly. The iridium FC components are shown in Figures 3.1.1-2 and 3.1.1-3, and the encapsulation requirements are defined in Reference 3.1.1-5.

3.1.1.3   Graphite Impact Shell (GIS)

Two FCs are encased in a Graphite Impact Shell (GIS) made of FWPF, a carbon-carbon composite material. The FCs are separated by a FWPF floating membrane within the GIS. The FCs are oriented such that the frit vents face the floating membrane. The cylindrical GIS is designed to provide impact protection to the FCs; its minimum wall thickness is 0.424 cm (0.167 inches). The GIS design is shown in Figure 3.1.1-4.

3.1.1.4   Aeroshell

Two GISs, each containing two FCs, are located inside each FWPF aeroshell. A Carbon Bonded Carbon Fiber (CBCF) insulator surrounds each GIS within the aeroshell to limit the peak temperature of the FC during inadvertent reentry and to maintain a sufficiently high temperature to ensure its ductility upon subsequent impact. The aeroshell serves as the primary structural member of the GPHS module as it is stacked inside the GPHS-RTG. It is designed to contain the two GISs under a wide range of reentry conditions and provide additional protection against impacts on hard surfaces at terminal velocity. It also provides protection for the FCs against overpressures and fragment impacts during postulated accident events. The aeroshell design is shown in Figure 3.1.1-5.

ø $\begin{matrix} 16.5 \\ 15.5 \end{matrix}$

0.8 - 3.2

$\begin{matrix} 4.5 \\ 3.5 \end{matrix}$

SCALE 2/1

ø $\begin{matrix} 0.51 \\ 0.38 \end{matrix}$ THRU

⊕ | A | B Ⓜ | 0.25 Ⓜ |

DASH NO.	MATERIAL	HOLE	REQ'D. PER ASSY.
-1	IRIDIUM	YES	1
-2	IRIDIUM	NO	1

ø $\begin{matrix} 29.82 \\ 29.60 \end{matrix}$

$\begin{matrix} 5.96 \\ 5.68 \end{matrix}$ RAD

(5.95)

$\begin{matrix} 15.12 \\ 15.04 \end{matrix}$

0.55 MIN.

(2.5)

| -A- |
| (⊘ 0.013) |

SHARP CORNER TO FULL RADIUS

0.03 BREAK PERMITTED TYP.

$\begin{matrix} 0.20 \\ 0.15 \end{matrix}$

0.35 or 0.60
0.25 or 0.45
(See Figure 4.1.1-3)

ENLGD VIEW
SCALE NONE

0.05 MAX.
BREAK TYP.

$\begin{matrix} 0.73 \\ 0.63 \end{matrix}$

| ·B· |
| ◎ | 0.08 |

ø $\begin{matrix} 29.88 \\ 29.73 \end{matrix}$

Dimensions in mm

Figure 3.1.1-2. Iridium Shield Cup

E.B. WELD

14.10
13.95

-A-

- B -

SINTERED AND
DIFFUSION BONDED
IRIDIUM FRIT VENT

E.B. WELD

VIEW A

Dimensions in mm

Figure 3.1.1-3. Iridium Vent Cup

7.899 cm
(3.110 in.)

45° CHAMFER x 0.127cm
(.050 in) FOUR PLACES

3.810 cm
(1.500 in.) DIA, TYP

3.937 cm
(1.550 in.) DIA, TYP

0.424 cm min.
(0.167 in.)
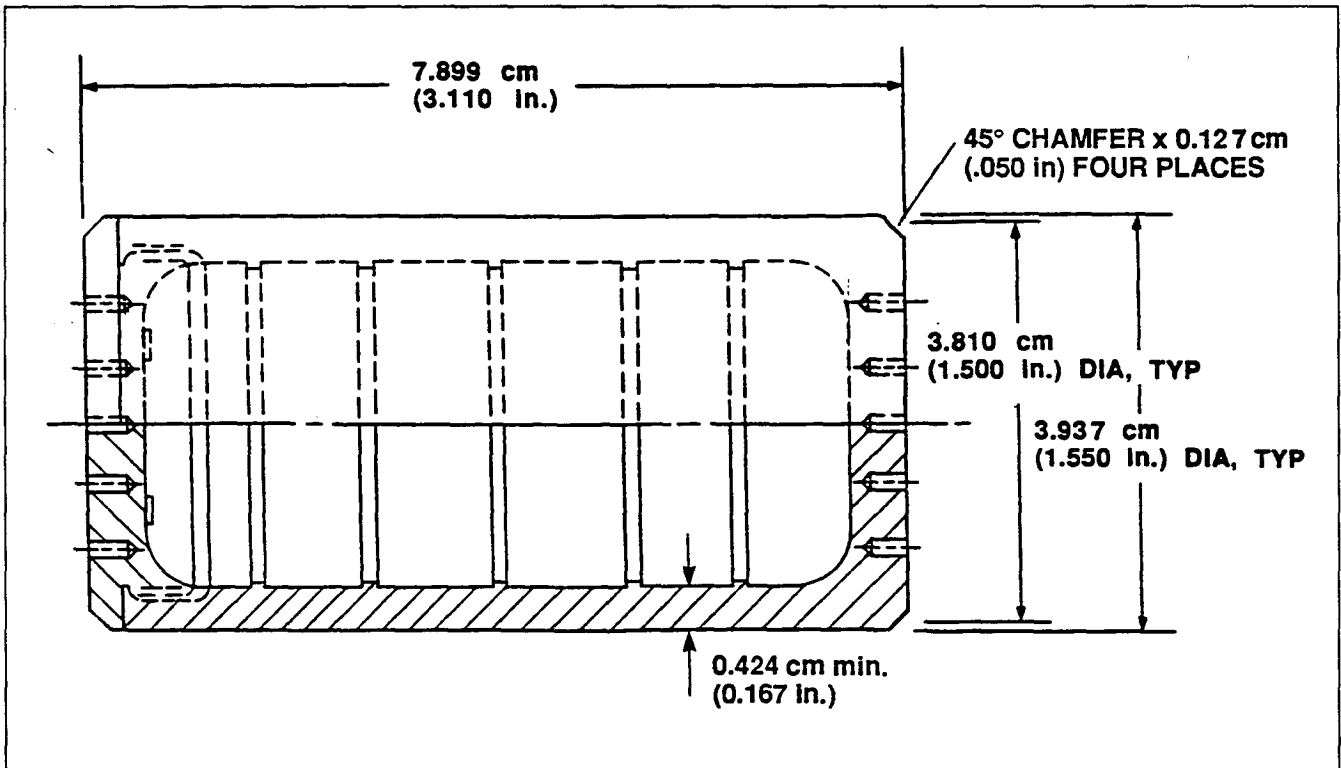
Figure 3.1.1-4. Graphite Impact Shell

CHAMFER CORNER

$.015^{+.005}_{-.000} \times 45°$

.544 SPHERICAL

1.913

2.090

1.045

0.095
TYP 4 PLS

1.050

1.720

3.826 ± .002

.080
2PLS

1.947 DIA.

1.720 DIA

.250
REF.

3.473
2 PLS

3.668 ± .002

.015 MAX
RADII TYP.

1.960

45° ± 0.30
2 PLS

0.854

1.282 DIA TYP

1.450
DIA TYP.

Dimensions in inches.
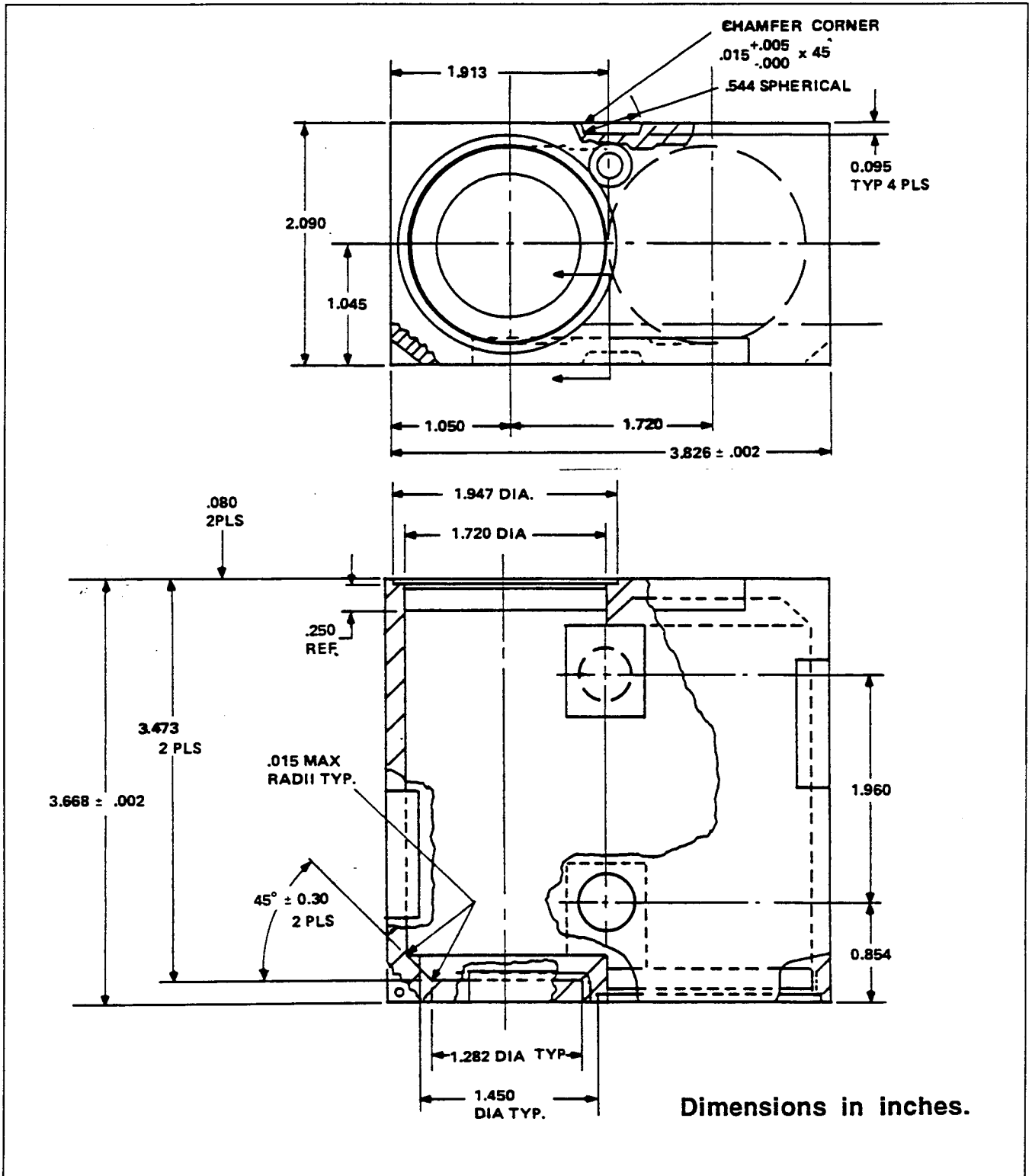
Figure 3.1.1-5.   Aeroshell

3.1.1.5   *Materials and Weights*

A summary of the heat source components, materials, and their associated weights are presented in Table 3.1.1-2. The weights shown in this table are averages for actual components.

Table 3.1.1-2.   GPHS Component Mass Summary

Component	LMMS-VF Reference Drawing	Material	No. Per Heat Source	Unit Weight (kg)	Total Weight (kg)
Fueled Clad	47C305993	PuO_2/Ir	72	0.207	14.893
Graphite Impact Shell	47D305396 47D305397	FWPF Graphite	36	0.091	3.266
Floating Membrane	47C305610	FWPF Graphite	36	0.007	0.245
Insulator	47D305608	CBCF Graphite	36	0.004	0.155
Aeroshell	47D305398 47D305399 47D305609	FWPF Graphite	18	0.402	7.242
Lock Members	47B305212	FWPF Graphite	32	0.001	0.044
Midspan Plate	47E305117	FWPF Graphite	1	0.259	0.259
GPHS Assembly	47D305112	– –	– –	– –	**26.104**

Note: Unit weights are rounded to the nearest gram and cannot be used to accurately determine total weight.

3.1.2   Thermopile Assembly and Outer Shell

The thermopile consists of 572 thermoelectric unicouples, multifoil insulation, and an internal frame. The unicouples, shown in Figure 3.1.2-1, are individually fastened to the outer shell. The two SiGe legs of the couple and their corresponding sections of the hot shoe are doped to provide thermoelectric polarity; the N-type material is doped with phosphorous and the P-type with boron. The silicon alloy thermocouple is bonded to a cold stack assembly of tungsten, copper, molybdenum, stainless steel, and alumina. Copper
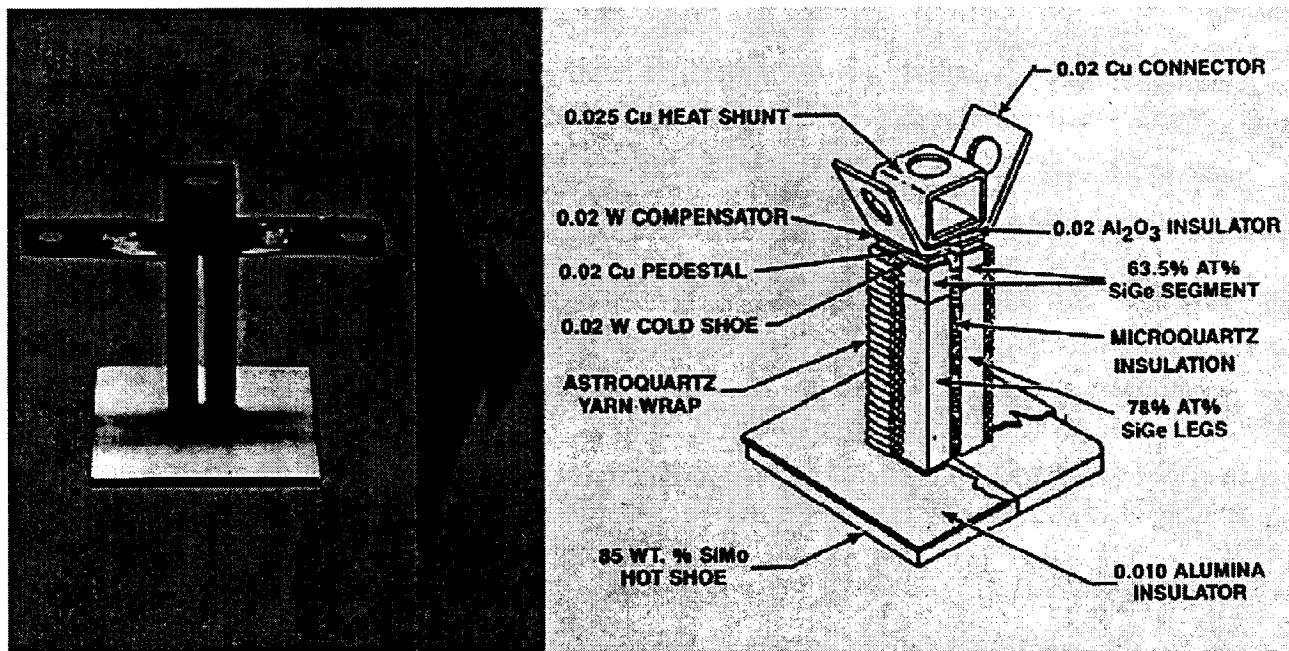
Figure 3.1.2-1. Silicon Germanium Unicouple

together in the space between the inside of the outer shell and the outside of the insulation system to form the thermopile electrical circuit. A two string, series-parallel, electric wiring circuit is used. This permits continued operation in the event of a single thermocouple open circuit or short circuit failure. Each unicouple is electrically insulated from the multifoil insulation.

Thermal insulation for the thermopile assembly consists of an axial section and two end caps that are a part of the inboard and outboard heat source support assemblies (Figure 3.1-1). All of the insulation is of multifoil construction, consisting of 60 alternate layers of 0.0003 inch molybdenum foil and Astroquartz cloth. An additional metallic layer is provided by a thicker foil on the inside of each end cap, and by an inner molybdenum frame that supports the axial section of the insulation. In an unrestrained condition, the 60 layers of insulation stack up to approximately 0.7 inch in thickness. The insulation assembly has 572 penetrations through which the thermocouples pass, and four penetrations for supports for the inner molybdenum frame. The two end caps each have four penetrations for the heat source support preload studs. The inboard insulation cap has four additional penetrations

that are plugged during RTG assembly and one penetration (previously used for electric heat source instrumentation wires) that is left open as a vent.

The converter shell is composed of the outer shell and the end domes, which are the major structural elements of the RTG. They are composed of aluminum, with sufficient strength to withstand launch loads, but intended to burn up in the event of a postulated reentry. The outer shell incorporates eight external fins to enhance radiative cooling in space.

The converter heat source support system consists of an inboard and outboard heat source support assembly, and four midspan support assemblies. The function of the heat source support system is to support the GPHS modules with respect to the outer shell and dome assemblies.

Accessories mounted on the outer shell include the Gas Management Valve (GMV), Pressure Relief Device (PRD), Active Cooling System (ACS), RTG power connector, and four Resistance Temperature Devices (RTDs).

The GMV is a component of the gas management system that permits control of the internal atmosphere in the converter. During storage and ground operations of the RTG, the converter is filled with inert gas. The end domes and all penetrations are sealed with C-seals, capable of retaining the gas for periods of at least 30 days without refilling. After launch, the PRD is actuated and punctures a diaphragm in the converter shell, thereafter allowing the RTG to operate with an internal vacuum environment.

The ACS on the converter permits circulation of cooling water through tubing passages near the base of each fin. This cooling lowers the temperature of the outer shell during the period of launch when the RTG is enclosed. This system was originally designed for launches on the Shuttle and was not used on the Titan IVB Cassini mission.

The RTG power connector, mounted on the converter shell, provides the electrical interface with the spacecraft. The instrumentation connector provides an interface that enables measurement of the outer shell temperature by means of RTDs which are located at four radial locations near the inboard end.

3.1.3 Electrically Heated Thermoelectric Generator (ETG)

All RTGs are first configured as ETGs during their initial assembly and processing. In this configuration they are heated by an Electric Heat Source (EHS). A special dome is mounted on the inboard end, and a spool piece is mounted between the inboard dome and the converter outer shell. In addition, ETGs have specific instrumentation used during processing. The special dome incorporates a valve used in processing and testing. The spool piece provides penetration for instrumentation connectors, needed for internal instrumentation, and four separate single-pin connectors provide electrical power to the EHS. During conversion of an ETG to an RTG, the EHS is replaced by GPHS heat source modules. The spool piece and internal instrumentation leads are removed, and the special dome is replaced by one of flight configuration.

3.1.4 Mass Summary

Table 3.1.4-1 is a summary of weights for RTGs F-2, F-5, F-6, and F-7.

Table 3.1.4-1. Weight Summary (lbs)

F-2	F-5	F-6	F-7
124.16	123.34	124.48	124.62

A typical mass summary for a flight RTG is summarized in Table 3.1.4-2.

Table 3.1.4-2. Component Weight Summary

	Quantity	Weight (lb.)
Housing		
Outer Shell	1	14.34
Fins	8	4.22
Emissive Coating	x	0.33
Auxiliary Cooling Tube Manifold	1	0.57
Nuts	8	0.11
Converter		
Unicouples	572	11.90
Unicouple Sealing Screws	576	1.54
Thermoelectric C-Seals	576	0.13
Rivets	672	0.65
Thermoelectric Spacers (Al_2O_3)	572	0.64
Nut Plates	286	0.84
Foil Insulation - Thermopile	1	12.15
Insulation Support Frame	1	1.91
Power Connector	1	0.29
Gas Management Assembly	1	0.36
Electrical Straps	x	1.65
PRD	1	0.94
C-Seal (Domes)	2	0.08
Other Insulation	x	0.20
Pressure Dome	2	1.68
Screws (Pressure Dome)	44	0.18
Assembly - RTD	1	0.67
Inner Frame Support Assembly		
Fitting	2	0.35
Leg	4	0.08
Shoe	8	0.06
Nut	4	0.004
Clip	4	0.003

Table 3.1.4-2. Component Weight Summary (Cont'd)

	Quantity	Weight (lb.)
Heat Source Support System		
Outboard Support Assembly		
Frame	1	0.91
End Cap Insulation Assembly	1	0.64
Pressure Plate	1	0.68
Retainer Screw	1	0.006
Stud Insulator	4	0.27
Barrier (Iridium)	4	0.01
Barrier (Tungsten)	4	0.004
Preload Stud	4	0.15
Insulation, Fibrous	AR	0.004
Insulation, M49A1	AR	0.002
Foil Disk	4	0.004
Shim	4	0.004
Latch	4	0.20
Stud, Latch	4	0.08
Screw, Latch	8	0.03
Heat Source Support System		
Inboard Support Assembly		
Frame	1	1.12
Pressure Plate	1	0.79
End Cap Insulation Assembly	1	0.58
Spring Washer	3	1.13
Collar	1	0.15
Guide	1	0.37
Preload Stud	4	0.15
Pressure Plate	1	0.49
Insulation, Fibrous	AR	0.004
Insulation, M49A1	AR	0.002
Barrier (Iridium)	4	0.01
Barrier (Tungsten)	4	0.004
Washer	1	0.03
Foil Disk	4	0.004
Washer, Inboard	1	0.03
Stud Insulator	4	0.27
Latch	4	0.08
Screw, Latch	8	0.03

Table 3.1.4-2. Component Weight Summary (Cont'd)

	Quantity	Weight (lb.)
Heat Source Support System		
Midspan Support Assembly		
Cap	4	0.24
C-Seal	4	0.02
Pivot	4	0.13
Support	4	0.25
Nut, Lock	4	0.11
Nut, Spring Washer	4	0.24
Spring Washer	12	0.40
Seat	4	0.07
Insulator	4	0.07
Can Assembly	4	0.04
Barrier	4	0.004
Shoe	4	0.004
Ring	4	0.03
Locating Pin	4	0.05
Insulation	AR	0.02
Washer	4	0.04
Washer	12	<u>0.02</u>
Converter		<u>65.96</u>
Midspan Plate	1	<u>0.57</u>
General Purpose Heat Source	18	
Fueled Capsule	72	32.832
GIS	36	7.200
Floating Membrane	36	0.540
CBCF Set	36	0.342
Aeroshell (Incl. caps, lock screws)	18	15.966
Lock Members	32	<u>0.096</u>
		<u>56.976</u>
RTG		123.51

3.2   GROUND SUPPORT EQUIPMENT (GSE)

The GSE required for processing and testing of the ETG for the Cassini program is described in this paragraph. Use of the GSE is illustrated in the following typical sequence of events. The ETGs are delivered to Building 800 (the processing and test facility) in the ETG shipping container (ETG-SC). After initial inspection and completion of resistance measurements, the ETG is removed from the ETG-SC using the outboard handling fixture and the ETG lifting fixture. It is then placed into the Loading and Assembly Station (LAS) for processing and test. With the ETG outboard dome removed, the LAS is evacuated to 1.0×10^{-5} torr, and a slow heat-up of the ETG is performed using the EHS until an input power of 4400 watts and a vacuum pressure of 1.0×10^{-5} torr are maintained. Control of applied EHS power and ETG parameters are accomplished using the Readout Console (ROC). This sequence of increasing heat as a function of chamber pressure (a measure of outgassing) is a final step in the manufacturing process. After this processing cycle is completed, an ETG performance test is run while still in the LAS. Following the performance test the LAS is backfilled with argon gas using the gas management system (GMS), thus enabling the use of the LAS as a glove box.

After doming operations are completed (during which the LAS GMS maintains the inert, oxygen-free environment) a pressure decay test is performed using the gas service cart (GSC). After removal from the LAS, the ETG is again placed in the ETG-SC for transport to Mound Laboratory (Miamisburg, Ohio) for conversion to a RTG and subsequent flight acceptance tests. The RTG is then put in storage and the portable test unit (PTU) is used for monitoring the RTG performance as required.

The following is a list of the GSE used on the Cassini program for those tasks mentioned. This GSE was built and used first on the GPHS-RTG program. The GSE was refurbished and retested as required for the Cassini program. Each is described in more detail in the paragraphs indicated.

Paragraph	GSE Item	Product Specification	Operating Procedure
3.2.1	ETG Shipping Container	CP 47A14648	
3.2.2	RTG Shipping Container	CP 47A14647	
3.2.3	Readout Console	CP 47A14638	SI 249703
3.2.4	Portable Test Unit	CP 47A25002	GESP 7167
3.2.5	Gas Service Cart	CP 47A25000	SI 249229
3.2.6	ETG/RTG Handling Equipment	CP 47A14649	

Additional tools and special fixtures are utilized as required to complete preparation of the ETGs for delivery. These items are covered in other sections of this report.

3.2.1 ETG Shipping Container (ETG-SC)

The ETG-SC is used to provide physical protection to the ETG during handling, shipping, and storage. The ETG-SC (47E305499G1) is constructed of two welded stainless steel assemblies: a domed upper half which measures 30 inches in diameter and is approximately 44 inches high, and a lower base assembly measuring 48 inches wide by 68 inches long. With the upper assembly mated to the base, and with the metal wheels lowered, the ETG-SC is 72 inches high and weighs approximately 1800 pounds (Figure 3.2-1). A gas monitoring and pressurization system is built into the ETG-SC. One system is built into the base assembly with an internal Wiggins quick-disconnect interface for the ETG and an external pneumatic fitting for the GSC. This system makes use of a 30 inch Hg to 30 psig gauge and two Nupro bellows valves (modified to allow safety wiring) for isolation and control of gas flow. The second system, built into the upper dome half, has a valve and gauge configuration that is the same as the base assembly. However, instead of the Wiggins interface this system opens through a port into the internal cavity formed by the upper half when secured to the base assembly. Two pressure relief valves are incorporated into the dome to prevent over-pressurization. This second system provides for servicing of the argon gas used to enclose the ETG in a protective environment. Stainless steel tubing is used throughout with the system enclosed in a box structure. The 10 inch steel wheels are manually retractable to provide a stable configuration when tied down for shipment.

Figure 3.2-1. ETG Shipping Container

3.2.2 Base and Protective Cover Assembly (BPCA)

The BPCA is used to provide physical protection to the GPHS-RTG during handling and storage at the launch site. The BPCA shares a common base assembly (47E305499G2) with the ETG-SC. The domed upper half is replaced with the protective cover (47E305551) for designation as the RTG BPCA (47E305060, Figure 3.2-2). The cover is of open mesh construction which allows ventilation for the RTG and protects personnel from the heated surface of the RTG. The entire RTG transfer container is of welded stainless steel construction and measures 48 inches wide by 68 inches long by 74 inches high with the metal wheels lowered and weighs approximately 1800 pounds.
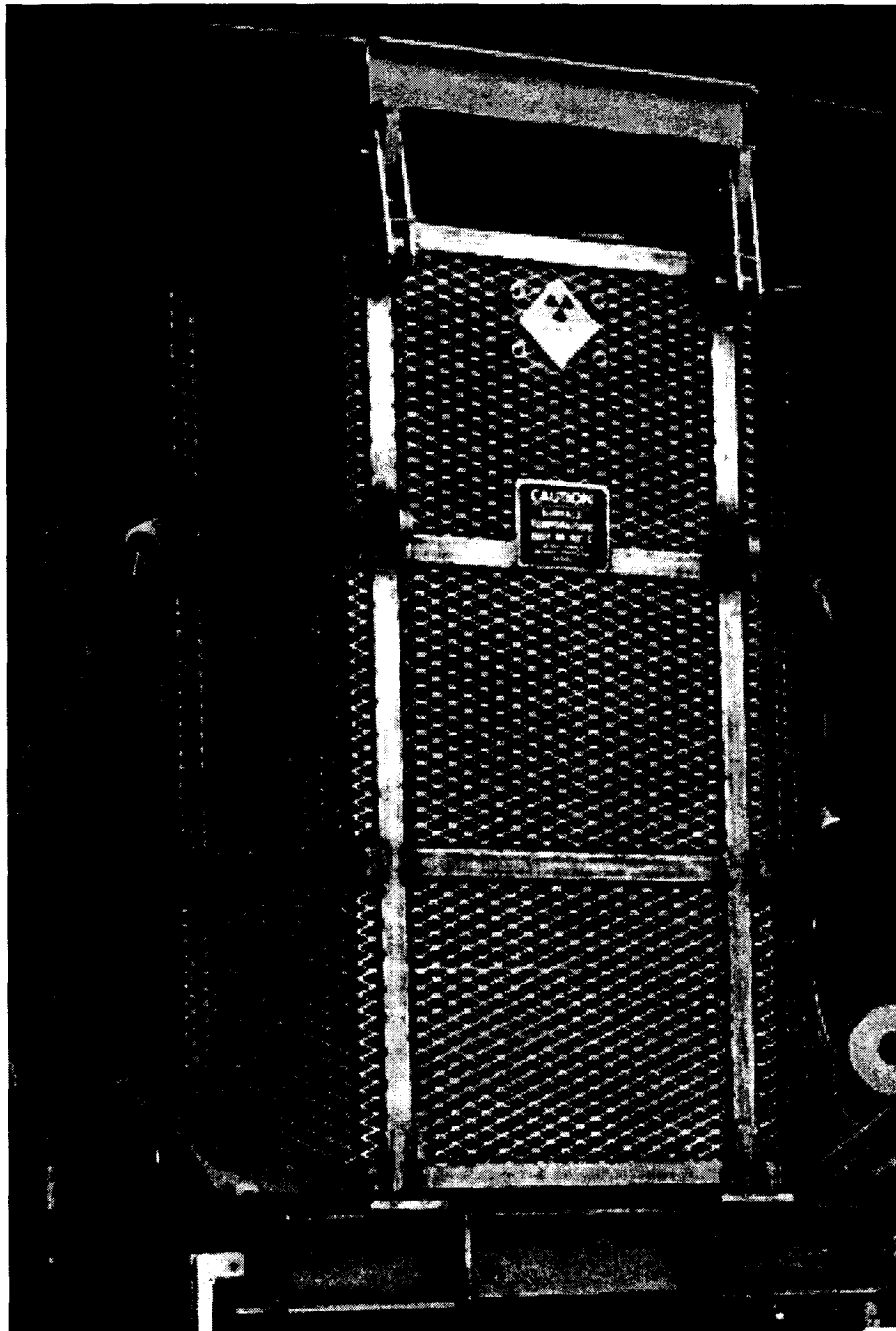
Figure 3.2-2. Base and Protective Cover Assembly

A gas monitoring and pressurization system is built into the base assembly with an internal Wiggins quick-disconnect interface for the RTG and an external pneumatic fitting for the GSC. This system makes use of a 30 inch Hg to 30 psig gauge and two Nupro bellows valves (modified to allow safety wiring) for isolation and control of gas flow. Stainless steel tubing is used throughout with the system enclosed in a box structure. The 10 inch steel

wheels are manually retractable to provide a stable configuration when tied down for shipment. During the Cassini program the protective cover assembly was modified by adding a four inch high hat section to the top of the cover. This allows proper clearance with the RTG when the JPL adapter is installed on the RTG for transfer to the launch site.

3.2.3 Readout Console (ROC)

The ROC provides the capability to monitor the performance of an RTG/ETG and to supply power for the EHS. It also includes the equipment to monitor, switch, and display the ETG/RTG temperatures and output voltage and current. A programmable data acquisition system provides the normal data acquisition sequence and test parameters. Programs are loaded into the data logger at the start of the test by floppy disk. An alarm system monitors critical ETG/RTG parameters and signals out-of-limit conditions. Temperatures and performance data, such as ETG/RTG voltage, current, thermopile-to-case, and foil shunt resistances, are recorded. ETG/RTG operation times are displayed on elapsed time meters. The ROC also monitors the voltage, current, and temperature of the EHS, providing out-of-limit alarms for these parameters as well. The ROC is a two bay rack (Figure 3.2-3) which requires a 208 Vac, 3 phase, 60 Hz, 50 amp power source. The Digitec Model 3000 data logger (with a Model 3300 scanner) was upgraded to an HP 75000 Data Acquisition System (DAS). In addition to the DAS upgrade, an HP Deskjet 500 printer was added to provide hard copies of normal interval data as well as alarm data. A Fluke Model 8520A digital multimeter (DMM) displays real time and/or backup manual data acquisition and a Sorensen Model DCR-150-70A power supply provides power for the EHS heat source. The ROC also contains six additional panels. The console control panel controls rack power and power status indicators, an RTG simulator panel for ROC checkout, a DMM input selector panel, the EHS monitor panel, ETG/RTG monitor panel, and a load panel. The load panel displays open circuit and shunt resistance readings as well as real time current and voltage.
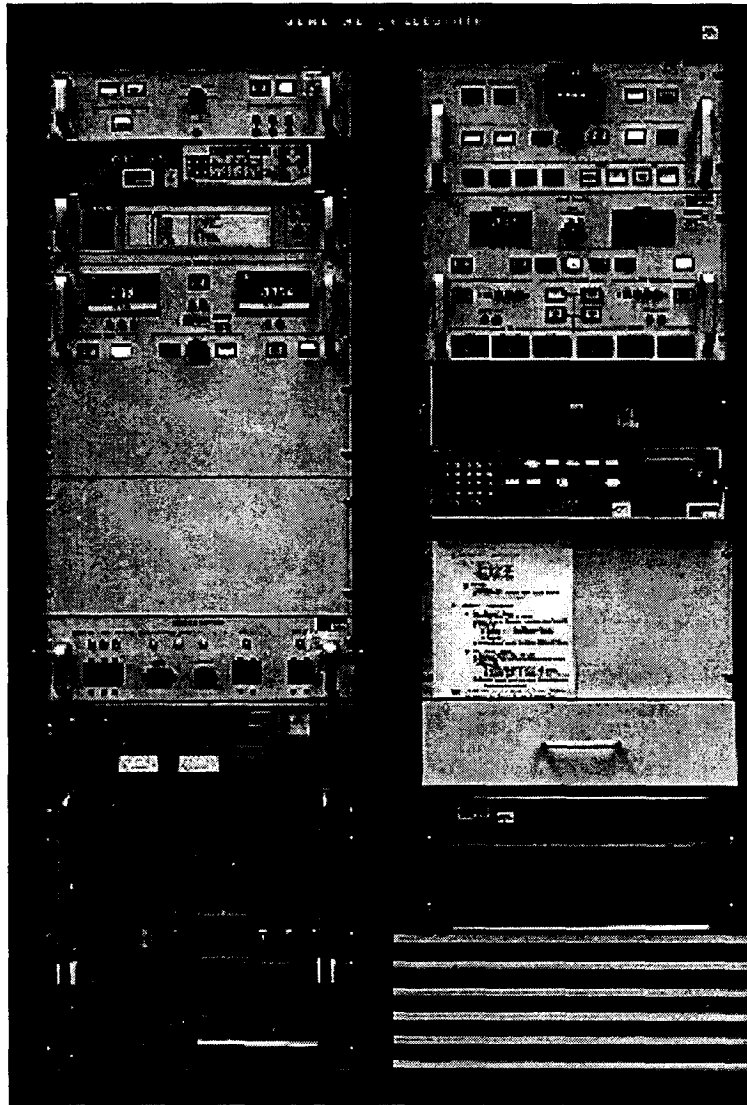
Figure 3.2-3. Readout Console

3.2.4 Portable Test Unit (PTU)

The PTU is a suitcase-sized package 24 inches long by 20.5 inches wide by 6.5 inches high and weighs approximately 40 pounds. The PTU is an AC/DC powered instrument which measures the RTG voltage, current, and shunt resistance, usually when the RTG is in the BPCA. The PTU contains a Fluke model 8600A DMM, internal self test circuits and a switching network which, in conjunction with the DMM, allows the RTG short/open circuit voltage, current, and resistance measurements to be displayed. The DC power supply (batteries) in the DMM provides for approximately six hours of continuous operation. The batteries can be charged continuously from a 120 volt AC source. Operation of the PTU in

the AC mode does not affect the charging rate of the batteries, since the batteries always supply operating power. Operation of the PTU is identical in either the AC or DC mode. The PTU/RTG interface cables and the AC power cable are housed in each lid of the PTU.

3.2.5 Gas Service Cart (GSC)

The GSC is a portable, self contained, pneumatic system approximately 4 feet wide by 2.5 feet deep by 5 feet high. The GSC is capable of storing and supplying various gases from different supply bottles secured to the cart and is used primarily to pressurize shipping containers, ETGs, and RTGs. A Welch mechanical pump is utilized for evacuation prior to backfilling operations. This pump is equipped with an oil free filter to preclude any oil backstreaming. An in-line thermocouple gauge is installed to allow vacuum pressure to be monitored and an absolute filter in the exhaust train provides radiological safety. A Wallace Tiernan 0.35 psia pressure gauge with 0.05 psia subdivisions accurately monitors pressure conditions. A micrometer valve is installed in the system for gas flow rate control during backfilling operations. This valve has an in-line 60 micron filter to prevent particulate contamination of the system or the test specimen. A gas sample port is available for taking RTG gas sampling.

3.2.6 ETG/RTG Handling Fixtures

Special fixtures are required for handling and lifting the ETG/RTG, for personnel safety as well as mechanical necessity. These fixtures are briefly described below.

The outboard handling fixture (47D305498) is a circular aluminum ring which clamps onto the outboard end of the ETG/RTG and provides an interface for the lifting sling (47D305505 G1/G2). The lifting sling is a four point aluminum fixture designed for either outboard use (G2) as described above or inboard use (G1). The inboard configuration mates with the mid-ring assembly (47D306262) which is the mounting interface with the ETG shipping containers and BPCAs. The RTG handling sling assembly (47D305515) is a two piece aluminum fixture used to rotate the ETG/RTG to provide access to the inboard end for mid-ring removal. This fixture is more commonly referred to as the turnover fixture. The RTG BPCA lifting yoke (47C305560) is a steel I-beam fixture which mates to the lifting lugs of the BPCA protective cover. This lifting yoke is used in the removal of the protective cover or for

lifting the entire BPCA (with or without the RTG) by crane. The dome clamping ring (47D306459) is a special fixture which facilitates proper seating of the C-seal during doming operations.

References for Section 3

3.1.1-1 Carpenter, R. T. (OSC) to B. A. Cook (DOE/NE-50), "Cassini F-2 RTG Fuel Composition," 4 December 1995.

3.1.1-2 Carpenter, R. T. (OSC) to B. A. Cook (DOE/NE-50), "Cassini F-7 RTG Fuel Composition," 23 July 1996.

3.1.1-3 Carpenter, R. T. (OSC) to B. A. Cook (DOE/NE-50), "Cassini F-6 RTG Fuel Composition," 16 December 1996.

3.1.1-4 "GPHS 238-PuO$_2$ Feed Powder Specification," LANL, 26Y-318180, 30 January 1996.

3.1.1-5 "GPHS 238-Plutonium Dioxide Fueled-Clad Specification," LANL, 26Y-318182, 30 January 1996.

Section 4

Detailed Design History
and
Special Studies

SECTION 4
DETAILED DESIGN HISTORY AND SPECIAL STUDIES

4.1 HERITAGE FROM GPHS-RTG PROGRAM

4.1.1 GPHS

The General Purpose Heat Source for the Cassini program is virtually identical in design to that for the Galileo and Ulysses missions. However, several minor modifications were made to the GPHS to facilitate manufacture, assembly, and inspection processes for the Cassini program. These included changes to the fueled clad weld shield, weld vent notch, fuel mass, and allowable impurities. The differences from the heritage design are summarized below.

Weld Shield

During the Cassini program the weld shield design was revised to eliminate the shield-to-cup attachment welds and facilitate clad vent set fabrication. Further, the absence of the shield attachment welds simplified clad vent set inspections. Figure 4.1.1-1 (based on Lockheed Martin Energy Systems Drawing M2D920101A009) shows the heritage shield design which included weld tabs for fastening the shield to the non-vented cup. To simplify the use of the weld shield, the revised configuration (designated type II) is shown in Figure 4.1.1-2 and was developed by Oak Ridge, Savannah River Plant, and Los Alamos personnel. The type II weld shield is not welded into one of the two clad cups and therefore is non-integral. Instead, it is installed separately in the non-vented cup at the time of fuel pellet loading. It is positioned inside the receiving cup by sliding it down until it reaches the wall curvature near the cup bottom. For this reason, the nominal height of the blank from which the type II shield is formed (13.97 mm) had to be greater than the heritage weld shield (8.14 mm nominal) which was welded to the cup wall at a location above the bottom curvature. (The type II shield is held in place by spring action of the shield against the inside wall of the cup.) The required shield height in each case was chosen to ensure that
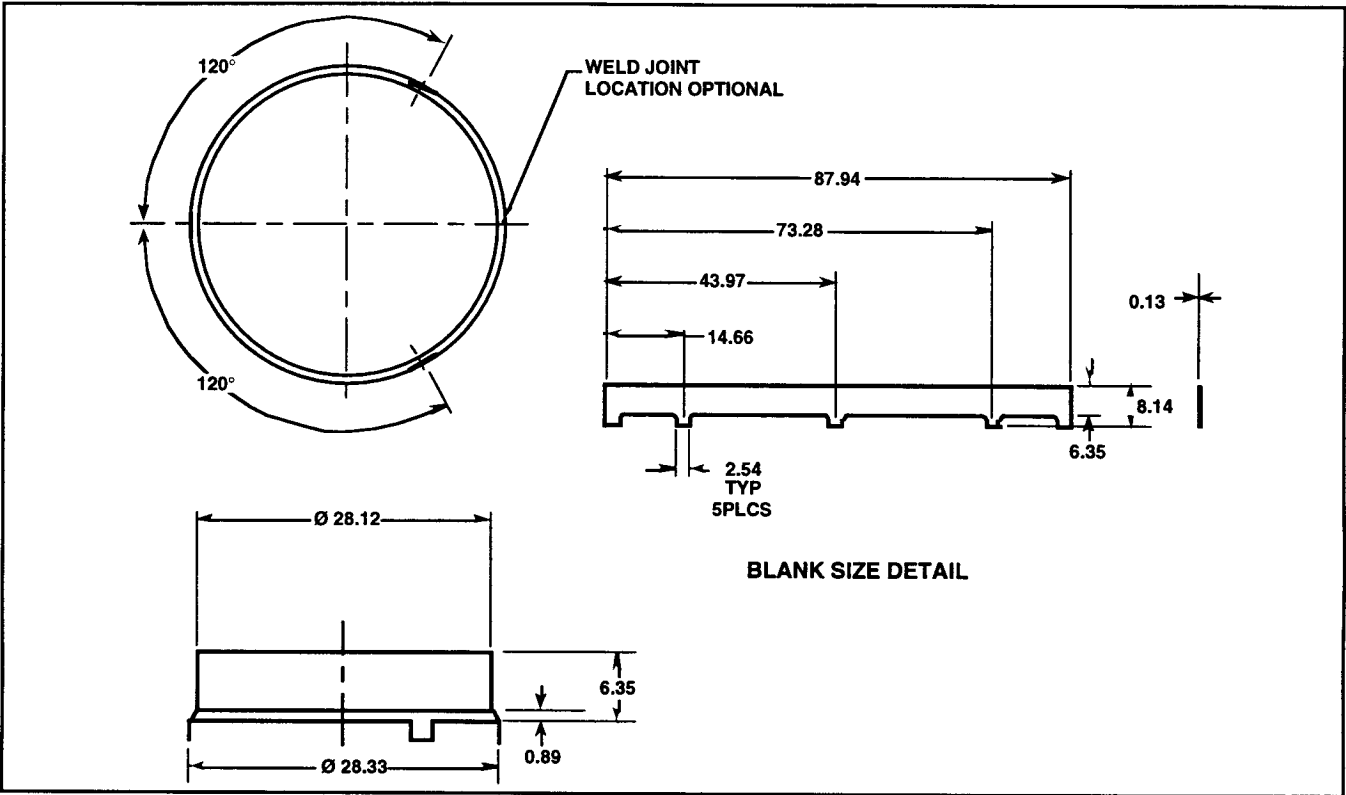
Figure 4.1.1-1. Heritage Weld Shield (Nominal Dimensions in mm)
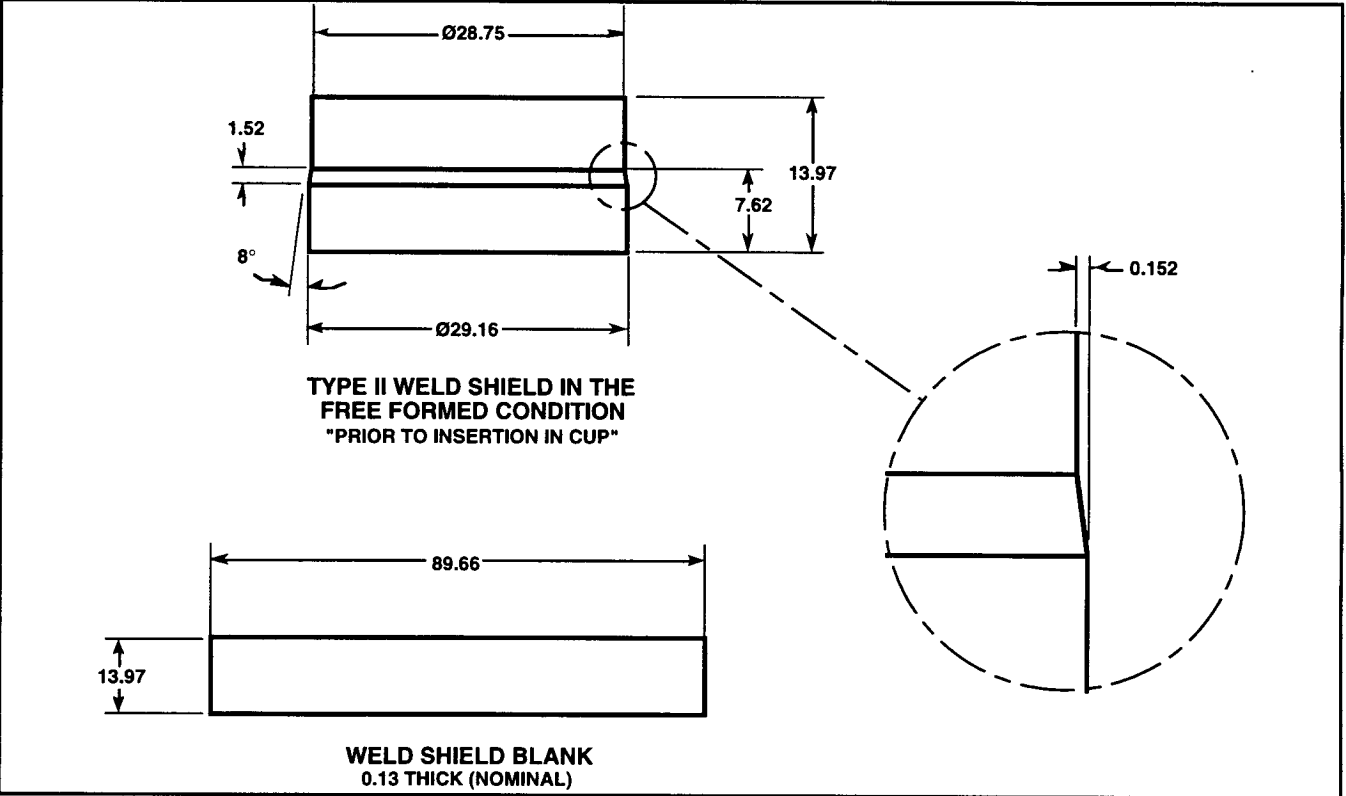
Figure 4.1.1-2. Type II Weld Shield (Nominal Dimensions in mm)

the shield was positioned behind the clad girth closure weld center line. The added mass of the type II weld shield was quite small and was easily accommodated within the overall RTG mass requirement of 125 pounds.

Weld Vent Notch

To provide greater venting area for the interior of the fuel cladding during girth closure welding, the weld vent notch in one of the two mated cups was widened during the Cassini program. The change affected only the width of the notch, not the height and is shown in Figure 4.1.1-3. The notch width increased from 0.25-0.35 mm to 0.45-0.60 mm, while the notch height remained unchanged at 0.15-0.20 mm. Weld thickness and bulge measurements (comparing mated cups with two standard vent notches against cup pairs with one enlarged and one standard vent) showed that the widened notch did not cause unacceptable welds and that acceptable welds could not be made with standard size notches. For this reason, both weld vent notches were considered acceptable for use on Cassini fueled clads.
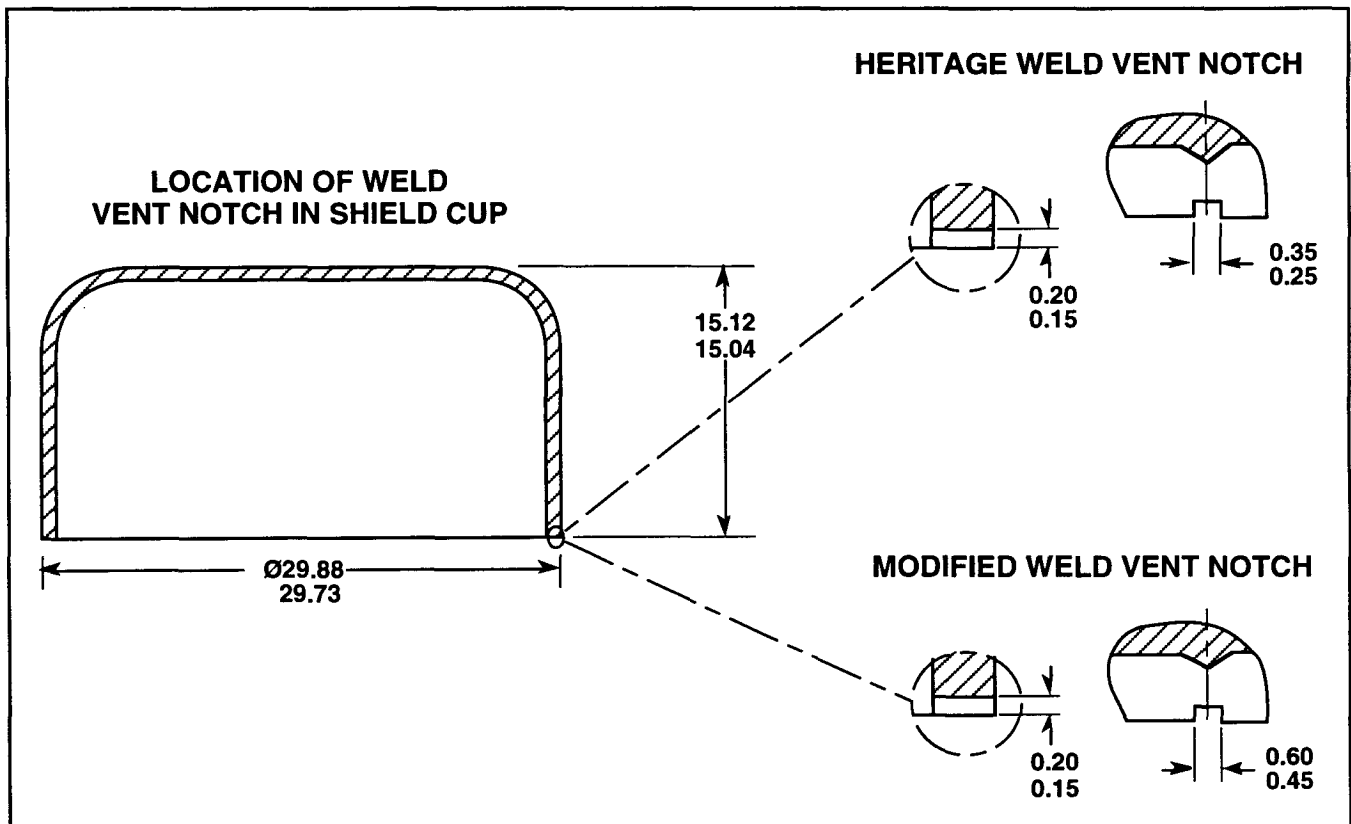
Figure 4.1.1-3. Weld Vent Notch Change (Nominal Dimensions in mm)

Fuel

For the Cassini program, fresh fuel derived from newly exposed targets was not used. Instead, existing fuel was returned to the DOE Savannah River Plant and reprocessed. The LANL fuel powder and pellet specifications were revised to reflect the use of reprocessed fuel with the revisions primarily affecting Pu^{238} content and allowable levels of some cationic impurities. These new Cassini limits are documented in LANL specifications 26Y-318180 and 26Y-318182 and are based upon the fuel actually produced by SRP during reprocessing.

Finally, during the Cassini program, nominal pellet weight was increased by one gram to 151 grams. This was done to slightly favor higher pellet thermal output, judged to be a prudent step using reprocessed fuel. The added mass was accommodated within the 125 pound RTG mass limitation.

4.1.2 Converter Assembly

4.1.2.1 Electric Heat Source

The Electric Heat Source (EHS) was used during processing and testing of the Flight Unit converters prior to their conversion from an ETG to an RTG. The EHS was required to duplicate the thermal and mechanical characteristics of a GPHSA, that is, an assembly of 18 GPHS modules and lock members, together with a midspan plate. In addition to meeting requirements for thermal power output, operating surface temperature, external geometry, mass, and mass distribution, the EHS was required to have sufficient strength and rigidity to withstand support preloads and the mechanical environment encountered during dynamic testing.

The EHS, shown in Figure 4.1.2-1, consisted of the following major components: (i) a graphite aeroshell that simulated the outside geometry of the aeroshells of stacked GPHS modules, (ii) graphite end caps that simulated the interfaces with the inboard and outboard heat source support assemblies, (iii) a graphite midspan plate that simulated the interface with the midspan supports, (iv) alumina insulators that supported the heating elements and provided electrical isolation, (v) graphite heating elements for the upper and lower sections,
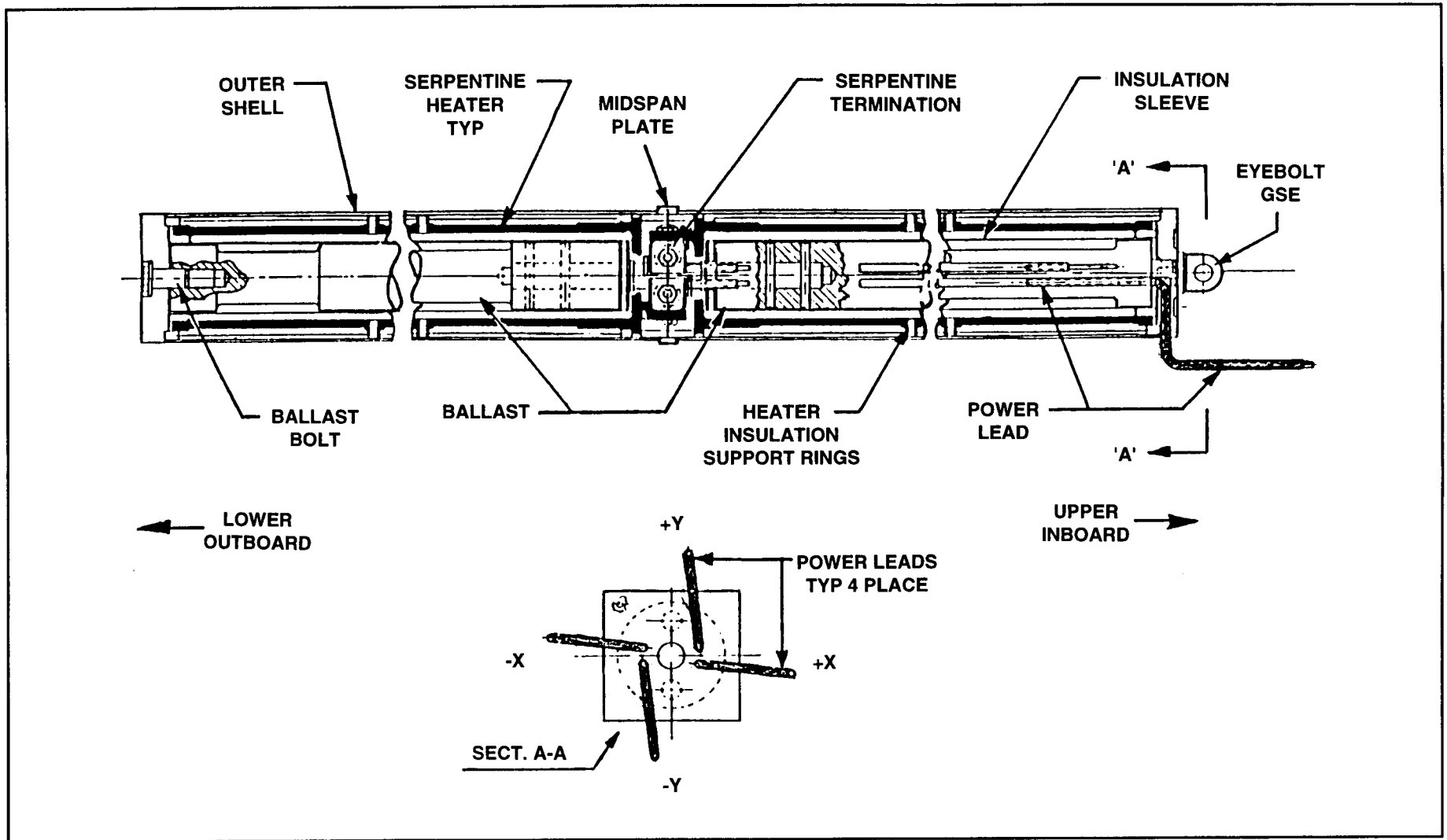
Figure 4.1.2-1. Electric Heat Source

(vi) tungsten power leads that attached to the heating elements and penetrated through the inboard end cap, and (vii) a molybdenum ballast that added to the mass and heat capacity of the EHS. The EHS was capable of operating from a power source of variable voltages up to 150 volts dc, providing power up to 4500 watts.

4.1.2.1.1 Heritage from GPHS Programs

The design of the Electric Heat Source was based on the design that was used on the MHW and identical to that used on the GPHS-RTG program. The graphite serpentine heater element, POCO outer shell, serpentine termination connections, tungsten power leads, alumina intermediate support rings, molybdenum ballast and the POCO end caps were all similar to features of the MHW program electric heat source. The GPHS electric heat source was smaller in cross-section and twice as long with almost twice the power output as the MHW electric heat source.

4.1.2.1.2 Design Features and Rationale

This paragraph describes the EHS in more detail, and provides some of the rationale for design selections. Table 4.1.2-1 provides a simplified parts list for the EHS from drawing 47J306060. Additional details of construction and materials can be obtained by reference to the drawings listed.

The outer shell of the EHS was made from POCO graphite, grade AXF-5Q. The decision to use this material, rather than the FWPF graphite from which the GPHS aeroshell was fabricated, was made on the basis of cost and delivery. FWPF had a long lead time and was not normally made in billet sizes large enough to make the EHS shell, even in two pieces. To compensate for the higher coefficient of thermal expansion of POCO, the EHS was made appropriately shorter so that it matched the length of the Isotope Heat Source (IHS) at operating temperature. This difference also meant that when required for dynamic testing, it was necessary to apply a calculated preload such that the preload occurring at launch temperature would match the preload on an IHS. Even with POCO, the billet size available necessitated machining the outer shell in two halves, with a separate midspan plate.

Table 4.1.2-1. Parts List for Electric Heat Source
(Reference LMMS Drawing 47J306060)

Reference Drawing Number	Part Nomenclature
47D305001	Upper Shell
47D305002	Spacer Sleeve
47D305003	Heater Element
47C305004	Support Tube
47E305581	Ballast, Lower Half
47D305007	End Cap, Upper
47D305008	End Cap, Lower
47B305009	Eye Bolt
47E305581	Ballast Bolt
47C305012	Support Ring, Center
47C305011	Support Ring, End
47C305013	Support Ring, Intermediate
47C305017	Sleeve, Center
47B305015	Angle Terminal
47B305016	Clamp Washer
47B305019	Power Lead
47E305581	Ballast, Upper Half
47C305014	Support Ring
47C305021	Midspan Support
47B305023	Bolt, Terminal
47B305024	Nut, Terminal
47B305025	Bolt, Terminal
47B305026	Nut, Terminal
47B306061	Screw, Locking
47C305027	Dowels
47D305018	Lower Shell
47B301557	Washers
47B302017	Bead
47B305006	Spacer, Insulator
47B302110	Sleeve, Insulating

The length of the heater elements was also limited by available billet sizes, so that separate elements were made for the upper and lower halves. In order to extend the heater elements as close as possible to the end caps and to provide more uniform heating near the ends, the heat element terminations were located at the midspan. Upper and lower halves were made symmetrically so that the only contributions to non-uniform heating were the I^2R losses in the power leads between the inboard end and the midspan. This non-symmetrical heating was identifiable in thermal vacuum testing of the GPHS-RTG Engineering Unit, where the temperature of the outer shell was consistently higher on the inboard half than on the outboard half. The heater elements were machined in a serpentine pattern, following the practice used for the heater element used in the EHS for the MHW-RTG program. To account for slight variations in the electrical resistivity of POCO from one heater element to another, final machining was performed after precision measurement of the resistance of each heater element. Machining was performed to reduce the cross-sectional area of each leg of the serpentine without affecting the fit of the heater element with adjacent parts.

Alumina tubing was used as the primary support for the heater elements on their outside diameter. This was a design deviation from the practice used in the EHS for MHW-RTG which incorporated a flanged cylinder. The choice of standard alumina tubing facilitated procurement, but meant that without a flange the sleeve was less readily restrained in the axial direction. After this design weakness was revealed in dynamic testing, it was necessary to make selective fit of specially ground spacers in order to limit the amount of possible axial movement.

Each heater element had two power leads attached to its terminals at midspan and extended through the inboard end cap. The four tungsten wires projected through holes in the multifoil insulation in the inboard heat source assembly. In the cavity of the spool piece, the ends of the EHS power leads were connected to four single-pin connectors by means of mechanically fastened cable assemblies. Through the multifoil insulation, the power leads were insulated by alumina tubing. Once inside the cavity of the spool piece, Varglas sleeving was used for electrical insulation on the power leads and interconnecting cables.

In addition to the major components described above, the EHS incorporated nine instrumentation thermocouples on its outer surface. These thermocouples were used to monitor EHS temperatures during heat up and processing of the ETG. The thermocouples used tungsten-rhenium wire and the junction was covered with a foil strip of niobium. The junction was secured to the outer shell of the EHS with clips and screws machined from POCO, and the wires were insulated with alumina tubing. Two bundles of insulated instrumentation wires passed through two separate holes in the multifoil insulation of the ETG inboard heat source support assembly. Inside the cavity of the spool piece, the wires were insulated with Varglas sleeving and attached to a multipin connector in the spool piece.

The molybdenum ballast in the EHS was made in three pieces to facilitate assembly. The center piece of the assembly was a dowel, slip fit into holes in the upper and lower halves, then double pinned. During handling and storage of the EHS, the ballast served as the structural core. The outboard end cap was attached to the ballast with a through molybdenum bolt, torqued and keyed. At the inboard end, the ballast projected through the inboard end cap and was secured with an eye bolt. When lifted by the eye bolt, the load path was through the ballast to the outboard end cap. Installed in the ETG, the eye bolt was removed and the load path for the preload was through the end caps and outer shell, while the ballast was restrained at one end only.

4.1.2.2 Heat Source Supports

4.1.2.2.1 Heritage from MHW

The design concept for the heat source support system on the Cassini RTG was similar to that used on the MHW RTGs. Similar material combinations and surface treatments were used in order to take advantage of proven material compatibilities. The primary differences were due to size and number of supports used. The Cassini and GPHS-RTGs utilize heat source supports at each end of the RTG and a set of midspan supports. The MHW-RTG utilized supports at each end, but no midspan supports were necessary. In addition the MHW-RTG heat source support system used a single, larger preload stud, attached to a titanium spider frame which reacted the loads through latches attached to a beryllium outer

shell. Because of the shorter length of the MHW-RTG heat source and the similarity in the thermal expansions of the materials used, the deflection range for which the preload was required to be maintained was smaller. The MHW-RTG spider frame was designed to have sufficient elasticity to accommodate deflections without the need for other springs.

Similarities in the design of the heat source support system included the tapered preload stud, wrapped with Astroquartz yarn and stuffed with quartz fiber insulation. The zirconia insulator on the MHW-RTG was larger, and to avoid cracking due to high thermal stresses, was assembled in three segments. The corresponding zirconia insulators for the Cassini RTG were designed to have lower thermal stresses and were assembled in one piece. A design detail adapted from MHW-RTG was the use of tungsten and iridium washers as diffusion barriers between the zirconia and the graphite pressure plate.

4.1.2.2.2 Design Features and Rationale

The Cassini RTG heat source support system consists of an inboard heat source support assembly (IBSA), an outboard heat source support assembly (OBSA), and four midspan support assemblies (MSA).

Inboard Heat Source Support Assembly

The major components of the IBSA are identified in Figure 4.1.2-2. The following is a detailed description of these components, roughly in order of the load path from the heat source to the outer shell. Further details on the construction and materials used in the IBSA can be found by reference to the drawings listed in Table 4.1.2-2.

The pressure plate in contact with the top GPHS module is fabricated from FWPF graphite and has two truncated hemispherical buttons machined on the outboard side of the plate. These buttons nest in the pockets of the top module to resist shear loads. The plate has a pair of tapered ears at each outboard corner. These ears aid in installing the IBSA onto the top module of the GPHSA and ensure engagement of the buttons into the module pockets. On the inboard face of the pressure plate are four (4) equally spaced pockets and a center 10-32 UNF threaded hole. Nested within the pockets are zirconia insulators, with thin
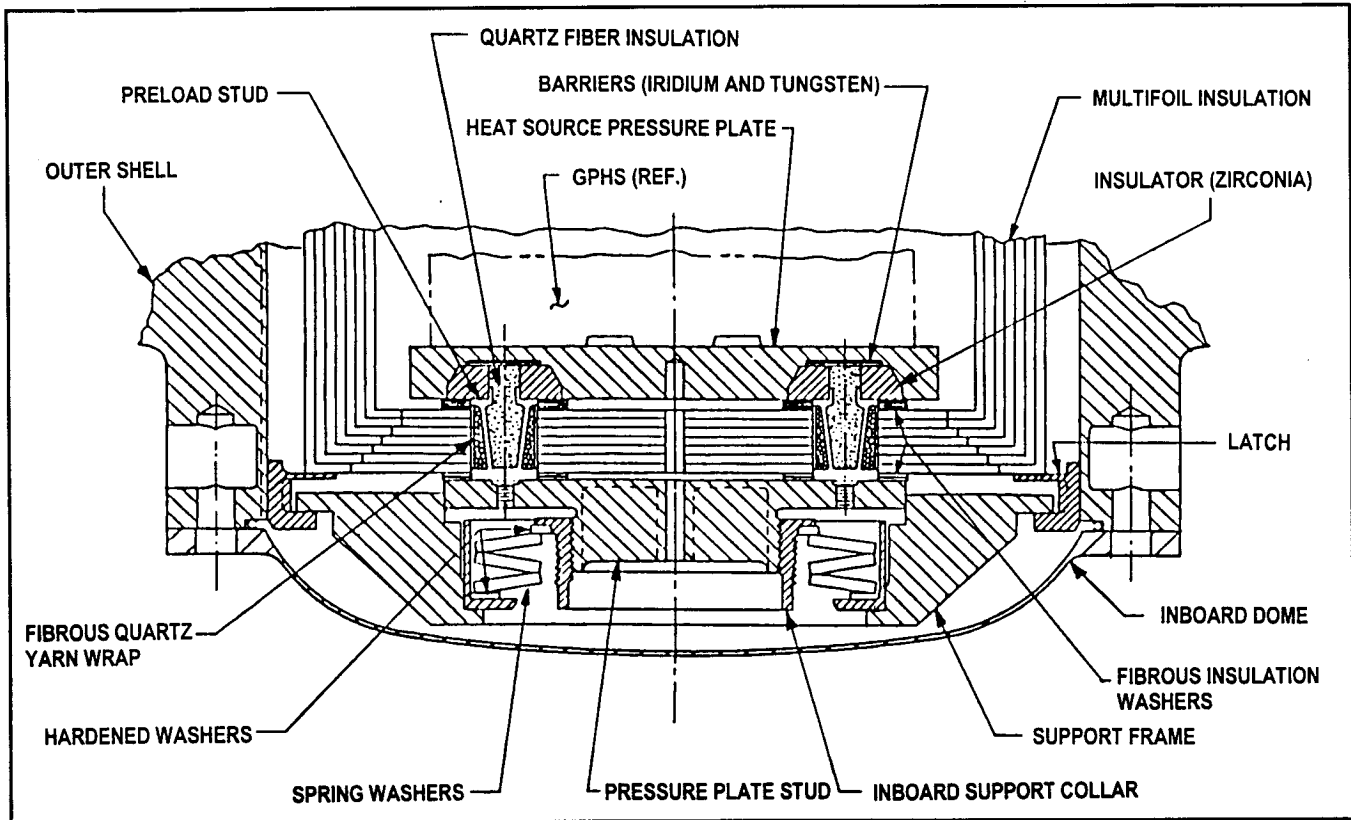
Figure 4.1.2-2. Inboard Heat Source Support

**Table 4.1.2-2. Components of the Inboard Heat Source Support Assembly
(Reference LMMS Drawing 47D305125)**

Reference Drawing No.	Part Nomenclature
47D305126	Pressure Plate, Stud
47C305147	Spring Washer
47C305128	Collar
47C305129	Guide
47C305130	Nut (Adjusting Tool)
47C305131	Screw (Holding Tool)
47C305132	Stud
47C305061	Pressure Plate, Heat Source
47C305229	Insulation Pad
47C305135	Insulator (Zirconia)

**Table 4.1.2-2. Components of the Inboard Heat Source Support Assembly
(Reference LMMS Drawing 47D305125) (Cont'd)**

Reference Drawing No.	Part Nomenclature
47C305136	Barrier (Tungsten)
47C305137	Barrier (Iridium)
47E305109	Insulation Assembly
47B305133	Washer
47B305382	Washer, Inboard
47E305064	Frame
47B305391	Barrier, Preload Stud

barriers of tungsten and iridium separating the zirconia from the FWPF graphite of the GPHS. Adjacent to and inboard of the pressure plate are 60 layers of octagonally shaped molybdenum insulation foil, separated by layers of Astroquartz cloth. Through this pack of insulation there are four holes corresponding in location to the zirconia insulators. A second pressure plate sits atop the insulation package with its four studs, penetrating the insulation and nesting on the zirconia washers, separated only by a stainless steel washer barrier. Each tapered stud, made from Inconel X-750, is wrapped on its exterior with Astroquartz yarn and stuffed in its interior with quartz fiber insulation.

Extending from the inboard side of the stud pressure plate is an externally threaded sleeve. Three large spring washers approximately 4.0 inches in diameter are stacked in series between a threaded collar and a spring washer guide. The collar is then threaded onto the sleeve of the pressure plate. Mounted over the spring assembly and pressure plate is the inboard frame. This frame transfers axial and lateral loads from the pressure plate to latches bolted to the inboard rim of the converter shell. By adjustment of the collar, axial load is applied to the GPHSA and the frame transfers this load through the same latches to the outer shell. A nut adjusting tool is used to hold the spring assembly together when the frame was not latched to the shell. A center holding tool is inserted through the pressure plate and insulation package. This is then threaded into the center hole in the graphite pressure plate. These two tools are required to hold the various pieces in relative position until the assembly has been installed in the converter, then they are removed.

Outboard Heat Source Support Assembly

The major components of the OBSA are identified in Figure 4.1.2-3. The following is a detailed description of these components, roughly in order of the load path from the heat source to the outer shell. Further details of the construction and materials used in the OBSA can be found by reference to the drawings listed in Table 4.1.2-3.
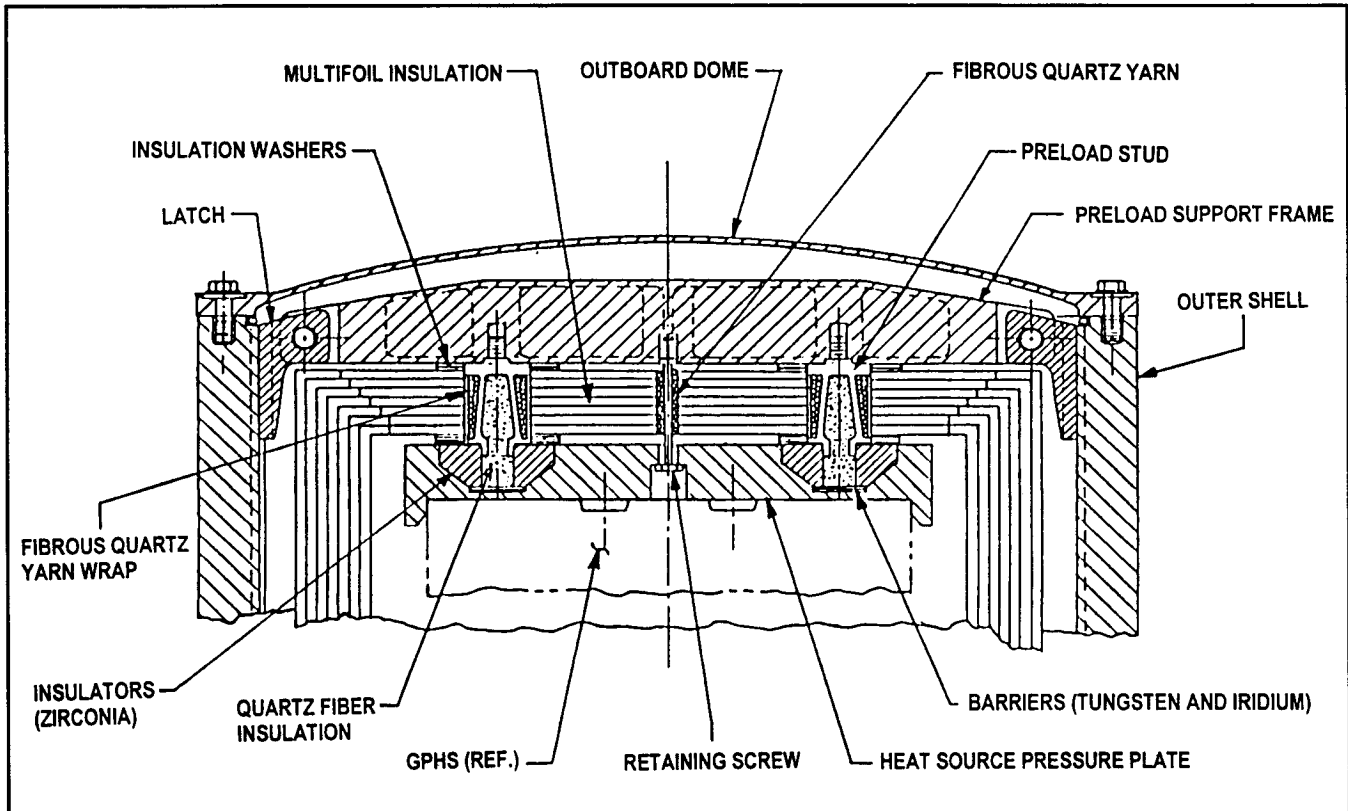
Figure 4.1.2-3. Outboard Heat Source Support

**Table 4.1.2-3. Components of the Outboard Heat Source Support Assembly
(Reference LMMS Drawing 47D305155)**

Reference Drawing No.	Part Nomenclature
47D305041	Frame
47E305109	End Cap Insulation Assembly
47D305105	Pressure Plate, Outboard
47B305042	Screw, Retainer
47B305135	Insulator

**Table 4.1.2-3. Components of the Outboard Heat Source Support Assembly
(Reference LMMS Drawing 47D305155) (Cont'd)**

Reference Drawing No.	Part Nomenclature
47B305137	Barrier (Iridium)
47B305136	Barrier (Tungsten)
47C305132	Stud
47D305229	Insulation Pad
47B305305	Stud, Ratch
47B305391	Barrier, Preload Stud

The OBSA is very similar to the IBSA with the following exceptions. There is no adjustment of the preload required in the OBSA, so there are no spring washers and the tapered studs are threaded directly into the frame. The frame is fastened into the latches on the outer shell through clevis fittings and all the pieces are held together until after installation into the converter with a small molybdenum retaining screw passing through the pressure plate, insulation assembly and threaded into the frame. After installation of the OBSA and just prior to installation of the electric heat source assembly, the bolt is backed off several turns to allow for thermal expansion of the assembly.

Midspan Support Assembly

The major components of the MSA are identified in Figure 4.1.2-4. The following is a detailed description of these components. Further details of construction and materials used in the MSA can be found by reference to the drawings listed in Table 4.1.2-4.

Each midspan support assembly is composed of three parts: a pivot, an insulation plug assembly, and a spring washer assembly. The insulation plug assembly has a locating pin fabricated from FWPF graphite, which engages in a hole in the GPHSA midspan plate. Centered on the outboard surface of the FWPF flange, and separated by 0.001 inch thick tungsten and iridium barrier washers is a thick walled cylinder of zirconia which acts as the preliminary thermal insulator for the MSA. Mounted on the zirconia is a spherical seat
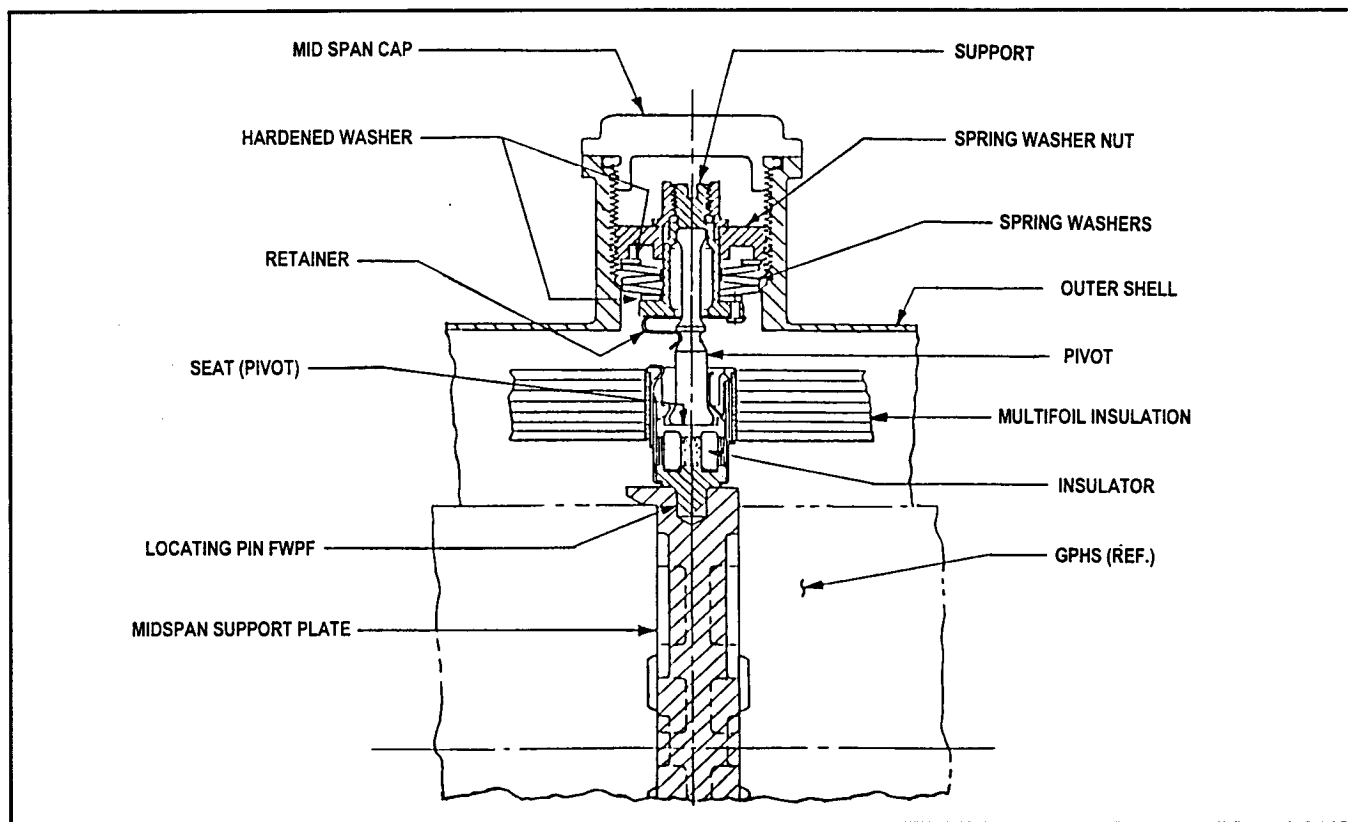
Figure 4.1.2-4. Midspan Support

**Table 4.1.2-4. Components of the Midspan Support Assembly
(Reference LMMS Drawing 47D306036)**

Reference Drawing No.	Part Nomenclature
47B306039	Nut, Spring Washer
47C305147	Spring Washer
47B305102	Support
47B305291	Screw
47B305099	Pivot
47B305136	Barrier (Tungsten)
47B305121	Barrier (Iridium)
47B306524	Nut (Tool)
47B305123	Washer
47B305106	Spring, Centering

**Table 4.1.2-4. Components of the Midspan Support Assembly
(Reference LMMS Drawing 47D306036) (Cont'd)**

Reference Drawing No.	Part Nomenclature
47C306031	Retainer Assembly
47B306034	Seat
47B305103	Insulator
47C306027	Can Assembly
47C306033	Pin, Locating
47B305517	Washer

which matches the end of the pivot. All these pieces are stacked in an iridium can, packed with fibrous insulation, and trapped on the end of the pivot by wiring the ears of the iridium can with Inconel safety wire. The spring washer assembly consists of a spring washer guide with three spring washers stacked in series and loaded by means of an Inconel-X750 nut threaded into a helicoil installed in a midspan boss in the outer shell. The nut is locked in place by a lock nut threaded into the same boss. The pivot is fitted inside the spring washer guide and contacts a matched spherical seat. These pieces are held together by an Inconel-X750 centering spring, wired with Inconel safety wire.

4.1.2.3 Thermopile

The thermopile is an assembly of multifoil insulation, molybdenum inner frame, two inner frame supports, 572 unicouples, and cold side electrical connecting straps. The multifoil insulation surrounds the heat source and is penetrated by the unicouples. Most of the radiated heat from the heat source is collected by the hot shoes and passed through the unicouple where it is converted into electrical power. The waste heat passing through the unicouples and bypassing the unicouples through the insulation is conducted through the outer shell to radiating fins. The multifoil lay up was modified for the two RTGs fabricated for the Cassini mission.

4.1.2.3.1 Heritage from MHW

The design of the Cassini RTG thermopile is based on the design of the MHW-RTG thermopile. The Cassini and GPHS-RTGs are smaller in diameter but about twice as long

as MHW-RTG and have almost twice as many unicouples and generate almost twice the electrical power. The unicouples are identical, the multifoil insulation is made of the same numbers of molybdenum foils and Astroquartz cloth. Because of the length, the insulation in the Cassini and GPHS-RTGs are made in five sections while MHW-RTG insulation was in three sections. MHW-RTG required a degaussing loop around the circumference to compensate for its single electrical circuit in the thermopile. The Cassini and GPHS RTGs on the other hand, have two electrical circuits, opposing each other. The intent is to balance the magnetic fields generated by the two circuits.

4.1.2.3.2 Silicon Germanium Unicouple

The silicon germanium unicouple is the same as that used on the GPHS program. The unicouple, as shown in Figure 4.1.2-5, consists of an 85 weight percent silicon molybdenum heat susceptor, or hot shoe, to which the N and P couple legs were bonded. Two compositions of silicon-germanium are used in the legs, 78 atomic percent silicon for most of the length and a short 63.5 atomic percent section at the cold end. The lower content segment is used to provide improved matching for thermal expansion of the bonded parts. The two SiGe legs and their corresponding sections of the hot shoe wae doped to provide thermoelectric polarity; the N-type material is doped with phosphorus and the P-type with boron. The SiGe thermoelectric elements are coated with silicon nitride (Si_3N_4) to reduce sublimation at operating conditions. The silicon alloy couple is bonded to a cold stack assembly of tungsten, copper, and alumina parts which separate the electrical and thermal currents. The thermal current crosses the alumina insulator and passes through the radiator attachment into the outer shell. The electric current flow between couples is shunted through separate copper straps bonded to each leg assembly. These straps are riveted together after insertion into thermopile assembly to form the thermopile electrical circuit. The cold stack is designed to flex laterally to ensure unicouple load sharing from insulation loads and thermal deformations. The unicouples are electrically insulated by several layers of Astroquartz yarn tightly wound around the couple legs and by an alumina wafer beneath the hot shoe, separating it from the foil insulation.
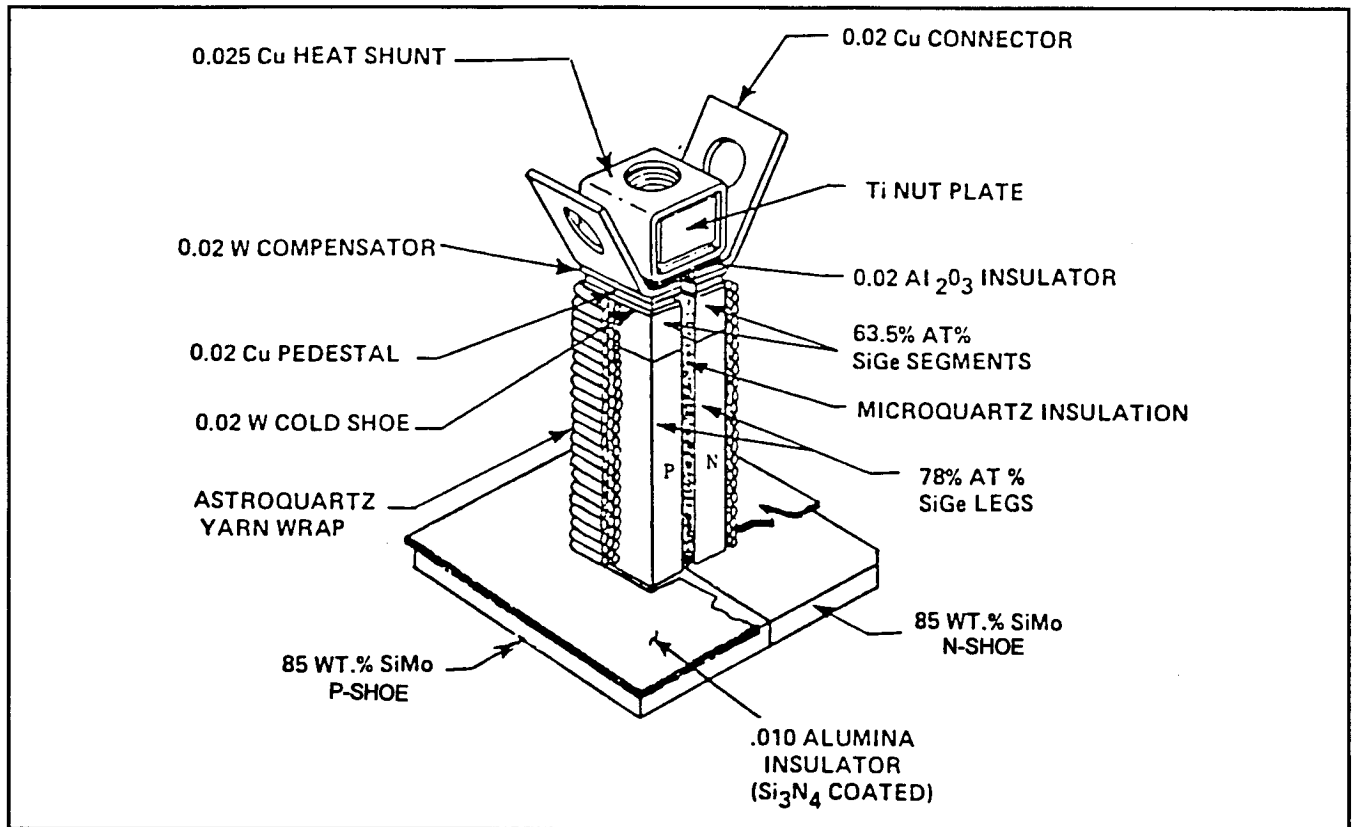
Figure 4.1.2-5. Silicon Germanium Unicouple

Instrumented Silicon Germanium Unicouple

The 18-couple modules use a special configuration of the unicouple that is instrumented with a thermocouple. An instrumented unicouple has a tungsten/rhenium thermocouple embedded in the hot shoe at the base of , and adjacent to, the "N" leg. The wires extend up the corners of the "N" leg, trapped between the first and second layers of yarn, as shown in Figure 4.1.2-6. Cold side thermocouples are formed by twisting the thermocouple wires, spot welding to a nickel shim and riveting the shim in place with the same rivet used to connect the unicouple straps together. From the point where the hot shoe wires exit the wrap at the cold end of the unicouple and for the entire length of the cold end wires, they wae sleeved in Varglas until their connection to tungsten/rhenium connector pins. The insulated thermocouple wires are tied to the electrical connector straps for support.
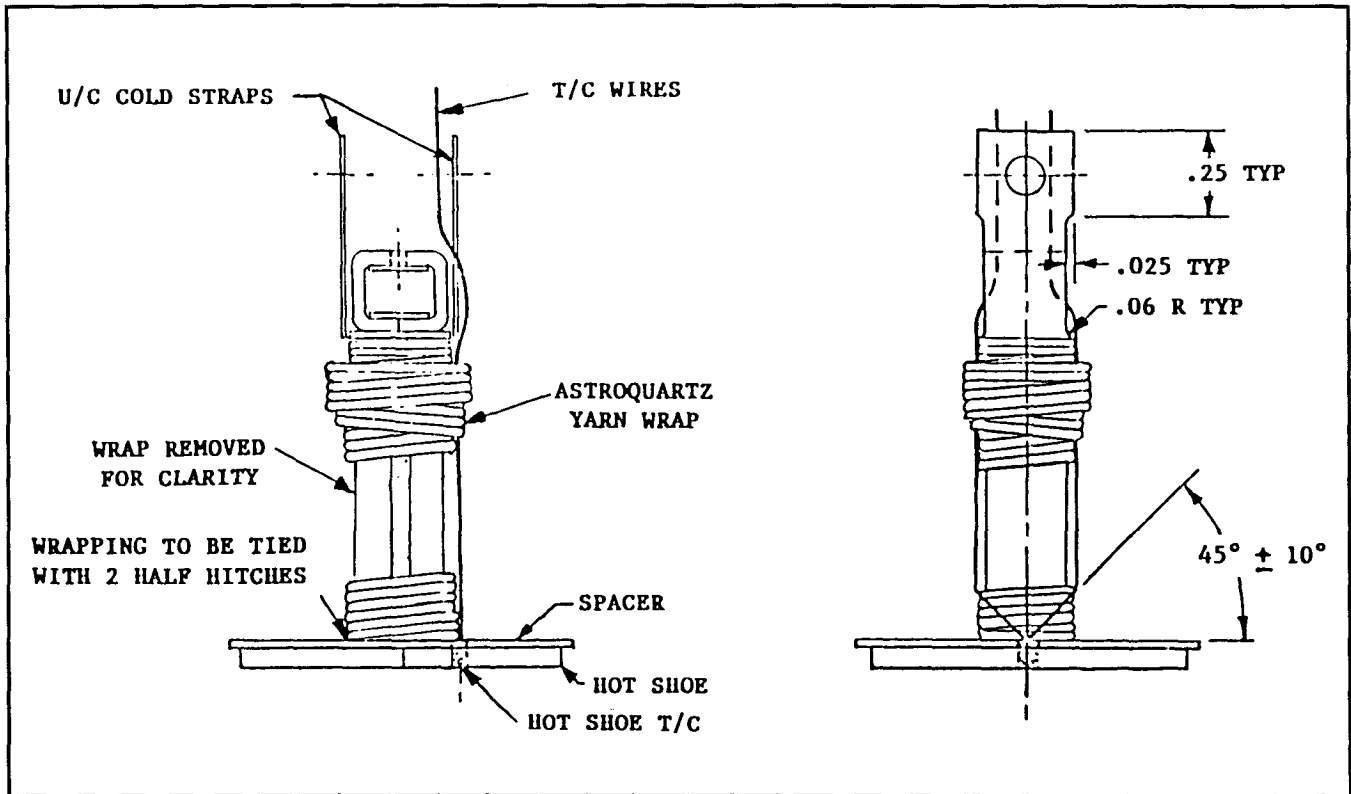
Figure 4.1.2-6. Instrumented Silicon Germanium Unicouple

4.1.2.3.3 Insulation System

The multifoil insulation assembly, shown in Figure 4.1.2-7, consists of 60 layers of molybdenum foil and 60 layers of Astroquartz (SiO_2) cloth with two types of cloth weave alternately laid up on the molybdenum inner frame assembly. The inner frame is made up of six 0.01 inch thick octagonal frames, with 0.01 inch thick back-to-back flanged ribs at each corner. The eight sides are covered with 0.0022 inch thick foil panels. Each side panel has two rows of thirty-six, 0.75 inch diameter lightening holes, separated into five groups by the frame locations. There is also one 1.0 inch diameter midspan hole at the center of each panel. The frames, ribs and panels are assembled using 0.01 inch thick clips and 0.032 inch diameter rivets to form a 6.25 inch regular open octagon frame, 40.0 inches long. All materials are molybdenum. The molybdenum insulation foils are trimmed, approximately 8.0 inches long, punched with square holes and folded, to form a fifth of two sides of the octagon's length. The Astroquartz cloth is also trimmed and punched with

2 LAYERS FIBROUS
ASTROQUARTZ CLOTH

INNER MOLY FRAME
2.2 MILS THK

LEVEL 1
LEVEL 2
LEVEL 3
LEVEL 4
LEVEL 5
LEVEL 6
LEVEL 7

LEVEL 1
10 LAYERS MOLY FOIL 0.3 MILS THK.
10 LAYERS FIBROUS ASTROQUARTZ
LEVELS 2 AND 3
11 LAYERS MOLY FOIL 0.3 MILS THK.
11 LAYERS FIBROUS ASTROQUARTZ
LEVEL 4,5,6 AND 7
7 LAYERS MOLY FOIL 0.3 MILS THK.
7 LAYERS FIBROUS ASTROQUARTZ

RETAINING BAND
MOLY 2.2 MILS
(3 PLACES)

2 LAYERS FIBROUS
ASTROQUARTZ

OUTER LAYER
MOLY 2.2 MILS THK
(END SECTIONS ONLY)

Longitudinal View

CORNER GAP
TYPICAL FOR
ALTERNATE
LAYERS, LEVEL 7

CORNER GAP
TYPICAL FOR
ALTERNATE
LEVELS 1-6

CORNER GAP
TYPICAL FOR
ALTERNATE
LAYERS

LEVEL 7

LEVEL 7

LEVEL 6

LEVEL 6

FOIL LAYER TYP

FOIL LAYER TYP
CLOTH LAYER TYP

CLOTH LAYER TYP

OVERLAPPING
LEVELS
LEVELS 1-6

OVERLAPPING
LAYERS

OVERLAPPING
LAYERS
LEVEL 7

INNER MOLY FRAME

INNER MOLY FRAME

F6 & PREVIOUS RTG'S

F7 & SUBSEQUENT RTG'S

Cross Section View

Figure 4.1.2-7. Multifoil Insulation Assembly

square holes. With the aid of a lay-up fixture these parts are then laid up on the inner frame assembly starting with cloth and alternating with foil for ten layers each. Each layer of foil was rotated circumferentially, so that the fold in each successive layer covers the gap in the previous layer. This lay up procedure is continued along the length of the inner frame until there are five sections, each with ten layers of foil and cloth, butted together along the entire length of the frame. This was the first layer of insulating foil. The six other levels of insulation cloth and foil are laid up in similar fashion, with each successive level overlapping the circumferential joints between sections of the previous level.

For the E-6 thermopile, each level was also shifted circumferentially by one flat (45°) from the underlying level such that the fold in each successive level covered the gap in the previous level.

The cloth used in all sections of the first three levels was 0.004 inches thick close weave cloth (Astroquartz #507, M9A2). Improper fit of the foil panels over the alignment pins of the E-6 thermopile was experienced at levels 4, 5, and 6 due to tolerance stack up and a drawing error in panel dimensions. The cloth thickness and distance between the fold-line and centerline of the rows of punched holes (dimension C) were changed from that specified on the assembly drawing by MRB direction. For level 4, the first three cloth layers were changed from 0.008 inches thick open weave (Astroquartz #594, M9A3) to 0.004 inches thick M9A2 and the remaining four cloth layers were 0.008 inches thick M9A3. An Engineering Change Notice (ECN RTG-0332) formally changed the cloth type for layer 1 from M9A3 to M9A2. For level 5, the first two cloth layers were changed from 0.008 inches thick M9A3 to 0.004 inches thick M9A2 and the remaining five cloth layers were 0.008 inches thick M9A3. In addition, the first cloth layer was installed without a 45° offset from the underlying level 4 panel sections as specified on the assembly drawing. For level 6, the cloth for all layers 1, 2, and the end sections of layer 3 were changed from 0.008 inches thick M9A3 to 0.004 inches thick M9A2. Also, cloth panels at layer 1 were not offset 45° from the underlying level 5 panel sections. For level 7, the first four cloth layers were 0.008 inches thick and the last two or three cloth layers were 0.004 inches thick.

Changes to the foil insulation lay up were formally made by an Engineering Change Notice (ECN RTG-0372) to reduce the "bunching" effect at the corners and tearing of the panels due to stretching the foil over the alignment pins. The manufacturing planning was updated and was used to fabricate the E-7 foil insulation assembly. The notched corner of the cloth panel was oriented to match the position of the notch in the subsequent foil panel. Each layer of cloth and foil within a level was shifted one flat (45°) with respect to the previous layer of cloth and foil such that the fold covered the gap between the previous layer. The cloth thickness was not changed from that specified on the 47J305231G1 assembly drawing.

Circumferential 0.0003 inch thick molybdenum bands are placed at each section joint around the outside of levels 3, 5, and 7. Each band is spot welded at each corner to one section only. Nickel shims are sandwiched between the band and foil to weld the molybdenum bands. (The rippling or bunching of the foil and cloth layers after spot welding the retaining bands after levels 3 and 5 on the E-6 insulation assembly also confirmed a panel misfit problem discussed above).

The end foil panels are notched and folded radially inward at 90°. A 0.0022 inch thick molybdenum ring is placed on top of the level 2 inwardly folded cloth and foil. The folded cloth and foils of level 3 are held in place by a similar ring spot welded to the circumferential band by 16 molybdenum clips and nickel shims. This spot welded assembly also constrains levels 1 and 2. Levels 5 and 7 had similar ring, clip, shim, and band spot welded assemblies to constrain the remaining layers of cloth and foil. The first layers of cloth and foil in levels 4 and 6 do not have flanges. Overall thickness of the total insulation assembly is approximately 0.70 inch.

An analysis on the possible impact of insulation modifications on RTG performance and a summary of the E-6 foil insulation fabrication history are detailed in Cassini Memo No. 251, Reference 4.1.2-1.

4.1.2.3.4 Thermopile Assembly

As the next step in assembly of the thermopile, the completed octagonal insulation assembly is removed from its assembly fixture and mounted to the thermopile assembly fixture. Two layers of 503 Astroquartz cloth are laid against the hot side molybdenum insulation foil to provide added electrical insulation between the foil and the hot shoe. Each completely wrapped unicouple assembly is individually installed through 572 of the 576 rectangular holes in the thermopile insulation from the inside, using the hot shoe chamfer to orientate the unicouples in an "N - P" sequence. The inboard rows adjacent to the +X and - X axes have only 17 unicouples each. The other hole in each row is taken up with the posts for the inner frame support. Two more layers of Astroquartz cloth are laid against the cold side foil, and tied in place with Astroquartz yarn.

Electrical Circuit

The thermopile electrical circuit as shown in Figure 4.1.2-8 was formed by straightening the unicouple copper electrode straps and riveting nineteen "N" straps to "P" straps in sequence, together with redundant cross-over straps. This forms 16 two string series-parallel circuits. Copper jumper straps were used to join the 8 inboard strings in series; similarly, the outboard strings are joined in series. This circuit permits continued converter operation in the event a single unicouple fails in either the open or short mode. Two adjacent unicouples would have to fail open to cause complete loss of power from one of the two circuits. Four main power straps redundantly connect the inboard and outboard strings of unicouples and terminate at the inboard end of the thermopile with two positive and two negative straps. Flexible, stranded, sleeved wires connect these straps with a hermetically sealed, five pin power output connector. The fifth pin is used for a ground connection to the outer shell of the converter. The circuit is designed so that the inboard half is electrically a mirror image of the outboard half. This reduced the magnetic fields and negates the need for a degaussing loop. All connecting straps are covered with Astroquartz insulation as required to prevent subsequent shorting to the outer shell. The completed thermopile, as shown in Figure 4.1.2-9, is then ready for insertion into the outer shell.
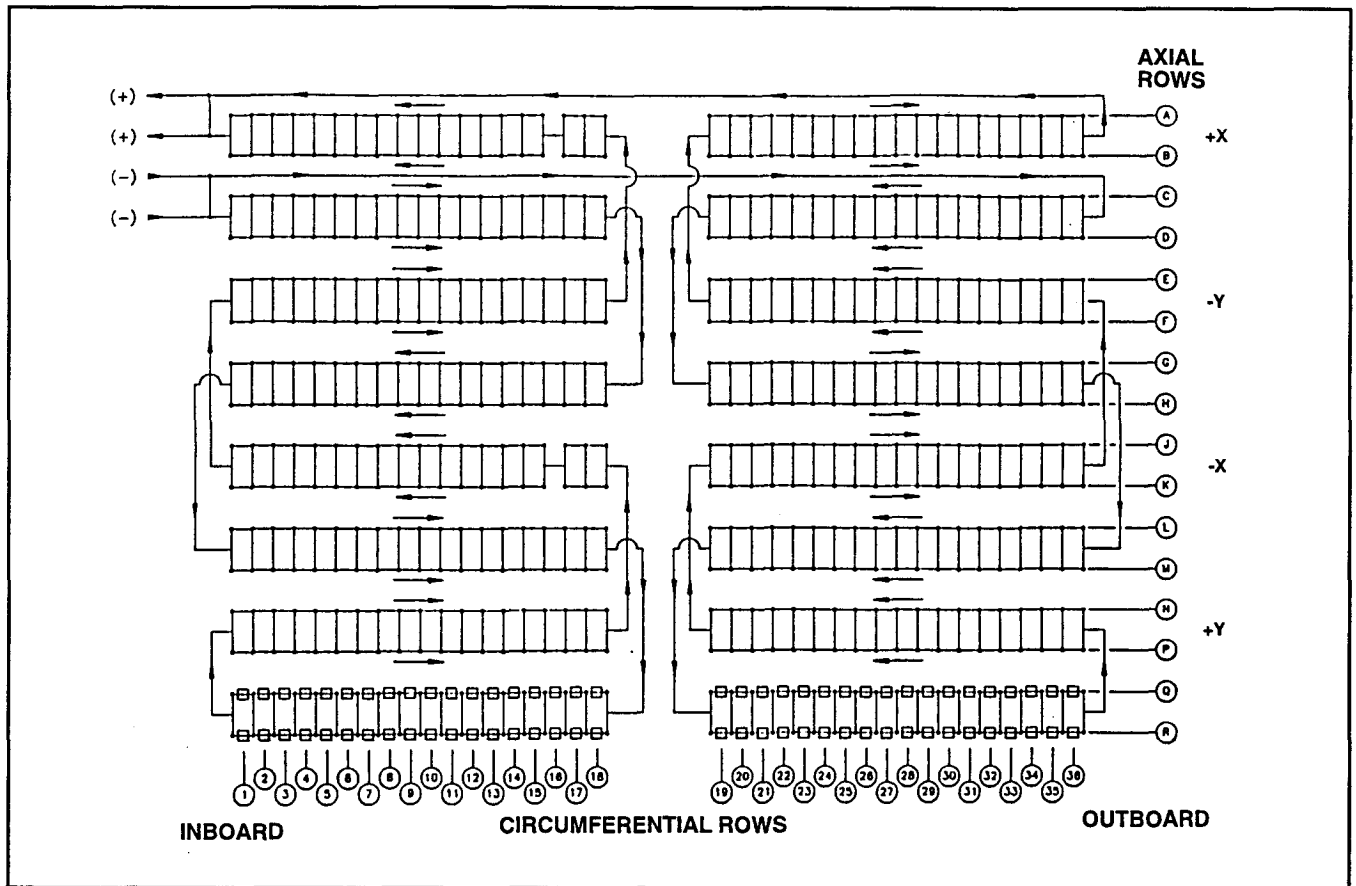
Figure 4.1.2-8. Thermopile Electrical Circuit
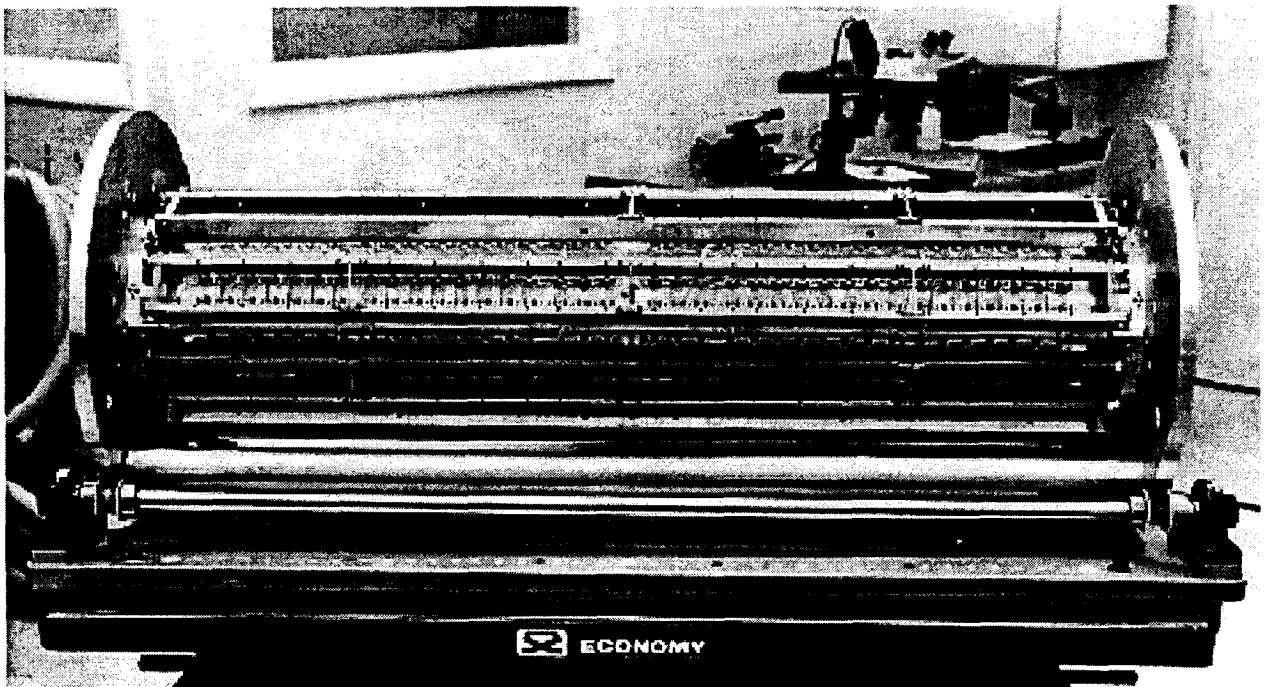
Figure 4.1.2-9. Thermopile Assembly

Electrical Interconnect

Pop rivets have been the fastener originally used to make the strap to strap electrical connections in the thermopile assembly 47J305306G1. Pop rivets were used in the MHW RTG design and were subsequently incorporated into the GPHS-RTG design.

Continuous monitoring of pop rivet joints in the E-6 thermopile showed that, in general, rivet joint resistances were increasing. Approximately 10% of the total 668 pop rivet joints in E-6 had changes in resistance that were higher than desired with the initial (just after installation) resistance in the 0.1 to 0.2 mΩ range increasing to a typical range of 0.8 to 1.5 mΩ after several weeks. In some instances, high resistance pop rivet joints within the E-6 thermopile also exhibited unstable behavior with measured values changing both high and low in the 0.2 to 1.0 mΩ range. The realization of a pop rivet joint resistance problem caused a significant delay in the assembly of the E-6 thermopile and initiated parallel activities to:

a) evaluate the impact of high resistance joints on RTG performance;

b) remove and replace the pop rivets from the most undesirable high resistance joints;

c) optimize the installation (pulling and swaging forces) parameters of the pop rivet used in the E-6 thermopile to achieve improved electrical performance;

d) seek alternate rivets, both pop and solid, with improved performance; and

e) determine the cause for the instability/increase of rivet joint resistance.

An engineering evaluation of high resistance joints in the E-6 thermopile determined that these joints would not have a significant impact on RTG power output. If all (688) rivet joints had a resistance of 1.0 mΩ, the RTG power loss would be 5 watts. Relating this to the E-6 thermopile, with approximately 60 high resistance joints, the power loss was estimated to be only 0.5 watts, which is less than 0.2% of the total RTG power output. Furthermore, it was assessed that rivet failure resulting in an open circuit was not credible. This analysis concluded that pop rivet replacement was not required. Despite this conclusion, limited rivet replacement was performed as a conservative measure. The principal motivation for

replacing rivets was the concern that rivet joint resistances would increase during RTG vibration testing. Replacement was a precautionary measure to prevent future test data interpretation problems. A total of 64 pop rivets were replaced in the E-6 thermopile. Replacement work was halted when testing work on rivet joint samples provided an understanding of the problem's cause and demonstrated that high resistance joints were returned to acceptably low resistance values after being subjected to ETG/RTG thermal-vacuum (and inert) processing environments. Testing showed the increase of rivet joint resistance to be related to a connecting strap surface oxidation (chemical) process which was reversed by thermal vacuum processing. These test results eliminated the concerns of rivet joint resistance variation during vibration testing since the structural (mechanical) integrity of the high resistance rivet joints was determined to be sound.

A development task was completed which demonstrated that a modified MS20615-4CU3 solid copper rivet could be successfully used in place of pop rivets to connect the electrical straps within the GPHS-RTG thermopile assembly. All the tooling and processes needed to install and remove solid rivets were developed and functionally tested. Fabrication of representative samples showed that solid rivets produce joints with the desired low and stable resistance characteristics. Supporting analysis showed that the weight increase of modified solid rivets in comparison to pop rivets was insignificant. Despite the successful development and demonstration results, the implementation of solid rivets into the thermopile design for the Cassini program (units E-7 and subs) was deemed unnecessary. Concurrent improvement work completed on pop rivets has resulted in achieving acceptable electrical performance from this fastener. As a consequence, solid rivets were not needed as an option.

4.1.2.4   Outer Shell

The outer shell assembly consists of a flanged cylinder with 8 radial fins and four midspan bosses. Rows of holes on both sides of each fin are used to mount the unicouples and hot frame supports. Other components such as the electrical power connector, four Resistance Temperature Devices (RTDs), Gas Management System (GMS), and Pressure Relief Device (PRD) are mounted to the shell and sealed by the use of C-seals. Likewise the end

flanges and midspan bosses also provide for c-sealing surfaces. The inboard flange has four barrel nuts mounted at the four main load carrying ribs. These are used to mount the GPHS-RTG to the spacecraft. For a list of components, see Table 4.1.2-5.

Table 4.1.2-5. Components of the Outer Shell
(Reference LMMS Drawing 47J305033)

Reference Drawing Number	Part Nomenclature
47D305095	Electrical Receptacle Assembly
47D305293	Gas Management Assembly
47C305292	Bracket, GMS
47E305744	RTD Installation
47B305963	Washer - Connector
47C305934	Mounting Plate Assembly - PRD
23003754	Adapter Plate
47B305935	Vent Chamber
47J306130	Shell and Fin Assembly
47D305036	Dome Inboard
47D305302	Dome Outboard
47C302638	C-seals
23003764	PRD Assembly
23009127	Bracket, RTD

4.1.2.4.1 Heritage from MHW

Many design features of the outer shell such as the unicouple mounting, fin/ribs, electrical power connector, RTDs, PRD, GMS, end domes and C-seals are the same as, or similar to, the features on the MHW converter. The unicouple mounting is the same as the GPHS-RTG. The short radial fin/ribs on MHW are integrally machined with the shell. The fin/ribs for GPHS and Cassini extend 4.0 inches beyond the shell and consist of short stubby radial ribs integrally machined into the shell, with 3.50 inch radial fins electron beam welded to the ribs. The mounting of the electrical power connector on Cassini is identical to that for GPHS and MHW. The connector is a 5 pin for Cassini and GPHS, two positive, two negative and a ground termination, whereas MHW had only 4 pins, two positive and two negative terminations. The RTDs are similar to the ones used on GPHS. There arre four RTD sensors on GPHS and Cassini and only three on MHW. The GMS for Cassini and GPHS is

the same as MHW except that the valve is mounted on standoffs on the cylindrical shell. On MHW the valve was mounted on the fin/rib. End domes with the exception of being smaller in diameter and aluminum, function the same as those of MHW. C-seals are clamped between the flanges of the domes and the flanges of the shell with the aid of screws passing through holes in the dome flanges and engaging helicoil inserts housed in the shell flange. Because the GPHS is designed to be mounted to the spacecraft by the inboard end, the dome screws in the inboard dome flange are countersunk to provide a flush mounting surface. Screws in the outboard dome flange are hex head, similar to those used in both dome flanges on the MHW-RTG. The PRD mounting is similar to the MHW-RTG. See Section 4.2.1 for details.

4.1.2.4.2 Design Features And Rationale

The outer shell is made from a 2219-T6 aluminum alloy forging and is approximately 8.50 inches in diameter and 42.50 inches long. Because no forging existed to accommodate these dimensions, a specially forged 8 foot long billet was manufactured by Weber. The billet was then cut in two, the outside machined to 12.0 inch diameter and the inside was cored to 4.0 inch diameter. This 48.0 inch long cylinder with a 4.0 inch thick wall was then heat treated to a T6 condition and quenched in a glycol/water bath to minimize the residual thermal stresses. After heat treatment of the cylinders, a simple sawcut test was performed to verify the absence of any residual stresses. If the sawcut opened or closed, there were residual stresses that must be relieved. Upon completion of a satisfactory sawcut test, a 4.0 inch long, ring-shaped prolongation was removed from one end of one forging in each lot. Specimens were taken from the ring section in an axial, tangential and radial direction and tested to verify the mechanical properties were compatible with the values listed in Table 4.1.2-6.

Table 4.1.2-6. Mechanical Properties

Direction	Tensile Strength, Minimum, PSI	Yield Strength at 0.2 Percent Offset, Minimum PSI
Axial	54,000	36,000
Tangential	55,000	37,000
Radial	52,000	35,000

The forgings were sent to Speedring to be numerically machined in incremental steps to obtain the thin walled, ribbed cylinder approximately 8.50 inches diameter and 42.50 inches long with inboard and outboard flanges and a midspan ring. The eight radial ribs, approximately 0.50 inches high and 0.055 inches thick, run the full length of the converter shell except when interrupted by the midspan ring and four midspan bosses equally spaced around the circumference, and located on the four main load bearing ribs at the midspan ring. Each boss is provided with an internal C-seal groove at its entrance. A large threaded helicoil insert is installed in each of the four bosses. Each rib was paralleled on both sides by a row of 36 holes. These holes are adjacent to the fins and are used to mount the unicouples. Four of these holes are used for the inner moly frame supports. There are three other through holes in the converter shell. At the inboard end are holes for the electrical power connector and the GMS. At the outboard end there is a hole for the PRD.

The spacecraft mounting holes in the inboard flange consist of a 0.386 inch diameter master hole, a 0.386 inch wide radial slot 180° opposed to the master hole, and two 0.410 inch diameter holes, 180° opposed to each other and each 90° from the master hole. Silver plated barrel nuts with stainless steel retainers are nested in the main load carrying ribs, in line with, and just outboard, of the four spacecraft mounting holes. These mounting holes and barrel nuts are all outside the sealed converter cavity. There are also two sets of two approximately 3/8 inch diameter mounting holes, spaced 180° apart on the X axis in the mid-ring, which could be used for spacecraft mounting. The inboard flange also had 20 #8-32 helicoil inserts interspaced with the mounting holes and a large internal C-seal groove. Twenty countersunk screws are used to clamp and seal the dome with the aid of the C-seal. The countersunk screws provide a flush surface for spacecraft mounting. The outboard dome is mounted and sealed in a similar manner, but with a bolt circle of 24 hex head screws and washers.

4.1.2.4.3 Radiation Fins

The fins are machined from aluminum 2219-T87 plates. These fins were approximately 18.0 inches long and 3.50 inches wide. The 18.0 inch length is divided into five sections by 3.0 inch long relief slots cut across the 3.50 inch width from the fin tip. At the base of each

slot is a 0.25 inch diameter hole. A 0.19 inch diameter flow passage with a 0.055 inch weld prep runs continuously along the entire length of one edge, with side ports at each end. The thickness of the fin tapers across the width from 0.055 at the flow passage to 0.015 at the tip.

The flow passages are gun bored through the 18.0 inch long fin. In order to accomplish this, the vendor required a precisely machined plate 0.472 x 5.000 x 22.00 long with sides flat and parallel within 0.002 inches and all sides free of scratches and gouges. After gun boring, the plate is machined to provide the thin wall flow passage and tapered fins. The converter shell has a built-in active cooling system (ACS) which consists of an inlet/outlet manifold, flow passages at the base of each fin, and 0.25 inch diameter aluminum 6061-T6 tubing. Coolant fluid could be pumped through the manifold, externally mounted at the outboard end of the shell. From the manifold, the coolant splits into two serpentine flow paths through the fins in circumferentially opposite directions. The 0.25 inch diameter tubing joins the manifold to the fins and fins to each other via their side end ports. The two flow paths join at the -Y axis at the outboard end, where it is transported back to the manifold through a 0.375 inch diameter tube. Special fixtures, as listed in Table 4.1.2-7, are manufactured to protect, handle, weld, ship, and store the shell and fin/tube welded assembly, used to assemble and align the fins, tubes and manifold, ready for attachment to the shell. Tubes are welded to the fin side ports and the manifold. The tube-to-tube connections are only mated at this stage of the assembly. Each of the eight fins and tube assemblies are individually removed from this fixture and placed in the individual fin/tube support fixtures to provide access to the free tube ends for proof pressure testing with water at 800 psi. When all eight fin/tube assemblies have been successfully tested and reassembled to the weld assembly fixture, it is placed in the double walled wooden box. The shell is placed in the shell/fin assembly storage/shipment can and both items are shipped to the Ebtech Company for e-beam welding. The individual fin/tube assemblies are once again disassembled from the fixture and one-by-one reinstalled and e-beam welded. During the e-beam welding of the GPHS unit, the free edges of the fins warped because not enough heat sink material was provided.

Table 4.1.2-7. Shell and Fin Assembly Fixtures

Item	Uses
Individual fin/tube support fixture	Pressure test individual fin/tube assemblies.
Fin/tube weld assembly fixture	Weld tubes to fins. Align fins and tubing for attachment to shell. Shipment.
Shell and fin assembly storage and shipment can	Storage and shipment of shell and shell and fin assembly.
Rotational handling fixture	Radiographic inspection of E-Beam welds. Final tube/tube welds. Final proof pressure test of ACS. Clean ACS lines. Mask for painting. Paint. Airbake cure of paint.
Mounting plate and handling sling	100 hour vacuum bake-out. Etch exterior of shell/fin assembly.
Double walled wooden base	Shipment of fin/tube weld assembly fixture.

For the first Cassini units, copper heat sinks are attached to the shell and the fins. To protect the shell/fin assembly from the weld gun, copper shields are provided at the beginning for start-up and at the end for run-off. Back-up copper shields are also used behind the material being welded, in case of blow-through. The shell/fin assembly is mounted on the rotational handling fixture and the e-beam welds were inspected radiographically for defects. After passing inspection the units were placed in the shell/fin assembly storage/shipment can and the weld fixture was packed in the double walled wooden box and returned to Lockheed Martin. The units are again mounted on the rotational handling fixture, the final tube to tube welds are made and the ACS is proof pressure tested with water at 800 psi. The ACS lines are cleaned with water, blown dry and back filled with argon. The manifold is sealed with a GSE cover and gasket. The unit is removed from the rotational handling fixture and, with the aid of the handling sling, the shell is acid etched. The unit is reinstalled on the rotational handling fixture and the flanges, sealing surface, and

area for component mounting, etc. are masked for painting. The unit is painted with a silicone-base thermal control coating, PD-224, as specified in LMMS specification NS0060-05-25 and allowed to air dry at room temperature. Once again, the unit is removed from the rotational handling fixture, installed on the mounting plate, the ACS manifold cover is loosened and the unit transferred to the vacuum bakeout chamber where it is baked out in vacuum at 485°F for 100 hours. The unit is packaged in mylar or aluminized mylar film, mounted in the shell and fin assembly storage and shipment can, and is ready for component mounting.

4.1.2.4.4 Emissivity Coatings

The thermal control and material protective coatings used on the Cassini RTG external and internal surfaces were created to be stable for a period of 8.1 years at mission operating conditions after a storage life of 5.5 years, or 4.8 years operating life after 6 years of storage. These thermal control coatings were selected for their stability and durability. A new coating had to be developed for GPHS because the coating (Radifrax RC) used externally on the beryllium outer shell of MHW RTGs, was not compatible with the 2219-T6 aluminum material used for GPHS, because of the high temperature associated with the application of the coating. Emissivity tests were conducted on various coatings and the results are shown in Table 4.1.2-8, Part I. From these first tests, a GE silicone (B6A) gave the best emissivity measurements. However, hairline cracks were observed in the coating when aluminum plates were prepared for static charge tests. To correct the cracking problem, mica was added and this coating material became PD-113. Because of outgassing at operating temperatures and results from the electrostatic charging characterization, another 3% carbon was added to the PD-113. This coating became PD-224 and was the thermal control coating used externally on the GPHS-RTG. PD-113 and PD224 emissivity test results are shown in Table 4.1.2-8, Part II. PD-224 was also used on the internal dome surfaces. Tests conducted with the PD-224 coating showed that after initial outgassing that occurs during vacuum processing, outgassing continues, but at a greatly reduced rate with no measurable change in coating properties. The Qualification RTG, on life test at Mound

Table 4.1.2-8. Emissivity Tests

Part I		
Coating		*Comments*
Pyromark 2500	.88	Commercial Product
	.87	(Silicone)
(B6A)	.92	1.5% Carbon
GE	.90	
Clear Silicone	.80	
	.79	
B6A Modified	.80	Ceramic oxides instead
	.81	of Carbon Black
Part II		
PD 113	.92	Mica Added
	.906	1.5% Carbon
PD 224	.91	3% Carbon
	.90	

Laboratories from November 1984 through 1990, had accumulated approximately six years of operation with no abnormal change in the case temperature which indicates no degradation of the external coating. In addition, the coating samples used for the higher temperature excursion tests were in storage for four years and no degradation was detected. Therefore, no significant change in properties were expected in extrapolating the coating performance over the extended storage and mission duration. The thermal control coating (Radifrax RC) used on some GPHS internal components was a borosilicate-iron titanate, used externally on both SNAP-27 and MHW RTGs. The performance degradation observed on Voyager missions was such that it could be explained solely in terms of fuel decay and dopant precipitation, implying no significant degradation of emissive characteristics of the coating.

4.1.2.4.5 Alternate Paint Formulation

The silicone-based PD-224 paint used to achieve a high thermal emissivity on the exterior surfaces of the RTG outer shell and other parts was developed in 1980, using resins commonly available from General Electric at that time. To facilitate preparation of the paint, alternate sources of silicone resins were sought during the Cassini RTG program. Using Dow 805 and Dow 1-2530 silicone resins in place of the General Electric materials, a batch

of PD-224 paint was prepared and the paint was applied to samples for the purpose of qualification testing. These tests included measurements of thickness, solar absorptance, total emittance, and adhesion, both as applied and after exposure to thermal vacuum conditions at a temperature of 300°C and for various durations up to 400 hours. These tests verified that paint prepared using alternate silicone resins meets all qualification requirements. In addition, tests were conducted to demonstrate the shelf life of the prepared paint, after storage at room temperature for periods of six months and twelve months. All the tests were successful. For use on future programs, the specifications for PD-224 paint will be modified to permit the use of alternate silicone resins procured from Dow, and to permit a shelf life of twelve months for the mixed paint before being applied.

Table 4.1.2-9 summarizes the data from Engineering Tests (ETs) used to qualify alternate resins for the PD-224 paint. Preparation of the paint, except for the use of alternate silicone resins, was performed in accordance with specification NS0060-05-25, Revision G, "Material Specification, Coating, Silicone, High Temperature, PD-224." All test samples were prepared by painting in accordance with specification NS0060-05-24, Revision J, "Process Specification for the Application of a High Emissivity, High Temperature Silicone Coating."

Table 4.1.2-9. Summary of Paint Qualification Engineering Tests (ETs)

ET No.	Date	Title
5229	11/21/96	Preparation of PD-224 Paint Using Alternate Silicone Resins
5233	2/14/97	Absorptance and Emittance of Alternate PD-224 Paint after Vacuum Treatment at 300°C
5234	2/14/97	Preparation of PD-224 Paint Samples for Qualification Testing
5236	6/25/97	Six Month Shelf Life Test for PD-224 Paint (July 1997)
5237	6/25/97	Twelve Month Shelf Life Test of PD-224 Paint (January 1998)

Table 4.1.2-10 provides a summary of the sample test results to qualify the alternate paint formulation. In all cases, the measured solar absorptance and total emittance exceeded minimum specification requirements.

Table 4.1.2-10. Summary of Qualification Test Results

	As Applied	After Vacuum at 300°C *	After Six Month Storage	After Twelve Month Storage
Thickness (mils)	1.6 (Passed)	Not measured	2.0 (Passed)	1.0 (Passed)
Surface Finish	Passed	Passed	Passed	Passed
Absorptance				
Requirement	0.94 min	0.94 min	0.94 min	0.94 min
Test Samples	0.95, 0.95, 0.95	0.96, 0.96, 0.96	0.96, 0.96, 0.96	0.995
Emittance				
Requirement	0.88 min	0.88 min	0.88 min	0.88 min
Test Samples	0.94, 0.94, 0.94	0.93, 0.93, 0.93	0.94, 0.94, 0.94	0.915, 0.914
Adhesion	Passed	Passed	Passed	Passed

* Samples removed after 100 hours, 200 hours, and 400 hours exposure

4.2 NEW DESIGN ELEMENTS

Almost all of the GPHS-RTG design configurations used on the Cassini program are of heritage design, however, there are two exceptions. New designs were incorporated for the Pressure Relief Device (PRD) and for the RTD Cable Assembly. These new designs and their related development activities are described in the following paragraphs.

4.2.1 PRD

The PRD is a pressure relief device to vent the internal pressure of the converter. It attaches to a mounting plate bolted to the access boss on the converter shell with the use of an adapter plate. The PRD has two primary functions:

1. Maintain a seal, isolating the internal RTG from the air environment during all ground testing, handling, and launch pad operations.

2. Vent the RTG to space during the ascent period of launch, and provide an orifice large enough to maintain the converter internal pressure below a desired value during space operations.

The PRD assembly, as shown in Figure 4.2.1-1, consists of a housing, lance, adapter plate, and pressure activated bellows. The bellows is a heritage design from the MHW program PRD and has the same three springs as the GPHS-RTG program PRD. Similarly, the lance
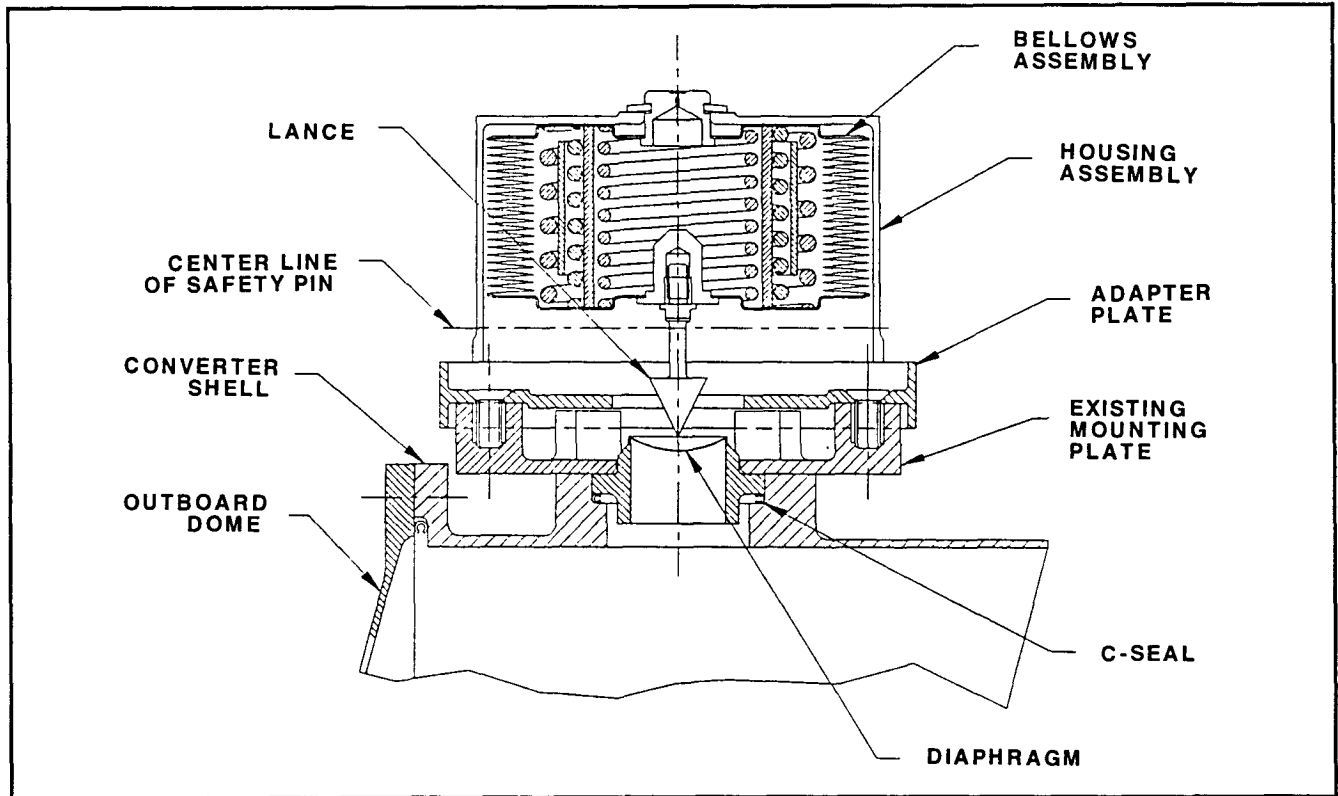
Figure 4.2.1-1. Cassini PRD Installation

Table 4.2.1-1. Components of the PRD (Reference Drawing 23003764)

Part Nomenclature	Reference Drawing #	Design History
PRD Housing Assembly	23003743	New Design
Bellows	47D303452	Heritage-MHW-RTG
Lance	47B305800	Heritage-GPHS-RTG
Safety Pin	47B305775	Heritage-GPHS-RTG
Quick Release Safety Pin	MS17986C338	Military Standard
Adapter Plate	23003754	New Design
Protective Cover Assembly	23003740	New Design
Mounting Plate Assembly	47C305934	Heritage-GPHS-RTG
Vent Chamber Assembly	47B305935	Heritage-GPHS-RTG

At atmospheric pressure, the evacuated bellows is compressed against one of its internal spring guides. During launch the bellows expands, forcing the lance through the diaphragm of the vent chamber assembly. This action creates a hole which vents the gas inside the PRD to space. A nut and bolt is used to prevent an inadvertent puncture during transport and ground handling operations. A standard safety pin with a quick release mechanism is used on the PRD during activities just prior to launch.

At atmospheric pressure, the evacuated bellows is compressed against one of its internal spring guides. During launch the bellows expands, forcing the lance through the diaphragm of the vent chamber assembly. This action creates a hole which vents the gas inside the PRD to space. A nut and bolt is used to prevent an inadvertent puncture during transport and ground handling operations. A standard safety pin with a quick release mechanism is used on the PRD during activities just prior to launch.

4.2.1.1 PRD New Design Overview

Several design improvements were made for the Cassini PRD as a result of experiences with previous RTG programs. Two view ports were added to the housing to allow verification of a gap between the safety pin and the bellows. The housing design included a tapped hole for mounting an accelerometer during dynamic testing. A hard, corrosion-resistant coating is applied to the inside surface of the housing to prevent galling by the bellows during operation.

The housing assembly uses captured titanium screws having solid film lubricant. The screws also have large fillet radii specified. This approach ensured that none of the PRD installation problems that occurred during the GPHS program (broken screw with Ulysses mission, extra washers with Galileo mission) would occur with Cassini.

The use of an adapter plate allows the PRD to be mounted to the GPHS mounting plate (reference Drawing 47C305934). This is an important consideration since a redesign of the mounting plate would have affected F-2 and F-5 RTGs and would have required refueling of F-5. The adapter plate uses different sets of holes to attach the storage cover assembly than those that are used to attach the PRD assembly. This eliminates PRD installation problems associated with the repeated use of inserts when the protective cover is installed and removed.

The quick release safety pin minimizes the radiation exposure of technicians preparing the RTG for launch. Its large handle makes visual verification of its removal prior to launch easier.

4.2.1.2 PRD Reliability Testing

The reliability of the PRD in venting the RTG internal pressure was established by the use of heritage design components, taking advantage of the extensive database of testing and flight experience from the MHW and GPHS RTG programs. A reliability demonstration program was conducted for the bellows assembly during the MHW program. These tests resulted in 34 successful diaphragm punctures by the bellows and included subjecting the bellows assemblies to mission defined thermal and dynamic environments prior to, and during, operation. Further reliability demonstration tests were conducted of the force capability of the springs used in GPHS-RTG, the same springs used in the bellows assembly. These tests consisted of measuring the stroke force of a PRD assembly (without a lance) 50 times at operating temperature.

Reliability analysis identified the quick release pin as a Category I Single Point Failure. No quantitative reliability goals for operations of the PRD were established. However, the likelihood of failure to remove the quick release pin is very low. Compensating provisions which prevent this event from occurring include: (1) the pin has a large handle and is visually obvious when it is in place, (2) written instructions for removal are provided in the pre-launch check list, (3) operators are trained in this procedure, and (4) supervision and QA verification are present during the operation of pin removal.

For the Cassini program, several engineering tests were conducted to expand the understanding of the Cassini PRD. A bellows force characteristic test was conducted to measure the available force provided by the bellows. A corresponding lance-diaphragm test was conducted to measure the force required by the lance to penetrate the diaphragm. Finally, a series of tests were conducted to assess the capabilities of several candidate coatings for the inside surface of the PRD housing. The conclusion of these tests shows a large margin exists (at least a factor of +1.18) between the force available to puncture and the force needed to puncture the diaphragm. A description of these tests follows.

Bellows Force Characteristic Test

Force tests were performed on the engineering bellows, S/N 38. The purpose of the tests was to characterize the bellow's available force at different displacements and external pressures at both room temperature and operating temperature (180°C). Tests were

conducted with displacements between 0.001 and 0.540 inches and with pressures between 0.1 and 13+ psia. An adapter assembly was screwed into the bellows in lieu of the lance. The bellows was enclosed in an insulated furnace from which the adapter assembly protrudes. The entire fixture, including the load cell, was placed in a vacuum chamber. A temperature controller connected to one of the heaters maintained the bellows' temperature during the elevated temperature tests. The other heater was controlled by a Variac. Figure 4.2.1-2 shows a schematic of the entire test setup.
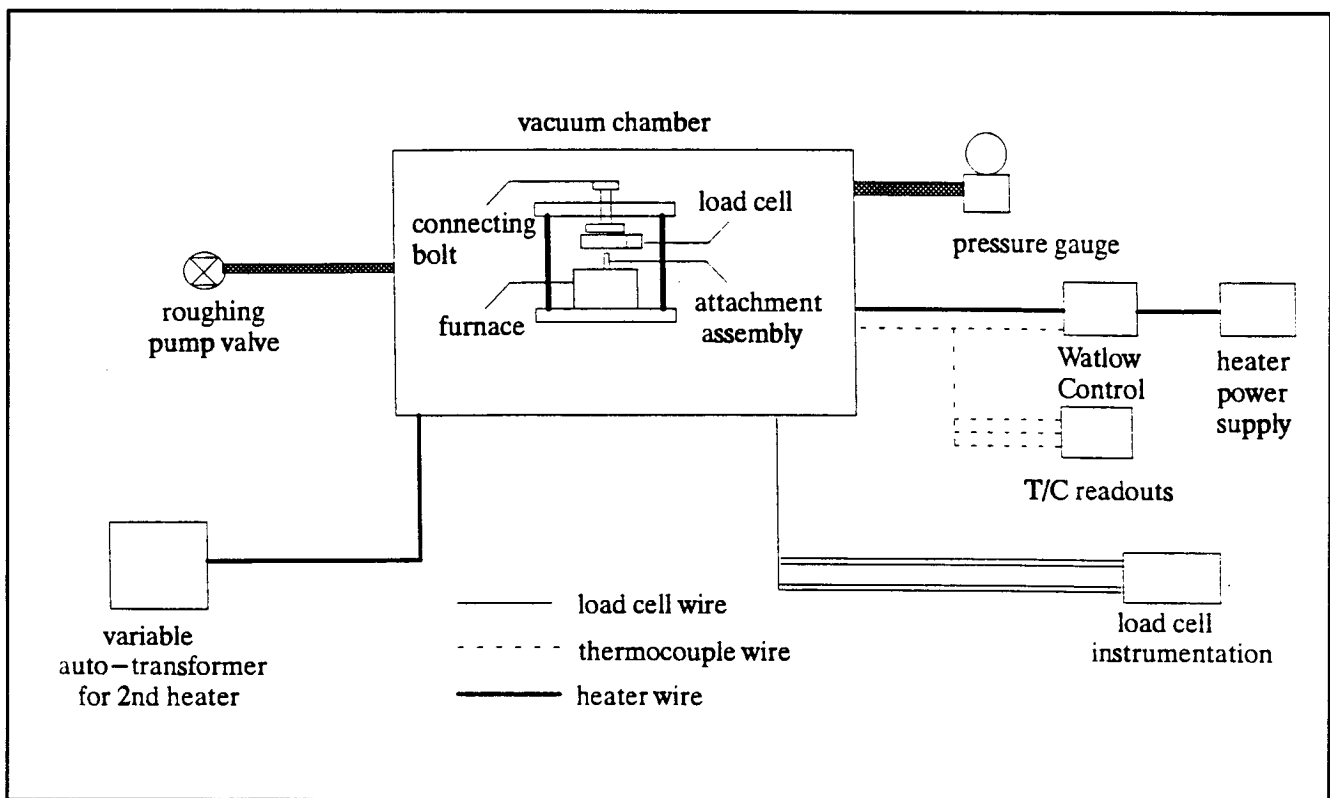
Figure 4.2.1-2. PRD Bellows Force Characteristic Test Schematic

Figure 4.2.1-3 shows the force generated by the bellows for the room temperature tests. Also shown for comparison are the results of the lance-diaphragm tests. Similarly, Figure 4.2.1-4 shows the force generated by the bellows for the operating temperature tests. In both figures it can be seen that sufficient force is generated by the bellows once it gets down to an external pressure of 4 psia. These plots provide an indication of the margin that is available for puncture along the entire stroke of the bellows.
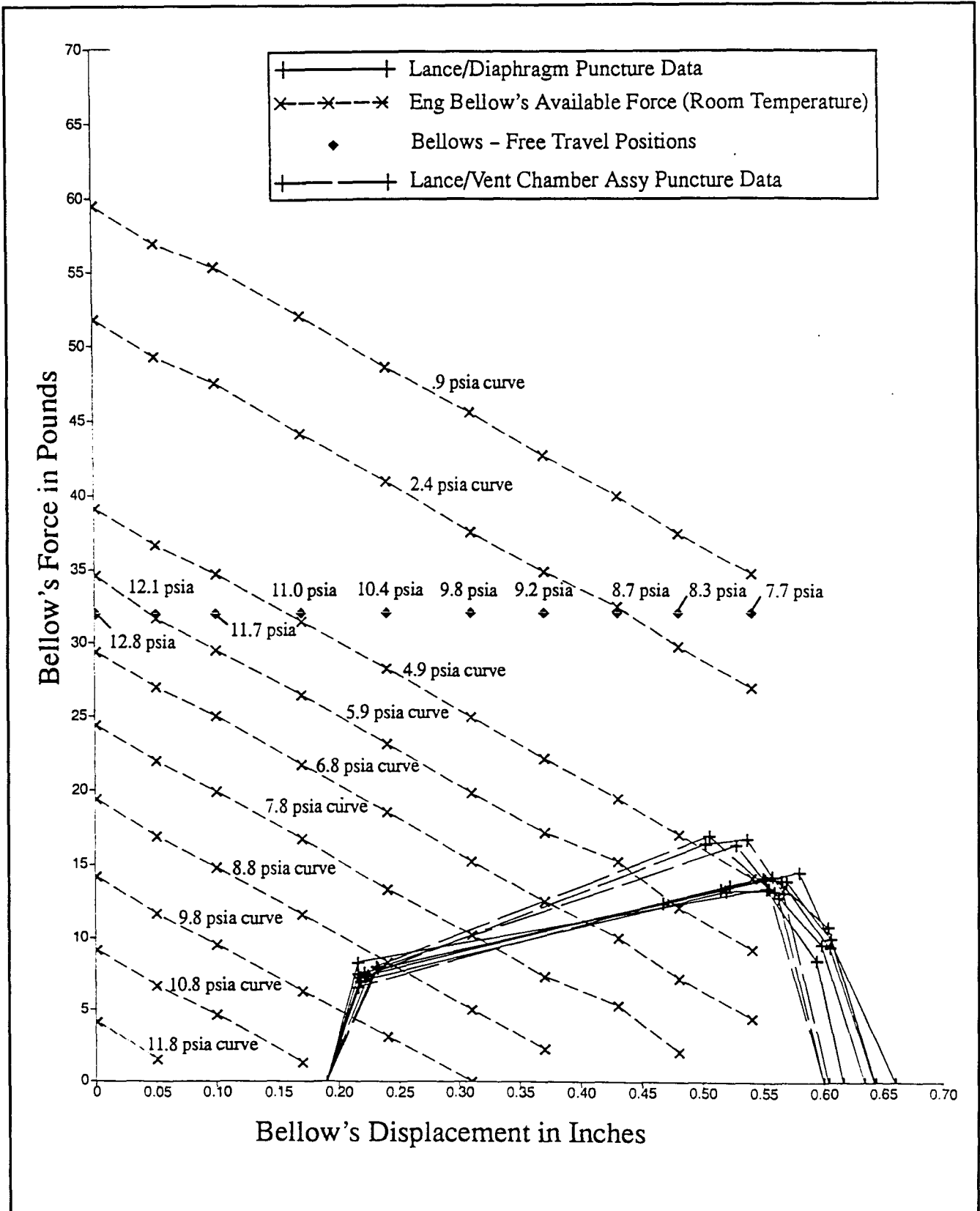
Figure 4.2.1-3. Bellows Force Test Room Temperature Data
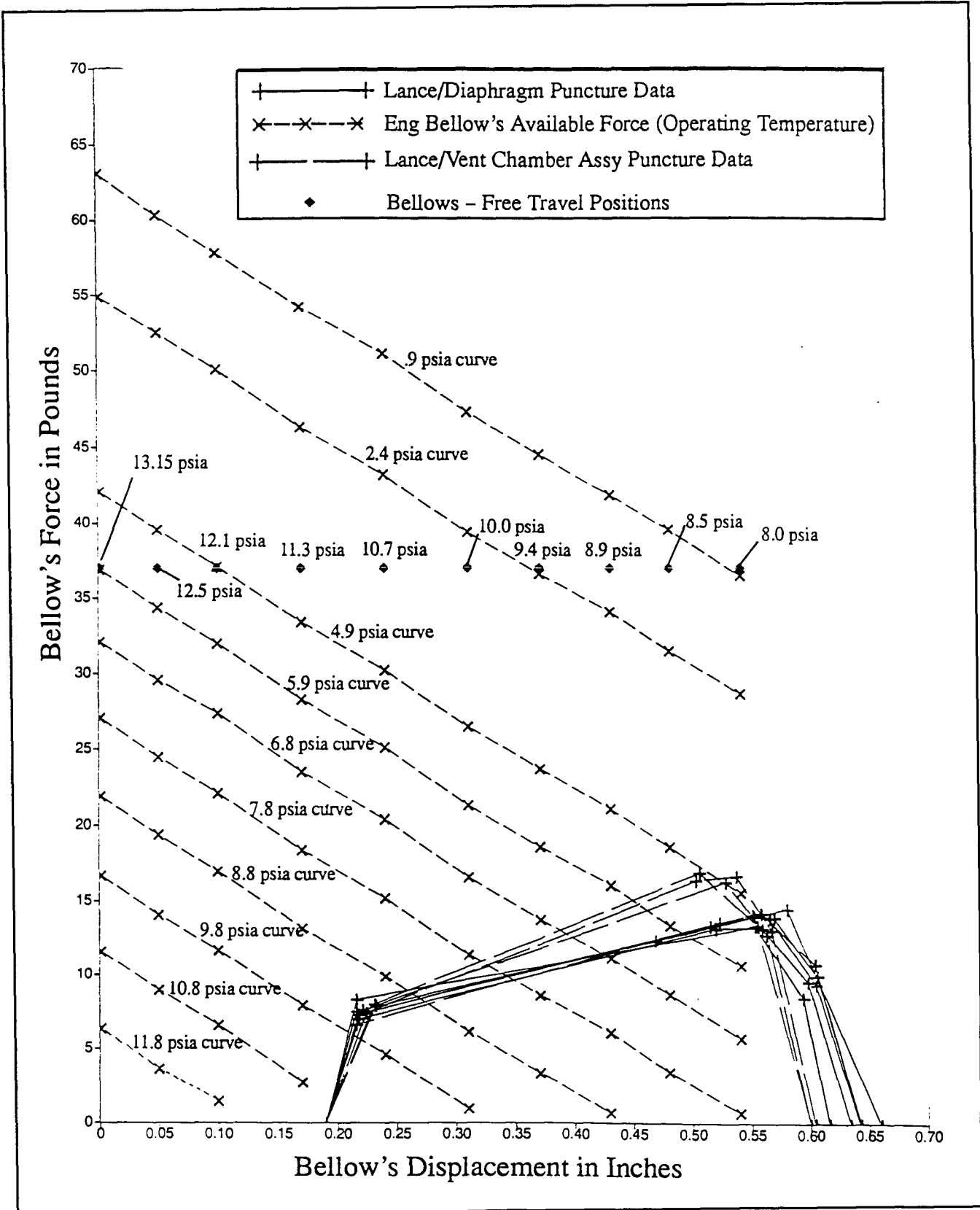
Figure 4.2.1-4. Bellows Force Test Operating Temperature Data

Lance-Diaphragm Puncture Tests

Five flanged diaphragms from lot CC11337 were punctured during these tests. Four vent chamber assemblies (VCA) were punctured (including three during lot acceptance testing). Both setups used a Tinius Olsen 10000 machine. The purpose of this test was to determine the force required to puncture and penetrate fully two different diaphragm mounting configurations(welded and clamped) as well as to measure the size of the holes in order to verify VCA conductance compared with specification requirements.

For all tests but one, the Tinius Olsen traveled at a constant rate of 0.02 inches/minute while the lance punctured. In the case of diaphragm S/N 2, the speed of puncture was increased to 14.4 inches/minute to demonstrate that the puncture force did not differ significantly with speed. Three different lances were used for the test. Two lances were from PO HHMC70293, one considered prime and one designated "engineering use only." The other lance was a residual lance from the GPHS-RTG program.

Table 4.2.1-2 lists the peak forces reached during the tests as well as the puncture travel and area. The puncture travel is the distance the lance moved from first contact with the diaphragm until the force returns to zero after puncture is complete. All of the puncture areas were calculated by taking the area of the triangle defined by the three corners of the puncture hole for each diaphragm/VCA and subtracting 0.003 in^2 which is the approximate area of the curls that remain after puncture. The average distance between corners of the puncture holes created by the residual, engineering, and prime lances were 0.420, 0.421, and 0.437 inches, respectively.

Table 4.2.1-2. Lance-Diaphragm Puncture Test Results

	Peak Force lb$_f$	Puncture Travel in	Puncture Area in^2	Lance Used
Diaphragm S/N 1	14.1	0.45	0.074	Engineering
Diaphragm S/N 2	14.5	0.47	0.074	Engineering
Diaphragm S/N 3	13.2	0.44	0.074	Engineering
Diaphragm S/N 4	14.0	0.45	0.074	Engineering
Diaphragm S/N 15	13.4	0.43	0.073	Residual
VCA S/N 1	14.2	0.45	0.074	Engineering
VCA S/N 4	16.7	0.41	0.080	Prime
VCA S/N 5	16.3	0.41	0.080	Prime
VCA S/N 11	16.9	0.41	0.081	Prime

The larger puncture holes and higher forces for the three prime lance punctures correspond to the slightly larger head size of the prime lance. The test showed the significance head size has on required puncture force. The rate of travel of the lance, however, had little effect on the puncture force. The conductance of the hole created by the punctures is sufficient to allow proper venting of the RTG by reason of the following:

The relative area of the diaphragm holes is the square of the ratio of the corner-to-corner distance of the puncture hole to MHWs:

$$(0.419 \text{ inch}/0.313 \text{ inches})^2 = 1.79$$

The overall conductance is:

$$1/F2 = 1/(2.7 \times 2901) + 1/(1.79 \times 3750)$$
(penetration) (diaphragm hole)

F2 = 3617 cc/sec which is 4.7 times greater than LES 8/9

The differential pressure can be calculated from these results using LES 8/9 ΔP data:

Delta P = 4.3E-5/4.7 = .915E-5 torr (which meets the PRD Product Specification criteria of <2.5E-5 torr).

An item of interest for the reliability of the PRD is the number of springs that the bellows needs to puncture. The bellows has three springs. Figure 4.2.1-5 shows the force of one, two, and three springs versus the required force for puncture for the stroke of the bellows. This shows that two springs would be sufficient to puncture.

PRD Housing Coating Tests

Tests were performed to aid in the selection of a coating for the inside of the PRD housing. The purpose of the coating is to prevent galling of the housing by the bellows. A wear test and a galling test were completed for the two candidate coatings, Nedox NH-1 and Nedox CR. Nedox NH-1 was selected due to its superior performance in the galling test and its ease of processing.

The wear test was a modification of the procedure from ASTM Standard Test Method D 2714. The machine was run at 72 rpm with the equivalent of 45 pounds of bearing force on test rings coated with the candidate coatings. The initial frictional force was recorded and when the frictional force reached 110% of the initial value the number of revolutions was recorded. Nedox CR took 4330 revolutions to reach 110% while Nedox NH-1 took 5710 revolutions. This test gave an indication of how well the coating was bonded to the metal surface.

The galling test simulated the worst case dynamic load of the bellows against the inner surface of the PRD housing. At a maximum of 70 g's, the bellows exerts an inertial force of 40 pounds. For this test, up to 40 pounds was assumed to act through only one convolution of the bellows and to act as a constant force. Thus, the test has a simulated convolution bearing against a test plate while the Tinius Olsen machine pulls the test plate in a direction perpendicular to the simulated convolution and measures the force required to do so. One uncoated plate and three coated plates were tested.

The results of the galling tests are shown in Table 4.2.1-3. The uncoated plate required significantly more force to move than the coated plates. Before the test, it was expected that the coated plates would lose their coating either before or upon reaching the 40-pound bearing load. On the contrary, two of the three coated test plates did not lose their coatings even at 40 pounds. Only the Nedox CR coating on a 63 rms plate lost its coating and then only at 40 pounds of bearing load. The overall conclusion of the test is that the coating
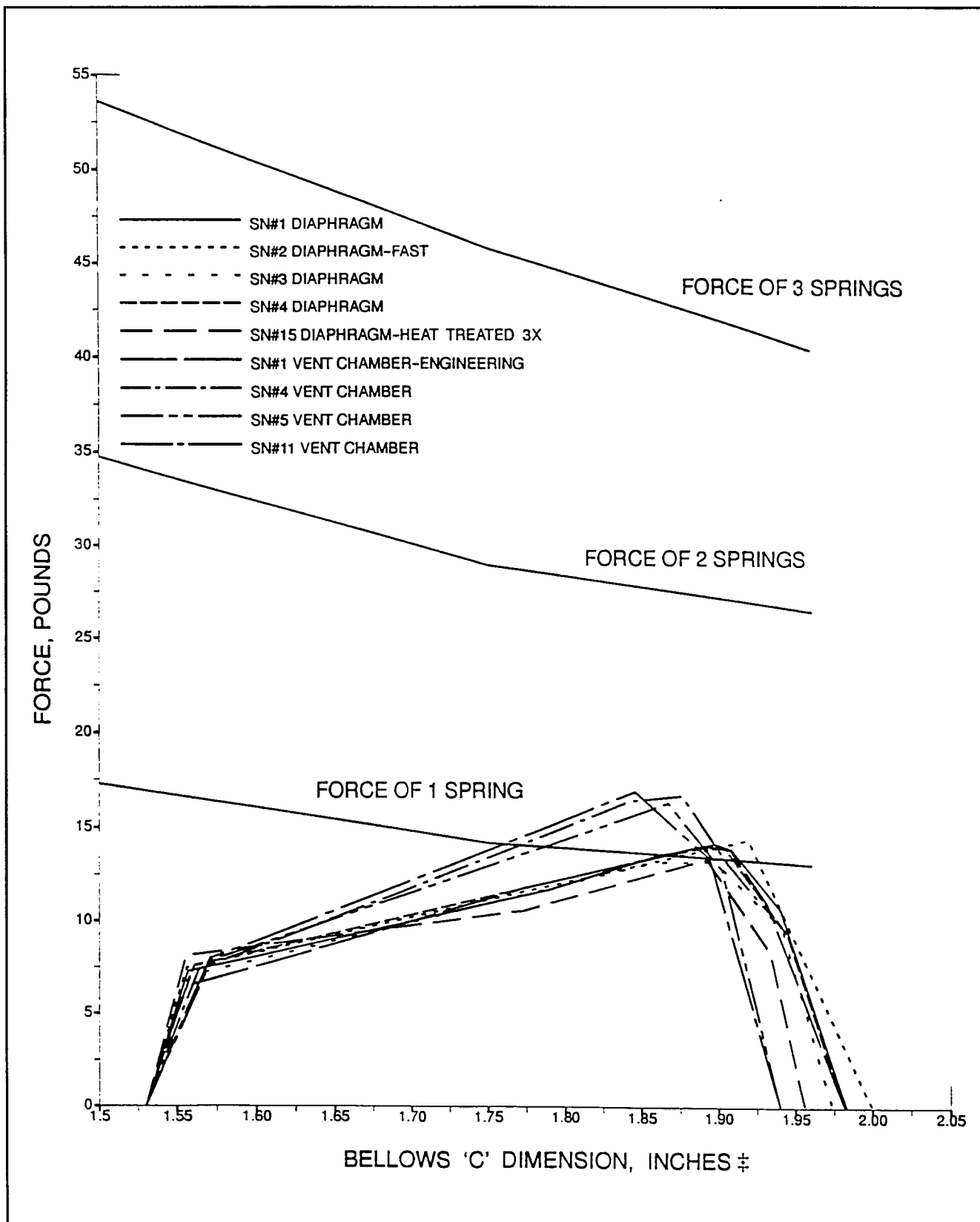
**Figure 4.2.1-5. Comparison of Bellows Spring Force Versus Measured
Lance-Diaphragm Puncture Data**

Table 4.2.1-3. Coating Galling Test Results

Bearing Load (lb$_f$)	Uncoated Al Alloy 2219 Plate (125 rms) (lb$_f$)	Nedox CR Coated Al Aly 2219 Plate (125 rms) (lb$_f$)	Nedox CR Coat Al Aly 2219 Plate (63 rms) (lb$_f$)	Nedox NH-1 Coated Al Aly 2219 Plate (63 rms) (lb$_f$)	Steel Bar (frictional force only) (lb$_f$)
5	4.9	2.4	2.5	1.9	.64
10	7.5	3.2	3.2	3.3	.90
20	16.2	7.0	6.8	7.2	1.63
30	18.6 *	8.8	10.1	8.7	3.0
40	23.3 *	11.1	16.7 * **	10.2	3.8

*   These runs resulted in damaging the simulated convolution to the point of being unusable.

**   This is an average of two runs (15.6 and 17.8 lb$_f$), both of which involved removal of coating.

did provide significant resistance to galling and, that of the two candidates, Nedox NH-1 was superior. This coating was, therefore, applied to the inside surface of the PRD housing.

4.2.1.3 PRD Qualification Program

The PRD qualification program was intended to demonstrate the suitability of the PRD design for the Cassini mission. This was done by a combination of inspections, analyses, and qualification tests. The qualification tests included a PRD assembly dynamic test followed by a PRD dynamic operational demonstration.

PRD Qualification Dynamic Tests

The qualification unit PRD was exposed to acceptance level dynamic testing at ambient pressure. This was followed by a force test on the qualification bellows to verify that no damage occurred during the vibration testing. Next, the PRD was exposed to qualification level vibration testing at operational temperature. Finally, the PRD was successfully demonstrated at operational temperature while exposed to the acceptance level random vibration testing in two axes.

The test environments employed during the dynamic testing were derived from the responses measured at the outboard end of the Q1 RTG during qualification testing for the GPHS-RTG program. The notching to the Q1 data due to the response of the GPHS-RTG

PRD design was removed from the input environments for the Cassini PRD. Notching to the environment required to limit the response of the Cassini PRD was determined during testing.

Figure 4.2.1-6 shows a schematic of the test setup used for these tests. The PRD was instrumented with one accelerometer triax mounted on top of the PRD housing which measured the overall response of the PRD. Another triax of accelerometers was mounted to the base of the test fixture and was used to control the vibration environments. Figure 4.2.1-7 shows the plot of the PRD dynamic operational demonstration test pressure versus time. The initial puncture of the diaphragm took place at a pressure of 11.5 psia which corresponds to an altitude of approximately 6700 feet.
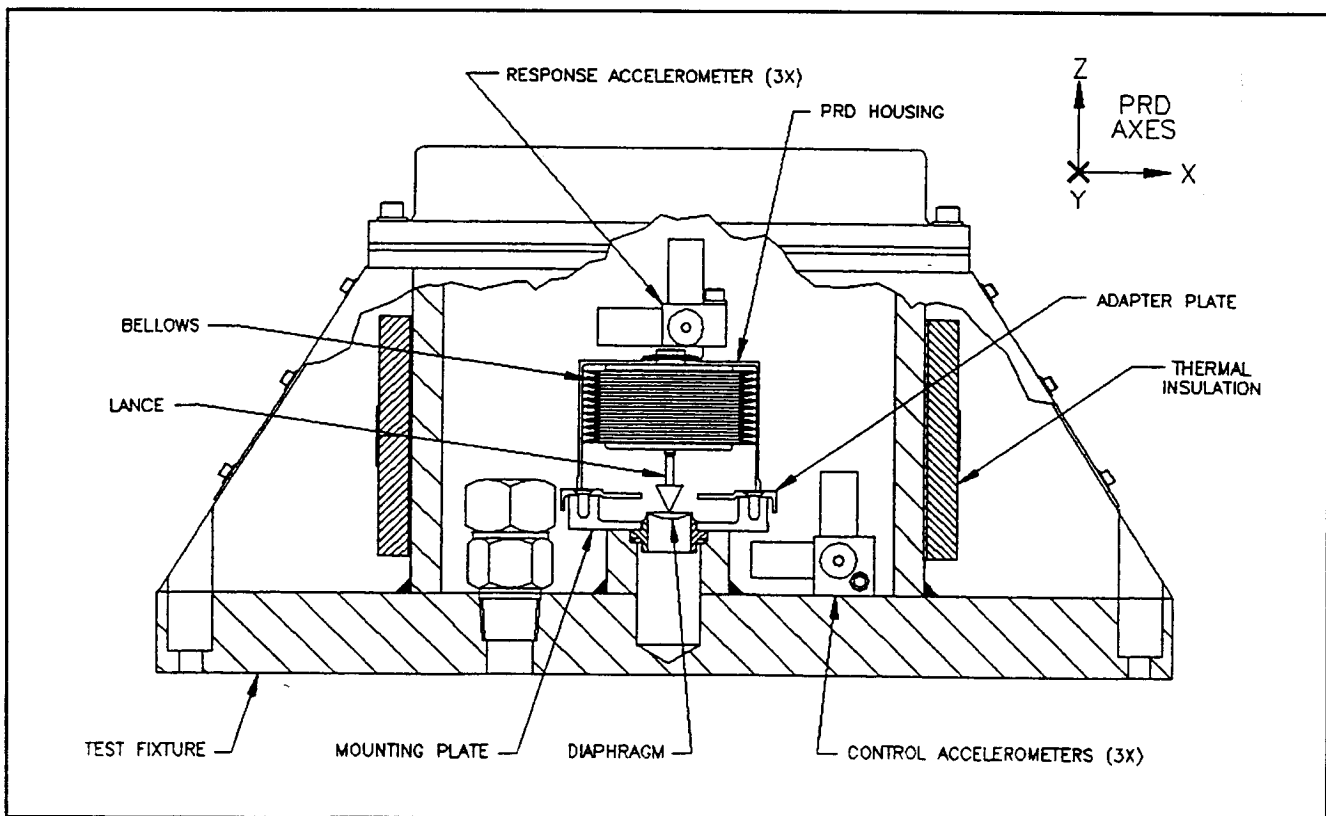
Figure 4.2.1-6. PRD Qualification Dynamic Test Schematic
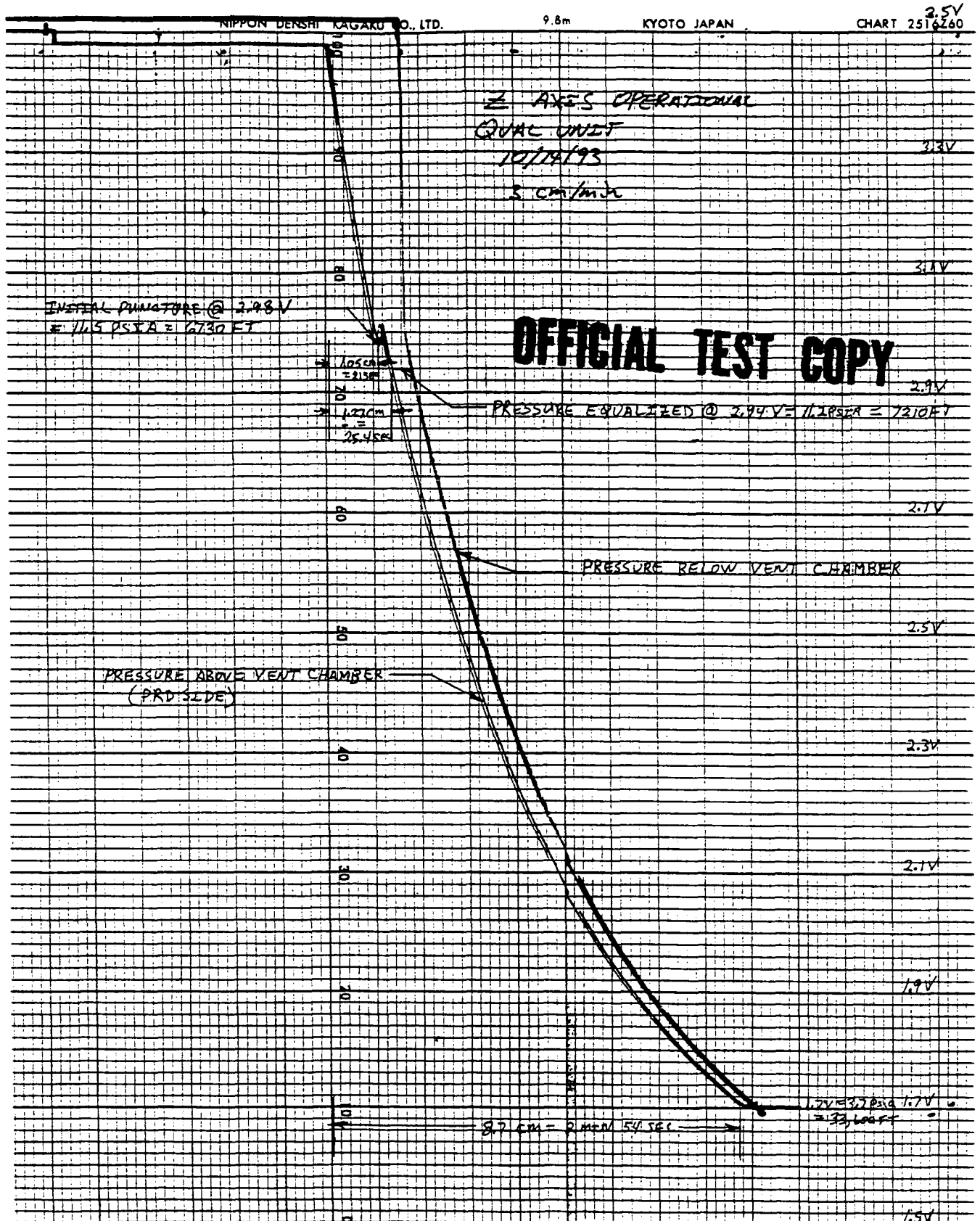
Figure 4.2.1-7. PRD Operational Demonstration Pressure Versus Time

PRD Bellows Qualification Force Test Failure

During force testing of the qualification bellows, a failure occurred. This test was similar to an acceptance force test which measures the pressure at which the bellows first moved and the force available at 0.54 inch stroke and 0.1 psia, except that the qualification test was performed at an operating temperature of 180°C. The qualification bellows, S/N 37, began to expand at 13.8 psia at operating temperature. The specification requirement is that the bellows should not expand at an ambient pressure above 13.0 psia. Prior to this test, S/N 37 had passed the acceptance force test. Following the failure, all eight prime bellows underwent qualification force testing. Only one bellows, S/N 29, passed the test with an initial expansion of 12.95 psia. All nine bellows easily met the force requirement of the test. After analyzing the data from these tests, it was concluded that trapped gas was present inside the bellows. Although all nine bellows had passed leak tests, they were returned to Metal Bellows, Inc. and rewelded with tighter controls. At the same time, the requirements were changed to require operating temperature tests to be performed on all bellows. Following rework, all nine bellows passed room temperature and operating temperature acceptance force tests.

4.2.1.4 PRD Acceptance Test Program

Acceptance tests were conducted on each flight PRD in order to establish acceptability for flight use. The acceptance test program consisted of the following:

a) **Bellows Force Test.** In this test, the force exerted by the bellows assembly was measured, both at room temperature (25°C) and at operating temperature. This test demonstrated that the bellows had adequate stroke length and force to puncture the diaphragm. Tests were conducted before and after dynamic testing in order to demonstrate that no damage occurred during dynamic tests.

b) **Diaphragm and Lance Vent Test.** This destructive test was performed on three diaphragms taken from the same lot as the flight unit diaphragms, and one lance taken from the same lot as the flight unit lances. The force required to puncture the diaphragm was measured and compared with specification requirements.

c) **Seal Integrity Test.** This test was a proof pressure and leakage test performed on each vent chamber assembly.

d) **Acceptance Dynamic Test.** This test subjected the PRD to dynamic environments at the Flight Acceptance (FA) levels.

e) **Bellows Seal Integrity Test.** This leak test was performed prior to launch in order to confirm previous leak testing. Test methods included detection of both gross leakage and fine leaks, compared with specification requirements.

4.2.1.5 PRD Documentation

Additional information on the PRD can be found in the following documents:

1. Fry, J., "PRD Dynamic Acceptance Test," Test Requirements Document No. 1310-0803-1, 22 March 1995.

2. Kauffman, R. R., "Results of F-5 PRD Acceptance Level Vibration Testing," PIR 1VC2-Cassini-0093/7063, 9 May 1995.

3. Kauffman, R. R., "Cassini Pressure Relief Device Transient and Random Vibration Test Environments," PIR 1RS1-C/C-0024/6937 Rev. B, 4 August 1993.

4. Klee, P., "PRD Bellows Gross Leak Test Methodology," PIR 1VC2-Cassini-108, 31 December 1995.

5. Kauffman, R. R., "Results of Flight Spare PRD Acceptance Level Vibration Testing," PIR 1VC2-Cassini-137/7107, 12 June 1996.

6. Kauffman, R. R., R. D. Cockfield, "Qualification Report for the Cassini PRD," PIR 1RS1-Cassini-051/6997, 29 October 1993.

7. Berger, E., "Product Specification for the Cassini Pressure Relief Device (PRD)," Specification PS23003753 Rev. C, 11 May 1993.

8. "Bellows, PRD," Drawing 47D303452 Rev. F.

9. Rickenbach, J., "Standing Instruction for Proof and Leak Testing of the GPHS Vent Chamber Assembly 47B305935," SI No. 249718, 20 July 1981.

10. Klee, P., "PRD Engineering Tests - Lance/Diaphragm and Bellows Interaction," PIR 1RS1-C/C-44/6971, 13 September 1993.

11. Klee, P., "PRD - Requirement Change for Timing of Bellows Leak Testing," PIR 1VC2-Cassini-105/7079, 2 November 1995.

12. Kauffman, R. R., "PRD Stress Calculations - Rough Notes Supporting Design Review," PIR 1AF1-Cassini-0062/7030, 24 February 1994.

4.2.2 Resistance Temperature Device (RTD) Assembly

The Cassini RTDs are identical to the ones used on GPHS, including the sheaths being bent at 90° to enable the mounting of the sensors on the converter shell's forward intermediate ring. There are four RTD sensors mounted on the ring equally spaced

around the circumference. (See Figure 4.2.2-1.) During flight operations, the temperature of the case of the GPHS-RTG is monitored using only three of the four existing RTDs. The three used were selected by JPL.
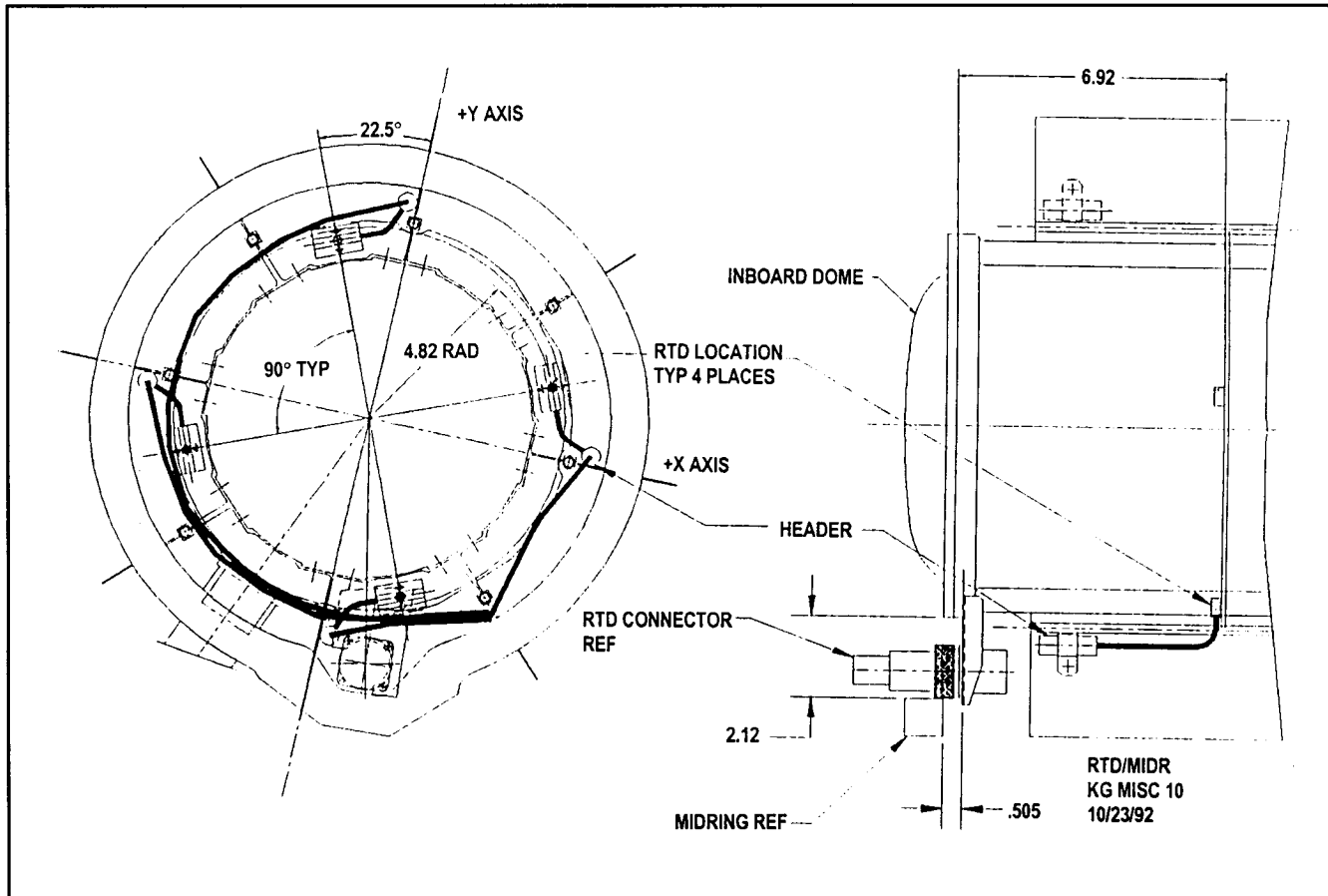
Figure 4.2.2-1. RTD Mounted on the Ring

During ground operations, the temperature of the case of the GPHS-RTG was monitored using four resistance temperature devices. A ten-pin electrical connector provides the interface with test monitoring equipment or with a cable to the spacecraft. The temperature readings provided useful diagnostic information on the health of the RTG, but were not essential to proper operation of the RTG.

The first indication that there might be a design deficiency with the sensor cable assembly came in 1984 when erratic readings were recorded between connector pins A and B, serving RTD No. 1 on RTG F-5. No anomalies were observed on any of the other flight units at that time. A Failure Review Board evaluated the impact of this on pre-launch and flight

operations, assessed the risks of replacing the RTD cable, and determined that no repair or replacement should be attempted. The F-5 RTG was a flight spare for the Galileo and Ulysses missions and after 1990, remained in storage at Mound laboratory, where the RTD continued to operate without anomalies at approximately 438°C (165°C). However, when flight data became available from the Galileo mission, it was observed that temperature readings dropped out (indicating an open circuit condition) during extreme temperature excursions, occurring during Venus flybys. Before proceeding with the RTGs for the Cassini mission, it was decided to pinpoint the cause of erratic behavior on RTD No. 1 on RTG F-5.

Radiography, confirmed by destructive disassembly of the RTD cable assembly, showed that the fault lay in the connection between the wire conductor from the RTDs and the connector pins. Figure 4.2.2-2 shows the details of the wire connections. These connections were made by brazing the copper wires to cups that were slipped over the end of the pins and spot welded, and then potting the end of the connector with RTV 566. Testing also demonstrated that additional strands within the wire could be broken when the assembly was raised to elevated temperatures. Although this type of connection had been used successfully on many previous RTGs, the manual braze operation depended on the skill of the operator to avoid raising the copper wire to an excessive temperature. Weakening or failure of a single strand in the multistrand wire could not easily be detected by visual or radiographic inspection. Examination of the failure point was performed using SEM/EDS (Scanning Electron Microscope/Energy Dispersive Spectroscopy) as well as optical microscopy techniques. The failure mechanism was determined to be tensile failure of the wire at the brazed connection due to forces imposed by thermal expansion of the potting compound. The wire at this point was weakened by excessive heating during the brazing operation, leading to excessive grain growth and possible intergranular diffusion of Ni, Cd, and Zn. The design solution was to eliminate the brazing process by using an alternate joining process. This was accomplished by selecting a connector type with removable pins with socket ends. This allowed the pin socket to be crimped to the wire before insertion into the connector and potting of the assembly, as shown in Figure 4.2.2-3.
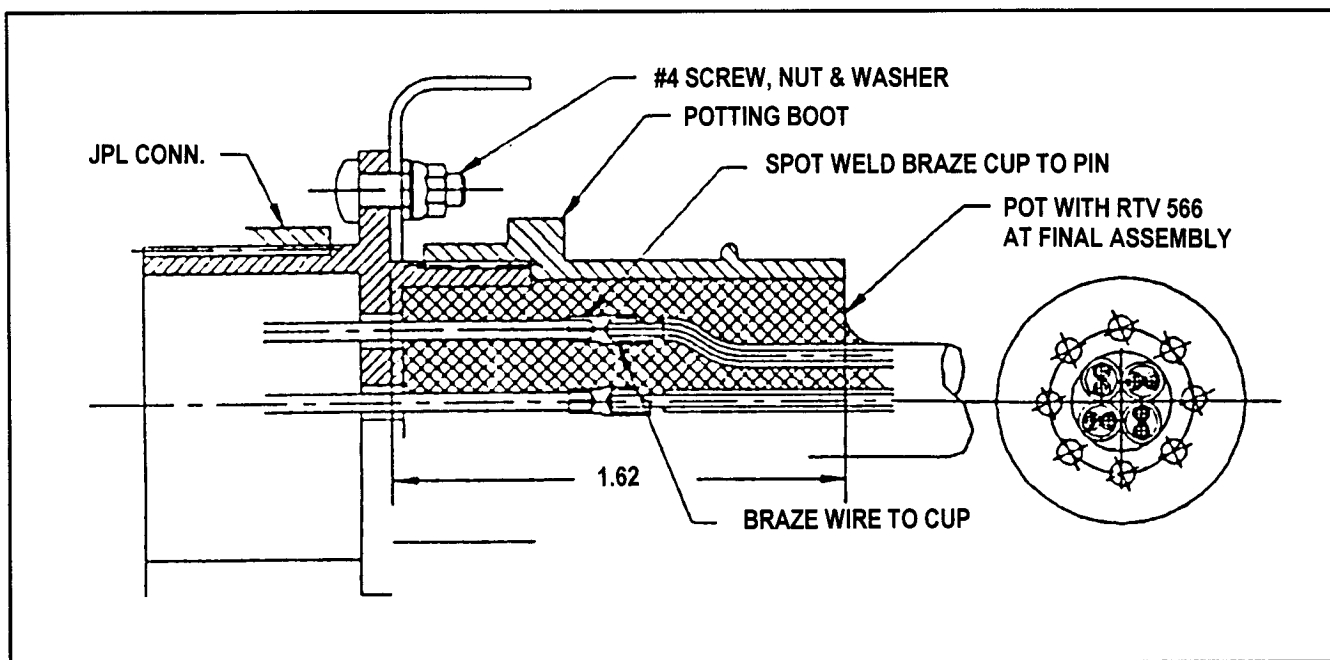
Figure 4.2.2-2. Detail of RTD Cable Connection
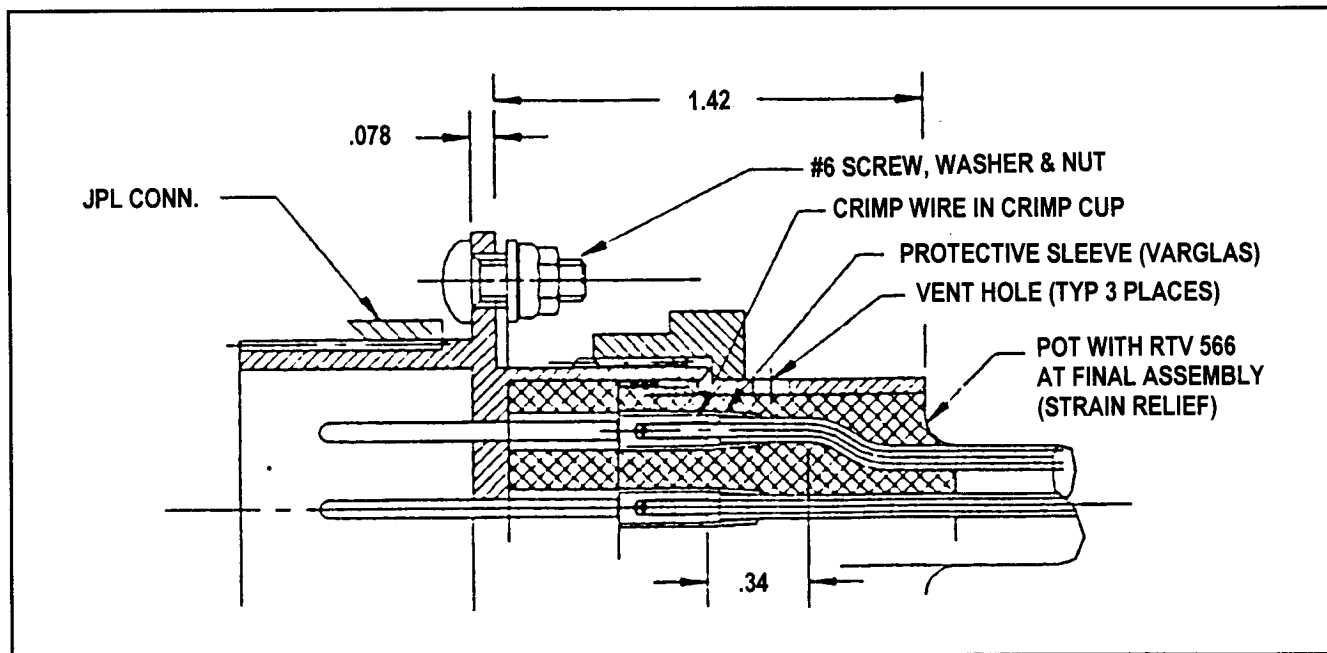
Figure 4.2.2-3. Detail of Revised RTD Cable Connection

The original connector design and method of attaching the wires was qualified for the MHW-RTG program and intended for operation at temperatures up to 543°K (270°C). The weakened condition of the copper wire at the brazed connection was not revealed until the Galileo mission pushed the service temperature beyond its limit, and was not understood until extensive testing and evaluation at the temperature extreme was performed.

All strands used in the manufacture of the conductors were soft annealed, nickel clad, oxygen free, high conductivity copper. Each #20 AWG strand consisted of 19 strands of #32 AWG wire. These #20 AWG wires were sleeved and were individually sleeved with quartz cloth insulation and twisted in pairs to form a 1.50 inch left hand lay, secured at both ends with quartz cloth ties and sleeved with an additional liner of quartz cloth (Figure 4.2.2-4). The cables were attached to the RTD headers in the same manner as those for GPHS. The cables were formed on a fixture resembling the converter. The cables were wrapped with nickel foil from the headers to the connector where the foil was terminated with grounding straps (Figure 4.2.2-5).
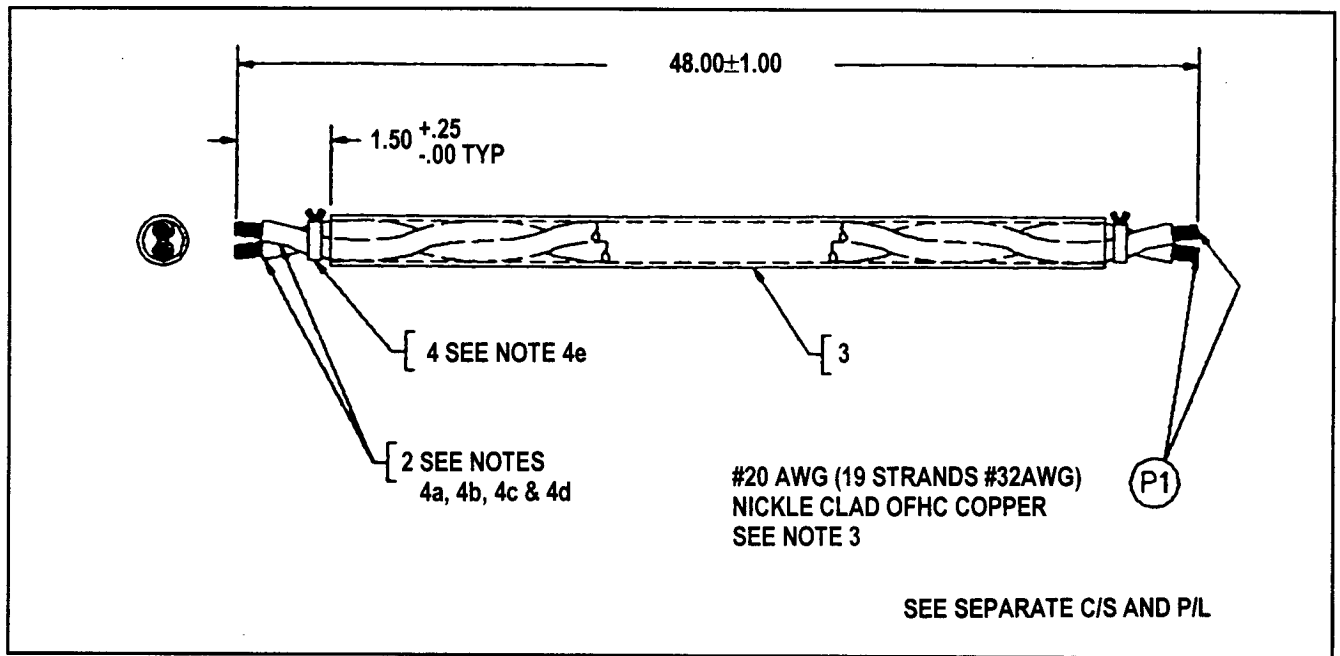
Figure 4.2.2-4. Wire Used in RTD Cable Assemblies

The connector mounting bracket is the same configuration as for the GPHS-RTG except the stock thickness was increased from 0.40 inches to 0.62 inches to provide additional stiffness and to prevent accidental deformation of the bracket during handling, as had occurred on several occasions.
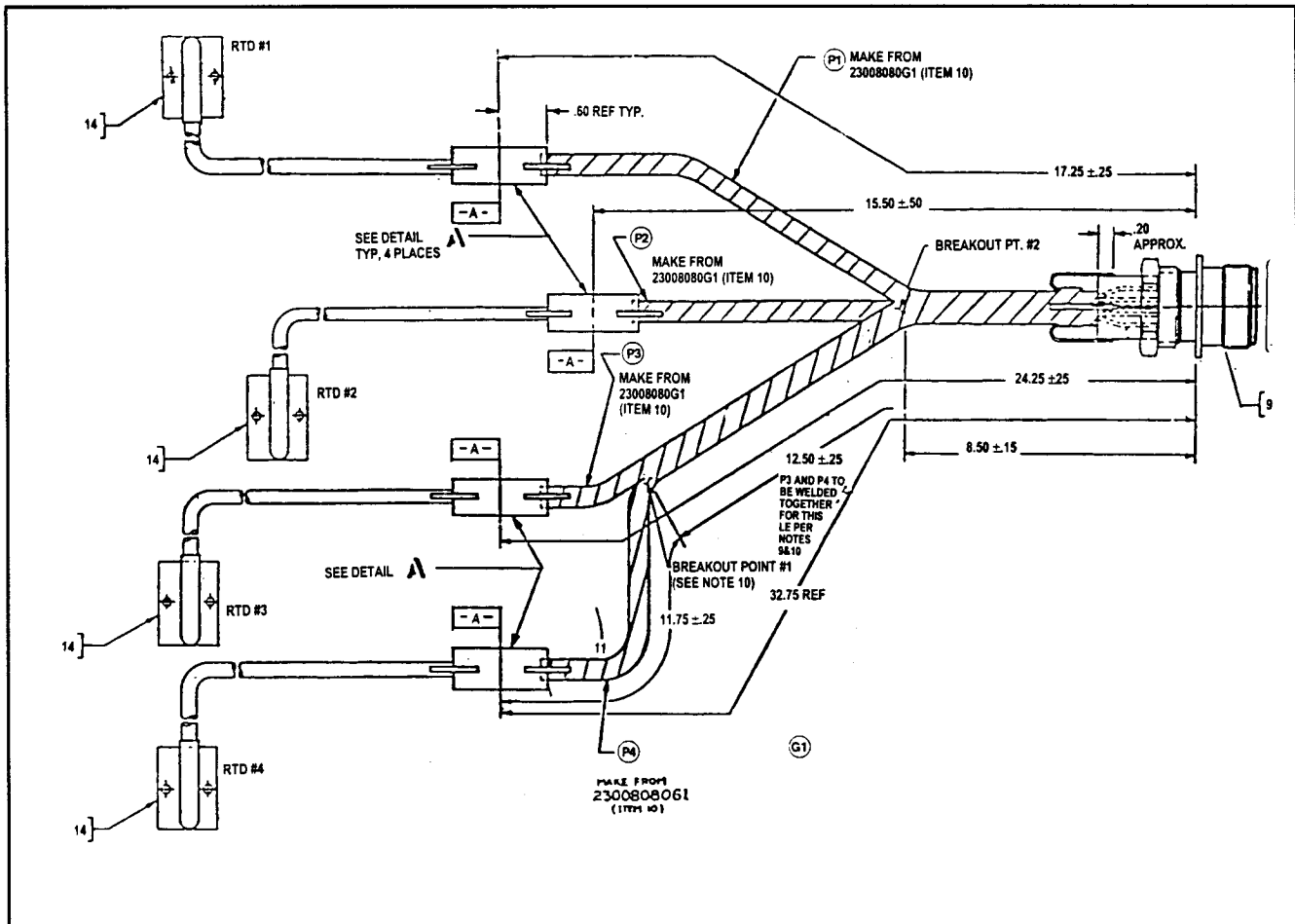
Figure 4.2.2-5. RTD Cable Assembly

The RTD cable assembly was qualified for the Cassini mission by a program that included inspections, demonstrations, tests, and analysis. Dynamic qualification testing was performed with the RTD cable assembly mounted on a test fixture that simulated its installation on the RTG. Testing was performed at 180°C, as measured on the RTD cable support bracket, the temperature expected to occur during the critical dynamic environments of launch. Dynamic environments included both random and transient inputs at the TA (Type Acceptance) level, applied in sequence in the direction of each of the three RTG axes. RTD resistances and insulation resistances were measured both before and after dynamic testing to verify that no damage had occurred. In addition, wire terminations at the connector and headers were radiographed to verify that there were no broken wire strands or separated connections.

Thermal vacuum tests were conducted for qualification of the RTD cable assembly from ambient temperature to 305°C, holding at 305°C for a minimum of four hours. RTD resistances were monitored continuously throughout the test to verify that no momentary open failure occurred, similar to those observed on the Galileo mission. Insulation resistance was measured at both ambient temperature and at 305°C. Visual examination and radiographic inspection were again performed to verify that there were no broken wires or separated connections.

Acceptance testing was performed on all flight RTD cable assemblies, both as mounted on the fixture used for qualification testing, and as mounted on the RTG during acceptance testing of the RTG. Thermal vacuum testing on the fixture included testing from ambient temperature to 300°C, with RTD resistance monitored continuously throughout the test. Insulation resistance was measured at both ambient temperature and at 300°C. Visual examination and radiographic inspection were again performed after removal from the test fixture to verify that there were no broken wires or separated connections.

Dynamic acceptance testing of flight RTD cable assemblies was similar to dynamic qualification testing, except that input levels were raised only to the FA (Flight Acceptance) level, and the tests were conducted at 175°C as measured on the RTD cable support bracket. RTD resistances and insulation resistance were measured before and after dynamic testing, and the wire terminations were again radiographed to verify that there were no broken wires or separated connections.

4.3 SMALL RTG DESIGN STUDY

4.3.1 Objective

A Small RTG Conceptual Design Study was performed in 1996. The objective was to evaluate various designs for a small radioisotope thermoelectric generator suitable for missions with modest power requirements. The designs evaluated include those previously proposed by Orbital Sciences Corporation and those proposed by Lockheed Martin. The target for these designs was 70 watts of electrical power at the end of a ten year mission. Assumptions regarding fuel age were treated parametrically, ranging from F-5 to new fuel. A maximum load environment of 40 g's acting along any axis was assumed and is consistent with load environments assumed at the beginning of previous RTG programs.

4.3.2 Design Options

4.3.2.1 Baseline Description

A baseline design and four options were evaluated from a mass and performance viewpoint. Scoping structural and thermal analyses were completed in support of mass and performance predictions. The baseline design is a shortened version of the GPHS-RTG as configured for the Cassini converter, sized for six GPHS modules rather than eighteen. This design incorporates 192 unicouples. No attempt was made to optimize the mass of the baseline design. The heat source support system was identical to that of an 18 GPHS module converter except that the mid-span supports were eliminated. The heat source support system is capable of providing the preload required for an 18 GPHS module converter with mid-span support. The thermal insulation system consists of sixty layers of molybdenum foil with layers of quartz cloth between each foil. Aluminum is utilized for the outer shell and fins.

Design options were considered for both five and six GPHS modules. Figure 4.3.2-1 illustrates the various options for the five module version. In addition, for each option, the number of unicouples was varied by reducing the number of rows. For example, as shown later, the maximum power at EOM was achieved for the five module version of Option 1 with 144 unicouples, as compared with 192 unicouples for the baseline.
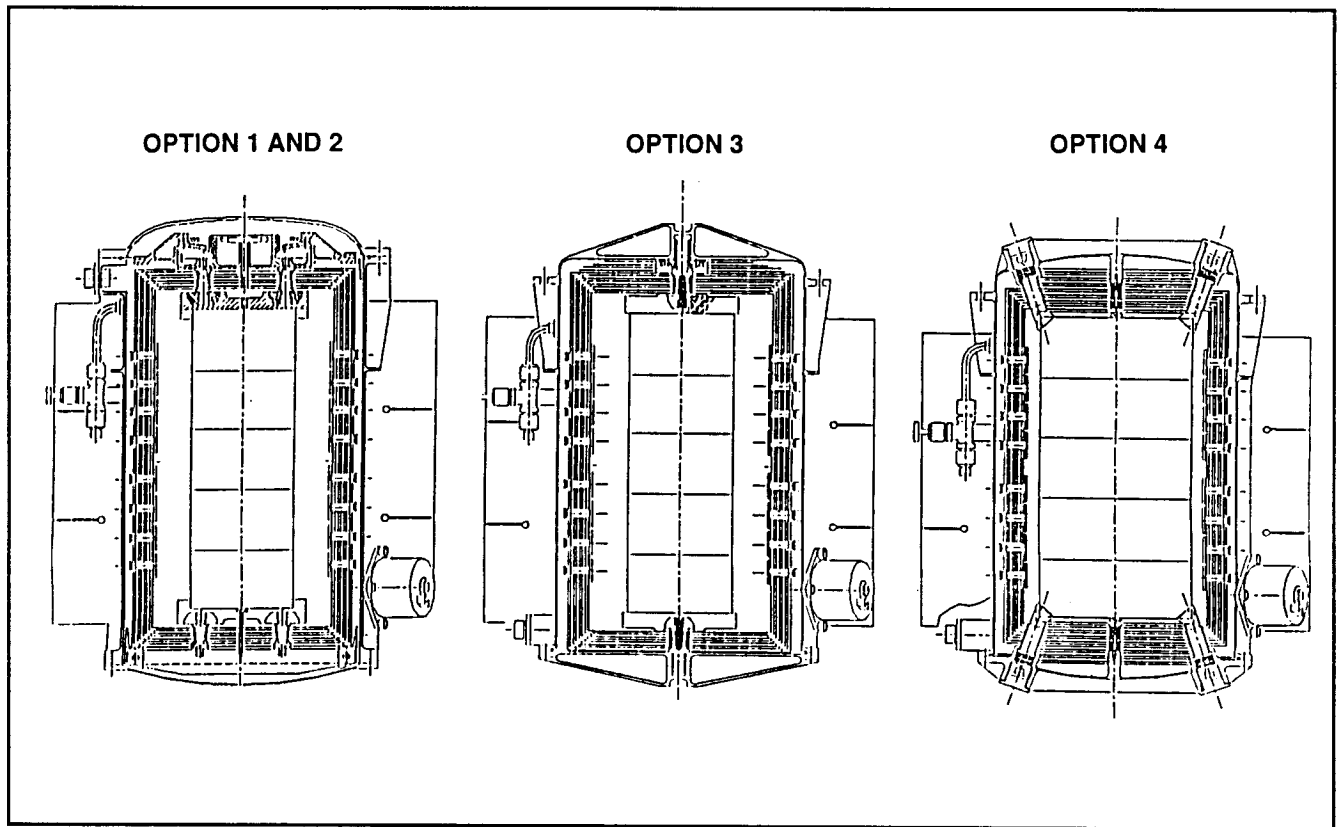
Figure 4.3.2-1. Small RTG Configurations Modeled

4.3.2.2 Option 1 Description

The only change from the baseline is to replace the three preload springs in the heat source system with a single spring which was sized for the lower axial preload required for six GPHS modules. This option has the minimum development risk of all the options.

4.3.2.3 Option 2 Description

The heat source support system is conceptually identical to Option 1, however, the individual components of the heat source support system were lightened to be compatible with the lower required preload for the small RTG. In addition, the PRD was downsized to be compatible with the lower internal volume of the small RTG.

The quartz cloth separator between the molybdenum foil in the multifoil insulation system was replaced with zirconia powder. This is a significant mass savings. The required development for this scheme constituted moderate technical risk.

4.3.2.4   Option 3 Description

This option utilizes design improvements representing significant technical risk. The most significant changes include a welded end closure at one end in place of the bolted flange and C-seal arrangement, and a single stud heat source support system in place of the four stud system used in Options 1 and 2. In addition, a graded multifoil insulation system with zirconia coated foils is employed.

"Graded insulation" utilizes selected variations in foil material through the thickness of the insulation package depending on temperature. Lighter weight materials were proposed on the cold side of the insulation package.

A variation of Option 3, utilizing a beryllium outer shell and end domes, is representative of design changes that attain mass savings by use of alternate materials. The current study evaluates material selections that include carbon-carbon composites, aluminum beryllium composites, and aluminum lithium alloys along with beryllium for the outer shell and fins.

4.3.2.5   Option 4 Description

Option 4 utilizes four pyrolytic graphite heat source support studs at each end of the heat source stack. This concept offers the advantage of lower heat loss through the pyrolytic graphite stud material because the material has a low conductivity perpendicular to the layers. However, because the material is weak in shear in the laminar direction, the support studs are positioned at an angle with the converter axis in order to take most of the load in compression.

Finite element analysis indicated that a significant increase in preload, and hence weight, is required for this concept since the supports were positioned at an angle to the converter axis. When sized for the higher preloads, the basic approach became less attractive from a mass viewpoint.

4.3.3 Summary

The power and mass summary are shown in Table 4.3.2-1. There are numerous combinations of fuel, number of GPHS modules, and design options available to meet the 70 watt electrical, EOM power requirement. Subsequent to determining fuel availability, the selected design option will determine the number of GPHS modules required to obtain 70 watts electrical EOM power.

Table 4.3.2-1. Power and Mass Summary

Option	F-5 Fuel		Cassini Fuel		New Fuel	
	5 Modules	6 Modules	5 Modules	6 Modules	5 Modules	6 Modules
1	EOM Power 58W	70	67	81	71 *	87 *
	Mass 43.95 lb.	49.40	43.95	49.40	44.38	49.83
2	61W	73	70	84 **	74 **	88 **
	40.05 lb.	45.50	40.05	45.50.	40.05	45.50
3	63W	76	67	81 **	71 **	85 **
	30.24 lb.	35.69	30.24	35.69.	30.24	35.69
4	61W	74	65	79 **	69 **	83 **
	29.54 lb.	34.99	29.54	34.99	29.54	34.99

* Only one row of unicouples removed

** These powers were estimated. Once the power requirement was met, cases for design changes which would drive hot junction temperature above 1000°C were not analyzed.

4.3.4 Design Recommendation

Option 2 is the design recommendation from the Small RTG Study. The Option 4 data illustrated in Table 4.3.2-1 are for a design for which the analysis has not been completed. A significant mass increase is anticipated when the preload is increased to provide comparable module separation gaps to the other options evaluated. Thermal analysis indicates that, from a thermal viewpoint, Option 4 has a slightly lower power output than Options 2 and 3. Hence Option 4 has no advantage over Options 2 and 3.

There is a significant mass saving between Option 1 and Option 2 for moderate development risk. Option 3 offers a significant increase in specific power over Option 2 (approximately 25%), however, the development risks are significant.

During the final design phase for a flight program it is anticipated that the mass delta between Option 2 and Option 3 could be reduced.

4.3.5 Structural Analyses Details

Structural analyses were performed to establish the sizes of critical components and areas of the RTGs. In addition, preload requirements were investigated for the three heat source support configurations as shown earlier in Figure 4.3.2-1. Two versions of Option 4 using pyrolytic graphite studs for support were investigated. One version incorporates spring washers at the inboard end only and the other incorporates spring washers at both the inboard and outboard ends. Preload requirements are important since they affect the weight of the heat source support structure and the heat losses through this structure.

4.3.5.1 Loads Environment

It was necessary to assume a structural load environment for this study. Figure 4.3.5-1, an expanded version of the curve provided in Reference 4.3.5-1 (Pluto Express Mission Science Investigation), provides an estimate of the dynamic loads as a function of effective component mass for some typical launch vehicles. Based on an assumed RTG weight of 22 kg, Figure 4.3.5-1 yielded an acceleration of 28 g acting along any axis. Reference 4.3.5-1 also provides quasi-static loads of ±18 g for the thrust axis and ±0.05 g for the lateral axis. Combining the dynamic and quasi-static loads yields 46 g for the thrust axis and 25.9 g for the lateral axis. However, the launch vehicle and the mounting orientation of the RTG were not defined. Therefore, for the purposes of this study, a maximum load environment of 40 g is assumed to act along any axis. This load environment is consistent with the load environment assumed at the beginning of previous RTG designs and was a reasonable compromise for the 46 g and 25.9 g levels derived above.
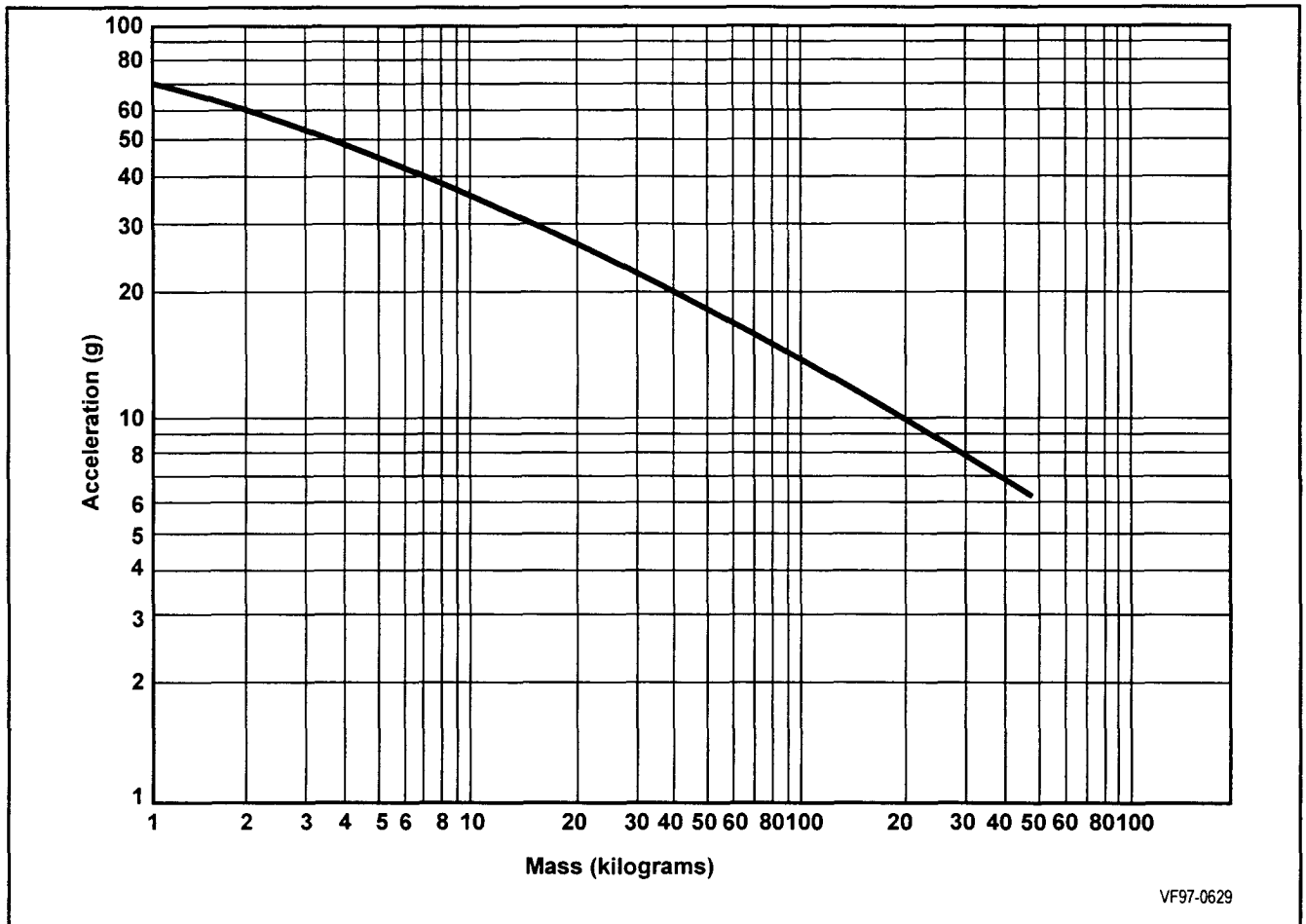
Figure 4.3.5-1. Mass Acceleration Curve

The conditions at lift off were assumed to be:

40 g		Longitudinal
40 g		Lateral
10 psig		Cover Gas (Argon)
172°C	(342°F)	Outer Shell (Avg.)
921°C	(1690°F)	Heat Source (Avg.)

4.3.5.2   Heat Source Module Finite Element Model

The finite element model of the heat source module used throughout this study is shown in Figure 4.3.5-2. The model consists of 360 elements and 372 nodes. Only the aeroshells (without the GIS caps) are assumed to carry the structural loads. The lateral shear restraints provided by the lock members are represented by rigidly coupling adjacent module interface nodes in the lateral directions at the lock member locations. The total weight of the complete module assembly is included by adjusting the density of the aeroshell material.

Y = -1.015

ELEMENTS PER MODULE	360
NODES PER MODULE	372
TOTAL WEIGHT OF MODULE	3.164 LBS.
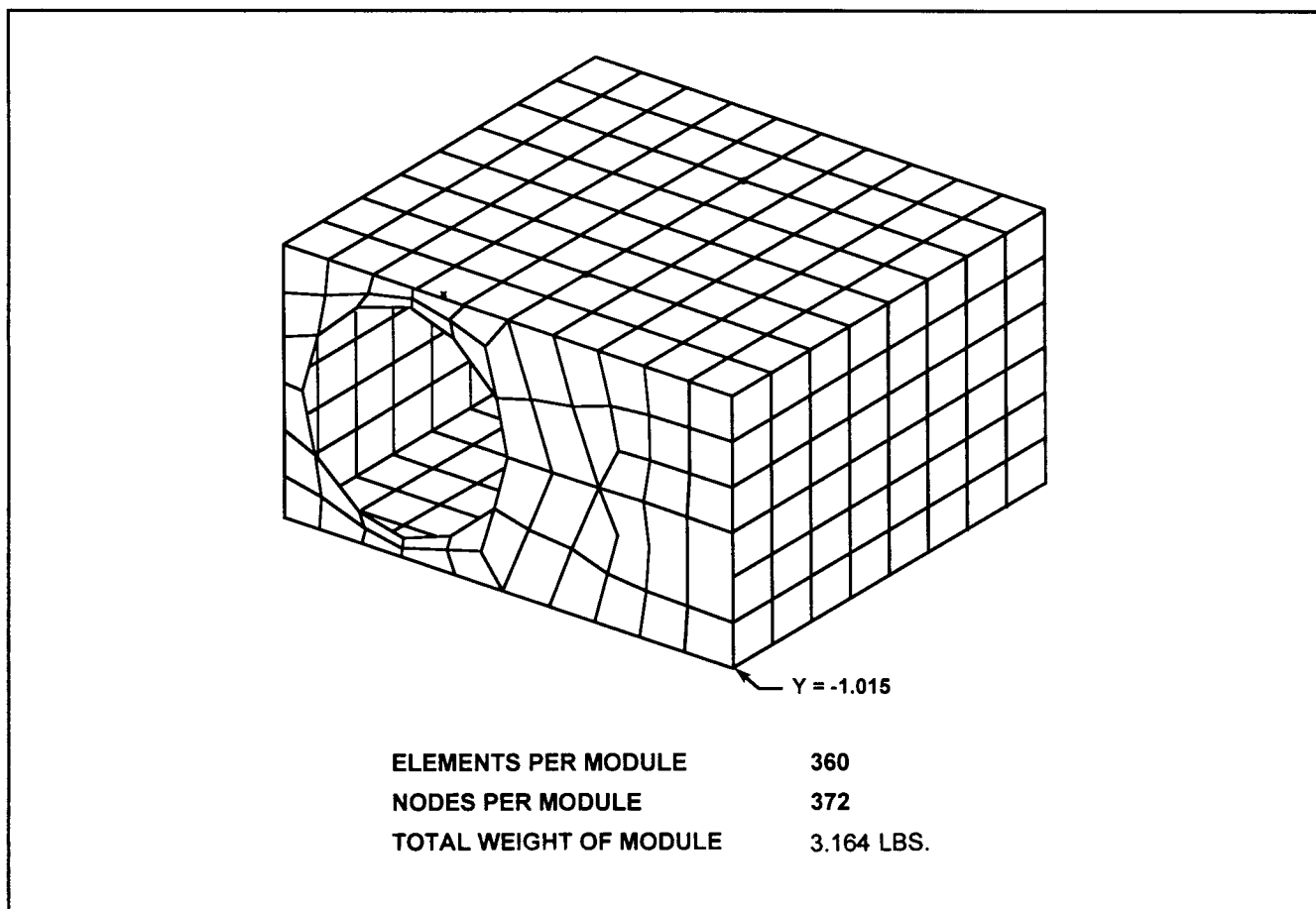
Figure 4.3.5-2. Heat Source Module Finite Element Model

4.3.5.3 Options 1 and 2

Options 1 and 2 employs the GPHS RTG heat source support system design which has been successfully tested and flown on previous missions. Four Inconel X-750 preload studs support the heat source assembly at each end through zirconia insulators and FWPF graphite pressure plates. The preload studs transmit the loads to the outer case through a titanium frame at the outboard end and through titanium support structures which include a Belleville type spring washer at the inboard end. The spring washer assembly provides a means for adjusting the longitudinal preload and accommodates relative thermal expansions between the heat source and the outer case. Changes in the stiffness characteristics of the support system based on the numbers of heat source modules were not included in this parametric study.

Figure 4.3.5-3 shows the finite element model developed for Options 1 and 2 based on a heat source consisting of five heat source modules. Beam elements are used to represent the outer shell and the heat source support members with the exception of the spring washer, which is represented as a spring element having translateral and rotational stiffness characteristics. This model consists of 2159 elements and 1906 nodes. The length of the outer shell was adjusted as required to be compatible with heat sources consisting of two to seven modules.

4 Preload Studs at Each End

INTERFACE ELEMENTS
BETWEEN MATING MODULES

O/B FRAME

I/B FRAME (4)

O/B STUDS (4)

I/B STUDS (4)

OUTER CASE

OUTBOARD

MODULE

PART	MAT'L	E	D
MODULE	FWPF	3.5 MSI	0.3
STUD	INCONEL	21.2 MSI	0.3
CASE	AL 2219-T6	8.8 MSI	0.3
FRAME	Ti 6-2-4-2	14.0 MSI	0.3

Number of Elements   2159
Number of Nodes   1906
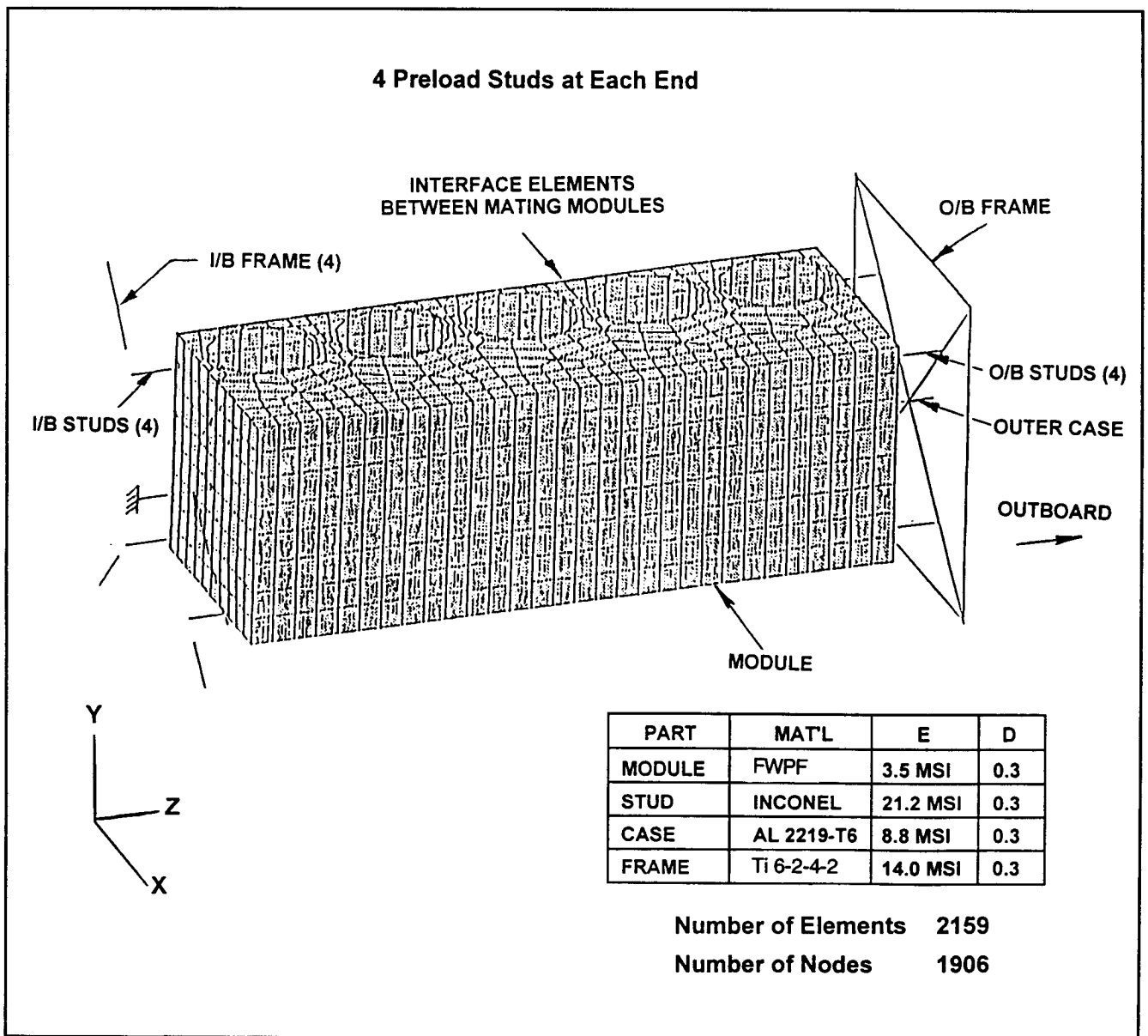
Figure 4.3.5-3. Finite Element Model of RTG (Options 1 and 2)

The longitudinal separation at the module interfaces was calculated as a function of longitudinal preload for a lateral load of 40 g. The results are shown in Figures 4.3.5-4 and 4.3.5-5. For the purposes of this study it was assumed that a maximum separation of 0.0005 inches is acceptable. Based on this criteria, the required preloads for 5-module and 6-module configurations were found to be 733 pounds and 1080 pounds, respectively. The required preloads for separation criteria of 0.0005 inches and 0.001 inches are shown in Figure 4.3.5-5.
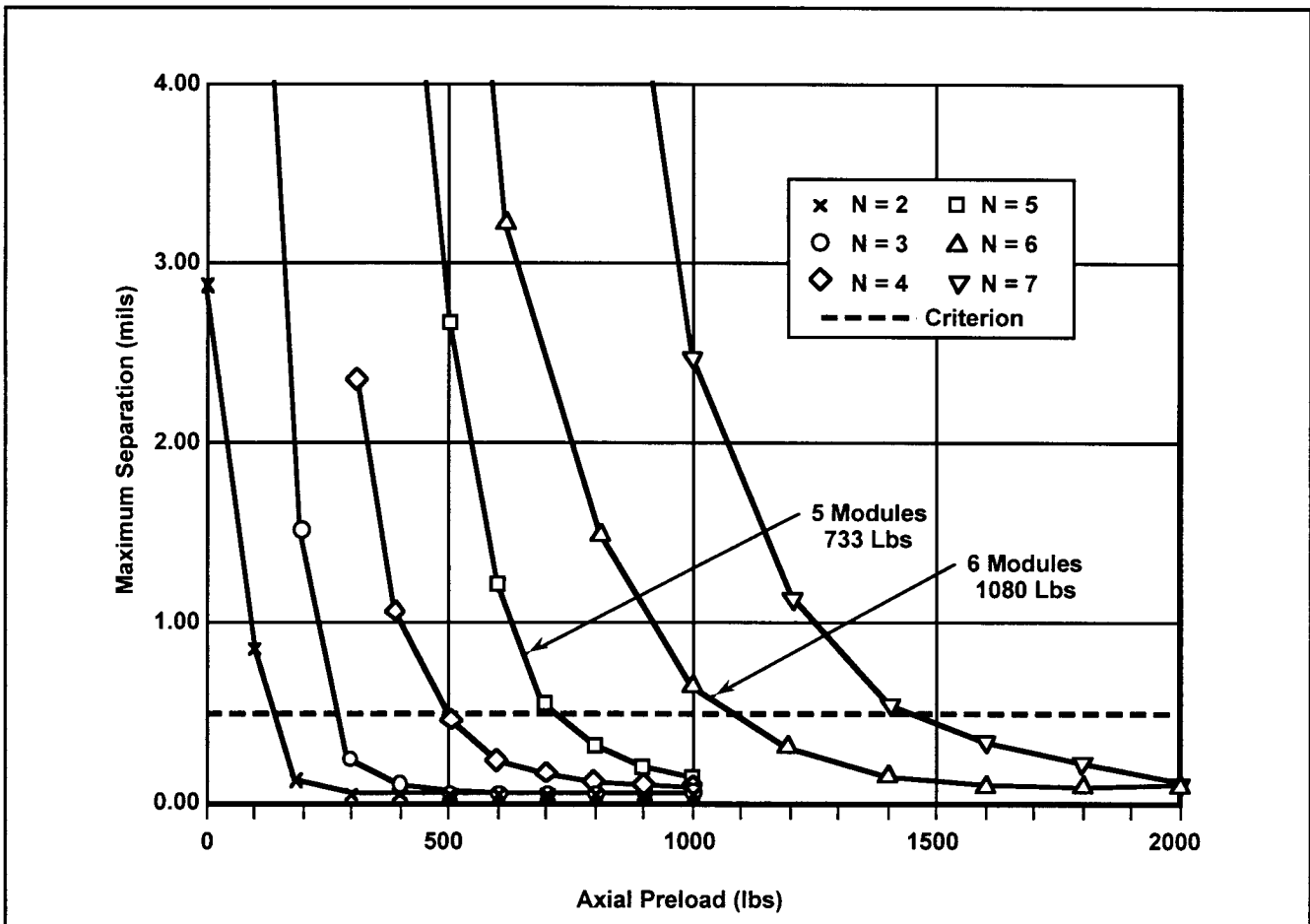
Figure 4.3.5-4. Effects of Number of Modules (Options 1 and 2)

**Required Preload vs Number of Modules for Two
Separation Criteria   40 g's   Y Axis**

VF97-0632
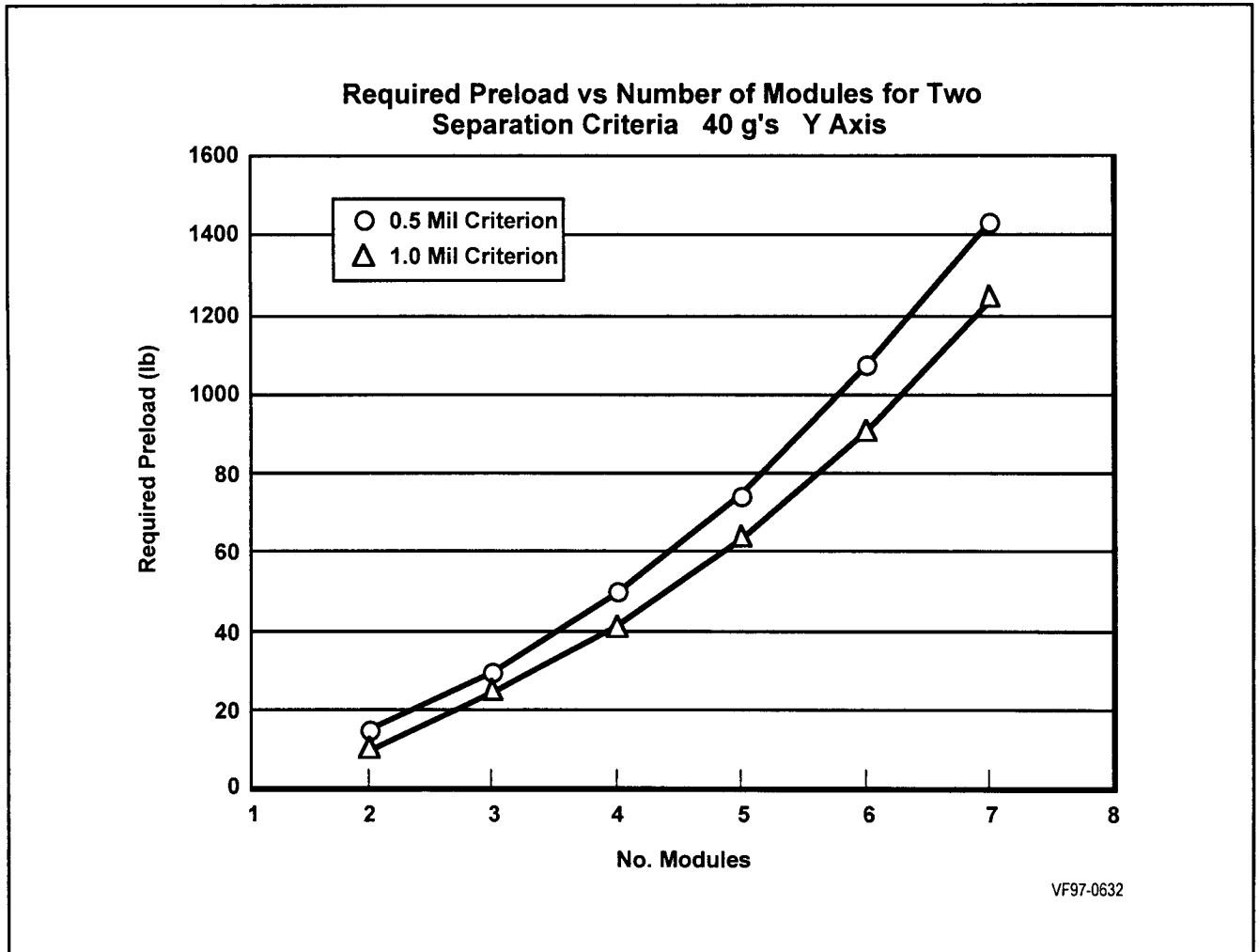
Figure 4.3.5-5. Effects of Allowable Separation (Options 1 and 2)

A contour map of the maximum separation for a configuration having 6 modules with a preload of 1000 pounds is shown in Figure 4.3.5-6, where the criterion of 0.0005 inches is slightly exceeded. The maximum separation is concentrated over a small area of the interface. It is believed that the 0.0005 inch separation criterion is conservative and should not result in any significant debris or damage to the aeroshells.   However, the corresponding preloads should be considered the minimum permissible level since the separation would increase rapidly with any decrease in preload. If the number of modules is reduced below five, a reassessment of the criterion is in order because of the rapid increase in separation with reduced preload.

6 Modules   40 g's   Y Axis   1000 lb Preload

~0.5 Mil Separation

Separation In.	
E11	**VALUE**
	+0.00E-00
	+1.00E-04
	+1.76E-04
	+2.53E-04
	+3.30E-04
	+4.06E-04
	+4.83E-04
	+5.60E-04
	+6.36E-04
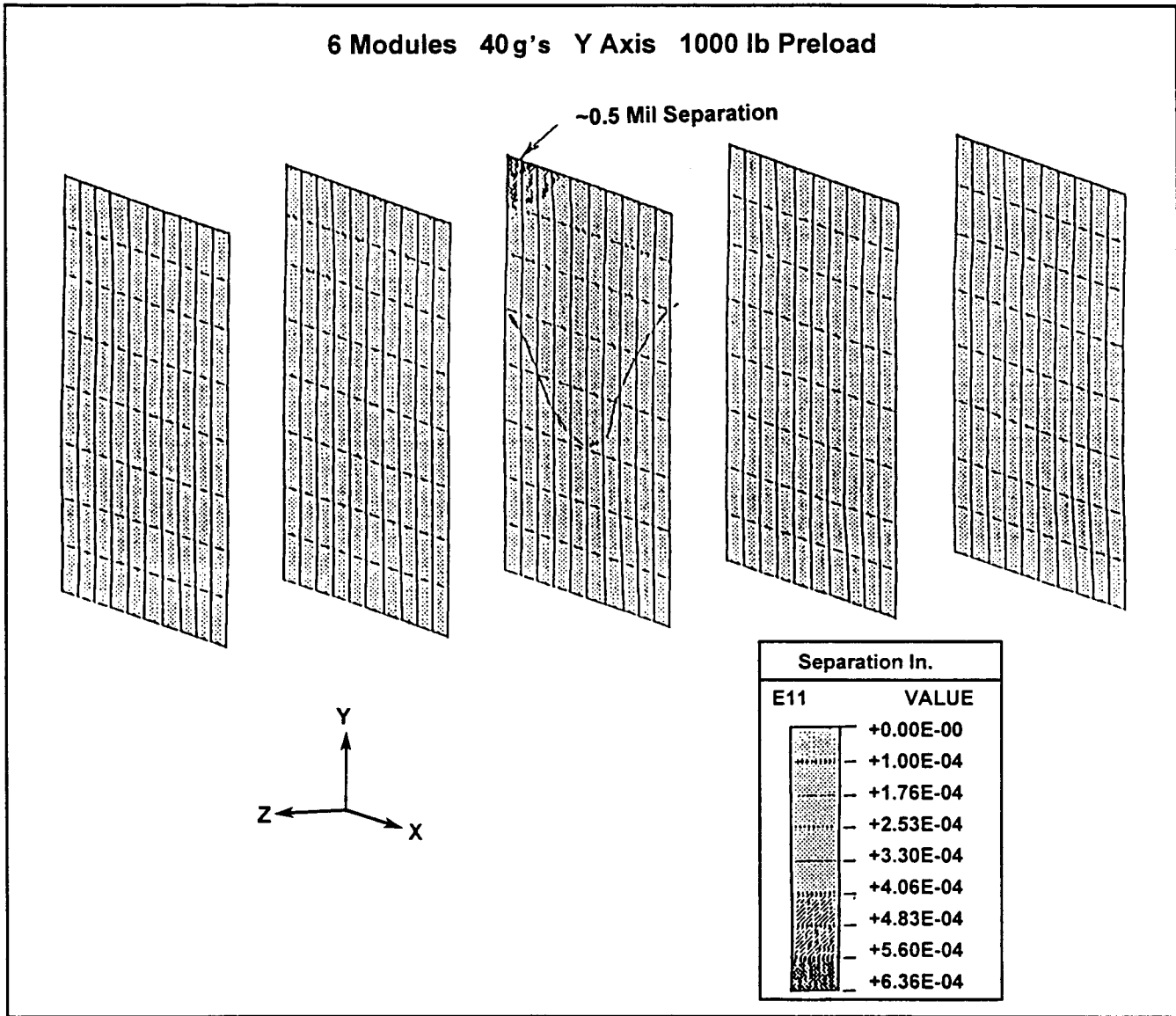
Figure 4.3.5-6. Interface Separation Profiles (Options 1 and 2)

Figure 4.3.5-7 shows the maximum compressive stress to be approximately 2090 psi at the module interfaces for the configuration having six modules and a preload of 1000 pounds. This is well below the compressive strength for the FWPF material of the aeroshell (>10,000 psi).

6 Modules   40 g's   Y Axis   1000 lb Preload

~2090 Psi
Compressive Stress

Stress Psi	
S11	VALUE
	+0.00E-00
	+2.22E-16
	+2.99E-02
	+5.99E-02
	+8.90E-02
	+1.19E-03
	+1.49E-03
	+1.79E-03
	+2.09E-03
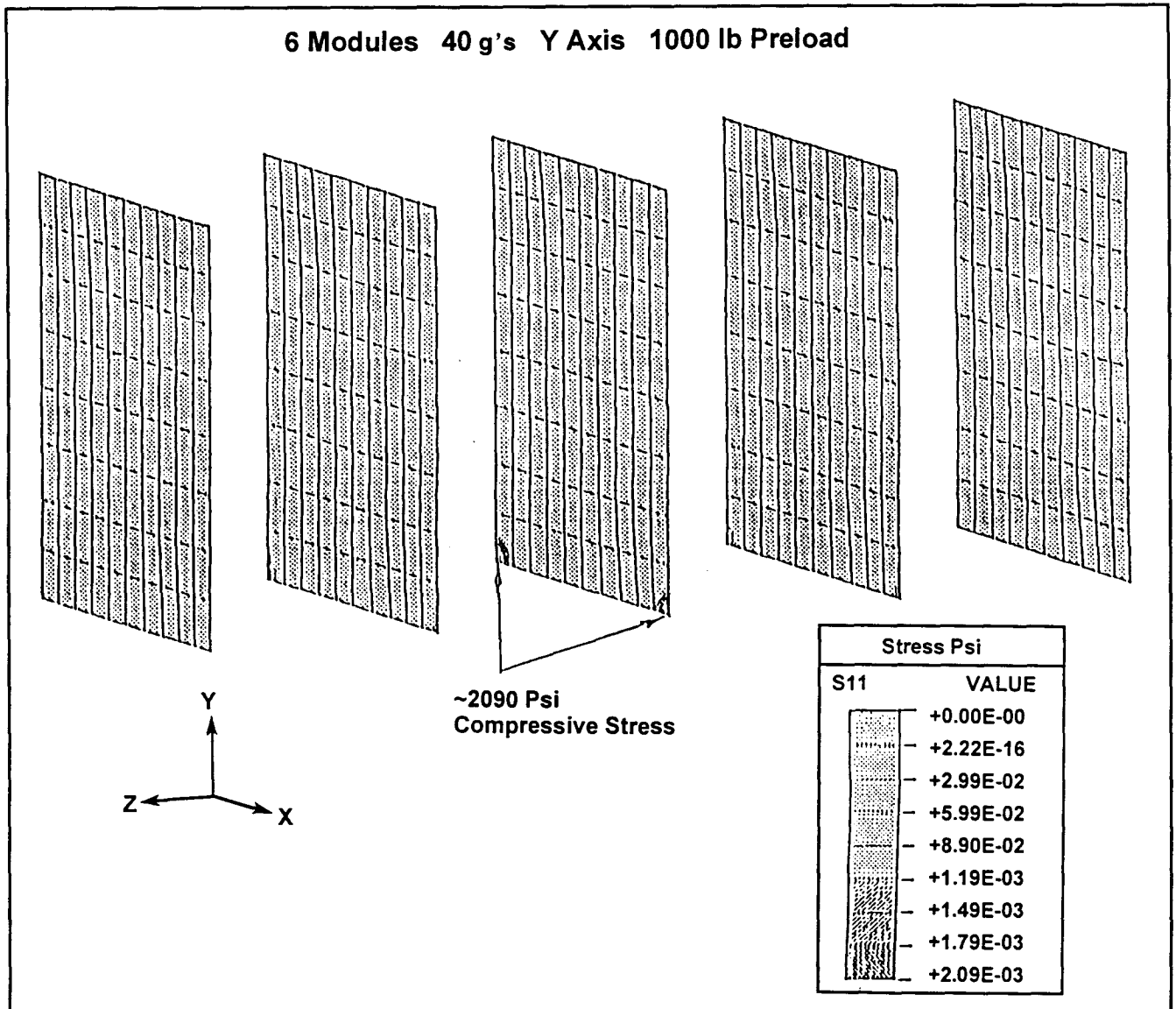
Figure 4.3.5-7. Interface Compressive Stress (Options 1 and 2)

4.3.5.4   Option 3

For Option 3, the number of preload studs is reduced from four to one for each end of the heat source supports, and the titanium support structures are eliminated by transmitting the loads directly to the end domes. This approach offers potential reductions in weight and heat loss. Spring washers are incorporated at one end to accommodate relative expansion between the heat source and the outer case.

The finite element model developed for Options 1 and 2 was modified to represent the Option 3 heat source support system and analyzed for a lateral load of 40 g. The results

compared to the Option 1 and 2 configurations are shown in Figure 4.3.5-8. For an RTG having 6 heat source modules, Option 3 required 1599 pounds of preload versus 1080 pounds of preload for Options 1 and 2 to meet the 0.0005 inch separation criterion. Based on these results, the end domes for Option 3 were designed with adequate reinforcing ribs to support the increased preload.

Separation vs Preload for Two Design Options
6 Modules   40 g's   Y Axis
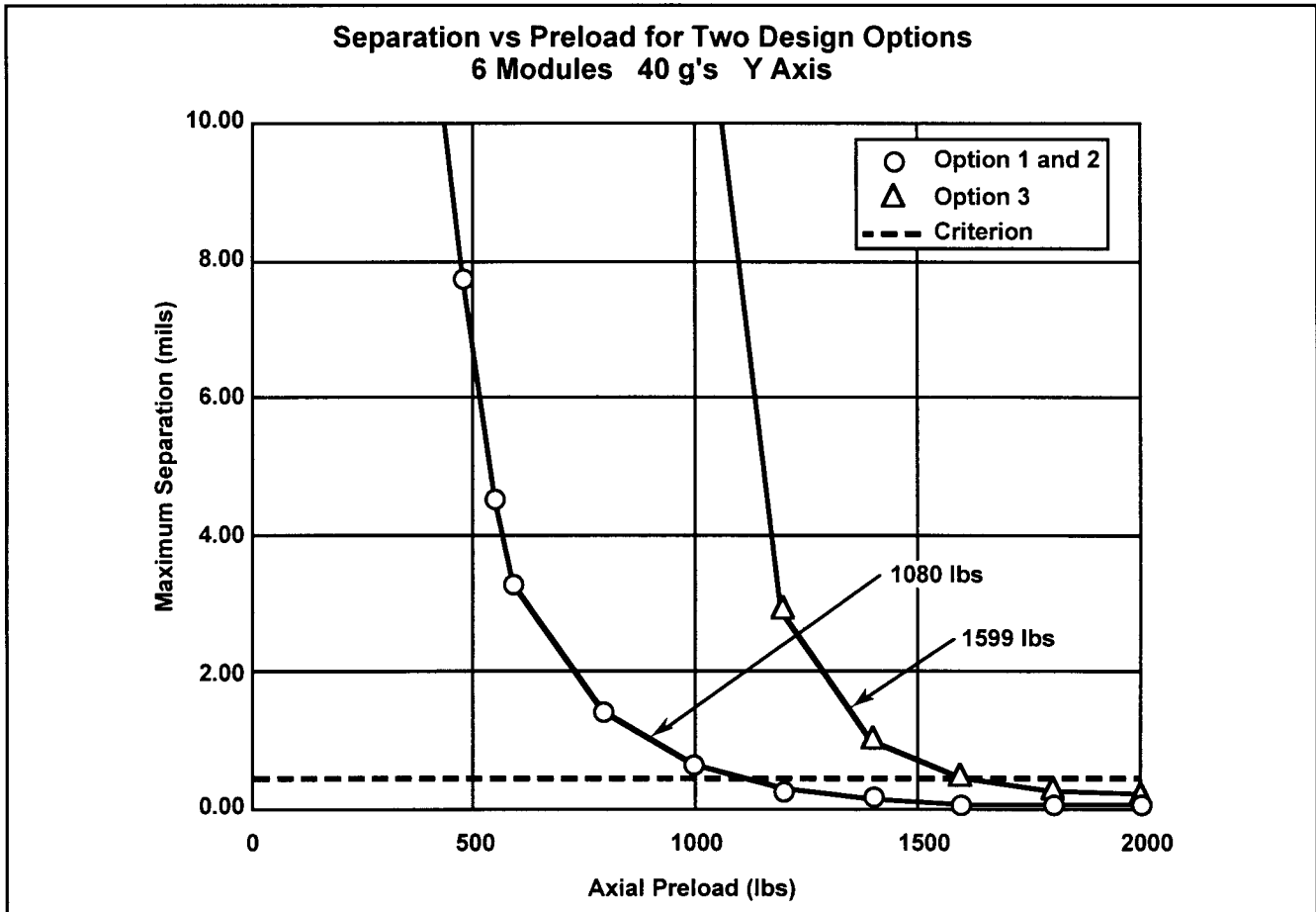
Figure 4.3.5-8. Effects of Heat Source Support Design Options

4.3.5.5   Option 4

The heat source support system for Option 4 consists of four pyrolytic graphite stud assemblies at each end of the heat source which transmit the loads directly from the corner of the heat source to the outer case. Details of the pyrolytic graphite stud assemblies are shown in Figure 4.3.5-9. This support system offers potential weight savings by eliminating the need for support frames to transmit loads to the outer shell. In addition, the low thermal conductivity of the pyrolytic graphite studs offers the potential for a reduction in heat losses.
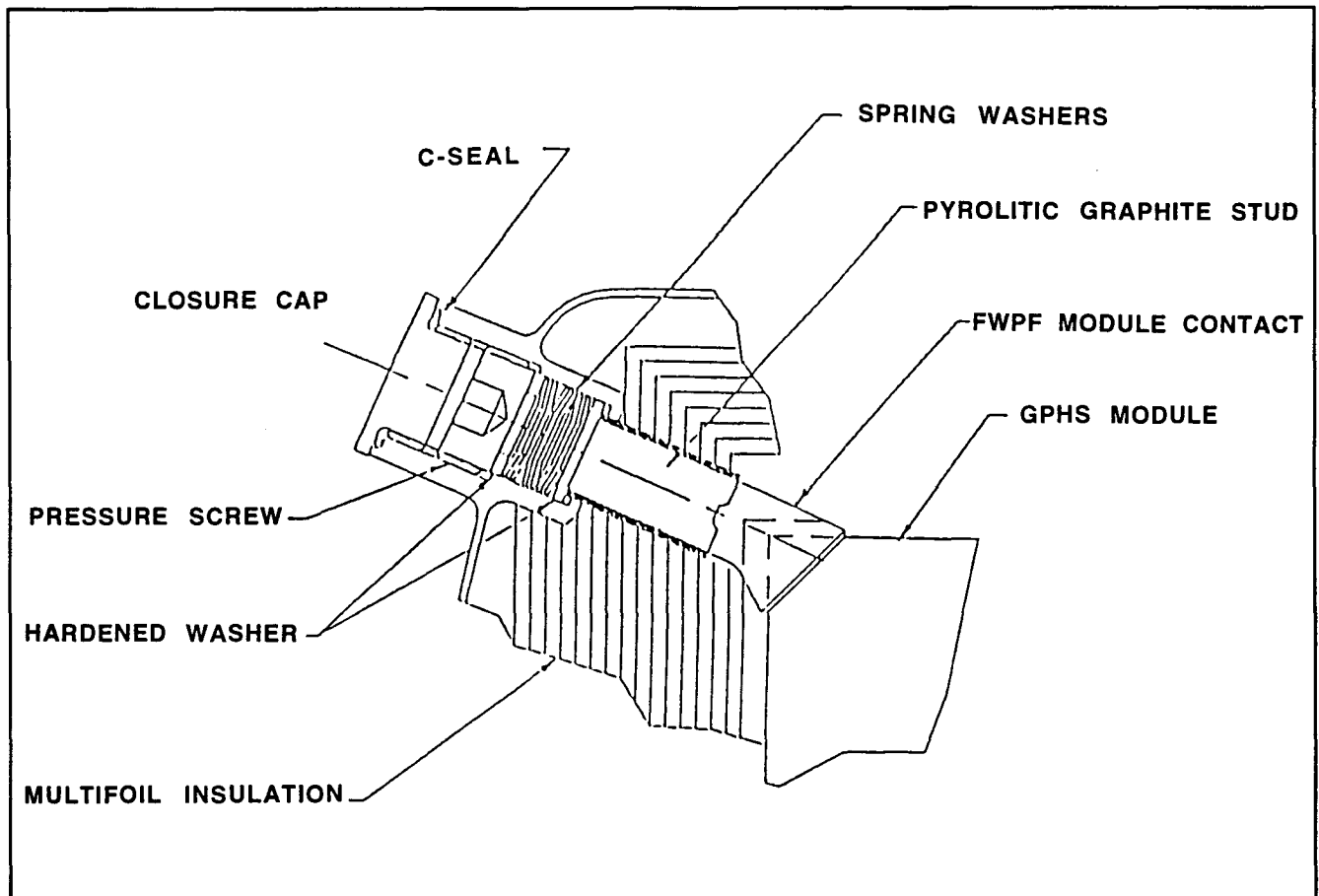
Figure 4.3.5-9. Pyrolitic Preload Stud Support (Option 4)

Two versions of this support system were analyzed. These versions are identical with the exception that the first, Configuration A, does not include spring washers at the outboard end while the second, Configuration B, includes spring washers at both ends.

The finite element model of Configuration A is shown in Figure 4.3.5-10. Based on the results of the analyses of Options 1 and 2, spring washers were selected to provide a longitudinal preload of 1000 pounds. The resulting spring constant for a stack of nine spring washers, arranged to provide a useful stroke of approximately 0.02 inches, was determined to be 8100 pounds per inch for each spring stack. The force vector line of action for each stud assembly was oriented to pass through the center of the heat source.

BELLEVILLE WASHERS (4)
(SPRINGS)
k = 8100 lb/in

INBOARD STUDS (4)
(BEAMS)

2160	SHELLS
16	BEAMS
4	SPRINGS
400	INTERFACE
TOTAL = 2580	ELEMENTS

OUTBOARD STUDS (4)
(BEAMS)

OUTER CASE
(BEAMS)

MODULE (SHELLS)

INTERFACE ELEMENTS
BETWEEN MATING MODULES

2

1

3
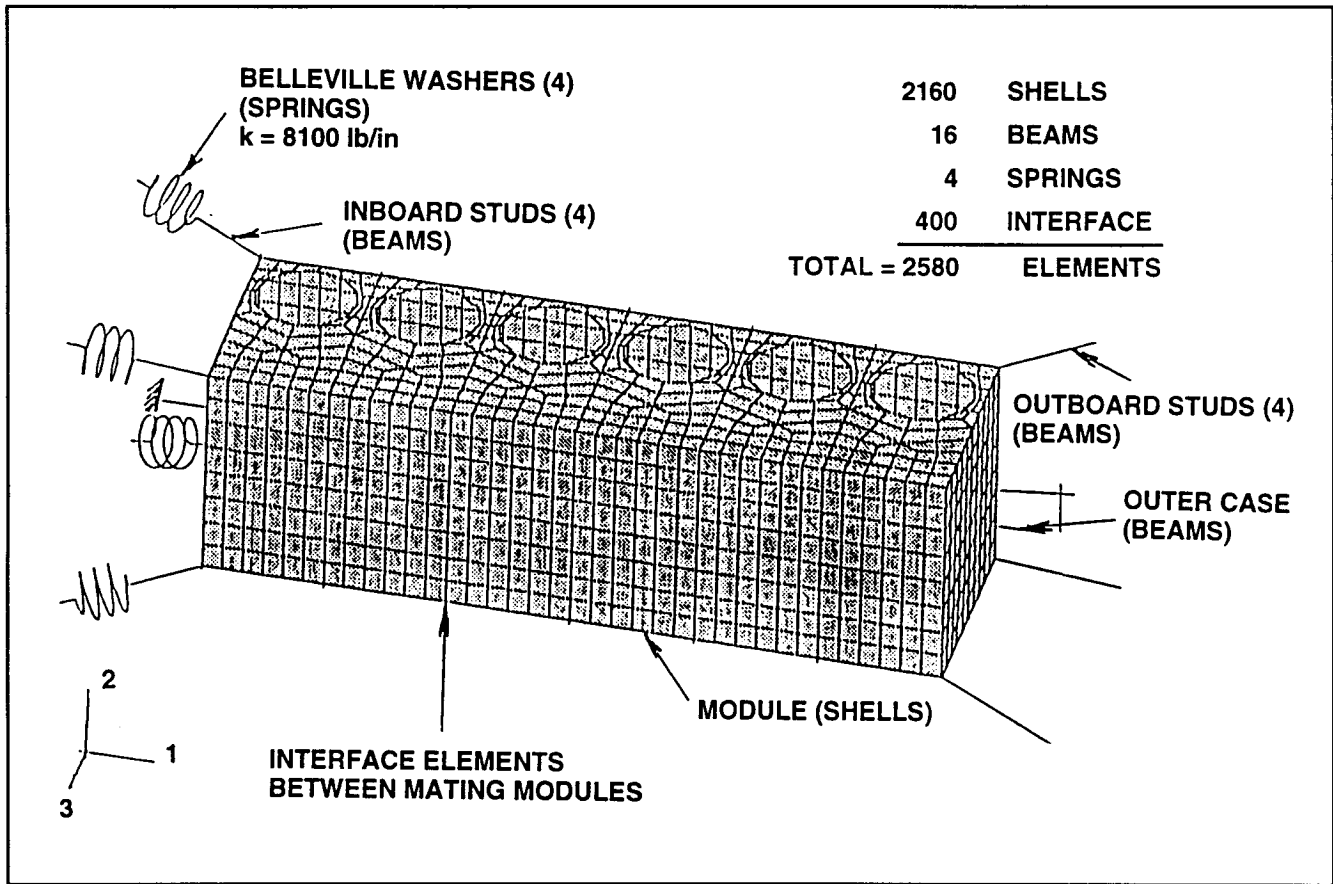
Figure 4.3.5-10. Six-Module RTG Finite Element Model (FEM) (Option 4)

The results of the analyses are summarized in Table 4.3.5-1. The required preload for Configuration A to meet the 0.0005 inch separation criterion is approximately 3500 pounds, which exceeds the capability of the selected springs. In addition, the lateral displacement at the inboard end of the heat source is excessive. The analysis of Configuration B is discontinued at a preload of 4000 pounds where the calculated interface separation is 0.0016 inches. As in Configuration A, the lateral displacement of the ends of the heat source is excessive. From these results it is apparent that the force vectors should be oriented to provide more lateral support of the heat source.

The analyses were discontinued when it was concluded that a considerable amount of additional analysis would be required to optimize these designs which had the potential for major weight increases and would require engineering test verification and development of special assembly and loading procedures.

Table 4.3.5-1. Maximum Separation at Heat Source Module Interfaces

Preload (lbs.)	Separation (in.)	
	Configuration A Belleville Springs One End	Configuration B Belleville Springs Both Ends
1000	Excessive	Excessive
2400	0.0043	0.0088
2800	0.0018	0.0058
3200	0.0008	0.0038
3600	0.0004	0.0025
4000	0.0002	0.0016

4.3.5.6 Conclusions

- A significant reduction in preload is afforded if a small separation is permitted to occur at the heat source module interfaces. For example, the required preloads for Option 1 and 2 are:

  No separation allowed   Preload = 1408 lbs.

  0.0005 inch separation allowed   Preload = 1080 lbs.

  This reduced preload will result in a weight reduction estimated to be up to 0.8 pounds and a reduction in heat loss.

- Separation of the heat source module interfaces is not a potential stability problem. Separation increases the length of the heat source stack, which compresses the preload springs, resulting in stabilizing increase in preload. Also, geometry dictates that the separation would be limited by the stroke of the springs when they bottom out and by the minor deflection of the remaining structure.

- The limiting criterion should be based on separation at the heat source module interfaces where excessive impacting could generate graphite debris, resulting in electrical shorts or damage to the aeroshells. A conservative separation criterion of 0.0005 inches has been selected. This results in very localized areas of separation and should result in no significant graphite debris.

- Options 1 and 2 are state-of-the-art designs and present no new structural problems.

- Option 3 is estimated to provide reductions in weight and heat loss compared to Options 1 and 2. However, creep of the end domes and the resulting loss of preload would have to be addressed. Several potential solutions are available including preconditioning to complete the primary creep prior to assembly or clamping to prevent creeping prior to lift-off.

- Option 4 would require additional analyses to optimize the direction of the force vector for the pyrolytic graphite stud assemblies and the sizes of the spring washers and surrounding structure before a fair assessment of this design concept could be made. Engineering unit tests would be required to verify the structural integrity. Assembly and fueling procedures would have to be developed, possibly requiring major modifications of existing tooling.

4.3.6 Thermal/Power Analysis Details

Thermal and electrical power analysis results are a function of fuel loading. Fuel loadings, assuming the use of F-5 fuel, other Cassini fuel, or new fuel, are shown in Table 4.3.6-1 for loading at the time of the Cassini launch and time of the Pluto launch, and ten years after the Pluto launch.

Table 4.3.6-1. Fuel Loading Summary (watts)

	F-5 Fuel	Cassini Fuel	New Fuel
Fuel Loading at Time of Cassini Launch (October 1997)	4029 (18 Modules)	4388 * (18 Modules)	--
Fuel Loading at Time of Pluto Mission Launch (March 2001)	218 (Per Module)	237 (Per Module)	254 (Per Module)
Fuel Loading at Ten Years from Pluto Launch	201 (Per Module)	219 (Per Module)	235 (Per Module)

* Average of F-2 and F-7

4.3.6.1 Baseline Models

The starting point for the thermal analysis was the SINDA model for a single RTG in a 100°F environment developed for the Cassini program. Before going to six or five modules, an intermediate SINDA model was created which eliminated the midspan ring and bosses, inboard ring, outboard ring and associated SINDA connections. Once this model was checked out, baseline models were created for six and five modules with Cassini fuel. The 6-module design was created first with a new TRASYS model, based on the layout for the 6-module design. Iteration between the SINDA run and the RTG performance code resulted in a final SINDA run for the 6-module baseline. The 5-module baseline design is based on a length of 2.09 inches (one GPHS module) shorter than the 6-module design. A summary of temperatures for the GPHS-RTG, 6-module and 5-module baseline designs is shown in Table 4.3.6-2.

Table 4.3.6-2. Summary of Temperatures for the GPHS-RTG, 6-Module and 5-Module Baseline Designs

Configuration	Temperature Averages °C			
	Outer Shell	Unicouple Hot Junction	Unicouple Cold Junction	ΔT h-c
GPHS RTG (18 Modules)	254	977	280	697
Six Module Design	208	896	231	665
Five Module Design	203	874	226	648

The purpose of creating these baseline models is:

1) Establish a starting point for design improvements. and

2) Show the dramatic drop in hot junction temperatures and ΔT_{h-c} when the number of modules decreases with same end conductances.

The resultant low hot junction temperatures of 6-module and 5-module RTGs indicate the need for design changes to increase the hot junction temperature. The design changes which produce the largest increases in hot junction temperature involve:

1) Reduce the heat losses through the inboard and outboard heat support systems, and

2) Reduce the number of unicouples.

4.3.6.2 Six and Five Module Designs - Cassini Fuel

Since all of the design changes were internal, no new TRASYS models were required. The SINDA models for 6-module and 5-module baselines were changed consistent with the proposed design changes. The resultant ΔT_{h-c} was used with the previous results to estimate electrical power increases and new Peltier cooling and heating values for the next SINDA run. The SINDA runs, after one or two iterations, were used as the basis for the initial performance code runs. The RTG Performance Program used the SINDA temperatures to calculate RTG performance. This resulted in a new power estimate and new Peltier cooling and heating terms. Several iterations between the SINDA models and the RTG performance code were necessary for convergence.

The predicted electrical power and hot junction temperatures for Cassini fuel are shown in Table 4.3.6-2.

Table 4.3.6-3. Electrical Power Predictions (Cassini Fuel: 237 Watts per Module at BOM)

Configuration	BOM Power (watts)	Unicouple Hot Junction Temperature (°C)	EOM Power (watts)	
			After 10 Yrs	After 12 Yrs + 2 Mos
Six Modules				
Baseline (Scaled GPHS RTG - 192 Unicouples)	85	896	70	67
Design Changes				
4 Pyrolytic Graphite Studs	94	918 Est.	77	74
176 Unicouples	93	943	76	73
One Pre-Load Stud	96	926	79	76
176 Unicouples + One Stud	101	968	83	80
160 Unicouples	99	989 Est.	81	78
Five Modules				
Baseline (Scaled GPHS RTG - 160 Unicouples)	71	877	58	56
Design Changes				
144 Unicouples	76	940	62	60
One Pre-Load Stud	79	907	65	62
144 Unicouples + One Stud	86	978	70	68
128 Unicouples	82	999 Est.	67	65
128 Unicouples + Smaller Studs	86	1010 Est.	70	67
128 Unicouples + One Stud	88	1043	* 67	65

* Could theoretically increase to 70W by operating in low voltage mode prior to Pluto arrival.

Note: Electrical power predictions based on RTG performance code for BOM (60°F sink) and flight unit data/TEG degradation code for EOM (0°F sink).

Convergence between the performance code and SINDA was completed for most of the cases listed. Temperatures shown with Est. were from SINDA only or were estimated by scaling. Likewise, BOM powers were also estimated when the temperatures were estimated. EOM powers were determined for periods of 10 years and 12 years plus 2 months after launch. The requirement in the statement of work was 70 watts after 10 years. The longer mission time is based on the JPL estimated time for first Pluto encounter. Electrical power for EOM is based on Flight Unit Data and the TEG Degradation Code which will be discussed in greater detail later in this report.

4.3.6.3 Six and Five Module Designs - F-5 Fuel

The primary issue is whether the 70 watt requirement can be met with five modules. Analysis indicates it can not. Most of the power predictions at BOM were estimated, based on the results for Cassini fuel. The F-5 cases which were actually calculated were obtained by iterating between SINDA and the RTG Performance Program. Power and temperature predictions for F-5 fuel are shown in Table 4.3.6-4. The low voltage option was considered as a way to minimize degradation losses throughout the mission. However, it was realized that most of the spacecraft power would be required for housekeeping throughout the mission, so operating at low voltage and low power was not a viable option.

Table 4.3.6-4. Electrical Power Predictions (F-5 Fuel: 218 Watts per Module at BOM)

Configuration	BOM Power (watts)	Unicouple Hot Junction Temperature (°C)	EOM Power (watts) After 10 Yrs	After 12 Yrs + 2 Mos
Six Modules				
Baseline (Scaled GPHS RTG - 192 Unicouples)	76		62	60
Design Changes				
176 Unicouples	81		66	64
One Pre-Load Stud	84		69	66
176 Unicouples + One Stud	88		72	69
160 Unicouples	86		70	68
160 Unicouples + Smaller Studs	89		73	70
160 Unicouples + One Stud	93		76	73
Five Modules				
Baseline (Scaled GPHS RTG - 160 Unicouples)	61	825	50	48
Design Changes				
144 Unicouples	66		54	52
One Pre-Load Stud	69		56	54
144 Unicouples + One Stud	75		61	59
128 Unicouples	71		58	56
128 Unicouples + One Stud	77	987	63	61
112 Unicouples + One Stud	83	1062	* 62	60
112 Unicouples + Smaller Studs	81		63	61

* Could theoretically increase to 67W by operating in low voltage mode prior to Pluto arrival.

Note: Electrical power predictions based on RTG performance code for BOM (60°F sink) and flight unit data/TEG degradation code for EOM (0°F sink).

4.3.6.4 Six and Five Module Designs - New Fuel

Only a few power predictions were calculated for the new fuel as the requirement was easily met, even with five modules. Hot junction temperatures were estimated to show that, due to the high fuel loading, only minimal design changes could be made before driving the hot junction temperature above 1000°C. Most of the power predictions for new fuel were scaled from Cassini fuel values by the relationship, electrical power equals one-eighth of fuel loading. The power prediction for new fuel are summarized in Table 4.3.6-5.

Table 4.3.6-5. Electrical Power Predictions (New Fuel: 254 Watts per Module at BOM)

Configuration	BOM Power (watts)	Unicouple Hot Junction Temperature (°C)	EOM Power (watts)	
			After 10 Yrs	After 12 Yrs + 2 Mos
Six Modules				
Baseline (Scaled GPHS RTG - 192 Unicouples)	99		81	79
Design Changes				
176 Unicouples	106	997	87	85
One Pre-Load Stud	110	978 Est.	90	87
176 Unicouples + One Stud	115	1020 Est.	89	86
160 Unicouples	111	1051 Est.	84	81
Five Modules				
Baseline (Scaled GPHS RTG - 160 Unicouples)	80		65	63
Design Changes				
144 Unicouples	87		67	65
One Pre-Load Stud	90		74	72
144 Unicouples + Smaller Studs	94		77	65
144 Unicouples + One Stud	96	1030	74	73
128 Unicouples	92	1060 Est.	69	69

Note: Electrical power predictions based on RTG performance code for BOM (60°F sink) and flight unit data/TEG degradation code for EOM (0°F sink).

4.3.6.5 Summary

A summary of the minimum design modifications to meet the 70W EOM requirement is shown in Table 4.3.6-6. Determination of EOM powers for all fuels is based on past experience with BOM hot junction temperature. For hot junction temperature less than 1000°C at BOM, Voyager flight data was used to obtain EOM/BOM = 0.82 for 10 years and 0.79 for 12 years and 2 months.

Table 4.3.6-6. Summary of Minimum Design Modifications for Each Fuel Type to Meet 70W EOM Requirement (Aluminum Shell and Fins)

	F-5 Fuel	Other Cassini Fuel	New Fuel
Six Modules	Two Rows Removed (Option 1) 70W	Two Rows Removed Option 1 81W	One Row Removed Option 1 87W
Five Modules	Two Rows Removed Only One Stud Option 3 63W Three Rows Removed Option 2 63W	Two Rows Removed Four Small Studs Option 2 70W	One Row Removed Option 1 70W

For BOM hot junction temperatures above 1000°C, the computer code, TEG, was used to calculate EOM powers. TEG calculates RTG performance with time accounting for dopant precipitation, silicon sublimation, multifoil insulation degradation and electrical insulation degradation. Analysis was first performed for several designs with BOM hot junction temperatures below 1000°C both to verify the program was giving reasonable answers and to justify the use of the same degradation factors for the lower temperature designs. The TEG program was then run for two 5-module cases, one with a BOM hot junction temperature of 1041°C and the other of 1062°C. These two runs were then used to estimate the degradation with time of other runs with hot junction temperatures exceeding 1000°C.

4.3.6.6 Fin Optimization Study

A study was also conducted on fin size using a fin optimization program called AXFIN. AXFIN optimizes fin length/thickness to minimize weight for a given heat rejection load, shell temperature, material selection, and converter size. The program assumes no end losses and allows options for rectangular, triangular, and trapezoidal cross section fins. In the study, the end losses from the domes were subtracted from the heat rejection load and the trapezoidal fin cross section was used. A variety of fin materials was investigated, including aluminum alloy 2219, beryllium, aluminum-beryllium alloy, aluminum-lithium alloy, and carbon-carbon. Both material and shell temperature had significant effects on the optimum fin length and thickness.

References for Section 4

4.1.1-1   Braun, J., R. Cockfield and L. DeFillipo, "Fabrication of E-6 Foil Insulation Assembly," Cassini RTG Program Memo No. 251, 23 November 1993.

4.3.1-1   "Pluto Express Mission Science Investigation," Draft Report A096-OSS-XX, NASA, Office of Space Sciences, 2 August 1996.

Section 5

Performance

SECTION 5

PERFORMANCE

5.1 FLIGHT UNIT PERFORMANCE AS ETGs

Each converter undergoes a series of tests as both an ETG and an RTG as indicated in Figure 5.1-1. ETG tests are performed under vacuum conditions and in air with an argon gas fill. Vacuum tests consist of processing and stability tests. Air testing is used to obtain a stable reference performance point with an argon gas fill and to measure the converter leak rate.
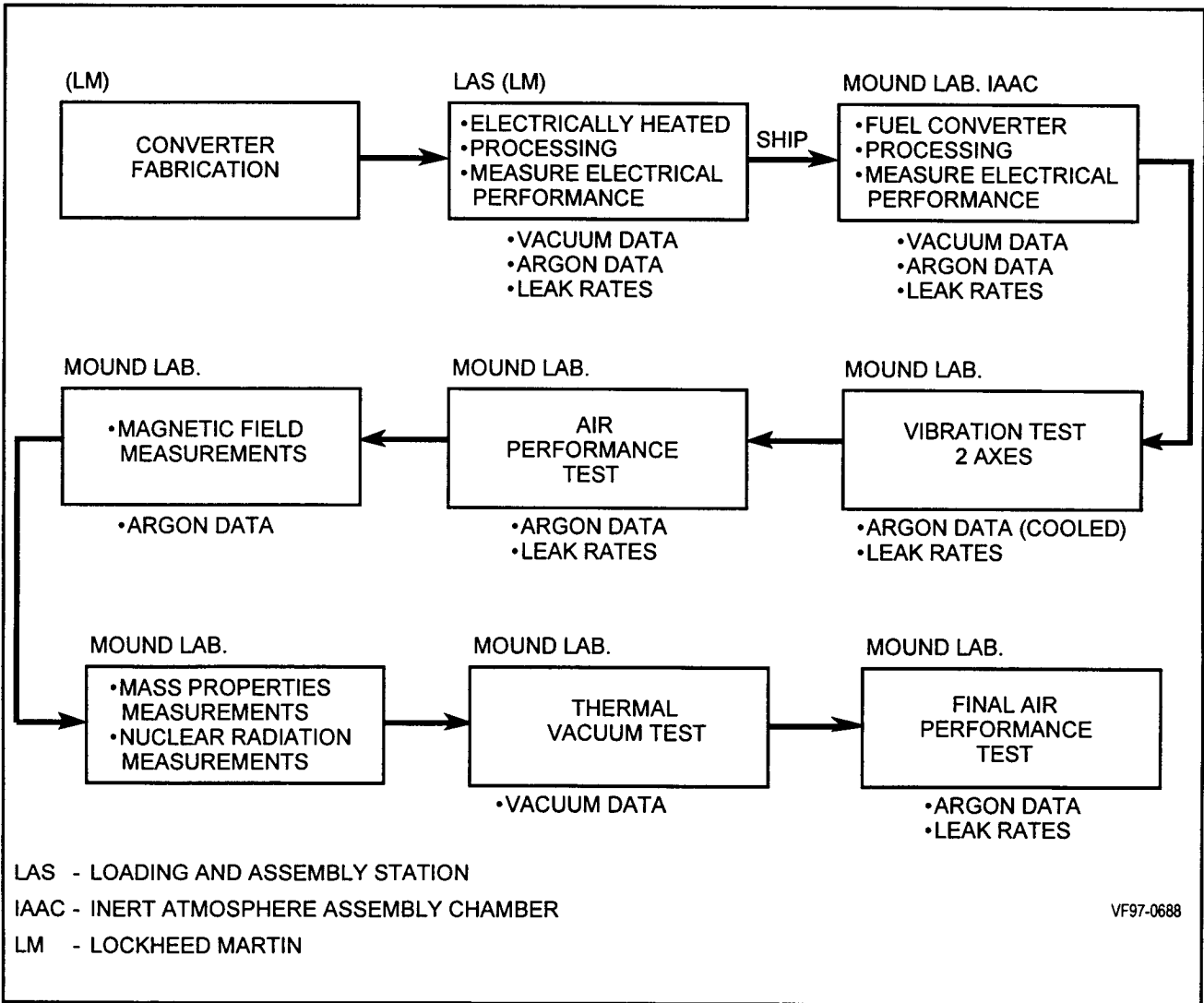
Figure 5.1-1. Flight Units Test Nominal Sequence and Data Acquisition

Vacuum Tests

Following fabrication, each unit is processed and tested with an electric heat source in the LAS (Loading And Assembly Station). The processing consists of a gradual heat-up, in vacuum, to full operating temperatures. The intent of the processing is to outgas absorbed moisture and other potentially degrading gases before achieving full operational temperature. This process typically takes about thirty days as shown in Figure 5.1-2. After achieving a heat input of 4415 watts, the ETG is subjected to a 24-hour stability test followed by a 76-hour stability test at 4402 watts input. The stability tests are performed to demonstrate that the electrical performance of the ETG (i.e., power, voltage, internal resistance, and isolation resistance) is stable and consistent with previously tested ETGs.
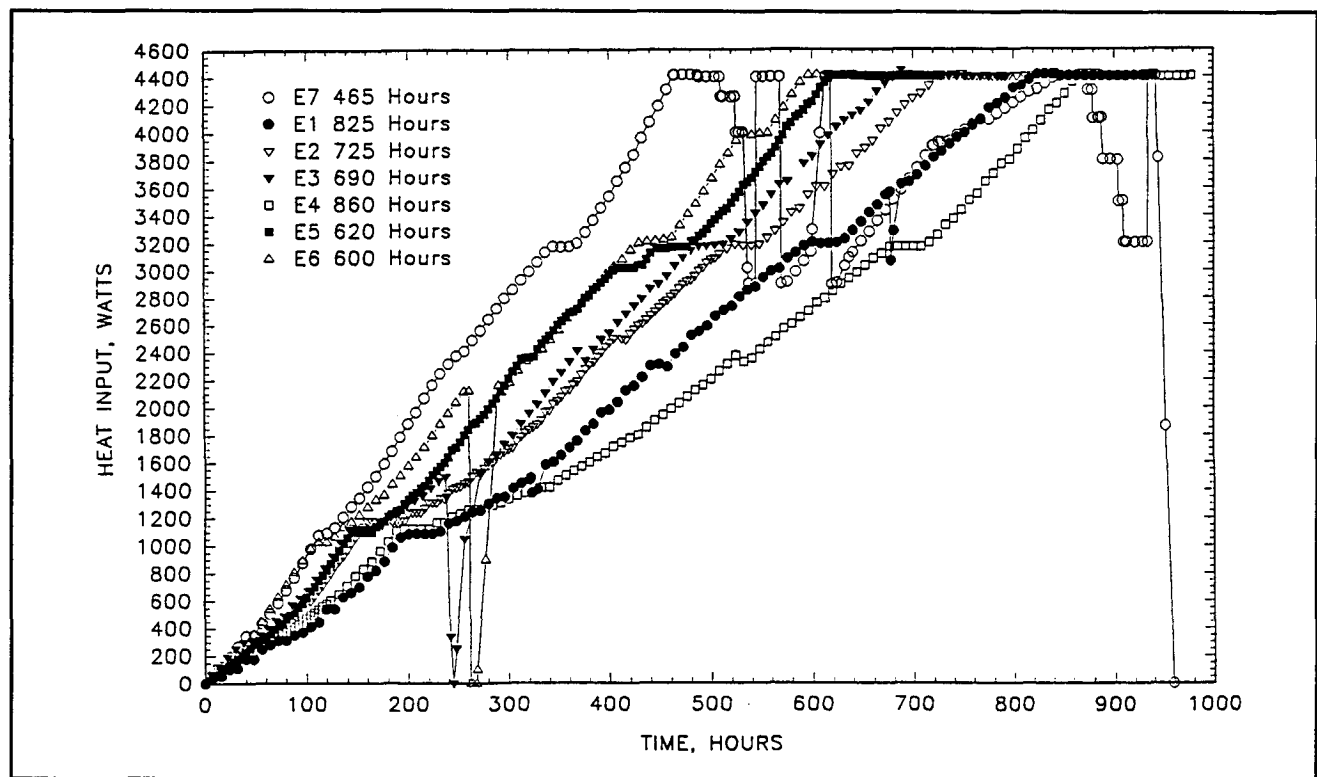
Figure 5.1-2. Heat Input Versus Time to Reach Full Power

Converter E-2

Converter ETG-2 was processed and tested in October 1983 during the Galileo/Ulysses program. It showed normal performance during processing and vacuum testing. At this point only the qualification unit and E-1 had been tested. Power output, internal resistance and isolation resistance were all within a small range for the three units as shown in Table

5.1-1. Following vacuum performance, the next step was to place the end dome on the converter and measure the argon performance and the leak rate. During this operation the converter was exposed to air for a brief period due to an imploded glove port. To assess the effect of the air exposure, an additional vacuum test was performed. Results, also in Table 5.1-1 showed that the converter lost 2.6 watts between the first and second vacuum tests. Analysis of the internal resistance and open circuit voltage changes resulted in a calculated power loss of 0.7 watts due to dopant level changes associated with the temperature cycles and 1.9 watts due to the oxygen effect. The effect of the air exposure was to form an oxide layer on some of the molybdenum foil surfaces, which increased their emissivity and resulted in a larger heat loss. Following vacuum testing, the argon tests were performed as shown in the next section.

Converter E-6

E-6 was the first converter built for the Cassini program and was processed in February 1995. Processing and vacuum performance were normal. Its electrical performance, shown in Table 5.1-1, is seen to be in good agreement with the previously built ETGs. The average normalized power output of the GPHS qualification unit and units E-1 through E-5 was 296.2 watts as shown in Table 5.1-2. Normalized power output for E-6 was 293.4 watts, which was the lowest value of any unit but within one percent of the average of the previous six units. Table 5.1-2 used the initial stability test data for E-2 rather than the second test in order to compare initial performance. E-2 measured 294.8 watts at the end of the first test and 292.2 watts at the end of the second test following the air exposure. Internal resistance of E-6 was 2.150 ohms, which was the highest value measured for any of the ETGs. Open circuit voltage, however, was not higher. This could indicate a small effect due to higher than normal rivet resistances as discussed in Section 3.1.3 of this report. The isolation resistance between the circuit and outer shell was measured at 4,200 ohms, which was higher than measured in four of the six previous converters.

Table 5.1-1. Comparison of ETG Performance

	Qual		E-1		E-2			E-3		E-4		E-5		E-6		E-7	
	Start	End	Start	End	Start	End	End	Start	End	Start	End	Start	End	Start	End	Start	End
Date	1/15/83	1/22/83	7/26/83	8/1/83	9/27/83	10/1/83	10/8/83	2/9/84	2/12/84	4/20/84	4/23/84	6/27/84	6/30/84	2/12/95	2/15/95	2/3/96	2/19/96
Heat Input, watts [2]	4388	4393	4391	4393	4391	4390	4391	4391	4387	4390	4388	4393	4391	4405	4405	4400	4403
Power Output, watts [1] (Measured)	292.7	291.9	292.8	292.6	292.3	291.5	288.9	295.5	294.4	292.9	292.4	295.0	294.3	292.5	291.8	294.4	292.7
Load Voltage, volts	30.04	30.02	30.01	30.04	30.02	30.08	30.02	30.04	30.06	30.07	30.04	30.04	30.02	30.06	30.01	29.99	30.00
Open Circuit, volts	50.28	50.75	50.50	50.85	50.56	50.85	50.99	50.53	50.82	50.48	50.76	50.55	50.85	50.61	50.90	50.70	51.40
Current, amps	9.744	9.724	9.759	9.739	9.735	9.692	9.626	9.838	9.793	9.741	9.735	9.821	9.802	9.730	9.730	9.820	9.760
Internal Resistance, ohms	2.076	2.132	2.100	2.137	2.110	2.143	2.179	2.083	2.120	2.095	2.129	2.089	2.125	2.112	2.150	2.108	2.189
RTD Temp, °C	250.8	250.8	251.8	251.8	252.4	252.4	254.2	247.8	247.6	249.8	249.9	252.3	252.2	247.8	247.7	252.4	252.0
EHS Avg. Temp, °C	—	—	1039	1040	—	—	—	1043	1042	1049.2	1048.4	1055	1054	1042.9	1041.9	—	—
Circuit Isolation to Case, ohms x 10^{-3} 2 Seconds	1.93	1.48	2.2	2.1	2.0	1.9	—	2.2	2.2	4.0	3.1	5.0	4.6	3.3	2.6	2.6	1.2
2 Minutes	3.77	2.33	4.2	3.9	3.6	3.1	2.7	3.4	3.4	7.0	7.8	9.5	9.7	6.0	4.2	3.5	1.4
EHS Isolation to Shell, ohms x 10^{-3} 2 Seconds	8.16	4.19	7.5	9.3	4.6	6.0		6.0	9.6	9.0	15.0	9.0	10.7	13.0	13.0	—	—
2 Minutes	4.52	4.3	6.0	6.3	3.8	4.6	4.7	6.4	7.4	6.0	9.0	13.0	11.0	8.3	8.5	—	—
Normalized Power [3] at 4402 watts Input, at Pins, watts	296.3	294.9	296.0	295.6	295.5	294.8	292.2	298.7	298.1	296.2	296.0	298.0	297.5	294.1	293.4	296.6	294.6
Elapsed Time, hours		171		84		76			76		76		76		76		51

[1] Thermopile power output is approximately 2 watts higher than measured.

[2] Includes lead loss correction of 25 watts.

[3] Using 0.12 w(e) per w(th).

5-4

Table 5.1-2. Average Power, Internal Resistance, and Open Circuit Voltage at End of LAS Vacuum Test (30 Volts) for Qualification and E-1 through E-5 ETGs

Power Output [1] at RTG Pins (watts)	Average	296.2
	Low (F-2) [2]	294.8
	High (F-3)	298.1
	Range	3.3 (1.1%)
Internal Resistance (ohms)	Average	2.131
	Low (F-3)	2.120
	High (F-2) [2]	2.143
	Range	0.023 (1.1%)
Open Circuit Voltage (volts)	Average	50.83
	Low	50.76
	High	50.85
	Range	0.09 (0.2%)

[1]   Normalized to 4400 watts; 25 watt total heater lead correction

[2]   E-2 used first LAS test data

Converter E-7

E-7 was the second and last of the new converters built for the Cassini program and was processed in February 1996. It showed normal power output, internal resistance, and open circuit voltage during heat-up and during stability testing as shown in Table 5.1-1. The isolation resistance trend for E-7, however, was observed to be abnormal. This abnormal trend is discussed in detail in Reference 5-1. A summary of the report is provided here.

The isolation resistance began to show a slightly steeper than normal slope after the heat input reached 4,200 watts. The EHS did not have any thermocouples, but based on E-6 measurements, this would correspond to an average EHS surface temperature of 1010°C as shown in Figure 5.1-3. During the stability testing at the 4400 watt level, both the isolation resistance value and the isolation resistance trend fell outside the previous database as shown in Figure 5.1-4. Extrapolation of the data indicated that the resistance
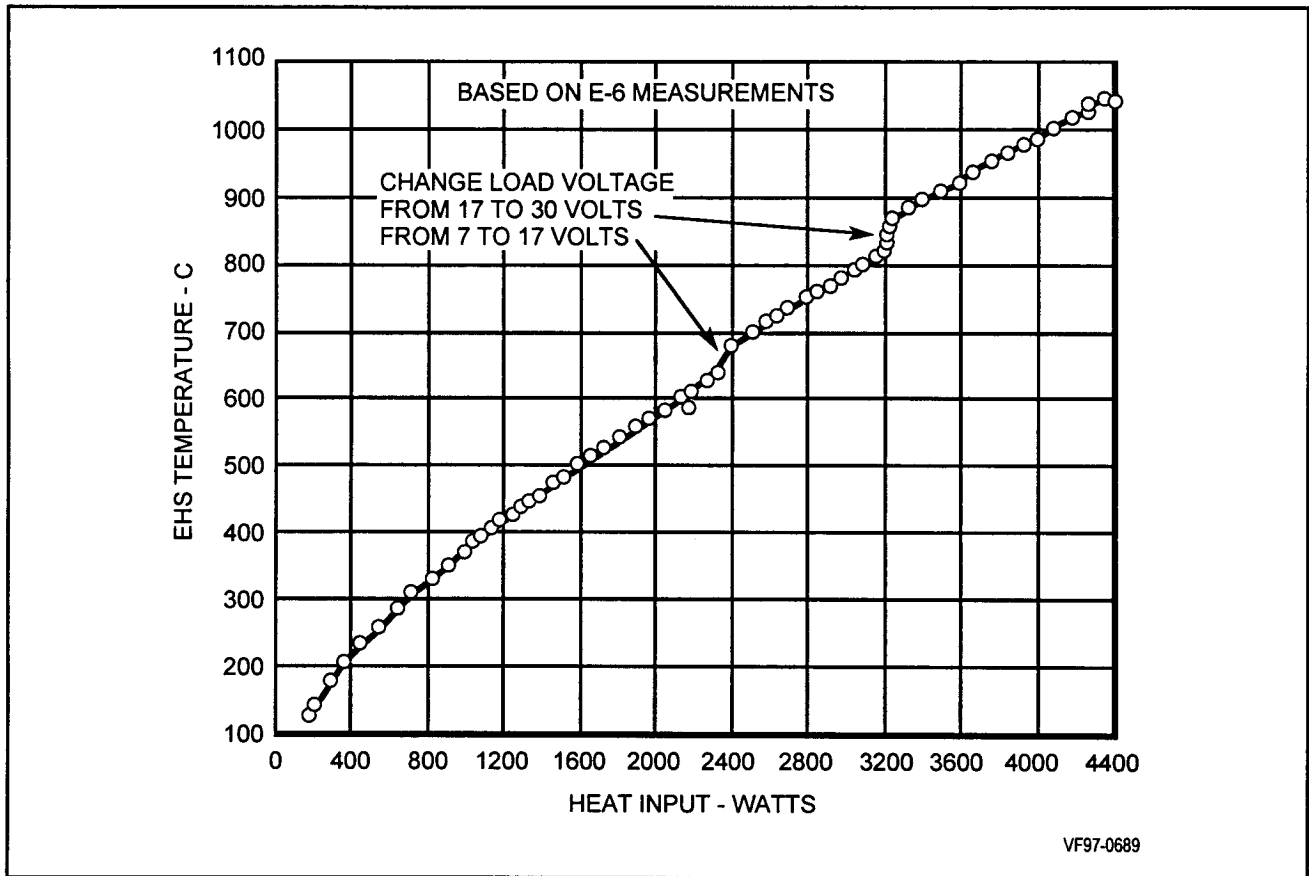
Figure 5.1-3. EHS Temperature Versus Heat Input during E-7 Processing

might fall below the 1,000 ohm requirement before the end of the stability test. Efforts were taken to halt the downward isolation resistance trend. Because the water vapor partial pressure, as indicated by residual gas analyzer (RGA) measurements, was higher than observed during E-6 processing, it was decided to decrease the power input and remove water at a lower temperature. In addition, it was decided to backfill the LAS with dry argon and use the scrubber system to help remove some of the water vapor. The scrubber was operated for approximately 24 hours after which vacuum processing was restarted. Isolation resistance trends during the reprocessing are shown in Figure 5.1-5. Figure 5.1-6 shows the isolation resistance during the first and second stability tests along with the qualification ETG trend.
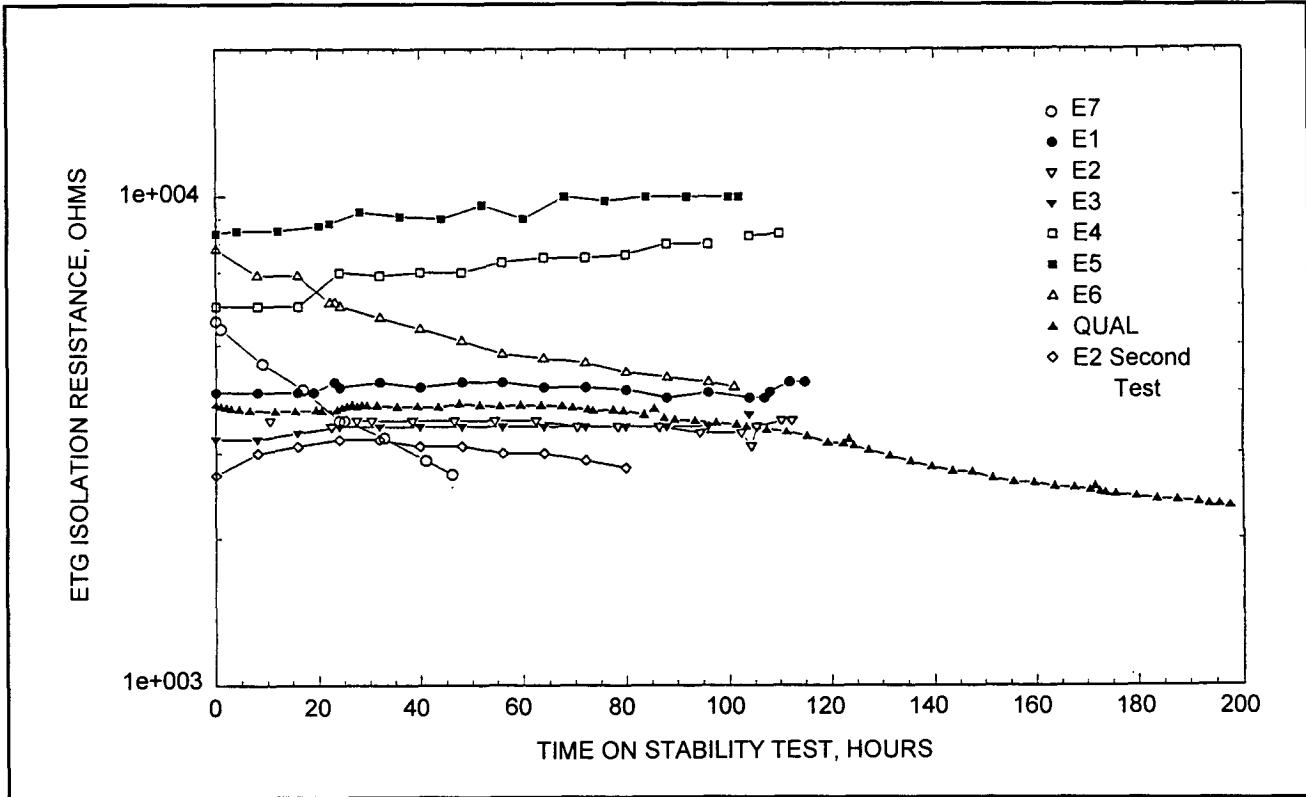
Figure 5.1-4. ETG Isolation Resistance Versus Time during Stability Tests
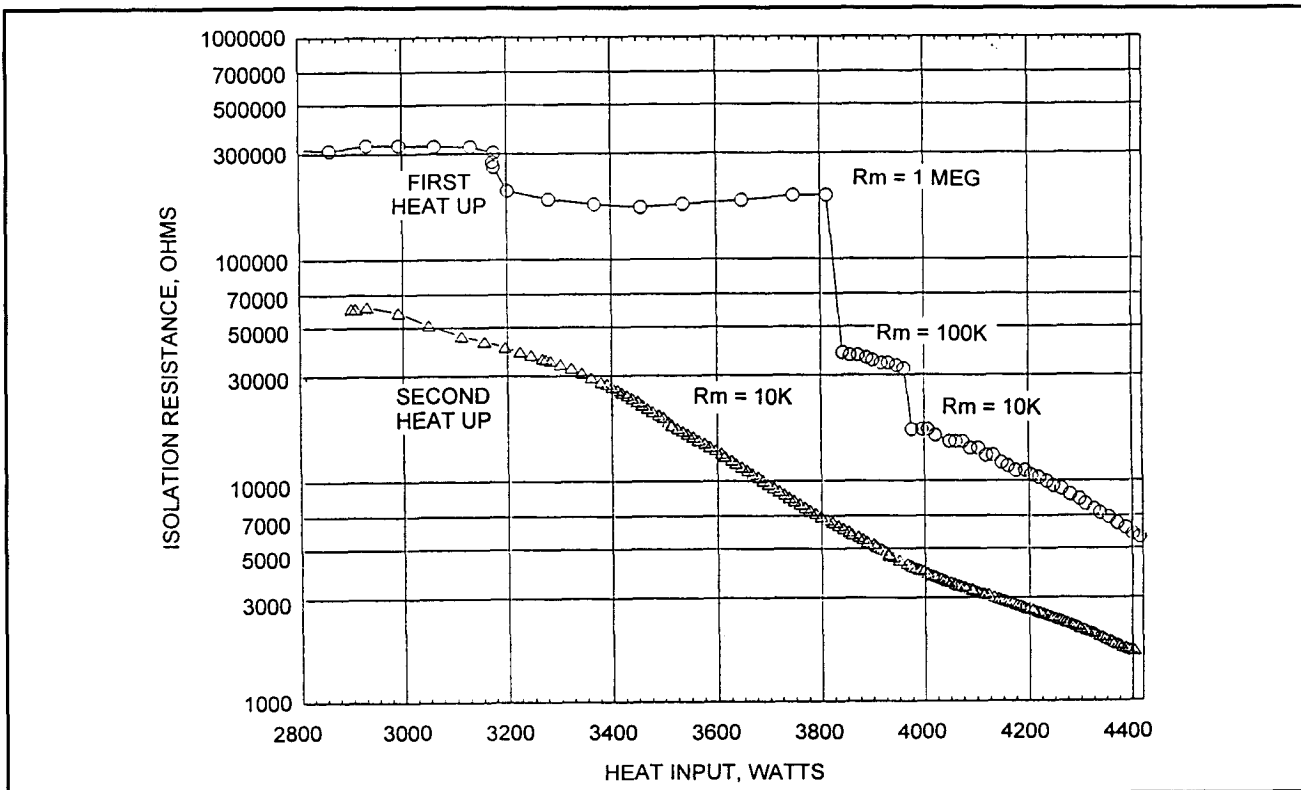
Figure 5.1-5. E-7 Isolation Resistance during First and Second Heat-Ups
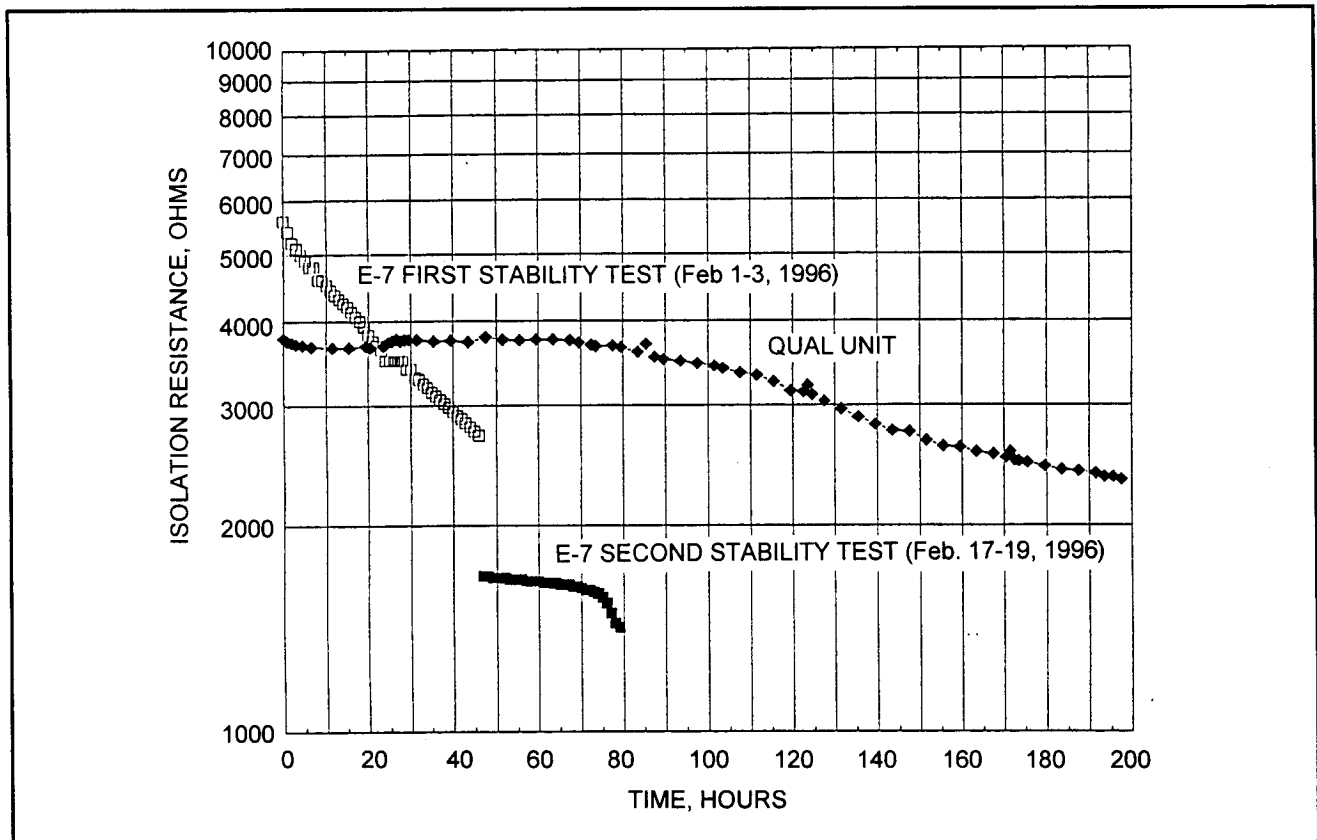
Figure 5.1-6. E-7 Isolation Resistance during Stability Tests

The decrease in isolation resistance between the end of the first and the start of the second stability test was attributed to the deposition of conductive material during the slow reheat, over a period of 220 hours, from 2900 watts. The resistance was nearly constant through the first 26 hours of the second test, but then began to decrease and reached 1,400 ohms. The resistance decrease was accompanied by an increase in the ETG internal pressure as shown in Figure 5.1-7. (The ETG internal pressure was measured by an ion gauge which penetrated the inboard dome as shown in Figure 5.1-8.) Stability testing was terminated at this point, with MRB approval, because of the concern that higher than normal effluent gases were emanating from the EHS which could further degrade the ETG isolation resistance.

Investigation Results

An investigation was initiated to identify the source and cause of the lower-than-expected isolation resistance and to determine if there may be long term adverse effects on RTG performance. The investigation reviewed and identified differences between the E-7 ETG

ISOLATION RESISTANCE AND ETG PRESSURE CHANGE AS HEAT INPUT IS REDUCED

ISOLATION RESISTANCE

ETG PRESSURE

—4400 WATTS— | 4300 | 4100 WATTS

TIME - HOURS
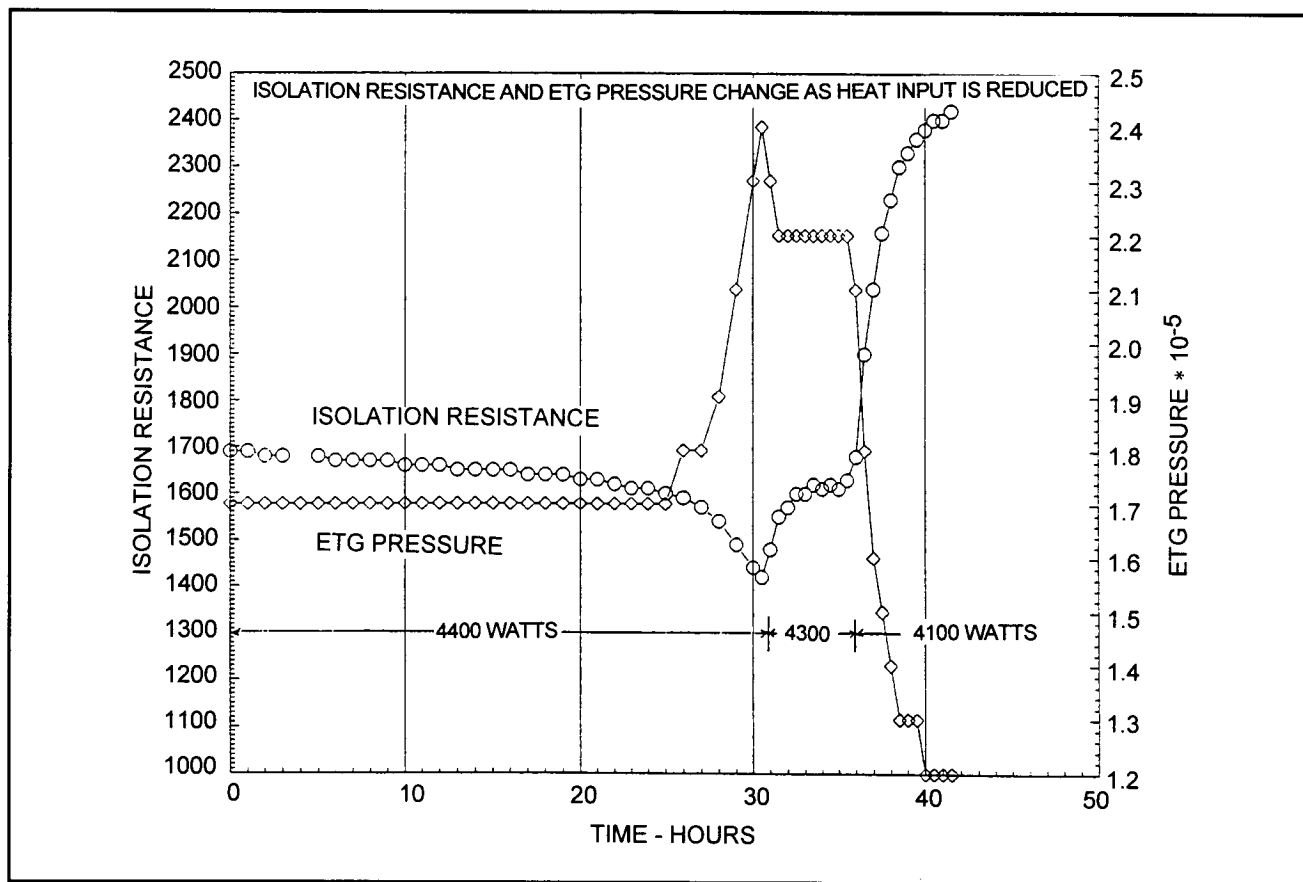
Figure 5.1-7. E-7 ETG Pressure Versus Time during Second Stability Test

and previous ETGs. Differences in materials, configuration, and processing parameters were evaluated. Gaseous effluents from the EHS were a suspected cause and emphasis was placed on EHS material and configuration differences. Equilibrium thermodynamic analyses were performed by Lockheed Martin (LM) and Battelle Columbus Lab (BCL) to predict the chemical reactions taking place in the EHS and converter during heat-up and stability testing which could cause a reduction in ETG isolation resistance. Verification tests were performed at BCL to confirm the hypothesized reactions. Based upon these evaluations, an assessment was made regarding long term adverse effects on RTG performance.

The investigation concluded that the E-7 isolation resistance was most likely degraded by the deposit of gaseous aluminum effluent from the EHS onto the silica wrap between the unicouple and foil insulation. These deposits normally occur during ETG processing, but
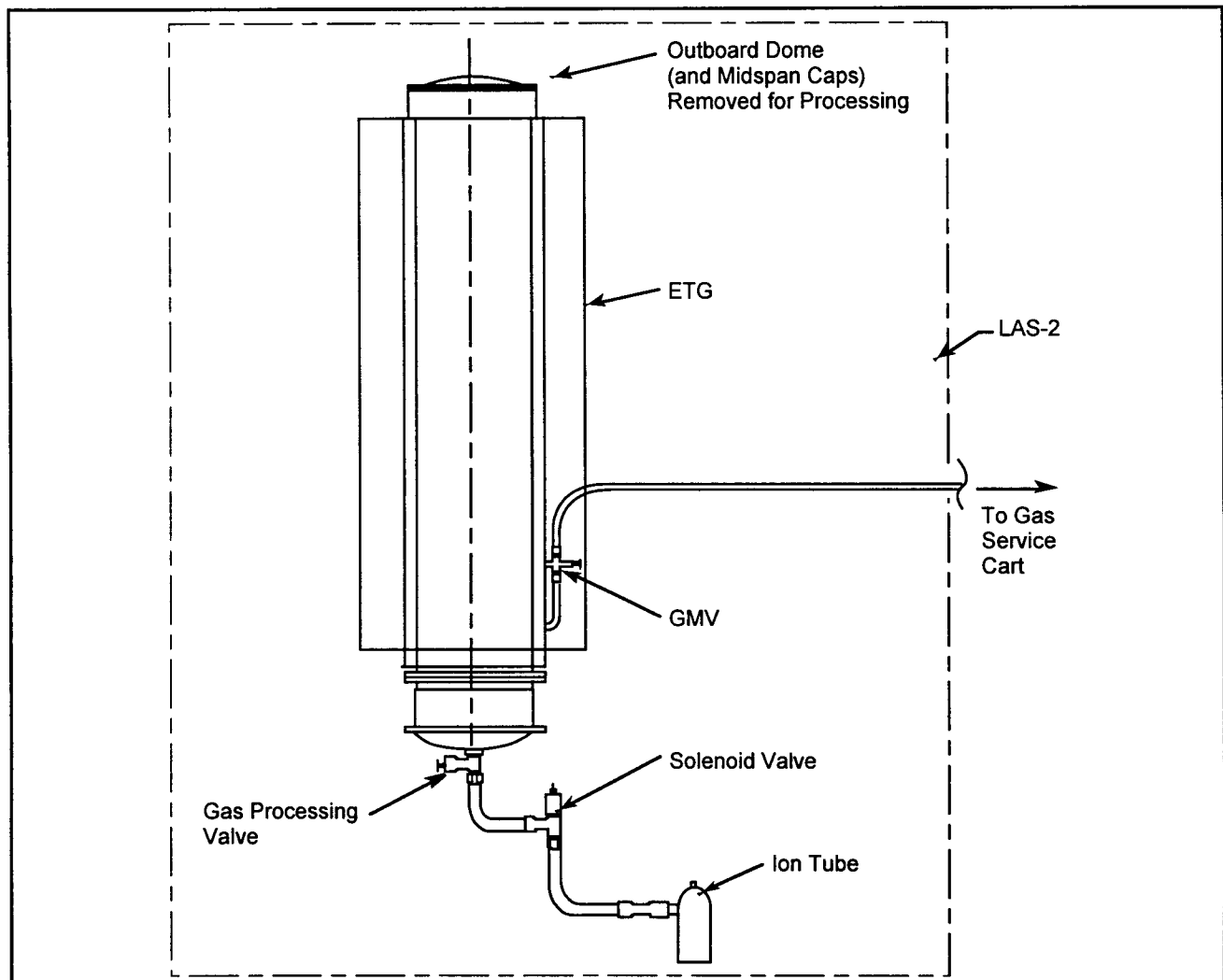
Figure 5.1-8. E-7 Processing Configuration

were aggravated during E-7 processing because of several factors. The initial EHS heat-up rate was faster than for E-6 and the moisture level in the ETG was approximately twice as high as indicated by RGA scans. The E-7 EHS configuration was different in that it had more venting area because its thermocouples were not installed due to a thermocouple wire cracking problem. This resulted in the EHS operating at lower pressures than in previous ETGs. Thermogravimetric analyses (TGA) at BCL verified that the EHS alumina/graphite reaction rate was enhanced as the total pressure decreased and that sufficient aluminum was generated to account for the lower E-7 isolation resistance. These results were supported by thermodynamic analyses conducted by LM and BCL. In addition, verification tests performed at BCL indicated the E-7 EHS ceramics were three to five times more reactive than those used in the E-6 EHS.

These deposits represent less than a single layer (monolayer) of aluminum distributed over the surface of the silica wrap of the unicouples and are not expected to have any adverse, long term effect on the F-7 RTG performance. Its performance is expected to be within the database of the previous RTGs. The interior of the F-7 thermopile (heater cavity) was inspected at Mound when the EHS was removed in preparation for fueling. There was no evidence of any deposits or foreign material. Final confirmation that the isolation resistance was stable and acceptable was obtained after stable performance data were observed during and after thermal vacuum testing of the F-7 as described in Section 5.2.5.

5.2 FLIGHT RTG ACCEPTANCE TESTING

5.2.1 IAAC Assembly and Performance Testing

Argon Performance (Pre-Vacuum)

After ETG acceptance testing at the Lockheed Martin Valley Forge facility the units were fueled at Mound Laboratories. The fueling operation is performed in the Inert Atmosphere Assembly Chamber (IAAC). Fueling takes place in an argon atmosphere and the first electrical performance data are obtained at this time. Table 5.2.1-1 summarizes the stabilized data which is taken with the upper end dome off.

Table 5.2.1-1. IAAC Performance (Dome Off) Argon Environment

	F-5 RTG	F-2 RTG	F-7 RTG	F-6 RTG
Date	12/7/84	2/10/96	9/4/96	11/16/96
Hour	1000	1700	0700	0700
Heat Input, watts	4459.5	4435	4435	4437
Power Output, watts				
As Measured	174.7	168.0	169.5	158.3
Corrected to Pins	175.4	168.6	170.1	158.9
Load Voltage, volts	30.00	30.012	29.98	30.04
Open Circuit Voltage, volts	41.65	41.793	41.615	40.681
Current, amps	5.823	5.597	5.653	5.270
Internal Resistance, ohms	2.000	2.105	2.053	2.019
Average RTD Temperature, °C	181.3	177.7	179.9	179.6
Bell Jar Temperature, °C	45.3	37	35.5	33.6
Isolation Resistance to Shell (2 minutes), Ohms	—	60.7K	58.3K	66.5K

F-5 was fueled during the Galileo program in December 1984 with a fuel thermal loading of 4459.5 watts. The Cassini RTGs had a fuel loading approximately 25 watts lower. This accounts in part for the lower power. F-2 had already been through two thermal vacuum tests and had air exposure in 1983. These all contributed to a lower power. In addition, comparison of ETG and RTG thermal vacuum open circuit voltage data had indicated that the true fuel loading in the Galileo RTGs was approximately 30 watts higher than the reported value. Comparison of F-6 with other RTGs led to the conclusion that the end dome foil package was not seated as well. This led to higher convective heat losses and lower power output. The effect is less in vacuum as shown in the next section.

Vacuum Performance

Vacuum performance data is obtained in the water cooled bell jar located in the IAAC. Table 5.2.1-2 summarizes the measured performance. The power requirement for a 4410 watt input was 291 watts for F-2, 293 watts for F-6 and F-7 and 292 watts for F-5 (at 30+0.7/-0.5 volts). A second requirement was that the electrical isolation between the thermopile and outer case be 1,000 ohms minimum. Both of these requirements were met as shown in Table 5.2.1-2. Additional requirements were that bell jar pressure be 1x 10^{-5} torr or less and that the CO (carbon monoxide) partial pressure be 1 x 10^{-7} torr or less. These requirements were not met. Although the total bell jar pressure was only slightly above the requirement, the CO partial pressure was 11 to 40 times higher.

CO Level Investigation

The CO investigation was reported in detail in Reference 5-2. The CO problem surfaced during processing of the F-2 RTG when it was not possible to reach a bell jar pressure below 1x10^{-5} torr and a calculated CO partial pressure equal to or less than 1 x 10^{-7} torr. The CO partial pressure was estimated to be 4 x 10^{-6} torr. The bell jar transient pressure history had shown a trend indicative of either a pump problem, outgassing or an air leak. RGA scans showed a peak at mass 78 indicating off-gassing and an oxygen partial pressure of 2.6 x 10^{-6} torr, which was a clear indication of an air leak. Subsequent trouble-

Table 5.2.1-2. IAAC Vacuum Performance (Dome Off)

	F-2 RTG	F-5 RTG	F-6 RTG	F-7 RTG
Date	2/18/96	12/16/84	11/21/96	9/10/96
Hour	1800	1400	1000	1200
Heat Input, watts	4435	4458.6	4437	4435
Power Output, watts				
As Measured	295.9	305.5	298.2	297.9
Corrected to Pins	297.8	307.6	300.2	299.9
Normalized to 4410W Input *	294.8	301.8	295.8	296.9
Load Voltage, volts	30.034	30.070	30.144	30.031
Open Circuit Voltage, volts	51.751	51.94	51.873	52.305
Current, amps	9.851	10.158	9.891	9.921
Internal Resistance, ohms	2.205	2.152	2.197	2.245
Average RTD Temperature, °C	262.5	262.6	261.2	261.4
Insulation Resistance, k-ohms				
Thermopile to Case (2 minute)	2.7	6.42	4.12	2.49
Chamber Pressure, torr	4×10^{-5}	2.8×10^{-6}	1.1×10^{-5}	8.2×10^{-6}
Average Sink Temperature, °C	68.3	68.8	57.8	61.3
CO Partial Pressure, torr	4×10^{-6}	2.3×10^{-8}	3.3×10^{-6}	1.1×10^{-6}

* Normalized using 0.12 watts electric per thermal watt input

shooting, after the RTG was removed from the IAAC, showed that the pump performance was erratic. One test with a controlled leak injected into the bell jar showed a calculated pumping speed of 5 liters/sec. At the time it was thought that the pumping speed should have been about 165 liters/sec. Numerous other trouble shooting tests failed to identify the source of the air leak, but the liquid nitrogen cold trap was highly suspect. The oil diffusion pump and cold trap were subsequently replaced with a turbomolecular pump prior to the fueling the F-7 RTG.

During IAAC vacuum processing of the F-7 RTG, a total pressure of 8 x 10⁻⁶ torr was obtained, however, the CO partial pressure requirement again was not satisfied. The calculated CO partial pressure was reported as 1.1x10⁻⁶ torr. Prior to the November 1996 fueling of the third RTG (F-6), the CO partial pressure limit was increased from 1 x 10⁻⁷ to 5 x 10⁻⁶ torr. The calculated CO partial pressure for the F-6 RTG was 3.3 x 10⁻⁶ torr which was

below the new limit. It was apparent that a more detailed knowledge of the vacuum system was needed to understand the observed results. The following areas were considered during the investigation.

Vacuum system pumping speed

Effect of 90° elbow

Comparison of helium partial pressures

Vacuum measurement and RGA sampling methods

Comparison of CO pressures in the LAS

Outgassing of PD224 high emissivity paint on the outer shell

CO released from the fuel

The major findings were (1) that the elbows in the pumping system (Figure 5.2.1-1) control the net pumping speed (Figure 5.2.1-2) and not the size of the pump. If operating properly, both the turbomolecular or the oil diffusion pump would provide the same (within 10%) pressure for a given gas generation rate, (2) the measured partial pressures of helium for the Cassini RTGs are in good agreement with the values calculated from the known helium generation rate and the calculated net pumping speed. The helium partial pressures reported for the Galileo/Ulysses RTGs, on the other hand, were about a factor of 50 lower than predicted as shown in Figure 5.2.1-3.

The reported CO partial pressures in the IAAC bell jar for both programs are also shown in Figure 5.2.1-3. There is a striking similarity in the relative differences in the magnitude of both.

BELL JAR

BELL JAR AND 6" VACUUM LINE

HIVAC VALVE

TURBO PUMP

IAAC WALL
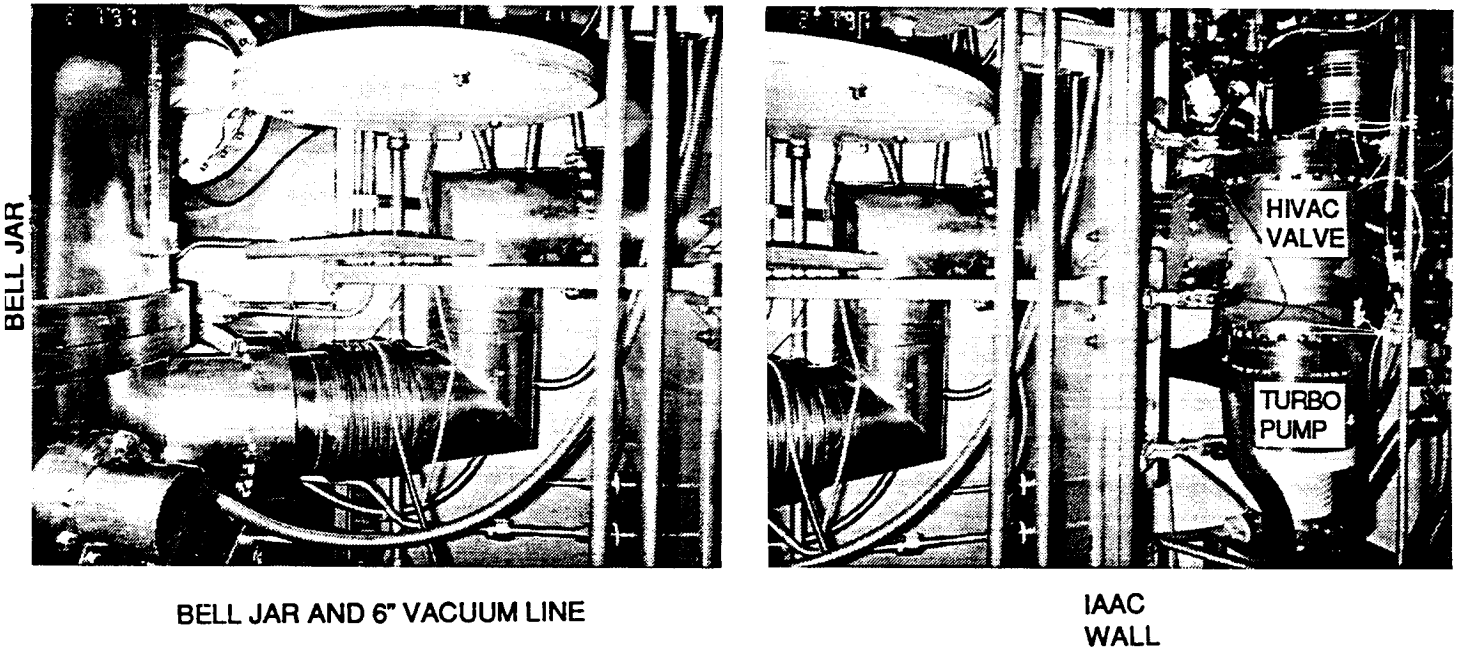
Figure 5.2.1-1. IAAC Vacuum Chamber with Turbomolecular Pump
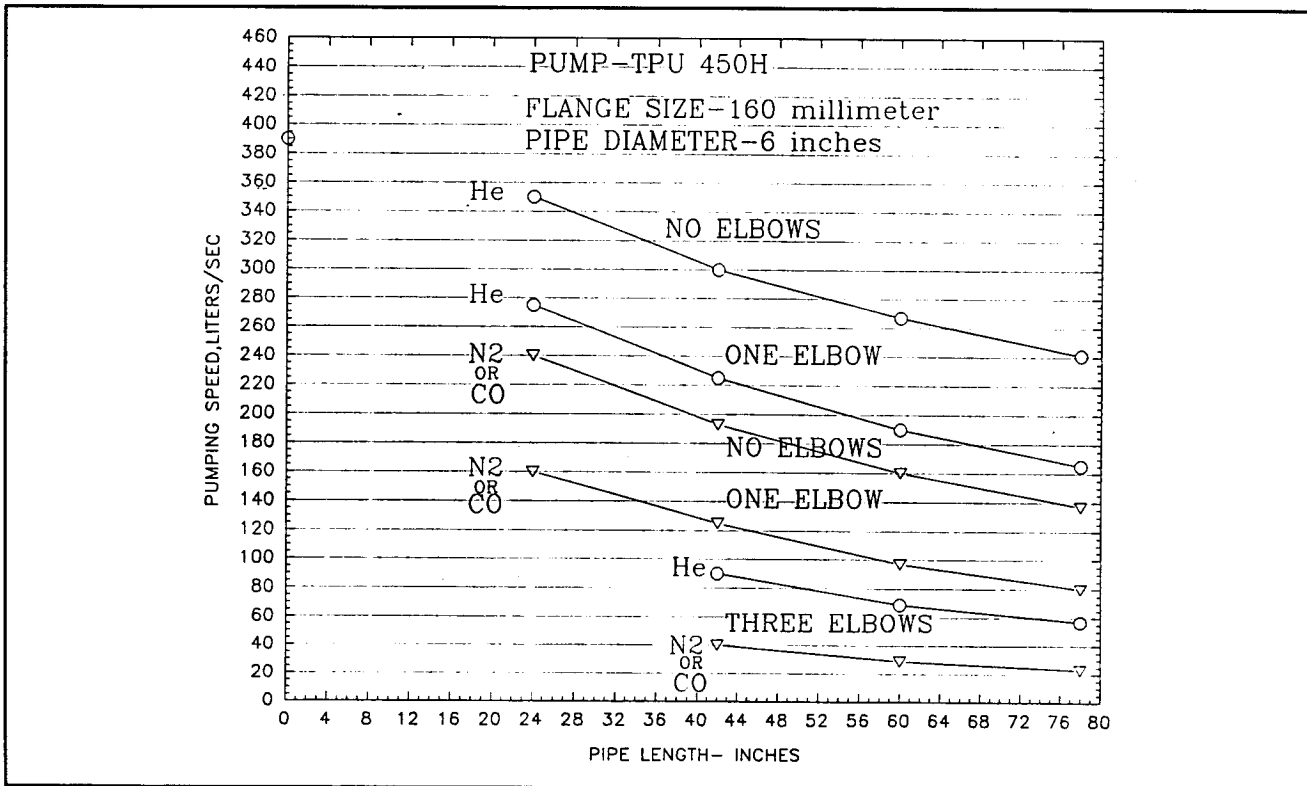
**Figure 5.2.1-2. Effect of Elbows on Net Pumping Speed of He and CO
(Calculated by Pfeiffer Vacuum Technologies)**
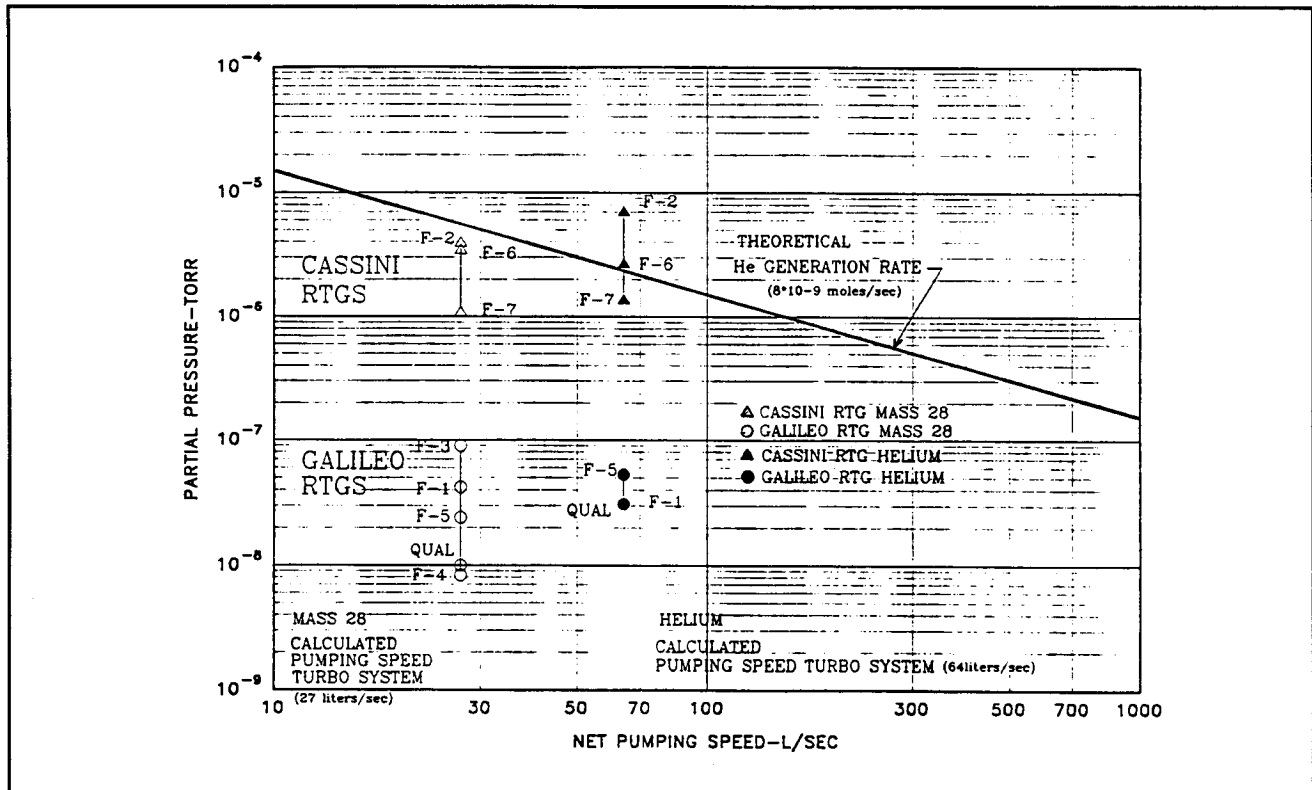
Figure 5.2.1-3. Comparison of the He and CO Partial Pressures and IAAC Net Pumping Speeds for the Cassini and Galileo/Ulysses RTGs

He and CO

The CO levels in the Cassini RTGs were also a factor of 50 higher than those for the Galileo/Ulysses RTGs. In vacuum systems, uncertainties in measurement are often such that pressure deviations of a factor of 2 or 3 or sometimes a factor of 5 are not necessarily considered unusual. It is further noted that the Cassini RTG total pressures, as measured by an independent vacuum gauge, were about a factor of 3 higher than those reported for the Galileo/Ulysses RTGs (Table 5.2.1-3). This smaller difference, as compared to the factor of 50 difference in He and CO partial pressures, suggests that systematic differences related to the RGA system are responsible for the apparently higher CO levels in the Cassini RTGs.

A review of the RGA differences was made as well as the methods used to calculate the partial pressures from the raw data. The differences were found to be significant as discussed in detail in Reference 5-2. The new system used for Cassini was found to be much less prone to error than the old system.

Table 5.2.1-3. Total Pressure in the IAAC Vacuum Chamber

Date Processed	Unit	Total Pressure (torr)	Vacuum Pump	Calculated Mass 28 Pumping Speed with 3 Elbows (liters/sec)
Galileo/Ulysses RTGs				
Feb 1984	Qual	3.2×10^{-6}	Oil Diffusion	28.3
Sep 1984	F-1	1.8×10^{-6}	Oil Diffusion	28.3
Dec 1984	F-5	2.8×10^{-6}	Oil Diffusion	28.3
Feb 1985	F-3	4.5×10^{-6}	Oil Diffusion	28.3
June 1985	F-4	4.7×10^{-6}	Oil Diffusion	28.3
Cassini RTGs				
Feb 1996	F-2	$\sim 4 \times 10^{-5}$	Oil Diffusion	28.3
Sep 1996	F-7	8.2×10^{-6}	Turbomolecular	27
Nov 1996	F-6	1.1×10^{-5}	Turbomolecular	27

CO measurements made in the LAS when scaled up by the ratio of pumping speeds showed that the Cassini levels were consistent. LAS CO data from the Galileo program Qual unit when scaled by the pumping speed ratio should have resulted in an IAAC bell jar pressure of 1.1×10^{-6} torr whereas the value reported was 1×10^{-8} torr or 100 times lower.

Conclusion

The higher CO partial pressure and total pressure of the Cassini RTGs measured during IAAC processing were primarily due to improved vacuum measurement and residual gas analysis methods. Secondary contributions included a reduced vacuum pumping speed, outgassing of the PD224 outer shell coating and transient release from the PuO_2 fuel. (The latter two were responsible for the higher levels from F-2 and F-6 relative to F-7.) It was determined that the CO and He partial pressures reported for the Galileo/Ulysses RTGs were found to be artificially low and the actual CO partial pressures for the Cassini RTGs were not significantly different than those that actually existed for the Galileo/Ulysses RTGs. The difference was attributed to possible errors introduced by conversion of a current signal to a voltage and comparison of a pen trace to a calibration curve associated with the method used for the Galileo/Ulysses RTGs compared to the microprocessor controlled data acquisition and analysis method used for the Cassini RTGs. Active pumping on the RGA during processing of the Galileo/Ulysses RTGs could also have contributed.

All the Cassini RTGs processed in the IAAC bell jar were affected by the systematic RGA problem. In addition, the F-2 RTG was processed in the IAAC bell jar equipped with a faulty oil diffusion pump and some outgassing from the touch-up PD224 outer shell paint contributed to the CO level. For the F-6 RTG, some residual CO was released from the fuel due to a shorter (Modular Reduction and Monitoring Facility) MRMF processing time.

The CO partial pressures measured subsequently in the thermal vacuum chamber indicated normal generation rates for all Cassini RTGs (References 5-3, 5-4, 5-5). Analyses of both the IAAC and the thermal vacuum chamber RGA data suggest that the internal CO generation rates were not significantly different from those seen in the Galileo/Ulysses program. Consequently, the Cassini RTG power performance is expected to be comparable to that of Galileo/Ulysses RTGs.

Isolation Resistance

The isolation resistance between the thermoelectric circuit and outer shell is measured during IAAC operations. Figure 5.2.1-4 shows the isolation trends for the Cassini RTGs during the time of vacuum operation. The initial point is the time at which the RTG is switched from short circuit to 30 volts. The isolation trend of F-7 was of particular interest because of the low isolation resistance measured during ETG testing in the LAS.

GESP-7247 (Reference 5-6) was issued predicting the expected isolation resistance behavior of F-7. A minimum resistance in the range from 670 to 850 ohms was predicted. In addition a gradual rise to between 850 to 1220 ohms after 20 hours was also predicted. The measured minimum was 1150 ohms and in 20 hours the isolation resistance had risen to 1700 ohms. The normal resistance trend lends credence to the conclusion expressed in Reference 5-1 (E-7 Processing Investigation Final Report) that the problems observed in the LAS were directly related to the electric heat source and would cease when the heat source was removed and replaced by the isotope heat source.
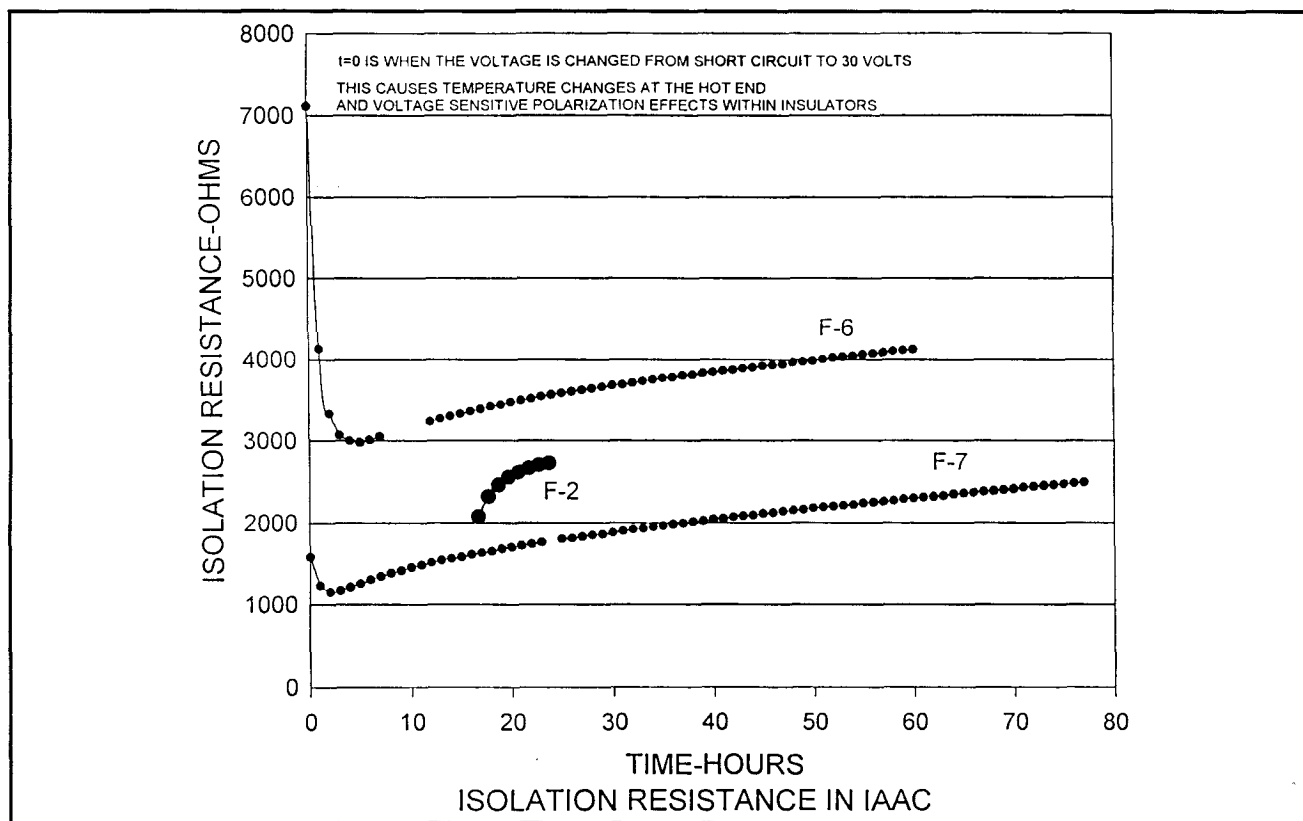
Figure 5.2.1-4. Isolation Resistance in IAAC

Figure 5.2.1-5 shows the isolation resistance trends for both the Cassini and the Galileo/ Ulysses RTGs. All RTGs show an upward trend after the minimum is reached in less than ten hours. Additional isolation resistance measurements made during thermal vacuum testing (Section 5.2.5) continued to show normal isolation resistance trends for the Cassini RTGs.
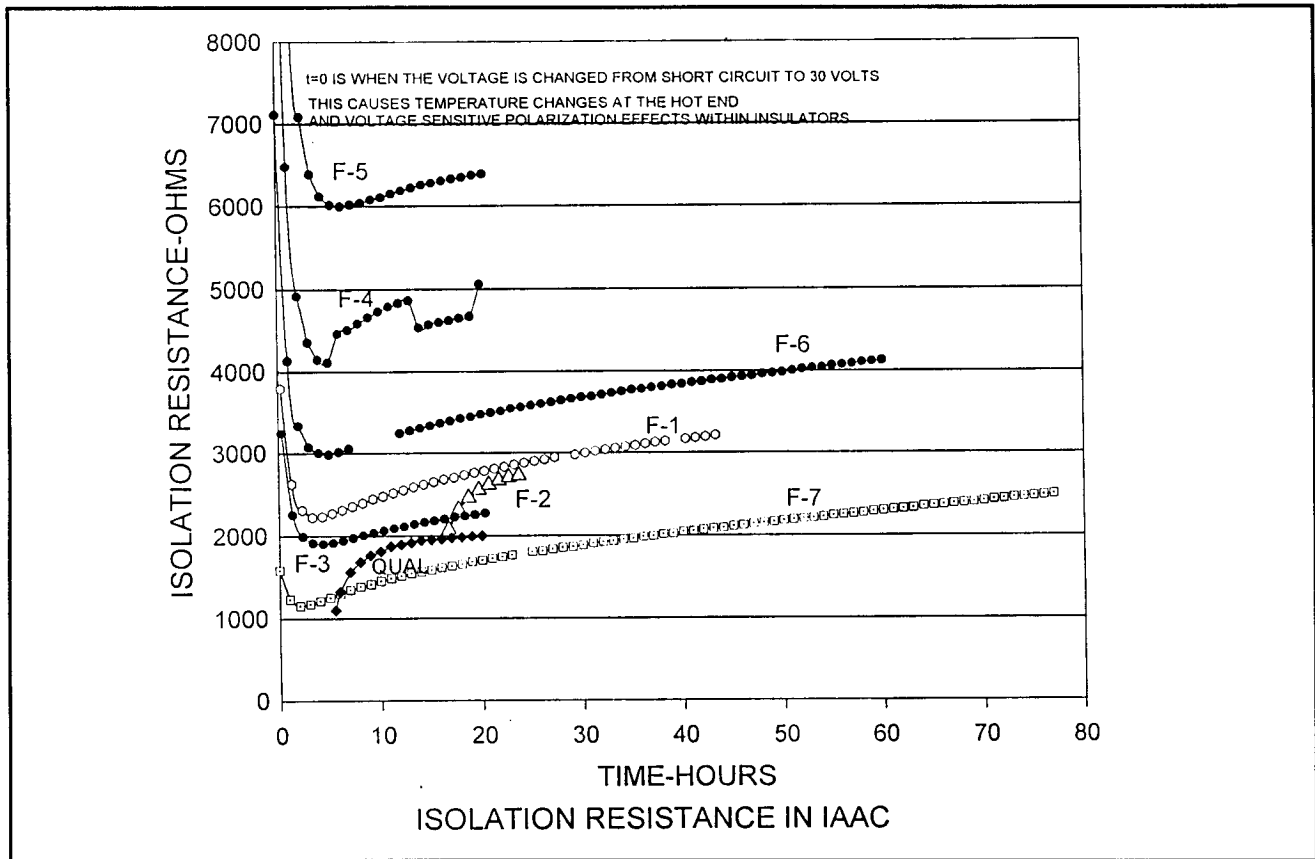
Figure 5.2.1-5. Cassini and Galileo/Ulysses RTGs

5.2.2 Vibration Testing

All of the RTG Flight Units for the Cassini mission (F-2, F-6, and F-7) were subjected to dynamic acceptance tests in accordance with Specification 23009150. The spare RTG (F-5), having previously been acceptance tested for the Galileo and Ulysses missions, was subjected to a reduced set of acceptance tests in preparation for the Cassini mission. These tests did not include dynamic testing. (F-5 was subjected to a one-time low level dynamic test at the request of JPL which argued that it served to confirm that the response of the component engineering test (CET) dynamic model did correspond to the response of an actual RTG and that the response of F-5 had not materially changed since its acceptance test.)

Each RTG was subjected to dynamic acceptance tests in the sequence summarized in Table 5.2.2.-1. Functional performance tests performed before and after dynamic testing, and measurements of internal resistance, open circuit voltage, power output, and insulation

resistance performed before and after each change in axis or environment confirmed, in each case, that no damage to the RTGs resulted from these dynamic environments.

Table 5.2.2-1. Vibration Test Sequence Summary

Test No.	Axis	Environment	Duration
1	Y	1/2 g Sine Sweep	10-2000 Hz, 2 Oct/Min
2	Y	FA Random	1 Minute at 0 dB
3	Y	FA Transients	1 Pulse at 0 dB 4 Frequencies
4	Y	1/2 g Sine Sweep	10-2000 Hz, 2 Oct/Min
5	Z	1/2 g Sine Sweep	10-2000 Hz, 2 Oct/Min
6	Z	FA Random	1 Minute at 0 dB
7	Z	FA Transients	1 Pulse at 0 dB 4 Frequencies
8	Z	1/2 g Sine Sweep	10-2000 Hz, 2 Oct/Min
Random and transient environments as defined in Specification 23009150.			

Response to sine and random vibration is summarized in Tables 5.2.2-2, 5.2.2-3, and 5.2.2-4 for RTGs F-2, F-6, and F-7, respectively. These tables show measured frequencies and transmissibilities (amplification factors) for instrumented locations on the RTGs: at midspan, and on the PRD. Overall, the responses were comparable on all three RTGs. The similarity of responses in pre-test and post-test sine sweeps is a good indication that no damage or permanent distortion occurred in any of the RTG structural members as a result of being subjected to the dynamic environment.

Flight Acceptance (FA) level random vibration tests were performed in the lateral and longitudinal axes of the RTG. The tests were begun at -15 dB test level and the test levels were increased in 3 dB increments until the 0 dB test level was achieved. The random vibration tests were controlled by the average power spectral density response of the four in-axis accelerometers attached to the RTG interface mounting plate. For all tests, the applied Random spectra were within the ±3 dB test tolerance abort limits of the defined environment. No significant changes in the dynamic characteristics or electrical performance occurred during or after the random tests.

Table 5.2.2-2. Random Vibration Test Result Summary for RTG F-2

Location	Mode	Pre-Test Sine Sweep (1/2 g) Freq. (Hz)	Q	Random Freq. (Hz)	Q	Post Test Sine Sweep (1/2 g) Freq. (Hz)	Q
Midspan Y Axis	First	48.7	3.03	40.2	2.50	48.2	3.44
	Second	227	1.81	226	1.29	221	1.61
PRD Y Axis	First	51.6	6.26	44.1	4.57	50.9	6.97
	Second	215	3.23	227	2.29	223	2.79
	Third	—	—	469	2.73	—	—
PRD Z Axis	First	—	—	188	2.85	—	—
	Second	307	14.8	312	5.88	306	14.9
	Third	426	22.9	412	8.76	407	20.8

Table 5.2.2-3. Random Vibration Test Result Summary for RTG F-6

Location	Mode	Pre-Test Sine Sweep (1/2 g) Freq. (Hz)	Q	Random Freq. (Hz)	Q	Post Test Sine Sweep (1/2 g) Freq. (Hz)	Q
Midspan Y Axis	First	50.8	3.20	48.0	2.40	50.6	3.47
	Second	210	1.60	205	1.43	205	1.50
PRD Y Axis	First	51.9	7.40	48.0	4.70	51.4	7.35
	Second	210	2.50	202	2.66	208	2.85
	Third	—	—	490	2.49	—	—
PRD Z Axis	First	144	2.00	182	3.0	135	2.05
	Second	370	14.9	310	4.42	330	13.0
	Third	430	32.8	405	9.83	420	29.0

Table 5.2.2-4. Random Vibration Test Result Summary for RTG F-7

Location	Mode	Pre-Test Sine Sweep (1/2 g)		Random		Post Test Sine Sweep (1/2 g)	
		Freq. (Hz)	Q	Freq. (Hz)	Q	Freq. (Hz)	Q
Midspan Y Axis	First	49.0	3.00	45.8	2.36	48.8	3.27
	Second	223	1.44	210	1.16	208	1.13
PRD Y Axis	First	52.2	6.69	48.1	4.62	52.6	7.23
	Second	230	2.34	208	2.21	210	1.80
	Third	—	—	461	2.252	—	—
PRD Z Axis	First	152	2.27	204	2.81	149	2.25
	Second	336	21.1	378	7.05	335	13.8
	Third	399	29.7	406	8.77	399	30.0

Flight Acceptance level Transient tests were also performed in the lateral and longitudinal axes of the RTG. All of the Transient pulses were within the ±2% tolerance limit of the required pulse frequencies. The Shock Response Spectrum (SRS) for each FA pulse met the requirement that harmonic distortion at frequencies above the fundamental frequency be at least 6 dB below the shock spectrum amplitude at the pulse fundamental frequency.

The first and second lateral modes observed on RTGs F-2, F-6, and F-7 were very similar to those previously observed for other RTGs, except that the frequencies were about 10% lower than those observed during testing for the Galileo/Ulysses program. This can be attributed to the extra flexibility of the fixturing, a result of incorporating load measuring capability. (Load cells were incorporated in the fixture to enable dual-mode testing, a technique proposed by JPL, but not adopted.)

Force measurements were made during dynamic testing for Engineering information only. In general, the force data are somewhat consistent with the acceleration data in that the peaks are coincident. However, neither the PRD nor the inner moly frame responses were obvious in the force data, nor is it clear that the heat source response can be readily

separated from that of the rest of the RTG in the absence of any internal instrumentation. Again, the similarity of responses in pre-test and post test sine sweeps, in this case as indicated by force measurements, is a good indication that no damage or permanent distortion occurred in any of the RTG structural members as a result of being subjected to the dynamic environment.

No significant changes in the parameters that define electrical performance were observed during the course of dynamic testing. Changes in internal resistance were acceptably low, no more than one milliohm, whereas an open thermoelectric couple might be expected to cause a change in internal resistance of at least eight milliohms.

A minor test anomaly was observed, similarly on all three RTGs, when the 3.78 g input level slightly exceeded that maximum specified environment during the Z-axis 15.75 Hz transient. This deviation was still well below the 6.0 g nominal FA level which was used for acceptance testing of the GPHS-RTG for the Galileo and Ulysses missions.

Additional information on vibration acceptance testing may be found in the following documentation:

1. "F-2 Engineering Report," (B.3 Topical Report), Lockheed Martin Missiles and Space Document GESP-7249, 22 November 1996.

2. "F-6 Engineering Report," (B.3 Topical Report), Lockheed Martin Missiles and Space Document GESP-7251, 7 March 1997.

3. "F-7 Engineering Report," (B.3 Topical Report), Lockheed Martin Missiles and Space Document GESP-7250, 24 January 1997.

5.2.3 Magnetic Testing

Magnetic measurements were performed as part of acceptance testing on the three flight unit RTGs, F-2, F-6, and F-7, as well as on the flight spare F-5.

Measurements were made with the RTG in two different positions: in Position 2 (-y axis up), readings were taken in the x-z plane of the RTG and in Position 5(-x axis up), readings were taken in the y-z plane. Three triaxial probes were used, all at a distance of 1.5 m from the geometric center of the RTG; Probe No. 1 above the table, Probe No. 2 at table level, and

probe No. 3 below the table. In accordance with test specifications, only data from probes located at table level in the horizontal plane through the RTG center of gravity were used for comparison with acceptance criteria. (The X, Y and Z designations for the axes of each probe were fixed with respect to the test cell, and are not related to the RTG X, Y, and Z coordinate axes.) Measurements were made by rotating the RTG through 360° past the probes, recording every 10°.

A total of 12 test runs were performed on each RTG, six in Position 2 and six in Position 5. To compensate for drift of the ambient field during the test, the magnetic field strength amplitude was recorded as the maximum reading, minus the minimum reading, divided by two. For each magnetometer (identified by the probe number and axis of the magnetometer), the maximum of the six runs was recorded. For comparison with acceptance criteria, this value was then normalized to rated current and to a distance of one meter. Rated current was taken as the estimate of current at the time of Saturn Orbit Insertion (SOI). The results are summarized in Table 5.2.3-1.

Table 5.2.3-1. Summary of Magnetic Testing

	F-2	F-5	F-6	F-7
Date of Test	5/23/96	9/13/95	1/15/97	10/23/96
Magnetometer Identification	2X	2X	2X	2X
Current during Test, amps	9.15	7.147	—	—
Current at SOI, amps	8.3	8.63	8.2	8.2
Maximum Magnetic Field Strength (nT)				
As Measured	23.2	16.7	—	—
Normalized to One Meter	78.4	56.3	—	—
Normalized to Rated Current	71.2	68.1	127.8	122.3
Specification Requirement	78	78	78	78

Note: Data listed in Table 4-10 of GESP-7250 was for F-2 and was incorrectly identified as applicable to F-7.

A review of the magnetic test measurements showed that there were fundamental differences in the characteristics of RTGs F-6 and F-7, the two units that were assembled as ETGs and RTGs on the Cassini RTG program, as compared with RTGs F-2 and F-5, previously assembled for the Galileo and Ulysses missions. The peak magnetic field was measured in Position 2, on probe 2X on all RTGs. However, on RTGs F-6 and F-7, the maximum field strength far exceeded the specification limit of 78 nT, and on F-6 that limit was also exceeded on probe 2X in Position 5.

Additional runs were made of magnetic measurements, a total of 22 on both F-6 and F-7. Rather than use the maximum field strength measured for any one test run, as was the practice agreed upon for F-2 and F-5, the probe readings were averaged for all the runs with closed circuit for each RTG. Readings during all these runs did not vary significantly, not to the extent that any one test reading could be discarded. In addition, the first and last readings for each probe were compared against each other to verify that the background fields did not drift appreciably.

Analysis of the magnetic measurements by JPL and ESA showed that the anomalous magnetic field of RTG F-6, as on F-7, was due to a significant permanent moment located near the inboard end. All suspect components, such as the gas management valve and the electrical connectors, were checked and found to have no significant magnetic field. A set of three spring washers, fabricated from PH17-4 corrosion resistant steel, taken from the same fabrication lot as those used in F-6 and F-7, were also checked and found to have no significant magnetic field. At first it was thought that there was some significance in the fact that RTGs F-6 and F-7 were the only units to not undergo degaussing prior to magnetic measurements. However, records showed that F-2, when tested as an ETG, showed no significant magnetic field in the as-built condition, and showed no change after degaussing.

The acceptance criteria for magnetic measurements was based on the assumption that the measured field is entirely current-induced, and could be represented as a pure dipole with a field that decreases inversely with the cube of the distance from the RTG. These assumptions were obviously not valid for RTGs F-6 and F-7, and the field strengths calculated using these assumptions were not meaningful. JPL and ESA analyzed the data

by first separating the permanent field from the current-induced. When the field strength was calculated by this method, it was estimated to be 80 nT at 1 meter for RTG F-6, with an uncertainty of ±4 nT. JPL therefore concluded that the field measured on RTG F-6 was acceptable, without the need for installing compensating magnets. (Specification PS23009148 allows the magnetic field requirement to be met "with or without" compensating magnetics.) Accordingly, JPL prepared a waiver to the magnetic field requirements for RTG F-6. By the same analysis, JPL showed that field strength on RTG F-7 was 74 nT, thereby meeting specification requirements. Further, JPL has been able to demonstrate analytically that by clocking of the RTGs on the spacecraft, acceptable magnetic fields can be obtained at both spacecraft magnetometers.

5.2.4 Mass Properties

Mass properties were measured on all of the RTG flight units, F-2, F-6, and F-7, as well as the spare RTG F-5. After subtraction of the mass of the ground support equipment, fixtures, and other non-flight items that were attached to the RTG during weighing, the flight mass for each RTG was determined to be as summarized in Table 5.2.4.-1. All units were within the specification limit of 125.0 lb. In addition, the requirement that all units are within 1% was also satisfied.

Table 5.2.4-1. Flight Unit Mass Comparison

Unit	Flight Mass (lb)	Difference from Lightest Unit (lb)	(%)
F-2	124.16	0.82	0.7
F-5	123.34	-	-
F-6	124.48	1.14	0.9
F-7	124.62	1.28	1.0

Center of mass was also determined for each RTG, including corrections in translating the reference coordinates from the measuring apparatus to the RTG spacecraft interface, and corrections for non-flight hardware in place at the time of measurement.

The specification requirement is that the center of mass of all units lie within a right circular cylinder, 0.64 cm (0.25 in.) in diameter by 1.27 cm (0.5 in.) long. Table 5.2.4-2 summarizes the data for all flight units. The envelope is shown to be a cylinder that is 0.14 in. diameter, 0.02 in. long, satisfying the specification requirement.

Table 5.2.4-2. Flight Unit Center of Mass Comparison

Unit	X (in)	Y (in)	Z (in)	Difference along X Axis (in)
F-2	0.045	0.058	-21.003	.013
F-5	0.022	0.041	-20.997	.007
F-6	0.031	0.045	-20.99	-
F-7	0.023	0.038	-21.009	.019

Envelope: Diameter $= 2 \, (.045^2 + .058^2)^{1/2} = 0.14$ in.
          Length $= 0.02$ in.

5.2.5   Thermal   Vacuum   Tests

Following dynamic tests, the RTGs were subjected to thermal vacuum tests in accordance with specification PS23009148. Specification requirement was a power output of 293 watts at the RTG pins for RTGs F-6 and F-7 (at a 4410 watt fuel load) 291 watts for F-2 (4410 watt fuel load) and 255 watts for F-5 (4100 watt fuel load). The required power is to be delivered at a voltage of 30 +0.7/-0.5 volts. Also specified was the requirement that the isolation resistance between the thermopile circuit and the outer shell be 1,000 ohms minimum. All RTGs met the requirements.

A summary of flight unit thermal vacuum test data is given in Table 5.2.5-1. Four values of power output are shown. "Measured power" is the power at the voltage tap location in the cable; "Corrected to pins " was calculated using the measured current and a 20 milliohm connector contact resistance to obtain the power where the specification applied; "normalized power" was at the pins and adjusted for a 4410 watt fuel inventory; the final power is the normalized power increased by 3 watts to take into account the Gas Management Valve(GMV) vent effect. This adjustment took into account the fact that the RTGs were vented through the GMV system which is more restrictive than the flight PRD.

Table 5.2.5-1. Flight Unit Thermal Vacuum Performance

	F-2	F-5	F-6	F-7
Date	3/6/96	10/5/95	2/8/97	11/21/96
Heat Input (watts)	4416.5	4091.1	4429.7	4427.7
Power Output (watts)				
As Measured	297.2	254.6	295.2	296.6
Corrected to Pins [1]	299.2	256.0 [3]	297.2	300.6
Normalized [2] to 4410W Input	298.4	257.1	294.8	298.5
With GVM Vent Correction (3W)	301.4	260.1	297.8	301.5
Requirement	291	255	293	293
Load Voltage (volts) 30+0.7/-0.5	30.018	30.033	29.95	29.979
Open Circuit Voltage (volts)	52.093	50.279	51.878	52.338
Current (amps)	9.801	8.479	8.857	9.960
Internal Resistance (ohms)	2.229	2.387	2.225	2.245
Average RTG Temperature (°C) Requirement <260°	243.9	236.4	245.2	246.1
Insulation Resistance (k ohms) Thermopile t Case (2 minute) Requirement >1.0	3.73	29.31	6.5	3.44
Chamber Pressure (torr)	9.8×10^{-7}	8×10^{-7}	5.4×10^{-7}	7.4×10^{-7}
Average Sink Temperature (°C)	26.7	35.8	33.1	27.9

[1]   Corrected = Measured $+0.02 \, I^2$

[2]   Normalized using 0.12W electric per thermal watt input; F-5 normalized to 4100W

[3]   Power still increasing at end of test; 258W estimated final power

The residual gas pressure resulted in an increase in thermal conductance of the foil insulation system and subsequently a loss of some power. Experience in the MHW converters showed this to be about 0.6% to 1.0% of the measured power. This same percentage was applied to the Cassini RTGs resulting in a power increase of 1.8 to 3.0 watts.

F-2 RTG

Chamber evacuation was started on 3 September 1996. It took 45 minutes to reach 0.1 torr from atmospheric pressure. Venting of the RTG internal argon/helium gas mixture through the GMV was initiated at 0633 on 4 September 1996.

Stability criteria were met at 0100 on 5 September. The 30 volt stability test was completed at 0700 on 6 September. Table 5.2.5-2 summarizes the vacuum performance. Measured power output was 297.2 watts with a fuel loading of 4416.5 watts. The power trend shown in Figure 5.2.5-1 shows that stability was reached. The correction for the connector contact resistance (20 milliohms) raises the power to 299.2 watts at the RTG power pins. Normalization to a 4410 watt thermal input reduces power to 298.4 watts. A final correction of 3 watts is added to account for the more restrictive venting of the GMV relative to the flight PRD. The corrected normalized power output is therefore 301.4 watts. This exceeds the specification requirement of 291 watts by 10 watts. The RTG internal resistance trend shown in Figure 5.2.5-2 exhibits normal behavior.

Table 5.2.5-2. F-2 Thermal Vacuum Test

Date	9/6/96
Hour	0700
Heat Input, (watts)	4416.5
Power Output, (watts) As Measured	297.2
Corrected to RTG Pins, (watts)	299.2
Normalized to 4410W (watts)	298.4
With GMV Vent Correction (3w) (watts)	301.4
Load Voltage, (volts)	30.018
Open Circuit Voltage, (volts)	52.093
Current, (amps)	9.901
Internal Resistance, (ohms)	2.229
Average RTD Temperature, (°C)	243.9
Insulation Resistance, (k-ohms)	
Thermopile to Case (2 minute)	3.73
Chamber Pressure, (Torr)	9.85×10^{-7}
Average Sink Temperature, (°C)	26.7

* Normalized using 0.12 watt electric per thermal watt input
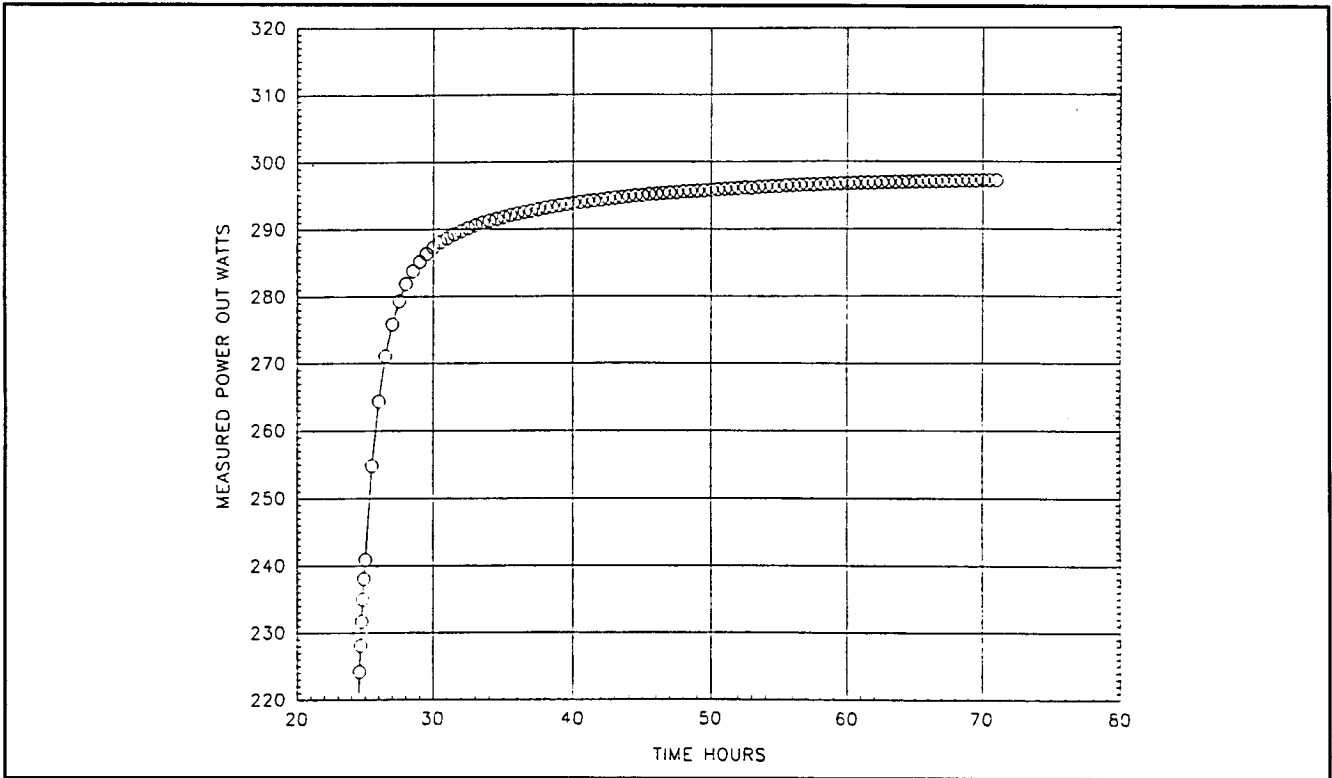
Figure 5.2.5-1. F-2 Measured Power during Vacuum Testing
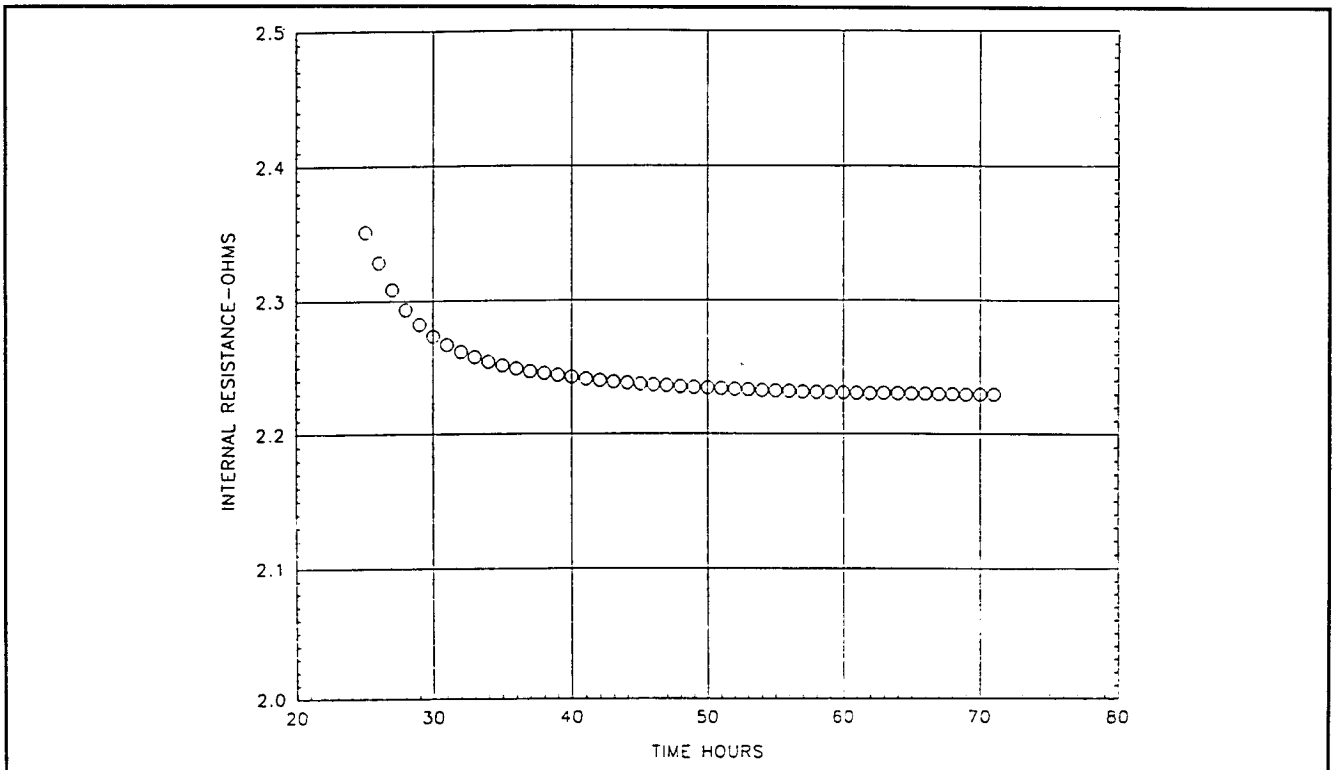
Figure 5.2.5-2. F-2 Measured Internal Resistance during Thermal Vacuum Testing
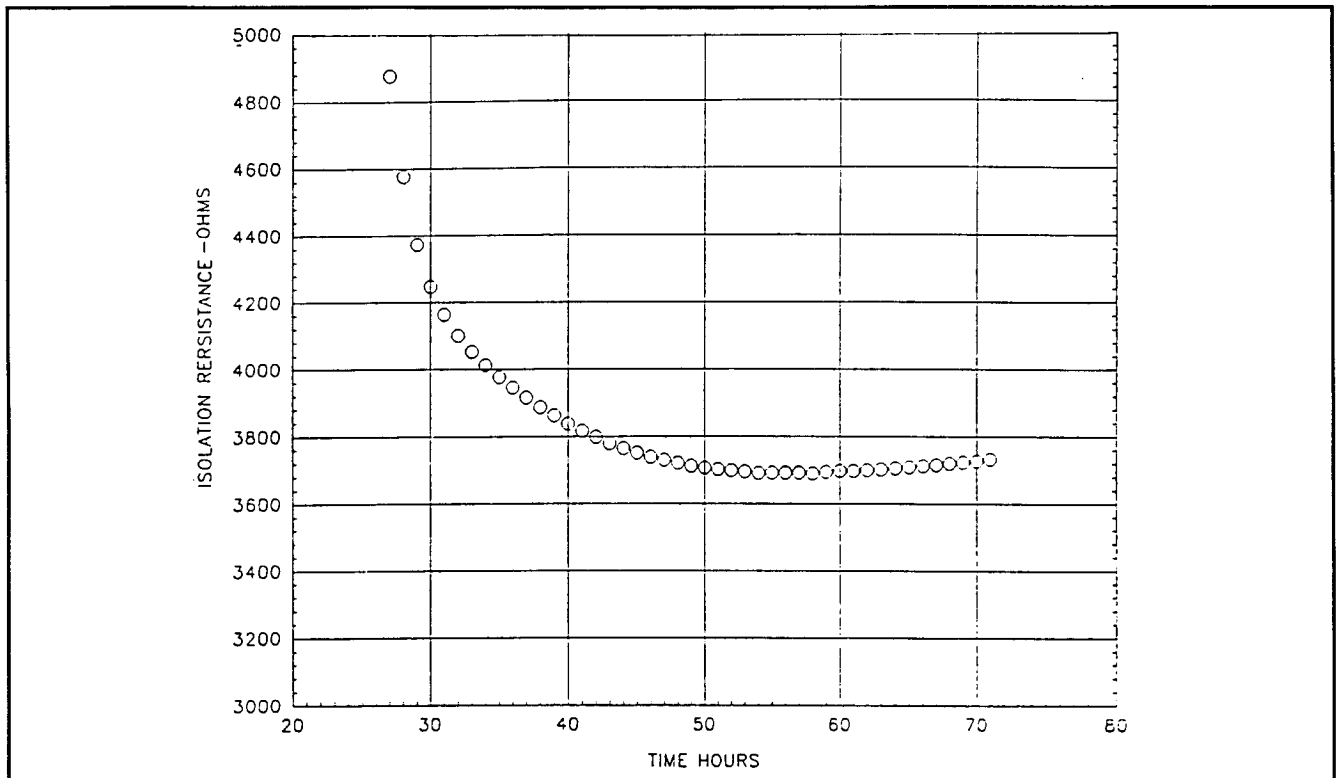
Figure 5.2.5-3. F-2 Measured Isolation Resistance during Thermal Vacuum Testing

Carbon Monoxide Partial Pressure and Generation Rate

Since carbon monoxide and nitrogen both are mass 28, there is always an ambiguity in gas samples analyzed by mass spectroscopy. Since nitrogen concentration may be an indication of air leakage it is useful to be able to distinguish between the two gases.

An RGA (residual gas analyzer) was added to the thermal vacuum chamber to enable an estimation of the CO partial pressure, and controlled leak rate calibration runs were made to determine the RGA fragmentation patterns for CO and nitrogen. From the calibration runs it was determined that an upper limit on the CO partial pressure can be obtained by multiplying the mass 12 partial pressure by 28.8. At the end of the stability test and during most of the test, mass 12 was below the detection limit of 1×10^{-10} torr. This indicated a CO partial pressure of less than 3×10^{-9} torr in the vacuum chamber. The net vacuum system pumping speed was determined to be 4100 liters/second from a CO controlled leak rate test. From the vacuum system pumping speed and the upper limit estimate of the CO partial pressure, an upper limit on the CO generation rate was calculated as 0.66×10^{-9} moles/second. This was in good agreement with the expected generation rate range of 0.35×10^{-9} to 1×10^{-9} moles/second that was documented in pre-test predictions.

F-5 RTG

Chamber evacuation was started on 2 October 1995 at 14:45 and venting of the RTG internal argon/helium gas mixture through the GMV was initiated 17 hours later at 07:37 on 3 October. The stability criteria were met and final data at 30 volts were recorded at 07:00 on 5 October. Table 5.2.5-3 summarizes the vacuum performance. Power output normalized to 4,100 watts was 257.1 watts compared to the specification requirement of 255 watts.

Table 5.2.5-3. F-5 Thermal Vacuum Test

Date	5/22/85	10/5/95
Hour	0830	0700
Heat Input, watts	4443.5	4091.1
Power Output, watts		
As Measured	305.2	254.6
Corrected	307.3	256.0
Normalized to 4410W input	303.3	
Normalized to 4100W input		257.1
Load Voltage, volts	30.030	30.033
Open Circuit Voltage, volts	52.310	50.279
Current, amps	10.164	8.479
Internal Resistance, ohms	2.191	2.387
Average RTD Temperature, °C	243.6	236.4
Insulation Resistance, k-ohms		
Thermopile to Case		
(2 minute)	8.508	29.3
Chamber Pressure, torr	8×10^{-7}	2.48×10^{-7}
Average Sink Temperature, °C	35.8	25.5

* Normalized using 0.1 2 watt electric per thermal watt input.

Power output was still rising very slowly at the end of the test, as shown in Figure 5.2.5-4, due to the gradual decrease in the helium release rate from the fuel matrix and dopant redistribution effects within the thermoelectric elements. Curve fits, as indicated by the two lines in Figure 5.2.5-4, were used to extrapolate the data to steady state conditions. Extrapolated power was determined to be in the range 257-260 watts.
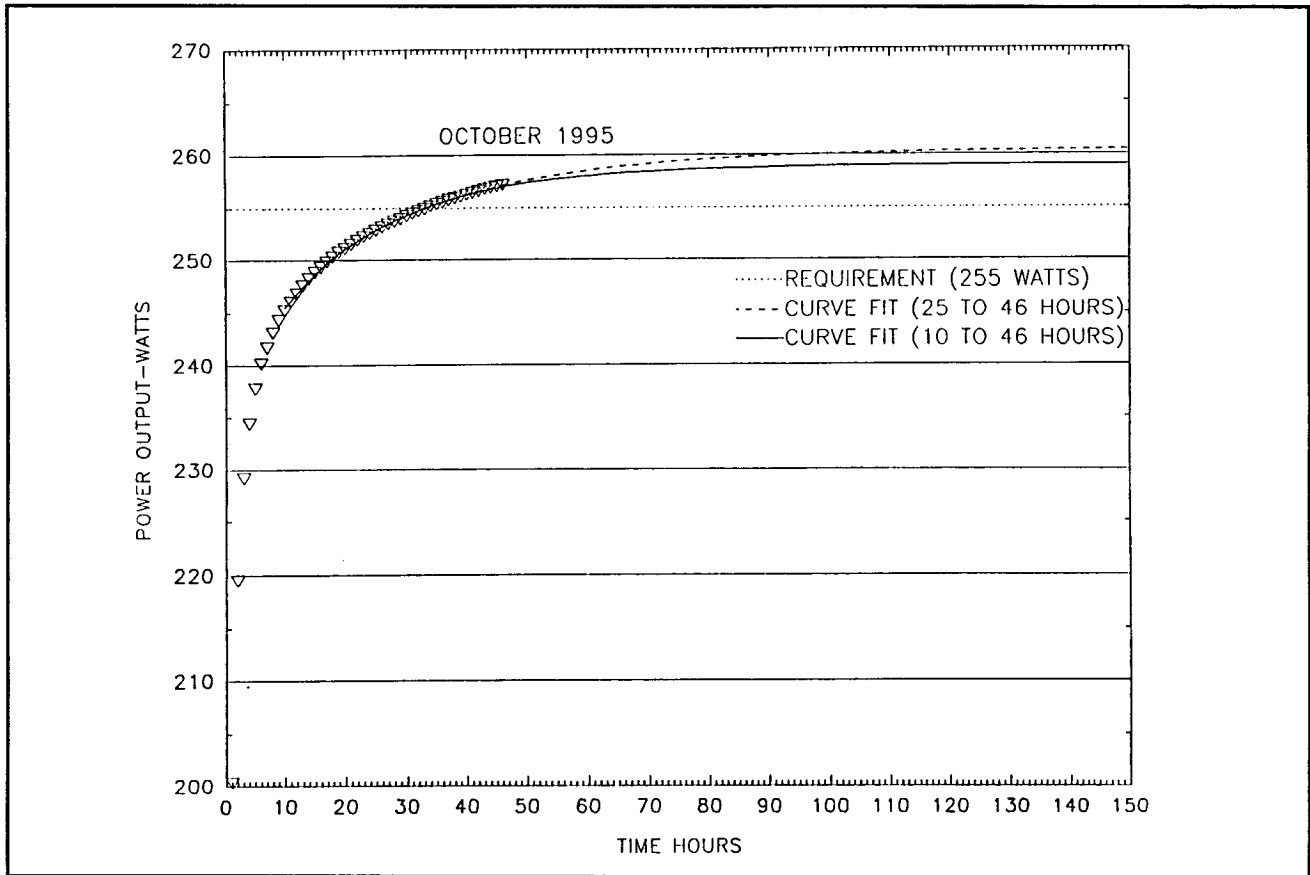
Figure 5.2.5-4. RTG Power vs. Time Rise

The previous thermal vacuum test was conducted in May of 1985 and, in the interim, a large amount of helium was stored in the fuel. This was evident from the pressure rise test run at the end of thermal vacuum testing. In this test the GMV was closed and the RTG internal pressure and power output were recorded. Figure 5.2.5-5 shows the pressure rise for both tests. The rise was much more rapid in the 1995 test. The test, which is normally run for two hours, was terminated after 50 minutes when the pressure exceeded 300 microns. Power output trends and power loss for both tests are shown in Figures 5.2.5-6 and 5.2.5-7. The power decrease was larger in the 1995 test and indicated a larger correction for GMV venting was appropriate. In the past, when predicting BOM power, a correction of 1.8 to 3.0 watts was added to the measured power output to account for the more restrictive venting characteristic of the GMV compared to a flight PRD.
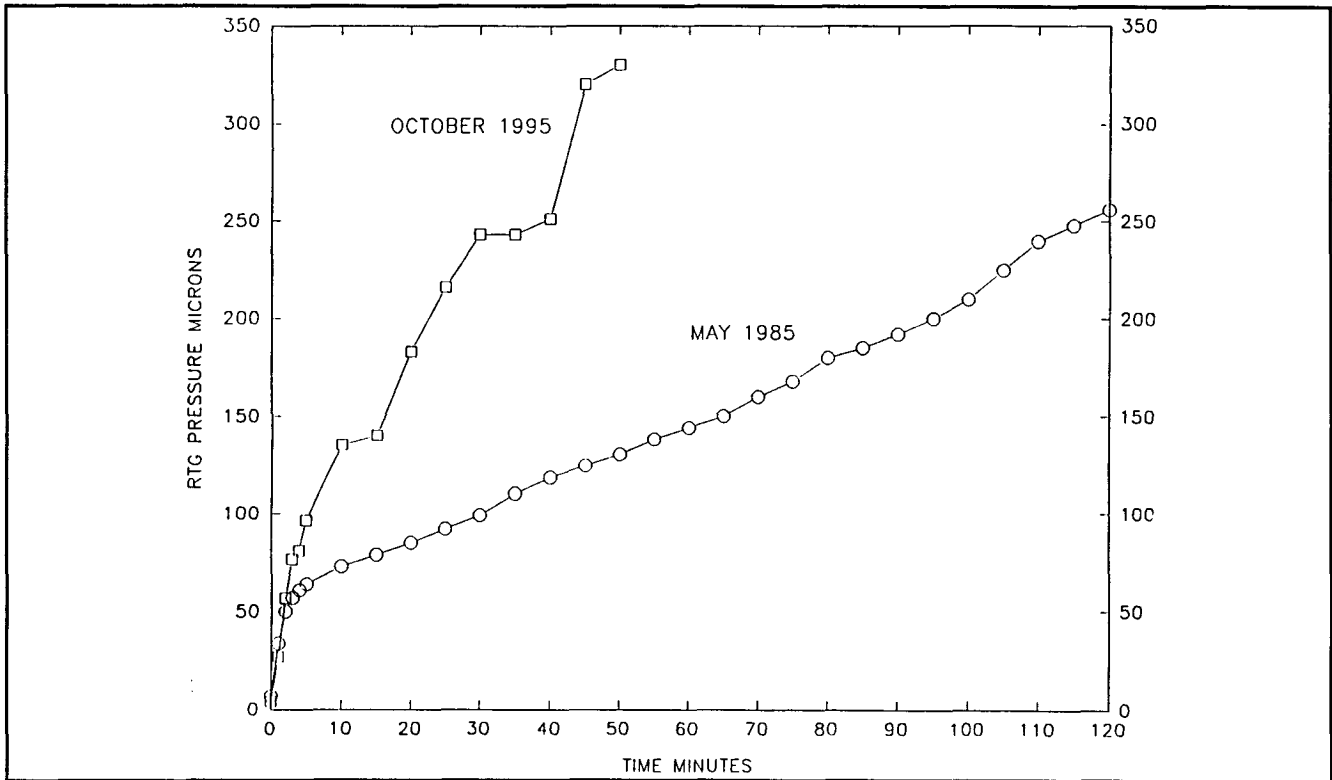
Figure 5.2.5-5. Pressure Rise
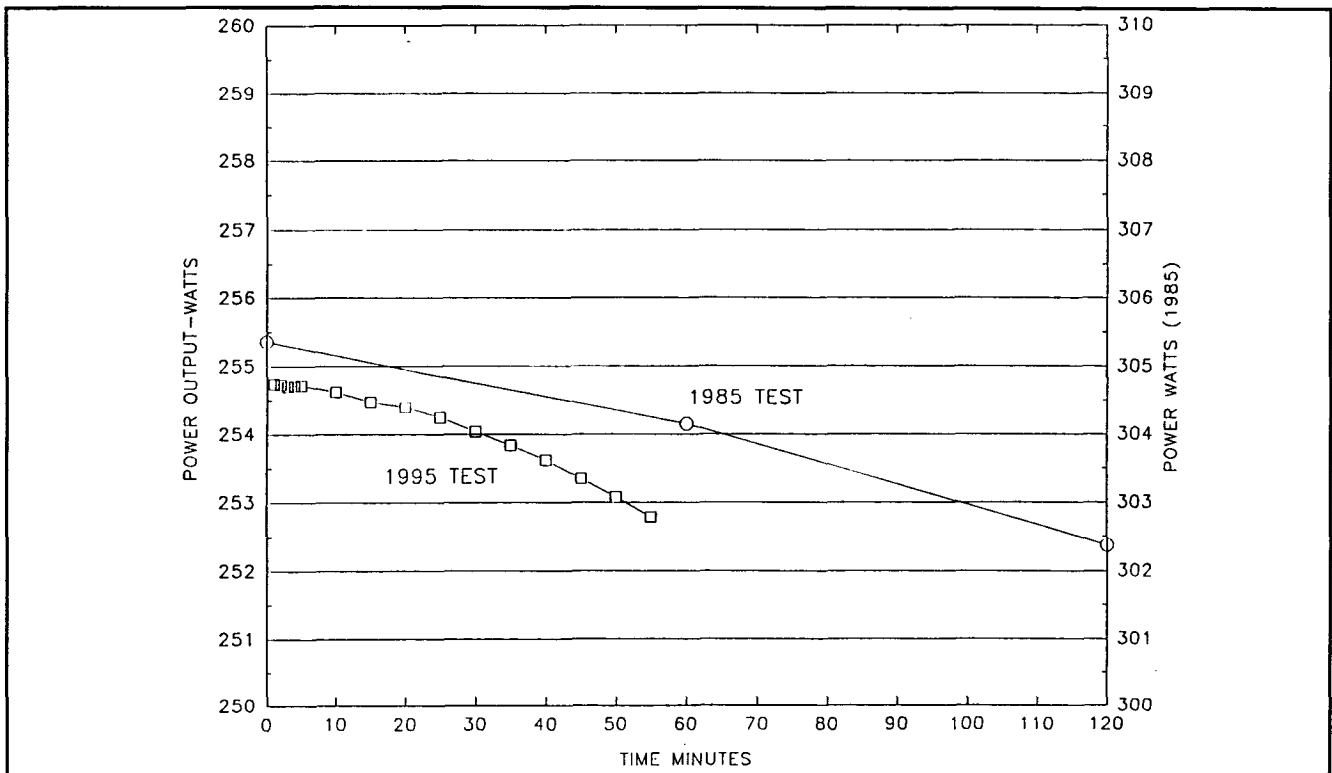
Figure 5.2.5-6. GMV Closed Power Loss
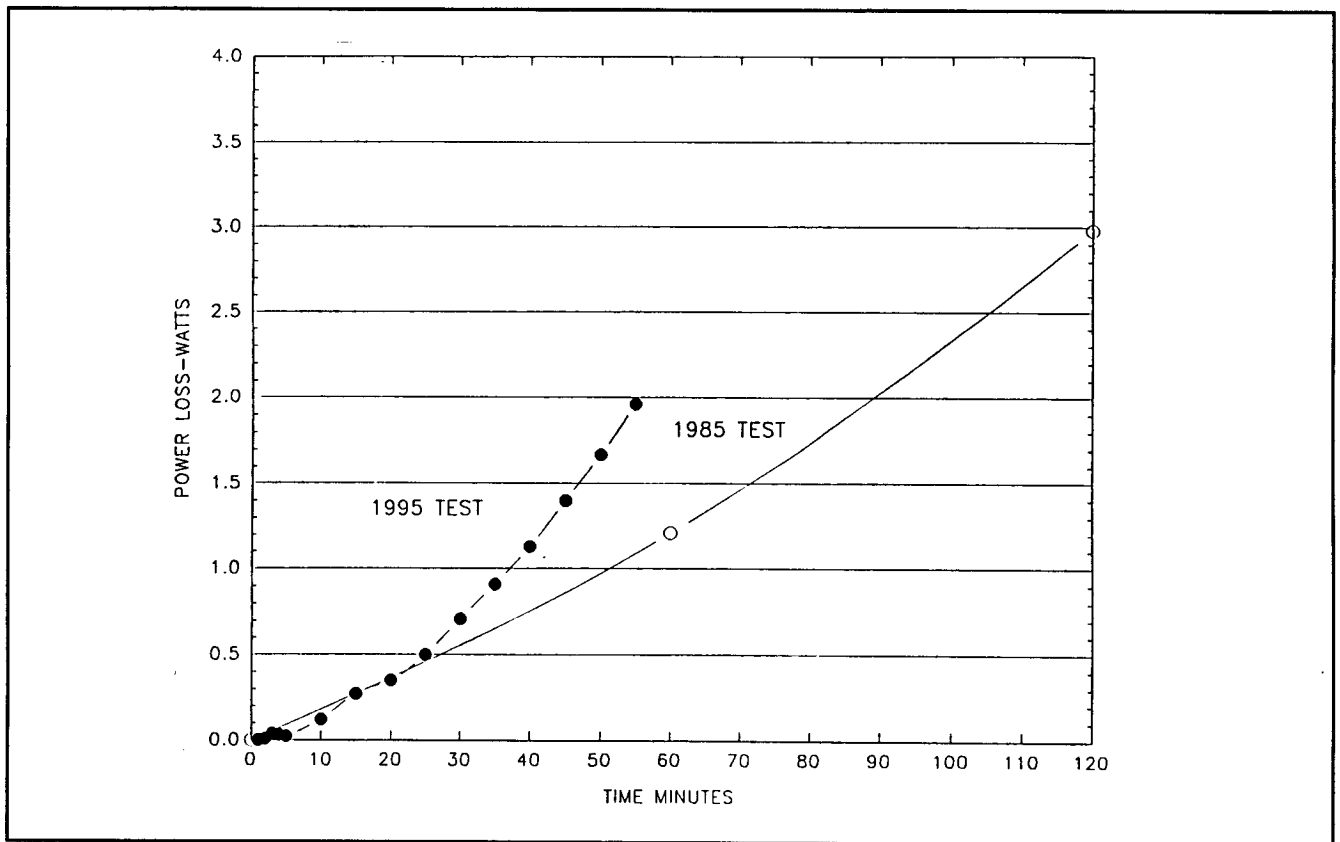
Figure 5.2.5-7. Power Loss after GMV Closed

Dopant redistribution effects, resulting from 10 years of low temperature storage, were evident from the internal resistance trend shown in Figure 5.2.5-8. The internal resistance showed a decrease as the dopant was going back into solution in certain regions of the thermoelements. The resistance had not quite reached the minimum when the test was terminated. The long term trend in SiGe alloys was an increase in resistance and a decrease in power output as the dopants precipitated from solution, so that a resistance upturn would have been observed if the test had been run longer. However, the test was terminated when all test objectives were met.
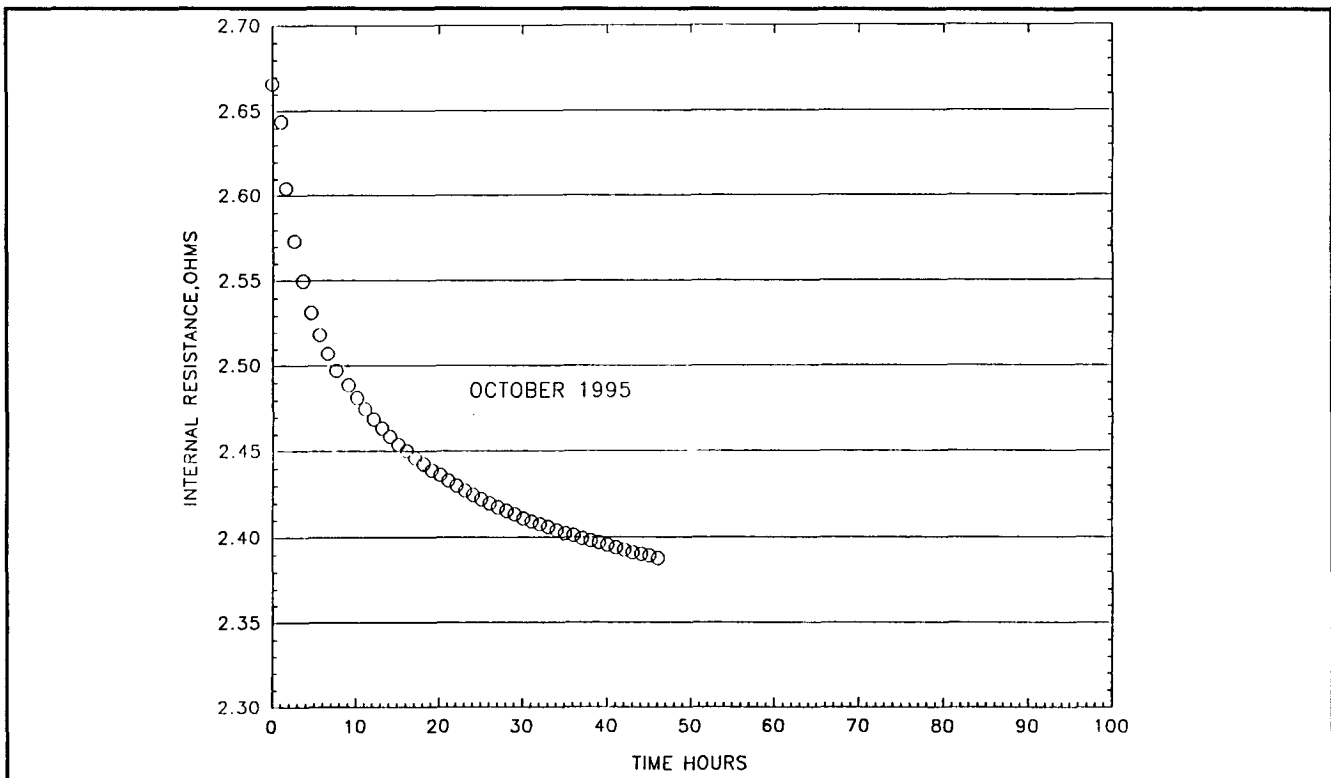
Figure 5.2.5-8. F-5 Internal Resistance during Thermal Vacuum Testing

The measured performance at 30 volts including the internal resistance and open circuit voltage were used in conjunction with the RTG performance computer program to calculate the current-voltage-power characteristic over the range from 20 to 35 volts.

RTG F-5 had also been tested in May 1985 when it was part of the Galileo RTG program. A comparison of test data is given in Table 5.2.5-3. As previously discussed, the power output was still drifting up at the end of the 1995 test and 2 watts were added to account for this. Power output degraded by 49.3 watts or 16 %. Of this, approximately 42.3 watts was due to fuel decay. The remaining 7 watts or 2.3 % loss is due to dopant precipitation effects during the 10 years of storage. This is in good agreement with storage models which predicted up to 9 watts power loss for the 12 year period from 1985 to the 1997 launch.

Figure 5.2.5-9 shows the voltage -power characteristic curves for both the 1985 and 1995 tests. Maximum power occurred very close to 30 volts in both cases.
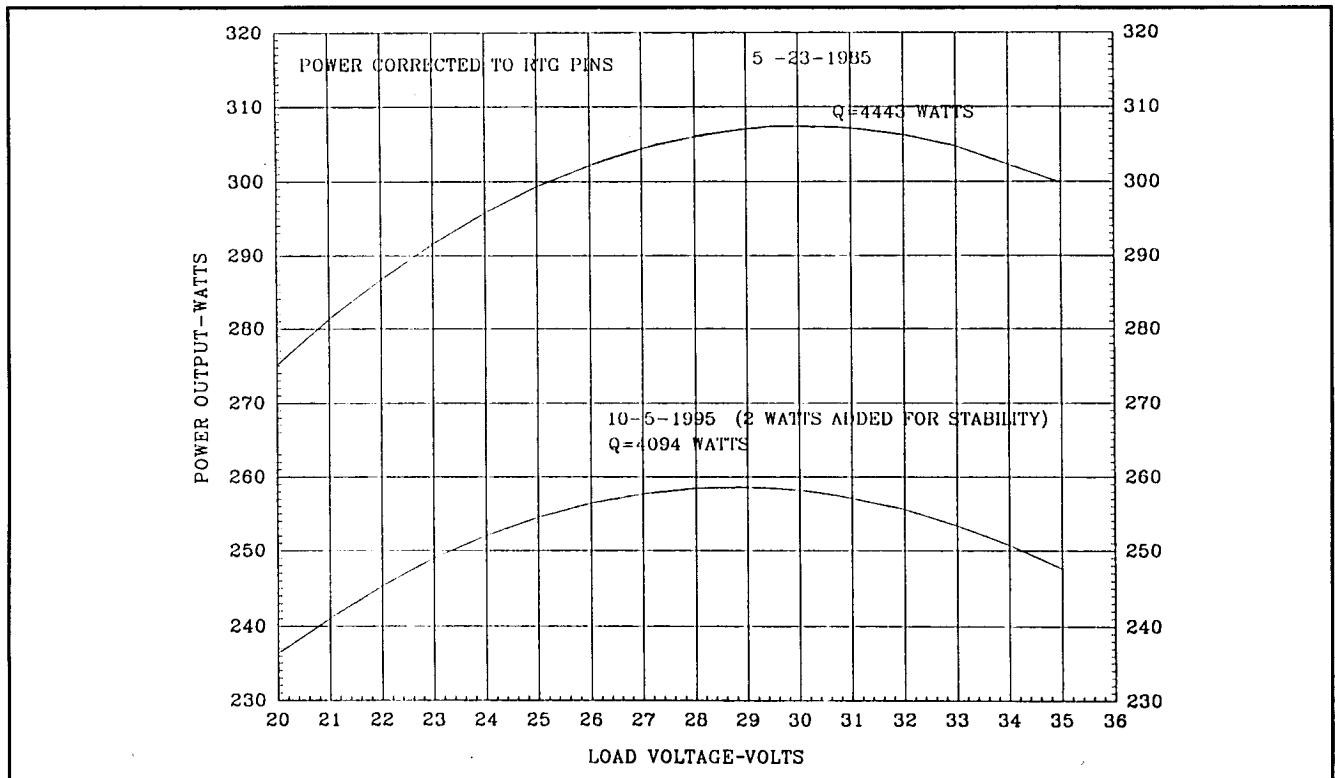
Figure 5.2.5-9. F-5 Power Vs. Voltage

F-6 RTG

Chamber evacuation was started at 1515 hours on 4 February 1997. Time to reach 0.1 torr was 50 minutes. Venting of the RTG internal argon/helium gas mixture through the GMV was initiated at 0650 on 5 February.

Stability criteria were met at 0300 on 6 February. The 30 volt stability test was completed at 1600 on 7 February, however, stability testing was extended to 0600 on 8 February and the later data are listed. Table 5.2.5-4 summarizes the vacuum performance. Measured power output was 295.0 watts with a fuel loading of 4429.7 watts. The power trend shown in Figure 5.2.5-10 showed that stability was reached. The correction for the connector contact resistance (20 milliohms) raised the power to 297.0 watts at the RTG power pins. Normalization to a 4410 watt thermal input reduced power to 294.6 watts. A final correction of 3 watts was added to account for the more restrictive venting of the GMV relative to the flight PRD. The corrected normalized power output was therefore 297.6 watts. This exceeded the specification requirement of 293 watts by 4.6 watts. The RTG internal resistance trend shown in Figure 5.2.5-11 exhibited normal behavior.

Table 5.2.5-4. F-6 Thermal Vacuum Test

Date	2/8/97
Hour	06:00
Heat Input, (watts)	4429.6
Power Output, (watts)	
As Measured	295.2
Corrected to RTG Pins	297.2
Normalized to 4410W Input	294.8
With GMV Vent Correction (3w)	297.8
Load Voltage, (volts)	29.96
Open Circuit Voltage, (volts)	51.878
Current, (amps)	9.855
Internal Resistance, (ohms)	2.225
Average RTD Temperature, (°C)	245.2
Insulation Resistance, (k-ohms)	
Thermopile to Case (2 minute)	6.50
Chamber Pressure, (Torr)	5.4×10^{-7}
Average Sink Temperature, (°C)	33.1

* Normalized using 0. 1 2 watt electric per thermal watt input.

Isolation resistance between the thermoelectric circuit and case was 6,370 ohms at the end of the stability test, and this exceeded the requirement of a minimum of 1,000 ohms. The observed performance was as predicted and normal isolation trends were observed as shown in Figure 5.2.5-12.
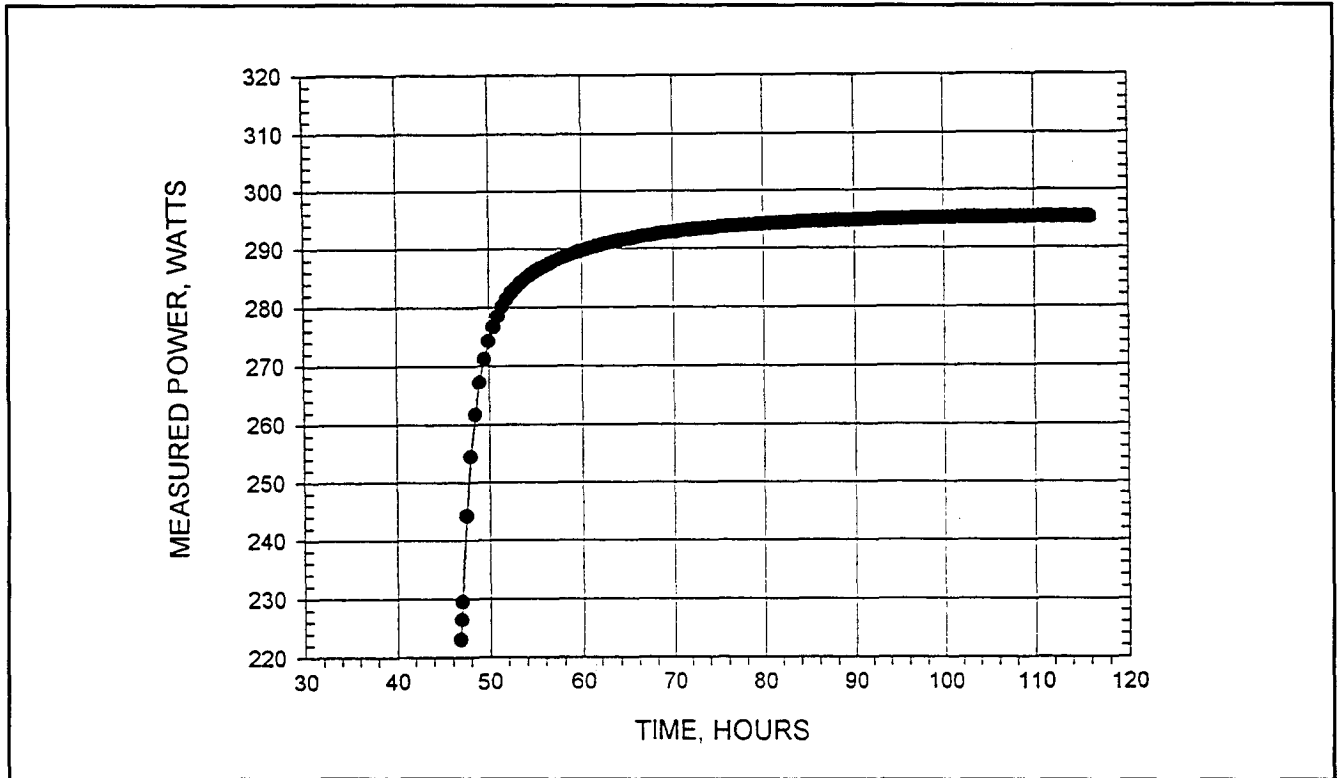
Figure 5.2.5-10. F-6 Measured Power Output during Thermal Vacuum Testing
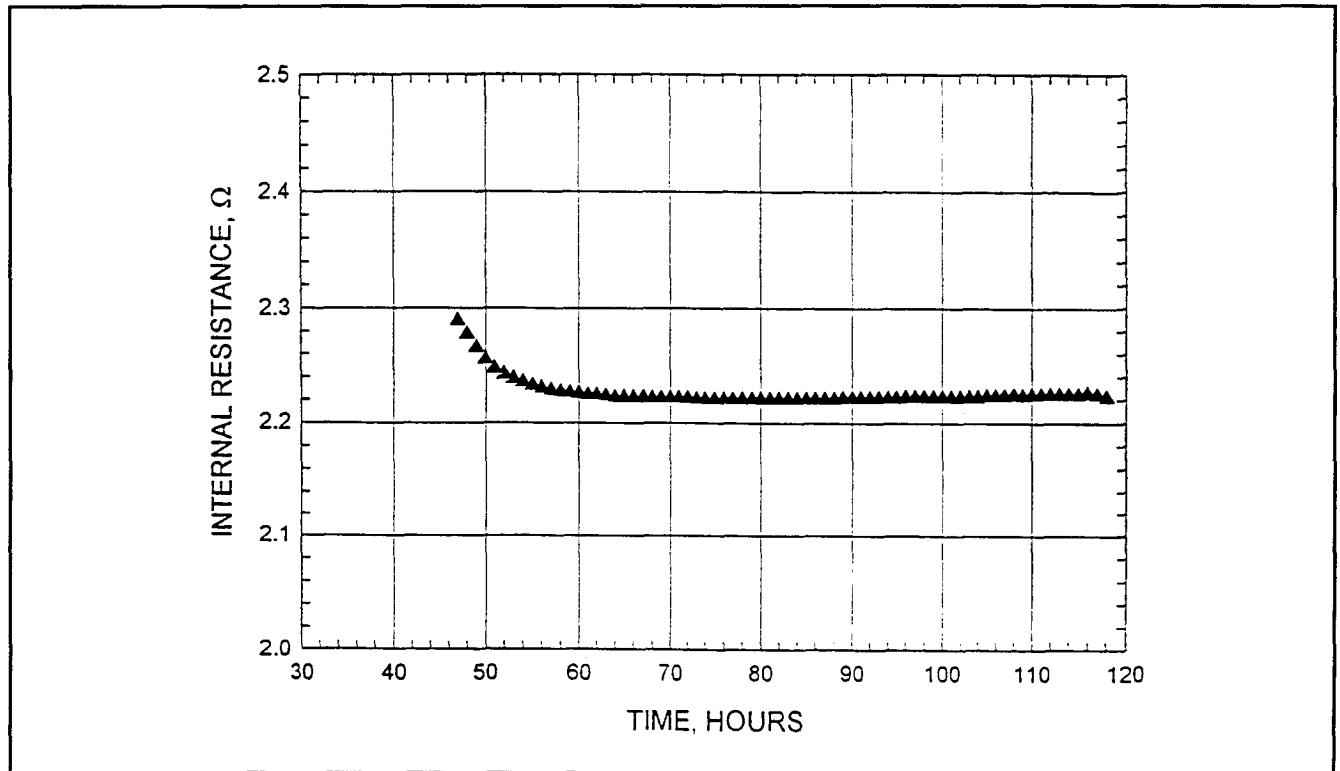
Figure 5.2.5-11. F-6 Measured Internal Resistance during Thermal Vacuum Testing
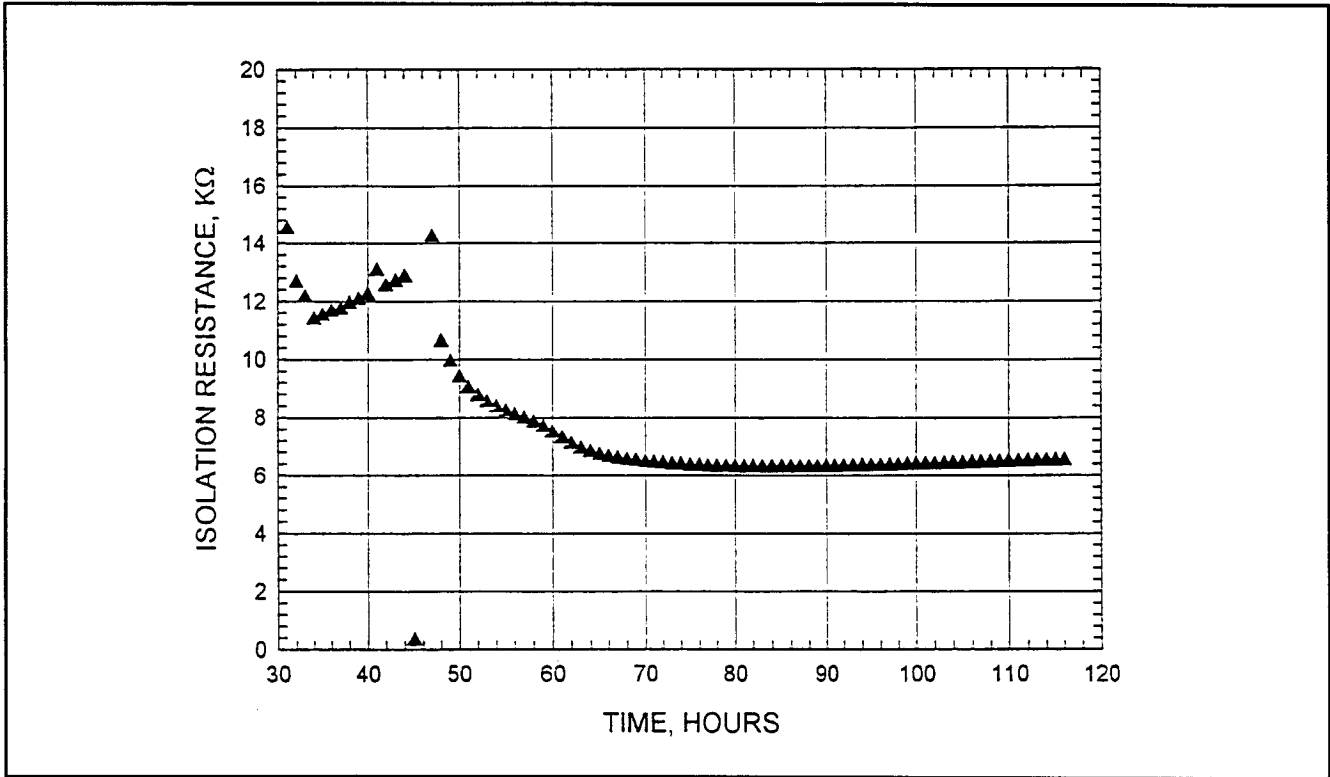
Figure 5.2.5-12. F-6 Measured Isolation Resistance during Thermal Vacuum Testing

F-7 RTG

Chamber evacuation was started at 1550 on 18 November 1996. In 45 minutes 0.1 torr was reached. Venting of the RTG internal argon/helium gas mixture through the GMV was initiated at 0739 on 19 November.

Stability criteria were met at 0100 on 20 November. The 30 volt stability test was completed at 0800 on 21 November. Table 5.2.5-5 summarizes the vacuum performance. Measured power output was 298.6 watts with a fuel loading of 4427.7 watts. The power trend shown in Figure 5.2.5-13 showed that stability was reached. The correction for the connector contact resistance (20 milliohms) raised the power to 300.6 watts at the RTG power pins. Normalization to a 4410 watt thermal input reduced power to 298.5 watts. A final correction of 3 watts was added to account for the more restrictive venting of the GMV relative to the flight PRD. The corrected normalized power output was, therefore, 301.5 watts. This exceeded the specification requirement of 293 watts by 8.5 watts. The RTG internal resistance trend shown in Figure 5.2.5-14 exhibited normal behavior.

Table 5.2.5-5. F-7 Thermal Vacuum Test

Date	11/21/96
Heat Input, (watts)	4427.7
Power output, (watts)	
As Measured	298.6
Corrected to RTG Pins	300.6
Normalized to 4410W Input	298.5
with GMV Vent Correction (3w)	301.5
Load Voltage, (volts)	29.979
Open Circuit Voltage, (volts)	52.338
Current, (amps)	9.960
Internal Resistance, (ohms)	2.245
Average RTD Temperature, (°C)	246.1
Insulation Resistance, (k-ohms)	
Thermopile to Case (2 minute)	3.44
Chamber Pressure, (Torr)	7.4×10^{-7}
Average Sink Temperature, (°C)	27.9

* Normalized using 0.12 watt electric per thermal watt input.

Isolation Resistance

Isolation resistance between the thermoelectric circuit and case was 3,440 ohms at the end of the stability test, and this exceeded the requirement of a minimum of 1,000 ohms. During ETG processing, gaseous species released from the heat source had caused an abnormal trend in the isolation resistance. Engineering studies addressing causes and mechanisms were reported in Reference 5-1 and summarized in Section 5.1. A visual inspection of the interior of the unit was performed on 27 August 1996 after the EHS was removed and prior to fueling operations. All thermoelectric rows of unicouples were examined for discoloration and deposits. The Astroquartz cloth on the inside of the multifoil insulation between the hot shoes was white in color, as installed. The hot shoes had normal grayish color and the inner moly frame was bright and shiny as installed. There was no evidence of any deposits or foreign material. Predictions of the isolation trends during the thermal vacuum test were made in Reference 5-6. The observed performance was as predicted and normal isolation trends were observed as shown in Figure 5.2.5-15.
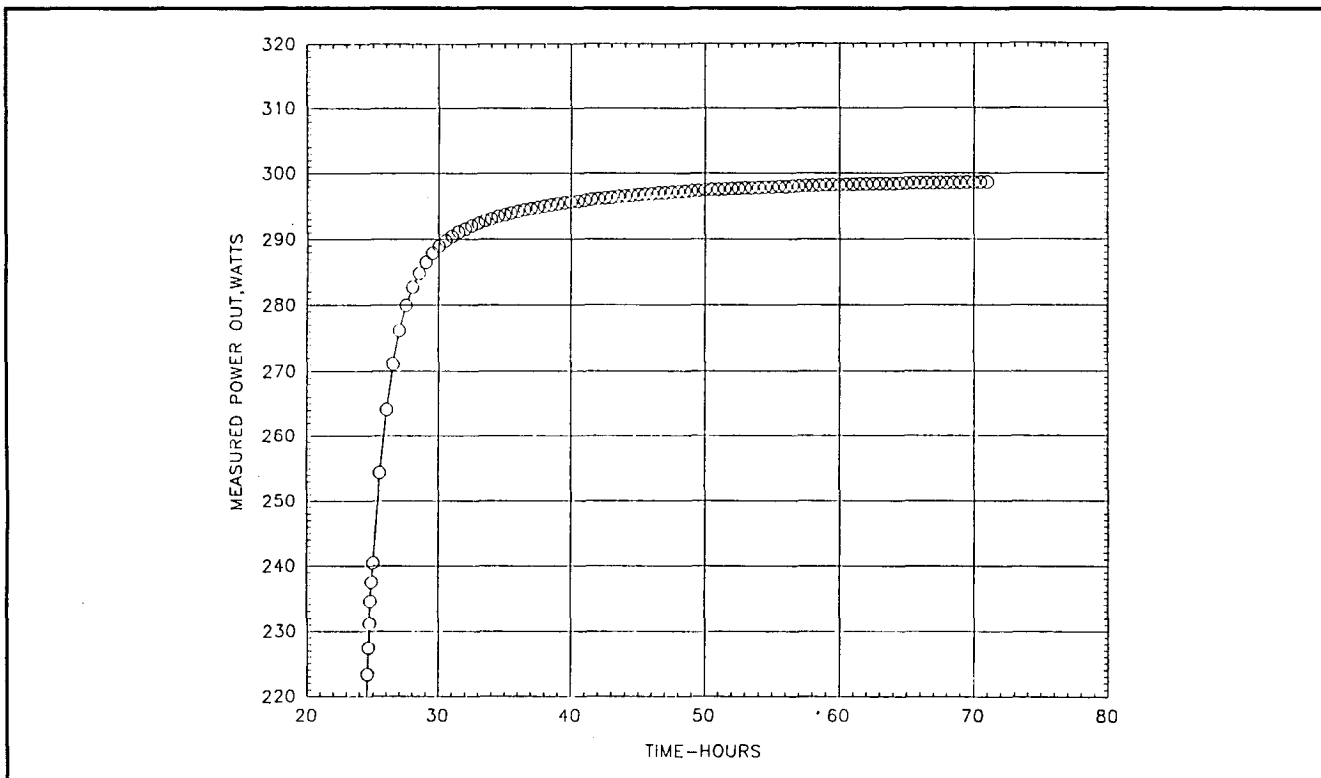
Figure 5.2.5-13. F-7 Measured Power during Thermal Vacuum Testing
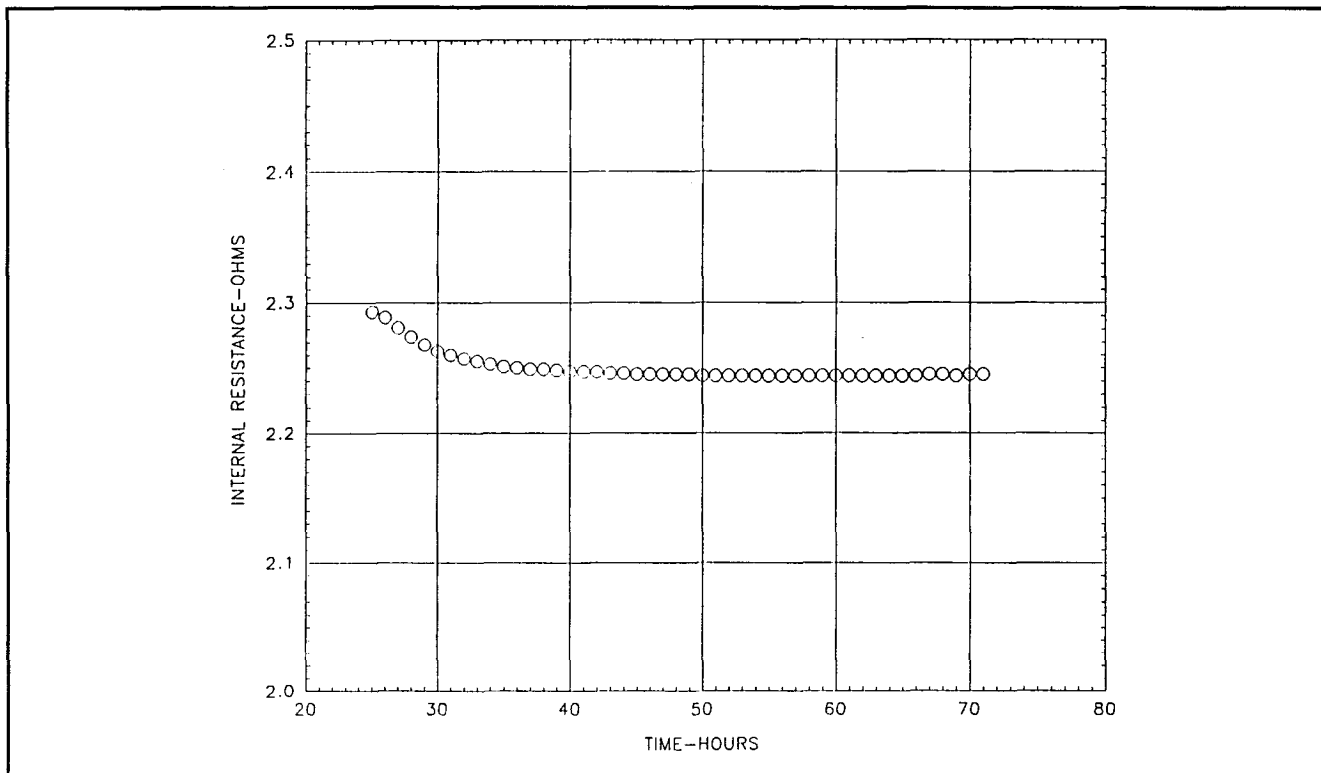
Figure 5.2.5-14. F-7 Measured Internal Resistance during Thermal Vacuum Testing
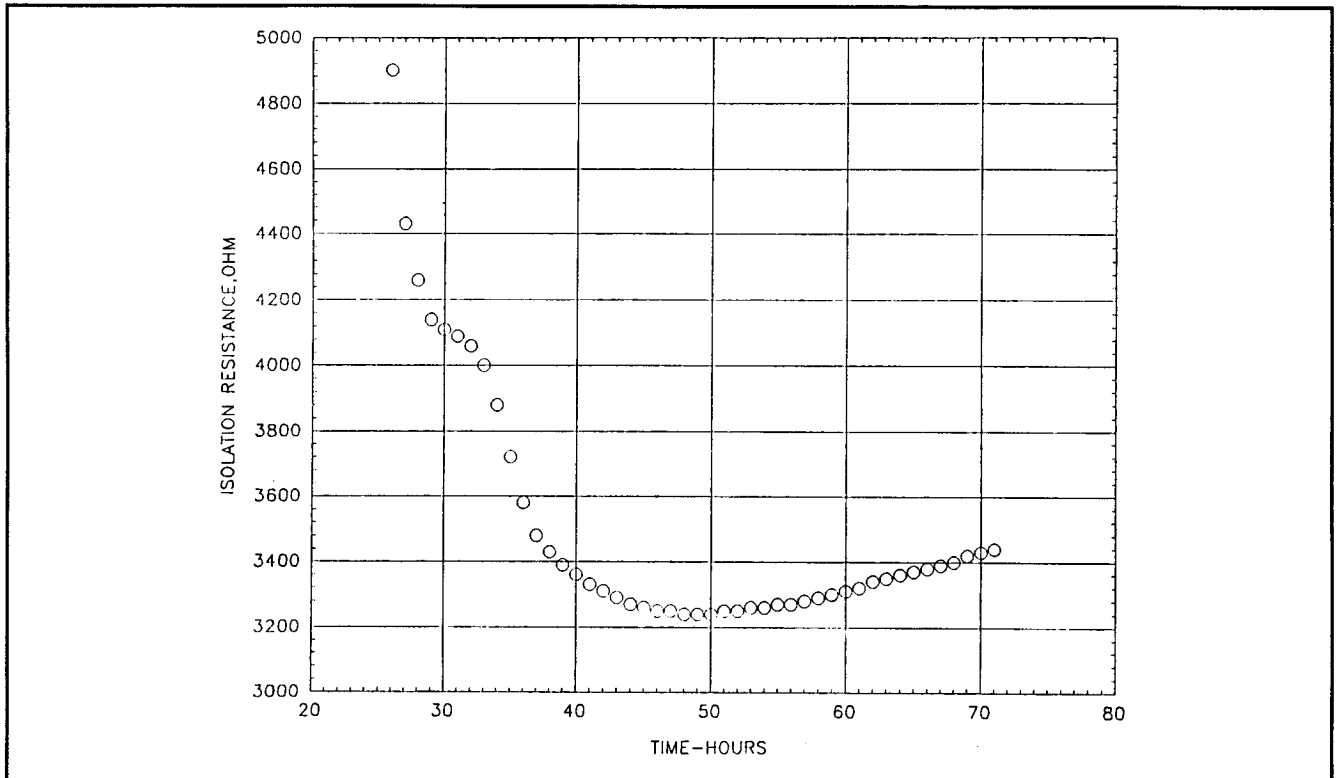
Figure 5.2.5-15. F-7 Measured Isolation Resistance during Thermal Vacuum Testing

Carbon Monoxide Partial Pressure and Generation Rate

Following is a discussion of the carbon monoxide gas sample measurements made on RTG F-7.

A gas sample taken prior to the thermal vacuum test showed 1.83 mole percent N_2/CO. Subsequent mass spectrometer analysis involving high sensitivity resolution of the mass 28 peaks showed that the composition was 95% CO or 1.7 mole percent CO. Further analysis was performed to determine the relative isotopic abundance of O^{18} and O^{16} in the CO. This was done to determine if the oxygen in the CO came from the fuel. The fuel is deliberately depleted in O^{17} and O^{18} to reduce neutron radiation arising from alpha-neutron reactions. The analysis compared the mass 28 and mass 30 peaks. The O^{18}/O^{16} ratio was found to be 0.061%, whereas the natural abundance ratio is 0.204%. This is a depletion factor of 3.3 for O^{18}. Calculations show that for this depletion factor, at least 70 percent of the CO in the gas tap came from the fuel. Mass 28 levels were subsequently closely monitored during the thermal vacuum test.

5-44

An RGA was added to the thermal vacuum chamber (prior to F-2 RTG thermal vacuum testing) to enable an estimation of the CO partial pressure. Controlled leak rate calibration runs were made to determine the RGA fragmentation patterns for CO and nitrogen since both are mass 28. From the CO controlled leak test a net vacuum system pumping speed of 4,100 liters/second was determined. From the calibration runs it was determined that an upper limit on the CO partial pressure can be obtained by multiplying the mass 12 partial pressure by 28.8. At the end of the stability test and during most of the test, mass 12 was below the detection limit of 1.0×10^{-10} torr. This results in a CO partial pressure of less than 3×10^{-9} torr in the vacuum chamber. From the vacuum system pumping speed and the upper limit estimate of the CO partial pressure, an upper limit on the CO generation rate was calculated as 0.66×10^{-9} moles/second. This is the same result obtained from RTG F-2 thermal vacuum testing and is in good agreement with the expected generation rate range of 0.35×10^{-9} to 1×10^{-9} as given in Table 1 of Cassini Memo No. 461 (F-2 RTG Predictions in Thermal Vacuum Test).

The normal CO level observed during the thermal vacuum testing indicated that the high CO level found in the pre-thermal vacuum gas tap was a residual quantity, generated, stored in, and released from the heat source and not a continuing generation process. Further evidence was obtained from a gas tap taken three weeks after the thermal vacuum test, wherein the mass 28 quantity was less than 0.02%.

5.2.6 RTG Power Projections

Based on the thermal vacuum test results, predictions were made for launch pad performance and BOM and EOM performance. References 5-3, 5-4, and 5-5 document the details of the factors taken into account in making the predictions. Launch pad power predictions considered fuel decay, dopant precipitation, air in-leakage (F-6 only), residual helium from the argon to xenon gas exchange and helium buildup after the gas exchange. The predictions allowed for a possible 30-day hold after the scheduled launch date. Conservative assumptions were made in calculating the pad power. BOM power also had to consider fuel decay, dopant precipitation, and air in-leakage effects from the time of thermal vacuum testing to launch. EOM predictions were made using the TEG degradation

model which includes thermal insulation degradation due to sublimation as well as the normal fuel decay and dopant precipitation effects.

Table 5.2.6-1 shows the conservative launch pad power predictions after a 30-day hold for the individual RTGs and for the combinations F-2, F-6, F-7 (596 watts) and F-2, F-5, F-6 (559 watts).

Table 5.2.6-1. Launch Pad Power

RTG	Pad Power (watts)	
	Requirement	Predicted
F-2	172	203
F-6	174	188
F-7	174	205
F-5	155	168
F-2, F-6, F-7	520	596
F-2, F-5, F-6	501	559

BOM and EOM power predictions are given in Table 5.2.6-2. EOM predictions are shown for 10.8 and 16 years after launch. Nominal and minimum EOM predictions were made in the TEG model. The values in Table 5.2.6-2 are the minimum values. (For comparison, the values listed in parentheses are the corresponding power output requirements as defined in the RTG Product Specification.) BOM power was predicted to be 888 watts for the combination F-2, F-6, F-7, and 841 watts for the back-up combination F-2, F-5, F-7. Figures 5.2.6-1 and 5.2.6-2 show the predicted nominal and minimum power for both RTG combinations throughout the 16 year mission.

Figure 5.2.6-3 shows the predicted minimum total RTG power for the two combinations of RTGs throughout the 16 year mission and compared to the spacecraft power requirements. The predictions show that the spacecraft power requirements will be met throughout the entire mission.

Table 5.2.6-2. Measured and Projected Power Output

Unit	Electrical Power Measured at Acceptance Tests (watts)	Fuel Thermal Power at BOM (watts)	Projected Power (watts)		
			BOM	10.8 Years after BOM	16 Years after BOM
F-2	301.2	4378	296 (274)	231	213 (198)
F-6	299.2	4407	294 (276)	230	212 (199)
F-7	302.6	4397	298 (276)	233	215 (199)
F-5	261	4029	251 (249)	198	183 (182)
F-2, F-6, F-7		13182	888 (826)	694	640 (596)
F-2, F-5, F-6		12814	841 (799)	659	608 (579)

Specification values in parentheses
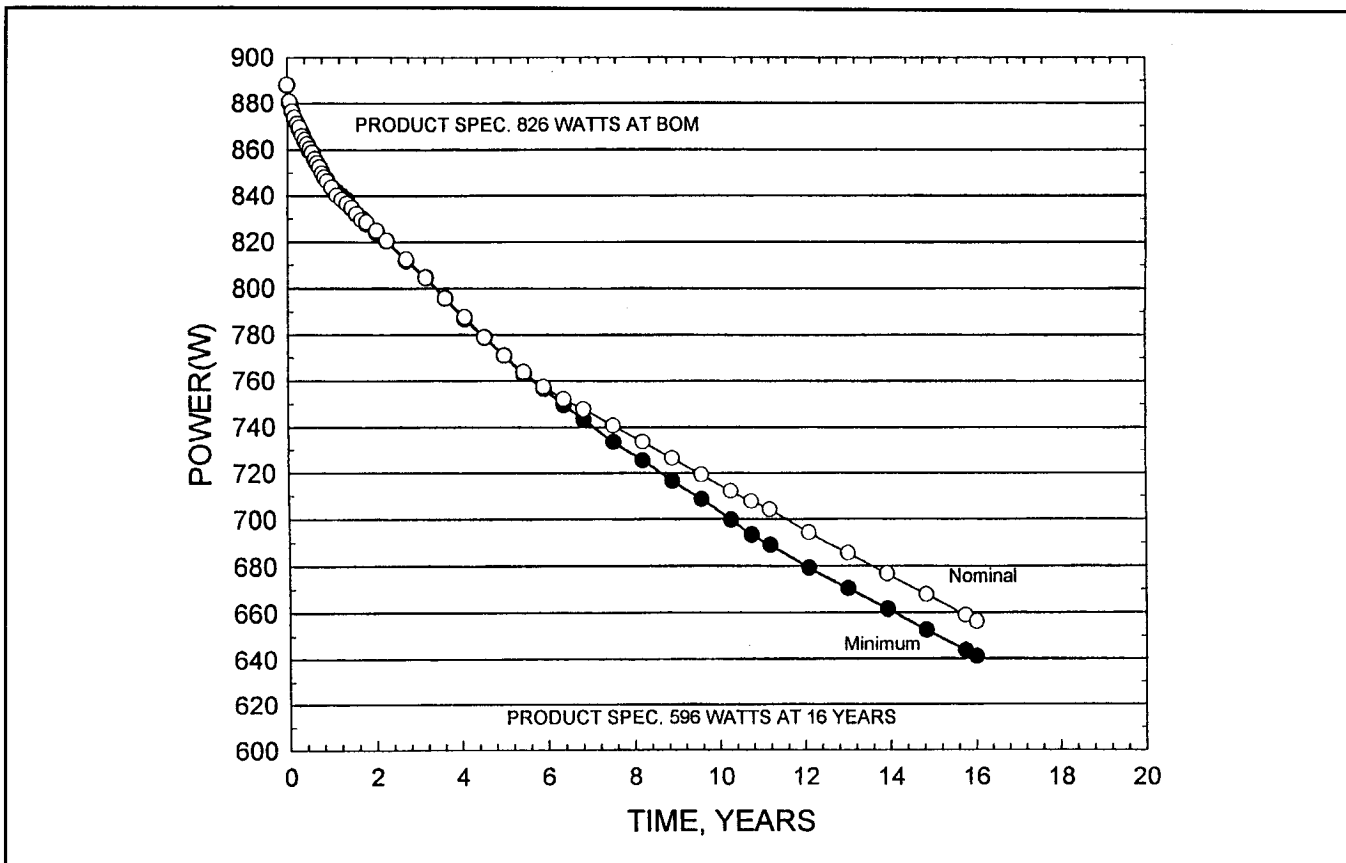
Figure 5.2.6-1. F-2, F-6, and F-7 Total Power
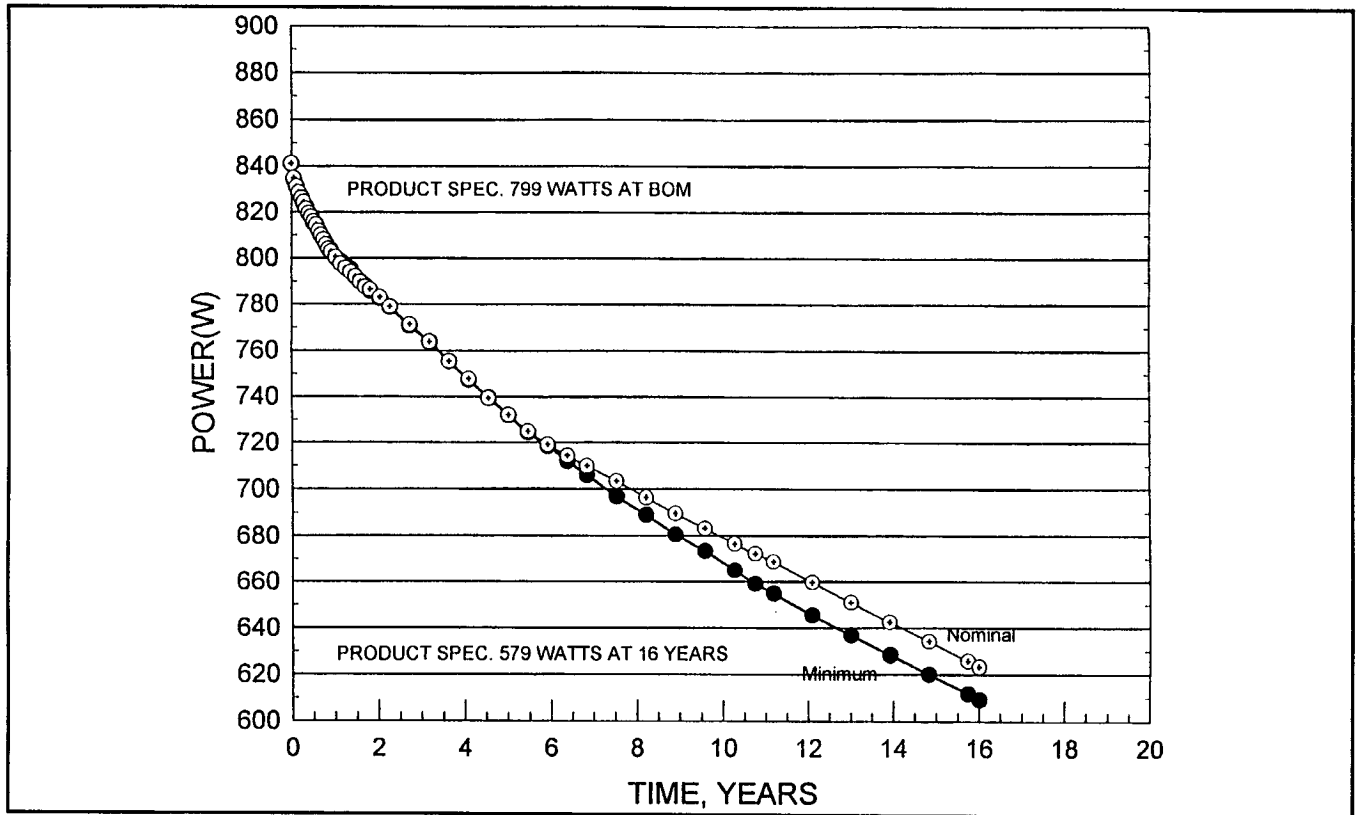
Figure 5.2.6-2. F-2, F-5, and F-6 Total Power
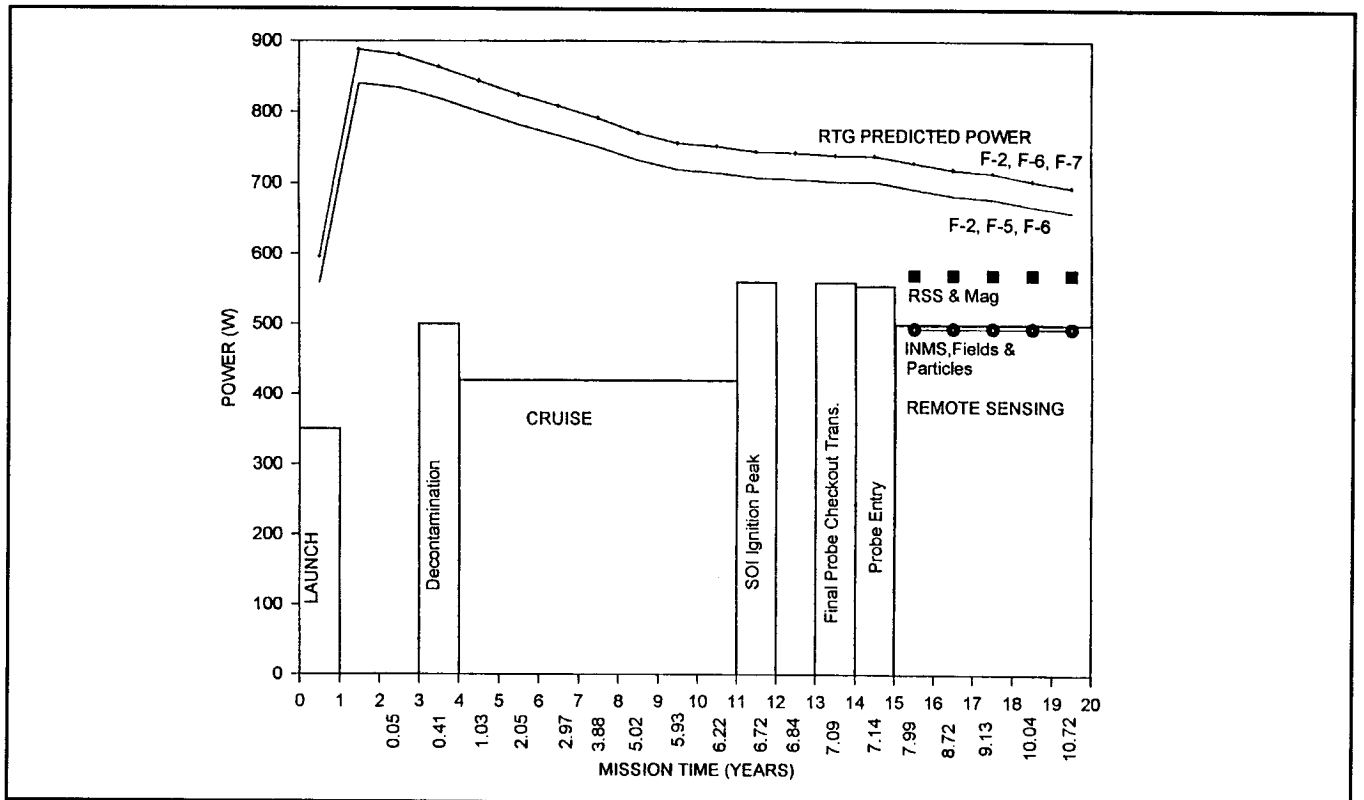
Figure 5.2.6-3. Cassini Required Power and RTG Predicted Power

Flight Telemetry Power

The actual Cassini flight configuration consisted of RTGs F-2, F-6, and F-7. Telemetry data, after correcting for cable losses, showed that measured RTG BOM power output to be 887 watts compared to the predicted value of 888 watts. This is well within the telemetry accuracy of 1% or 9 watts.

5.3 QUALIFICATION PROGRAM

The GPHS-RTG was previously qualified for the Galileo/Ulysses missions, and was accepted for the Cassini mission without the need for testing of an additional qualification unit RTG. The differences between the Galileo/Ulysses and Cassini missions were handled two ways: (1) differences in the environments were addressed analytically, and (2) components that were newly designed to meet Cassini mission requirements (PRD) or were modified in design (RTD cable assembly) were qualified separately as components.

Qualification of the GPHS-RTG for the Cassini mission, as defined by the requirements of the Product Specification for the GPHS-RTG for Cassini, PS23009148, was based on the results of analyses, inspections, and tests used to qualify the GPHS-RTG for the Galileo/Ulysses missions. These were supplemented by analyses, inspections, and component tests for those instances where the requirements or design definition were changed for the Cassini mission.

Qualification of the GPHS-RTG for the Cassini mission was documented in report GESP-7242, "Design Qualification for GPHS-RTG for Cassini," issued 11 August 1995. In this report, each of the requirements for qualification defined in Specification PS23009148 was addressed and evidence of verification was provided.

The dynamic environments defined by Specification 23009150 for the Cassini mission differ slightly from those defined in Specification NS0020-05-04 for the Galileo/Ulysses missions. To demonstrate that the RTG remained qualified, those differences were addressed analytically. The following paragraphs discuss differences in transient, random vibration, acoustic noise, shock, and quasi-static accelerations resulting from significant launch events.

The transient vibration environment defined for the Cassini mission was slightly less severe than the Galileo/Ulysses environment to which the RTG was initially qualified. Therefore, the transient vibration environment was not an issue.

Random vibration environments defined for the Cassini mission differed only slightly from those defined for the Galileo/Ulysses missions, and are compared at the acceptance test level in Figures 5.3-1 (lateral axis) and 5.3-2 (longitudinal axis). Notching to limit response of the inner molybdenum frame and of the heat source support system, as determined during qualification for the Galileo/Ulysses mission, was retained. The frequency range in which the Cassini random environments exceeded the Galileo/Ulysses environments represented the notching intended to protect the PRD. Dynamic testing of the PRD as a component and low level dynamic testing of the F-5 RTG demonstrated that notching of the random environment was not required for the barometrically operated PRD designed for the Cassini mission.

During the RTG qualification program for Galileo/Ulysses, acoustic tests were performed on the Engineering Unit ETG to demonstrate the capability to withstand the acoustic environment. The acoustic environment defined for the Cassini mission is compared with test environments in Figure 5.3-3. It can be seen that the test environment was within a tolerance band of ±3 dB for frequencies below 400 Hz and then exceeded requirements above 400 Hz. It was therefore concluded that the RTG remained qualified to the requirements for dynamic capability under acoustic environments.

Point	Frequency (Hz)	PSD (G²/Hz)
1	80	0.04
2	170	0.04
3	205	0.016
4	245	0.016
5	280	0.04
6	320	0.04
7	352	0.025
8	500	0.025
9	72	0.032
10	180	0.032
11	275	0.032
12	450	0.032

Total GRMS

Cassini 4.78
Galileo/Ulysses 4.84
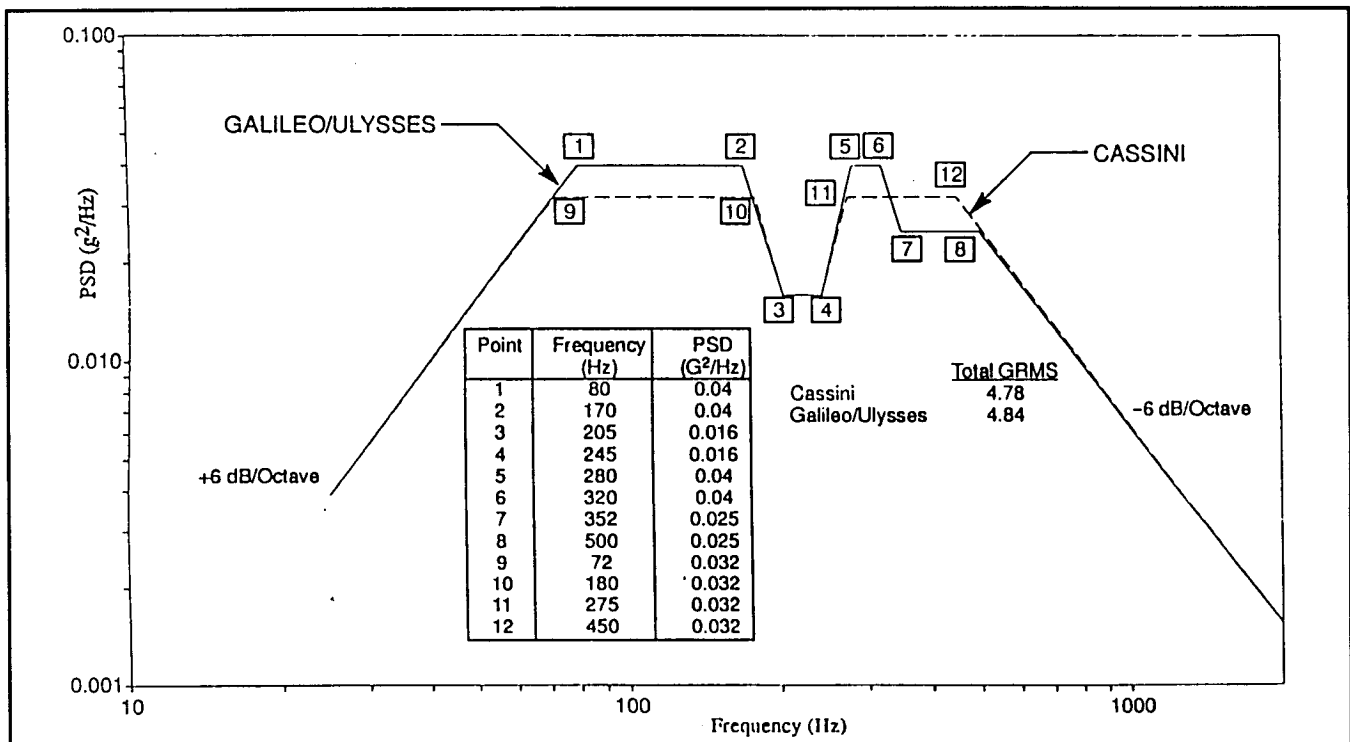
Figure 5.3-1. Comparison of Cassini and Galileo/Ulysses Lateral Acceptance Level Random Vibration Environments
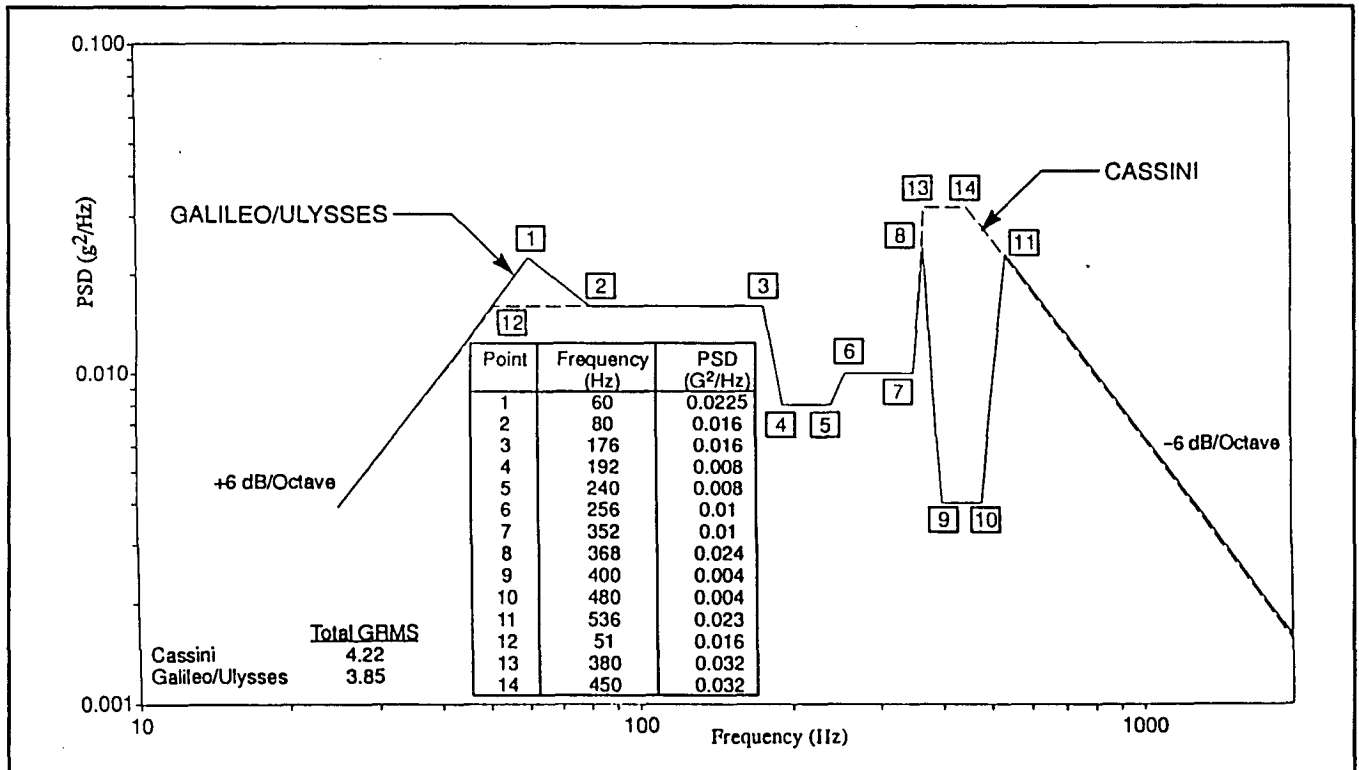
Figure 5.3-2. Comparison of Cassini and Galileo/Ulysses Longitudinal Acceptance Level Random Vibration Environments

Point	Frequency (Hz)	PSD (G²/Hz)
1	60	0.0225
2	80	0.016
3	176	0.016
4	192	0.008
5	240	0.008
6	256	0.01
7	352	0.01
8	368	0.024
9	400	0.004
10	480	0.004
11	536	0.023
12	51	0.016
13	380	0.032
14	450	0.032

	Total GRMS
Cassini	4.22
Galileo/Ulysses	3.85
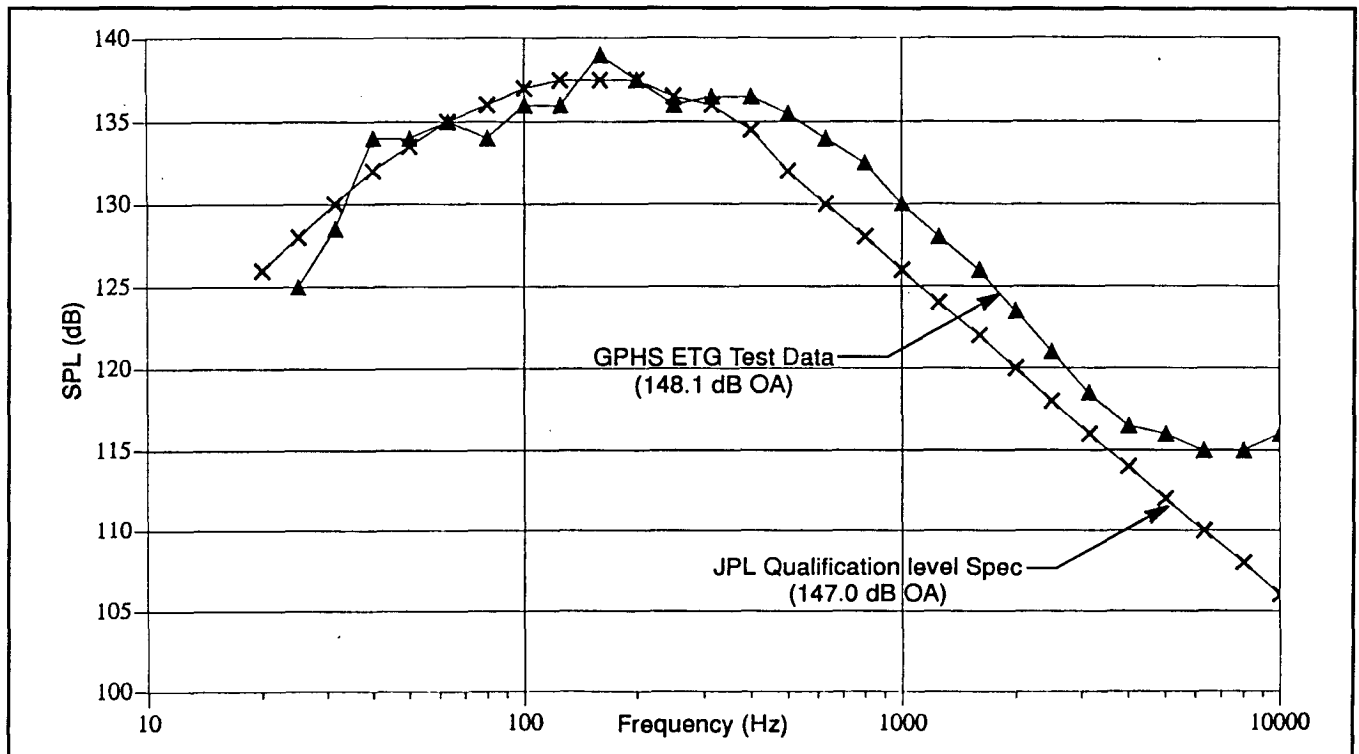
Figure 5.3-3. Comparison of Acoustic Test Data with Qualification Requirements

Shock testing was also performed on the Engineering Unit ETG as part of qualification for the Galileo/Ulysses missions. When mounted on the Galileo spacecraft, the RTGs were supported at the midspan as well as at the inboard end. Pyrotechnic actuators used to release the midspan supports were the primary source of shock loading, and shock testing consisted of three firings of these devices. Test data compared with the specified shock environment for the Cassini mission, Figure 5.3-4, showed that the response greatly exceeded requirements over most of the frequency range, and was only slightly below at frequencies above 3000 Hz. These test data were judged to be adequate demonstration of dynamic capability for shock environment, taking into account the following:

a. The shock environment defined for Cassini was conservative, in that there are no pyrotechnic devices in close proximity to the RTGs.

b. The shock environment was defined to be at the inboard mounting interface whereas shock tests were conducted with input at the midspan and closer to vulnerable components of the thermopile.

c. Mechanical damage was most likely to be expected at lower frequency inputs.
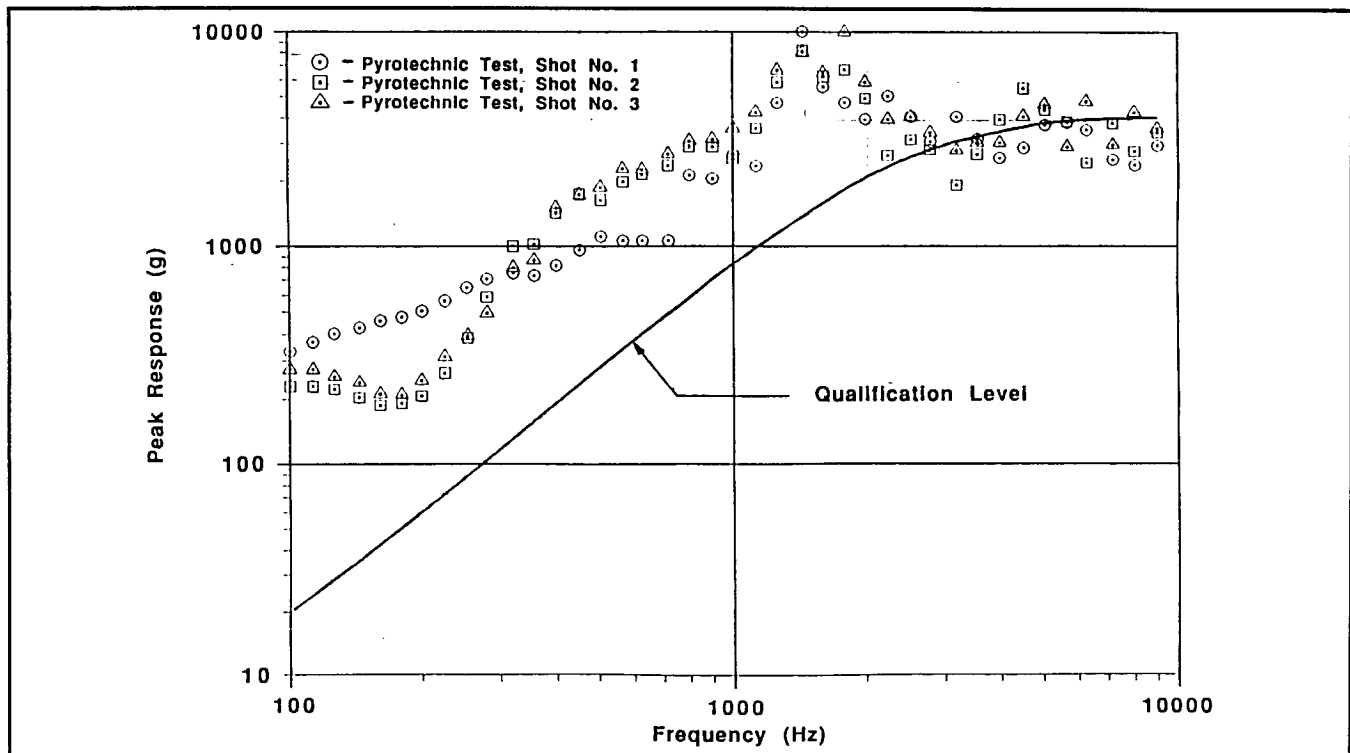
Figure 5.3-4. Comparison of Shock Test Data with Qualification Requirements

Dynamic environments in the 0 to 80 Hz frequency range were represented by quasi-static accelerations. These events included lift-off, maximum aerodynamic buffeting, maximum aerodynamic pressure, ignition of launch vehicle first stage, forward bearing (payload fairing) release, engine shut down of the first stage, engine shut down of the second stage, Centaur main engine shut down after first burn, and Centaur main engine shut down after second burn. Accelerations at the RTG mounting interface, occurring at each of these events, were evaluated to determine the impact on the qualification status of the RTG. Included in the evaluation was analysis that took into account the differences in component temperatures. These temperature differences were a result of uncooled launch on the Titan IV as compared with conditions during qualification testing for the Galileo/Ulysses missions, which was performed with the Active Cooling System (ACS) in operation. Positive Margins of Safety were demonstrated on all critical components within the RTG structural load path.

Quasi-static acceleration loads were also analyzed to determine if adequate axial preload existed on the heat source at all of the significant launch events. The analysis concentrated on the F-5 RTG, since it was likely to have the lowest preload of all flight RTGs at the time of launch. This analysis demonstrated that F-5 (and all other flight RTGs) would have adequate preload to withstand launch dynamic environments.

5.4 GALILEO AND ULYSSES FLIGHT PERFORMANCE

5.4.1 Galileo

The Galileo spacecraft was launched in October 1989 on a six year journey to Jupiter and its surrounding moons. The spacecraft is powered by two RTGs, designated as F-1 and F-4. In spacecraft terminology, F-1 is labeled as the -x RTG and F-4 the +x RTG.

The mission requirements called for a BOM power of 568 watts and EOM power of 470 watts after 71,000 hours (8.1 years). Table 5.4-1 summarizes BOM characteristics. BOM power, as reported by telemetry data, was 577.2 watts. Telemetry accuracy is 1.2 % or ±3.5 watts. Predicted BOM power was in the range of 571 to 576 watts. All power values were at the RTG pins. The Galileo spacecraft measures the bus voltage and the output current from each RTG. There is a voltage drop and power loss from the RTG pins to the spacecraft

Table 5.4-1. Galileo RTG Power, BOM and EOM

	Requirement (watts)	Predictions (watts)	Measured (watts)
BOM	568	571 to 578	577
EOM (8.1 Years)	470	475 to 489	482

bus through the connecting cable. This power loss is accounted for by using a 41 milliohm resistance value supplied by JPL. Figure 5.4-1 shows the power output at the RTG pins throughout the mission as indicated by telemetry and the prediction from the Lockheed Martin degradation model. Predicted power was normalized to the BOM power as determined by telemetry in order to more clearly compare the measured and predicted power slope. Predicted and measured performance was in very good agreement. EOM power on 7 December 1997 was 482 watts. This exceeds the specification requirement of 470 watts by 12 watts (2.6%). The predicted EOM power range was 475 watts to 489 watts.
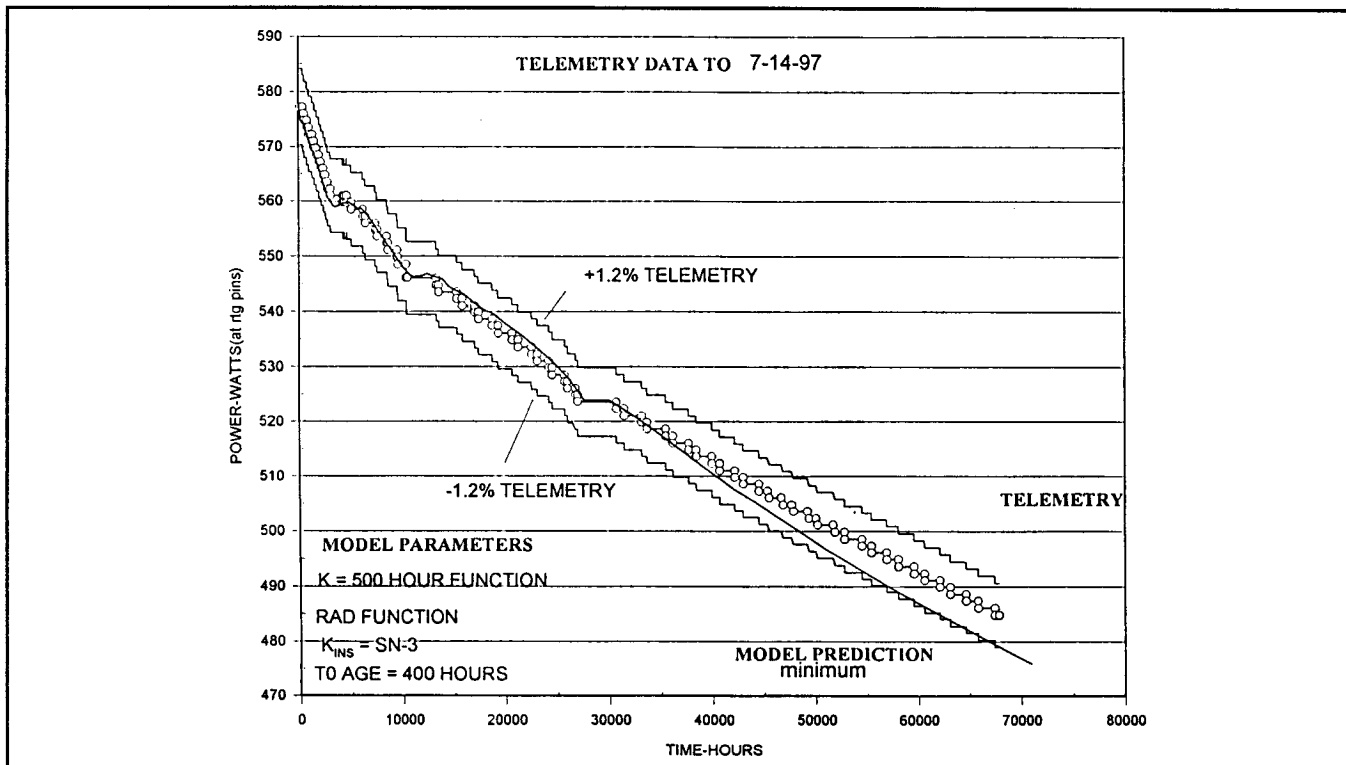
Figure 5.4-1. Galileo RTGs Power Output (F-1 + F-4)

Performance of the individual RTGs is shown in Figures 5.4-2 and 5.4-3. The performance of both are nearly identical with F-1 being slightly higher as shown in Figure 5.4-4.
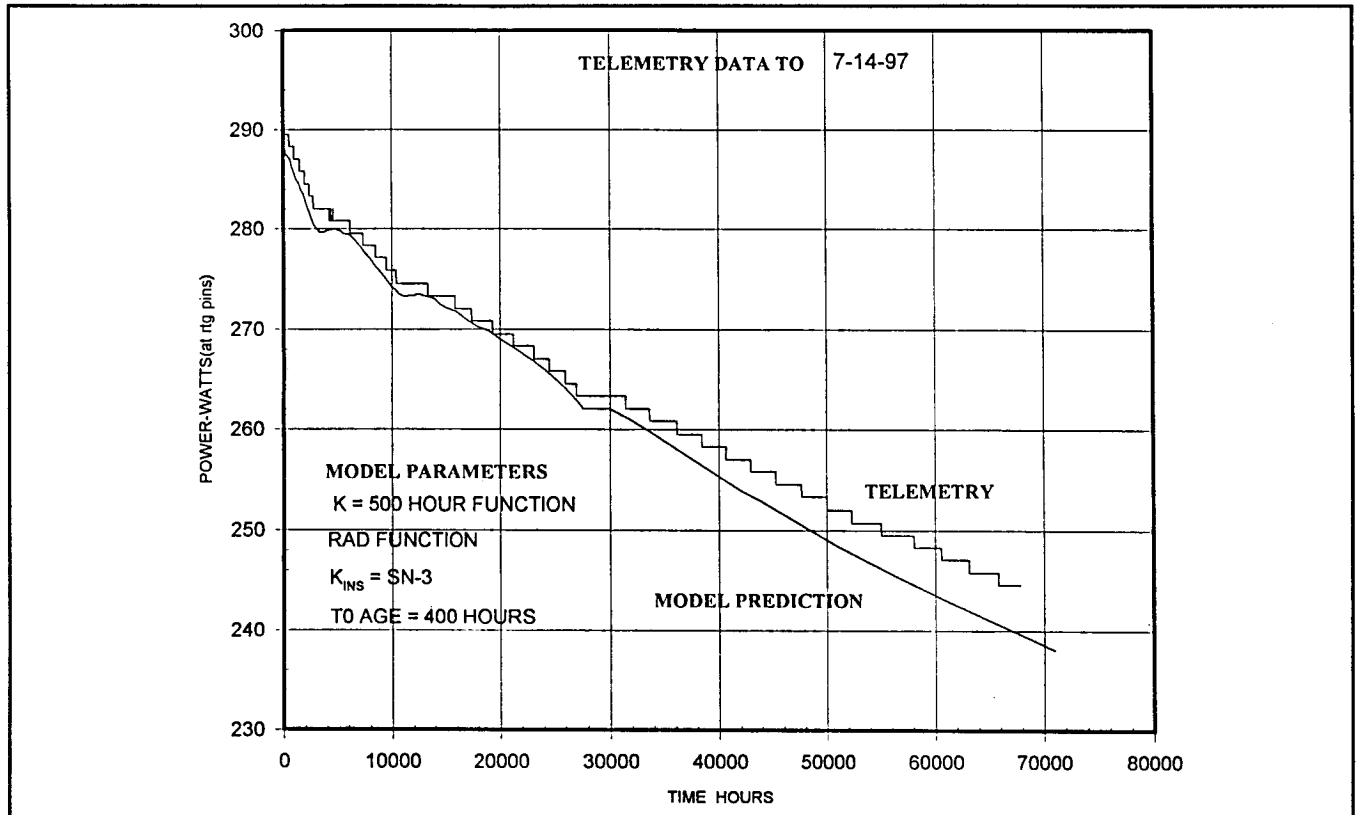
Figure 5.4-2. Galileo RTG F-1 Power

During the first 3.5 years of the mission there were changes in the power output slope. These were the result of changes in operating temperature as the distance to the Sun changed during the various planetary flybys. RTG outer shell temperatures (individual RTD readings), as reported by telemetry, are shown in Figure 5.4-5 along with the predicted average RTD temperature from the JPL TEG2 degradation model. The power output slope was steeper as the RTGs were increasing in temperature because insulation heat losses (proportional to T^4) increased causing the temperature difference across the thermopile to decrease. Conversely, as the RTG temperature decreased the thermopile temperature drop increased, tending to increase power output. This effect was sufficient in magnitude to counterbalance the normal degradation mechanisms and resulted in the observed power plateaus.
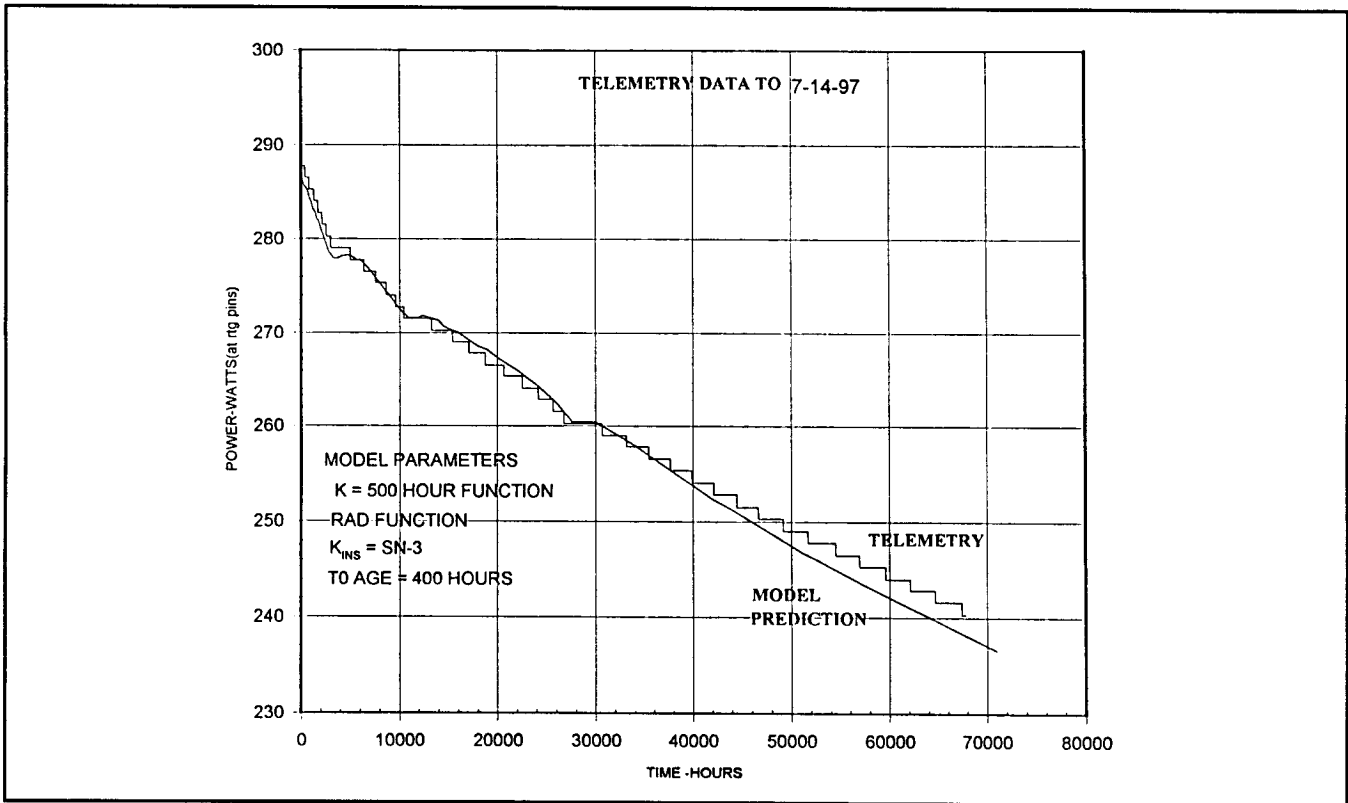
Figure 5.4-3. Galileo RTG F-4 Power
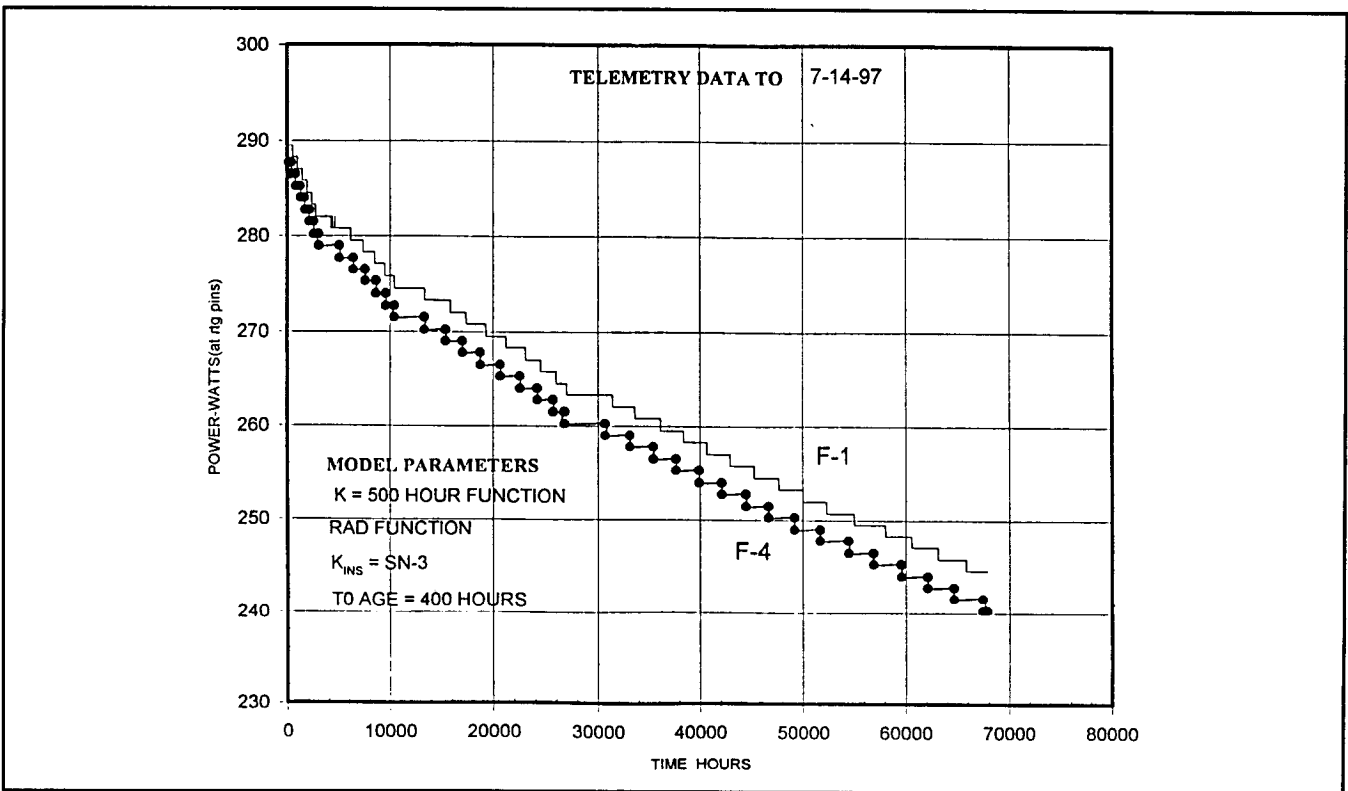
Figure 5.4-4. Galileo RTGs F-1 and F-4
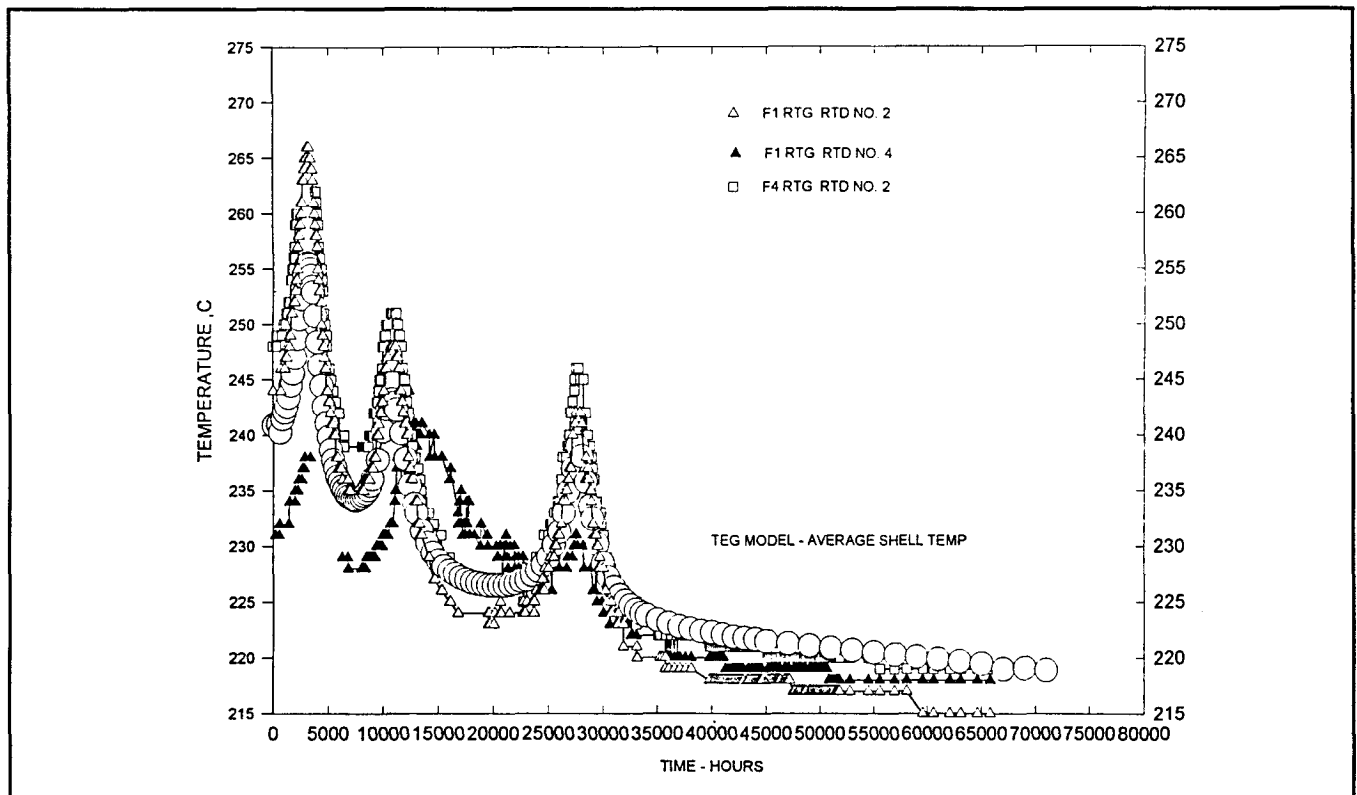
Figure 5.4-5. Galileo RTD Temperatures

Figures 5.4-6 and 5.4-7 , provided by JPL, shows the RTG power available at the spacecraft bus and the required power during the various phases of the primary mission, which was completed on 7 December 1997. All mission power requirements were met and the entire primary mission was successfully performed and included ten encounters; with Ganymede (four times), Callisto (three times), and Europa (three times). The Galileo mission was extended for two years to conduct a detailed study of Europa over a 14 month period followed by close flybys of Io in October 1999.

5.4.2 Ulysses

The Ulysses spacecraft was launched in October 1990 with a single RTG, F-3. Its trajectory led it to the planet Jupiter, where in February 1992, it received a gravitational assist that sent it out of the plane of the Earth's orbit and eventually over the poles of the sun. It passed over the South Pole in October 1994 and the North Pole in 1995. The power estimates for F-3 are shown in Figure 5.4-8. Unlike Galileo, there is no direct measurement of RTG power
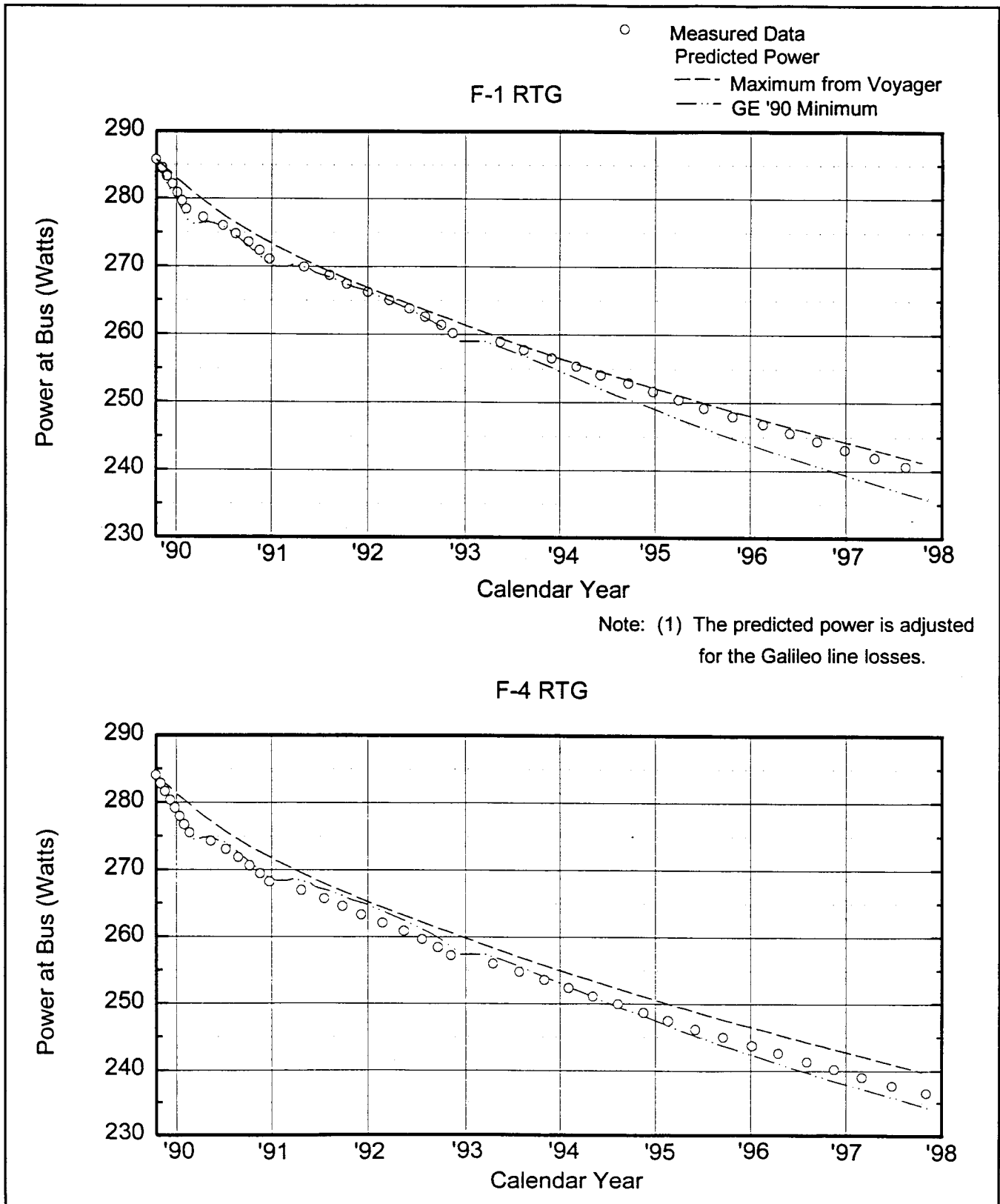
Figure 5.4-6. Galileo — RTG Power at Spacecraft Bus
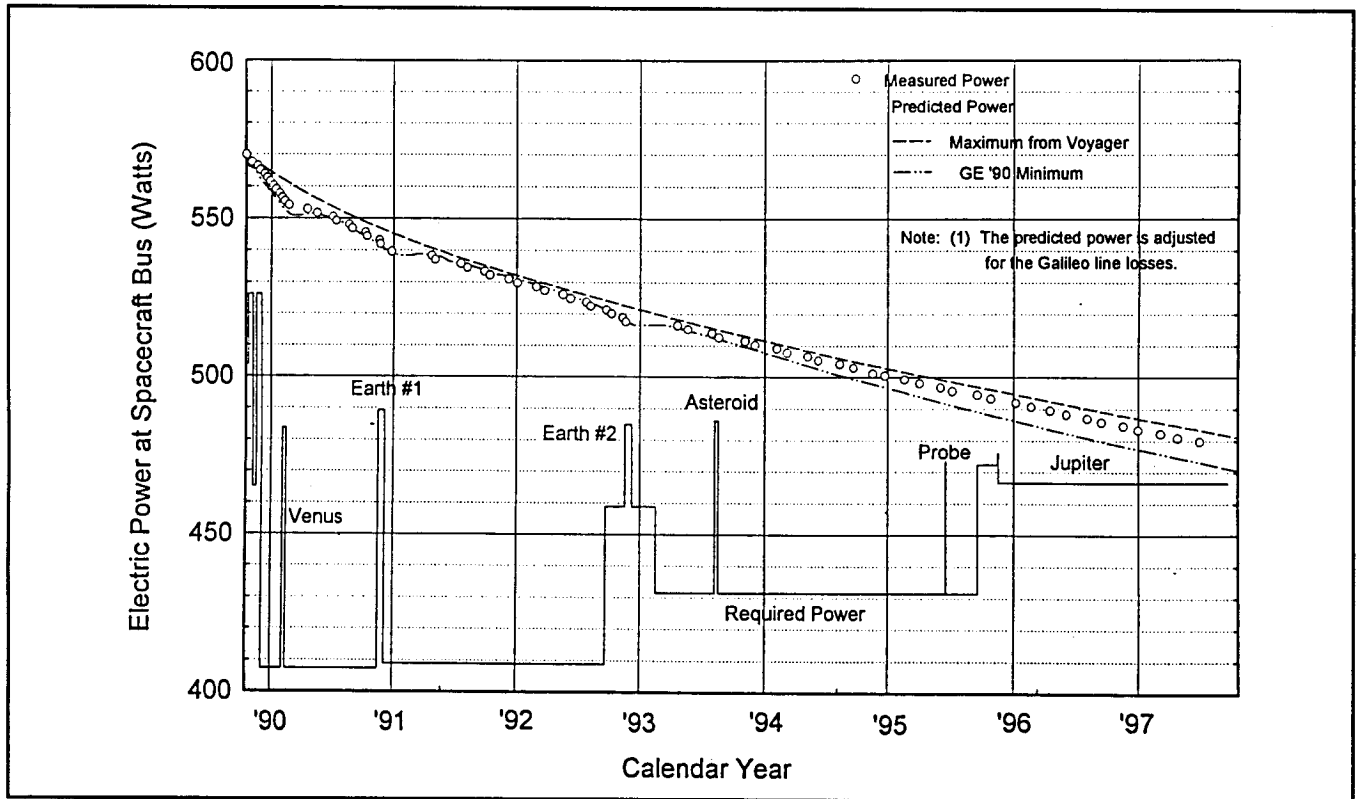
**Figure 5.4-7. Galileo Spacecraft — RTG Power Status Report
(Launch 18 October 1989)**
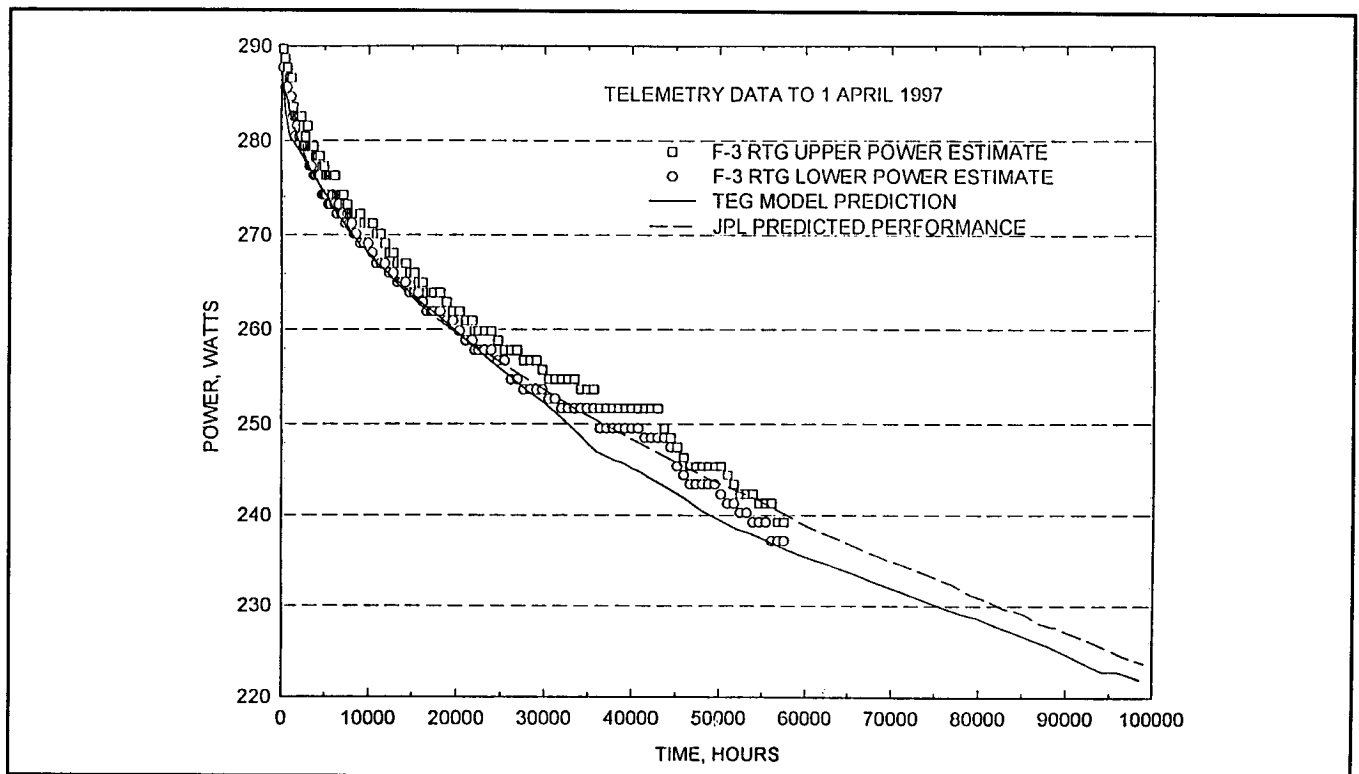
Figure 5.4-8. Ulysses RTG F-3 Power

output. RTG power output was estimated from an algorithm which considered (1) the main bus current, (2) an internal power dump current, (3) nominal power consumption values for ten spacecraft components if they are operating at the time, and (4) unlike the Galileo spacecraft, the Ulysses spacecraft operates at a nominal load voltage of 28 volts. Initial telemetry power was reported to be 284 watts at the bus and 289 watts at the RTG connector (45.7 milliohm resistance between RTG and bus). This exceeded the specification requirement of 277 watts at the RTG connector. (The pre-launch prediction of BOM power was in the range 282 to 287 watts at the connector. The RTG continued to meet all spacecraft power requirements throughout the 42,000 hour (4.8 year) mission which ended in August 1995. Power at EOM was reported as 248 watts. The EOM requirement was 245 watts. JPL has reported that during the periods leading up to and following perihelion in March 1995, there were several spacecraft power reconfigurations in response to the large changes in solar heating as the spacecraft-Sun distance decreased and then increased. Since the algorithm used to estimate power is configuration dependent, these reconfigurations have clearly introduced artifacts into the data set. Table 5.4-2 summarizes BOM and EOM performance.

Table 5.4-2. Ulysses RTG Mission Requirements

	Requirement (watts)	Telemetry Power (watts)
BOM Power [1]	277	289
EOM Power	245	248

[1] Pre-launch predicted power 282 to 287 watts

The Ulysses mission was also extended beyond its primary mission and is now slightly over two years into the extended mission which includes a second polar orbit. The spacecraft is heading to aphelion at the orbit of Jupiter in April 1998, a south polar pass of the Sun in September 2000 and a north polar pass beginning in September of 2001. Figure 5.4-9, provided by JPL, shows the estimated bus power from telemetry to the end of 1997. The JPL TEG model predicts that 220 watts will be available at the spacecraft bus at the end of the extended mission.
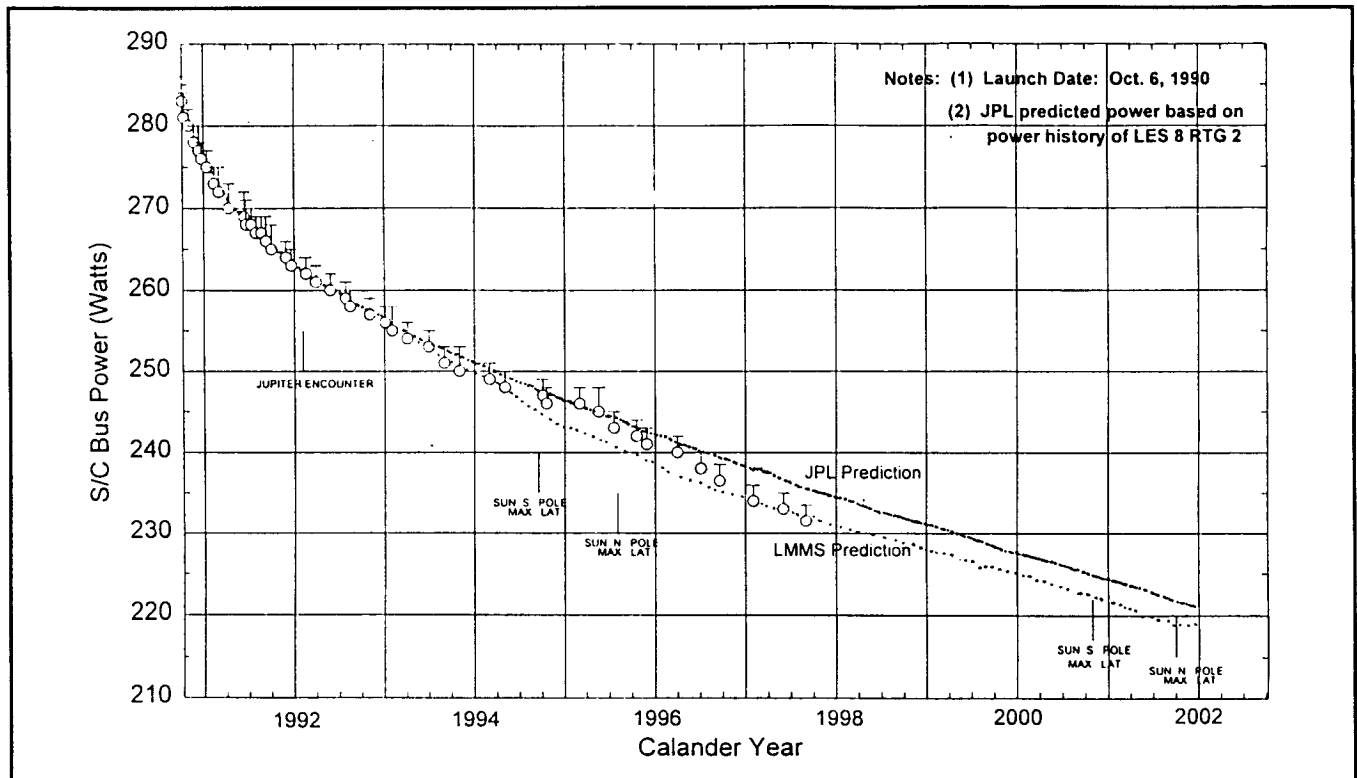
Figure 5.4-9. Ulysses Extended Mission Power

References for Section 5

5-1 Nakahara, J. F., C. E. Kelly, S. Loughin, and R. F. Hartman, "E-7 Processing Investigation - Final Report," Lockheed Martin Missiles & Space Document GESP 7248, Cassini RTG Program, 16 August 1996.

5-2 Kelly, C. E. and J. F. Nakahara, "Carbon Monoxide Levels in Cassini RTGs," Lockheed Martin Missiles & Space Document GESP 7253, Cassini RTG Program, 16 April 1997.

5-3 Cockfield, R. D. and C. E. Kelly, "F-2 Engineering Report," Lockheed Martin Missiles & Space Document GESP 7249, Cassini RTG Program, 22 November 1996.

5-4 Cockfield, R. D. and C. E. Kelly, "F-6 Engineering Report," Lockheed Martin Missiles & Space Document GESP 72451, Cassini RTG Program, 7 March 1997.

5-5 Cockfield, R. D. and C. E. Kelly, "F-7 Engineering Report," Lockheed Martin Missiles & Space Document GESP 7250. Cassini RTG Program, 24 January 1997.

5-6 "Predicted Isolation Resistance for RTG F-7," Lockheed Martin Missiles & Space Document GESP-7247, Cassini RTG Program, 31 July 1996.

Section 6

Safety

SECTION 6

SAFETY

6.1 MISSION AND SYSTEM DESCRIPTION

6.1.1 Mission Overview

The Cassini mission is an international cooperative undertaking of the National Aeronautics and Space Administration (NASA), the European Space Agency, and the Italian Space Agency (ASI). The mission involves the use of the Cassini spacecraft, including the detachable Huygens Probe, to conduct a 4-year scientific exploration of the planet Saturn and its moons. Cassini is one of the two missions under NASA's Outer Solar System Exploration program that were planned in 1991, the Comet Rendezvous Asteroid Flyby (CRAF) being the other mission. The CRAF mission was subsequently canceled in 1992.

The primary Cassini mission was scheduled for launch within a 41-day period beginning 6 October 1997 from Launch Complex 40 (LC-40) at the Cape Canaveral Air Station (CCAS). Launch took place on the 10th day of the launch period (15 October) at 0443 EDST. Using the Titan IV/Centaur launch vehicle, the spacecraft was injected into a 6.7-year Venus-Venus-Earth-Jupiter-Gravity-Assist (VVEJGA) trajectory to Saturn, as shown in Figure 6.1-1. (The dates shown in this figure are based on a launch date of 6 October 1997.) A brief description of the mission, obtained from Reference 6.1-1, is presented below.

The first Venus swingby will occur in April 1998. In December 1998, a maneuver will place the spacecraft on course for the second Venus swingby in June 1999. Due to the Earth's unique orientation relative to Venus during this time period, the spacecraft will swing by Earth in slightly under two months, where it will obtain another gravity assist in August 1999.

After Earth flyby, the spacecraft will travel toward Jupiter, passing through the asteroid belt. In December 2000, the spacecraft will swing by Jupiter to obtain a fourth and final gravity assist.

For several months prior to arrival at Saturn in July 2004, the spacecraft will perform science observations of the Saturnian system as it draws nearer to its destination. During the Saturn Orbit Insertion (SOI) phase, the spacecraft's approach (about 1.3 Saturn radii), is the closest of the entire mission.
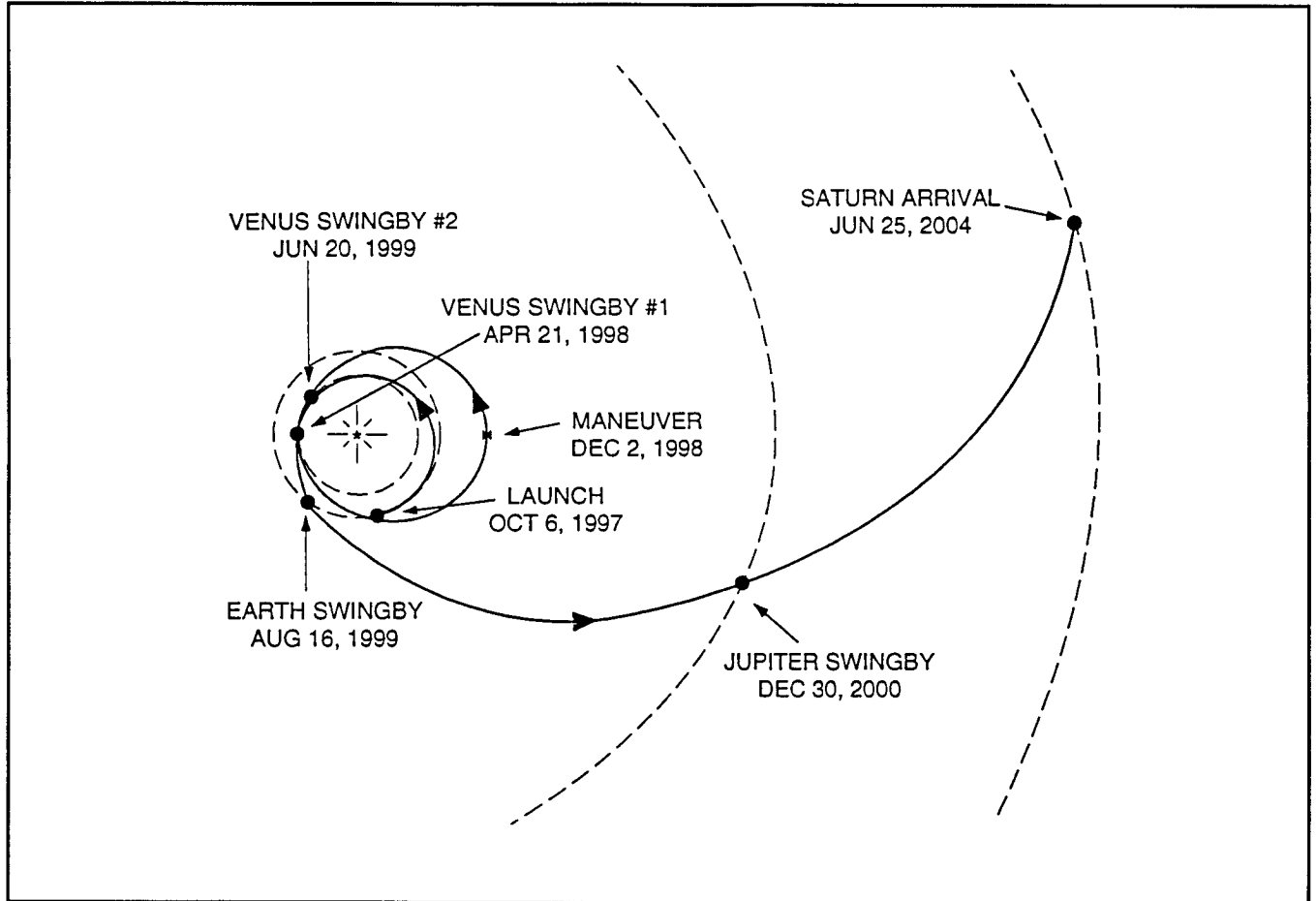
Figure 6.1-1. Cassini Interplanetary Trajectory, VVEJGA

After SOI, the spacecraft will move to the most distant point in its orbit around Saturn (about 180 Saturn radii). It will then return for an encounter with Titan, its largest moon, in November 2004. Approximately three weeks prior to Cassini's first flyby of Titan, the spacecraft will release the Huygens Probe, targeted for entry into Titan's atmosphere. Two days after Probe release, the Orbiter will perform a deflection maneuver to be in position to receive scientific information gathered by the Huygens Probe throughout its estimated 2.5-hour parachute descent to Titan's surface.

The spacecraft will continue on its tour of the Saturnian system, including multiple Titan swingbys for gravity assist and science acquisition. The Titan swingbys and Saturn orbits will be designed to allow maximum science coverage, including the acquisition of science data from Saturn's icy satellites. The 10.7-year nominal mission will end in June 2008.

The Cassini launch phase mission timeline is shown in Table 6.1-1. Solid Rocket Motor Upgrade (SRMU) ignition is used as the time zero reference point for the mission elapsed time (MET). The initiating and final events that define each of the launch mission phases are listed along with the corresponding METs. Table 6.1-2 lists the nominal sequence of significant trajectory events starting at SRMU ignition and continuing until the Cassini spacecraft is inserted into its interplanetary trajectory. Each event is given along with a MET referenced to SRMU ignition. Also shown is the corresponding inertial vehicle velocity and altitude at the start of each event. The altitude listed is the vehicle center-of-mass altitude above the Earth's surface as defined by the SAO-67 Reference Ellipsoid, taken from Smithsonian Astrophysical Observation Report 264. At the launch site (LC-40), this reference ellipsoid is 103.75 feet above mean sea level. The vehicle center-of-mass is at Vehicle Station 852, which is 91.45 feet above mean sea level. Therefore, Table 6.1-2 shows a vehicle center-of-mass altitude of approximately -12 feet at SRMU ignition.

6.1.2   Launch Vehicle and Space Vehicle

6.1.2.1 Launch Vehicle

The Titan IV launch vehicle for the Cassini mission consists of a Core Vehicle which has two liquid propellant stages, an upper stage, a Payload Fairing (PLF), and two SRMUs mounted on opposite sides of the Core Vehicle. The Centaur upper stage is mounted atop the core vehicle second stage. Physical features of the Titan IV/Centaur flight vehicle are illustrated in Figure 6.1-2.

The solid rocket motors upgrades were newly developed by Alliant and were successfully demonstrated in their first launch (aboard a Titan IVB vehicle) in early 1997. Cassini is the second mission using these new motors. The SRMUs are built in three segments, identified as forward, center, and aft. These segments are cased in a graphite epoxy, filament-wound, composite material. The forward closure is also made of composite material. Each SRMU is 112.4 feet long and has a 10.87-ft outer diameter at the steel field joints. The nominal propellant weight of the SRMU is 695,428 lbm and the total weight with inerts is 775,928 lbm.

Table 6.1-1. Cassini Mission Timeline

Mission	Event Description		Mission Elapsed Time seconds	
	Phase	Finish	Start	Finish
0	Complete RTG Installation	SRMU Ignition	-48 hours	0
1	SRMU Ignition	SRMU Jettison	0	143
2	SRMU Jettison	PLF Jettison	143	206
3	PLF Jettison	Stage 1 Jettison	206	320
4	Stage 1 Jettison	Stage 2 Jettison	320	554
5	Stage 2 Jettison	Centaur MECO 1	554	707
6	Centaur MECO 1	Centaur MES 2	707	1889
7	Centaur MES 2	Earth Escape	1889	2277
8	Earth Escape	Centaur MECO 2	2277	2349

**Table 6.1-2. Nominal Cassini Flight Sequence of Events
(Referenced for 6 October 1997 Launch Date)**

MET (sec)	Inertial Velocity (fps)	Altitude (ft)	Event
0	1,341	-12	SRMU Ignition
0.4	1,341	-12	Lift-off and vertical flight
11.0	1,352	817	Begin ramped pitch over
21.0	1,453	3,562	Orient to zero - lift flight
56.5	2,552	34,173	Max. dynamic pressure (950 lbf/sq. ft.)
131.3	7,297	190,396	Stage 1 ignition
143.2	7,635	222,316	SRMU separation
206.3	9,574	362,133	Jettison PLF
319.0	16,577	537,345	Stage 2 ignition
319.7	16,584	538,439	Stage 1/Stage 2 separation
554.2	23,398	674,149	Stage 2/Centaur separation
577.4	23,400	673,293	Centaur first burn ignition, MES 1
706.7	25,663	646,937	Centaur shutdown of first burn, MECO 1
1889.2	25,723	604,679	Centaur second burn ignition, MES 2
2348.6	38,524	1,657,864	Centaur shutdown of second burn, MECO 2
2948.6	33,502	10,882,678	Centaur/Spacecraft separation

Legend:

- **Titan IV Flight Vehicle**
  1) Satellite Vehicle

- **Titan IV Launch Vehicle (LV)**
  2) Payload Fairing (PLF)
  3) Centaur Upper Stage
  4) Solid Rocket Motor Upgrade
     (SRMUs, Stage 0)

- **Titan IV Core Vehicle**
  5) Centaur Adapter Extension
     (CP2492)
  6) Forward Skirt Extension (CP2490)
  7) Stage 2 Forward Oxidizer Skirt
     (CP2460)
  8) Stage 1
  9) Stage 2
  10) Liquid Rocket Engines
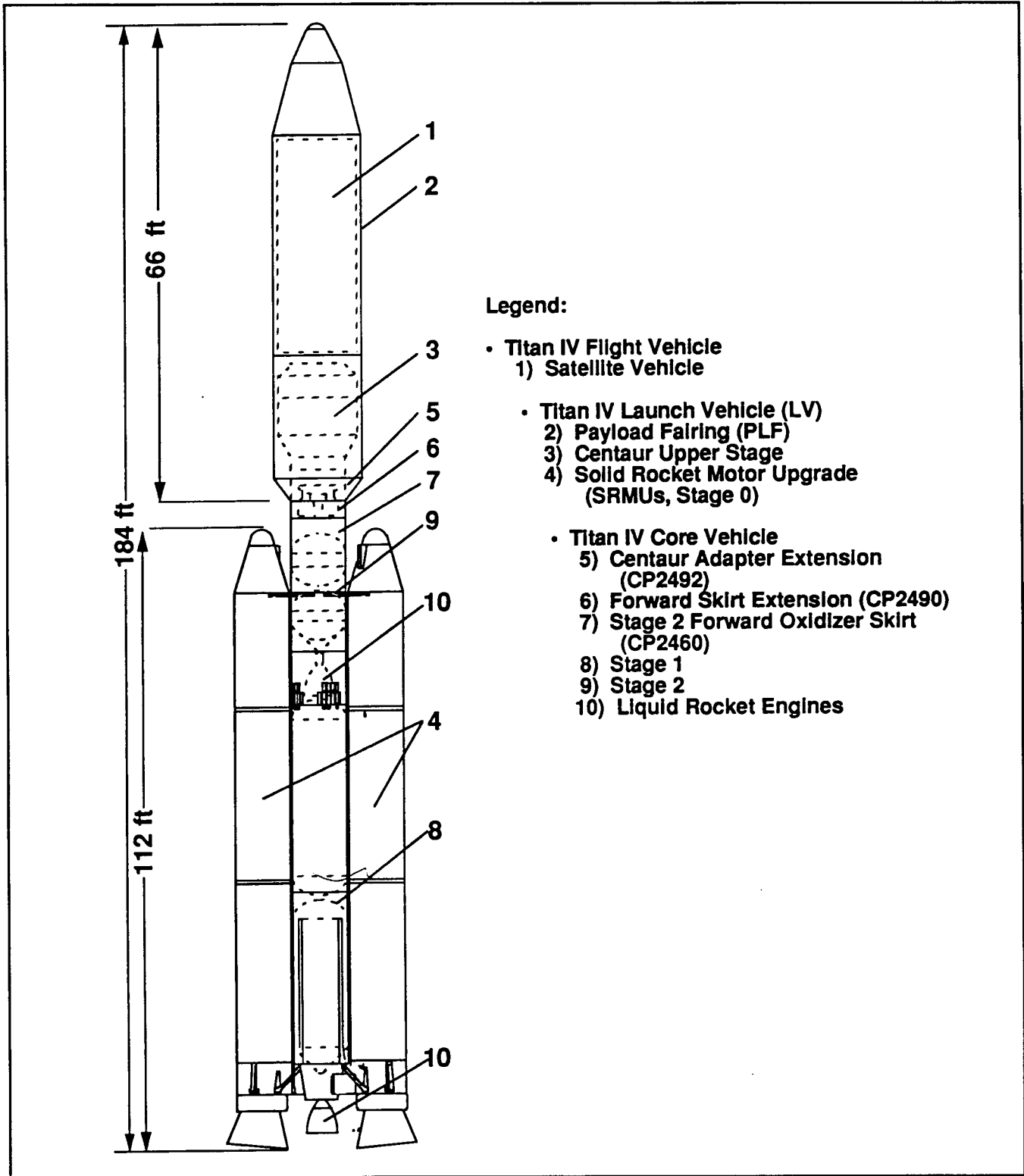
Figure 6.1-2. Cassini Titan IV Launch Vehicle Features

Alternative missions using the conventional Titan IV SRM (Solid Rocket Motor) configuration were considered in the event the SRMU was not available. The mission design in this case would have been limited by the smaller mass injection capabilities of the SRMs, thus reducing the propellant mass onboard the spacecraft and consequently the amount of science return from the mission. The SRM configuration was identified in the Final Environmental Impact Statement (Reference 6.1-2), but was dropped as an alternative once schedule considerations precluded such a change without missing the launch windows.

For flight safety, the Titan IV launch vehicle flight termination system (FTS) provides ground personnel with the capability to shut down the core engines during flight and to destroy the Titan IV launch vehicle in flight. The FTS will also automatically destroy the vehicle if any element should inadvertently separate. The FTS consists of the Command Shutdown and Destruct System (CSDS) and the Automatic Destruct System (ADS). Both the CSDS and the ADS have the capability to destroy the vehicle. The CSDS has the additional capability of shutting down the Titan IV Stage 1 and 2 engines without destruction. The CSDS responds to commands transmitted from the ground while the ADS is activated when certain electrical paths are interrupted as a result of inadvertent separation of stages in flight.

There is a range safety requirement that an automatic FTS must be activated by vehicle breakup or premature separation of any stage interface above or below the stage containing the command system. The command system for Titan IV is located in Stage 2. Stage interfaces are Centaur/Stage 2 above the command system and Stage 0/1, Stage 1/2 interfaces below. Premature separation of any of the Titan IV Stage interfaces will result in activation of the automatic FTS in stages below the sensed separation. Each stage of the Titan IV contains its own ADS. A Thermal Barrier ADS was added to the Titan IV Stage 2. It has the ability to destroy the Titan IV Core Vehicle in the event of a Centaur liquid oxygen tank rupture or a hydrogen/oxygen explosion following rupture of both tanks. Each system is armed before liftoff to provide command destruct or inadvertent separation destruct capability through the Titan IV Stage 2 powered flight. Further detailed description of the Titan IV launch vehicle and the Centaur upper stage can be found in Reference 6.1-3.

6.1.2.2 Space Vehicle

The Cassini space vehicle (SV) is shown on Figure 6.1-3. The information in this section has been obtained from Reference 6.1-4. The main body of the SV is comprised of a Lower Equipment Module, the Propulsion Module, an Upper Equipment Module, and the High Gain Antenna. The two equipment modules are used for external mounting of the magnetometer boom and the three GPHS-RTGs that supply power to the SV. The SV electronics bus is part of the Upper Equipment Module. The High Gain Antenna and two Low Gain Antennas are used to transmit data and receive commands.
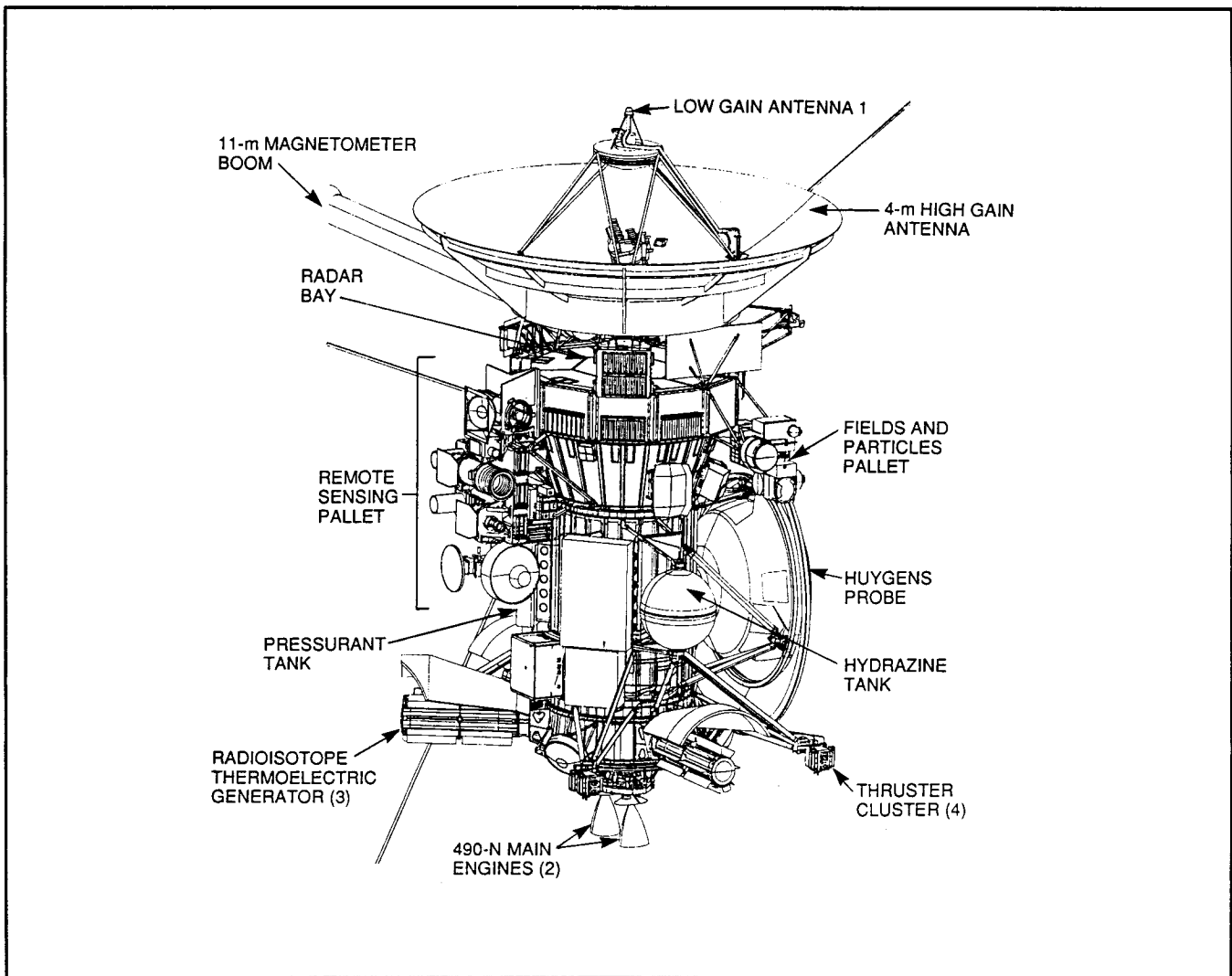
Figure 6.1-3. Cassini Spacecraft Configuration

The overall height of the SV is 7.0 m and its maximum diameter, at the High Gain Antenna, is 4 m. The SV carries 687 kg of scientific instruments, including the Huygens Probe System. After separation from its Titan IV/Centaur launch vehicle and adapter, the SV has a baseline total mass allocation (including margin) of 5,655 kg. The SV dry mass allocation is 2,150 kg, including 335 kg for science payload. A mass properties summary of the integrated space vehicle is provided in Table 6.1-3 (Reference 6.1-4).

Table 6.1-3. Mass Properties Summary (with Respect to SV Coordinates)

Item	Mass (kg)	Center of Gravity (m)		
		X	Y	Z
SV @ Launch	5625.9	-0.02	-0.01	1.37
GPHS-RTG 1	56.0	1.29	0.74	2.80
GPHS-RTG 2	56.0	0.00	1.49	2.80
GPHS-RTG 3	56.0	0.00	-1.49	2.80
Tank + Fuel (BOM)	1204.5	0.00	0.00	0.46
Fuel Tank (Dry)	72.9	0.00	0.00	0.49
Tank + Oxidizer (BOM)	1941.3	0.00	0.00	2.16
Oxidizer Tank (Dry)	72.9	0.00	0.00	2.27
Pressurant + Tank for Bipropellant (BOM)	49.6	0.00	0.99	1.48
Monopropellant + Tank (BOM)	150.8	0.00	-1.09	1.60
Pressurant + Tank for Monopropellant (BOM)	3.5	0.64	-0.65	2.12

6.2 LAUNCH SAFETY RISK ANALYSIS PROCESS

6.2.1 Analysis Objectives

Any U.S. space mission employing radioisotope power sources is subject to a launch approval process that includes a detailed safety analysis and review of the health risks to the public associated with the mission. The requirements for approval have evolved over more than three decades beginning with the launch of the SNAP-3 RTG in June of 1961. The risk analysis process focuses on nuclear safety and has developed, along with the launch approval process, with each new mission building upon the accomplishments of earlier risk analysis efforts. The objective here is to perform the risk analysis associated with the pre-launch, launch, Earth-orbit and Earth-swingby segments of the mission and to document this risk analysis in a Safety Analysis Report (SAR) which is provided to the Interagency Nuclear Safety Review Panel (INSRP) for critical review and as input into the Safety Evaluation Report (SER).

6.2.2 Analysis Overview

The launch approval process consists of a risk analysis documented in a SAR, followed by an interagency review, documented in a SER. Both reports are subject to a critical examination by appropriate agencies of the executive branch prior to a recommendation by OSTP to the Office of the President as to whether or not to approve the launch. This process is shown schematically in Figure 6.2-1.
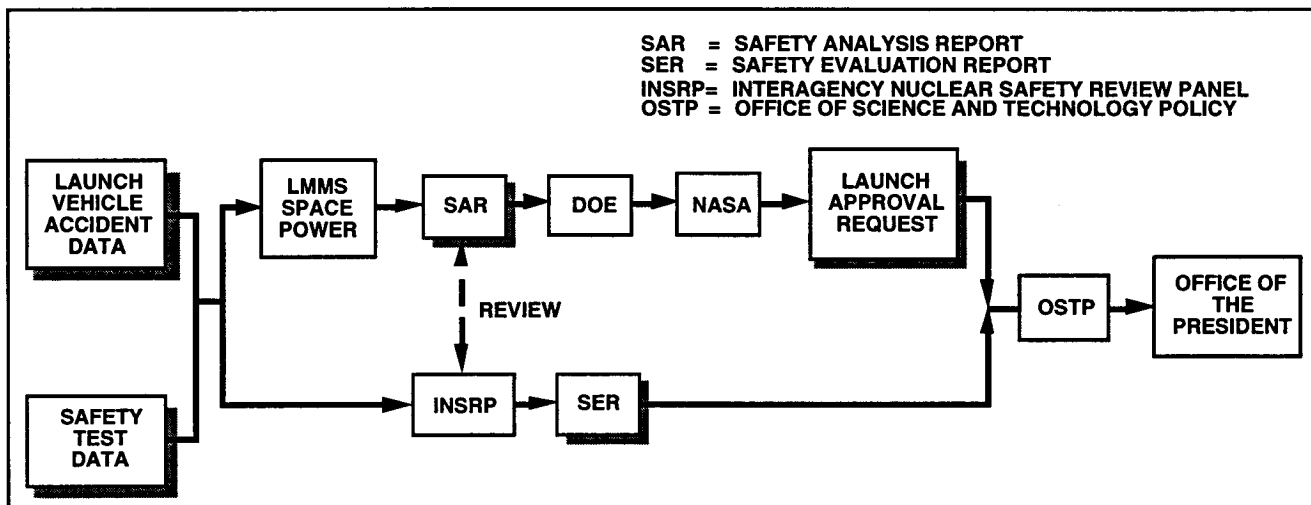
Figure 6.2-1. Schematic of the Launch Approval Process

The risk analysis process employed in the Cassini program builds upon the analysis performed for the Galileo and Ulysses missions, and incorporates many new refinements. Figure 6.2-2 presents an overview of the risk analysis process that was implemented in the Cassini program. The process of determining risk associated with the pre-launch, launch, and Earth swingby segments of the Cassini mission consists of four steps. The first step, that of accident definition, is embodied in the Cassini/Titan IV Centaur RTG Safety Databook and the Cassini Program Environmental Impact Statement Supporting Study, Volume 3: Earth Swingby Plan. The Databook defines those accidents which may occur during the pre-launch, launch, and earth-orbit phases of the mission. (The Databook is supplemented by several JPL technical memoranda (Reference 6.2-1) for conditions related to Earth reentries during the launch segment.) The Swingby Plan defines those accidents which may occur after escape from Earth orbit and which may initiate during the interplanetary cruise. These documents provide the fundamental definition of the accident cases, and the resulting environments that may present a threat to the plutonia fuel containment capability of the RTGs. Each also defines the probability of occurrence (i.e., of failure or POF) for the accident cases described therein.

6.2.3 Analysis Methods

Response modeling is based on an extensive set of test data that have been acquired to support GPHS-RTG safety analyses on this and earlier programs. The mathematical models used to simulate potential launch and reentry accidents are based on these test data on RTGs and RTG components, as well as standard engineering models, computer simulations, and fundamental physical principles. Specifically, the test data are supplemented by a series of 'hydrocode' calculations, which rely on continuum mechanics codes to calculate the time dependent deformations of the RTG components when subject to specific accident conditions. These calculations are semi-empirical in nature, and the empirical parameters have been selected so as to make the calculations agree with actual test data where such data are available.
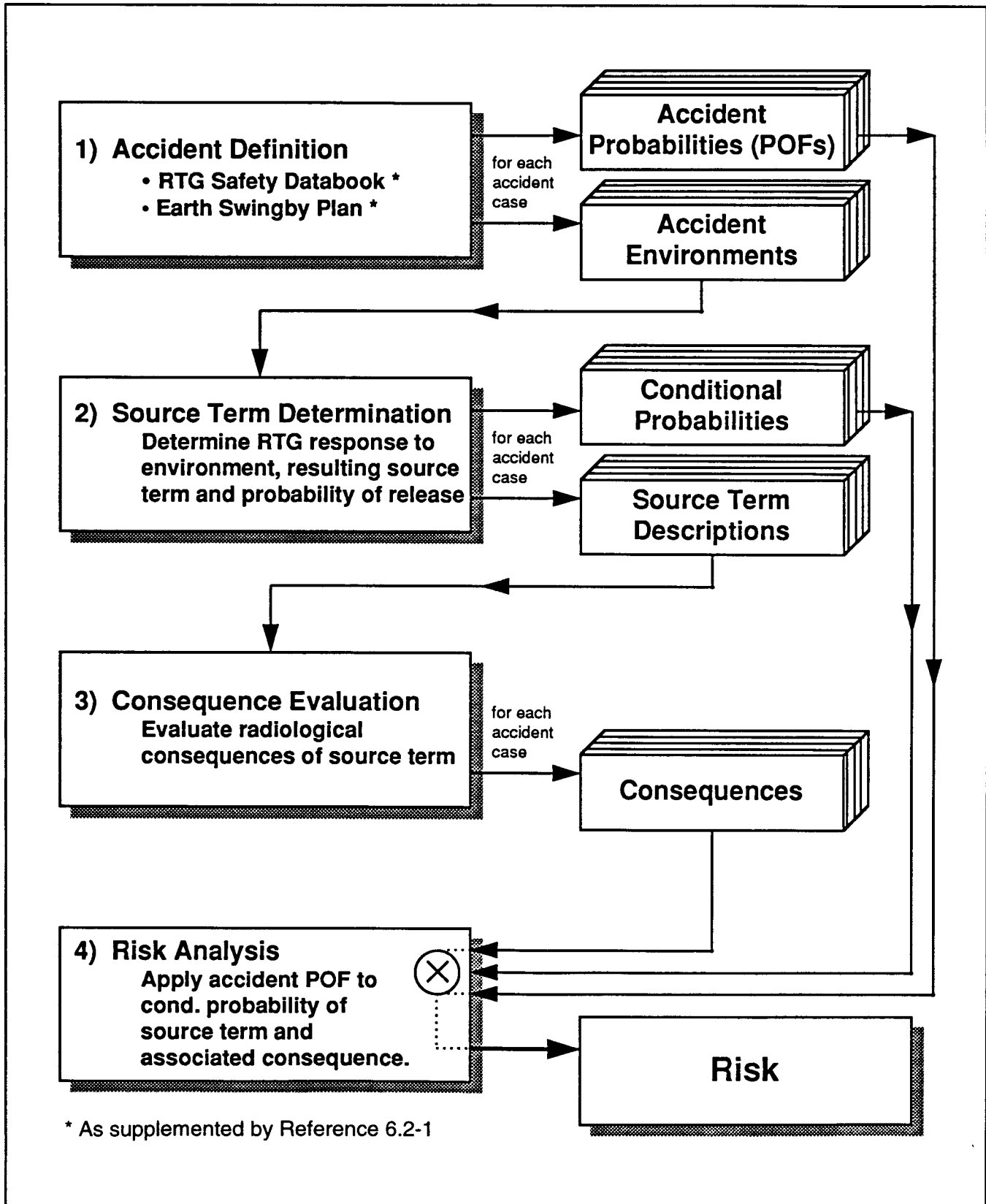
Figure 6.2-2. Top-Level View of the Basic Elements in the Risk Analysis Process

Launch accident analyses were performed, employing these test data and calculations, using a computer code entitled Launch Accident Scenario Evaluation Program for the Titan IV (LASEP-T). This code permitted evaluation of RTG response in the pre-launch and early launch phases of the Cassini mission by simulating the effects of various threatening environments that might result from the launch accidents defined in the Databook. The location and state of each RTG and RTG component was modeled from the initial insult, generally at-altitude, through the final insult upon Earth impact. The outcome of the simulation consisted of determining whether a release occurs, and if so, the salient characteristics of the release. Releases which occurred within a liquid propellant fire were subject to particle size modification, reflecting vaporization effects. The simulation was repeated thousands of times, drawing the initial conditions for each cycle from relevant probability distributions, to create a statistical description of the response to the subject accident case, including the conditional probability of release, and the range of source terms that may result. Modified versions of LASEP-T were used for simulation of pre-launch and full vehicle intact impact accidents.

For launch accidents which included the potential for solid propellant fragments to strike RTG components on the ground, a separate code, FALLBACK, determined trajectory characteristics with a modified version of LASEP-T employed for predicting fuel release. Vaporization effects associated with proximity to solid propellant fires were modeled with the SRESP code.

For out-of-orbit accidents which occur late in the launch segment and subject RTG components to reentry conditions, fuel containment survivability was predicted using a 3-degree-of-freedom trajectory model that includes the aerothermal environment. The reentering bodies are assumed to be modules, in either a face-on-stable or random-tumbling condition. The graphitic aeroshell of the module is designed to survive reentry by ablative cooling. Ablation mass loss was modeled using a finite difference thermal conduction code entitled Reaction Kinetics and Ablation Program (REKAP). The effect of ground impact were evaluated using the same methods as were used to evaluate ground impact for the LASEP-T simulation discussed above. This resulted in a similar statistical distribution of source terms.

In an inadvertent reentry during Earth swingby, reentry velocities exceed 19 km/s, as compared to less than 8 km/s for non-skip out-of-orbit reentries. NASA-JPL performed a breakup analysis of the Cassini spacecraft to predict the initial conditions for RTG components released from the spacecraft. The flight dynamics of the modules for such reentries were predicted by Johns Hopkins University's Applied Physics Laboratory (JHU/APL). The JHU/APL model provided a 6-degree-of-freedom (3 translational and 3 rotational) analysis of the trajectory. The aeroshell response was predicted using computational fluid dynamics (CFD), coupled with thermal analysis to determine transient temperature distributions and surface recession. In addition, the structural response to these transient conditions was modeled using a detailed nonlinear finite element method to determine the structural integrity of the aeroshell when subject to these thermal, aerodynamic, and inertial loads. The codes and methods employed have been adapted from those previously used to successfully predict the behavior of ballistic reentry vehicles that reach similar temperature regimes. Based on the results of these calculations, once again, a set of source terms was defined to provide a statistical description of the potential releases from this type of accident.

The above discussions indicate how source terms were obtained for various types of potential accidents. The next step was to evaluate the radiological consequence of these releases. Accident source terms were input as a set of released particles distributed by size. Those releases that occur in a fireball were pre-processed using the PUFF code from Sandia National Laboratory's ERAD model to calculate plume rise and the dimensions of the fireball cloud. Latin Hypercube Sampling (LHS) with stratified sampling was applied to provide adequate statistical sampling of the database of source terms and other parameters that affect consequence, while limiting the calculation to a tractable size. The Space Accident Radiological Release and Consequence (SPARRC) family of computer codes were used to perform this evaluation. SPARRC consists of the following modules: SATRAP, for modeling site specific transport and dispersion of radioactive particles; GEOTRAP, for modeling global transport and dispersion of radioactive particles; HIAD, modeling high altitude aerosol transport and dispersion; and PARDOS, for modeling dose and health effects.

Each of the three transport models were applied to model transport and dispersion of the different fuel particle size ranges and dispersion time scales. PARDOS was used to model dose and health effects for all transport / dispersion models. By rank ordering the consequences, cumulative complementary distribution functions (CCDFs) were obtained to provide a picture of the relative likelihood of consequences of various magnitudes. These were the output of the consequence calculations and were used, along with probability calculations, to quantify risk.

Risk was expressed in the safety analyses in two forms: 1) as a probability distribution of potential consequences for a given situation, and 2) as the mathematical expectation value of the consequence, given by the sum of the products of the consequences and their associated probabilities.

The models used in the calculation of consequences from potential accidents for the FSAR are based upon experimental and observational data and known physical principles. The models cannot provide completely precise descriptions of the accident situations they simulate due to limitations in the amount of data available and limitations in the level of understanding of the processes which might occur in an accident. Therefore, the consequences of a potential accident could be somewhat different than those calculated by the analysis. As a result, an uncertainty analysis was performed for the establishment of bounds enclosing the accident consequence levels, to a high level of confidence.

6.3   SAFETY ANALYSIS REPORTS

6.3.1   Overview of Safety Analysis Reporting Activities

At the outset of the CRAF/Cassini program, effort was applied towards preparing an Early Safety Assessment (ESA), based upon a Titan RTG Safety Databook to be provided by Martin Marietta under contract to NASA. The Titan Databook was to include only those accident scenarios considered by the RTG Working Group to present potentially significant threat environments to an RTG. The RTG Working Group consisted of representatives from DOE, GE, Martin Marietta, and NASA, organized to define requirements for CRAF/Cassini Databook content.

Delays in receipt of this Databook, identified as the EIS Databook, precluded delivery of the ESA prior to October 1991, the initially defined release date for the CRAF/Cassini EIS. A Draft EIS Databook was received in July 1991, with updates in September and November of 1991. A Preliminary ESA was provided to DOE in October 1991, and updated in February 1992, addressing risks associated with four postulated scenarios:

> SRMU Fail-to-Fire
>
> Centaur Tank Failure/Collapse
>
> Command Shutdown and Destruct
>
> Inadvertent Reentry

Comments received from DOE, DOE contractors, and affiliated national laboratories were incorporated into the Preliminary ESA, resulting in the release of the Draft ESA in September 1992. The Final ESA, retitled the RTG Safety Assessment (RSA), was released by DOE in May 1993.

Activities for the preparation of the next databook version, titled the Preliminary Databook, kicked off in June 1992 with a meeting of the RTG Working Group. In contrast to prior mission databooks, the Preliminary Databook was to include probabilistic risk assessments for all included accident scenarios. Creating this type of document required intensive interactions between the RTG Working Group, NASA/LeRC, and INSRP through 1993 and 1994. Event sequence diagrams were created for all credible accident scenarios and reviewed by the safety community for completeness.

EIS supporting analyses were performed in mid-1993 in the areas of GPHS module thermal response to EGA reentry environments and a bounding estimate consequence assessment for EGA reentry. An event sequence tree describing probabilities for an individual module to occupy various states (e.g., tumbling vs. non-tumbling, rock impact vs. water impact vs. soil impact, etc.) was provided to NASA via DOE along with the analysis results listed above.

During mid-1994, NASA considered the possible use of heritage design solid rocket motors (SRMs) in lieu of the as-yet untested solid rocket motor upgrades (SRMUs). Agreement was reached at that time between DOE and NASA to proceed with the Preliminary Safety Analysis Report (PSAR) under the assumption that only the SRMU configuration would be analyzed. As mentioned above, potential use of SRMs was identified in the June 1995 EIS but removed from consideration soon thereafter.

The Preliminary Cassini Titan IV/Centaur RTG Safety Databook was received from NASA in October 1994 and incorporated into the RTG PSAR (Preliminary Safety Analysis Report), which was issued in December 1994. PSAR material was briefed to the INSRP in February 1995. Subsequently, a compilation of over 350 comments was received from INSRP.

Due to ongoing delays in the release of each Databook update, NASA agreed in late 1994 to provide accident description and environment data packages in advance of the final release of the Databook. Data packages were received in February through April 1995 for all then-defined scenarios other than SRMU fragmentation and propellant fallback. Formal issuance of the Databook, Rev. 0, occurred in September 1995. Open items not fully addressed in this release included the SRMU environments and details regarding the Flight Hardware/RTG Impact environment. Databook definition for these environments was provided in November and December 1995. Given the time required to update and validate launch accident models to reflect these added items, accident cases including SRMU and Flight Hardware/RTG Impact effects were identified for inclusion in an addendum to the FSAR, to be issued several months after the FSAR.

A replan of the entire safety analysis task was completed in June 1995. The effort related to treatment of variability and uncertainty was identified as significantly greater in scope than initially anticipated. This additional work was authorized by DOE under Task 8. The

approach adopted for handling variability and uncertainty within launch accident analyses was reviewed with INSRP between August and December 1995. To assist both uncertainty analysis activities and accident modeling, DOE provided funding for support from the Sandia National Laboratory (SNL) Risk Assessment Department staff. Work scope for the SNL effort included consultation regarding uncertainty analysis methods, definition of consequence uncertainty parameter distributions, development of a liquid propellant fireball model, and providing a plume rise model for transport analyses.

Due to severe schedule compression from delayed delivery of the RTG Safety Databook, the planned Updated Safety Analysis Report (USAR) was replaced by a series of INSRP presentations in which preliminary risk analysis methods and results were provided. Meetings in November 1995 provided updated definition of the analysis models while meetings in January and February 1996 provided analysis results from both launch and EGA swingby postulated accidents.

In early 1996, NASA initiated an effort to more fully address the accident scenario in which an intact Titan IV/Centaur veers off-course and impacts the ground before the Range Safety Office can issue a destruct command. This accident type was termed a Full Stack Intact Impact (FSII). Lockheed Martin participated in the development of accident environments during mid-1996, providing an early assessment of fuel release, health and land contamination risks. Results of this assessment were briefed to NASA in August 1996 in support of a decision to request ground system enhancements at CCAS to preclude such an accident. The complete FSII risk analysis was detailed in the FSAR Addendum.

The Draft Final Safety Analysis Report (DFSAR) was issued in July 1996, approximately coincident with the release of Rev. A of the Databook. The DFSAR provided source term and consequence results for the pre-launch, early launch and late launch mission segments. Pre-launch and early launch results did not include effects due to SRMU coincident impact, Flight Hardware/RTG environments, or Full Stack Intact Impact. Inadvertent EGA reentry source term and consequence results were not provided in the DFSAR, as this work was ongoing at the time. DFSAR comments were received from INSRP, NASA, DOE, and DOE contractors and subsequently reviewed for disposition.

The Final Safety Analysis Report (FSAR) was issued in November 1996. It included the EGA source term results and the consequence results for all four mission segments, but did not include environment changes from Rev. A of the Databook. The results of the FSAR uncertainty analysis were issued in December 1996 as an attachment to Volume III of the FSAR. An Executive Summary of the FSAR was also released that month.

Databook Rev. B was provided by NASA in draft form over a period from July 1996 to January 1997. Rev. B updates included a reduction in the overpressure resulting from Centaur propellant explosion (based on joint NASA/NASDA Hydrogen Oxygen Vertical Impact (HOVI) cryogenic tank destruct tests), new FSII environments, a revision to the SRMU propellant burn rate, and a change in accident probabilities for a number of launch accident scenarios. Results of calculations incorporating Databook Rev. A and Rev. B changes were presented in the FSAR Addendum, released in April 1997. The two most significant changes in the consequences were 1) an increase in predicted early launch consequence due to a greatly increased probability of space vehicle intact impact, and 2) a reduction in the probability of late launch accidents.

The FSAR Addendum Supplemental Analyses Report, released in May 1997, presented an updated uncertainty analysis, updates in the reentry consequence analysis to reflect consequence modeling changes, and an analysis of the risks associated with the secondary launch window. An updated Executive Summary was released at the end of May 1997. Concurrent with release of the Updated Executive Summary, NASA issued a revised Earth Swingby Plan which specified lower Earth impact probabilities and higher nominal swingby altitude (~800 km vs. 500 km) than previously defined. These updates could not be incorporated into the FSAR Addendum documents but were subsequently evaluated in a consequence analysis and provided to DOE.

A Supplemental Environmental Impact Statement was released in June of 1997. Its release was necessitated by new information developed since the EIS was issued in June 1995, including the HOVI test results and the higher consequences predicted in the FSAR and FSAR Addendum for pre-launch and late launch accidents than previously identified.

6.3.2 Summary of Safety Analysis Results

A summary of safety analysis results from the EIS, FSAR, FSAR Addendum (FSAR Add), and the Supplemental EIS (SEIS) is given in Table 6.3-1. Early launch and late launch risks calculated for the FSAR were over an order of magnitude higher than the values calculated for the EIS. However, the FSAR risk for EGA was over an order of magnitude lower than the risk calculated for the EIS. The environment changes from Rev. A and Rev. B of the Databook resulted in an increased risk for early launch and a decreased risk for late launch in the FSAR Addendum, as discussed previously.

Table 6.3-1 Summary Statistics for the Cassini Safety Analyses (Mean Values)

Mission Segment	Analysis	Probability of Failure	Probability of Release	Source Term (Grams)	50 Year Collective Dose [a] (Person-rem)	50 Year Health Effects [a] (Excess Fatalities)	50 Year Risk [a] (Excess Fatalities)
Pre-Launch	EIS*						
	FSAR	1.4×10^{-4}	1.4×10^{-4}	0.3	3.6	1.8×10^{-3}	2.5×10^{-7}
	FSAR Add	6.7×10^{-5}	5.2×10^{-5}	3.8	130	6.6×10^{-2}	3.4×10^{-6}
	SEIS	6.7×10^{-5}	5.2×10^{-5}	3.8	13	6.6×10^{-2}	3.4×10^{-6}
Early Launch	EIS	2.0×10^{-3}	1.1×10^{-3}	0.37	1.2	4.1×10^{-4}	4.6×10^{-7}
	FSAR	5.8×10^{-3}	6.9×10^{-4}	0.57	21	0.10	7.3×10^{-6}
	FSAR Add	6.2×10^{-3}	6.6×10^{-4}	15	140	7.1×10^{-2}	4.7×10^{-5}
	SEIS	6.2×10^{-3}	6.7×10^{-4}	14	140	7.1×10^{-2}	4.7×10^{-5}
Late Launch	EIS	3.7×10^{-2}	9.3×10^{-4}	0.12	0.23	4.0×10^{-4}	3.8×10^{-7}
	FSAR	2.9×10^{-2}	4.1×10^{-3}	0.21	90	4.5×10^{-2}	1.9×10^{-4}
	FSAR Add	2.1×10^{-2}	2.1×10^{-3}	0.20	89	4.4×10^{-2}	9.4×10^{-5}
	SEIS	2.1×10^{-2}	2.1×10^{-3}	0.20	88	4.4×10^{-2}	9.2×10^{-5}
EGA	EIS	7.6×10^{-7}	**	1.2×10^{4}	6.6×10^{6}	2.3×10^{3}	1.7×10^{-3}
	FSAR	8.0×10^{-7}	6.3×10^{-7}	2.6×10^{4} ***	2.5×10^{5}	1.3×10^{2}	8.0×10^{-5}
	FSAR Add	8.0×10^{-7}	6.3×10^{-7}	2.6×10^{3}	2.5×10^{5}	1.4×10^{2}	8.6×10^{-5}
	SEIS	8.0×10^{-7}	6.3×10^{-7}	2.6×10^{3}	2.6×10^{5}	1.4×10^{2}	8.8×10^{-5}

*   Pre-launch was not considered in the EIS

**   Not given. Source term mass is an expectation value

***   Not given in the FSAR

a   Without de-minimis applied

FSAR Addendum results are presented in greater detail in the remainder of this section.

Table 6.3-2 presents mean probabilities of failure and release as well as source term statistics by accident case, for the mission segment. The fact that the mean release values in the table are higher than the 50th percentile releases indicates that the source term distributions are asymmetric.

Figure 6.3-1 provides source term complimentary cumulative distribution functions (CCDFs) for phase 0, phase 1, and phases 3-8 launch accident cases, and EGA reentry. These CCDFs give the probability of the source term exceeding any given amount. For example, there is approximately a 2×10^{-4} (1 in 5000) probability that a phase 1 launch accident will occur that will result in a plutonia release exceeding 1 gram.

Mean 50 year consequence values by mission segment are given in Table 6.3-3. Collective dose and health effect values are given with and without de-minimis. A calculation with de-minimis assumes that no effects result from doses below a set level, which was 0.001 rem per year for the results shown.

CCDFs for 50 year health effects without de-minimis are provided in Figure 6.3-2 by mission segment. The curves show the overall probability that health effects will exceed a given value. These probabilities include the POF and the conditional probability of plutonia release given that an accident has occurred.

Table 6.3-2. Source Terms by Mission Segment

Mission Segment	Mission Phase(s)	Probability of Release	* Mean Release (grams)	Release Percentiles *, **			
				5th (grams)	50th (grams)	95th (grams)	99th (grams)
PRE LAUNCH	0	5.2×10^{-5}	3.8	0.026	0.43	2.1	23
EARLY LAUNCH	1	6.6×10^{-4}	15	0.027	0.38	52	3.6×10^{2}
LATE LAUNCH	3-8	2.1×10^{-3}	0.10	0.014	0.064	0.23	0.37
EGA SWINGBY a (Short Term)		6.3×10^{-7}	2.6×10^{3}	0.050	1.2×10^{3}	9.7×10^{3}	1.2×10^{4}
TOTAL MISSION		2.8×10^{-3}	4.1	0.016	0.084	2.0	61

*　For trials which produced fuel releases (grams of PuO_2)

**　5th Percentile: 5% of trials produced mass release smaller than this value
　　50th Percentile:　　　50% of trials produced mass release smaller than this value
　　95th Percentile:　　　95% of trials produced mass release smaller than this value
　　99th Percentile:　　　99% of trials produced mass release smaller than this value

a　For 500 km swingby altitude
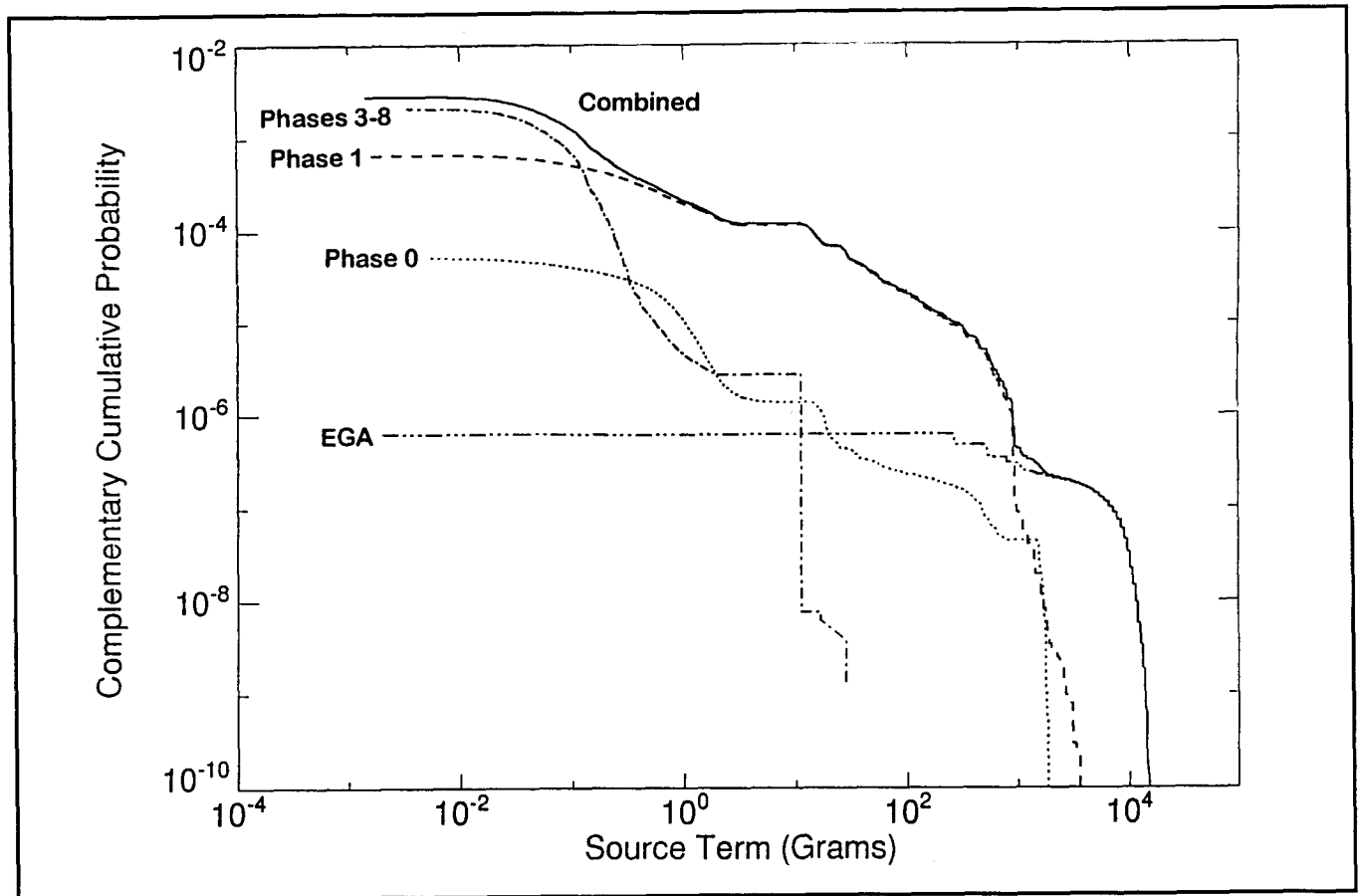
Figure 6.3-1. Source Terms by Mission Segment

Table 6.3-3. Probabilities, Mean 50 Year Consequences and Risk for the Primary Launch Opportunity by Mission Segment

Mission Phase(s)	Mission Segment Description	Probability of Release	Health Effects (without de-minimis)	Health Effects (with de-minimis)	Risk (without de-minimis)	Risk (with de-minimis)	Land Area Exceeding 0.2 μCi/m^2 (km^2)
0	Pre-Launch	5.2×10^{-5}	0.066	0.053	3.4×10^{-6}	2.7×10^{-6}	1.5
1	Early Launch	6.6×10^{-4}	0.071	0.044	4.7×10^{-5}	2.9×10^{-5}	1.6
3 through 8	Late Launch	2.1×10^{-3}	0.044	0.040	9.4×10^{-5}	8.4×10^{-5}	0.057
	EGA	6.3×10^{-7}	140	26	8.6×10^{-5}	1.6×10^{-5}	19
	Total Mission	2.8×10^{-3}	0.081	0.047	2.3×10^{-4}	1.3×10^{-4}	0.44
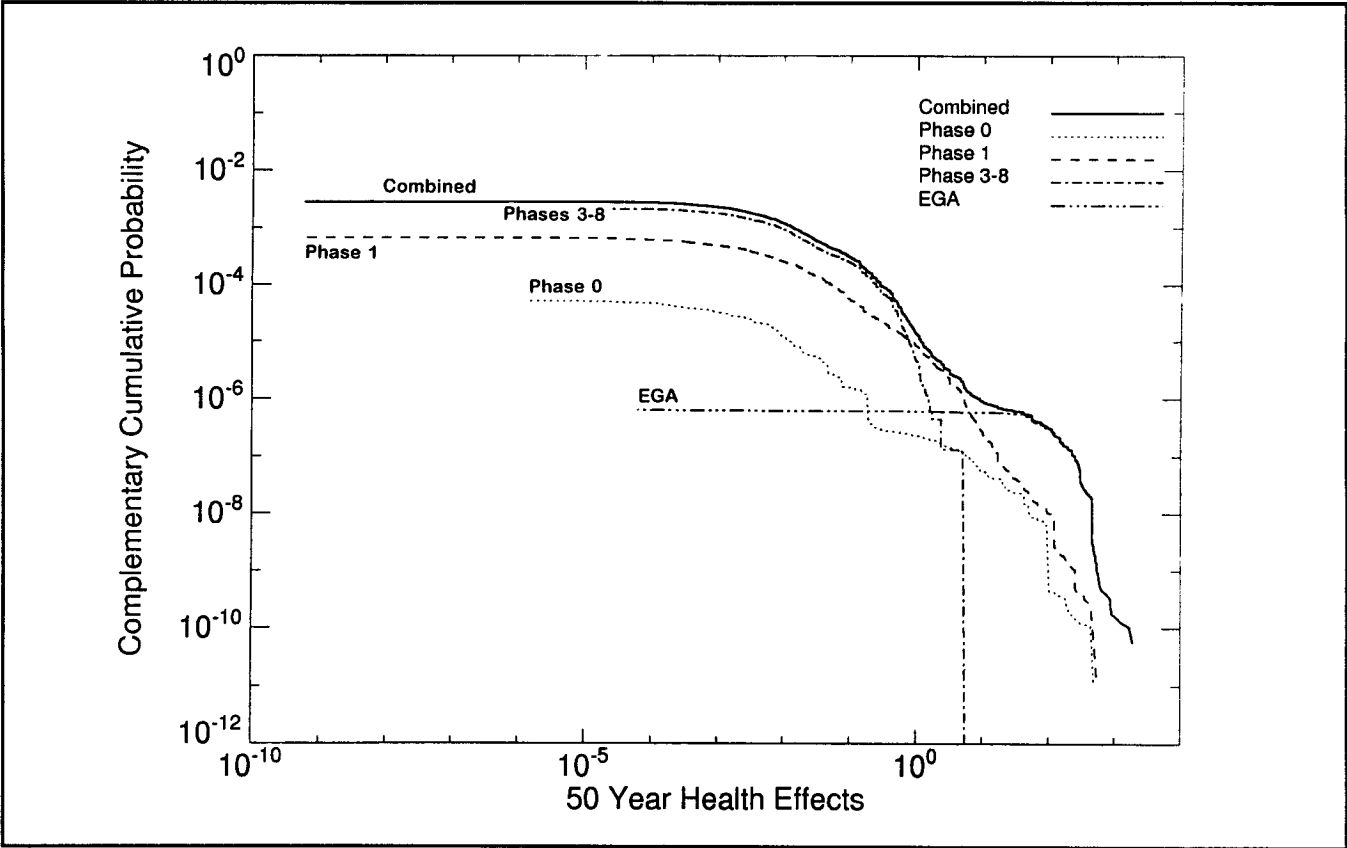
Figure 6.3-2. 50 Year Health Effects without de-minimis (by Mission Segment)

6.4   POSTULATED ACCIDENT SCENARIOS

6.4.1   Launch Accidents

Launch accident scenarios were first developed in 1991 by Martin Marietta Space Launch Systems (Reference 6.4-1) as part of NASA's effort in the preparation of the Cassini EIS. Four specific accident scenarios, along with their initiating probabilities, were identified as representative of failures in the Titan IV SRMU/Centaur launch vehicle that could potentially occur during launch of the Cassini spacecraft: Command Shutdown and Destruct, Titan IV (SRMU) fail-to-ignite, Centaur tank failure/collapse, and inadvertent reentry from Earth orbit. These scenarios were chosen based on the collective expert judgment that the resulting environments could pose potential threats to the RTGs.

In support of the Cassini FSAR, the Titan IV/Centaur RTG Safety Databook was developed by NASA by further expanding and adding to these postulated accidents as the Cassini mission design evolved and significant changes were made to the spacecraft and launch vehicle hardware.

Using a Probabilistic Risk Assessment (PRA) approach, the Databook analysis estimated the known probabilities of the basic component or subassembly failures of the launch vehicle, referred to as Basic Initiating Events (BIEs). One or more of these BIEs will lead to a certain launch vehicle behavior, or vehicle-level accident event, known as Accident Initiating Condition (AIC). One or more of these AICs, in turn, will propagate to an Accident Outcome Condition (AOC), representing the first potential threat environment to the RTGs. The PRA process ends with a Final Environment (FE) which represents the last significant potential threat to the RTGs from the launch vehicle.

A total of 111 AOC-to-FE pathways were identified in Databook Rev. A, each representing a unique sequence of RTG insults and includes a probability distribution function denoting the relative likelihood of occurrence. These event sequences were further grouped into 15 representative accident scenarios (RASs), as shown in Table 6.4-1.

Table 6.4-1. Representative Launch Accident Scenarios

Scenario	Launch Vehicle Configuration *						
	0	1	2	3	4	5	6
1. Common Core Automatic Destruct (ADS)			X	X	X		
2. Thermal Barrier Automatic Destruct (ADS)			X	X	X		
3. Total Boost Vehicle Destruct Activation		X					
4. Command Shutdown and Destruct (CSDS)		X	X	X	X	X	
5. Ground Impact		X					
6. Water Impact		X					
7. Flight Hardware/RTG Impact		X					
8. Hard Surface Impact		X					
9. Centaur Propellant Explosion		X	X				
10. SRMU Forward Segment Explosion		X					
11. SV Propellant Explosion		X	X	X			
12. On-Pad Propellant Explosion	X	X					
13. Sub-Orbital Reentry				X	X	X	
14. Orbital Reentry						X	
15. Environment Resulting from Escape		X	X	X	X	X	X

* Configuration Codes:
0 - Entire Launch Vehicle with no Centaur Propellants
1 - Entire Launch Vehicle, fully fueled
2 - Launch Vehicle minus SRMUs
3 - Launch Vehicle minus SRMUs and PLF
4 - Launch Vehicle minus SRMUs, PLF, and Stage 1
5 - Centaur and Cassini Space Vehicle
6 - Cassini Space Vehicle only

The scenarios in Table 6.4-1 can be classified into those that can potentially result in release of PuO_2 fuel and those which cannot, based on the severity of the associated FEs. Because of the low ambient pressure at altitude, the in-air environments for vehicles in configurations 2 or higher (generally in mission phases 2 or higher) are insufficient to cause release during ascent. Moreover, the remnants from these late accidents will impact on water, which produces insufficient force to cause release. Consequently, only those accidents postulated to occur in Phases 0 or 1 require launch accident simulation.

Of the 111 AOC-to-FE pathways described in the Databook, 26 describe Phase 0 accidents and 28 describe accidents that have at least some probability of occurrence in Phase 1. Recognizing that the analysis of 54 separate accident cases is impractical, the Databook defines a series of binned RASs that describe the environment characteristics and the sequence of RTG insults associated with each RAS.

Each composite accident case combines a unique set of AOC-to-FE paths with identical time distributions, such that the probability of the composite accident case may be regarded as the sum over the probabilities of occurrence of each of the constituent paths. Each composite accident case also leads to application of the environments of a single RAS or, in the flight hardware/RTG impact cases, two closely related scenarios. Consolidation of AOC-to-FE paths yielded one phase 0, thirteen phase 1, and four reentry composite accident cases, as listed in Table 6.4-2 along with their associated mean POFs.

6.4.1.1 *Out-of-Orbit Reentry*

Out-of-orbit accidents encompass situations leading to reentry of the Cassini spacecraft into the Earth's atmosphere prior to insertion into the mission's interplanetary trajectory. These out-of-orbit reentry accidents are grouped as follows:

Sub-orbital: Reentry due to accidents that occur prior to the attainment of the nominal Earth parking orbit, as completed by the Centaur first burn. These accidents can lead to surface impacts in the Atlantic Ocean, southern African continent, and Madagascar.

Nominal orbital: Reentry due to decay from the nominal Earth parking orbit caused by a loss of directed thrust during the Centaur first or second burn. These accidents can lead to surface impacts between the northern and southern latitudes bounded by the park orbit inclination, which may be as high as 38 degrees. The nominal park orbit has a lifetime of approximately 10 days.

Off-Nominal Orbital, Elliptic Decayed: These accidents involve reentry due to decay from elliptical Earth centered orbits, caused by a misdirected Centaur second burn. These accidents can result in surface impacts identically distributed to those resulting from decay from the nominal park orbit. The lifetime of these elliptic orbits may vary from slightly more than 10 days to tens of years based on the baseline trajectory.

Table 6.4-2. Composite Launch Accident Case Descriptions

Mission Segment	Accident Case Number	Case Description	Case Mean Probability of Failure (POF)
Pre-Launch	0.0	On-Pad Explosion, Configuration 1	6.7×10^{-5}
Early Launch	1.1	Total Boost Vehicle Destruct (TBVD)	4.2×10^{-3}
	1.2	Command Shutdown and Destruct (CSDS)	6.6×10^{-4}
	1.3	TBVD with SRMU Aft Segment Impact	8.1×10^{-4}
	1.4	SRMU Explosion	1.2×10^{-4}
	1.5	Space Vehicle (SV) Explosion	7.6×10^{-14}
	1.6	TBVD without Payload Fairing (PLF)	9.1×10^{-6}
	1.7	CSDS without PLF	1.5×10^{-6}
	1.8	SV Explosion without PLF	1.4×10^{-6}
	1.9	Centaur Explosion	1.4×10^{-4}
	1.10	Space Vehicle/RTG Impact within Payload Fairing	2.3×10^{-4}
	1.11	Payload Fairing/RTG Impact	1.9×10^{-6}
	1.12	Payload Fairing/RTG Impact, RTG Falls Free	1.9×10^{-6}
	1.13	Full Stack Intact Impact	1.6×10^{-6}
Late Launch	3.1	Sub-Orbital Reentry	1.4×10^{-3}
	5.1	Sub-Orbital Reentry from CSDS Configuration 5	1.2×10^{-2}
	5.2	Orbital Reentry, Nominal	8.0×10^{-3}
	5.3	Orbital Reentry, Off-Nominal Elliptic Decayed	3.0×10^{-7}

Off-Nominal Orbital, Powered, Elliptic Prompt/Delayed: A misdirected Centaur burn may result in reentry from an off-nominal Earth centered park orbit. In this case, the orbit's perigee lies within the Earth's atmosphere, leading to a prompt or delayed direct reentry. These accidents can lead to surface impacts between northern and southern latitudes of approximately 55 degrees.

The sub-orbital accidents are classified in the Databook as those that occur after 275 seconds MET. The nominal orbital, elliptic orbital, and off-nominal orbital accidents are those that occur after the start of the Centaur first burn, Main Engine Start (MES1).

When the space vehicle (SV) reenters the atmosphere due to a launch vehicle or SV failure aerodynamic heating and loads cause structural failure at relatively high altitudes and the SV rapidly breaks apart. For the orbital decay condition the spacecraft breakup is predicted by NASA-JPL to occur between 330,000 feet at the earliest to 300,000 feet at the latest, consistent with observed spacecraft breakup altitudes. When SV breakup occurs, the 54 GPHS modules from the three RTGs (18 per RTG) are released and become independent bodies directly exposed to the reentry environment.

6.4.2 Earth Gravity Assist (EGA) Reentry

The Cassini mission relies on planetary swingbys to reduce launch energy requirements and achieve the necessary velocities and orbit shaping required to reach Saturn. The baseline trajectory incorporates a Venus-Venus-Earth-Jupiter gravity assist. A reentry occurring during Earth swingby (i.e., entering Earth's atmosphere at an entry angle sufficient for capture (defined as less than or equal to -7 degrees) is considered a short-term Earth impact. Loss of spacecraft control during the interplanetary cruise could potentially result in a long-term Earth impact decades to millennia later as the spacecraft drifts in its orbit around the Sun. Cassini safety analyses considered only the short term reentry scenario in calculating mission risk.

Micrometeoroid-induced rupture of a propellant or pressurant tank is the principal contributor to short-term Earth impact probabilities causing an anomalous velocity change and may cause a loss of spacecraft control. Other failure modes include failure of the main engine valves, the thruster valves, the accelerometer, the main engine gimbal actuator, the stellar reference unit, or the inertial reference unit. A failure that causes loss of spacecraft

control such as a propellant tank failure would prevent recovery of the spacecraft. Most of the failure modes would require subsequent failures or would need to occur very close to the time of the planned Earth swingby to prevent recovery.

The total probability of short-term Earth impact was calculated by NASA-JPL from the constituent probabilities of individual failure modes for the VVEJGA trajectory, taking into account both the probability of failure occurrence and the probability of non-recovery from that failure. As defined in the updated EGA Swingby Plan (Reference 6.4-2), the mean probability of short-term Earth impact for a 800 km Earth swingby VVEJGA trajectory was calculated to be 6.2 x 10^{-7}. Conditional reentry angle and latitude impact probability distributions for the preliminary 500 km and updated 800 km swingby altitudes are illustrated in Figures 6.4-1 and 6.4-2 relative to latitude band population from a 1990 U.N. Survey (Reference 6.4-3).
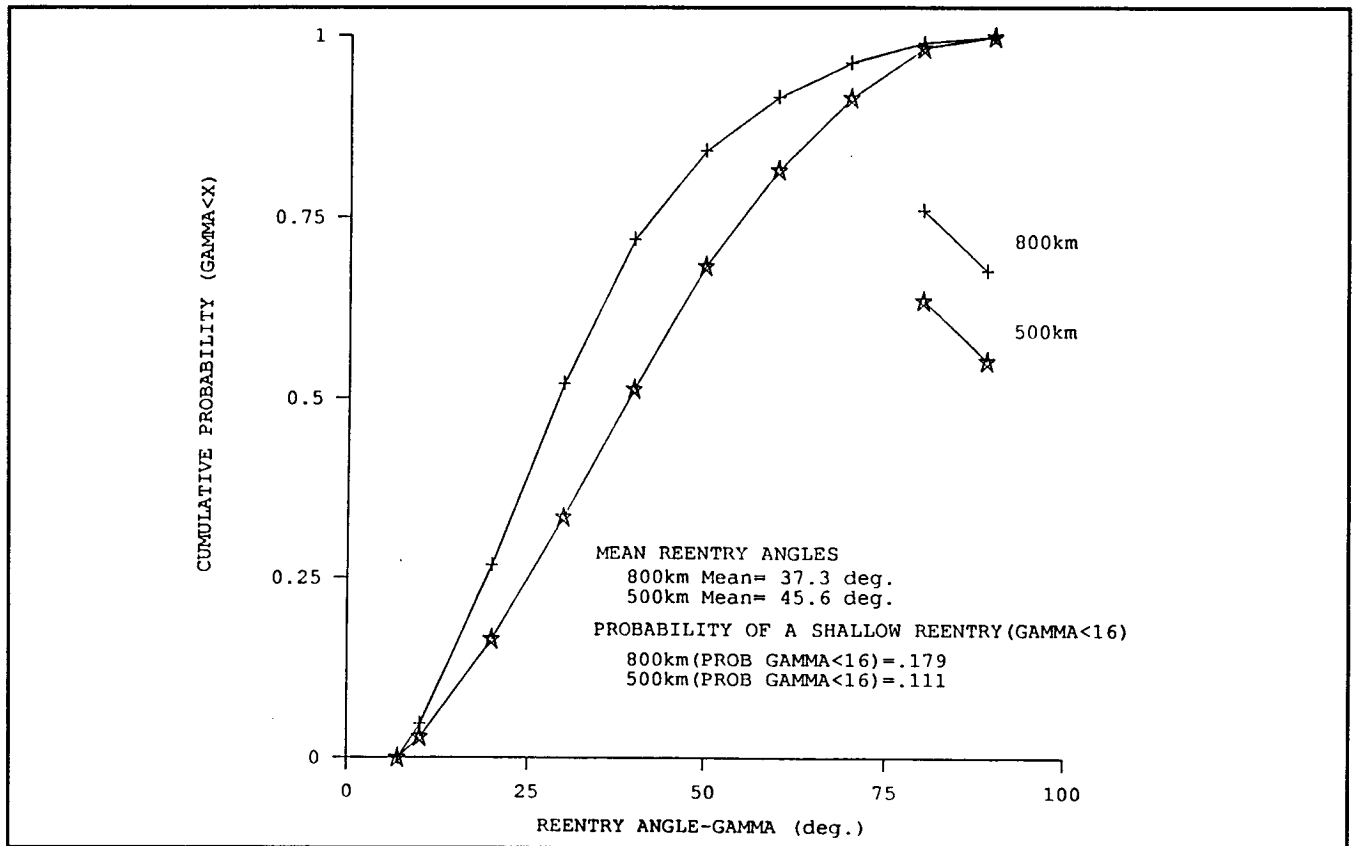
Figure 6.4-1. EGA Short Term Reentry Angle Conditional Probability Distributions for 800 km and 500 km Swingbys
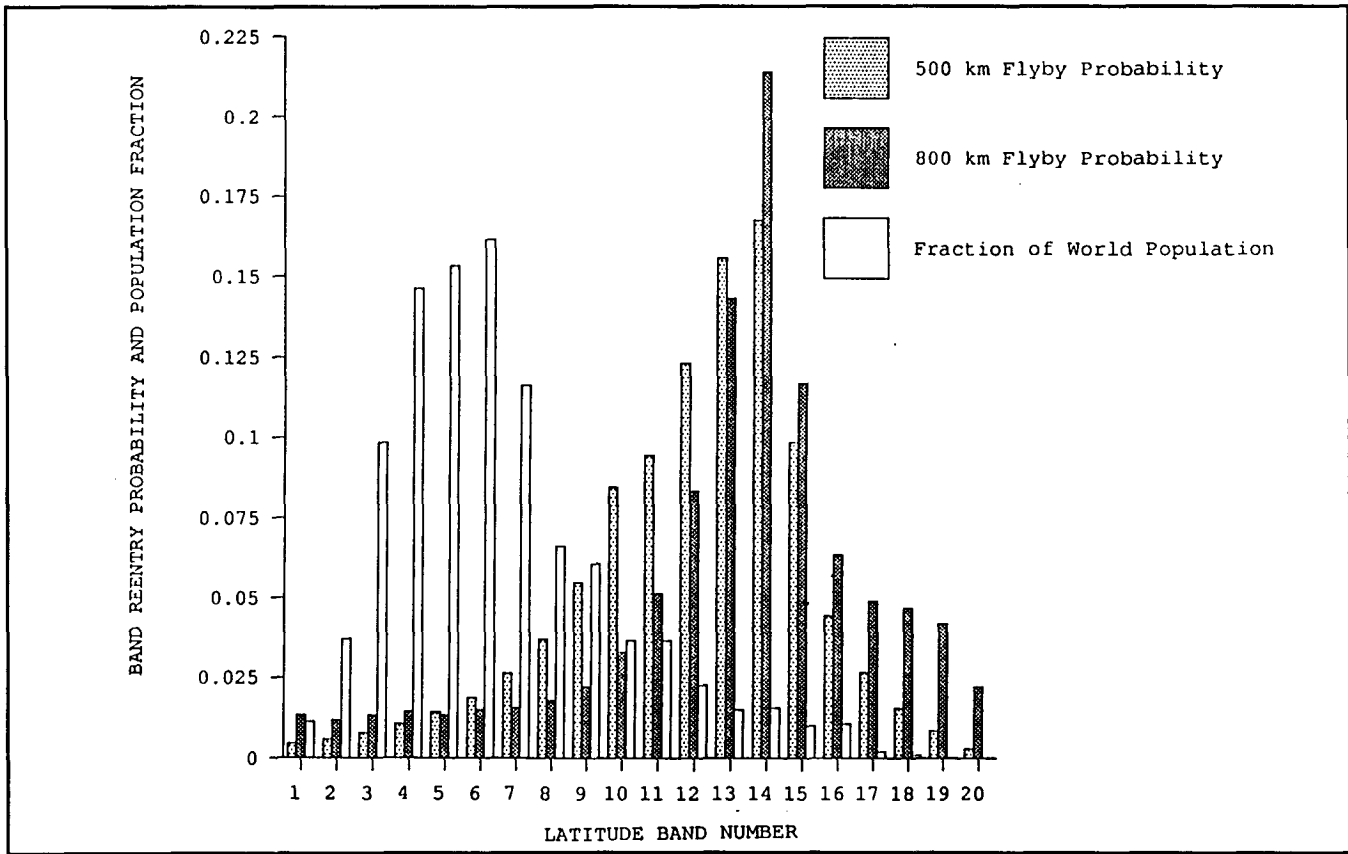
Figure 6.4-2. EGA Short Term Latitude Impact Conditional Probability Distributions for 800 km and 500 km Swingbys

6.5 ACCIDENT MODELING

Cassini mission accident modeling and analyses consist of three separate, parallel activities, each corresponding to one segment of the mission timeline:

1. On-pad and early launch accidents (mission phases 0 to 2)
2. Late launch accidents due to unsuccessful Earth escape (phases 3 to 8)
3. Inadvertent reentry during Earth swingby

This section provides a summary description of the methodology and modeling for each portion of the mission timeline.

6.5.1 On-Pad and Early Launch Accidents

A computer code entitled Launch Accident Scenario Evaluation Program for the Titan IV (LASEP-T) was developed to evaluate the response of the RTGs to threatening environments resulting from accidents during the pre-launch and early launch phases of the Cassini mission.

The LASEP-T code follows the same model structure as that of the LASEP code, created to perform launch safety analyses for the Galileo and Ulysses missions using the Space Shuttle. Though some of the LASEP utility programs were carried over to the LASEP-T code, the majority of the accident models were re-written due to the differences in launch vehicle environments, significant updates to the various RTG response models, and the incorporation of uncertainty analyses.

The development of LASEP-T was initiated in late 1994, with code executed for mission analyses through April 1997. During this period, LASEP-T was revised several times in response to the changes and additions to the postulated accidents and environments defined in the Databook, as well as updates to the RTG response models resulting from hydrocode analyses performed by OSC and the incorporation of RTG safety test results.

6.5.1.1 Model Structure

RTG response to a postulated accident depends not only on the threats from the local environment, such as blast overpressure and fragment impacts, but also on the timing of these relative to the launch sequence. Because the configuration of the launch vehicle and its position relative to the ground change as a function of time of flight, the model must include time as a variable. Moreover, because of the complexity and probabilistic nature of

the dependence of RTG response on dynamical variables and vehicle configuration, the evaluation is performed by a Monte Carlo simulation.

LASEP-T permits evaluation of RTG response in the pre-launch and early launch phases of the mission (Phases 0 and 1) by simulating the effects of the various threatening environments defined in the Databook resulting from launch accidents. The location and state of each RTG or RTG component is simulated from the initial insult, generally at altitude, through the final insult upon Earth impact. The outcome of the simulation consists of determining whether or not a release of PuO_2 fuel occurred, and if so, the salient characteristics of the release, including mass, location, particle size distribution, and particle density.

The model is executed thousands of times to characterize each composite accident case, simulating a large number of accidents occurring at different times, and developing differently. Each execution cycle, simulating one accident occurrence, is called a trial.

To simplify this process, LASEP-T includes an executive program which performs the simulation repeatedly until the desired number of trials has been achieved, recording the outcomes for each trial for subsequent statistical analysis. The iterative function of the executive program is illustrated in Figure 6.5.1-1 as the "MAIN LOOP", encircling the elements of the LASEP-T model which are performed repeatedly to simulate the desired number of trials.

In each simulated trial, an AIC is first selected randomly based on the probability distributions given in the Databook. This condition represents the first point of departure from the nominal mission. At AOC, which may occur instantaneously with AIC or at any time thereafter, the accident has developed to a point at which the first threat to the RTGs can occur. At this point in the time sequence, the models of at-altitude environments must be applied to determine the state of the RTGs and RTG components. The typical sequence for these environments is a blast overpressure, followed by a fragment field, followed by a fireball. After the at-altitude environment models have been applied and the state of the RTGs and RTG components have been determined, the next element of the sequence is
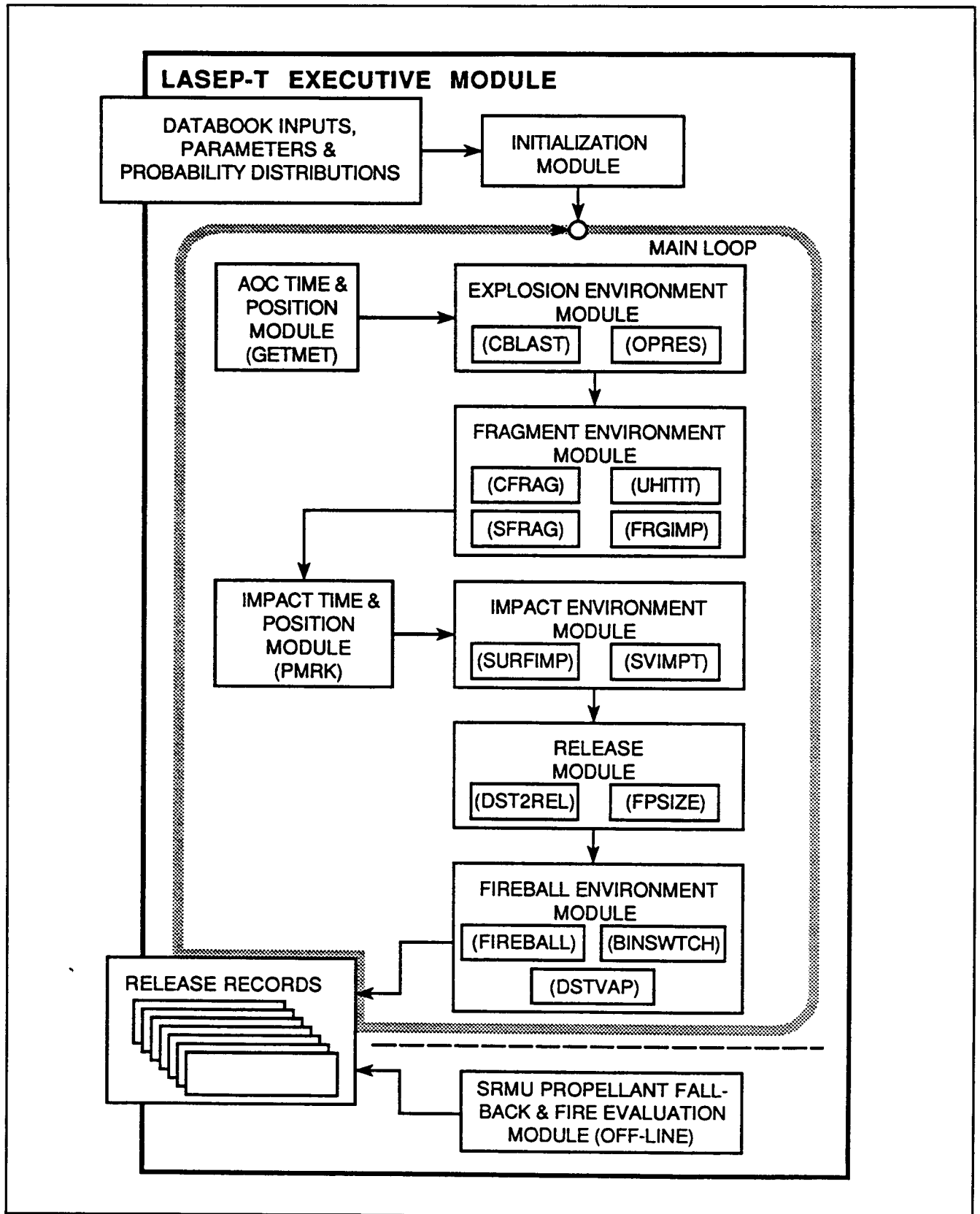
Figure 6.5.1-1. Structure of LASEP-T Model

their flight to the ground, either attached to the space vehicle, or separated and falling independently. The ground impact environments are then applied which include the mechanical effects of impact on steel, concrete, soil, or water, possibly in combination with overpressure, fragments, and fireball effects. Finally, some accidents will require application of an environment model to determine the effects of solid propellant impact and fires, when fragments of the SRMU propellant land in proximity to RTGs and RTG components. With the exception of phase 0 and Full Stack Intact Impact (FSII) accidents, these effects are not considered as part of the general simulation within LASEP-T, because the probability of proximity is sufficiently small that this event would occur rarely, even in a large number of trials. Rather, proximity probabilities are determined by analysis and the outcomes are then evaluated by a separate, stratified Monte Carlo simulation, as delineated in Section 6.5.1.3.

For phase 0 on-pad explosion and FSII accidents, tailored versions of LASEP-T code were developed to include the SRMU propellant impact and fire effect which has significantly higher probability of occurrence than in an at-altitude accident. These accident models are described in Sections 6.5.1.4 and 6.5.1.5, respectively.

6.5.1.2 Model Description

This section provides a brief description for each of the key model subroutines that are used in LASEP-T to simulate various insult environments and corresponding RTG and RTG component responses in a launch accident.

Mission Elapsed Time (GETMET) - This subroutine is used to define a Mission Elapsed Time (MET) and the launch vehicle state vector for when the accident is postulated to occur.

Centaur Blast Model (CBLAST) - This subroutine simulates the blast overpressure from a Centaur tank failure/destruct, resulting in an LO_2/LH_2 explosion.

The Centaur blast overpressure estimate was updated in the Revision B of the Databook as a result of the joint NASA/NASDA HOVI (Reference 6.5.1-2). The test data indicate a mean ignition delay time that is much shorter than the 80 milliseconds previously assumed in the Databook. This resulted in lower predicted overpressures at RTG locations from a mean of 120 psi static to about 30 psi.

Overpressure Damage Assessment Model (OPRES) - This subroutine determines the effect of a Centaur propellant explosion. Threshold values for removal of RTG components (i.e., RTG shell, GPHS aeroshell, fuel cladding) are compared to the overpressure. If the overpressure exceeds any of these, then the components are assumed to be stripped away, releasing the internal constituents. The maximum overpressure environment specified in the Databook is marginally greater than the iridium clad plastic deformation threshold, and well below the threshold to breach a fueled clad.

Fragment Environment (CFRAG and SFRAG) - A blast overpressure environment can accelerate blast fragments which may threaten the RTGs. The fragment speed is determined by the overpressure impulse, as well as the mass projected cross-sectional area, and drag coefficient of the fragments. This model yields a postulated field of fragments with the initial positions and velocities of each fragment from the Centaur and from the SRMUs.

Fragment Damage Assessment (UHITIT and FRGIMP) - This subroutine determines which, if any, of the fragments hit the RTGs or RTG components. The damage sustained in fragment collision is determined by comparing the kinetic energy of the fragment and the RTG relative to their center-of-mass to a set of threshold values. The center-of-mass, kinetic energy, E, is given by

$$E = \frac{\mu V^2}{2} = \frac{m_1 m_2}{m_1 + m_2} \bullet \frac{|v_1 - v_2|^2}{2}$$

[6-1]

where μ is the reduced mass, $m_1 m_2 / (m_1 + m_2)$, and V is the relative velocity, $v_1 - v_2$, for a fragment of mass, m_1, and an RTG component of mass, m_2, respectively. The threshold values are 54.8 kJ for an intact RTG, and 12.6 kJ for the individual modules.

Any modules suffering fragment impact are evaluated individually for damage. Whether the aeroshell ruptures or not, distortion is calculated for the fueled clads within the module based on the center-of-mass kinetic energy of the impacting entities, the state of the RTG or module when the impact occurred, and the impact configuration. If any RTGs remain attached to the space vehicle they are presumed to fall to the Earth's surface with the space

vehicle intact. Released modules and fueled clads are assumed to fall to the Earth's surface independently.

Post-Accident Trajectory Model (PMRK) - This subroutine tracks each RTG and/or RTG components to eventual impact on the Earth's surface after sustaining at-altitude insults.

The impact location or intercepting structure, is compared with the KSC/CCAS site map and a table of structure data, to determine the impact surface: water, sand (soil), steel, or concrete. The record for each independent RTG or RTG component is updated with impact location, impact velocity, time of impact, and impact surface.

Surface Impact Assessment (SURFIMP) - Impacting the Earth's surface, or an intervening structure at a substantial velocity will result in distortion to the fueled clads, and possibly in the release of PuO_2. The model for this response is based on the results of BCI and SVT tests. In addition to experimental data, extensive hydrocode analyses have been performed to supplement the test data.

If released modules or fueled clads impact water, then no distortion is presumed to result. If the impact surface is sand, then a nominal distortion of 5% (based on BCI data for sand impact) is presumed to result. If the impact surface is concrete or steel, then the distortion is calculated from the correlations of BCI and SVT test data.

The standard deviations for maximum-likelihood fits to BCI and SVT data are used to estimate the variation in fueled clad responses to surface impact.

SV Intact Impact Damage Assessment (SVIMPT) - In the event that the RTG remains attached to the SV, impact with the Earth's surface will include the additional threats of a hypergol blast and a field of SV fragments accelerated by the blast. Extensive hydrocode analyses have been used to assess the response of the RTG to this environment (Reference 6.5.1-2). This subroutine simulates all defined environments and predicts RTG response during an SV impact.

Two possible scenarios of sequential insults to the RTGs have been postulated, depending on the SV impact orientation.

(A) 1. Ground surface impact
2. Propellant pressurant tanks overpressure and fragment impact
3. Hypergol blast overpressure
4. SV fragment impact

(B) 1. Propellant pressurant tanks overpressure and fragment impact
2. Hypergol blast overpressure
3. SV fragment impact
4. Secondary ground surface impact

In the first sequence (LVA-leading orientation), the RTG impacts the ground first, then the propellant pressurant tanks rupture producing an overpressure and fragment environment. This is followed by the hypergol blast overpressure and impact of SV fragments. In the second sequence (high gain antenna-leading orientation), where the RTG is still above ground when the hypergol explosion occurs, the propellant pressurant tanks rupture first, with attending overpressure and fragments. Next the hypergol blast occurs producing an overpressure and accelerating SV fragments toward the RTG. Finally the RTG, or RTG components, experience a secondary ground impact.

Calculation of Fuel Release (DST2REL and FPSIZE) - After assessing how much distortion of the fueled clads will be induced by each of the environments, the next step in the accident simulation is to determine how much, if any, PuO_2 fuel is released, the size distribution, and the release location. This is accomplished by two subordinate modules, one which evaluates distortion to determine the amount of fuel released (DST2REL), and one which distributes the release into particle size bins (FPSIZE).

The DST2REL model evaluates release due to distortion, based on the results of the BCI, SVT, and FGT tests. It is assumed that in any one insult, the probability of developing a breach in the fueled clad depends only on the severity of the insult, and not on the severity of any prior insults.

From the safety test data cited above, two release types are evident: small releases, in which cracks appear and some small particles of PuO_2 escape the iridium cladding, and large releases in which a larger amount of the PuO_2 pushes through the clad. There is no apparent correlation between fractional release and distortion within the two release types

based on analysis of the available test data. The DST2REL model includes variations in the amount of fuel released for both small and large releases.

Once a clad is breached, a release is calculated for every insult even if the current insult is inadequate to produce a breach. The model FPSIZE, employed to determine the particle size distribution is based on the database of measured particle size distributions, from samples obtained in safety tests as described in Reference 6.5.1-3.

The model for particle size distribution assumes that the maximum particle size for a given release is determined by the maximum crack width, and that for any given insult, the particles released will be limited to those less than the maximum size accommodated by the maximum crack width.

The mass released is then distributed into "bins" to provide a piecewise distribution. In order to preserve resolution over a large range of sizes, a logarithmic sequence has been selected for the particle size bins, as shown in Table 6.5.1-1.

Table 6.5.1-1. LASEP-T Particle Size Bins

Bin	Minimum Diameter (μm)	Geometric Mean Diameter (μm)	Maximum Diameter (μm)
1	<0.1	----	0.1
2	0.1	0.15	0.215
3	0.215	0.32	0.464
4	0.464	0.68	1.0
5	1.0	1.47	2.15
6	2.15	3.16	4.64
7	4.64	6.81	10.0
8	10.0	14.7	21.5
9	21.5	31.6	46.4
10	46.4	68.1	100.0
11	100.0	146.6	215.0
12	215.0	----	>215.0

Liquid Propellant Fireball (FIREBALL/BINSWTCH and DSTVAP) - The FIREBALL model assesses the effect of a liquid propellant fire on released PuO_2. The fireball environment is applied if the release location lies within the diameter of the fireball. Equations describing fireball parameters (such as diameter and combustion duration) as

functions of propellant mass are described in the Databook, and implemented within the FIREBALL model.

FIREBALL calculates PuO_2 vaporization within a propellant fire. The net effect of vaporization is to reduce the diameter of the particles as the outer surface evaporates. This has the effect of shifting particles from higher size bins to lower size bins, with an adjustment to the mass in each bin to account for material converted to the vapor phase.

Homogeneous agglomeration is simulated by the DSTVAP model, including PuO_2 condensation into a sub-micron size aerosol, solidifying as the fireball temperature declines, and agglomerating into larger particles.

6.5.1.3 SRMU Propellant Fallback Code

The average conditional probability of an SRMU propellant impacting a RTG entity resulting from an at-altitude accident was initially estimated as approximately 10^{-3}. To get a statistically significant contribution from this accident scenario in the simulation, SRMU effects were analyzed outside of the LASEP-T Monte Carlo code, using LASEP-T trial-by-trial data for vehicle conditions and accident timing as input. The analysis consists of three separate steps: (1) FALLBACK to calculate the probability of direct or near-miss impacts by SRMU fragments onto RTG entities; (2) SRESP (SRMU Propellant Fallback Response Model) to determine the RTG response from the mechanical impact and subsequent solid propellant fires; and (3) a series of utility programs that combine these probabilities and source terms with those from the non-SRMU environments to provide an integrated input to the risk and consequence analysis.

Calculation of the conditional probability for the SRMU coincident impact is partitioned into two components. The first is the probability of coincident impact, and the second is the probability that such impact will apply to more than one module. This latter consideration stems from the fact that the impact of a large segment upon the debris field of an early phase 1 accident will potentially involve multiple modules, particularly if impact occurs in the vicinity of an intact space vehicle impact.

From the first 500 LASEP-T trials of a composite accident case which resulted in RTG components impacting land, FALLBACK calculates trajectories of freed modules or SV-attached modules from Space Vehicle Intact Impact (SVII) and that of the SRMU fragments.

For each trial, the expectation value of the probability of coincident impact was calculated using the module and space vehicle positions and velocities at AOC as initial conditions. The expectation values were determined as functions of 16 binned SRMU fragment sizes, 12 binned fragment impact velocities, explosion strengths, impact surfaces (sand or concrete), and RTG entities (freed modules or SV-attached modules).

These expectation values for single module or SV are then adjusted to account for the actual spatial distribution of modules about the SV debris centroid, and for the possibility that a single SRMU fragment impacts multiple isolated modules. Both of these can be accounted for by analysis of the actual module distribution associated with the specific trial results from LASEP-T. For intact SV impact, an offset vector is added to each module to account for random displacements during the impact and subsequent hypergol blast.

Estimates of fuel releases due to SRMU impact and subsequent exposure to SRMU fire were calculated from the modified versions of LASEP-T's DST2REL, FIREBALL, SBINSWITCH and SDSTVAP subroutines. Modifications were required to extend the fuel release model to the large distortions which can result from coincident impact. The fueled clad distortion model was constructed using the hydrocode calculations performed by Orbital Sciences Corporation for varying SRMU fragment sizes and velocities and impact surfaces (Reference 6.5.1-4).

The response of the RTG components to the SRMU propellant fire was based on a safety test in which a bare fueled clad with urania simulant survived a 10.5 minute fire from burning UT-3001 solid propellant. These results were confirmed for the current propellant material using a computer-aided thermal analysis employing the SINDA computer code. The response of any released radioisotope fuel in the presence of an SRMU propellant fire was determined by analysis of the vaporization and agglomeration effects for the fire description given in the Databook, and is similar to the liquid propellant FIREBALL subroutine described above.

6.5.1.4 Full Stack Intact Impact (FSII) Code

A modified version of the LASEP-T Monte Carlo code was generated to simulate the FSII accident. In contrast to LASEP-T simulation of other phase 1 launch accidents where the initiating launch vehicle conditions are determined randomly from probability distribution functions provided in the Databook, the launch vehicle conditions in an FSII are

intercorrelated and thus can not be randomly selected from distribution functions. As a result, detailed vehicle conditions from 4045 Lockheed Martin Astronautics simulations used to define the Databook environments are used to define the initial states of the launch vehicle as input to the modified LASEP-T/FSII code. Also unique to FSII code is the inclusion of SRMU fragment impact and fire models, as the probability of coincident impact is significantly higher than other phase 1 accidents. The parameters that characterize each FSII trial include:

- Mission elapsed time when the vehicle c.g. (center of gravity) impacts the ground
- Velocity of vehicle c.g. at impact
- The total accumulated vehicle rotation from the initial launch position
- The angular rate of the roll axis in the pitch plane at impact
- Surface location of vehicle c.g. impact point

Given the vehicle's Earth surface impact angle, the impact can be identified as either tail-first or nose-first. For nose-first FSII, the SV/RTG assembly impacts the ground intact, producing insult environments for RTGs similar to that for the SVII scenario in other launch accident cases (i.e., surface impact, hypergol blast and SV fragments). In addition to the SVII environments, fragments resulting from the breakup of Titan IV stages 1 and 2 and the Centaur could potentially impact the RTGs in a nose-first FSII accident.

For tail-first impacts, an ADS triggered destruct of the entire vehicle would be activated within milliseconds of initial vehicle contact with the Earth's surface. The blast overpressure from the Centaur auto destruct could damage the RTG housing, resulting in the free fall of GPHS modules to the ground, or separate the SV/RTG assembly from the Centaur, leading to an SVII.

In all accidents, a ADS triggered SRMU destruct will lead to SRMU fragmentation and the possibility of SRMU coincident impact with modules on the ground. The effects of both liquid and solid propellant fires on any released fuel are determined, with the assumption that fuel released into a liquid propellant fire is lofted by the fireball and is not subject to the solid propellant fire environment. Figure 6.5.1-2 summarizes the two possible sequences of insult environments that the RTGs will experience in an FSII accident. The models utilized to simulate each of the accident environments provided in Figure 6.5.1-2 are the same as those used for LASEP-T and SRMU propellant fallback codes described above.

Nose-First Impact	Tail-First Impact

– SVII Environments
  • Ground surface impact
  • SV/tank fragments
  • Hypergol blast
– Centaur Blast
– LV Fragment Impact
– SRMU Fragment Impact
– Liquid Propellant Fire
– SRMU Fire
	– Centaur Blast
	– Module Ground Surface Impact or SVII Environments
	– SRMU Fragment Impact
	– Liquid Propellant Fire
	– SRMU Fire

Figure 6.5.1-2. FSII Environment Paths for RTGs

6.5.1.5 Phase 0 On-Pad Propellant Explosion Code

After the start of LH_2 filling, an on-pad propellant explosion can be caused by a Centaur LOX/LH_2 cryogen explosion or by inadvertent activation of the core or SRMU flight termination system destruct charges after the Titan IV destruct system is armed at T-17 seconds. For a Centaur explosion prior to ADS arming, the core vehicle can remain intact. When this occurs, both the core vehicle and the SRMUs remain upright and the SV is propelled upward and eventually impacts the launch pad intact. In the event that the core vehicle explodes after the Centaur failure, the SRMUs will separate and fall outboard, away from the vehicle, and potentially impact the SV on the ground.

A separate LASEP-T-based Monte Carlo code was created to simulate the various event sequences of this accident. In all cases the space vehicle is assumed to impact concrete while intact (i.e., Centaur/core vehicle blast overpressure never result in RTG components being separated from the SV). This assumption is based on independent LASEP-T simulations which indicated intact SV impacts with three RTGs attached occur in ~80% of all Centaur blast-initiated trials. SRMU segments which strike the SV are assumed to impact all 54 modules as SRMU dimensions are greater than anticipated module dispersion distances. Releases caused by SRMU impact upon the SV are shielded from, and therefore unaffected by liquid propellant fireballs. Conversely, releases due to insults other than SRMU impact are assumed to be lofted by the appropriate liquid propellant fireball and are unaffected by solid propellant fire.

6.5.1.6 Summary of Source Term Results

Source terms from phase 1 accidents are tabulated for those cases selected for full accident analysis, including SRMU effects (Table 6.5.1-2). Collectively these cases capture over 85% of the phase 1 expected risk. No source terms are predicted for phase 2 of the early launch mission segment.

Table 6.5.1-2. Source Terms for Pre-Launch and Early Launch Accident Cases

Case #	Accident Case	Mean POF	Probability of Release	* Mean Release (grams)	Release Percentiles *, **			
					5th (grams)	50th (grams)	95th (grams)	99th (grams)
0.0	On-Pad Explosion, Configuration 1	6.7×10^{-5}	5.2×10^{-5}	3.8	0.026	0.43	2.1	23
1.1	Total Boost Vehicle Destruct	4.2×10^{-3}	4.5×10^{-4}	15	0.027	0.38	56	3.6×10^2
1.3	Total Boost Vehicle Destruct with SRMU Aft Segment Impact	8.1×10^{-4}	1.2×10^{-4}	17	0.032	0.52	56	4.6×10^2
1.10	SV/RTG Impact within Payload Fairing	2.3×10^{-4}	2.1×10^{-5}	5.8	0.045	0.44	15	1.0×10^2
1.13	Full Stack Intact Impact	1.6×10^{-6}	9.3×10^{-7}	13	0.032	0.49	32	3.2×10^2

* For trials which produced fuel releases (grams of PuO_2)

** 5th Percentile: 5% of trials produced mass release smaller than this value
50th Percentile: 50% of trials produced mass release smaller than this value
95th Percentile: 95% of trials produced mass release smaller than this value
99th Percentile: 99% of trials produced mass release smaller than this value

A summary of source terms and the probabilities for accident cases in mission phases 0 and 1 are provided in Section 6.3.2. Typical particle size distributions for the fuel releases representative of the pre- and early launch phases are shown in Tables 6.5.1-3 and 6.5.1-4 for case 1.1 (TBVD) and case 1.13 (FSII), respectively. The fuel release types are defined as:

- Type 1: a ground release outside of a fire
- Type 2: a ground release in a core fireball
- Type 3: a release in an SV hypergol fireball
- Type 4: a ground release in a core and SV fireball
- Type 13: a ground release due to SRMU impact, accompanied by SRMU propellant fire

Table 6.5.1-3. Case 1.1 Representative Particle Size Distributions (in gms of PuO$_2$)

Bin #	Min Dia (μm)	Max Dia (μm)	Type 1 Release No Fire		Type 2 Release Core Fireball		Type 3 Release SV Fireball		Type 4 Release Core + SV Fireball	
			50th Percentile	99th Percentile	50th Percentile	99th Percentile	50th Percentile	99th Percentile	50th Percentile	99th Percentile
1	<0.1	0.1	1.1×10^{-4}	5.7×10^{-3}	1.9×10^{-4}	9.6×10^{-4}	3.1×10^{-5}	1.0×10^{-2}	3.5×10^{-4}	3.1×10^{-2}
2	0.1	0.215	1.2×10^{-4}	6.4×10^{-3}	8.5×10^{-4}	4.3×10^{-3}	7.0×10^{-4}	0.23	1.5×10^{-3}	0.14
3	0.215	0.464	2.5×10^{-4}	1.4×10^{-2}	1.4×10^{-5}	7.3×10^{-5}	2.7×10^{-4}	7.6×10^{-2}	1.2×10^{-5}	1.2×10^{-3}
4	0.464	1.0	5.4×10^{-4}	2.9×10^{-2}	1.2×10^{-4}	6.5×10^{-4}	3.5×10^{-4}	4.4×10^{-2}	9.3×10^{-5}	9.7×10^{-3}
5	1.0	2.15	1.1×10^{-3}	6.0×10^{-2}	5.7×10^{-4}	3.0×10^{-3}	1.1×10^{-3}	0.19	6.2×10^{-4}	6.1×10^{-2}
6	2.15	4.64	2.4×10^{-3}	0.13	1.6×10^{-3}	8.1×10^{-3}	2.5×10^{-3}	0.51	2.0×10^{-3}	0.19
7	4.64	10.0	5.1×10^{-3}	0.27	3.5×10^{-3}	1.8×10^{-2}	5.4×10^{-3}	1.1	4.7×10^{-3}	0.44
8	10.0	21.5	1.1×10^{-2}	0.57	7.5×10^{-3}	3.9×10^{-2}	1.1×10^{-2}	2.4	1.0×10^{-2}	0.94
9	21.5	46.4	2.3×10^{-2}	1.2	1.6×10^{-2}	8.2×10^{-2}	2.4×10^{-2}	5.1	2.2×10^{-2}	2.0
10	46.4	100.0	4.7×10^{-2}	2.5	3.0×10^{-2}	0.17	5.0×10^{-2}	11	3.5×10^{-2}	4.2
11	100.0	215.0	9.0×10^{-2}	5.0	3.2×10^{-2}	0.33	0.10	22	4.7×10^{-2}	8.2
12	215.0	>215.0	5.9×10^{-2}	85	8.0×10^{-2}	0.56	0.88	4.5×10^{2}	3.1×10^{-2}	98
Total			0.24	95	0.17	1.2	1.1	490	0.15	110

Table 6.5.1-4. Case 1.13 (FSII) Representative Particle Size Distributions (in gms of PuO_2)

Bin #	Min Dia (μm)	Max Dia (μm)	Type 3 Release SV Fireball		Type 4 Release Core + SV Fireball		Type 13 Release SRMU Impact + Fire	
			50th Percentile	99th Percentile	50th Percentile	99th Percentile	50th Percentile	99th Percentile
1	<0.1	0.1	2.0×10^{-4}	2.4×10^{-3}	4.2×10^{-4}	9.7×10^{-3}	3.7×10^{-5}	4.0×10^{-3}
2	0.1	0.215	4.5×10^{-3}	5.4×10^{-2}	1.9×10^{-3}	4.3×10^{-2}	3.4×10^{-3}	0.37
3	0.215	0.464	1.5×10^{-3}	1.8×10^{-2}	2.0×10^{-5}	1.4×10^{-3}	0.18	19.17
4	0.464	1.0	4.6×10^{-4}	1.2×10^{-2}	1.7×10^{-4}	1.1×10^{-2}	0.38	40.90
5	1.0	2.15	2.6×10^{-3}	5.0×10^{-2}	9.5×10^{-4}	4.1×10^{-2}	6.4×10^{-5}	6.9×10^{-3}
6	2.15	4.64	7.7×10^{-3}	0.13	2.8×10^{-3}	0.10	3.4×10^{-6}	4.1×10^{-4}
7	4.64	10.0	1.8×10^{-2}	0.29	6.5×10^{-3}	0.23	2.5×10^{-4}	2.3×10^{-2}
8	10.0	21.5	3.8×10^{-2}	0.61	1.4×10^{-2}	0.48	4.6×10^{-3}	0.34
9	21.5	46.4	8.0×10^{-2}	1.29	3.0×10^{-2}	1.02	4.6×10^{-2}	4.17
10	46.4	100.0	0.17	2.68	6.2×10^{-2}	2.12	0.21	23.58
11	100.0	215.0	0.26	5.29	0.12	4.16	0.46	71.35
12	215.0	>215.0	0.27	73.40	0.13	56.00	0.50	1.2×10^3

The majority of fuel releases are types 3, 4 and 13 where liquid and solid propellant fires are present. The fire affects mostly the smaller particle size bins when compared to the type 1 releases. For liquid fireballs, vaporization and recondensation effects occur primarily in the first two bins, whereas for solid propellant fires, which have a much longer duration and are accompanied by a high concentration of Al_2O_3, the particle vapor recondenses over a wider range of size bins. Type 13 release is not shown for case 1.1 in Table 6.5.1-3, however, the distribution is very similar to that for case 1.13.

6.5.2 Late Launch Accidents

This section addresses the techniques applied and results obtained in assessing the potential for fuel release in the event of an accidental out-of-orbit reentry of the Cassini spacecraft into the Earth's atmosphere. For reentry accidents, the determination of source terms involve both the evaluation of fuel containment during reentry (to assess the potential for an in-air release) and also the evaluation of impact on the Earth's surface.

Out-of-orbit accidents encompass situations leading to reentry of the Cassini spacecraft into the Earth's atmosphere prior to insertion into the mission's interplanetary trajectory. These out-of-orbit reentry accidents are grouped as sub-orbital, nominal orbital, off-nominal (elliptic decayed), and off-nominal (elliptic prompt/delayed) and are described in detail in Section 6.4.1.

When the space vehicle (SV) reenters the atmosphere due to a launch vehicle or SV failure, aerodynamic heating and loads cause structural failure at relatively high altitudes and the SV rapidly breaks apart. When this occurs, the 54 GPHS modules from the three RTGs (18 per RTG) are released and become independent bodies directly exposed to the reentry environment.

Once the GPHS modules become independent reentry bodies their trajectory and associated aerothermal environment is predicted utilizing a three degree-of-freedom trajectory prediction tool (3DMP). This tool models the three translational equations of motion as influenced by the Earth's gravity, aerodynamic drag, and atmosphere. The simulation, as modeled here, utilizes a 1984 WGS Earth model with 8th order gravity harmonic, and a 1976 U.S. Standard atmosphere.

The graphitic FWPF aeroshell of the GPHS module is designed to survive the reentry environment by transporting the heat away from the aeroshell surface through ablation. Predictions of the mass rate of ablation for out-of-orbit reentries are performed using a finite difference thermal conduction code described later. Stagnation point recession has been calculated over the entire potential reentry accident envelope.

Analyses indicate that the GPHS modules will survive the reentry environment for all out-of-orbit accident cases, even under worst case conditions. The maximum aeroshell recession for non-multiskip trajectories is 0.068 inches, which is 37% of the aeroshell minimum thickness. If the module reenters under conditions that lead to multiple skips (reentries) the recession may increase to as much as 0.130 inches.

Because the individual modules survive out-of-orbit reentry, they will impact the Earth's surface intact. A statistical assessment of module response to surface impacts has been performed by Monte Carlo simulation. This simulation determines the impact position probability distribution on the Earth's surface, the surface characteristics (surface type and altitude), and the statistical response of the module to that impact. The impact position distribution is influenced by launch trajectory characteristics such as launch time and date, and velocity/position state condition, and reentry characteristics such as atmospheric variability and module drag condition. The surface demographics are based on a 720 equal-area worldwide grid data base developed by Halliburton NUS (Reference 6.5.2-1). The impact response, in terms of fuel release and particle size distribution is determined using launch accident evaluation models based on empirical safety test results as described in Sections 6.2 and 6.5.1.

6.5.2.1   Reentry Envelope

The envelope of all potential spacecraft reentry conditions, as defined by velocity (V) and flight path angle (γ) at 400,000 ft is illustrated in Figure 6.5.2-1. This is referred to as the V - γ envelope.
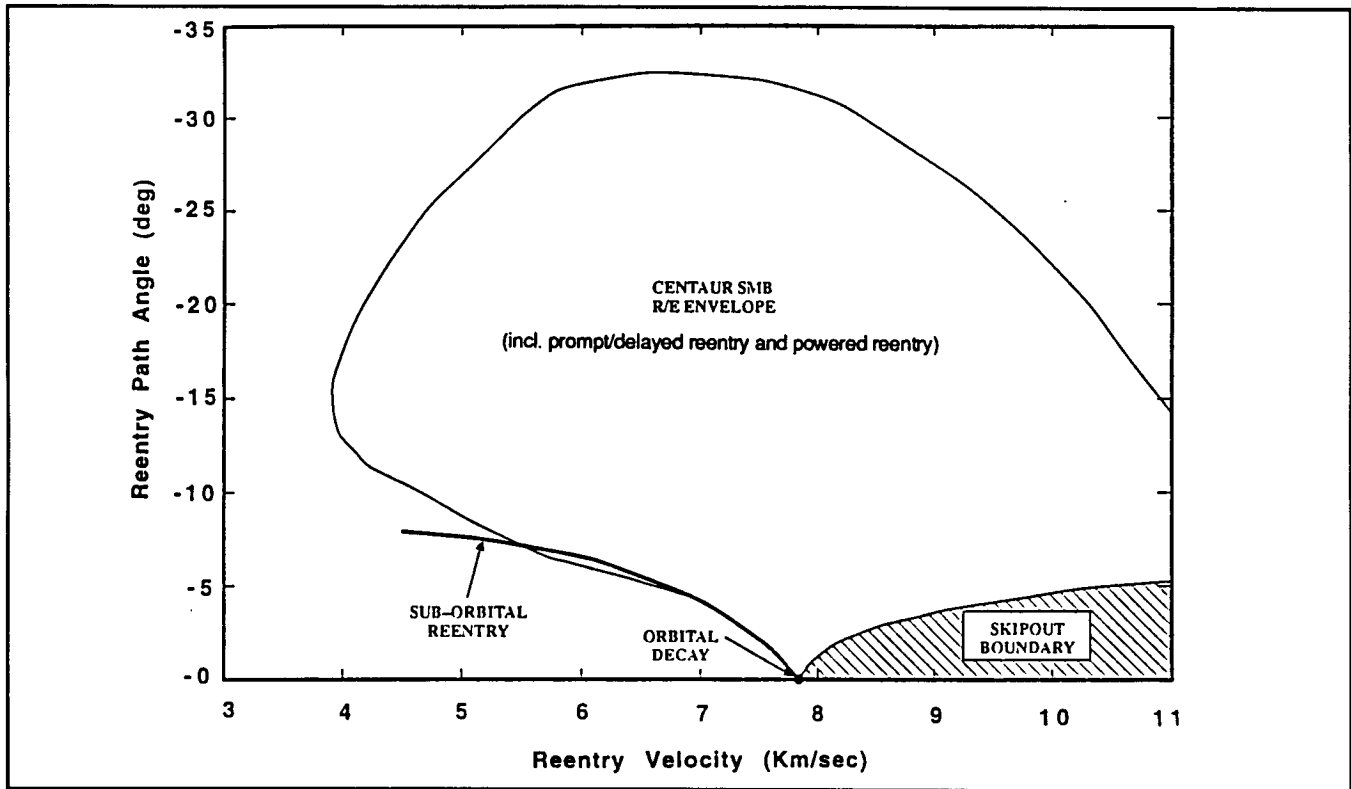
Figure 6.5.2-1. Reentry Envelope

The sub-orbital conditions are represented by the solid curve from approximately V = 4.5 km/s and γ = -8 degrees (corresponding to the earliest potential failure in the Titan IV stage 2 that would lead to reentry conditions) to approximately V = 7.9 km/s and γ = 0 degrees (corresponding to an accident just prior to the termination of the Centaur first burn park orbit injection).

The orbital decay reentry condition at 7.9 km/s, nearly zero flight path angle corresponds to reentry from the Earth park orbit (known above as nominal orbital reentry). This same condition is replicated for decays from elliptical orbits.

The skip-out boundary separates those reentry conditions where the SV or module, upon entering the atmosphere, continues to Earth impact (above the boundary) or penetrates to a given altitude, loses insufficient energy for capture, and exits the atmosphere temporarily (below the boundary). These skip-out conditions, up to super-orbital velocities, arise due to a highly unlikely steady misdirected burn (SMB) of the Centaur upper stage. Together the sub-orbital and skip-out conditions bound the lower edge (shallowest flight path angles) of the V - γ envelope.

The upper boundary of the V - γ envelope also arises due to a SMB of the Centaur resulting in reentry. In these cases the Centaur places the spacecraft into either highly elliptical orbits which reenter (perigee within the atmosphere) or literally drives the spacecraft out of its initial park orbit. Further, in some cases the Centaur may still be thrusting, producing a powered reentry. The SMB reentry envelope was developed by using 3DMP to model the Centaur burn with a finite duration and a randomly oriented thrust direction.

The above reentry conditions are utilized as initial 3DMP trajectory modeling conditions. The spacecraft, prior to RTG breakup, is modeled with a constant ballistic coefficient of 60 psf (per NASA-JPL). When the spacecraft reaches the breakup altitude predicted by NASA-JPL the GPHS module is regarded as exposed to the reentry aerothermal environment. At this point the trajectory simulation is continued with the aerodynamic and mass property characteristics of the module.

6.5.2.2 Out-of-Orbit Aerothermal Model

The primary model utilized for the out-of-orbit recession predictions is the Reaction Kinetics and Ablation Program (REKAP). This one-dimensional finite difference conduction and surface mass loss model is well suited for the determination of the aeroshell stagnation point recession.

REKAP solves the multi-layer heat conduction problem using an applied surface heating, accounting for transient material properties as a function of pressure and temperature. Energy is re-radiated from the surface using the appropriate temperature-dependent hemispherical emittance with the backface boundary condition assumed to be adiabatic and defined with either a heat loss input or as a backface temperature history. The REKAP code predicts in-depth decomposition and surface recession with models available for many reentry material heat shields. For this study a well-calibrated graphite thermochemical model/database is used based on flight and ground test data and results. This model has been validated over the past 25 years in the design of reentry vehicle thermal protection systems for MK12/12A (MINUTEMAN), MK21 (PEACEKEEPER), MK500, MK4, RVTO, MSV, and NASA planetary exploration missions such as Pioneer Venus and Galileo.

For purposes of analysis the 1D REKAP model approximates the 3-D GPHS module using one-dimensional layers of each module element's thickness and properties to the center of the PuO_2 (Figure 6.5.2-2).

	# NODES
AEROSHELL 0.19" FWPF	6
INSULATOR 0.07" CBCF	6
0.1675" FWPF	4
0.0255" CLAD	4
0.542" FUEL	4

ADIABATIC BACKFACE

NOTE: MODEL REPRESENTS SECTION THROUGH ONE GIS
i.e. LOCATION WHERE FWPF AEROSHELL HAS MINIMUM THICKNESS
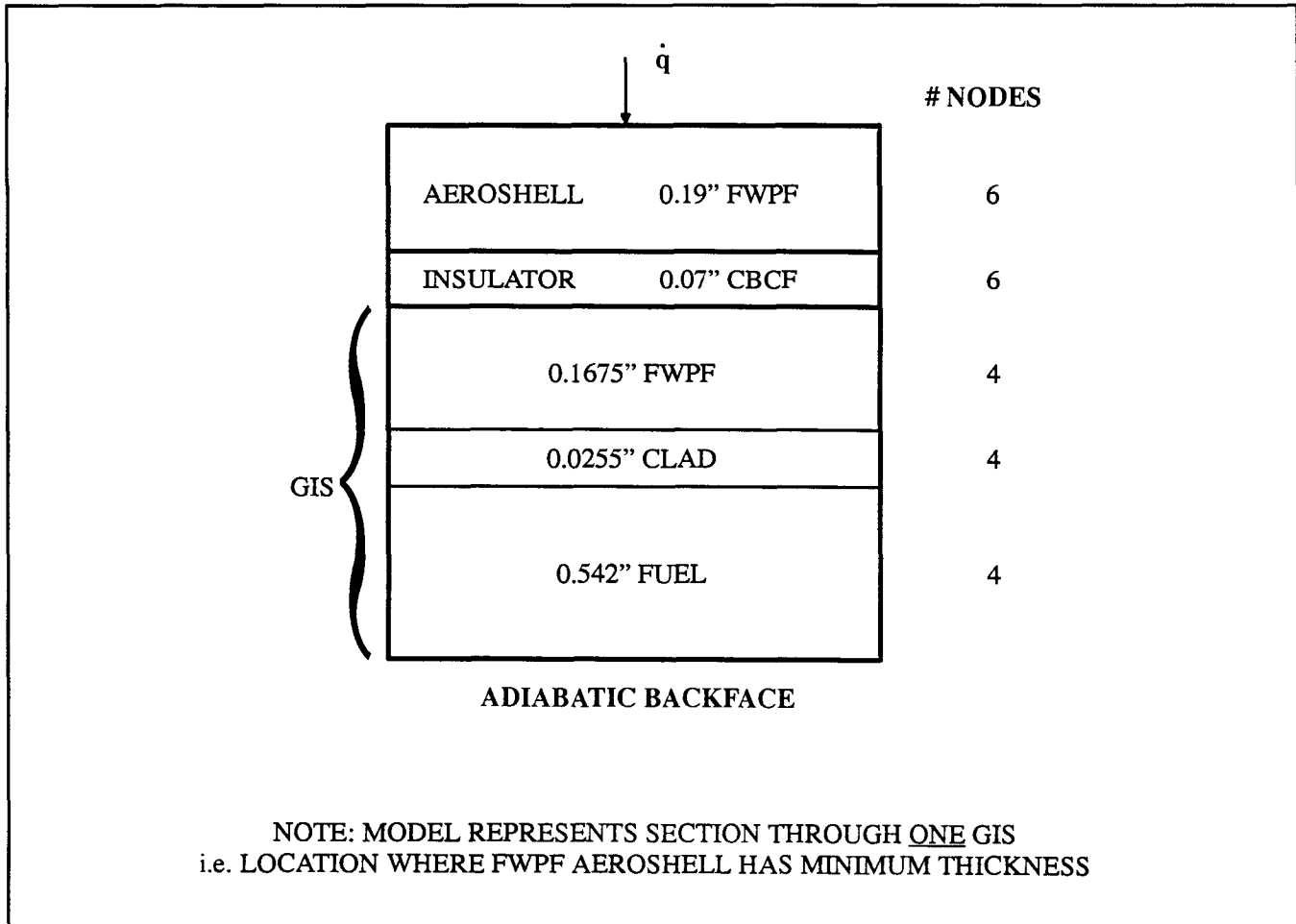
Figure 6.5.2-2. One Dimensional Layered REKAP Model for GPHS Module

The nominal stagnation point recession for the broad-face of the module has been predicted assuming a face-on (normal to velocity vector) stable orientation throughout reentry. This attitude exposes the aeroshell surface to the most severe, steady heating environment. Further, it is assumed that the RTG breakup occurs rapidly at the predicted altitude, releasing the modules to the free stream environment at the highest (earliest) opportunity. These two assumptions result in the most severe recession prediction.

The heating (free molecular, convective, and radiative) used for each reentry trajectory was computed in the 3DMP trajectory code using the techniques described, with recession calculated using the REKAP code.

The convective stagnation point heating rate to a sphere, without mass transfer effects, is calculated using approximations of the more rigorous formulations developed by Lees (Reference 6.5.2-2). The stagnation point heating for the aeroshell, with one face normal to the velocity vector, is estimated by applying a geometrical correction factor to the spherical stagnation point heating. Radiative heating is computed using the stagnation point radiative heating presented in Reference 6.5.2-3, by Tauber and Sutton.

The specific reentry trajectories evaluated were selected to enable a recession map to be developed for the entire V-γ envelope as shown in Figure 6.5.2-1. The resulting recession predictions for the stagnation point of the broadface of the aeroshell were utilized to generate the V-γ recession map shown in Figure 6.5.2-3.
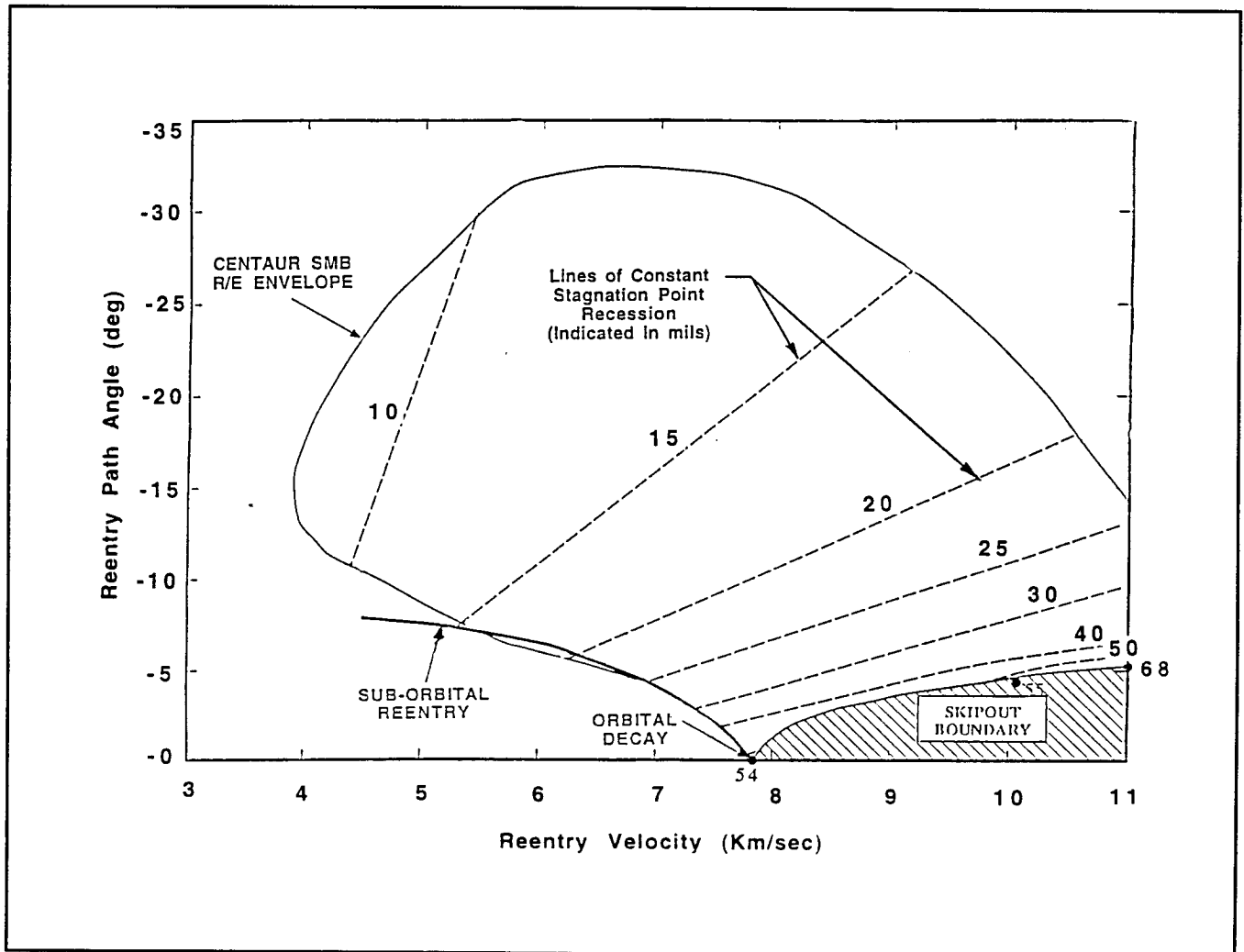
Figure 6.5.2-3. GPHS Module Stagnation Point Recession Contours

Sub-orbital accident reentries will result in recessions varying from 0.011 to 0.054 inches (or 6% to 29% of the minimum thickness). For accidents resulting in orbital decay reentries the expected recession is 0.054 inches.

The super-orbital, near skip-out condition of 11 km/sec and -5.1 degrees yields a maximum, non-multiskip recession of 0.068 inches or approximately 37% of the aeroshell thickness. This results from the combination of high velocity and long flight duration producing maximum integrated heating. For multiple skips (reentry below the skip-out bound), the stagnation point recession may increase to as much as 0.130 inches or 71% of the aeroshell thickness.

The surface temperature history for the FWPF aeroshell was computed using REKAP for the worst case, face-on stable, orientation of the GPHS module as well as the less severe random tumbling flight condition. The peak temperature experienced for a set of representative trajectories across the V-γ envelope is provided in Table 6.5.2-1.

Table 6.5.2-1. Maximum Surface Temperature for GPHS Module - Out-of-Orbit Accidents

Reentry Case	Velocity (km/s)	Flight Path Angle (deg)	Maximum Stagnation Point Temperature (and Altitude at Peak Temp.) - Face-on Stable -	Maximum Stagnation Point Temperature (and Altitude at Peak Temp.) - Random Tumbling -
Orbital Decay	7.9	0	3150°F (210 kft)	2300°F (200 kft)
Sub-orbital	6.5	-6.0	3120°F (160 kft)	2300°F (150 kft)
Sub-orbital	5.0	-9.0	2400°F	-
Super-orbital (Centaur SMB)	11.0	-5.1	4350°F (230 kft)	3160°F (225 kft)
Centaur SMB	4.5	-22.0	2200°F (120 kft)	-
Centaur SMB	6.5	-31.0	3000°F (115 kft)	-

The iridium clad reaches a temperature of 2570°F for the orbital decay, face-on stable, reentry condition, well below the melt temperature of 4440°F. For all other out-of-orbit cases the clad temperature will also remain well below the clad melt temperature.

6.5.2.3 Out-of-Orbit Reentry Ground Impact Analysis

The Module reentry ground Impact Model (MIM) is a Monte Carlo code that simulates the response of an intact module upon impact with the Earth's surface as the result of a reentry accident. The model randomly draws a module reentry point (latitude and longitude) propagates a reentry trajectory to impact (latitude, longitude, and altitude - above mean sea level), determines the impact surface type (water, soil, rock - based on a worldwide data base), and then characterizes the potential fuel release. Damage to the individual modules upon impact is modeled by use of LASEP-T subroutines SURFIMP, DST2REL, and FPSIZE which utilize release statistics extracted from impact tests of modules and bare fueled clads. The fuel release information includes mass release and particle size distribution.

The conditional probability distribution for impact location varies by accident case. Four accident cases have been selected for analysis, from potential out-of-orbit reentry accident scenarios defined in the Databook. Those scenarios leading only to water impacts have a zero conditional probability of release and therefore have not been analyzed. Cases selected for analysis are defined in Section 6.4.1 (case 3.1: sub-orbital reentry; case 5.1: sub-orbital reentry, CSDS configuration 5 accident; case 5.2: orbital reentry, nominal; and case 5.3: orbital reentry, off-nominal and elliptic decayed) . The case number prefix reflects the mission phase in which the POF (probability of failure) is a maximum.

For these four accident cases, two distinct probability distributions for impact location are identified. Orbital decay reentries result in globally distributed impacts, while suborbital reentries yield impacts that are confined to the Atlantic ocean, the southern African continent and Madagascar.

Accident cases 5.2 and 5.3 are orbital decay reentries, and result in impact locations which are latitudinally distributed, based on the park orbit inclination (the maximum north-south latitude can be no greater than the decay or park orbit inclination), and uniformly distributed longitudinally around the world. The latitudinal distribution is more probable at the extreme north-south latitudes and slightly less probable near the equator essentially due to the greater dwell time over these latitudes. The latitudinal band probability, P, can be represented mathematically as a spherical trigonometric function of the range of orbital argument of reentry, ω_1 to ω_2, or the latitude band , ϕ_1 to ϕ_2, and orbital inclination, ι:

$$P = \frac{1}{\pi}(\omega_2 - \omega_1) = \frac{1}{\pi}\left[Sin^{-1}\left(\frac{Sin\phi_2}{Sin\iota}\right) - Sin^{-1}\left(\frac{Sin\phi_1}{Sin\iota}\right)\right]$$

Table 6.5.2-2 shows the conditional probability of impacting within a given latitude band for accident cases 5.2 and 5.3. The probability of impacting any specific cell within a latitude band is 1/36th of the latitude band probability.

Table 6.5.2-2. Orbital Decay Conditional Impact Probabilities

Latitude Band	Cell Numbers	Latitude Range	Latitude Band Conditional Impact Probability
1	1 to 36	64.2 to 90 deg N	0
2	37 to 72	53.1 to 64.2 deg N	0
3	73 to 108	44.4 to 53.1 deg N	0
4	109 to 144	36.9 to 44.4 deg N	2.33×10^{-4}
5	145 to 180	30 to 36.9 deg N	0.0806
6	181 to 216	23.6 to 30 deg N	0.1400
7	217 to 252	17.5 to 23.6 deg N	0.0840
8	253 to 288	11.5 to 17.5 deg N	0.0701
9	289 to 324	5.7 to 11.5 deg N	0.0642
10	325 to 360	Equator to 5.7 deg N	0.0609
11	361 to 396	Equator to 5.7 deg S	0.0609
12	397 to 432	5.7 to 11.5 deg S	0.0642
13	433 to 468	11.5 to 17.5 deg S	0.0701
14	469 to 504	17.5 to 23.6 deg S	0.0840
15	505 to 540	23.6 to 30 deg S	0.1400
16	541 to 576	30 to 36.9 deg S	0.0806
17	577 to 612	36.9 to 44.4 deg S	2.33×10^{-4}
18	613 to 648	44.4 to 53.1 deg S	0
19	649 to 684	53.1 to 64.2 deg S	0
20	685 to 720	64.2 to 90 deg S	0

The impact point probabilities for suborbital accident cases 3.1 and 5.1 are essentially distributed along the Titan IV flight path from approximately 200 sec into the boost phase flight to just prior to park orbit insertion. This suborbital distribution can be represented by the Instantaneous Impact Point (IIP) predictions for the reference trajectory as defined in the Databook.

Based on the POF time history and range of potential park orbit inclinations for accident case 3.1, impacts will be distributed as shown in Figure 6.5.2-4 for typical variations from the reference trajectory. It can be seen that approximately 80% of the impacts will occur in the broad ocean area of the Atlantic, with a high concentration (55%) in the mid-Atlantic. This highly probable band corresponds to impacts resulting from failure of the Centaur at the first engine burn (fail-to-start conditions).

As discussed above, the surface impacts for the 54 modules, within a given Monte Carlo trial, are distributed spatially (dispersion) at impact due to varying flight characteristics during reentry. This distribution results in a degree of correlation with the surface type (rock, soil, water) within a given demographic cell. If the dispersion is much smaller than the characteristic dimension of the surface type the impacts may be considered completely correlated (all assumed to impact the same surface). If, however, the dispersion is much greater than the characteristic dimension of the surface type, then the impacts are completely uncorrelated (each module will have a probability of impacting any of the various surface types within the cell).

As shown in Figure 6.5.2-5, the probable module impact distribution for orbital decay reentries is depicted as a footprint of approximately 420 km in length by only 25 km in width, on the order of the typical dimensions of a worldwide grid cell. As a result, module impacts are assumed to be uncorrelated for surface impact type.
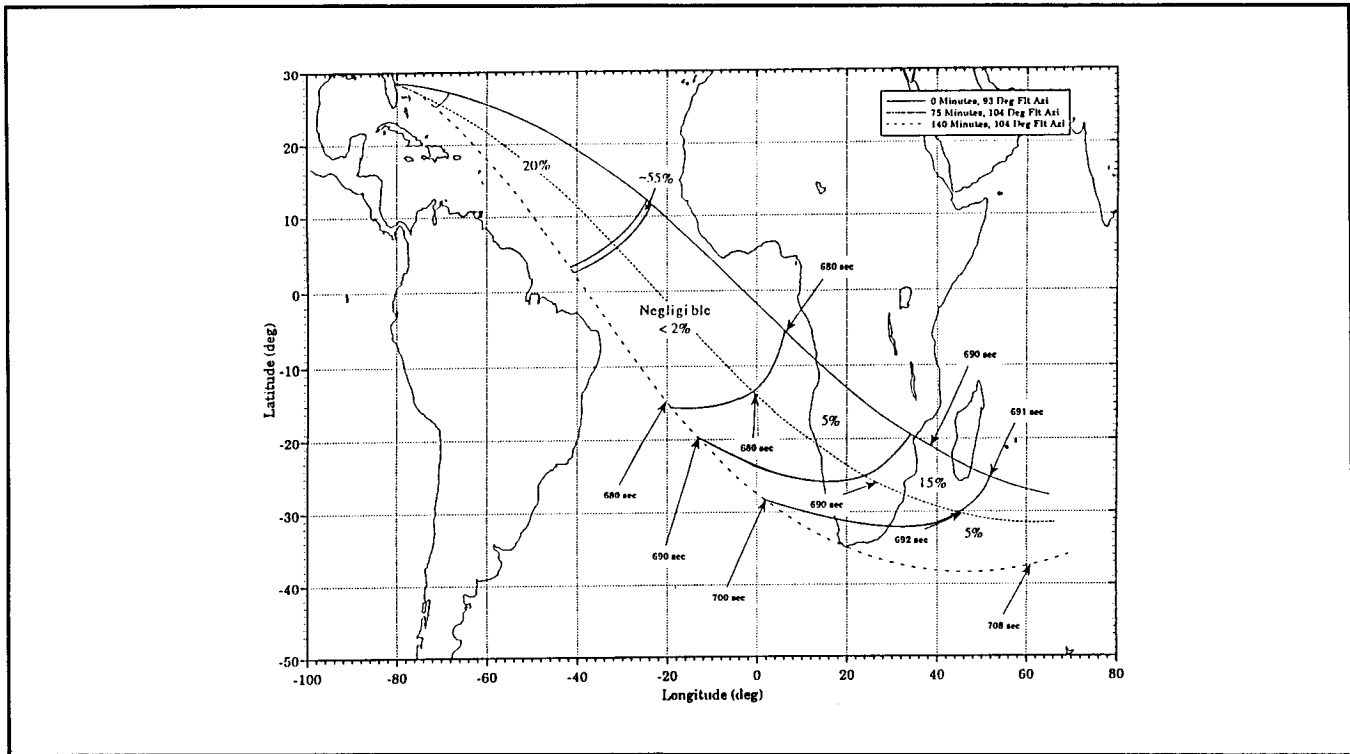
Figure 6.5.2-4. Cassini SV Instantaneous Impact Point Distribution
(Percentages Represent Relative Portion of Potential Sub-Orbital Reentries Expected to Impact within each Bounded Region)
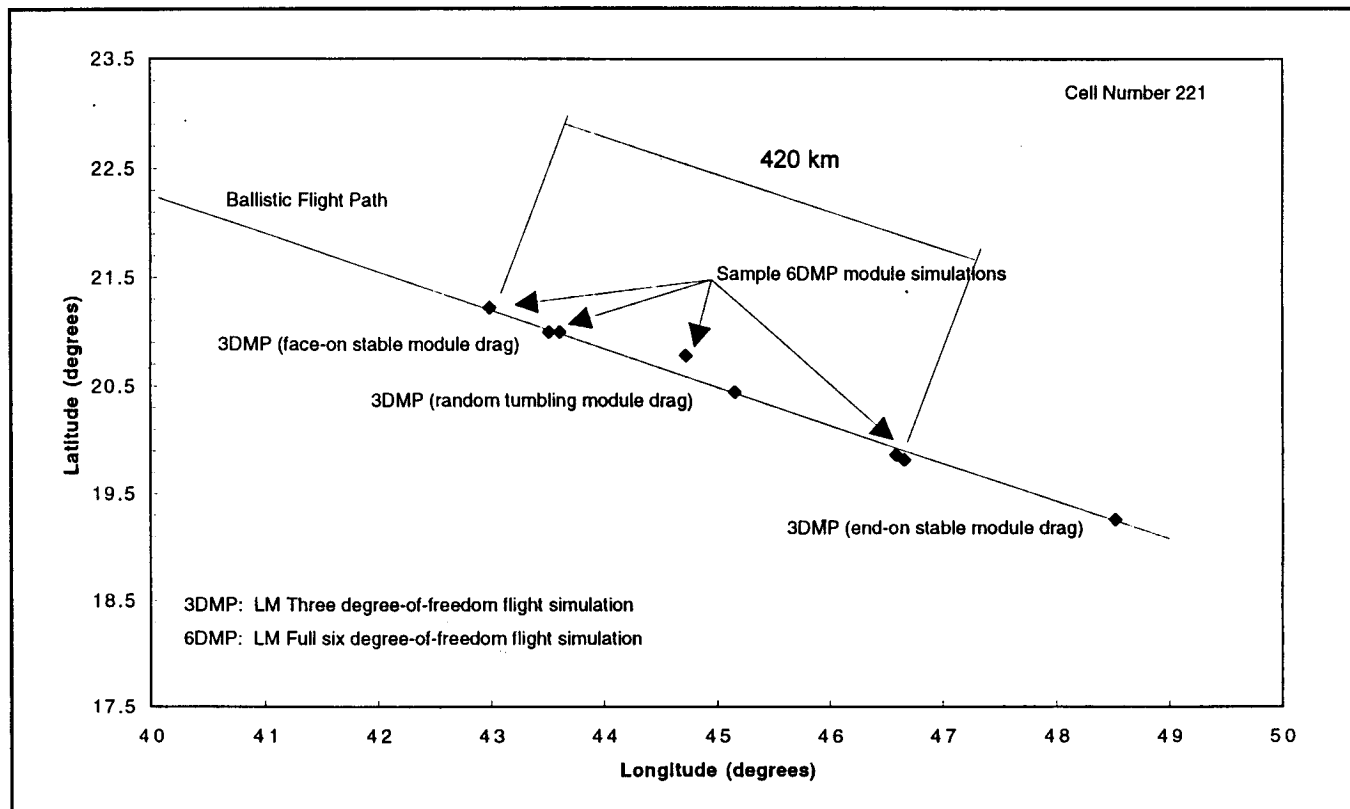
Figure 6.5.2-5. Module Dispersion within a Typical Demographic Cell

The evaluation of reentry accident consequence utilizes several sets of data generated by MIM: 1) a compilation, by worldwide database cells, of impact probability, 2) a set of 5000 release source terms for module impacts on rock surfaces from Monte Carlo simulation, (including correlated mass release and particle size distribution) , and 3) the conditional probability of a module releasing fuel given a rock surface impact. These data were provided to the SPARRC consequence model for health and land contamination consequence predictions. Statistics for the source terms from individual and combined out-of-orbit reentry accident cases are provided in Table 6.5.2-3. Representative source term particle size distributions are presented in Figure 6.5.2-6 for orbital decay reentries.

Table 6.5.2-3. Reentry Source Terms by Composite Accident Case

Accident Case	Mean POF	Probability of Release Given Failure	Probability of Release	Mean Release (grams)*	Release Percentiles*, **			
					5th (grams)	50th (grams)	95th (grams)	99th (grams)
3.1	1.4×10^{-3}	0.043	6.1×10^{-5}	0.097	0.014^{Δ}	0.063^{Δ}	0.212^{Δ}	0.298^{Δ}
5.1	1.2×10^{-2}	0.003	3.5×10^{-5}					
5.2	8.0×10^{-3}	0.25	2.0×10^{-3}	0.218	$0.019^{\bullet}$	$0.132^{\bullet}$	$0.696^{\bullet}$	$1.299^{\bullet}$
5.3	3.0×10^{-7}	0.25	7.5×10^{-8}					
Combined			2.1×10^{-3}	0.214	0.019	0.128	0.688	1.29

* Release in grams of PuO_2, for trials which produced fuel releases

** 5th Percentile: 5% of trials produced mass release smaller than this value
    50th Percentile: 50% of trials produced mass release smaller than this value
    95th Percentile: 95% of trials produced mass release smaller than this value
    99th Percentile: 99% of trials produced mass release smaller than this value

Δ A single Monte Carlo simulation was performed to reflect source terms for sub-orbital reentries (cases 3.1 and 5.1)

$\bullet$ A single Monte Carlo simulation was performed to reflect source terms for nominal orbit reentries (cases 5.2 and 5.3)

The conditional probability of release given a rock surface impact was computed by 400 MIM accident simulations, where each trial (and each of the 54 modules within the trial) was forced to impact a rock surface. Out of the 21600 modules that impacted rock, 12076 modules breached yielding a probability of release given rock impact, $P_{rel/rock}$, of 0.56. The first 5000 modules that resulted in a fuel release were also used to construct LASEP-T type release records which include the total mass released as well as the mass distributed into each of the 12 particle size bins.

BIN	MIN. DIA. (μm)	MAX. DIA. (μm)
1	<0.1	0.1
2	0.1	0.215
3	0.215	0.464
4	0.464	1.0
5	1.0	2.15
6	2.15	4.64
7	4.64	10.0
8	10.0	21.5
9	21.5	46.4
10	46.4	100.0
11	100.0	215.0
12	215.0	>215.0
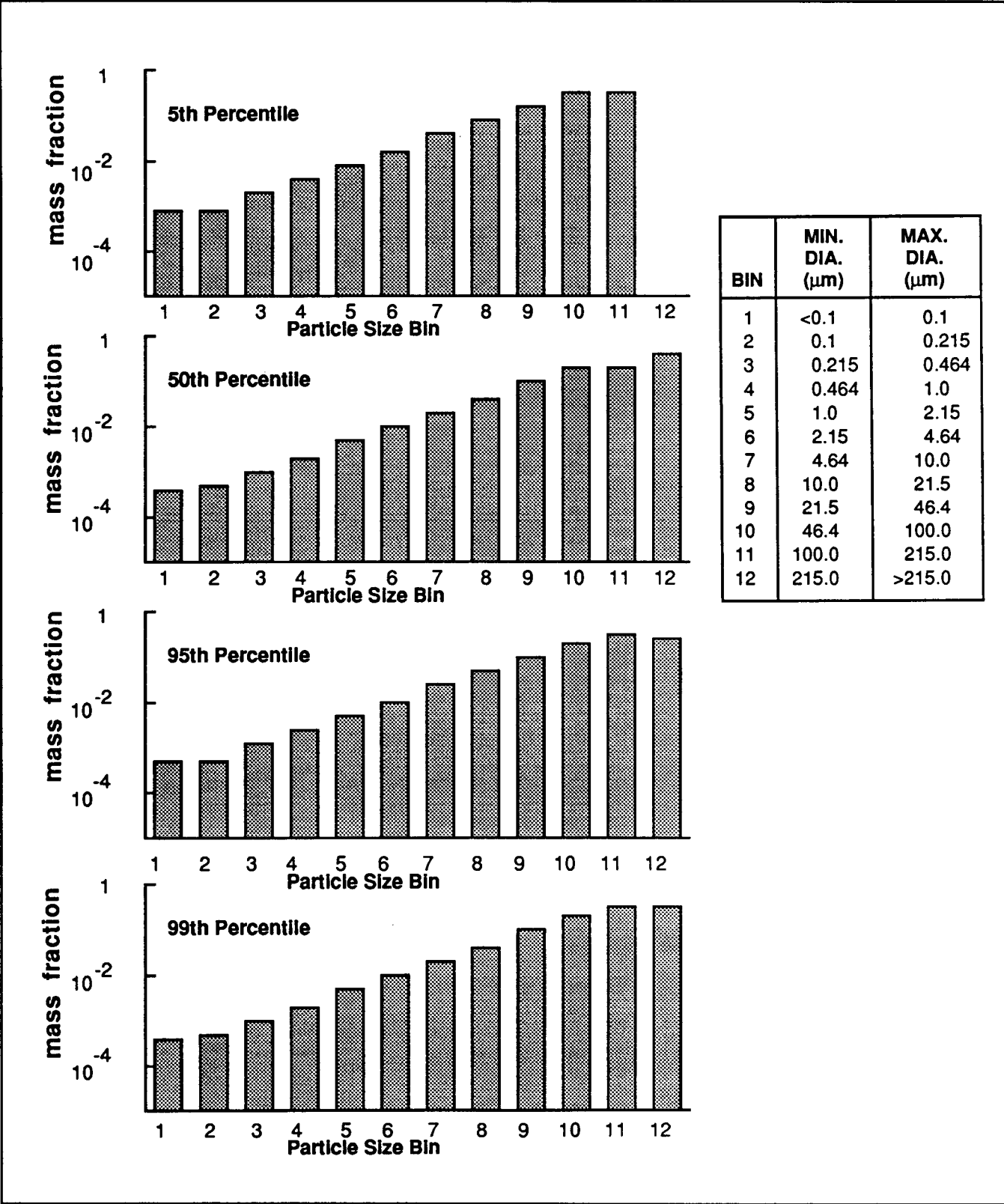
**Figure 6.5.2-6. Particle Size Distributions for Out-of-Orbit Reentry
Ground Impacts - Cases 5.2/5.3**

The cumulative probability distributions for each of the out-of-orbit accident cases were developed from 100,000 MIM trials which, for the orbital decay accident cases, 5.2 and 5.3, resulted in approximately 24600 trials yielding a fuel release. An average of 1 module breached per trial with a minimum of 1 and a maximum of 34. The average fuel release was 0.218 grams.

6.5.3 Earth Gravity Assist (EGA) Reentry Accidents

NASA-JPL has performed an assessment of the spacecraft breakup for inadvertent reentry during the Earth gravity assist swingby portion of the VVEJGA maneuver (Reference 6.5.3-1). The objective of this analysis was to predict the release conditions (altitude, velocity, and flight path angle) of the RTGs from the spacecraft. Table 6.5.3-1 summarizes the predicted release altitudes.

Table 6.5.3-1. RTG Release Altitudes

Reentry Flight Path Angle (deg)	Release Altitude (kft) Early	Release Altitude (kft) Late
-90	258	241
-45	264	247
-15	290	270
-10	306	284
-7	320	295

The flight dynamic behavior of the GPHS module during EGA inadvertent atmospheric reentry is predicted by JHU/APL (Reference 6.5.3-2). This behavior is simulated via a full six degree-of-freedom, 6DOF, (three translational, three rotational) trajectory program.

Since the GPHS may be released from the spacecraft with a wide range of initial conditions (initial body rates and angles) 850 distinct 6DOF simulations were performed for reentry trajectories ranging from -7 to -90 degrees reentry flight path angle. The statistical outcome of the 6DOF simulations is presented in Table 6.5.3-2 which shows the occurrence frequency as a function of total angle-of-attack observed for at least 15% to 20% of the heat pulse. As shown in Table 6.5.3-2, nearly 40% of the cases are considered face-on-stable (FOS) with the remaining 60% either tumbling or non-FOS.

Table 6.5.3-2. Statistical Results from GPHS 6DOF Reentry Motion Studies - VVEJGA Trajectory

α_R Average							
α_R	0-20	21-40	41-60	61-80	81-90	Tumbling	All *
No. of Occurrences	590	276	140	264	85	120	1475
Percent	40.0	18.7	9.5	17.8	5.8	8.2	100

* When an angle of attack occurred for 15% to 20% of the heat pulse, that angle was used in the analyses; this could occur as many as three times during a trajectory. Thus, the total number is greater than the 850 cases studied.

6.5.3.1 VVEJGA Reentry Environments

Figure 6.5.3-1 shows velocity - altitude profiles for a typical ballistic reentry vehicle (BRV) and the GPHS module at several flight path angles. The substantial differences in reentry time for each trajectory are evident by the spacing of the 1-second tick marks. Differences in the flight profile are due to very high reentry velocity experienced for the VVEJGA trajectory (over 2.5 times that of the BRV) and the low ballistic coefficient (β) of the GPHS module (about two orders of magnitude less than the BRV). The low-β and high initial velocity of the aeroshell cause severe heating at high altitudes where the freestream density and pressure are low. Table 6.5.3-3 highlights major differences between the BRV and GPHS module flight environments.

COMPARISON OF FREESTREAM VELOCITY
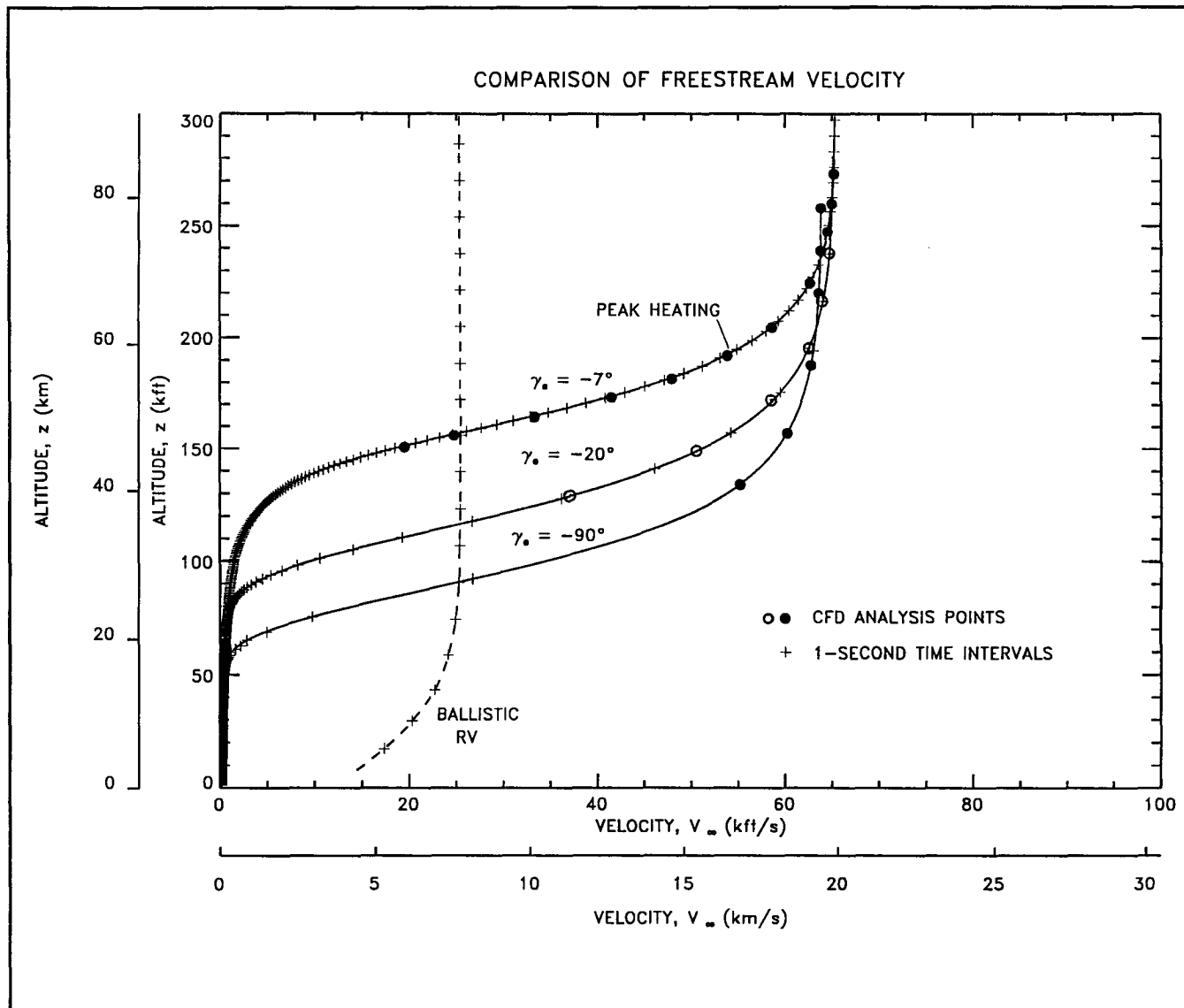
Figure 6.5.3-1. Comparison of Reentry Trajectories for a GPHS Module and a Typical Ballistic Reentry Vehicle (BRV)

Table 6.5.3-3. Comparison of BRV and GPHS EGA Flight Environments

Parameter	BRV	GPHS Module
Aeroheating		
- Peak	Lower altitude and higher pressure	High altitude with low density and pressure
- Duration	Short duration with high heat rate to impact	- Very short pulse for steep and about 10 times longer for shallow - Considerable time (minutes) for soak and cooling prior to impact
- Radiation	Insignificant	Shock-layer radiation dominates surface heating
Inertial loads	Approximately 100 Gs	About 1,000 Gs for steep. Less than 100 Gs for shallow.
Flow chemistry	Equilibrium during heat pulse	Nonequilibrium during heat pulse
Transition from laminar to turbulent flow	Approximately 40,000 feet for nosetip	Will remain laminar

6.5.3.2   EGA Reentry Analysis Approach

Techniques have been developed to compute the aero/thermo/structural response of:

- the GPHS aeroshell during reentry following release from the RTG shell

- the GIS in the event that the aeroshell fails

- the fuel particles in the event of GIS failure (and fueled clad melt).

These techniques are described below. Results of the analyses are presented in Section 6.5.3.3. Additional details on the analysis approach are presented in Appendix E of Reference 6.5.3-3.

Computations were performed over a range of trajectories in order to determine reentry path angle boundaries that delineate regions of aeroshell survival / failure, GIS survival/ failure, and fuel particle response. The fuel particle analysis was also extended into regions where nominal predictions showed no fuel air-release. This extended fuel particle analysis was performed in order to encompass effects of uncertainty and variability in the response predictions.

The GPHS aeroshell and GIS analyses provided estimates for probabilities for release employed in consequence calculations. The fuel particle analyses determined air-release

particle-size distributions with corresponding release altitudes and velocities as well as the particle-size distribution of the remaining intact fragments that impact the Earth's surface.

The trajectories for the GPHS aeroshell, GIS, and fuel aerothermal analyses are generated using the three degree-of-freedom trajectory program, 3DMP. For the purpose of these GPHS module studies the early (highest) breakup altitude (as presented in Table 6.5.3-1) is utilized leading to the longest exposure of the module to the reentry aerothermal environment. The velocity at the indicated spacecraft breakup altitude is 19.45 km/s (63,800 ft/sec), Earth Centered Inertial (ECI), and is considered to be independent of the given breakup altitude. The trajectories were flown with the initial velocity directed counter to the Earth's rotation (into the relative wind since the atmosphere rotates with the planet). This heading will provide the highest air-relative velocity and therefore the most severe aerothermal environment. The initial conditions for the subsequent GIS analyses are taken from the predicted structural failure points for the GPHS. The initial conditions for fuel analyses are defined by potential GIS burnthrough altitudes.

The procedure for the aero/thermo/structural analysis of EGA reentry utilized a sequence of computer codes. The three primary elements in this approach are: 1) CFD and coupled flowfield radiation techniques to compute the complex phenomena of reentry physics, 2) thermal analysis models to determine transient, in-depth temperature distributions and surface recession using CFD-supplied surface heat flux and ablation rates, and 3) detailed nonlinear finite-element structural analysis models to determine the response of the aeroshell to thermal, aerodynamic, and inertial loading. This approach is based on experience with BRVs and planetary atmosphere probes. Related analysis procedures have been very successful in predicting reentry vehicle performance, confirmed by carbon nosetips that survive to impact.

The structural analysis code that is employed for EGA reentry utilized the same technique previously used for carbon BRV nosetips that reach temperatures comparable to the GPHS aeroshell. The thermal analysis codes are also well validated and have been widely used throughout industry. However, the standard three-dimensional thermal analysis code was modified for Cassini EGA reentry to incorporate recession (moving boundaries). Both the three-dimensional and one-dimensional transient thermal codes were modified to solve the

surface energy balance using tables (from CFD) of surface heat flux, enthalpies, and ablation rates.

The CFD and flowfield radiation codes used for EGA reentry analysis are new and, of necessity, far more sophisticated than conventional reentry techniques. Because of the low ballistic coefficient and extremely high reentry velocities, peak heating occurs at high altitudes (relative to BRV reentry trajectories) and is dominated by hot-gas nonequilibrium radiation compounded by the effects of carbon ablation products. Approximate, semi-empirical, stagnation-point techniques, used for EGA analyses on previous missions, become suspect at the extremely high velocities of the Cassini EGA inadvertent reentry. The significant effects of coupled nonequilibrium chemistry, nonequilibrium radiation, and nonequilibrium carbon ablation cannot be confidently modeled using such simplified techniques. Conventional codes developed for BRVs such as Blottner's (Reference 6.5.3-4) chemically reacting boundary-layer technique, and codes developed for planetary reentry, such as Nicolet's H-He atmosphere, viscous-shock layer flowfield/radiation technique (RASLE, Reference 6.5.3-5), do not address all of the phenomena important for GPHS reentry. Even with substantial modifications, existing flowfield codes fall short of adequately modeling the GPHS reentry environments. Several state-of-the-art Navier-Stokes flow solvers were assessed for applicability to Cassini EGA reentry environments. The LAURA code (Reference 6.5.3-6) developed at NASA Langley, was initially selected because it incorporated much of the required physics. Furthermore, LAURA had been successfully coupled to the LORAN nonequilibrium radiation code (Reference 6.5.3-7). For Cassini EGA reentry, both LAURA and LORAN were extended to include carbon species and reactions. LAURA also required extensive modifications to treat ablation boundary conditions. These new versions of the flow solver and radiation code were designated LAURA-C and LORAN-C to denote the extension from 11-species, 20-reaction air chemistry system to a 19-species, 44-reaction air-carbon system.

The LAURA-C/LORAN-C codes were successfully applied at points along the steep ($\gamma = -90°$) trajectory. However, the LAURA-C code proved to be painfully slow to converge (several hours on a Cray C-90) and its stability was challenged by chemical and ablation rates. To enable the computation of the hundreds of cases that were required for EGA analyses, a new faster and more robust flow solver was needed.

A new full Navier-Stokes solver for Reacting, Ablating, Chemical Equilibrium/ nonequilibrium with Radiation (RACER) was developed to overcome the problems encountered with LAURA-C. The RACER code, described in References 6.5.3-3 and 6.5.3-8, employs a new hybrid, third-order, fast converging flux-vector splitting scheme. In addition, a new two-step, thermally-coupled chemical solution algorithm was devised to efficiently predict high-temperature, nonequilibrium, reacting and ionizing flows. RACER also includes nonequilibrium carbon-sublimation and heterogeneous-oxidation ablation models. With slight modifications, the LORAN-C code was linked to RACER to iteratively compute coupled flowfield / radiation solutions. At all stages of the development process RACER was validated with data, other techniques including LAURA and LAURA-C, and empirical relations and approximate theory. On benchmark test cases, RACER has proven to be 10 to 14 times faster to converge than LAURA-C. The speed of RACER makes it ideally suited to solve the required number of cases. In addition, RACER analyses can be readily performed on workstations rather than supercomputers.

6.5.3.2.1 GPHS Aero/Thermo/Structural Analysis Approach

The survival/failure of the GPHS aeroshell, in the event of accidental reentry during the Earth gravity-assist maneuver, is assessed using a multi-discipline approach. Aeroshell reentry response is computed along bounding trajectories; the shallowest flight-path angle just above skip-out ($\gamma = -7°$) and vertical ($\gamma = -90°$). In addition, an intermediate trajectory ($\gamma = -20°$) was selected to better establish survival/failure boundaries. For conditions where aeroshell failure is predicted, and the graphite impact shell (GIS) assemblies are assumed to be released, the response of the GIS is analyzed as described in Section 6.5.3.2.2.

This EGA analysis differs from other conventional approaches that either neglect thermal transients, by using "steady-state" ablation, or treat transients with simplified flowfield predictions and one-dimensional in-depth conduction techniques. Instead, a full Navier-Stokes code, coupled to a nonequilibrium radiation code, is used in conjunction with a three-dimensional, in-depth, transient thermal-response code. Nonlinear three-dimensional thermostructural analyses are subsequently performed at critical trajectory points to determine the structural adequacy of the GPHS module under combined aerothermal loading. In this approach, both the flowfield/radiation and structural analyses are performed at discrete points on the trajectory while the thermal analysis is a continuous

along the trajectory. This discrete-point application of flowfield and structural analysis codes is valid because flow-establishment times are measured in milliseconds and dynamic loads can safely be neglected (compared to static loads) for these conditions.

Coupling of CFD/Radiation and Transient-Heating Techniques: As shown schematically in Figure 6.5.3-2, flowfield and transient-heating computations are advanced together down the trajectory. The flowfield computations are performed for specified front-face and side-face temperatures. These temperatures are based on the transient-heating solution at the previous trajectory point. Three temperature estimates, labeled "low", "nominal", and "high", are supplied as boundary conditions for the flowfield and radiation analyses. The flowfield and radiation codes are run sequentially. Initially the flowfield is solved without radiation. This flowfield is used to obtain an initial radiation field. The flowfield and radiation codes are then globally iterated to convergence. This solution procedure provides a matrix of
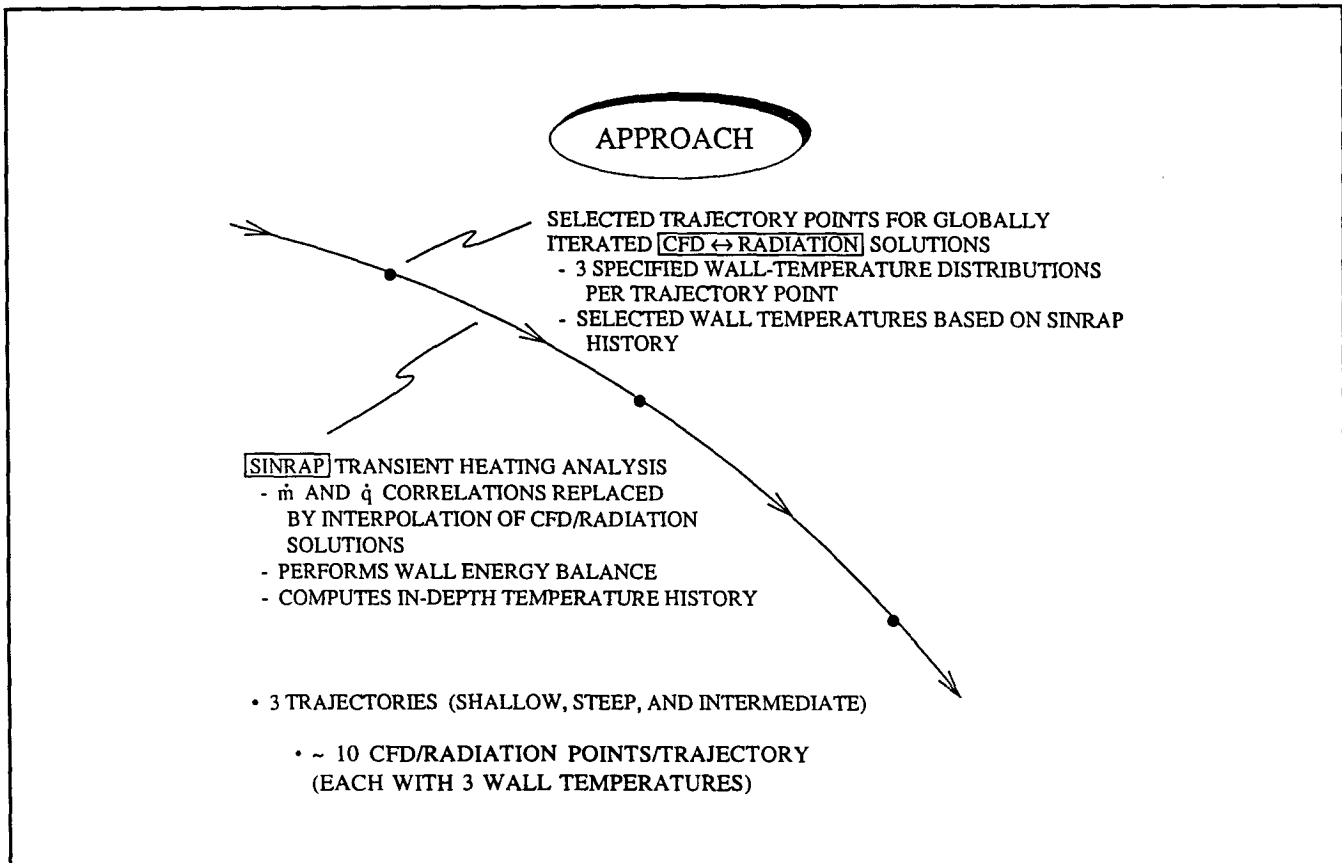
Figure 6.5.3-2. Trajectory-Based Coupling of Flowfield/Radiation Analyses with Transient Heating Computations

surface distributions of heat flux, enthalpy, and ablation rate as a function of altitude and wall temperature. These tables are then used by the SINRAP transient-heating code (Reference 6.5.3-9) to advance the solution of the module's temperature and surface recession through three trajectory points. The transient-heating code iterates at each time step on temperature at each surface and in-depth nodal point and satisfies the surface-energy balance.

Thermostructural Analysis Technique: The finite-element code ABAQUS (Reference 6.5.3-10) was chosen to perform the thermostructural assessment because of its advanced nonlinear capabilities, which includes the ability to utilize user-defined nonlinear constitutive material models. As shown in Figure 6.5.3-3, for the shallow (-7°) trajectory, the thermostructural analyses are performed at points along the trajectory where maximum

Note: Temperature and recession data from SINRAP analysis, loads from 3 DOF analysis
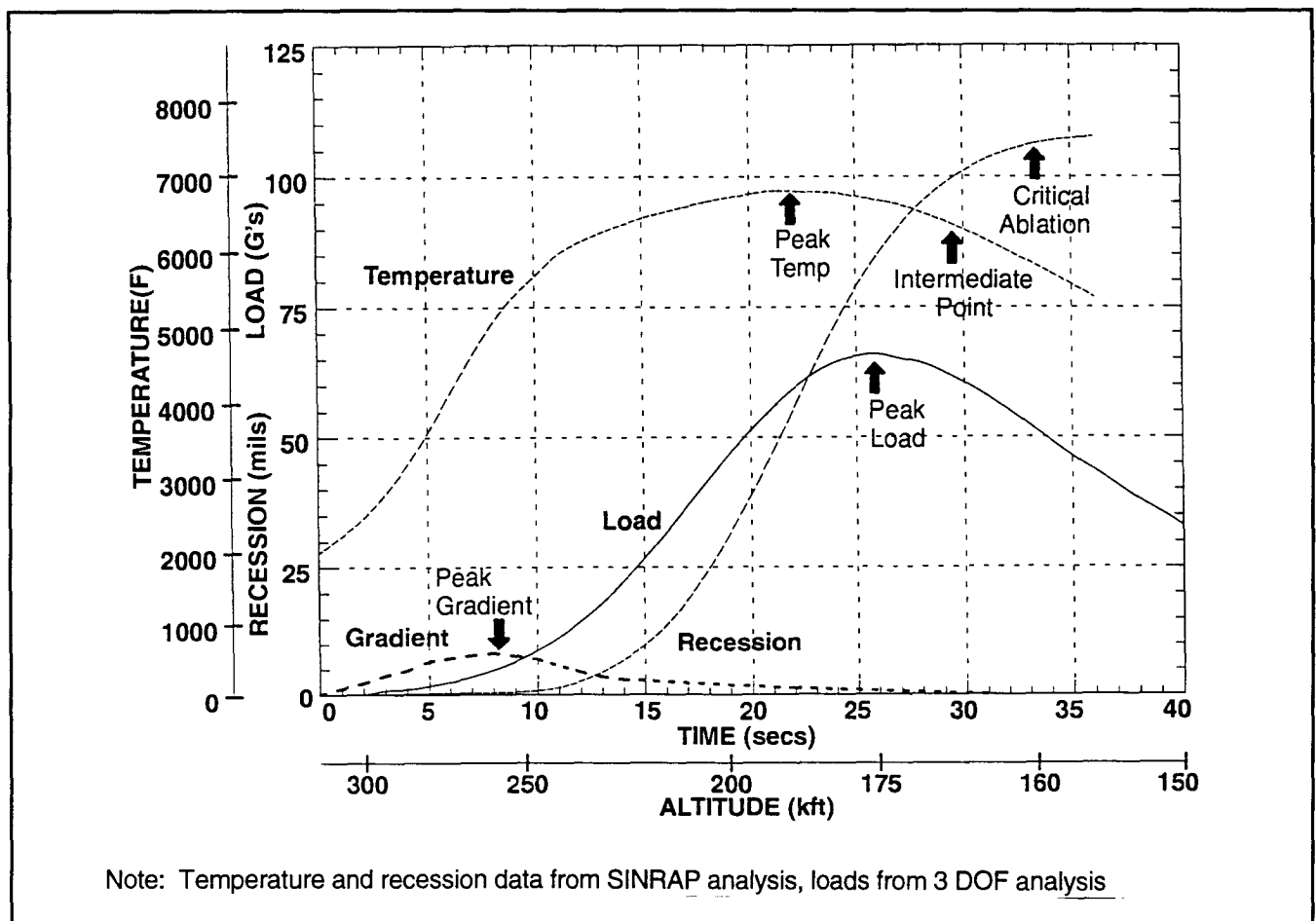
**Figure 6.5.3-3. Selection of Thermostructural Analysis Points -
Shallow (-7°) Trajectory**

stresses could potentially occur. These trajectory points generally correspond to instances of peak thermal gradients through the thickness of the aeroshell front face, maximum stagnation-point temperature, maximum reentry pressure and deceleration, maximum recession, and some intermediate points where combined load effects may be most severe. Surface pressures on the aeroshell are obtained from the flowfield predictions. Flight dynamic three-degree-of-freedom (3DOF) trajectory computations provide deceleration loads. Thermal loads for the ABAQUS model are obtained from the transient thermal predictions. The outer contour of the aeroshell is also modified to match the predicted ablation. Aeroshell stresses and strains predicted by the nonlinear ABAQUS analysis are then evaluated against FWPF material allowables to determine the structural adequacy of the module. The structural capability is expressed in terms of a "factor of safety" which is simply the material allowable divided by the predicted stress or strain. A factor of safety less than 1.0 indicates failure.

Enabling Assumptions: Each flowfield case requires global convergence of the Navier-Stokes code with the radiation code (generally three-to-five iterations). Over one-hundred cases are needed to adequately address the three trajectories examined in this study. In order to accomplish this extensive case matrix, without risk of under-predicting the aerothermal environment, it is assumed that:

1. The module is oriented (aerodynamically trimmed) broad face-on-stable (FOS).

2. The three-dimensional GPHS module is represented by an axisymmetric, flat-face, cylinder with a small radius corner blending the front face with the side of the cylinder.

3. Radiation is computed using the tangent-slab approach.

4. The wall is treated as an equilibrium-catalytic surface.

The flowfield is assumed to be in thermal equilibrium (single-temperature model).

These are conservative assumptions tending to overpredict heating.

6.5.3.2.2 GIS Aero/Thermo/Structural Analysis Approach

For this analysis, failure of an aeroshell during reentry is assumed to result in release of both GIS assemblies at altitude. Analysis has been performed for a side-on stable GIS condition. GIS assemblies which maintain an end-on stable condition (less than 3%) would

be expected to experience enhanced recession due to the blind crush holes, as indicated in Reference 6.5.3-11.

The GIS's cylindrical shape and side-on stable orientation permits the use of a stagnation-line flowfield/radiation approach. This stagnation-line technique greatly reduces the computational demand of the alternative two-dimensional (infinite cylinder) approach. An equivalent simplification is not possible for the GPHS module because the flowfield over the flat-face geometry is strongly influenced by the shoulder radius. In addition, the heat flux at the corners of the GPHS is large and is important in the overall thermal/structural response analysis.

A stagnation-line version of RACER and LORAN-C was developed for the GIS response analyses. The coupled flowfield/radiation/transient-thermal analysis scheme is similar to that used for the GPHS module. However, the three-dimensional SINRAP thermal analysis code is replaced by the one-dimensional REKAP code (Reference 6.5.3-12). REKAP solves the multi-layer transient heat conduction problem and accounts for material properties as a function of temperature as well as recession of the FWPF shell. RACER/ LORAN-C solutions are supplied as temperature dependent tables of the net heat flux and corresponding ablation rate at selected points along the GIS trajectory. The GIS is modeled in REKAP using cylindrical coordinates with radial internal conduction through the FWPF shell, iridium clad, and fuel. This approach is conservative because it neglects heat conduction in the circumferential direction to cooler regions away from the stagnation point.

The thermostructural analysis of the GIS is very similar to the approach utilized for the GPHS module. An ABAQUS finite element model of the GIS assembly is utilized in conjunction with the detailed nonlinear model of the FWPF material that was developed for the GPHS. Aeropressures are applied and balanced by deceleration loads. Thermal loads are applied concurrently with the reentry load conditions, and static analyses are run at selected points in the trajectory that could potentially produce the worst-case stress conditions in the FWPF shell. Stress and strain results are evaluated against temperature dependent material allowables for every element in the GIS.

The nonlinear ABAQUS finite element model of the GIS, composed entirely of solid elements, include the GIS, end cap, and floating membrane (all FWPF), as well as the

iridium clad and PuO$_2$ fuel pellets. The nonlinear, temperature-dependent material model utilized for the FWPF components is identical to the one utilized for the aeroshell. Temperature-dependent, linear isotropic material properties were developed for the clad and fuel pellet based on the material property database. A critical feature of the ABAQUS model of the GIS assembly is the utilization of nonlinear contact elements at the GIS/clad and clad/fuel pellet interfaces. These elements carry load in compression only and thus are ideally suited for applications where two unattached components may come into contact when loaded. In this case, there exists a diametral gap between the fuel pellet and clad body of approximately 0.036 inches. In addition, the fueled clad rests on internal rings in the GIS which are approximately 0.016 inches larger in diameter than the outer surface of the clad.

Reentry deceleration load conditions for the GIS were balanced by an applied pressure distribution on the outer surface. This pressure was assumed to have a cosine distribution, with the peak occurring at the model cut plane. Temperatures and ablations for the model were obtained from stagnation-line REKAP thermal analyses. The model shape was adjusted to match the predicted ablated shape. The entire outer surface was conservatively assumed to ablate the maximum (stagnation point) amount. In-depth temperatures were applied to all components in the model. Temperatures varied radially but were assumed to be constant in both the axial and circumferential directions. A single point on the axis of the model was constrained to eliminate any residual free-body motion.

6.5.3.2.3 Fuel Response Analysis Approach

The response of plutonia fuel particles for assumed release from a GIS assembly has been assessed to determine the particle size mass distribution for subsequent consequence analysis. If the fuel particles are released, they will melt, shedding microsphere droplets through the mechanism of liquid layer stripping. The resultant molten droplets will then begin vaporizing. Much of the basis of this analysis stems from previous studies by Gilbert and Eck reported in References 6.5.3-13 and 6.5.3-14, respectively.

The time dependent thermal environment for the fuel particles is modeled using the 3DMP trajectory code that accounts for the time varying mass and dimensional characteristics of the melting/vaporizing fuel particles and resultant droplets. It is assumed that the fuel

initially released from the GIS is already fragmented. The selection of initial fragment/particle size distribution is discussed below.

These fragments/particles are exposed to the hypersonic environment and begin to melt, shedding microsphere droplets which then begin to vaporize. The onset of droplet vaporization is delayed to account for the finite time required to raise the molten droplet from its melt temperature (4635°R) to the vaporization temperature of 8100°R. It is assumed that these microspheres are isothermal as verified by computing the Biot number, N_{bi}.

Initial Particle Size Distribution: The initial particle size distribution for air releases prior to ablation was determined by extrapolating SVT safety test data on particle size distribution versus distortion for fueled clads. The results are shown in Table 6.5.3-4. Relative contributions from small particles in the fueled clads prior to air release on the particle size distribution of the air release was felt to be negligible due to the large amount of small particles generated by ablation as indicated in the next section.

Table 6.5.3-4.   Particle Size Distribution Prior to Air Release

Particle Diameter	Mass Fraction
< 841 micrometers	0.0
841 to 2000 micrometers	0.133
2000 to 6000 micrometers	0.531
> 6000 micrometers	0.336

6.5.3.3   EGA Reentry Analysis Results

SINRAP in-depth heating and recession predictions, using tables of RACER (flowfield) and LORAN-C (radiation) results, followed by ABAQUS nonlinear structural analyses, show that the aeroshell survives the shallow (γ = -7°) trajectory in a face-on-stable (FOS) orientation. For the steep (γ = -90°) trajectory, results show that the FOS aeroshell experiences structural failure between 1.8 and 2.0 seconds. The intermediate trajectory (γ = -20°) also fails structurally (at 5.85 seconds). Subsequent structural analyses place the nominal threshold flight path angle for aeroshell failure at -16°. Results from RACER/LORAN-C, SINRAP, and ABAQUS are presented below.

Flowfield Results

On the shallow trajectory, RACER/LORAN-C solutions were obtained at eleven trajectory points (specified altitude and velocity) each with three prescribed surface-temperature distributions. On the steep and intermediate trajectories, CFD results were obtained at six and seven trajectory points, respectively. Each altitude-velocity/temperature case requires three-to-five global iterations of the flowfield with the radiation field. In addition, grid studies are periodically performed to assure that a sufficient number of points are used to resolve the flow physics. In total, about three-hundred and fifty RACER and two-hundred and eighty LORAN-C solutions were obtained for the three trajectories.

Transient-Heating Results

SINRAP, modified to accept surface-energy balance terms and recession-rate predictions from tables of RACER/LORAN-C solutions, computed in-depth nodal temperatures and surface recession histories which were then employed in thermostructural analyses.

The SINRAP solution for the GPHS temperature and recession histories is obtained by an iterative solution of the surface energy balance (SEB). The results, shown below, are based on a new form of the SEB developed by Bhutta et al. (References 6.5.3-15 to 6.5.3-21) during the course of the Cassini safety analysis. All analyses were then repeated using the conventional SEB. The effect of the SEB formulation on the GPHS is presented at the end of this section.

The three prescribed front-face wall temperatures for each CFD point along the shallow, steep and intermediate trajectories are shown in Figure 6.5.3-4, along with the converged SINRAP stagnation-point temperature history for each trajectory. On the shallow trajectory, the temperature peaks at 7260°R in about 22 seconds. At the last point on the steep trajectory, wall temperatures have surpassed 8000°R in only 2 seconds.

For the shallow (-7°) entry angle, a peak iridium temperature of 3514°R (1679°C) is reached at 58 seconds. This is far below the iridium/FWPF graphite eutectic temperature of 4625°R (2296°C). At impact, the iridium has cooled off to a minimum temperature of 2396°R (1058°C). For the steep case at the predicted time of aeroshell failure near 1.9 seconds, the iridium temperature is 2832°R (1300°C).
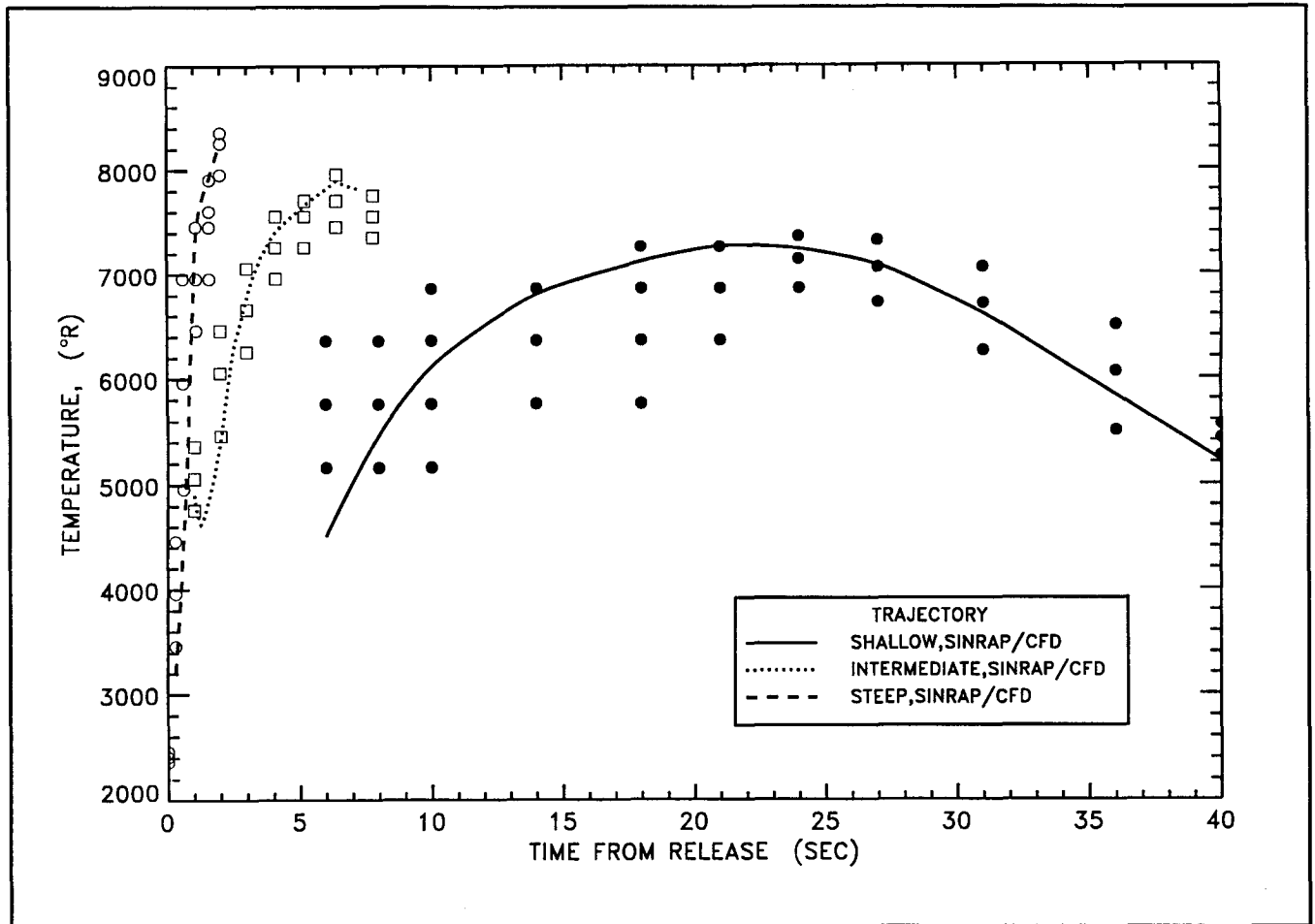
Figure 6.5.3-4   CFD Computational Matrix and Comparison of Steep, Shallow, and Intermediate Trajectory Stagnation-Point Temperature Histories

The total heat flux is shown in Figure 6.5.3-5. On the steep trajectory, flux levels approach 34,000 BTU/ft^2 sec at the stagnation point. This heating rate is more than 13 times the shallow peak-heating level. The radiation component of the steep trajectory heat flux is comparable to that encountered by the Galileo probe during its plunge into the Jovian atmosphere.

The resulting surface recession for the shallow, intermediate and steep trajectories is shown in Figure 6.5.3-6. Shallow trajectory recession continues out beyond 100 sec with leveling off at 0.125 inches. The minimum aeroshell thickness is 0.185 inches, so sufficient margin remains for the shallow trajectory (ABAQUS thermostructural analyses, presented below, verify structural integrity for the shallow trajectory). On the steep trajectory, recession is progressing rapidly at the time of structural failure.
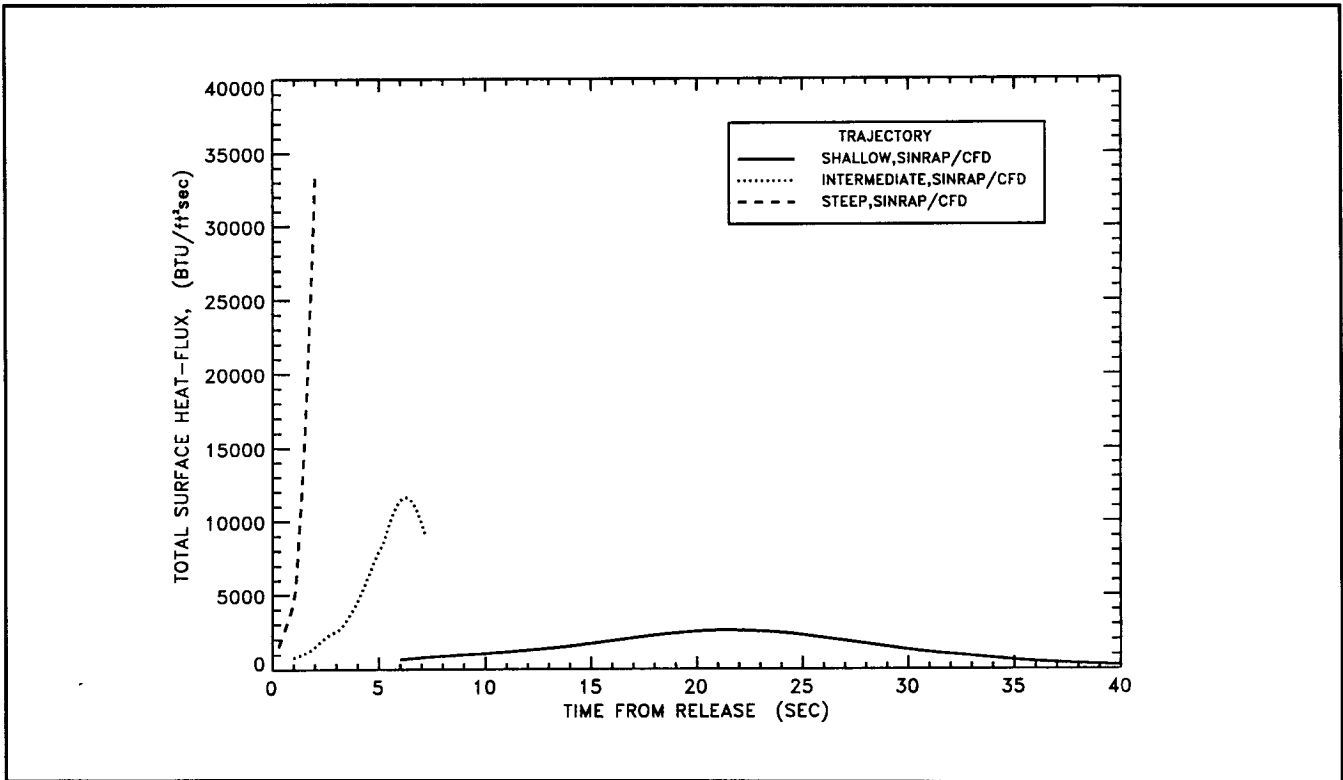
Figure 6.5.3-5. Comparison of the Total Heat-Flux at the Stagnation Point along the Steep, Shallow, and Intermediate Trajectories
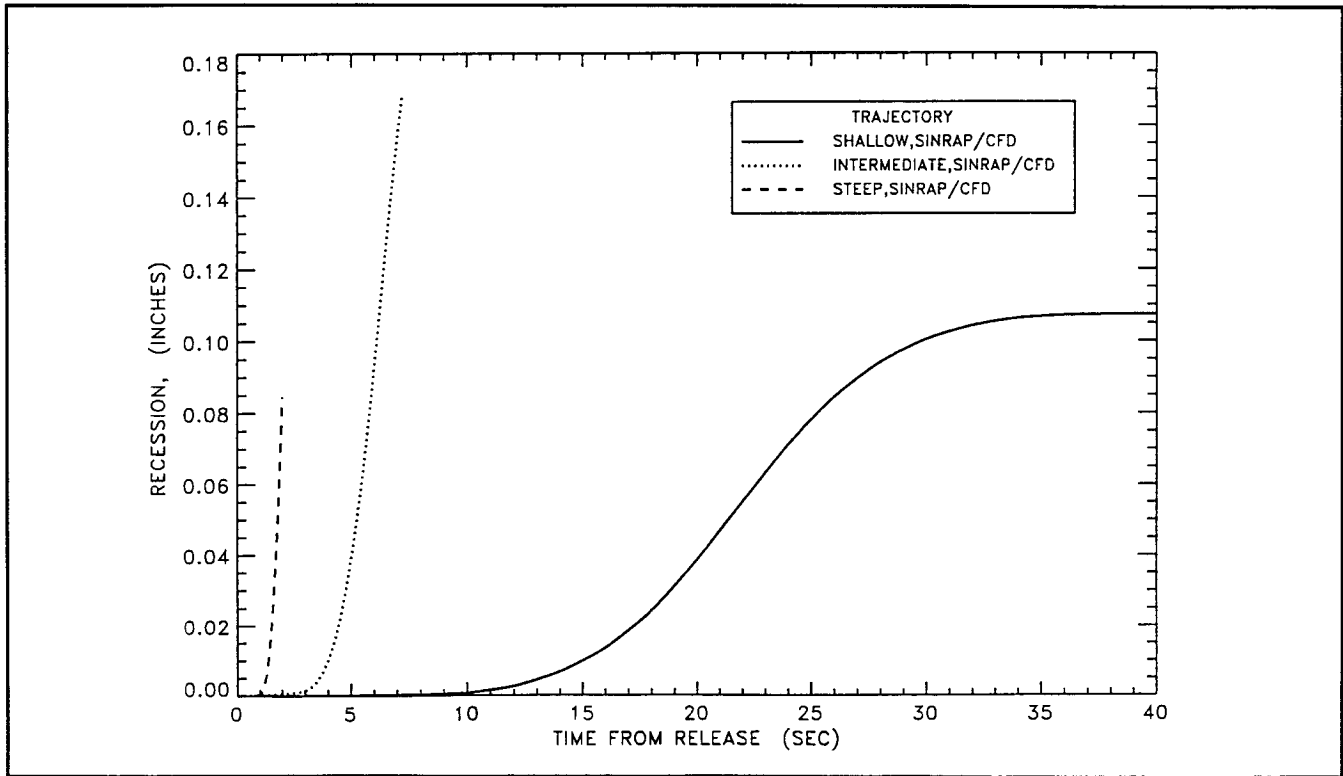
Figure 6.5.3-6. Comparison of the Stagnation-Point Recession along the Steep, Shallow, and Intermediate Trajectories

Thermostructural Results (Face-On Stable, Shallow Trajectory)

The FOS orientation provides a much more severe thermostructural environment than random-tumbling. Thermostructural analyses were performed at trajectory points that correspond to instances of peak thermal gradients, maximum stagnation point temperature, maximum reentry pressure and acceleration, and maximum surface ablation, as well as an intermediate point where combined load effects could be most severe.

Thermostructural results show that the aeroshell has sufficient structural capability to survive the shallow trajectory load conditions. For all but the high altitude point, minimum factors of safety were found to occur in the X direction near the center of the ablating surface due to bending induced by the aeropressure loads. (The X direction is defined as perpendicular to the flight path, in the plane of the front-face of the aeroshell, with Z direction defined as perpendicular to the aeroshell front-face.) The minimum factor of safety in stress in the X direction was found to be 1.47. However, significant structural capability still exists in the module, since the minimum factor of safety in strain (which is more significant) was found to be 3.87.

Thermostructural Results (Face-On-Stable Attitude, Steep Trajectory)

Four-trajectory points were analyzed along the steep trajectory, including the point of maximum stagnation-point thermal gradient through the wall thickness (t = 1.1 sec). The remaining three analysis points are at intermediate times in the trajectory up to and including the point at which structural failure of the aeroshell was predicted. It is important to note that the fourth analysis point occurs at only about half the maximum predicted aero loading for the aeroshell, and that the predicted front-face ablation is still rising rapidly.

The aeroshell fails at around t = 1.9 sec, which corresponds to an altitude of approximately 140 kft. Failure of the aeroshell in this context indicates the inability of the ablating surface to withstand further aero loading. Analytical predictions also indicate a 0.046 inch compression of the CBCF insulator by the bending aeroshell wall, sufficient to cause contact between the aeroshell and GIS in this region.

Thermostructural Results (Face-On-Stable Attitude, Intermediate Trajectory)

Analyses show that a FOS-oriented GPHS aeroshell will survive the shallow trajectory (-7°) with ample margin but will fail for steep (-90°) trajectory. Assuming release of the GIS following GPHS aeroshell failure, aerothermostructural analyses were performed to establish if the GIS survives reentry to impact. In order to bound these GIS analyses, a lower limit on the flight-path angle that will lead to GIS release was required.

Thermostructural analysis results for a γ = -20° trajectory show aeroshell front face failure occurring at t = 5.85 seconds (altitude = 160 kft). The minimum factors of safety in the X and Y directions are similar and are primarily a result of bending in the aeroshell ablating surface induced by the aeropressure loads.

Based on intermediate (γ = -20°) trajectory analysis results, an estimate was made of the reentry path angle above which aeroshell structural failure would nominally be predicted. The 160 kft failure altitude for the intermediate trajectory corresponds to a deceleration load of approximately 195 G's. Utilizing the plot of maximum deceleration load versus reentry path angle shown in Figure 6.5.3-7, and taking into account that the intermediate trajectory results slightly overpredict temperature and recession, a value of -16° was established for the critical reentry path angle for aeroshell failure.

Thermostructural Results (Tumbling Attitude)

The reentry analyses were performed primarily for the face-on-stable aeroshell attitude because this is the most critical condition. Due to lower temperature and ablations for the aeroshell, the random tumbling reentry can generally be considered less severe for the determination of aeroshell survivability. Despite this mitigation of stresses and strains for the random tumbling reentry, an assessment of aeroshell survivability for these conditions is still important to the probabilistic determination of aeroshell survivability. Transient SINRAP thermal analyses of a random tumbling aeroshell were performed for both the steep (-90°) and the intermediate (-20°) flight path angles. These SINRAP analyses did not incorporate CFD analytical techniques but were instead based on equilibrium heating values and extrapolated B' curves. This type of analysis has been shown to be somewhat conservative based on the results of FOS reentry analyses with CFD incorporated.
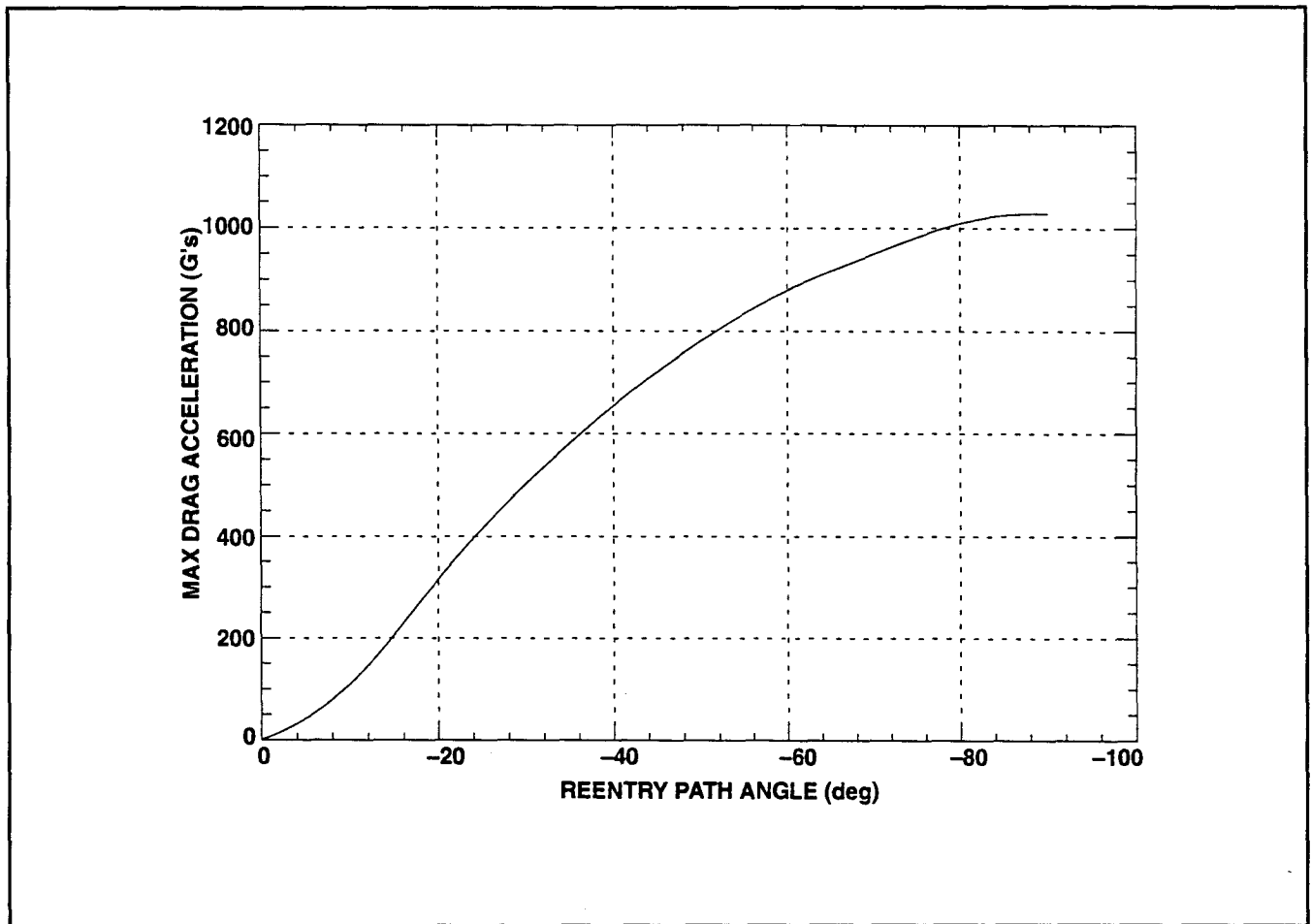
Figure 6.5.3-7. Maximum Drag Acceleration vs. Path Angle - Gravity Assist Reentry

Analysis of the shallow trajectory for a random tumbling aeroshell was not necessary because the aeroshell has sufficient structural capability to survive the same reentry conditions in the more severe FOS attitude. Similarly, since the FOS aeroshell failed structurally for the steep trajectory well before the peak heating and peak load conditions were reached, it can be inferred that the random tumbling aeroshell will also fail. As a result, the focus of the random tumbling analysis was the intermediate trajectory where FOS aeroshell survivability/failure is marginal.

Thermostructural analysis was completed for the intermediate trajectory (-20°) random tumbling reentry condition for the critical timepoint of t = 8.0 seconds where both maximum temperature and maximum load conditions are attained. An additional centrifugal force due to aeroshell tumbling was also applied to the model. This force was based on a nominal

tumbling rate of 500°/sec derived from motion studies and is relatively insignificant compared to the other forces on the aeroshell body.

Analysis indicates that the aeroshell has adequate structural capability to survive the reentry load conditions. The minimum factors of safety for X direction stress and strain are 1.093 and 1.189, respectively, indicating that the aeroshell has sufficient structural capability but cannot sustain much additional loading. In addition, some non-propagating local failures around the lock member are predicted for this load case. The Z direction minimum strain factor of safety of 3.486 indicates no critical loading in this direction, as temperature gradients are relatively minor for the random tumbling reentry.

The results of this random tumbling analysis, as well as the general trend of factor of safety versus deceleration load derived from the FOS analysis for the intermediate trajectory, were used to assess the critical angle for random tumbling aeroshell failure. The random tumbling aeroshell was estimated to fail at a deceleration load of 350 G's, which corresponds to a path angle of approximately -21°. As expected, this aeroshell failure threshold occurs at a higher angle than the -16° predicted for the FOS attitude

Effect of SEB on GPHS Survival/Failure Predictions

The GPHS transient-thermal analyses were repeated using the conventional surface energy balance (SEB) formulation. For the steep trajectory, structural failure occurs soon after release. Over this small time interval, the predicted module temperatures and surface recession were similar for both forms of the SEB.

For the shallow trajectory, the conventional SEB produces slightly higher temperatures over most of the trajectory. However, by 40 seconds (well past the peak heat pulse) the predicted temperatures from both SEBs are in good agreement while the conventional SEB yields 32% more recession than the LMMS SEB.

Use of the conventional SEB does not change the GPHS survival/failure results. With either SEB, the GPHS will fail at approximately 1.9 seconds on the steep trajectory. The module will also survive on the shallow trajectory for both forms of the SEB. Although the conventional SEB yields more recession for the shallow trajectory, the module will survive because the minimum factor of safety, which occurs at peak load, is reached at 26 seconds where both SEBs predict ample margin. Beyond 26 seconds, the load rapidly decreases,

so that, despite the enhanced thinning of the aero shell with the conventional SEB, the GPHS is predicted to survive.

Use of the conventional SEB will change the estimate for the critical reentry angle from -16° to about -14°.

6.5.3.3.3 GIS Aero/Thermo/Structural Results

GIS Orientation During the Heat Pulse

The orientation history of the GIS is determined by a combination of:

1. Initial conditions (orientation and rates)
2. Mass properties
3. Static-stability characteristics.
4. Dynamic-derivatives (such as the pitch-damping derivative, Cm_q)

A full six degree-of-freedom (6DOF) Monte Carlo simulation, with non-linear aerodynamics, has been utilized following release of the FSAR to determine the statistical distribution of GIS orientation during the heat pulse, following release from a failed GPHS module. This Monte Carlo assessment was performed for release of a GIS from either a face-on stable or random tumbling GPHS module.

Initial conditions (pitch, yaw, and roll rate, and angle-of-attack and angle-of-sideslip) for the GIS are derived from the dynamic conditions of the GPHS module at the time of release. The module dynamic conditions at release have been determined by JHU/APL for those cases where the module is face-on stable (FOS). Due to the symmetry, the pitch and yaw rate distributions are assumed to be identical. APL reports the module roll rate to be no more than 4000 deg/sec with an average value of approximately 1500 deg/sec. Also, the initial angle-of-attack for the FOS module can lie within 30 degrees of fully broadside. It has been assumed that the initial rates (pitch, yaw, and roll), for a random tumbling GPHS module, will be uniformly distributed between ±5000 deg/sec in each axis. Further, the initial angle-of-attack may be uniformly distributed between ±180 degrees.

GIS aerodynamic characteristics are based on the MHW-Heat Source Assembly (HSA), which is a cylinder with a length-to-diameter ratio very close to that of the GIS (approximately 2). The MHW-HSA aerodynamic data was obtained in a wind-tunnel test

series (at Mach 10) conducted by GE (Reference 6.5.3-22). The aerodynamic characteristics indicate that the GIS can statically stabilize in two orientations, broadside (90°) and near end-on (22°). The broadside orientation is, by far, the dominant condition. However, there is a finite potential for a near end-on orientation through the heat pulse.

The thermal-pulse duration for the GIS is approximately 5 seconds for the intermediate flight-path angle. This motion study determined how quickly the GIS will attain a stable orientation if it is initially given a high pitch/yaw rate from the GPHS at release.

Figure 6.5.3-8 shows the time required to attain a stable broadside orientation following release from a face-on stable (FOS) GPHS module, as determined from 1000 6DOF Monte Carlo trials. As shown, 60% of the samples stabilize broadside within 0.1 seconds of release. Further 80% stabilize broadside within 1 second and 98% within 3 seconds (the maximum is 3.2 seconds). None of the samples stabilized end-on.
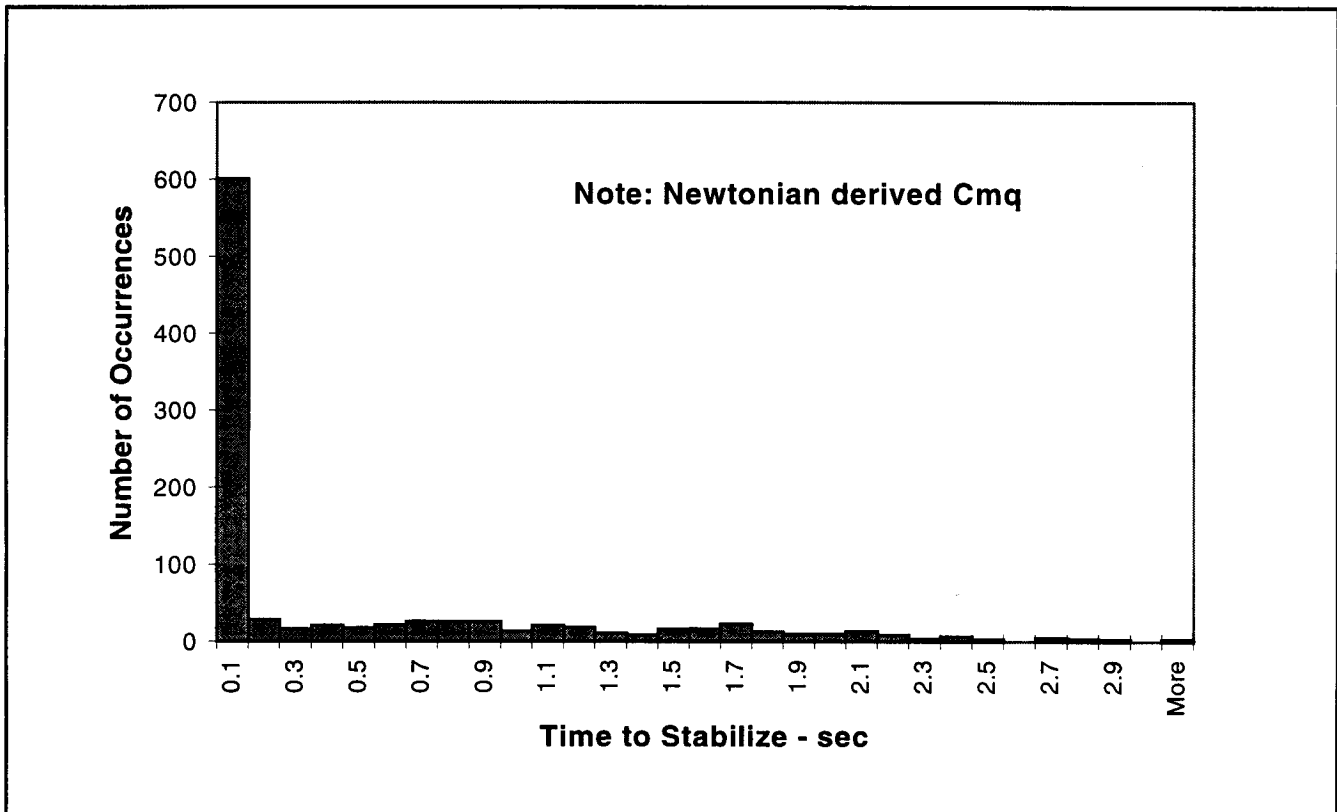
**Figure 6.5.3-8. Time to Stabilize "Broadside" for GIS
(Following Release from Face-On Stable Module) -20° Flight Path Angle/EGA**

Similarly, Figure 6.5.3-9 shows the time required to attain a stable orientation following release from a random tumbling GPHS module, as determined from 1000 6DOF Monte Carlo trials. As shown, 22% of the samples stabilize broadside within 0.1 seconds of release and 50% stabilize broadside within 1 second. The maximum time to stabilize is 2.3 seconds. One sample out of the 1000 trials stabilized end-on through the heat pulse.
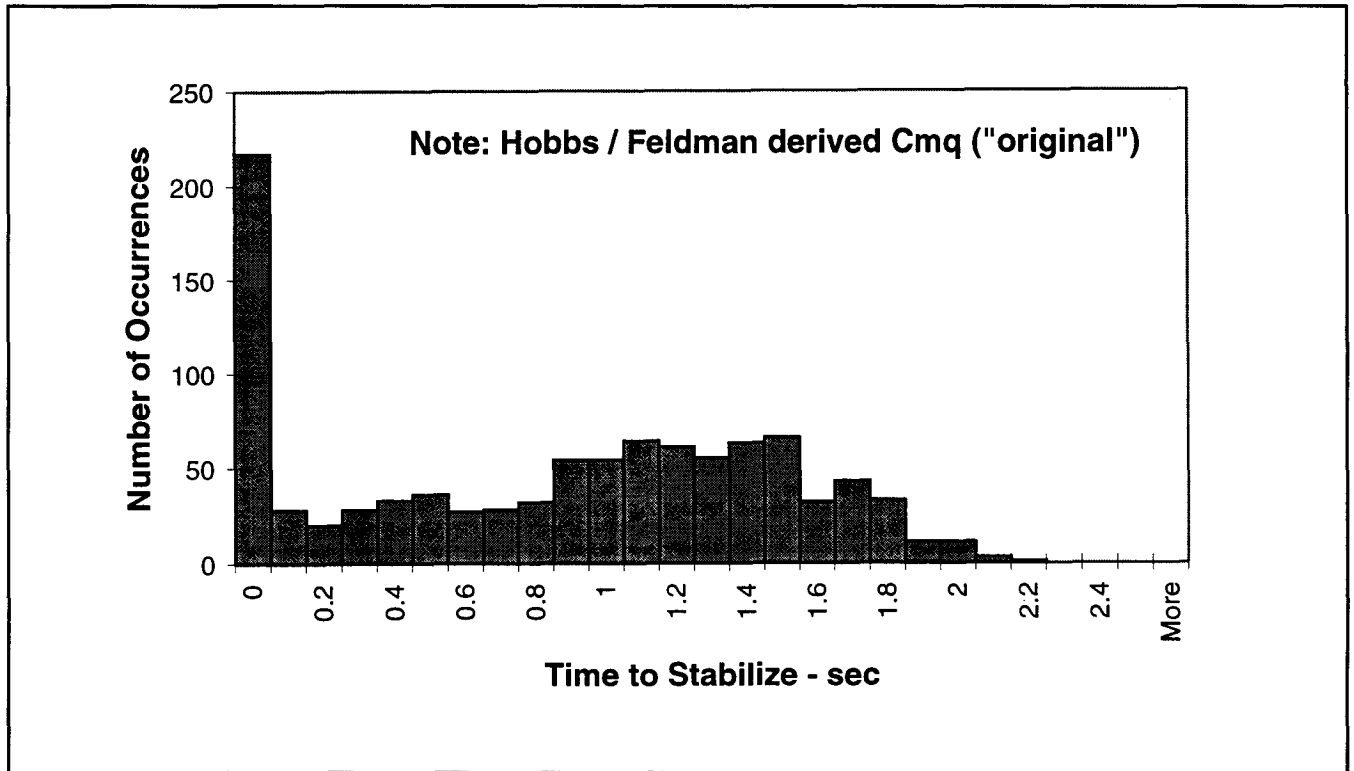
**Figure 6.5.3-9. Time to Stabilize "Broadside" for GIS
(Following Release from Tumbling Module) -20° Flight Path Angle/EGA**

The GIS is considered to be effectively spinning (from a thermal response perspective) if the roll rate is greater than 0.2 rev/sec (72 deg/sec). Based on the roll rate distribution at separation, as shown in Figure 6.5.3-10, 98.3% of all cases will be effectively spinning during the heat pulse for release from a FOS GPHS module. It is also expected that 97% of all cases, for release from a random tumbling module, will be spinning.
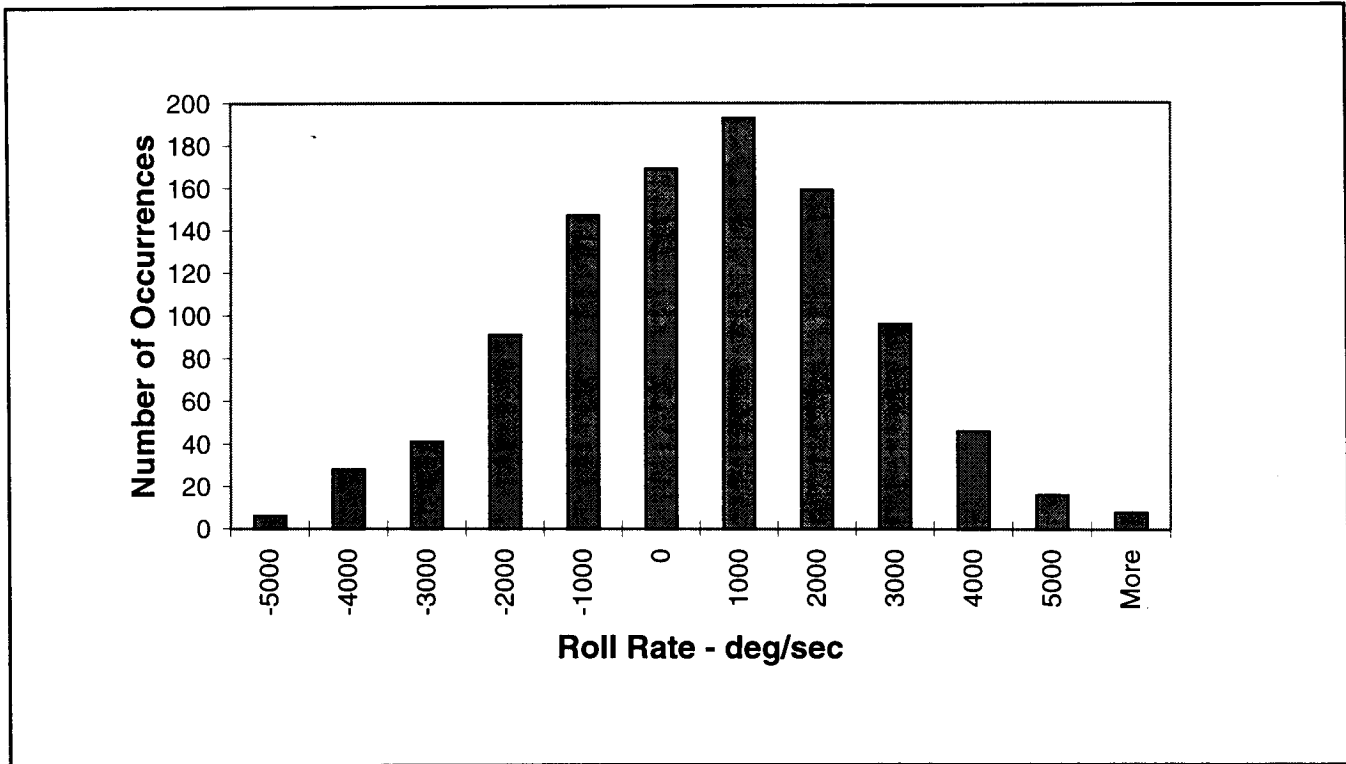
Figure 6.5.3-10. GIS Roll Rate Distribution (FOS Module)

These 6DOF motion studies show that the GIS effectively stabilizes broadside, through the heat pulse, for all releases from the GPHS module, whether face-on stable or random tumbling. Further, it is expected that the GIS will be effectively spinning for 97% to 98% of all cases, for release from a random tumbling or FOS GPHS module, respectively. With spin, the resultant spin-averaged heat fluxes are substantially reduced from the nonspinning levels.

GIS Aero/Thermal Analysis

The stagnation-streamline versions of the nonequilibrium, chemically reacting, Navier-Stokes flowfield code (RACER), and the nonequilibrium flowfield radiation code (LORAN-C), have been applied to compute the net-heat flux and ablation-rate of the GIS cylinder for the intermediate and steep trajectories. The GIS initial conditions for this analysis are shown in Table 6.5.3-5. Based on motion studies, the GIS is assumed to be oriented broad-side stable for these analyses. The analysis also assumes a nonspinning GIS because this provides worst-case heating. In addition, the nonspinning GIS heating can be systematically reduced (spin averaged) to predict temperatures and recession for a spinning GIS.

Table 6.5.3-5. GIS Release Conditions from FOS GPHS

Parameter	Initial Conditions	
Initial Aeroshell Reentry Angle	-90°	-20°
Time of GIS Release (sec)	1.9	5.85
Altitude (ft)	139,705	159,925
Velocity (ft/sec) (Relative)	56,820	55,192
Path Angle (deg) (Relative)	-88.624	-18.854
Component Nodal Temperatures (°R) GIS Iridium Clad Fuel	 2649 2834 3022-3327	 2752 2834 3022 - 3327

As with the previous GPHS module computations, the flowfield and radiation calculations were coupled by iterative applications of the codes (usually four-to-five cycles of RACER and LORAN-C were sufficient).

The detailed RACER/LORAN-C aerothermochemical analyses of the GIS were performed for the steep (γ = -90°) and intermediate (γ = -20°) trajectories. These trajectories encompass the wide range of path angles for potential GIS release from the GPHS module.

Transient, in-depth heating analyses of the GIS were then performed using a version of the REKAP code (modified to obtain the net surface heat-flux and ablation-rate along the trajectory by interpolating the RACER/LORAN-C solutions). Two solutions were obtained for each trajectory. One solution is based on the conventional surface energy balance (SEB), the other uses the SEB developed by Lockheed Martin.

The conventional SEB for an ablating, chemically reacting surface represents an upper bound for heating because of its treatment of the near-wall, gas-phase reactions. In the conventional SEB, it is assumed that the heat released by these homogeneous reactions is totally transferred to the surface. Alternatively, in the Lockheed Martin SEB, it is assumed that this heat is transferred to the adjacent gas-phase and is indirectly passed to the surface by an increased convective and/or radiative heat flux. Under high ablation conditions, the real scenario is expected to be closer to the Lockheed Martin model.

The REKAP prediction of the surface temperature history of the GIS along the steep trajectory is shown in Figure 6.5.3-11. Upon release from the GPHS, the GIS surface temperature rises, almost immediately, from 2667°R to 8000°R. As expected, use of the conventional SEB results in higher temperatures, with a peak value of 8400°R. After the initial temperature jump, the surface of the GIS begins to cool (within 1 second from release). At 2 seconds from release the temperature has dropped below 7000°R. The corresponding recession history is shown in Figure 6.5.3-12. Use of the conventional SEB yields more recession, however, burn-through does not occur.
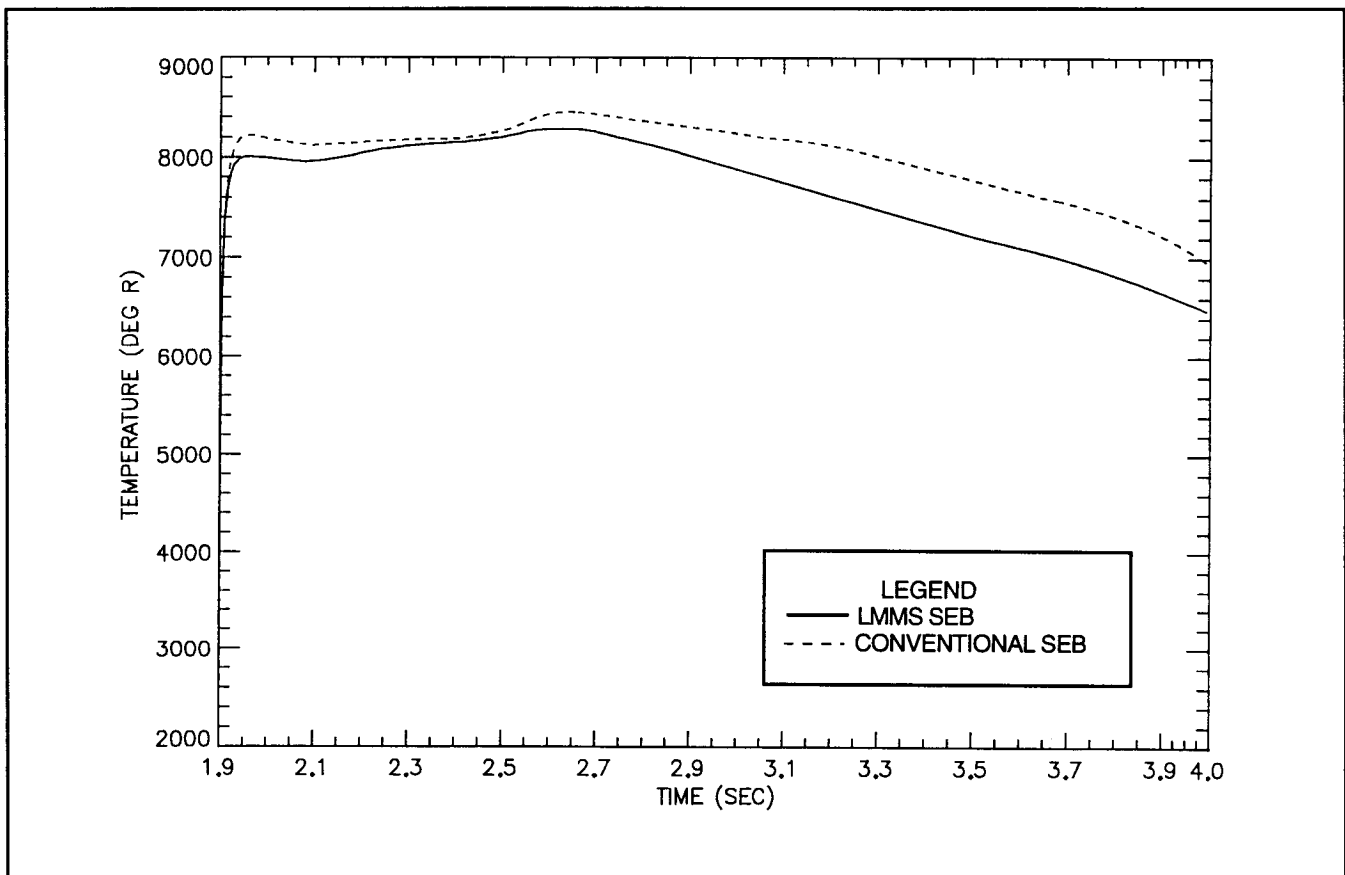
Figure 6.5.3-11. GIS Surface Temperature History. Non-Spinning, Broad-Side Stable along the Steep Trajectory
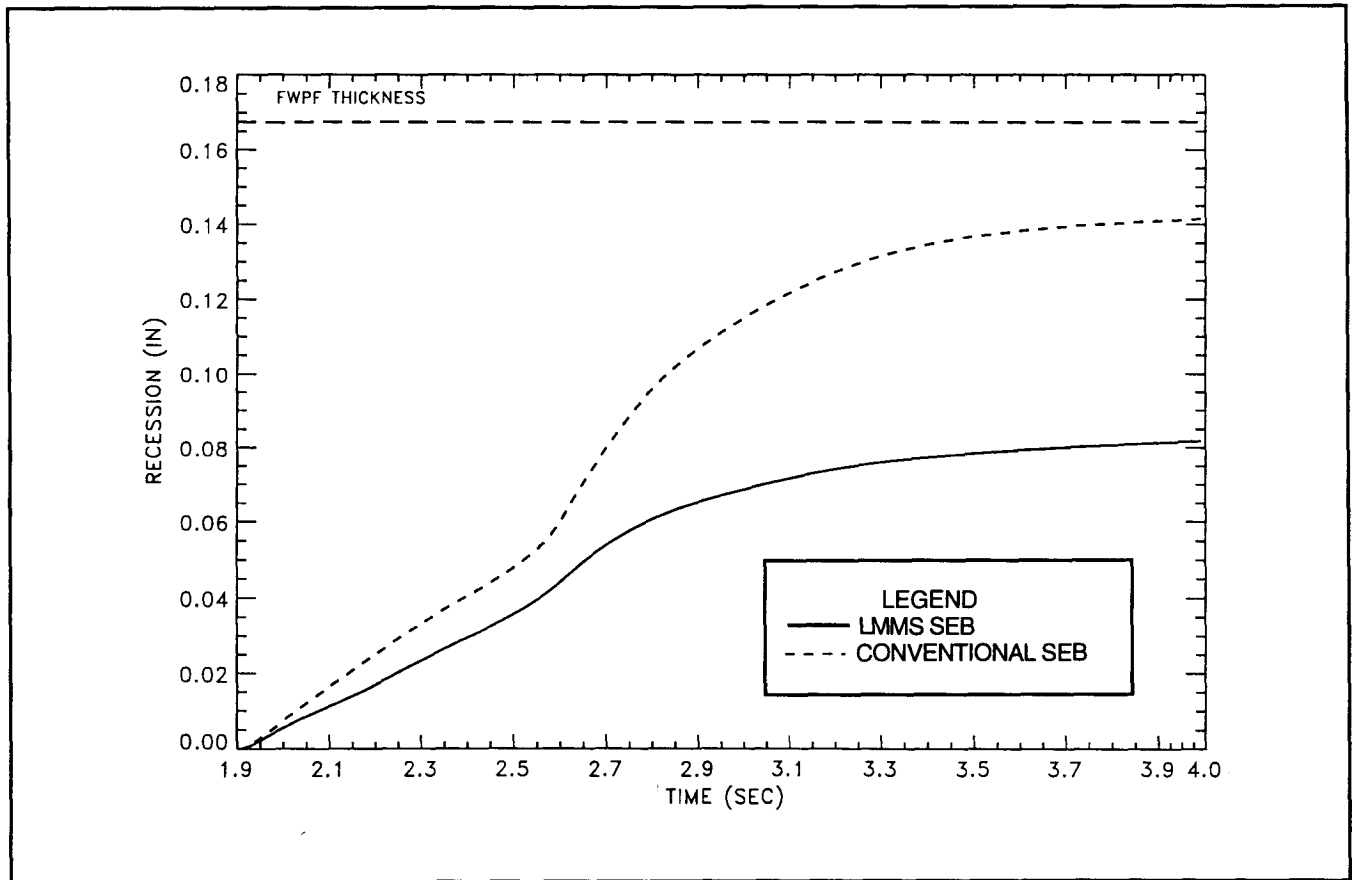
Figure 6.5.3-12. GIS Recession History. Non-Spinning, Broad-Side Stable along the Steep Trajectory

The predicted temperature history of the GIS along the intermediate trajectory is shown in Figure 6.5.3-13. On this trajectory, the surface temperature stays below 8000°R, but remains above 7000°R for almost 5 seconds. The net heat-flux levels are less than those encountered on the steep trajectory, but because of the longer duration of the heat pulse, recession is about 25% greater (as shown in Figure 6.5.3-14). With the conventional SEB, marginal burn-through will likely occur. However, as shown by the motion studies, the broad-side stable GIS will be spinning (about its long axis) for over 98% of all releases. This spinning motion will greatly reduce recession heat pulse so that burn-through will not occur for either SEB.
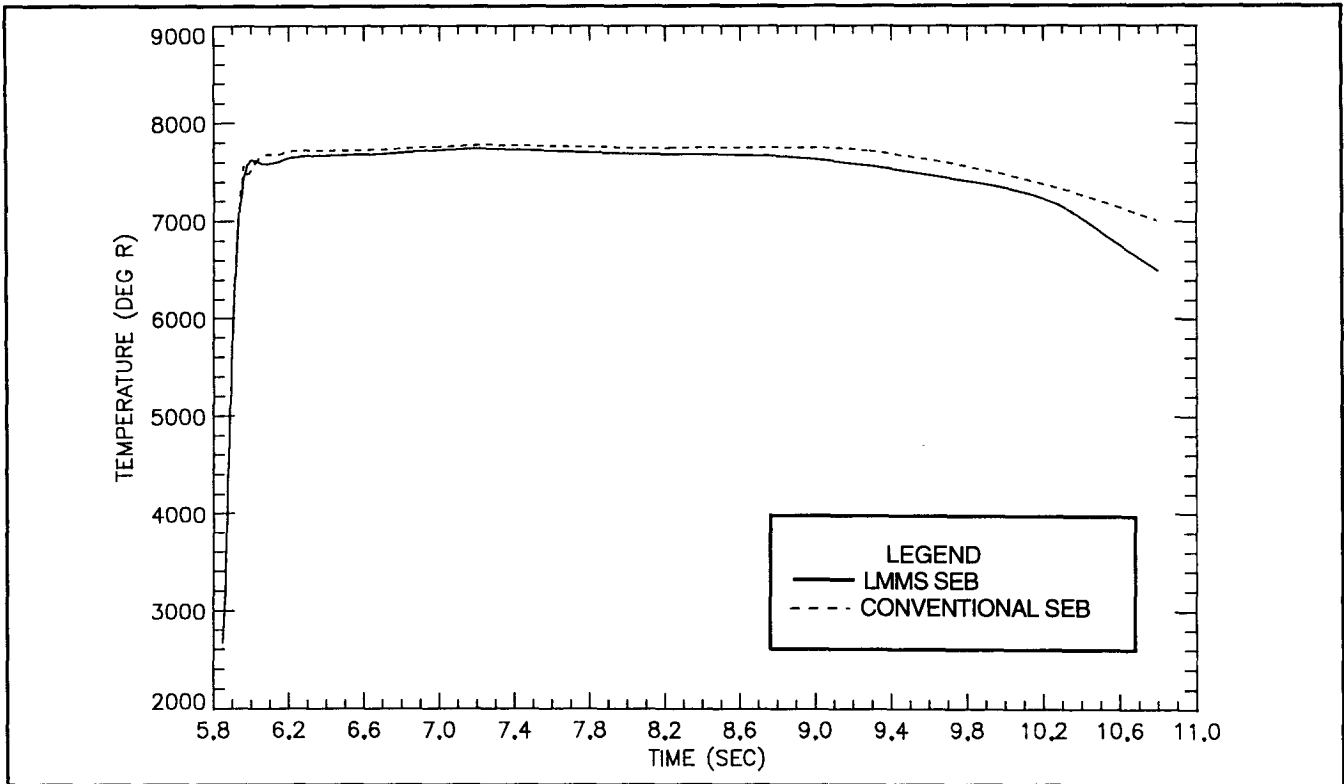
Figure 6.5.3-13. GIS Surface Temperature History. Non-Spinning, Broad-Side Stable along the Intermediate Trajectory
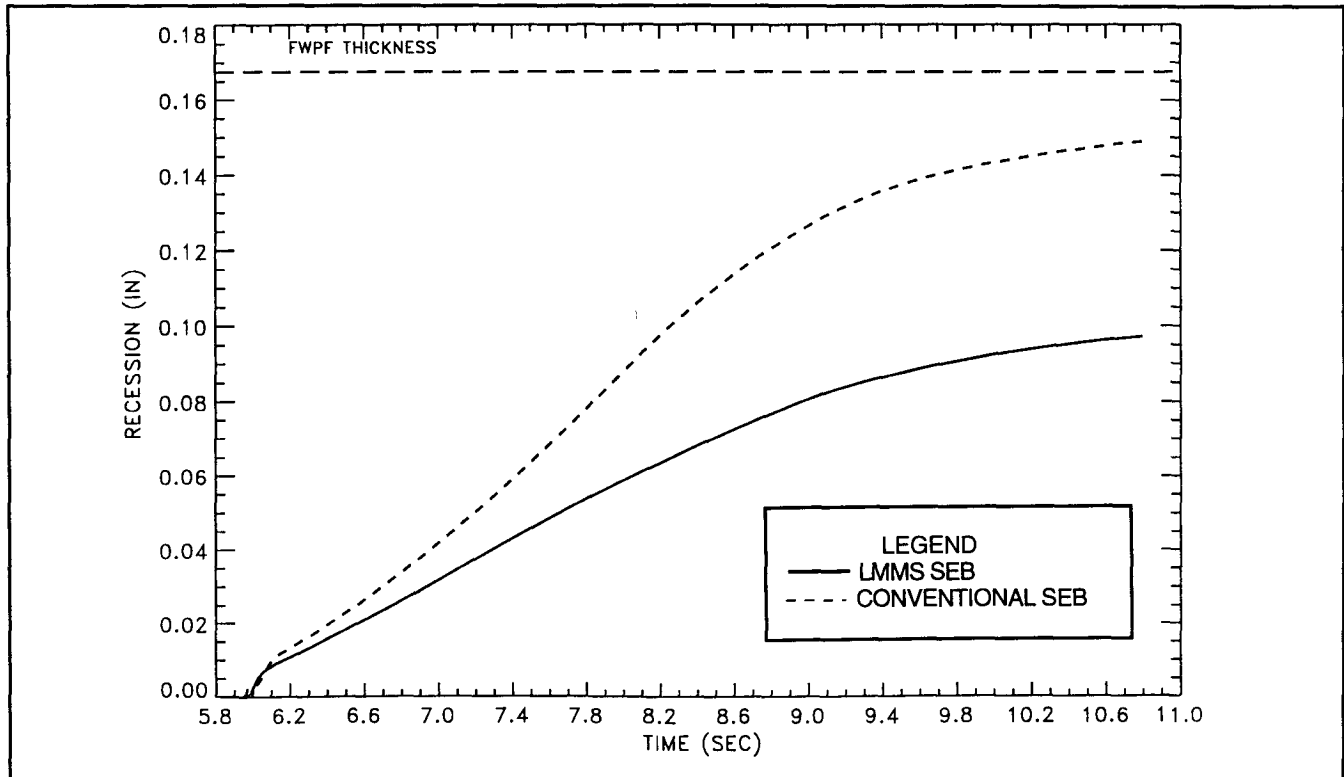
Figure 6.5.3-14. GIS Recession History. Non-Spinning, Broad-Side Stable along the Intermediate Trajectory

GIS Thermostructural Analysis (Non-Spinning)

Three points on the steep trajectory were selected for detailed analysis. These points represented critical times in the trajectory, specifically the maximum thermal gradient condition (t = 2.01 secs), the combined maximum temperature and deceleration load condition (t = 2.67 secs), and a critical ablation condition (t = 4.00 secs).

Load conditions at the various trajectory points are summarized in Table 6.5.3-6. The peak GIS temperatures and decelerations are comparable to those predicted for the aeroshell for the steep trajectory. As shown in Figure 6.5.3-15, the GIS decelerates rapidly following release, attaining maximum temperature and load conditions within the first second after being exposed to the flow. Thermal gradients are extremely high because of the sudden exposure to the reentry environments. Ablation rises rapidly before leveling off around t = 4.0 seconds as the loads and temperatures drop rapidly.

Table 6.5.3-6. Summary of Load Cases for GIS Assembly, Steep (-90°) Trajectory, 139.7 kft Release

	Analysis Time (secs)		
	2.01	2.67	4.00
Altitude (kft)	134.1	104.0	70.5
Flight Condition	Maximum Gradient	Maximum Temperature & Load	Critical Recession
GIS Weight (lbs)	1.11	1.03	0.99
Accel. Load (G's)	388.3	960.0	314.6
Stagnation Pt. Data			
Temperature (°F)	7642	8050	6109
Gradient (°F)	5146	2196	-104
Ablation (in)	0.0063	0.0902	0.1351
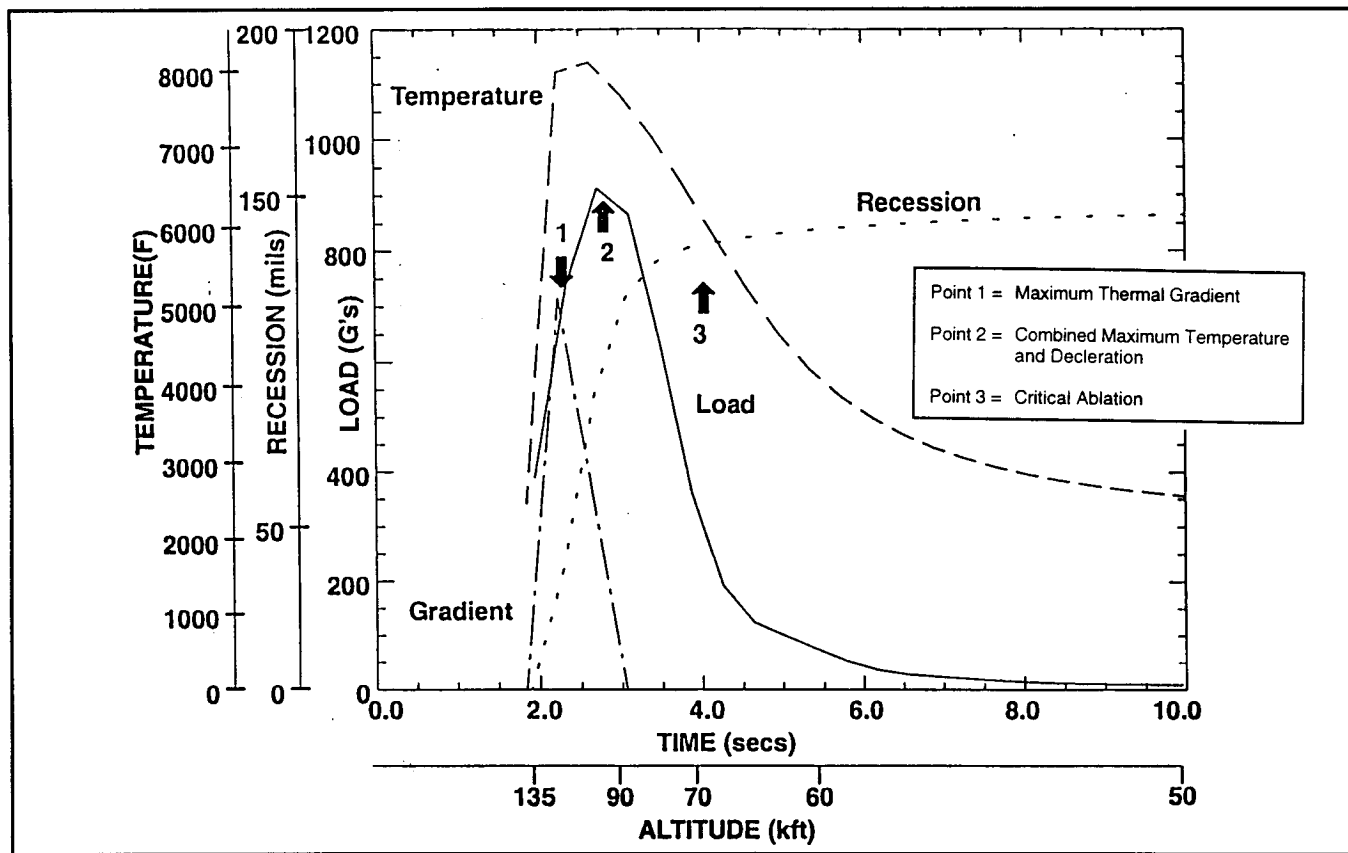
Figure 6.5.3-15. Critical Flight Data at Stagnation Point vs. Time - GIS Assembly Steep (-90°) Trajectory, Side-On-Stable Attitude, 139.7 kft Release

Stresses in the X direction are higher than those in the Y direction because of the asymmetrical loading of the inside of the GIS by the fueled clad as it shifts forward during reentry. The minimum predicted stress and strain factors of safety in the X direction of 1.42 and 2.40 occur at t = 2.67 seconds and indicate sufficient structural capability to withstand reentry load conditions.

Stresses and strains in the Z direction of the GIS are caused principally by the extreme thermal gradients resulting from the rapid reentry heating of the body, which causes much higher thermally-induced expansion on the outer surface of the GIS than on the inside. The factor of safety in stress reaches a minimum of approximately 1.0 at t = 2.67 seconds, which would seem to indicate potential GIS failure based on stress evaluation criteria. However, the Z factor of safety in strain at this time is 2.46, which demonstrates that the GIS does indeed retain structural capability. The critical area of the GIS is the outer surface near the cap, which is at a temperature approaching 8000°F. The material at this temperature is exhibiting perfectly-plastic behavior, in which the stress has reached its maximum value but

strain capability still remains. However, this is a highly localized stress and only the outer surface of the GIS cannot sustain additional loading, while the majority of the shell has significant structural capability remaining.

Thermostructural analysis of the GIS was also conducted for the intermediate (-20 degree) reentry condition. A total of four points along this trajectory were analyzed in detail, representing critical times in the trajectory for the maximum gradient condition (t = 6.05 secs), the maximum temperature condition (t = 7.85 secs), the peak deceleration load condition (t = 8.45 secs), and a critical ablation condition (t = 10.95 secs).

Load conditions at the various trajectory points are summarized in Table 6.5.3-7. The peak GIS temperatures and decelerations are much lower than the maximum values obtained for the GIS from the steep trajectory analysis. Also, due to the longer-duration reentry heating environment, thermal penetration into the GIS is increased such that the gradients are much lower than those for the steep trajectory at the comparable times of peak deceleration loading. This implies that the entire GIS is at an elevated temperature during the critical loading phase of the intermediate trajectory.

Table 6.5.3-7. Summary of Load Cases for GIS Assembly,
Intermediate (-20°) Trajectory, 159.9 kft Release

	Analysis Time (secs)			
	6.05	7.85	8.45	10.95
Altitude (kft)	156.4	128.5	121.1	101.2
Flight Condition	Maximum Gradient	Maximum Temperature	Maximum Load	Critical Recession
GIS Weight (lbs)	1.12	1.05	1.03	1.00
Accel. Load (G's)	159.6	286.0	293.3	157.6
Stagnation Pt. Data				
Temperature (°F)	7130	7422	7298	6204
Gradient (°F)	4522	330	64	−22
Ablation (in)	0.0044	0.0793	0.1023	0.1378

The minimum X, Y, and Z factors of safety in stress and strain indicate adequate structural capability in the GIS to withstand the reentry loading environment.

6.5.3.3.4 Fuel

Particle Size and Mass Distribution Results

The post-reentry mass and particle size distribution has been determined over a range of potential fuel release conditions from the GIS. These release conditions, in general, correspond to assumed GIS wall recessions from 75% to 85% for -20 degree and -90 degree EGA reentry flight path angles. Table 6.5.3-8 provides a summary of these conditions.

Table 6.5.3-8. Release Conditions Evaluated

Reentry Flight Path Angle (deg)	Percent GIS Wall Recession	Altitude (ft)	Velocity (ft/s)	Inertial Flight Path Angle (deg)
-20	75	110456	25628	-18.645
-20	80	104655	19939	-18.665
-20	85	101160	12331	-18.791
-90	75	82807	23668	-90
-90	80	72883	13430	-90
-90	85	57044	2181	-90

The two cases most likely representing potential fuel release conditions are the 85% recession at -20 degree flight path angle and the 80% recession at -90 degree flight path angle. Releases at lower altitudes for these two cases result in a thermal environment so benign as to not melt or vaporize the fuel fragments, while GIS recessions at higher altitudes are probably insufficient to yield a release of fuel.

For the above cases nearly half of the fuel will remain intact and continue to a surface impact. The remaining half will melt and stabilize into microspheres 2 to 50 μm in diameter. These microspheres will further lose 30% to 60% of their mass to vaporization.

The melting/vaporization process, for a given reentry, occurs within a very narrow band of altitude, between 23 and 25 km for a steep (-90°) reentry and 30 to 32 km for an intermediate (-20°) reentry. The melt is completed within one to two seconds while the vaporization occurs within 100 to 200 msec.

Figures 6.5.3-16 and 6.5.3-17 show the mass/particle size distributions per GIS for the above two cases binned into the same 12 bins defined for the LASEP-T launch accident models. The quantities within each mass bin represent in ascending order the cumulative total mass originating from the 841 to 2000 μm and 2000 to 6000 μm initial particle size groups. The quantity above each bar represents the total bin mass. Total mass within the "intact" bin represents the residual particle mass which did not experience melting. All of the particles in this bin exceeded 500 μm in diameter and are considered to be in the 12th bin for consequence analysis.

The mass release distribution illustrated above is assumed to be representative of releases, accounting for uncertainty, from both an end-on stable and a broadside stable, non-spinning GIS orientation.

BIN	MIN. DIA. (μm)	MAX. DIA. (μm)
1	<0.1	0.1
2	0.1	0.215
3	0.215	0.464
4	0.464	1.0
5	1.0	2.15
6	2.15	4.64
7	4.64	10.0
8	10.0	21.5
9	21.5	46.4
10	46.4	100.0
11	100.0	215.0
12	215.0	>215.0
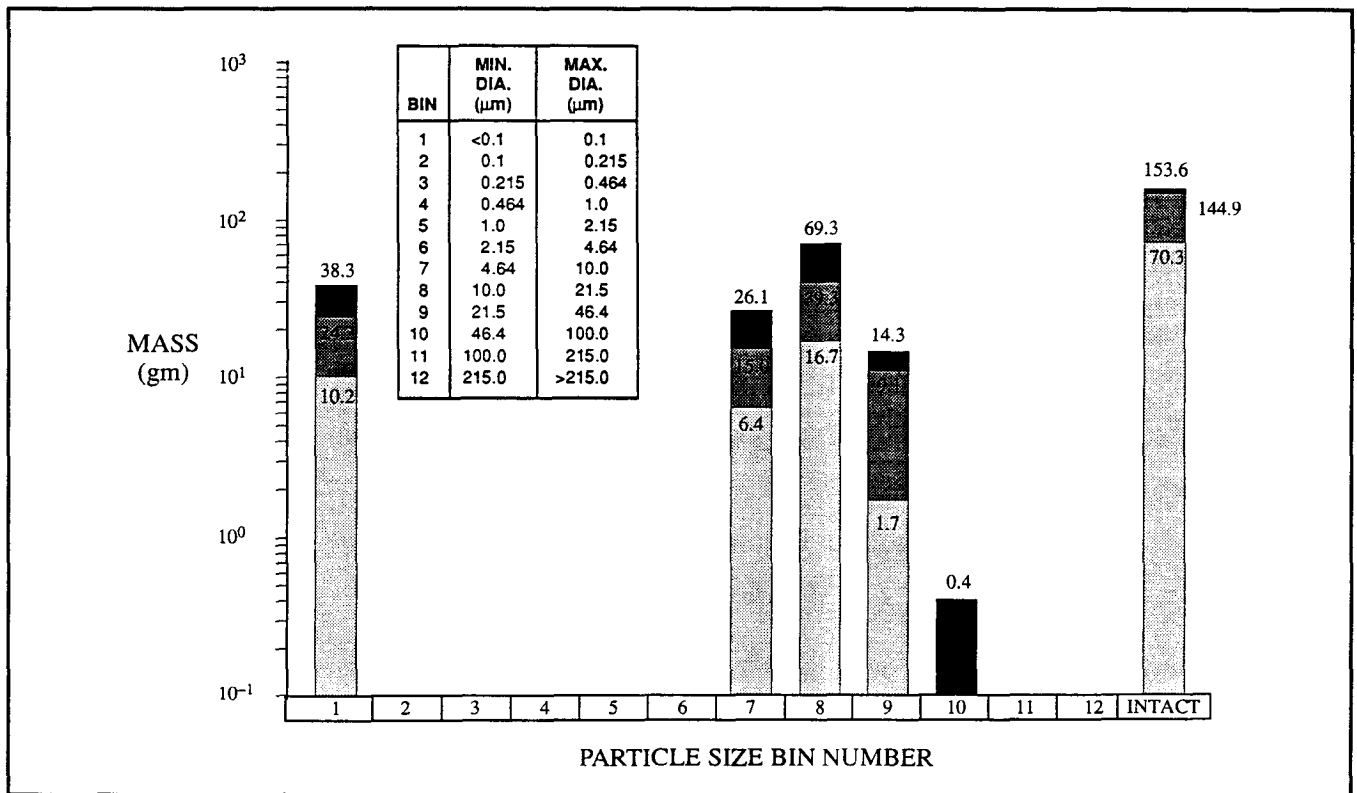
Figure 6.5.3-16. Particle Size Distribution for γ = -20°, Fuel Released at 85% GIS Ablation

BIN	MIN. DIA. (µm)	MAX. DIA. (µm)
1	<0.1	0.1
2	0.1	0.215
3	0.215	0.464
4	0.464	1.0
5	1.0	2.15
6	2.15	4.64
7	4.64	10.0
8	10.0	21.5
9	21.5	46.4
10	46.4	100.0
11	100.0	215.0
12	215.0	>215.0
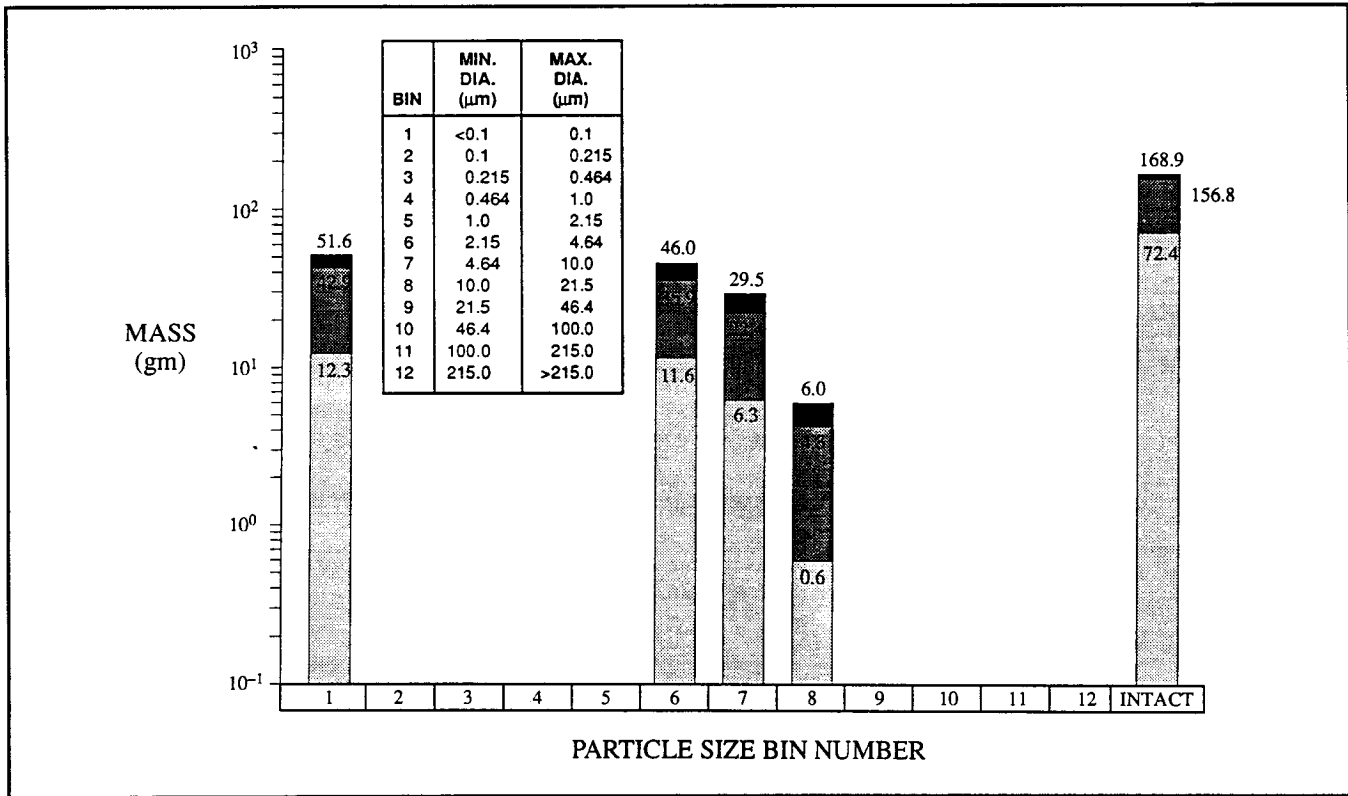
Figure 6.5.3-17. Particle Size Distribution for γ = -90°, Fuel Released at 80% GIS Ablation

6.5.3.4 EGA Variability Treatment

Reentry from Earth Gravity Assist is more complex than out-of-orbit reentry, as a result of the higher reentry velocity from EGA. The GPHS module and its components, the GIS and the fueled clad, may or may not survive reentry, depending upon the initial conditions of the reentry such as reentry angle, module orientation, module spin rate, etc. Furthermore, the sequence of events cannot be described in a deterministic fashion since the motion of the module or GIS can be chaotic.

Therefore, reentry from EGA is modeled using an event tree which explicitly describes the various possible sequences of events which may occur.

Variability assessments identify variations in atmospheric conditions (primarily density) to be the principal source of variability in the reentry response calculations. As the impact of atmospheric density variations on response results was found to be insignificant, variability in aeroshell, GIS and fuel response did not alter the nominal branch point probabilities defined in the event tree.

There are a small number of outcomes of the EGA event tree which involve fuel release. One of the event tree outcomes, GPHS module impact on rock, is modeled using MIM, which includes variability. Fixed source terms are used for the other outcomes. Some of the final branchings depend upon the type of surface impacted by the GPHS module or module component. Therefore the consequence calculation samples impact sites, using the same grid as used by the out-of-orbit reentry calculation.

Thus, reentry from Earth Gravity Assist is modeled as having a small number of discrete source terms and one variable source term.

The event tree is shown in Figure 6.5.3-18 through 6.5.3-20. Figure 6.5.3-18 is the top level event tree. Figures 6.5.3-19 and 6.5.3-20 are continuations. Conditional probabilities are shown in the ovals representing intermediate events and in the diamonds representing outcomes. The probabilities shown were used for FSAR analyses. Revised probabilities from post-FSAR GIS analyses described earlier in this section are not included. The possible sequences of events covered by the tree are the following:

1. The aeroshell of the GPHS module fails or does not fail.

2. If the aeroshell fails, the GIS is released or is not released.

3. If the aeroshell fails, the GIS fails or does not fail. (This can occur if the GIS is released or if the GIS is not released.)

4. If the GIS does not fail, the fueled clad melts or does not melt.

The complexity of the event tree reflects the fact that probabilities of the events typically depend upon the sequence of prior events. For example, the probability of aeroshell failure depends upon the reentry angle (steep or shallow) and upon the orientation of the module (face-on-stable or non-face-on-stable).

The first branch point (vertex) in the event tree is steep reentry versus shallow reentry. The conditional probabilities are given as P_1 and P_2 since the probability distributions for angle of reentry are dependent upon the latitude of reentry. Conditional probabilities for aeroshell failure for steep reentry with the module in the non-face-on-stable orientation are also dependent upon latitude and are given as P_3 and P_4. The conditional probability for aeroshell failure is 0.0 for shallow reentry, for any orientation, as discussed in Section 5.3.

Figure 6.5.3-18. VVEJGA GPHS Reentry Event Sequence Diagram

- FOS = Face-On-Stable

- P_3 and P_4 are equal to the probabilities of reentry at angles greater than or less than, respectively, the -21° threshold angle for non-FOS aeroshell failure

- P_1, P_2, P_3, P_4 calculated from NASA-JPL PDFs for each latitude band

- Pr, Pw & Ps provided by sampling worldwide database for each of 720 global cells

Figure 6.5.3-19. Reentry Sequence Diagram for Aeroshell Failure, Non-Face-On-Stable, Steep Reentry
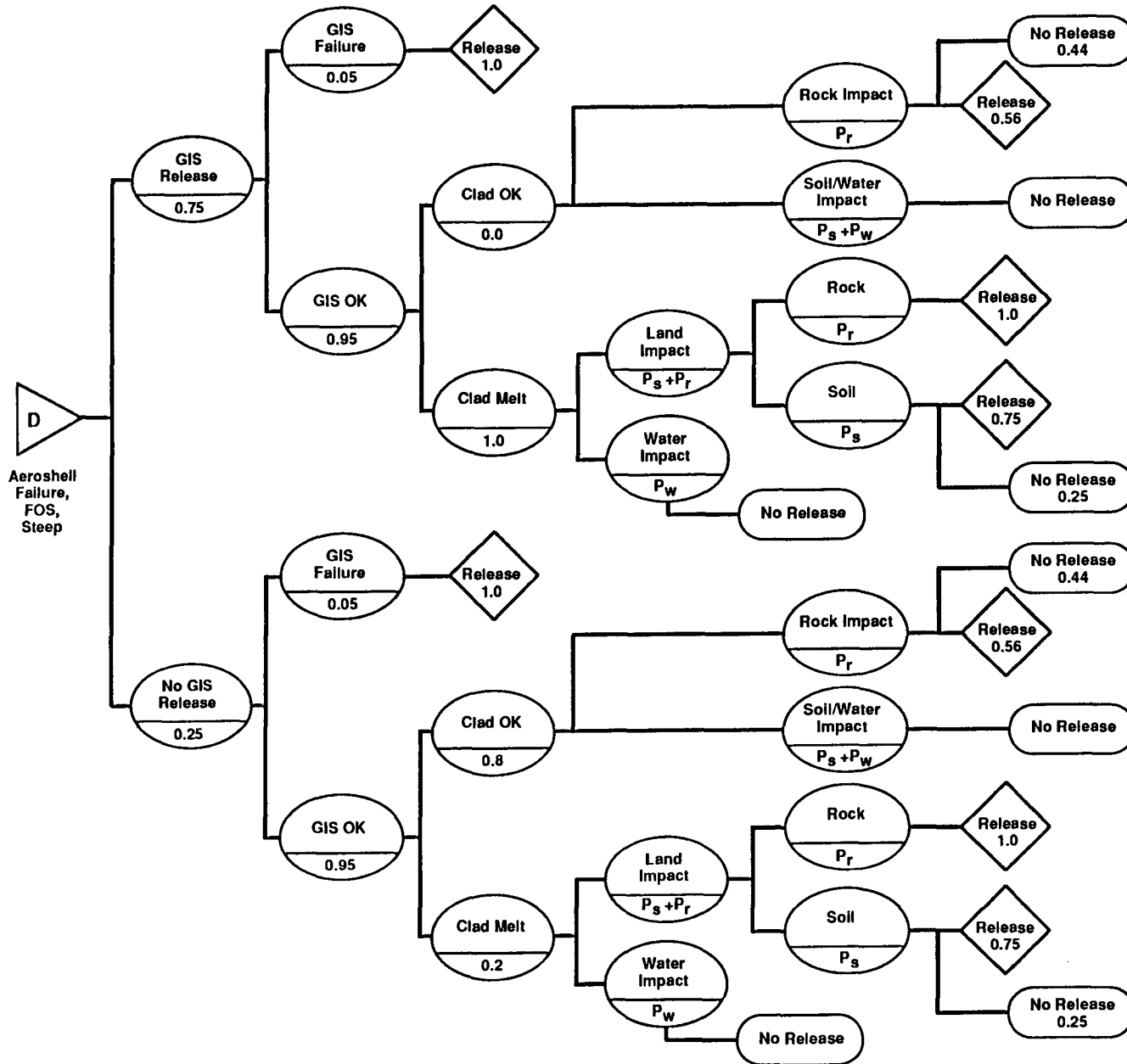
Figure 6.5.3-20.   Reentry Sequence Diagram for Aeroshell Failure, Face-On-Stable, Steep Reentry

If the aeroshell does not fail, the GPHS module impacts the Earth's surface. Fuel is only released in the event of rock impact (conditional probability = 0.56). The event tree for aeroshell failure is continued in Figures 6.5.3-19 and 6.5.3-20. These sub-trees have vertices for GIS release versus non-release, GIS failure versus non-failure, and clad melt versus clad OK, in the event of GIS non-failure. If the GIS fails, some of the fuel is released in the atmosphere and the remainder on the ground. If the GIS does not fail and the clad does not melt, fuel is only released if the GIS strikes rock (conditional probability = 0.56). If the GIS does not fail, but the clad melts, fuel is released for impacts on rock (conditional probability = 1.0) and for impacts on soil (conditional probability = 0.75).

6.5.3.5 EGA Source Terms

The following EGA event tree outcomes lead to fuel release:

1. Aeroshell No Failure - GPHS Module Impacts Rock

2. Aeroshell Failure - GIS OK - Clad OK - GIS Impacts Rock

3. Aeroshell Failure - GIS OK - Clad Melts - GIS Impacts Rock

4. Aeroshell Failure - GIS OK - Clad Melts - GIS Impacts Soil

5. Aeroshell Failure - GIS Failure

Source terms for these outcomes were developed as following:

1. Source terms for GPHS modules striking rock are calculated using the Module Impact Model (MIM) developed for out-of-orbit reentry.

2. The source term for outcome #2, GIS OK - Clad OK - Rock impact is the measured particle size distribution for released fuel from BCI test #5. In this test a fueled clad struck a steel target at a velocity of 53 meters/second, releasing 0.0073 grams of fuel. This test result was chosen since the particle size distribution of the released fuel had been measured and the velocity was reasonably close to the GIS terminal velocity of 61 meters/second.

3. The source term for outcome #3, GIS OK - Clad Melts - GIS Impacts Rock is the contained particle size distribution for BCI test # 31. In this test a fueled clad struck a concrete target at 61 meters/second, but did not breach. It is assumed that the rock impact results in a total release of the contained fuel since the clad melted during reentry.

4. A total release of fuel is also assumed for outcome #4, since the clad has melted during reentry. However, the soil impact is not expected to result in any fragmentation of the fuel. Therefore the particle size distribution should be that of a clad which has not been damaged. This data is not available for fueled clads but is available for a clad containing urania simulant, which was used here.

5. In the case of GIS failure, some fuel is released in the atmosphere and the remaining fuel impacts the Earth's surface. Calculation of the amount and size distribution of the air releases is discussed in Section 6.5.3.3. The particle size distribution of the ground release from the remaining fuel was calculated by multiplying the amount of remaining fuel by the mass fractions for the appropriate source terms. The source terms used were BCI 31 for rock impact and M-13 for soil impacts. The extrapolation approach was not used for the source term for impact on soil since it cannot give reliable results for small particles, which dominate consequence in that situation.

Table 6.5.3-9 summarizes the source terms for each EGA outcome which produces a release and Table 6.5.3-10 gives the actual particle size distributions within the 12 bins as defined for LASEP-T. Mass distribution within the largest bin (#12), for particles >215 μm, is further specified relative to the maximum inhalable particle size of 484 μm. This particle size corresponds to a 1500 AMAD which is is the largest particle size considered to be inhalable by the SPARRC dose model.

Table 6.5.3-9. Summary of Source Terms for Reentry from Earth Gravity Assist

Angle	Aeroshell	GIS	Clad	Location	POR*	Source Term	Release*** (grams)
Steep	Failure	Failure	-------	Air	1.0	steep air release	66.55
Shallow	Failure	Failure	-------	Air	1.0	shallow air release	74.2
Steep	Failure	Failure	-------	Rock	1.0	BCI 31 contained	84.45
Shallow	Failure	Failure	-------	Rock	1.0	BCI 31 contained	76.8
Steep	Failure	Failure	-------	Soil	1.0	M-13	84.45
Shallow	Failure	Failure	-------	Soil	1.0	M-13	76.8
Any	Failure	OK	Melt	Rock	1.0	BCI 31 contained	151
Any	Failure	OK	Melt	Soil	0.75	M-13	151
Any	Failure	OK	OK	Rock	0.56	BCI 5 released	0.0073
Any	OK	-------	-------	Rock	0.56 (**)	MIM	variable

*   Conditional probability of release per GIS unless otherwise indicated

** Conditional probability of release per aeroshell

*** Release per fueled clad

Section 6.7 includes results for the number of modules predicted for each end-state from FSAR and post-FSAR EGA analyses.

Table 6.5.3-10. Particle Size Distributions for Source Terms for Reentry from Earth Gravity Assist Given as Grams Per Bin

Bin #	Max Diam (μm)	GIS OK, Clad OK, Rock Impact	GIS OK, Clad Melt, Rock Impact	GIS OK, Clad Melt, Soil Impact	GIS Fail, Steep Reentry, Air Release	GIS Fail, Shallow Reentry, Air Release	GIS Fail, Steep Reentry, Rock Impact	GIS Fail, Shallow Reentry, Rock Impact	GIS Fail, Steep Reentry, Soil Impact	GIS Fail, Shallow Reentry, Soil Impact
1	0.10	3.9×10^{-5}	1.655×10^{-2}	4.38×10^{-3}	25.8	19.15	9.2559×10^{-3}	8.4175×10^{-3}	2.4496×10^{-3}	2.2277×10^{-3}
2	0.215	7.57×10^{-5}	2.513×10^{-2}	9.42×10^{-3}	0.0	0.0	1.4055×10^{-2}	1.2781×10^{-2}	5.2683×10^{-3}	4.7911×10^{-3}
3	0.464	1.5×10^{-4}	4.085×10^{-2}	2.032×10^{-3}	0.0	0.0	2.2846×10^{-2}	2.0777×10^{-2}	1.1364×10^{-3}	1.0335×10^{-3}
4	1.0	1.25×10^{-4}	8.297×10^{-2}	9.68×10^{-3}	0.0	0.0	4.6403×10^{-2}	4.2199×10^{-2}	5.4138×10^{-3}	4.9233×10^{-3}
5	2.15	4.01×10^{-4}	1.301×10^{-1}	1.7294×10^{-1}	0.0	0.0	7.2761×10^{-2}	6.6170×10^{-2}	9.6720×10^{-2}	8.7959×10^{-2}
6	4.64	5.72×10^{-4}	2.398×10^{-1}	2.0377×10^{-1}	23.0	0.0	1.3411×10^{-1}	1.2197×10^{-1}	1.1396×10^{-1}	1.0364×10^{-1}
7	10.0	1.238×10^{-3}	8.386×10^{-1}	2.9051×10^{-1}	14.75	13.05	4.6901×10^{-1}	4.2652×10^{-1}	1.6274×10^{-1}	1.4776×10^{-1}
8	21.5	1.955×10^{-3}	4.065	2.9926×10^{-1}	3.0	34.65	2.2734	2.0675	1.6737×10^{-1}	1.5221×10^{-1}
9	46.4	2.745×10^{-3}	13.199	5.9057×10^{-1}	0.0	7.15	7.3818	6.7131	3.3029×10^{-1}	3.0037×10^{-1}
10	100	0.0	7.100	6.9846×10^{-1}	0.0	0.2	3.9708	3.6111	3.9063×10^{-1}	3.5524×10^{-1}
11	215	0.0	9.070	7.1624×10^{-1}	0.0	0.0	5.0726	4.6131	4.0057×10^{-1}	3.6429×10^{-1}
12A	484	0.0	18.900	5.3311×10^{-1}	0.0	0.0	10.57	9.6127	2.9815×10^{-1}	2.7115×10^{-1}
12B	>10000	0.0	97.276	147.45	0.0	0.0	54.404	49.476	82.46	74.995
Total		0.0073	151	151	66.55	74.2	84.45	76.8	84.45	76.8

Notes: • All releases are tabulated per fueled clad

• A GIS failure results in a full release from each fueled clad, comprised of the sum of an "air release" distribution (encompassing mass lost due to vaporization and liquefied plutonia shed during reentry) and a ground release distribution (representing the post-impact particle size distribution for large particles which strike the Earth's surface). Ground release distributions are defined for impacts on either soil or a hard surface (rock).

6.6 TRANSPORT/BIOLOGICAL EFFECTS MODELING

Postulated Cassini accident scenarios could happen on the launch pad, during ascent or during Earth swingby. The source terms released from these hypothetical accidents can possess a wide range of particle sizes, from sub-micron to several thousands of microns. Overall, given an accident with a fuel release, the consequence analysis relies on two models: 1) a transport model to evaluate the ground and air concentrations resulting from the atmospheric dispersion of the released source terms and, 2) a radiological consequence model to predict the extent of contamination and health effects in the exposed population. Because virtually all mission phases are involved, the transport modeling must consider release altitudes ranging from near ground level to the higher altitudes of the stratosphere. The transport time of small particles could span from days to years as the release height increases, and thus specific models are needed for defined ranges of transport time. As an alpha-emitter, the fragmentation of the plutonia fuel poses a major concern in health effects through inhalation. Therefore the dosimetry and health effects calculation should be a particle-size dependent model. This section provides a description of the models and analysis processes adopted for the analysis of various accident scenarios.

6.6.1 Model Description

The process of determining the integrated nuclear risk for the Cassini mission employed three main transport/biological models. Figure 6.6-1 provides an overview of the analysis process with its feature models for a typical accident scenario. The SPARRC (Space Accident Radiological Release and Consequence) family of models, developed by LMMS, consists of SATRAP (Site-Specific Analysis of Transport and Dispersion of Radioactive Particles), GEOTRAP (Global Transport and Dispersion of Radioactive Particles), and HIAD (High Altitude Aerosol Dispersion) for the atmospheric transport and health effects prediction. In each of the three SPARRC codes, a common dose calculation method was implemented, namely PARDOS (Particulate Dose), to evaluate the radiological doses from various pathways and health effects. Two other codes were used in the analysis process both developed by Sandia National Laboratories: PUFF which evaluates the plume rise height for initialization of release dimensions, and LHS (Latin Hypercube Sampling) which provides sampled parameter values for each accident simulation.
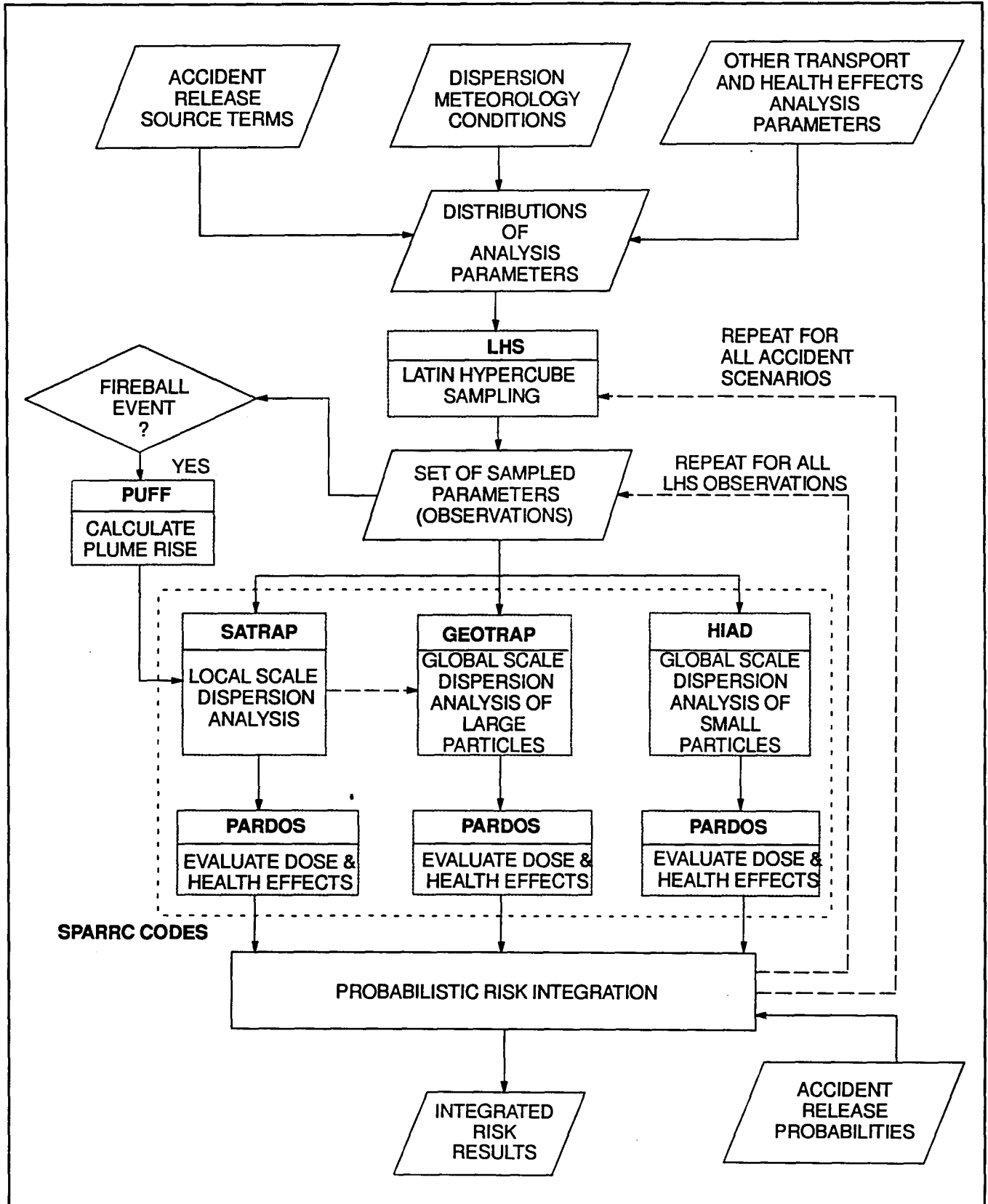
Figure 6.6-1. Overview of Consequence Analysis Process

In view of the transport time problem, the SPARRC models were each designed specifically for a range of particle sizes and dispersion time scales. Although this top level similarity can be found in the method used by HNUS for the Galileo and Ulysses analyses, the constituent models have significant differences in both transport and dose calculation modeling techniques. The range of applicability for the three transport codes is summarized in Table 6.6-1.

Table 6.6-1. Dispersion Scales and Applicable Codes

Example of Scenarios	Particle Size Range	Rel. Height	Dispersion Scale	Transport Time	Applicable Code
Explosion on launch Pad	$d\begin{cases} \geq 0.05\mu m \\ \leq 5000 \ \mu m \end{cases}$	0 to 5 km	Local	Minutes to hours	SATRAP
Random Worldwide Surface Impact	$d\begin{cases} \geq 0.05\mu m \\ \leq 5000 \ \mu m \end{cases}$	0.5 m to 3 m	Local	Minutes to hours	SATRAP
Reentry during Swingby	$d > 10 \ \mu m$	15 to 60 km	Global	1 – 2 Weeks+	GEOTRAP
Reentry during Swingby	$d < 10 \ \mu m$	15 to 60 km	Global	Weeks to Years+	HIAD

+: Depending on altitude of release and particle size.

SATRAP is used for local scale dispersion, mainly for releases inside the planetary boundary layer, such as accidents at the KSC launch site. GEOTRAP is used for the global scale dispersion of large particles, with diameter above 10 μm, released at high altitudes, between 5 and 60 km, which could induce travel time up to 2 weeks. HIAD is used for the global scale dispersion of small particles, with diameter less than 10 μm, which could have weeks to years of transport time because of high release altitudes (up to 60 km) and negligible settling velocity. The commonality in dose modeling and format outputs from PARDOS facilitates the integration of consequence results for release accidents that necessitate more than one analysis model.

6.6.1.1 SATRAP Model

The area of analysis considered for local scale dispersion analysis, around the launch pad, is quite complex in terms of meteorological characteristics, geographic features, and population density distribution. Due to the land-ocean interaction, the curved coast line and the presence of inland waterways, wind patterns at the KSC/CCAS launch site could vary strongly in space and time. Combined with the polydisperse source term problem, a Lagrangian-trajectory model coupled with a time varying 3-D wind field database was created to describe the many possible launch accident release conditions.

SATRAP was designed to independently track individual source term clouds, defined mainly by particle size and release dimensions, in time steps through a four-dimensional (x,y,z,t) wind field. The transport and diffusion calculations were based on the time and space varying meteorological data processed for a 200 km x 200 km Cartesian domain with a 5 km grid scale. The grid data include wind components, stability class, mixing height, and roughness length of the ground surface. In the Galileo and Ulysses analyses, the transport model did not qualify as a Lagrangian model because only one vertical profile of meteorological parameters was processed for the origin and along with other dispersion parameters uniformly applied to the whole 100 km radius range. The main characteristics of SATRAP as well as various adopted sub-models are summarized in Table 6.6-2.

Table 6.6-2. Principal Characteristics of SATRAP

Category	Description/Model Used	Notes
Diffusion Model Type	Lagrangian Puff Multiple source clouds	Use time and space varying wind field
Stability Scheme	Pasquill Stability Categories	Use stability classes A to G
Dispersion Coefficient Calculation	Split-sigma method	Horizontal and vertical diffusion treated separately
Source Cloud Definition	Particle size, Initial dimensions and locations	Tracked independently
Deposition Velocity	Sehmel-Hogdson	As a function of particle size, roughness length
Concentration Integration	Numerical	
Deposition Grid System	Nested Cartesian	Six levels, starting at 62.5m
Receptor Database	40,000 cells, each at 1 km x 1 km	Domain of analysis is 200 km x 200 km
Dose and Health Effects Calculation	ICRP-30, ICRP-60, BEIR IV and BEIR V	Detailed outputs for organ doses & dose levels
Ingestion Dose Calculation	Common food production model	Using site-specific analysis for inputs

To adequately evaluate ground concentrations of the multiple particle-size source terms at the impact point, a nested Cartesian grid with up to six levels was used in the deposition calculation. The receptor database which contains information such as population density and land usage, is assumed to have a different grid resolution because of different characteristic lengths. This modeling approach avoids both the smearing effect from the limitation of concentration grid points and the assumption that accident releases always occur at one fixed origin. In this application, the KSC/CCAS receptor database consists of 40,000 Cartesian cells, 1 km x 1 km each. Considering that ground impact releases could have very small initial dimensions, the smallest grid scale was set at 62.5 m. During cloud transport, the calculation of air and ground concentrations at grid points is initiated, whenever the cloud intersects the ground.

To cover the dispersion meteorology variability, a 5-year database for October and November, was generated for the Cassini primary launch opportunity. Both surface meteorological data and upper air rawinsondes data were used. Surface data measured at 20 different wind stations surrounding the launch site were collected and processed. The 15-minute average wind vectors were interpolated to the 5 km grid points and stored in separate files for 150 weather-days.

For reentry scenarios involving random ground impact during the orbit acquisition phase or Earth swingby phase, SATRAP is used with a simplified uniform wind field and receptor database. In this mode, only limited data can be obtained for the wind speed, stability categories and population distribution around the impact point, and therefore constant values are used as inputs. The main data required for this type of analysis include:

- Average wind speed for transport and dispersion

- Average Pasquill stability class

- Typical surface roughness length for deposition calculation

- Average population density.

- Source cloud definition in terms of particle size and initial dimensions.

In the simplified mode, the code treats the plume as a straight line diffusion at constant wind speed and provides output results in a format identical to the site-specific analysis. A uniform population density is assumed around the impact point.

6.6.1.2 GEOTRAP Model

When released at high altitudes, approximately between 5 and 60 km, particulate source clouds will travel several thousand kilometers before starting to deposit on the ground. A source cloud with particles less than 10 microns will spread throughout the globe and may take several years to completely deposit to the ground. In contrast, larger particles fall to the surface in a short time and form well defined footprints. A review of past mission analyses revealed that accident scenarios similar to the latter case were analyzed with greatly simplified assumptions: 1) one typical particle distribution, 2) all resulting deposition areas, provided in tabular forms, are confined within the same latitude band (no effects of global wind field) and, 3) land characteristics and population density are assumed uniform throughout the latitude band involved. In reality, large separation distances, both in longitude and latitude, of various surface deposition areas are induced by the gravitational sorting of released particles and the 3-D global wind field. The fall velocity of particles changes with altitude and atmospheric properties. A Lagrangian-trajectory method coupled with a global receptor database is necessary to solve such a problem. Considering those factors, GEOTRAP is designed to track individual Gaussian puffs in a 3-D global wind field and determines the final deposition locations where specific surface characteristics can be used for the consequence prediction. GEOTRAP is applicable to large particles with physical diameters from ten to several hundred microns. The transport time is limited to two weeks because the cloud diffusion scale reaches proportions where the Lagrangian tracking method becomes invalid. Source clouds with small particles and longer transport times are analyzed with the HIAD model.

Table 6.6-3 provides a summary of the main characteristics of GEOTRAP. For the wind field database, monthly average global wind fields from NASA's GRAM95 model were processed. The cloud trajectory was computed using the altitude-dependent particle fall velocity and the three component wind field. Atmospheric data such as air density and viscosity, which are used in the fall velocity calculation, were taken from the 1976 U.S. Standard Atmosphere (Reference 6.6-1). A fourth-order Runge-Kutta numerical integration, capable of handling space and time-varying parameters, successively calculates positions of cloud centers until reaching ground level.

Table 6.6-3. Principal Characteristics of GEOTRAP

Category	Description/Model used	Notes
Diffusion Model Type	Lagrangian Puff Multiple source clouds	
Windfield Model	GRAM95	Monthly average wind field
Receptor Database	720 equal-area grid cells	
Atmospheric Properties	U.S. Standard Atmosphere(1976)	Use for evaluation of particle fall velocity
Dispersion Coefficient Calculation	Based on statistical data for long range transport	
Source Cloud Definition	Particle size, Initial dimensions and locations	Tracked independently
Concentration Integration	Numerical	
Dose and Health Effects Calculation	ICRP-30, ICRP-60, BEIR IV and BEIR V	Detailed outputs for organ doses & dose levels

At the ground, deposition areas consist of overlapping footprints from dispersed clouds of various sizes. Instead of using the whole Earth surface as receptor reference grid, only a limited number of areas are examined for ground deposition calculation. From the cloud center location and dimensions, GEOTRAP determines the boundaries of deposition and appropriate grid scales with the smallest cloud size in each deposition area. The concentrations from deposition are computed at these grid points by taking account of all contributing clouds.

A receptor database for 720 equal-area cells covering the earth's surface was used for land characteristics and population density data. Note that in previous mission analyses the database applies to 20 latitude bands because it was assumed that all deposition areas have surface characteristics similar to those of the receptor latitude band. For GEOTRAP, the concentration grid resolution in deposition areas is determined uniquely from the overlapping cloud sizes and is independent of the demographic database. This separation of grids allows a better description of the ground concentration distribution for multiple particle source terms.

6.6.1.3 HIAD Model

HIAD is designed for the global scale dispersion of small particles. With plutonia fuel density about 10 g/cm^3, multiple year atmospheric residence time could apply for particles

with diameters less than 10 microns for releases between 45 and 60 km in altitude. A typical release condition for HIAD application is an inadvertent EGA reentry in which areo-thermal forces ablate RTG modules and components, resulting in the release of fine fuel particles in the stratosphere. Due to their long residence time in the upper atmosphere, the source clouds become globally diffused, and tend to deposit in the form of latitudinal bands. Table 6.6-4 provides a summary of the main characteristics of HIAD.

Table 6.6-4 Principal Characteristics of HIAD

Category	Description/Model used	Notes
Diffusion Model Type	Exponential Transfer Compartments	Horizontal and vertical diffusion treated separately
Average Residence Time for Mesosphere	4 years	
Average Residence Time for Stratosphere	14 months	
Average Residence Time for Troposphere	1 week	
Source Cloud Definition	Total mass of fuel release	Average particle size used for dose calculation
Concentration Integration	Analytical	
Receptor Database	20 equal-area latitude bands	
Dose and Health Effects Calculation	ICRP-30, ICRP-60, BEIR IV and BEIR V	Detailed outputs for organ doses & dose levels

In the Galileo and Ulysses FSARs, HNUS used a set of distributions for the latitudinal dispersion as a function of injection latitude, based on data of fallout studies (Reference 6.6-2). The same latitudinal distributions were adopted for the Cassini risk analysis. However, previous FSAR analyses did not account for variations in residence time during vertical transport nor factor in fuel decay during long residence time. In HIAD, the atmosphere was characterized, up to about 80 km, with three distinctive layers: the troposphere, the stratosphere, and the mesosphere. Each atmospheric layer is modeled as an exponential transfer compartment with an average residence half-time to describe the vertical transport. HIAD calculates the relative deposition fraction in each latitude band based on the initial injection latitude. The final deposition is assumed uniform for each latitude band and seasonal effects are neglected. Decay factor is considered in the concentration calculation.

6.6.1.4 PARDOS Model

The same model for dose and health effects calculation was implemented in each transport SPARRC code. The particle-dependent Dose Conversion Factor (DCF) calculation is based on ICRP-30 (Reference 6.6-3). The tissue weighting factors and health effects are from ICRP-60 (Reference 6.6-4). Radiation doses are calculated for seven organs: lung, liver, bone surface, red bone marrow, thyroid, gonads, and skin. Two exposure periods were calculated, the first year and 50 years from release time. As shown in Figure 6.6-2, the doses from the following pathways are computed:

- cloudshine or external irradiation from cloud immersion
- groundshine or external irradiation from ground deposition
- direct inhalation from the passing cloud
- ingestion
- resuspension inhalation
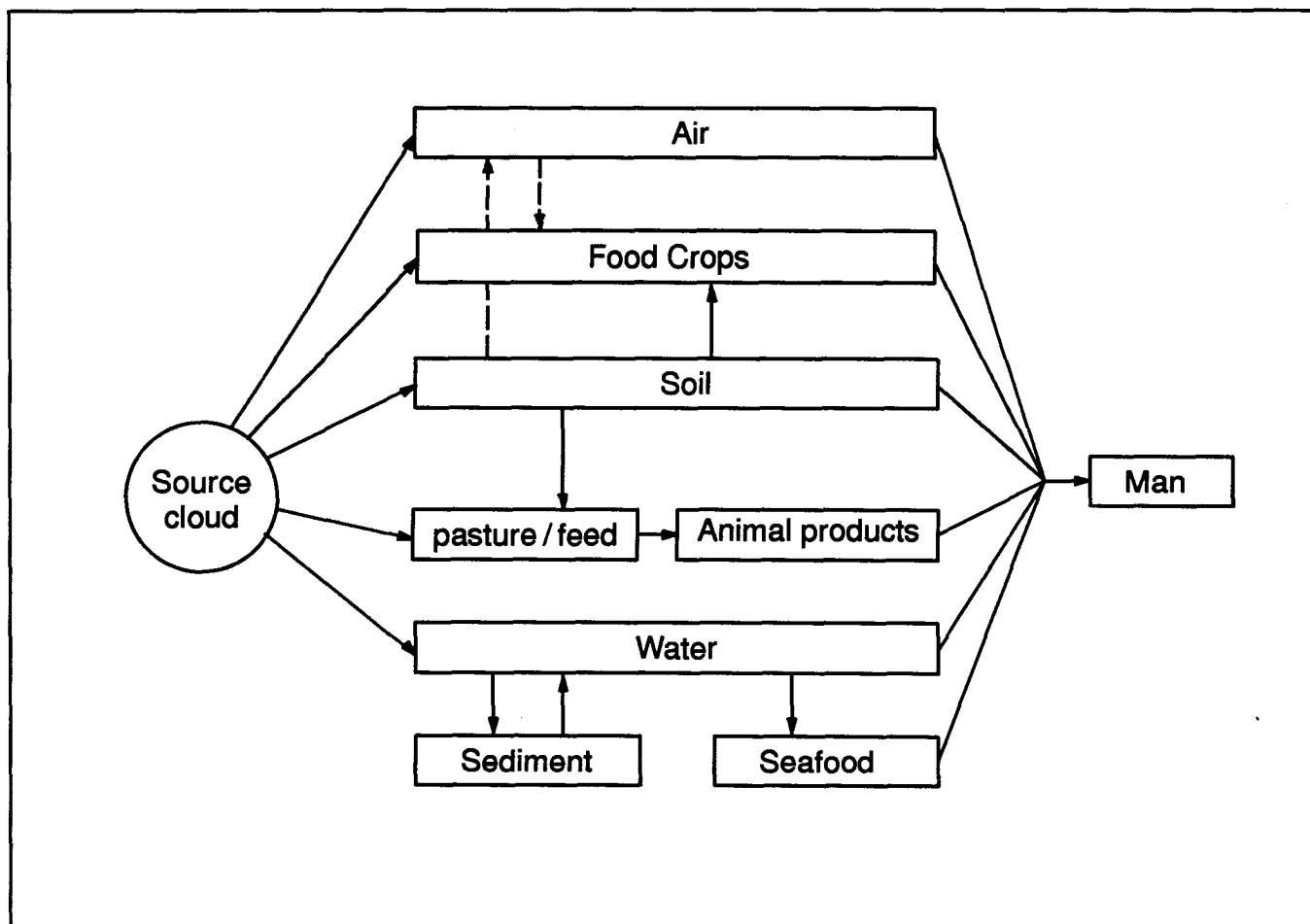
Figure 6.6-2. Exposure Pathways Considered in the Dose Calculation

Early in the project, attempts were made to implement a new lung model from ICRP-66 (Reference 6.6-5). The initial structure of PARDOS was designed to accommodate features such as age-dependent dose calculation. However, the late availability of bio-kinetic factors as well as recommended DCF values prevented the implementation of the new model. Per ICRP-30, the DCF values are highly dependent on particle size, and thus provisions were made to design PARDOS to be flexible to any particle size definition. In particular for plutonium bearing fuel, PARDOS derives the applicable DCF value based on particle size, density, solubility class, and gut absorption factor. The deposition fraction in three lung compartments is calculated during this process and the exposure doses are sorted by particle bins for the health effects calculation.

Two types of ingestion dose are considered in PARDOS: 1) the dose of contaminated foodstuffs produced inside the plume footprint, affecting people at the same location, 2) the dose from commercially distributed foods available in a large region, different from the contaminated production area. In this application, the distinction between these two ingestion doses is based on the size of the geographic cells used in the particular code. In the case of GEOTRAP, the receptor cells are quite large (about 843 km on each side) therefore the first type of ingestion dose is calculated with generic food consumption rates. In the case of SATRAP, the whole geographic area for which calculations are made (100 km) is comparable to or smaller than the area from which food is obtained. In this case, the ingestion dose to individuals at the specific geographic locations was obtained as the sum of ingestion doses from garden grown produce and an estimated average ingestion dose from commercially distributed foods. A KSC/CCAS site-specific screening analysis determined foodstuffs such as seafood and produce to be dominant contributors to the common ingestion dose. This extensive reliance on site-specific data is a significant advancement from the previous mission analyses

The health effects of each accident scenario is expressed in terms of the statistical expectation value for the numbers of latent cancers induced in the exposed population. The estimated cancers are an attributed excess above those naturally occurring in the population. In the Cassini risk analysis, the health effects are evaluated with the ICRP-60 risk estimator, equal to 5×10^{-4} per person-rem. The BEIR IV and BEIR V health effects (References 6.6-6 and 6.6-7) were also evaluated but used only for comparison. It was felt

that a distinction of risk estimators from ICRP and BEIR would provide a better health effects prediction than a scaled value from the two sources as used in previous mission analyses.

In addition to the non-threshold health effects results as described previously, health effects with a de-minimis criteria, set at 1 mrem per year, were also evaluated.

6.6.2   Pre-Launch/Early Launch Accidents

Postulated accidents occurring at the KSC launch site involve the definition of three key variables: 1) the released source term, 2) the meteorological conditions or weather-day for a daily-based archive, and 3) the accident time within the launch window.   The last two variables play a significant role in determining the atmospheric dispersion conditions of the released source terms.   SATRAP is the primary transport model used in pre-launch and early launch accident analysis.   The PUFF model from SNL was used to evaluate plume rise height and fireball dimensions, based on the local meteorological conditions and the available fuel energy.   All airborne source clouds leaving the SATRAP analysis domain (200 km x 200 km) are transferred to GEOTRAP for long range transport analysis.   As such all fuel is accounted for in the consequence analysis.

The following assumptions were adopted for the analysis of pre-launch/early launch accidents:

- The SRMU fuel fire plume is always present

- Liquid fuel fireballs lifting to altitudes higher than the SRMU fire plume are unaffected

- All fuel releases within the SRMU fire plume are well mixed and modeled as a uniform column with SRMU plume dimensions

- SRMU fire diameter applies to a dense burning zone whose radius is estimated from the mission elapsed time

- Fractions of the source terms to be tracked in the wind field are determined by the mixing height and contributing fire plume configurations.

The rise of liquid fireballs to high altitudes is expected to occur in a very short time, much faster than the solid fuel fire, and therefore are unaffected by the turbulent regime of the SRMU plume at lower altitudes.

Due to the varying extent to which releases from SRMU solid propellant impacts were integrated into the codes used for launch accident modeling, three different analysis processes were used to derive the consequence results for various accident cases, :

1) *Non-SRMU induced release and SRMU Coincident Impact Release evaluated in the same accident simulation:*
    - case 0.0 (On-pad Propellant Explosion, Configuration 1)
    - case 1.13 (Full Stack Intact Impact).

2) *SRMU Coincident Impact Release evaluated separately:*
    - case 1.1 (Total Boost Vehicle Destruct or TBVD),
    - case 1.3 (TBVD with SRMU Aft Segment Impact)
    - case 1.10 (Space Vehicle/RTG Impact within Payload Fairing).

3) *Non-SRMU induced release only:*
    - for accident cases associated with low probabilities (case 1.2, 1.4, 1.6, 1.8, and 1.9).

If the SRMU induced source term was evaluated with the Non-SRMU induced source term from the same LASEP-T simulation, the release source term is sampled along with other parameters such as weather-day and time of launch, then the consequence analysis is performed with the SPARRC code. In this analysis, the LASEP-T release records are not equally probable and their probability distribution function (PDF) is used in the sampling process. In particular for case 0.0, which could occur up to 55 minutes before midnight, the meteorological data required a concatenation of two successive 24-hour data files and an adjustment to the time boundary input of SATRAP.

If the SRMU induced source term was evaluated separately, two passes of analysis are required. Figure 6.6-3 shows the end states of release source terms considered in this analysis process. The first pass involves only the Non-SRMU induced source term, with equally probable release records. The second pass accounts for the SRMU induced source term and possible combinations with Non-SRMU induced releases. During the analysis process, this combination is performed if a sampled variable is less or equal to the mean conditional probability of SRMU induced release. The final consequence results are obtained by combining the results from the two passes of analysis.

ACCIDENT OCCURRENCE	NON-SRMU INDUCED RE-LEASE	SRMU INDUCED RE-LEASE	END STATES

NO
(1- POF)
LAUNCH
YES
(POF)
(1-POR)
(1-PCI)
(PCI)
(POR)
(1-PCI)
(PCI)

1: NO ACCIDENT
2: ACCIDENT BUT NO RELEASE
3: SRMU INDUCED RELEASE ONLY
4: NON-SRMU INDUCED RELEASE ONLY
5: SRMU-INDUCED PLUS NON-SRMU-INDUCED RELEASE
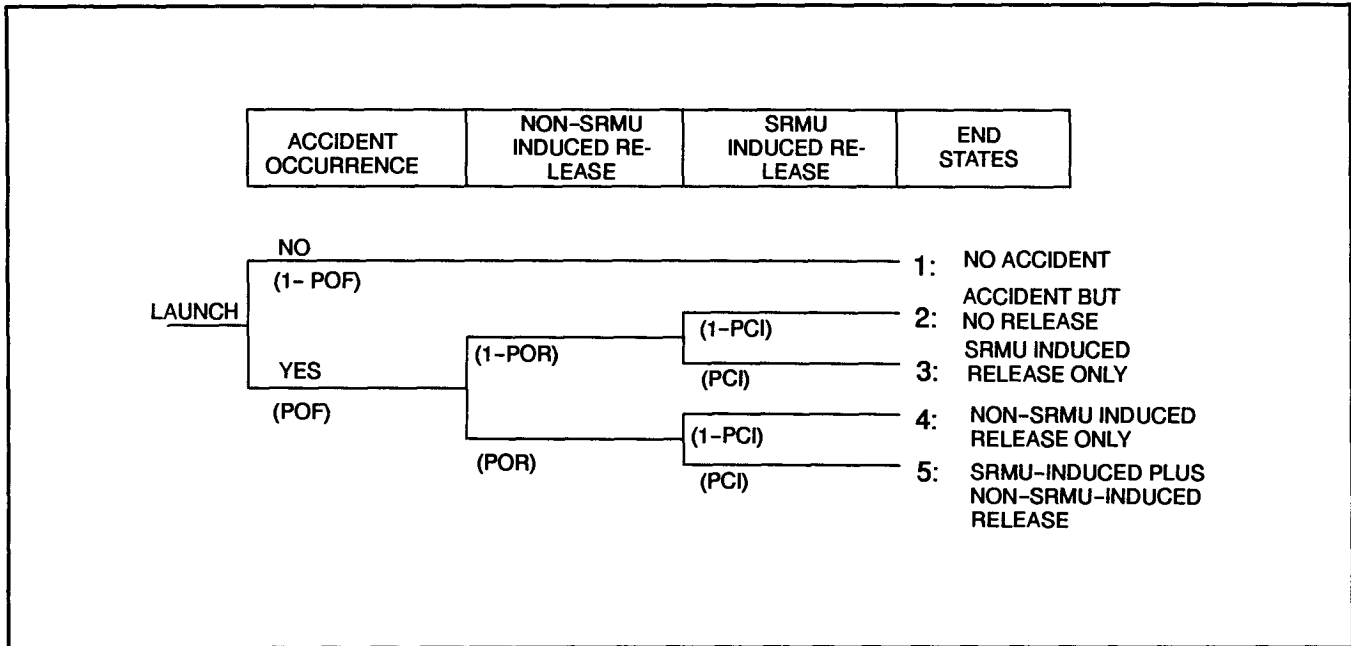
Figure 6.6-3. Combinations of Source Terms Considered in Phase 1 Consequence Analysis

For accident cases of low probability, the SRMU induced releases were not evaluated, and a different sampling process was implemented because all LASEP-T release records (from Non-SRMU induced environments) are equally probable.

The effects of variability from the source term and other transport conditions were evaluated with the stratified sampling method of the Latin Hypercube Sampling (LHS) code. To assure that LHS could sample all significant value ranges while maintaining a tractable number of analyses, three clusters of source term and 10 clusters of dispersion meteorology conditions were defined for the analysis process. For the variability-only analysis, accident cases in phase 0 (pre-launch) and phase 1 (early launch) were evaluated with either 30 or 60 LHS observations to obtain the distribution of consequence results. Each LHS observation consists of 30 SPARRC analyses. The high volume of analysis cases was made possible with the use of multiple workstations on a local network and a shell program designed to process the flow of data, executable codes and results. Consisting of high level Unix commands and C language programs, this shell program represents the link between LASEP-T outputs, LHS random sampling, and the SPARRC family of codes. Table 6.6-5 summarizes the number of SPARRC/LHS analyses performed for the variability-only analysis of launch accident cases.

Table 6.6-5. Summary of SPARRC/LHS Analyses

Case	Separation of SRMU-Induced Source term	Number of LHS Observations	Number of SPARRC Analyses
0.0	No	30	900
1.1	Yes	60	1800
1.3	Yes	60	1800
1.10	Yes	60	1800
1.13	No	30	900
1.2,1.4,1.6,1.8 & 1.9	N/A	30 each	900 each
Total			11,700

The selection of weather-day clusters was guided by the results of a sensitivity study performed in May 1996. In this study, an average source term was calculated for each release type over all launch accident cases. Then, a consequence analysis was performed for each average source term with the complete meteorology database, i.e., 150 weather-days, at assumed accident times of 3 a.m. and 7 a.m. The results were ranked and grouped in eight clusters. Later, two additional clusters were added grouping weather days with the highest and the lowest predicted consequences to assure adequate sampling of the extreme consequence values. From this study, the 3 a.m. results were used in a consequence scaling model to analyze accidents with low probabilities for the FSAR in June 1996. The scaling model employed the mass-normalized consequence for each weather-day and provided a scaled result for every release record and weather-day combination. The scaling factor depends upon the dominant contributing pathway of the normalized results. Those results that are dominated by the ingestion pathway would be scaled directly with total mass released. For direct inhalation and inhalation due to resuspension dominated results, the dose importance weighted mass scaling factor would be used. Although the scaling method ignores variability due to position of release and time of launch, it includes all the variability due to release mass, release particle distribution and weather-day.

The modeling approach for FSAR analyses, did not incorporate the effects of solid fuel fire plume on the transport process. Three new elements considered for launch phase accidents following FSAR analyses included the effects of the revised Centaur overpressure, the presence of SRMU fire plume, and SRMU coincident impact source terms. These changes were subsequently implemented in the consequence analysis

process and a new set of consequence results were provided for the FSAR Addendum issued in April 1997.

The key modeling detail for the updates, not present during the FSAR, was the diffusion of source terms in the presence of a large areal burning zone of solid fuel fragments. It was necessary to model this particular effect because virtually all accident cases in the launch phase are associated with an SRMU fire plume. Video footage and meteorological conditions from the Titan IV - 34D accident at Vandenberg AFB (April 1986) and a more recent Delta accident at CCAS (January 1997), were obtained to derive typical inputs for SRMU plume rise simulation. A calibration factor for the appropriate energy level input to PUFF was derived based on plume rise heights calculated for both accidents. The semi-empirical Briggs's model was also reviewed and provided reasonable results. However, the PUFF code reflects better local meteorology conditions defined for each weather-day and was implemented for automation in the analysis process. Regarding the diameter of the burning zone, results from SRMU footprint simulations were examined along with video footage and pictures taken from the Delta accident to determine an effective diameter identified as a "dense burning zone." This zone is where individual plumes join together with a strong buoyancy, forming a well-mixed column for any potential source term released inside its volume. A nominal factor of 0.5 times the SRMU fragment footprint diameter was adopted for the dense burning zone.

The population groups and pathways considered in the FSAR addendum launch site dose analysis is summarized in Table 6.6-6.

Contingency Planning Support

In support of contingency planning activities prior to launch, typical fire configuration plume and corresponding fractions of released source terms in various plume components, were transmitted to the emergency planning team. These configurations, which include the average stabilized plume heights and fireball diameters, were used as inputs to the ARAC code of Lawrence Livermore National Laboratories for analysis of hypothetical launch accidents. Two test cases were performed for comparison with ARAC. The input source term and dispersion conditions were defined by HNUS. A 99th percentile value of source term from both RTGs and LWRHUs was selected for the analysis. The wind field was assumed to be uniform throughout the analysis domain and the effects of mixing height was

not considered. Overall, the results from SATRAP compared favorably with those from ARAC.

Table 6.6-6. Population Groups and Pathways Considered for Launch Site Consequence Analysis

Population Group	Pathway					
	1	2	3	4	5	6
Workers - 3rd Shift - Outdoors	X		X	X	X	
Workers - 3rd Shift - Indoors		X	X		X	
Residents - Outdoors	X		X	X	X	X
Residents - Indoors		X	X		X	X
Spectators	X			X	X	

1: Direct inhalation during cloud passage
2: Reduced direct inhalation during cloud passage
3: Inhalation from resuspension
4: Cloudshine
5: Groundshine
6: Ingestion

6.6.3 Late Launch Accidents

In analyzing late launch consequences, ground releases are considered uncorrelated, that is the surface type impacted by one module is independent of the surface types impacted by any other modules. Given this assumption, the reentry analysis process for the late launch phase involves two levels of calculation: 1) determine the impacted cells and corresponding number of breached modules, and evaluate the consequences, normalized to 1 person/km², and 2) scale the consequence results to the number of breached modules and exposed population density classes. The number of breached modules is predicted by sampling a binomial distribution sampling based on the exposed rock fraction within the cell and the failure probability for the module. Multinomial distribution sampling provided a matrix of the number of modules breached and population density classes for each impacted cell.

A worldwide receptor database of 720 equal-area cells with 15 population density classes, ranging from 0 to 25,000 person/km², was used for the analysis. Based primarily on the launch trajectory and orbit inclination, the MIM analysis (Section 6.5.2) provided ground impact probabilities per cell for sub-orbital reentries and per latitude band for orbital reentries. The list of impacted cells were restricted to those containing both exposed rock surface and population for consequence analysis.

The variables sampled by the first level analysis, using a SPARRC/LHS process, include the impacted cell, source term from a single GPHS module, the number of releasing modules and the weather category. For the first level analysis, 900 LHS observations were performed for each reentry accident case. In the second level analysis, the multinomial distribution sampling was limited to 100 trials because, in some cases, there are a very large number of possible combinations of breached modules and population density classes, but at very low probabilities.

For transport analysis, the dispersion conditions in impacted cells consist of 14 meteorology categories and 7 Pasquill stability classes with average wind speeds. The bounce height of GPHS modules after rock surface impact was assumed to be 0.5 m above ground and all source terms are released at this height in a Gaussian cloud with $\sigma = 1$ meter in 3-dimensions. A simplified version of SATRAP modeled the transport as straight line Gaussian diffusion. Transport was evaluated for 100 km, however test cases showed that over 99% of the consequence resulted from dispersion in the first 60 km. A uniform distribution of population density was assumed for the area of impact.

Several refinements were implemented during the development of the late launch analysis process. For the DFSAR analysis, no credit was taken for the rocky soil types considered to be thinly covered with soil and a whole cell-dependent rock fraction was used in determining the number of breached modules. Also, all failed modules were assumed to release fuel into the same population density class. Later for the FSAR analysis, an exposed rock fraction based on a worldwide soil type database and ranging from 70% to 80% was used for the calculation of conditional probability of release. Multinomial distribution sampling was added to predict the combination of population density classes with breached modules, to provide a more correct evaluation of the probabilities associated with modules impacting various population density classes.

Compared to prior mission analyses, two significantly different features were used in the Cassini late launch analysis: 1) the conditional failure probability upon rock impact is evaluated per module instead of per fuel clad, and 2) the distribution of potential cells impacted were systematically sampled instead of relying on an average impact condition (defined as average values of rock fraction and population density).

6.6.4 EGA Reentry

Inadvertent reentry scenarios during the Cassini earth swingby maneuver could generate several types of fuel release. Fuel release might occur both at high altitudes and at the Earth's surface due to various failure modes for the 54 GPHS modules. The consequence analysis process for inadvertent EGA reentry is treated with two levels:

1) The first level of the process determines the partition of 54 modules into four possible end states based on failure modes and location of release, and calculates the normalized consequence result for each type of release.

2) The second level of the process predicts the set of combinations of breached modules (or GISs) and applicable population density classes for the impacted cell. Specific cell characteristics such as exposed rock fraction and joint probability of population density class - soil type surface, are input into the determination of conditional release probability. For each combination mentioned previously, the consequence value was calculated based on the number of predicted breached modules, the applicable population density and the normalized consequence result.

Based on the EGA event tree (Section 6.5.3), each module which releases fuel can be categorized into one of the end states as described in Table 6.6-7.

Table 6.6-7. Definition of Module Fuel Release End States for EGA Consequence Analysis

End State	Aeroshell	GIS	Clad	Location of Potential Release
A	OK	- - -	- - -	Rock
B	Failure	OK	OK	Rock
C	Failure	OK	Melt	Rock - Soil
D	Failure	Failure	- - -	Initial: Air Secondary: Rock - Soil

For end states A and B, fuel release can occur for module (or GIS) impacts upon rock. For end state C, fuel release from a degraded GIS could occur from either rock or soil impact. For end state D, both aeroshell and GIS have failed during reentry and fuel release is released at high altitudes. In this particular case, the remaining fuel inventory that proceeds to the Earth's surface is considered to fragment upon impact on rock or soil.

The key assumptions for each EGA reentry simulation include:

- All modules are subjected to the same reentry angle

- With a separation distance estimated at less than 80 km, air and ground releases occur in the same equal-area cell of the 720 cell worldwide cell grid.

- Surface types (soil or rock) within the impacted cell are not necessarily continuous and thus the impact of modules on these surfaces are uncorrelated.

- GISs within the same module have correlated impact surface types and failure modes. In other words, due to identical reentry conditions, both GISs from a given module would either survive or fail, and their separation distance is assumed smaller than the characteristic length of any surface type.

- For all surface types, fuel is released 0.5 m above ground.

- Deposition of fuel from in-air release (end state D) to water bodies has a negligible contribution to the total consequence, except for shallow ocean and inland water for which a mean seafood ingestion dose is calculated and scaled to the number of breached modules.

In the first level of the EGA analysis, the following parameters are sampled by LHS to evaluate the normalized consequence results:

- Latitude band of reentry

- Angle of reentry

- Equal-area cell of impact (or longitude of impact)

- Altitude of release (for in-air release only)

- Weather group, rock and soil fraction applicable to the impacted cell

- Mass and particle size distribution of source terms

- Distribution of 54 modules into four end states

For the first level of analysis, cells with potential consequence from ground impacts (i.e., with either population, soil or exposed rock surface) are clustered and sampled separately from the remaining cells. Variability of source terms was only defined for the rock impact of GPHS modules (end state A). An average source term was defined for all remaining release types. A random draw, using the multinomial distribution based on the probability of end states, determines the distribution of 54 modules into each of the four end states. With all the above parameters defined, the input files for the SPARRC codes were created and

the consequence analysis performed for a population density of one person/km². The consequence results calculated include health effects (with and without de-minimis), collective dose, maximum individual dose for each population density class, and land contamination areas.

The second level of the EGA analysis predicts the number of modules breached within applicable population density classes, combines the consequences from contributing releases, and provides the final set of consequence results. Based on the surface characteristics and population data of each impacted cell, the number of modules or GISs releasing fuel upon rock or soil impact is predicted. Since the concern is mainly for areas associated with people, a joint probability of having both population and rock/soil surface is used in determining the conditional probability of release. For each combination of population density class / rock (or combination of population density class/soil) a different probability of release is calculated. Having those probabilities applicable to the cell, multinomial distribution sampling is used to determine the partition of the breached modules or GISs among population density classes.

An impacted cell could have soil, rock and shallow ocean surfaces, therefore in accident simulations where the 54 reentry modules are subjected to all four end states, a combination of up to eight release types is possible. The release types include:

1) Intact module releasing on rock impact

2) Intact GIS releasing on rock impact

3) Intact GIS - melted clad releasing on soil impact

4) Intact GIS - melted clad releasing on rock impact

5) Small particle (<215 μm) release from in-air GIS failure

6) Large particle (> 215 μm) from in-air GIS failure, fragmenting upon soil impact

7) Large particle (> 215 μm) from in-air GIS failure, fragmenting upon rock impact

8) Large particle (> 215 μm) from in-air GIS failure, landing in shallow ocean or inland water.

In the above list, release type 5 would experience global dispersion and release type 8 could occur anywhere in the impacted equal-area cell. The exposure doses to these two fuel release types are calculated with the average population density of the impacted

latitude bands and equal-area cells respectively. The remaining release types have a limited range of dispersion (from 5 to 60 km) and thus areas with different population density classes are considered.

For the whole accident scenario, the distribution of population exposed to 18 dose levels was calculated. The dose distribution results were presented in the form of statistic values (mean and percentiles values) and CCDF curves.

6.7   CONSEQUENCE AND RISK PREDICTIONS

6.7.1   Mission Consequence and Risk Predictions

A summary of the mean value for collective dose, health effects, and dry land contaminated above 0.2 µCi/m2 is provided in Table 6.7.1-1 by accident case for cases which contributed significantly to risk within each mission segment. (Updates reflecting the 800 km Earth Swingby Plan and updated GIS reentry orientation analysis (Reference 6.7-1) are incorporated into the EGA consequence results discussed in this section. Predicted consequences for the 800 km swingby are compared to 500 km swingby consequence predictions from the FSAR Addendum: Supplemental Analyses in Table 6.7.1-2. The percentile values of land contamination above selected levels are provided in Table 6.7.1-3. For all combined postulated accident scenarios, from pre-launch to Earth swingby, the expected health consequence for the Cassini mission is calculated to be 0.07 incremental latent cancers. For the total mission, the probability of one or more latent cancer fatalities is slightly higher than 1 in 100,000. A breakdown of the results in terms of contribution from various phases shows the following characteristics:

- Accidents occurring near the launch site (i.e., in phases 0 and 1), would be expected to produce the lowest expected health consequences of any mission segment. The combined results from simulated accident cases of phase 0 and phase 1 account for 29% of the total mission risk. A total of 0.066 and 0.071 incremental cancer fatalities are predicted for the mean 50 year health effects without de-minimis resulting from exposure to fuel release in phase 0 and phase 1, respectively. From the segment consequence CCDF in Section 6.3.2 the probability of inducing one or more health effects due to exposure to accidental fuel release is about 1 in 4 million and 1 in 100,000 for phases 0 and 1, respectively. The probability of release in these phases is about 5 in 10,000. For the dominant accident case 1.1 (Total Boost Vehicle Destruct), which could occur in the first 20 sec MET, the majority of fuel releases are predicted to come from a Space Vehicle (SV) fireball engulfed in the SRMU fire plume. As a result, the fuel is well-mixed in a large plume column and lofted to high altitudes. This energetic areal release affects mostly off-site population. Table 6.7.1-4 provides the mean health effects by population group for pre-launch/early launch accident cases. Ground concentrations above 0.2 µCi/m^2 are contributed by large particles and are expected to be restricted to the KSC launch site. All analysis cases have a mean value of maximum potential individual dose less than 0.046 rem. In over 70% of the simulated analysis cases, inhalation of resuspended material was the dominant contributing pathway.

Table 6.7.1-1. Mean 50 Year Radiological Consequence Values by Accident Case

Accident Case	Accident Description	Collective Dose (Person-rem) (without de-minimis)	Collective Dose (Person-rem) (with de-minimis[b])	Health Effects[a] (without de-minimis)	Health Effects[a] (with de-minimis[b])	Maximum Individual Dose (rem)	Land Area with >0.2 μCi/m² (km²)
0.0	On-Pad Explosion, Configuration 1	130	96	0.066	0.053	0.013	1.5
1.1	Total Boost Vehicle Destruct (TBVD)	160	110	0.081	0.05	0.015	1.8
1.3	TBVD with SRMU Aft Segment Impact	130	88	0.067	0.045	0.046	1.3
1.10	SV/RTG Impact within PLF	80	51	0.04	0.021	0.020	1.1
1.13	Full Stack Intact Impact	240	180	0.12	0.098	0.028	2.2
3.1	Sub-Orbital Reentry	8.4	7.5	4.2×10^{-3}	3.8×10^{-3}	0.37	0.028
5.1	CSDS (Config. 5) Sub-Orbital Reentry	8.4	7.5	4.2×10^{-3}	3.8×10^{-3}	0.37	0.027
5.2	Orbital Reentry (Nominal)	92	82	0.046	0.041	1.1	0.058
EGA	EGA Reentry* (Short Term)	1.7×10^5	1.1×10^5	90	60	1780	21

a. Health Effects are incremental latent cancer fatalities.

b. The de-minimis dose level is 1.0×10^{-5} Sv (1.0×10^{-3} rem) per year.

* For 800 km swingby altitude

Table 6.7.1-2. Radiological Consequence Values for 800 km and 500 km EGA Swingby

Accident Case	Accident Description	Probability of Failure (POF)	Conditional Probability of Fuel Release	Health Effects[a] (without de-minimis)	Health Effects[a] (with de-minimis)	Maximum Individual Dose (rem)	Land Area with >0.2 μCi/m^2 (km^2)
EGA (500 km)	EGA Reentry (Short Term)	8.0×10^{-7}	0.79	140	26	650	19
EGA (800 km & Revised GIS End-State Probabilities)	EGA Reentry (Short Term)	6.2×10^{-7}	0.51	90	60	1780	21

[a] Health Effects are incremental latent cancer fatalities.

- For reentry accident scenarios occurring during late launch phases 3 to 8, the mean health consequence without de-minimis is 0.044. These reentry accidents are the dominant contributors to the combined risk curve below one health effect, for probabilities above 1×10^{-5}. The probability of more than one health effect due to reentry accidents is about 1 in 100,000. The high probability of fuel release, estimated at 2 in 1000, is attributed to the high relative probability of a loss of direct thrust of the Centaur or attitude control malfunction. Accident case 5.2 (nominal orbital reentry accident) is the dominant risk contributor to this mission phase.

- With a release probability estimated at less than 4 in 10 million, the highest mean health consequence without de-minimis is from Earth swingby scenarios. The probability of consequence for more than one health effect due to inadvertent reentry accidents is about 3 in 10 million. A total of 90 incremental cancer fatalities are calculated for an EGA reentry accident. Using a de-minimis dose level of 1 mrem/yr, the mean health effects consequence is reduced to 60 health effects. The de-minimis criterion affects mainly reentry accidents with low exposure doses from releases at high altitudes, doses which contribute 32% of the total mean health effects. An average value of 0.54 failed modules is predicted for the in-air high altitude releases. The releases on soil from a "GIS OK Clad Melt" condition accounts for 54% of the expected health effects and represent the highest consequence outcomes. An average of 6.9 failed modules is predicted for GIS OK Clad Melt releases on soil. Table 6.7.1-5 summarizes the evaluated number of persons exposed to various dose levels for the EGA reentry accidents.

Table 6.7.1-3. Land Area Contaminated above 0.2, 0.6, 1.2, and 2.4 μCi/m^2 for Dominant Accident Cases in Each Mission Segment

Contam. Level	Mean (km^2)	Expected Value (km^2)	5th Percentile (km^2)	50th Percentile (km^2)	95th Percentile (km^2)	99th Percentile (km^2)
Case 0.0						
>0.2	1.5	7.6×10^{-5}	5.1×10^{-3}	0.66	5.5	8.6
>0.6	0.5	2.6×10^{-5}	2.2×10^{-4}	0.17	2.0	2.8
>1.2	0.2	1.3×10^{-5}	0.0	0.030	1.1	1.6
>2.4	0.097	5.0×10^{-6}	0.0	6.5×10^{-3}	0.5	0.9
Case 1.1						
>0.2	1.8	8.1×10^{-4}	4.4×10^{-4}	0.59	6.8	23
>0.6	0.71	3.2×10^{-4}	0.0	0.11	2.7	10
>1.2	0.4	1.8×10^{-4}	0.0	0.032	1.6	7.3
>2.4	0.22	1.0×10^{-4}	0.0	0.01	0.99	5.1
Case 1.3						
>0.2	1.3	1.6×10^{-4}	1.3×10^{-3}	0.32	5.7	15
>0.6	0.51	6.1×10^{-5}	0.0	0.056	2.1	7.5
>1.2	0.28	3.3×10^{-5}	0.0	0.014	1.2	4.7
>2.4	0.15	1.8×10^{-5}	0.0	3.3×10^{-3}	0.6	3.1
Case 5.2						
>0.2	0.058	1.2×10^{-4}	0.0	0.031	0.25	0.35
>0.6	0.013	2.6×10^{-5}	0.0	0.0	0.062	0.12
>1.2	3.2×10^{-3}	6.5×10^{-6}	0.0	0.0	0.016	0.094
>2.4	8.0×10^{-4}	1.6×10^{-6}	0.0	0.0	0.0	0.047
EGA *						
>0.2	21	6.7×10^{-6}	0.0	8.7	85	124
>0.6	12.5	4.0×10^{-6}	0.0	5.0	53	63
>1.2	9.2	2.9×10^{-6}	0.0	3.7	39	45
>2.4	7.0	2.2×10^{-6}	0.0	2.4	30	35

* For 800 km swingby

Table 6.7.1-4. Mean 50 Year Health Effects Values by Population Group for Pre-Launch/Early Launch Accident Cases

Accident Case	On-Site Worker Health Effects (without de-minimis)	On-Site Worker Health Effects (with de-minimis*)	Off-Site Resident Health Effects (without de-minimis)	Off-Site Resident Health Effects (with de-minimis*)	Off-Grid Population Health Effects (without de-minimis)	Off-Grid Population Health Effects (with de-minimis*)
0.0	5.9×10^{-4}	4.2×10^{-4}	0.058	0.046	7.5×10^{-3}	6.6×10^{-3}
1.1	2.5×10^{-3}	1.8×10^{-3}	0.072	0.045	6.0×10^{-3}	2.8×10^{-3}
1.2	2.3×10^{-4}	6.0×10^{-5}	5.6×10^{-3}	9.6×10^{-4}	4.1×10^{-4}	6.3×10^{-6}
1.3	2.6×10^{-3}	2.0×10^{-3}	0.059	0.04	5.5×10^{-3}	3.2×10^{-3}
1.4	3.0×10^{-3}	2.1×10^{-3}	0.058	0.034	4.4×10^{-3}	1.4×10^{-3}
1.6	2.2×10^{-3}	1.6×10^{-3}	0.046	0.025	3.1×10^{-3}	9.2×10^{-4}
1.8	1.8×10^{-3}	1.3×10^{-3}	0.061	0.038	3.7×10^{-3}	1.2×10^{-3}
1.9	2.8×10^{-3}	2.0×10^{-3}	0.048	0.024	3.5×10^{-3}	9.7×10^{-4}
1.10	1.3×10^{-3}	7.6×10^{-4}	0.036	0.019	2.7×10^{-3}	1.3×10^{-3}
1.13	1.3×10^{-3}	9.0×10^{-4}	0.1	0.085	0.015	0.012

* The de-minimis level is 1×10^{-5} Sv (1×10^{-3} rem) per year

Table 6.7.1-5. EGA Analysis - Number of Persons Exceeding Doses above Levels (800 km Swingby)

Dose Level (rem)	Mean Number of Persons Exceeding Dose Level	Expectation Number of Persons Exceeding Dose Level
0.001	1.43×10^5	4.51×10^{-2}
0.05	3.29×10^4	1.04×10^{-2}
0.1	2.56×10^4	8.09×10^{-3}
0.4	1.39×10^4	4.40×10^{-3}
1	7.24×10^3	2.29×10^{-3}
5	1.85×10^3	5.85×10^{-4}
10	974.3	3.08×10^{-4}
100	144	4.56×10^{-5}
400	39.1	1.24×10^{-5}
500	24.1	7.61×10^{-6}
1000	10.8	3.43×10^{-6}
5000	1.6	5.1×10^{-7}

Final Technical Report
GPHS-RTGs for the Cassini Mission
Lockheed Martin Document No. RR18
August 1998

Overall, the consequences predicted for the Cassini mission are low when compared with other risks. Using a typical natural (background) radiation of 0.3 rem/year and a health effects estimator of 5 x 10⁻⁴ latent cancer fatalities/rem, the risk to an individual of developing fatal cancer from a 50 year exposure is estimated at 1 in 133. This estimated lifetime risk from background radiation is over 8 orders of magnitude higher than the Cassini mission average individual risk, estimated at 1 in 50 billion of incurring cancer due to exposure from an accidental RTG fuel release.

6.7.2 Discussion of Mission Consequence and Risk Predictions

Contributions to total mission risk for the pre-launch, early launch, late launch, and EGA swingby mission segments are 2%, 27%, 55%, and 16%, respectively. The characteristics of release and dominant pathways for each mission segment are discussed in this section.

6.7.2.1 Pre-Launch Accidents

A typical accident scenario during the pre-launch phase involves the inadvertent activation of the destruct system or the Centaur cryogen explosion resulting in the on-pad explosion of the Titan IV core propellant. Environment definitions from the Databook indicated the starting time of potential accidents to be no earlier than T-94 minutes. Since the October launch window spanned between 12:39 a.m. to 7:00 a.m., the starting time of accidents in phase 0 was sampled randomly between 55 min before midnight to 7:00 a.m. Analysis of accident environments and probabilities have led to a single LASEP-T simulation for pre-launch phase, namely case 0.0.

Pre-launch accidents include either a type 3 (SV) or type 4 (Core + SV) liquid fuel fireball. A total of 64% of the simulated accident cases have a type 4 fireball which could loft released fuel to altitudes between 1000 and 2000 m. As a result, the majority of source terms in the fireball cloud and stem will deposit in large off-site areas. Deposition to densely populated areas would have a higher consequence result through the resuspension pathway. If the deposition occurs in the Atlantic Ocean or in off-site areas to the southwest, very low health consequences would be expected, dominated by the ingestion pathway.

In general, the low ground concentration due to the large cloud dimension of fireballs would result in mean individual doses of less than 1 rem. As such, the direct inhalation pathway with its short exposure interval only contributes a modest part to the health effects. The

6-127

contribution from resuspension, mainly in urban (high resuspension rate) areas is the dominant pathway in 77% of the variability-only analyses.

For the source term that remains airborne after 100 km of transport from the launch pad, the mean health effects predicted without de-minimis applicable to off-grid population is 7.5 x 10^{-3}. The population in the vicinity of KSC/CCAS site and the off-grid population account for 89% and 11 % of the risk evaluated for case 0.0. Due to high altitudes to which source terms would be lofted, the number of health effects for on-site workers is about 2 orders of magnitude lower than the health effects for off-site residents.

6.7.2.2 Early Launch Accidents

Accidents in the early-launch segment could occur randomly between 12:39 AM and 7:00 AM. Dominant accident cases are represented by case 1.1 (Total Boost Vehicle Destruct) and cases 1.3 (Total Boost Destruct with SRMU Aft Segment Impact). From the variability-only results, their contribution to the phase 1 risk is 76% and 17% respectively. Typical releases in case 1.1 involve an SV impact source term dispersed within the SRMU fire plume which stabilizes at altitudes between 400 m and 1200 m.

As reported in Table 6.7.1-4, the population at risk in phase 1 is mainly off-site residents with mean health effects about a factor of 10 to 100 higher than the mean health effects of off-grid population and on-site workers. This is due to the elevation of releases associated by either the SRMU fire plume and or a liquid propellant fireball, both of which disperse the source term to large off-site areas but at very low concentrations. Land contamination exceeding 0.2 μCi/m^2 is primarily caused by large particles above 16 μm and would be expected to be restricted to the KSC launch site, composed of on-site facilities or unpopulated areas with marshes and dense vegetation.

Similar to pre-launch accidents, the resuspension pathway dominates the health effects results. This is attributed to the large areal releases through SRMU fire plume, primarily affecting urban off-site areas. In the variability-only analysis, 90% of simulated case 1.1 accidents include type 3 - SRMU fire plume releases. Source terms from a type 3 release would most likely be engulfed by the large SRMU fire plume. Therefore, the majority of the source term for case 1.1 is typically dispersed as a uniform column filling the mixing height. Table 6.7.2-1 summarizes the percentage of analyses in which each of the four primary pathways was most dominant.

Table 6.7.2-1. Dominant Exposure Pathways in Selected Phase 1 Accident Cases

Case	Inhalation - Cloud Passage	Inhalation - Resuspension	Produce Ingestion	Seafood Ingestion
1.1	2%	87%	5%	5%
1.3	4%	81%	9%	6%
1.10	10%	75%	7%	8%
1.13	3%	70%	15%	12%

6.7.2.3 Late Launch Accidents

Reentry accidents during the late launch phase involve the fuel release upon impacts of RTG modules on a hard rock surface. The dominant contributors to the late launch phase risk is accident case 5.2 or nominal orbital decay reentry. Based on the evaluated bounce height of RTG modules on a rock surface, the source term is modeled as a $\sigma = 1$ meter Gaussian cloud released at 0.5 m above ground.

While the major contributor to health effects of early launch accidents is resuspension, direct inhalation during cloud passage is dominant for late launch accidents. The typical contribution to health effects from direct inhalation and resuspension pathways for the late launch accidents are 60% and 40%, respectively. Reentry accidents during late launch have maximum individual doses equal to or less than 20 rem. A total of 55% of the surface impacts occur within population density classes 4, 5, and 6 (i.e., 6.5, 17.5, and 37.5 persons/km²). For the accident case 5.2, the average population density of impacted areas is at 98 pers/km², and an average of 2.46 modules release fuel upon rock impact.

Because of the relatively low release height in these accidents, ground depletion of the clouds has a significant influence on consequence predictions. As a result, most of the exposed population are located in the first 60 km of transport, with maximum exposure doses occurring between 1 and 3 km.

6.7.2.4 EGA Reentry Accidents

Up to eight release types could contribute to the health consequence result from an EGA reentry accident. Air releases at high altitudes (GIS failed - air release) and soil impact releases from GISs with melted clads (GIS OK - Clad melt on soil) dominate the EGA

consequence, contributing 32% and 54% respectively to the mean health effects. Table 6.7.2-2 provides the mean value of breached modules sampled for each release type. As shown, 49% of releases leading to health consequence are associated with air releases at high altitudes with a mean value of 0.54 failed modules. The GIS OK - Clad melt release type has a higher mean value of 6.88 failed modules but is present in 60% of the releases. Similar to out-of orbit reentry accidents, surface impacts in areas with population density classes 4, 5 and 6 are dominant, accounting for a total of 45% of all surface impacts. Releases in population density class 8 (175 persons/km^2) and above represent about 8% of all surface impact releases.

Each EGA reentry accident is a combination of various fuel release types with different characteristics. While fuel releases at high altitudes could have a worldwide exposed population, fuel releases at ground impacts affect only specific receptor cells. Fuel releases at high altitudes, due to the long atmospheric residence times that result in a low ground deposition rate over several years, contribute mainly to health consequence through the direct inhalation pathway. The fuel releases at ground impacts due to the relatively low altitude of the source term, could contaminate some surface areas with high ground concentrations, and thus, the resuspension pathway could be dominant in those cases. Adding to the complexity of this type of release, the number of breached modules determining the total source term, is dependent on the exposed rock fraction or soil fraction which can vary significantly with the 720 equal-area receptor cells.

Overall, the direct inhalation pathway is the dominant contributor to health consequence for EGA reentry accidents. For simulated accidents that have in-air release occurring in the stratosphere, the air concentration at ground level is dependent on the residence time within both the stratosphere and the troposphere. However, since the tropospheric residence time describes how fast the air concentration of fuel particles is depleted to the ground, it has a significant impact on the inhalation exposure pathway. The stratospheric residence time has virtually no influence on the health effects results because it only controls the transfer rate of material between the stratosphere and the troposphere, and the residence time considered for this atmospheric layer is shorter than both the decay factor for the plutonia fuel and the 50 year exposure period considered. For simulated accidents with ground impact releases, the relatively low height of release induces a rapid depletion of the source term cloud. Therefore, maximum exposure due to inhalation during cloud passage is expected to occur in the first few kilometers.

Table 6.7.2-2. Comparison of Consequence Contributions by GIS/Module End State between the 500 km and 800 km EGA Analyses

Released Type	Contribution to Mean Health Effects* 500 km EGA FSAR Suppl	Contribution to Mean Health Effects* 800 km EGA Post Suppl	Percentage Contribution to Mean Health Effects* 500 km EGA FSAR Suppl	Percentage Contribution to Mean Health Effects* 800 km EGA Post Suppl	Occurrence Probability Given Consequence* 500 km EGA FSAR Suppl	Occurrence Probability Given Consequence* 800 km EGA Post Suppl	Mean Number of Failed Modules 500 km EGA FSAR Suppl	Mean Number of Failed Modules 800 km EGA Post Suppl
Intact Module on Rock	4.98e-04	6.34e-04	0.00	0.00	0.0442	0.862	0.10	0.16
GIS OK - Clad OK on Rock	1.85e-02	1.04e-02	0.01	0.01	0.1656	0.1566	0.35	0.24
GIS OK - Clad Melt on Soil	19.4	49	14.17	53.96	0.4044	0.6004	3.17	6.88
GIS OK - Clad Melt on Rock	3.8	12.3	2.78	13.55	0.1820	0.3306	0.34	0.86
GIS Failed on Soil	2.91	0.61	2.13	0.67	0.2131	0.0667	0.31	0.07
GIS Failed on Rock	8.23e-02	6.8e-03	0.06	0.01	0.0253	0.0043	0.03	0.00
GIS Failed - Air Release	110.6	28.8	80.79	31.72	0.8882	0.4882	1.68	0.54
All Types	136.9	90.8						

* 50 Year without de-minimis

FSAR Suppl = From FSAR Addendum: Supplemental Analysis, issued May 1997
Post Suppl = From Reference 6.7-1, issued October 1997

6.8 CONSEQUENCE UNCERTAINTY ANALYSIS

The Cassini safety analysis included an integral evaluation of the uncertainty in the consequence results. This evaluation was complex in nature because the accident consequences were presented as probability distributions representing the variability in potential accident probability and severity. Evaluation of the uncertainty of a probability distribution is considerably more complex than the standard uncertainty analysis, which estimates the uncertainty in a number. This section discusses the reasons for performing an uncertainty analysis, the procedure that was followed to perform the analysis and the results of the analysis.

6.8.1 Analysis Methodology

The Cassini safety analysis consisted of a number of physical models of processes which are expected to occur in potential mission accidents which could result in the release of radioactive material. Many of these models described complex situations and were based upon a relatively modest amount of experimental and observational data. In such situations the usefulness of the results of an analysis are increased by a knowledge of the uncertainty in those results. This can arise from uncertainty in the inputs to the models (parameter uncertainty) or from uncertainty in the models themselves (model uncertainty). Results of uncertainty analyses are generally reported in terms of confidence levels or confidence intervals. For example there is a 95% "probability" that the actual consequence will be less severe than the 95% confidence level distribution. There is a 90% "probability" that the actual consequence distribution will lie in the 90% consequence interval between the 5% and 95% confidence levels.

The consequence analyses reported in the two FSARs for the Galileo and Cassini missions, as performed by HNUS, did not include quantitative evaluation of uncertainty. The Galileo SER, prepared by INSRP, had a qualitative uncertainty analysis whereas the Ulysses SER included a quantitative uncertainty analysis. The Ulysses FSAR mission health effects distribution was below the 5% confidence level health effects distribution as determined by INSRP and presented in the Ulysses SER. Without an uncertainty analysis for the FSAR result, it was not possible to determine if the disagreement in the results reflected a fundamental disagreement in the modeling or reflected uncertainty in the two models.

Therefore, it was generally agreed that the Cassini safety analysis should include an evaluation of uncertainty. The decision was made to restrict the uncertainty analysis to parameter uncertainty. Inclusion of model uncertainty is appropriate when the experimental data available does not allow one to distinguish between several existing models which give greatly differing results. This did not appear to be the situation for most of the models in the Cassini safety analysis.

Once the decision to perform an uncertainty analysis was made, it became necessary to choose the procedure for carrying out the uncertainty analysis. The method was developed in parallel with the development of the method for analyzing the consequence variability, which was being performed in-house for the first time. Previously HNUS had analyzed consequence variability using a two step process. The first step was a calculation of the consequence arising from the average source terms for each of the various accident phases. The second step was a Monte Carlo simulation of the variability which used the distributions of important source term and consequence model variables and the sensitivities of the consequence to the values of those variables.

The approach chosen for variability involved performing multiple consequence calculations using sampled source terms and sampled meteorological conditions. This approach was felt to be more accurate than the previously used method, as the actual variables and their effects are used, rather than models of the variable distributions and models of the sensitivity of the consequence to the variable values. Latin Hypercube Sampling (LHS) was chosen to increase the accuracy of the resulting consequence distributions for a given number of consequence calculations, since the complexity of the calculation limited the number of consequence calculations which could be performed for an accident case in a reasonable time to ~1000.

The standard method for performing an uncertainty analysis requires rerunning the variability analysis many times, with different sampled values of the uncertain parameters used for each run. Consequence distributions at various confidence levels are then determined from the family of consequence distributions which results. This approach was not practical due to the computationally intensive nature of the consequence variability calculation.

The first approach considered for the uncertainty analysis was similar to the HNUS approach to variability, namely a sensitivity study followed by a simulation. This approach was rejected in favor of a more general method based on deconvolution, a mathematical procedure used in signal and image processing to separate signals from distortion. Deconvolution is the inverse of convolution which combines two functions to produce a third. For example the probability density of the sum of two random variables is the convolution of the probability densities of the two variables. Deconvolution can be used to find the probability density of one of the variables if the density of the sum and the density of the other variable are both known.

The uncertainty analysis required two sets of consequence calculations: a variability-only calculation in which parameters are held at their most probable values and a variability-plus-uncertainty calculation in which variables and parameters were sampled simultaneously. Deconvolution was then used to separate the uncertainty distribution from the variability-plus-uncertainty distribution. The calculation was performed on the logarithm of the consequence, which resulted in an uncertainty multiplier distribution, since the logarithm of a product is the sum of the logarithms of the individual components. Furthermore, the logarithm of the uncertainty multiplier distribution was assumed to be normally distributed. The variability-only consequence distribution, the uncertainty multiplier, and the accident probability distributions were combined in the final step by a Monte Carlo simulation to determine the consequence distributions at various confidence levels.

The overall procedure for analysis of variability and uncertainty consisted of the following steps:

1. Classify quantities in the source term and consequence models as variables or parameters. Quantities representing physical properties such as temperatures, pressures, velocities, etc. were regarded as variables. Model derived quantities such as thresholds, yield strengths, moments of variable distributions, etc. were classified as parameters.

2. Determine distributions for the variables and parameters. Distributions of variables representing the accident environments came from the Databook. Meteorological variability was captured by using actual past meteorological data. Parameter distributions were determined by several different procedures. Standard statistical formulae were used to determine the uncertainty in parameter values resulting from limited experimental data for a number of the source term models. Engineering judgment was used in situations where the experimental data was insufficient to use quantitative methods. Sandia National Laboratories provided assistance in

determining parameter distributions for a number of consequence model parameters derived from observational data.

3. Structure the source term and consequence models so that the two types of calculations, the variability-only and the variability-plus-uncertainty calculations, could be performed. Parameters were held to their nominal values for the variability-only runs, but were sampled from their distributions for the variability-plus-uncertainty runs. The nominal parameter values were, in general, the values with the highest probability. Therefore these values were the median values in the frequent situation in which the parameter distribution was normal or lognormal. (The use of median values as nominal parameter values is desirable as it results in the variability-only calculation giving a "best-estimate" distribution.) In some cases the distributions were neither normal nor lognormal or the distribution was modified between the variability-only run and the variability-plus-uncertainty run. In those cases the nominal parameter values were often somewhat different from the median value of the parameter distribution. However there was no systematic bias on the nominal value, so that the result of the variability-only run was not systematically biased away from the "best-estimate". It should also be noted that the sampling procedures for variables and parameters were somewhat different in the variability-plus uncertainty runs. Source term variables were sampled for each use, excluding material properties, which were sampled once per trial. Source term parameters were sampled once per trial. Consequence variables and parameters were sampled once per LHS trial.

4. Perform the variability-only and the variability-plus-uncertainty runs for the various accident cases. The implementation of these runs differed for the various mission phases, as described elsewhere.

5. Perform deconvolution on the results of the variability-only and variability-plus-uncertainty runs for important accident cases. This procedure was carried out for two consequences: 50 year health effects without de minimis and 50 year collective dose without de minimis. The results of the deconvolution process were the mean and standard deviation of the logarithm (base 10) of the uncertainty multiplier distribution. Deconvolution was also performed on the source term mass distribution, in order to estimate what portion of the uncertainty was due to the source term model.

6. Perform the Monte Carlo simulation of uncertainty for individual accident cases, combined mission phases and the entire mission to obtain consequence distributions and distribution statistics at various confidence levels.

7. Perform a sensitivity analysis using the consequence parameter values and consequences from the variability-plus-uncertainty distribution to determine which parameters were the main contributors to the overall uncertainty. A linear regression of the logarithm of "normalized" health effects versus the logarithms of the parameters was used. These were combined with the standard deviations of the logarithms of the parameters to estimate the contribution of the important parameters to the overall uncertainty. The term "normalized" health effects refers to health effects divided by source term mass. This normalization reduced variability, resulting in more accurate regression coefficients. For EGA the parameter regression was performed for in-air releases, which represented approximately 80% of the total consequence of potential reentries from EGA. This precluded using the source term deconvolution in the parameter analysis since deconvolution was carried out on the entire source term, not the in-air release source term component.

6.8.2 Uncertainty Analysis Results

Deconvolution was carried out for accident cases 0.0 (pre-launch), 1.1 and 1.3 (early launch), 3.1, 5.1, and 5.2 (late launch) and EGA. The mean μ and the standard deviation σ of the log (base 10) of the uncertainty multiplier distribution are given in Table 6.8-1. The units of μ and σ are "orders of magnitude" since they are the mean and standard deviation of the log (base 10) of the uncertainty multiplier distribution.

Table 6.8-1. Deconvolution Results

Accident Case	Source Term		Health Effects		Collective Dose	
	μ	σ	μ	σ	μ	σ
0.0	0.21	0.67	0.35	1.06	0.45	1.10
1.1	-0.32	0.37	0.11	0.64	0.16	0.73
1.3	0.55	0.96	0.37	0.59	0.47	0.81
3.1	0.14	0.19	0.00	1.20	0.11	1.18
5.1	0.13	0.19	0.00	1.20	0.11	1.18
5.2	0.13	0.26	-0.07	1.33	0.05	1.35
EGA	0.31	0.15	0.33	0.90	0.44	0.85

The results of the parameter sensitivity studies are shown in Tables 6.8-2 through 6.8-5 for accident cases 0.0, 1.1, 5.3, and EGA. The tables include a comparison of the total variance calculated from the important parameters and the total variance as determined from deconvolution. The lack of close agreement between these quantities shows that the contributions to variance for each of the parameters must be regarded as a rough estimate.

Table 6.8-2. Case 0.0 (Pre-Launch): Parameter Regression Analysis

Source of Uncertainty	Regression Coefficient	Standard Deviation of Log (Parameter)	Contribution to Variance
Source Term Mass (from deconvolution)	--	--	0.45
Inhalation Dose Conversion Factor Multiplier	0.76 ± 0.04	0.66	0.25
Urban Resuspension Factor	0.22 ± 0.02	1.37	0.09
Total of Above			0.79
Deconvolution Result (Health Effects)			1.12

Table 6.8-3. Case 1.1 (Early Launch): Parameter Regression Analysis

Source of Uncertainty	Regression Coefficient	Standard Deviation of Log (Parameter)	Contribution to Variance
Source Term Mass (from deconvolution)	–	–	0.14
Inhalation Dose Conversion Factor Multiplier	0.74 ± 0.04	0.66	0.25
Urban Resuspension Factor	0.35 ± 0.02	1.37	0.23
Total of above			0.62
Deconvolution Result (Health Effects)			0.41

Table 6.8-4. Case 5.3 (Late Launch): Parameter Regression Analysis

Parameter	Regression Coefficient	Standard Deviation of Log (Parameter)	Contribution to Variance
Deposition Velocity Multiplier	-0.77 ± 0.03	0.92	0.50
Inhalation Dose Conversion Factor Multiplier	1.00 ± 0.04	0.66	0.43
Source Term Mass (from deconvolution)	–	–	0.07
Urban Resuspension Factor	0.18 ± 0.02	1.37	0.06
Health Effects Estimator Multiplier	1.00 ± 0.10	0.24	0.06
Inhalation Sheltering Factor	0.36 ± 0.04	0.49	0.03
Breathing Rate	1.01 ± 0.17	0.15	0.02
Total of Above			1.17
Deconvolution Result (Health Effects)			1.77

Table 6.8-5. EGA In-Air Release Parameter Regression Analysis

Parameter	Regression Coefficient	Standard Deviation of Log (Parameter)	Contribution to Variance
Inhalation Dose Conversion Factor Multiplier	0.97 ± 0.02	0.67	0.43
Troposphere Residence Time	0.90 ± 0.02	0.51	0.22
Health Effects Estimator Multiplier	0.98 ± 0.05	0.24	0.06
Breathing Rate	0.96 ± 0.08	0.15	0.02
Total of Above			0.73

Several results are noteworthy. The inhalation dose conversion factor multiplier is an important contributor to uncertainty for all four accident cases analyzed. This parameter is a direct multiplier for health effects resulting from inhalation (the primary pathway) and has a standard deviation of about two-thirds of an order of magnitude. Source term uncertainty is most important for pre-launch and early launch, reflecting the complexity of modeling these accident cases. The contribution to uncertainty in pre-launch and early launch from the urban resuspension factor reflects the fact that long-term resuspension is the dominant health effects pathway in those mission segments. The important role of the deposition velocity multiplier for late launch results from the facts that direct inhalation is the primary pathway for this mission segment and that the release is very close to the ground. Increased deposition depletes the release before it reaches more population, as indicated by the negative regression coefficient. Troposphere residence time is a significant uncertainty contributor for EGA in-air releases since it determines how long the particles are available for inhalation.

Figure 6.8-1 shows the CCDFs (complementary cumulative distribution functions) for 50 year health effects (without de minimis) for variability-only and the 5%, 50%, and 95% confidence levels for the mission. The near coincidence of the variability-only CCDF and the 50% confidence level CCDF shows that the variability-only result lies in the middle of the uncertainty range and is a "best-estimate". Table 6.8-6 provides expectation values of health effects for the three confidence levels, variability-only and variability-and-uncertainty for the mission phases and the combined mission. The variability-and-uncertainty expectation value is a mean over both variability and uncertainty.
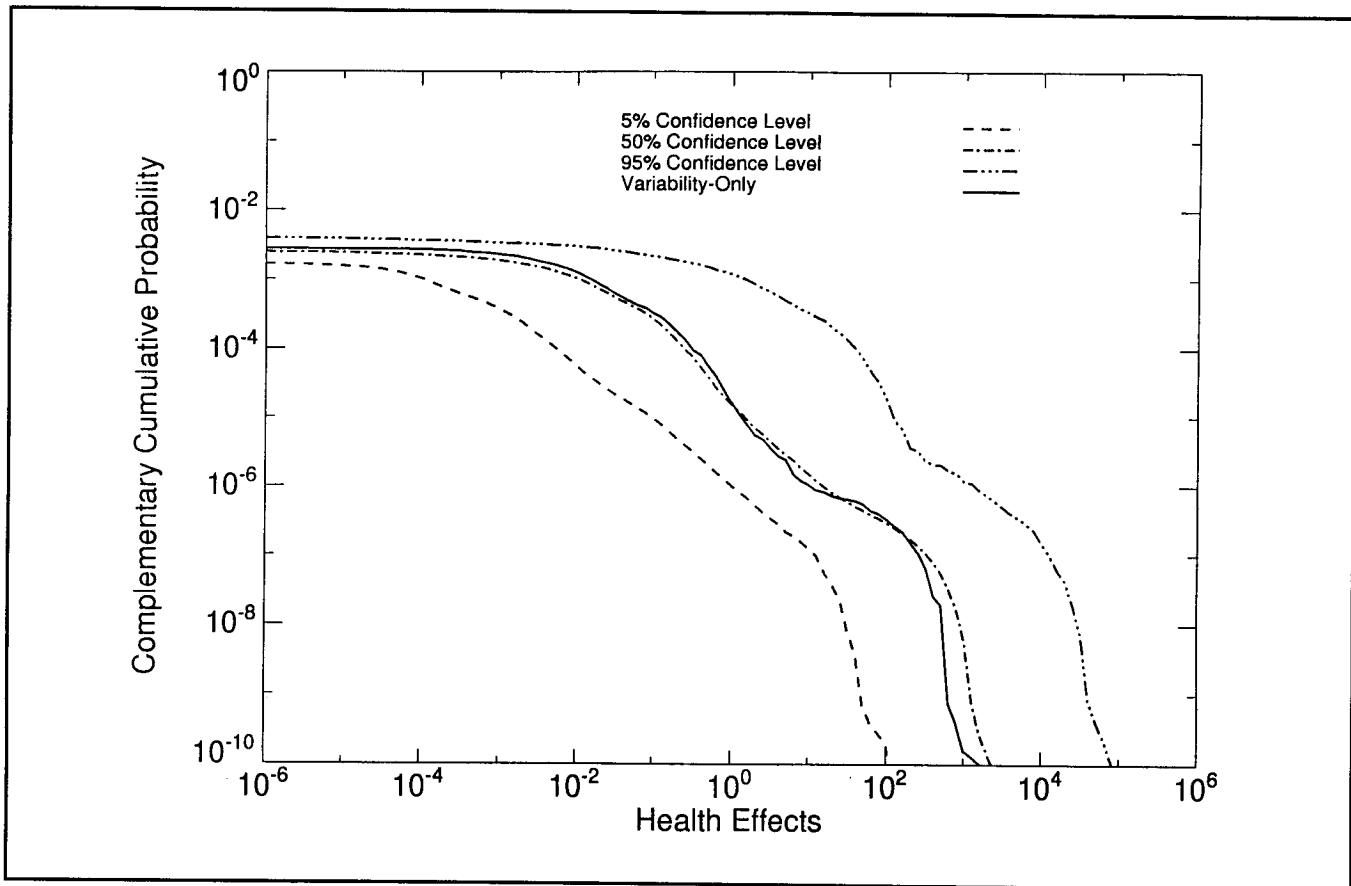
Figure 6.8-1. Total Mission 50 Year Health Effects (without de minimis)

Table 6.8-6. 50 Year Health Effects without de minimis Expectation Values

Mission Phases	Mission Segment	Variability- Only	Variability and Uncertainty	5% Confidence Level	50% Confidence Level	95% Confidence Level
0	Pre-Launch	3.4×10^{-6}	2.7×10^{-5}	7.6×10^{-8}	6.0×10^{-6}	4.2×10^{-4}
1	Early Launch	4.7×10^{-5}	9.4×10^{-5}	5.0×10^{-6}	6.2×10^{-5}	7.9×10^{-4}
3-8	Late Launch	9.4×10^{-5}	4.7×10^{-4}	4.0×10^{-7}	7.3×10^{-5}	1.3×10^{-2}
	EGA Reentry (Short Term)*	8.6×10^{-5}	4.8×10^{-4}	1.5×10^{-6}	8.7×10^{-5}	4.3×10^{-3}
	Total Mission: *	2.3×10^{-4}	1.8×10^{-3}	8.3×10^{-6}	2.2×10^{-4}	1.9×10^{-2}

* Based on 500 km Earth Swingby

6.9 CASSINI SAFETY TEST PROGRAM

A review of the safety analyses performed for the Galileo and Ulysses RTG missions concluded that there were several events for which new or modified RTG response models would improve risk assessment evaluation. Additional safety testing was identified to support modeling development activities, specifically: a) RTG terminal velocity impact; and b) edge-on collisions of plate fragments with an RTG. A description of each test and the test results are summarized herein from Reference 6.9-1.

6.9.1 RTG End-On Impact Test

6.9.1.1 Background

Analysis of RTG trajectories following near-pad release from an in-flight vehicle indicate that concrete targets can be impacted at speeds approaching terminal velocity. An RTG would be expected to undergo random tumbling and thus have a probability (though a low one) of impacting at an approximately end-on attitude. In this event, the maximum impact speed is the terminal velocity of the RTG in tumbling flight which is approximately 56 m/s.

The purpose of the RTG impact tests was to produce test data on fueled clad distortion versus GPHS module stack position in the RTG and the variability in distortion at each position. A secondary objective was to obtain data on fractional fuel-simulant release in the event of a breach in the fueled clad.

6.9.1.2 Test Description

Testing was conducted at the Sandia National Laboratory (SNL) Rocket Sled Test Track (Area III) and was coordinated by Los Alamos National Laboratory (LANL). The test schematic is shown in Figure 6.9-1. A stack of nine simulated GPHS modules was heated in a furnace with an argon atmosphere. The furnace was mounted on a test stand and positioned over a simulated RTG which was mounted to a rocket sled.

The heat source stack was heated to approximately 1210°C and lowered from the furnace into the simulated RTG. The simulated RTG was rotated 90°, after the heat source was latched in place, to orient it for impact at the outboard end, as shown in Figure 6.9-2. After allowing the heat source to cool to approximately 1090°C (the estimated impact temperature) the sled rocket was fired, propelling the simulated RTG into a concrete target.
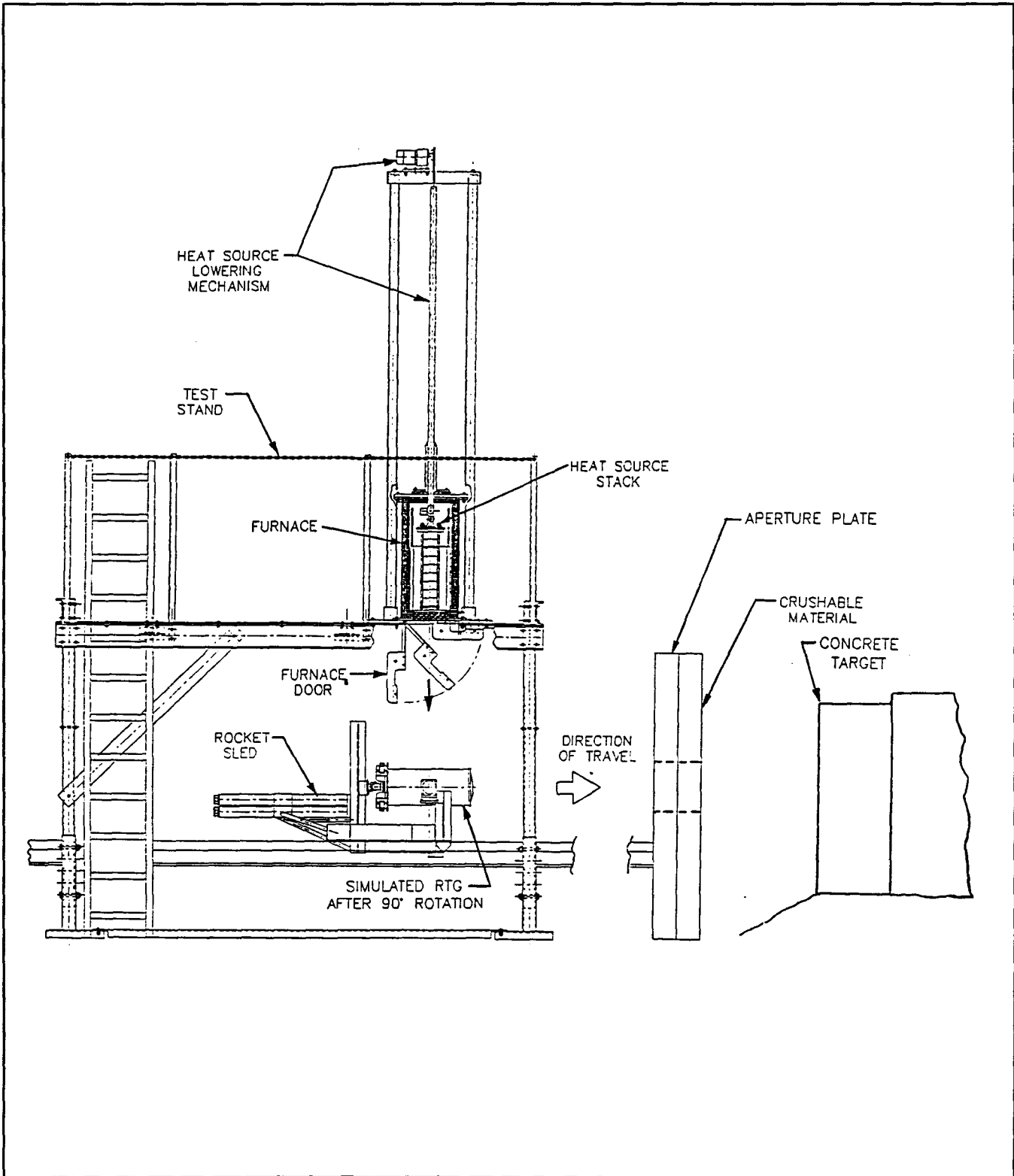
Figure 6.9-1. RTG End-On Impact Test Schematic
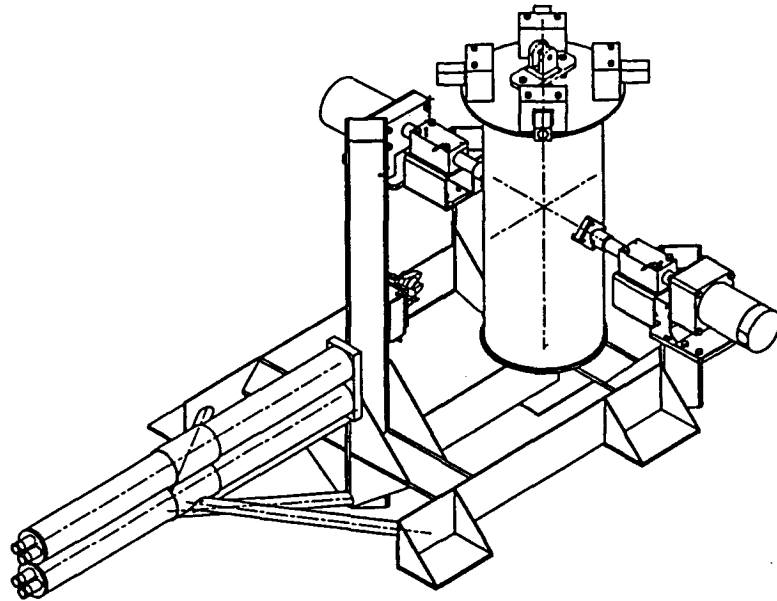
HEAT SOURCE LOADING POSITION
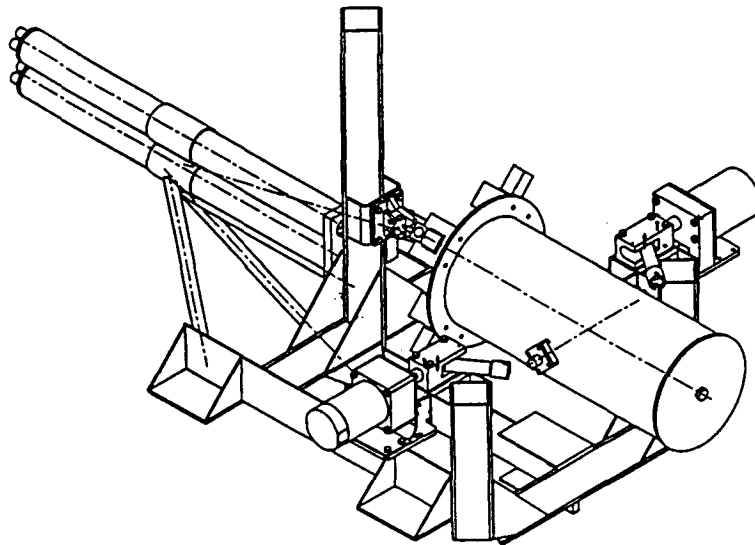
IMPACT POSITION

Figure 6.9-2. RTG End-On Impact Test Stand and Test Setup

The sled was designed to compress as it impacted a steel aperture plate, located approximately four feet in front of the concrete target (reference Figure 6.9-3). The aperture plate was designed to stop the sled while allowing the simulated RTG to pass through its opening and impact the concrete target.

The concrete target used for the test was obtained from the Cape Canaveral Air Station and was typical of the concrete used for installations in the vicinity of the launch pads. The concrete target dimensions were 36 inches x 48 inches x 18 inches thick.

Two impact tests were conducted. The first test (RTG-1) was conducted at a velocity of 57.6 m/s and the second test (RTG-2) was conducted at a higher velocity (77.1 m/s) in order to establish a threshold for obtaining a breach in the fuel clad.
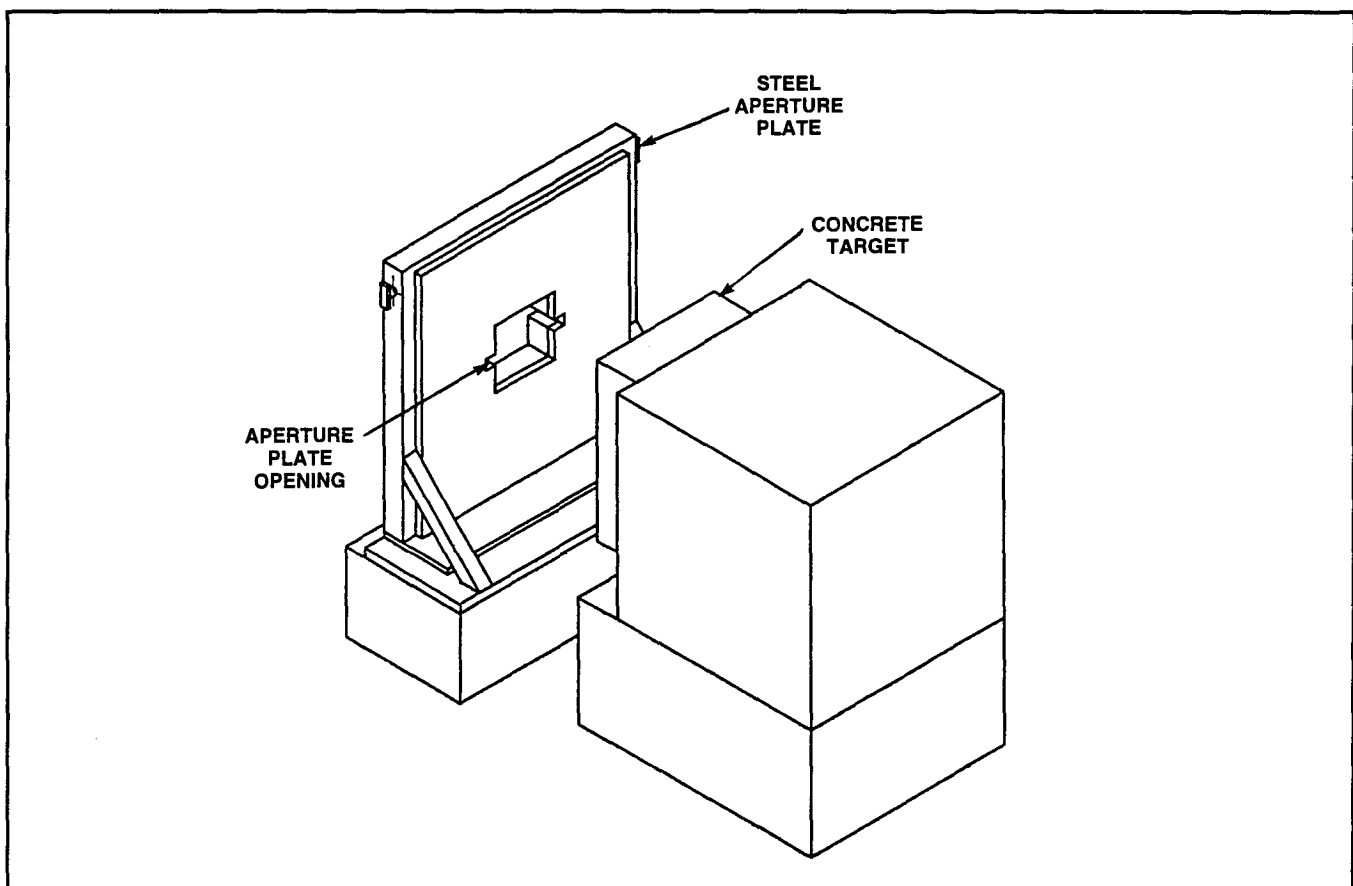
Figure 6.9-3. Setup of Steel Aperture Plate and Concrete Impact Target

6.9.1.3 Test Hardware

The simulated RTG test article consisted of approximately one half of a full length RTG converter shell. The outboard end of the converter, which was impacted against the

concrete target, was prototypical of the RTG design. It included an Al 2219 pressure dome and outboard heat source support system which was comprised of the outboard multifoil insulation end cap, titanium preload frame (spider), FWPF pressure plate, etc. Four spring loaded latches, located on the inboard end of the converter housing, secured the heat source stack in the converter. A blanket insulation (Cerafelt) was used inside the converter to maintain heat source temperature and a purge line was provided to maintain an inert cover gas to minimize oxidation. Two trunnions were provided to permit 90° rotation of the simulated RTG on the rocket test sled, after heat source loading, to orient it for impact. The simulated RTG test article is shown in Figure 6.9-4.

The heat source stack is shown in Figure 6.9-5. The heat source stack consisted of eight modules with FWPF aeroshells containing urania fueled clads or molybdenum mass simulants and a ninth module having a POCO™ AXF-5Q graphite aeroshell. The module stack positions were numbered 1 through 9 with the number 1 module located at the outboard end of the converter (first module at impact end). The modules were stacked using FWPF lock members and the modules were held in place with FWPF tie rods as shown in Figure 6.9-5.

6.9.1.4 Test Results

RTG-1 Test (Impact Velocity: 57.6 m/s)

The RTG-1 test was conducted in April 1995 at an impact velocity of 57.6 m/s representing the terminal velocity of an RTG in tumbling flight. Iridium fuel clad temperature, at time of impact, was 1071 ± 5°C.

The simulated RTG rebounded after impacting the concrete target with a modest twisting of the inboard (trailing) end of the housing. Deformation to the RTG outer shell, shown in Figure 6.9-6, was primarily at the outboard end, above the circumferential stiffening ring which is located 2.95 inches from the outboard flange. The outboard pressure dome remained intact but was compacted such that the imprint of the titanium support frame (part of the outboard heat source support system) was apparent. The deformation of the titanium support frame from the impact is believed to have contributed to the deformation of the GISs in modules #1 and #2. There was considerable breakup of the heat source stack inside the converter. A piece of the stack tie rod and lifting lug, along with one intact module (#9), were ejected from the back (inboard end) of the converter housing.
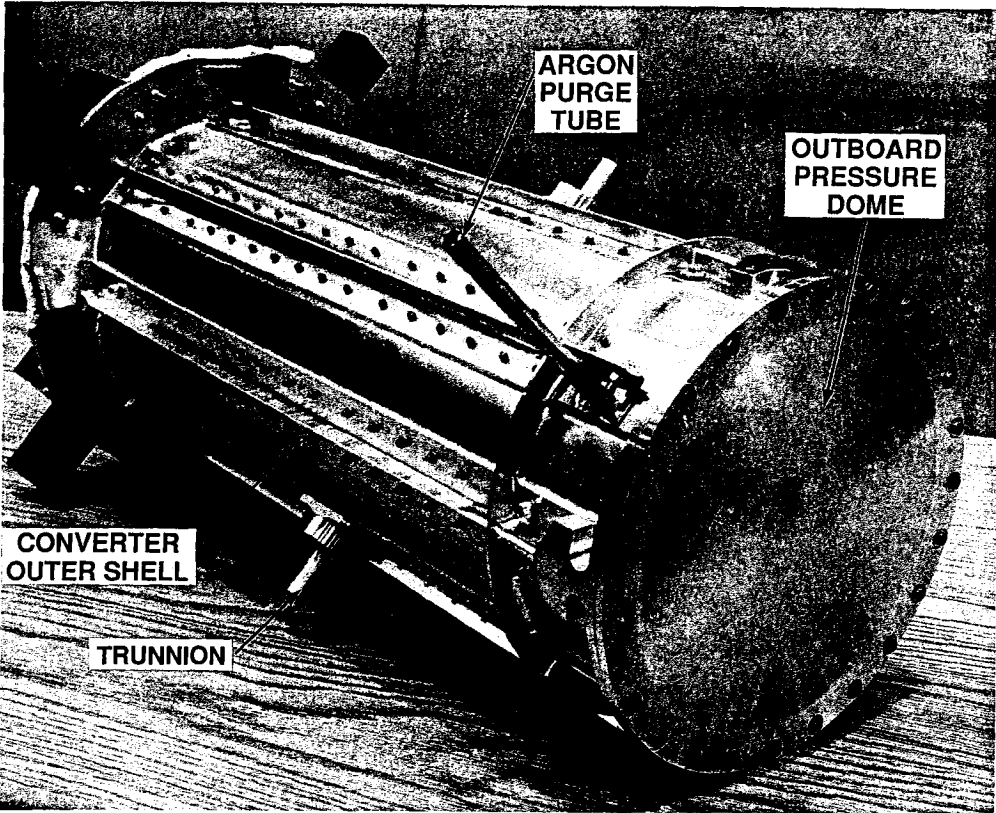
Side View
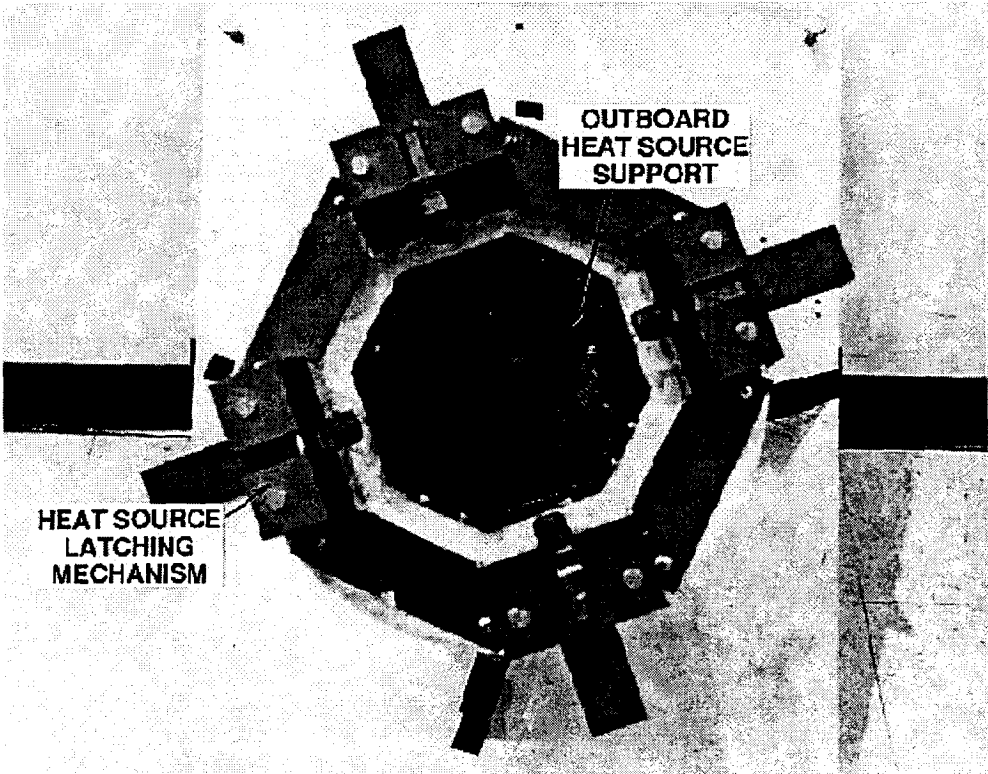
Top View

Figure 6.9-4. Simulated RTG Test Article – End-On Impact Test
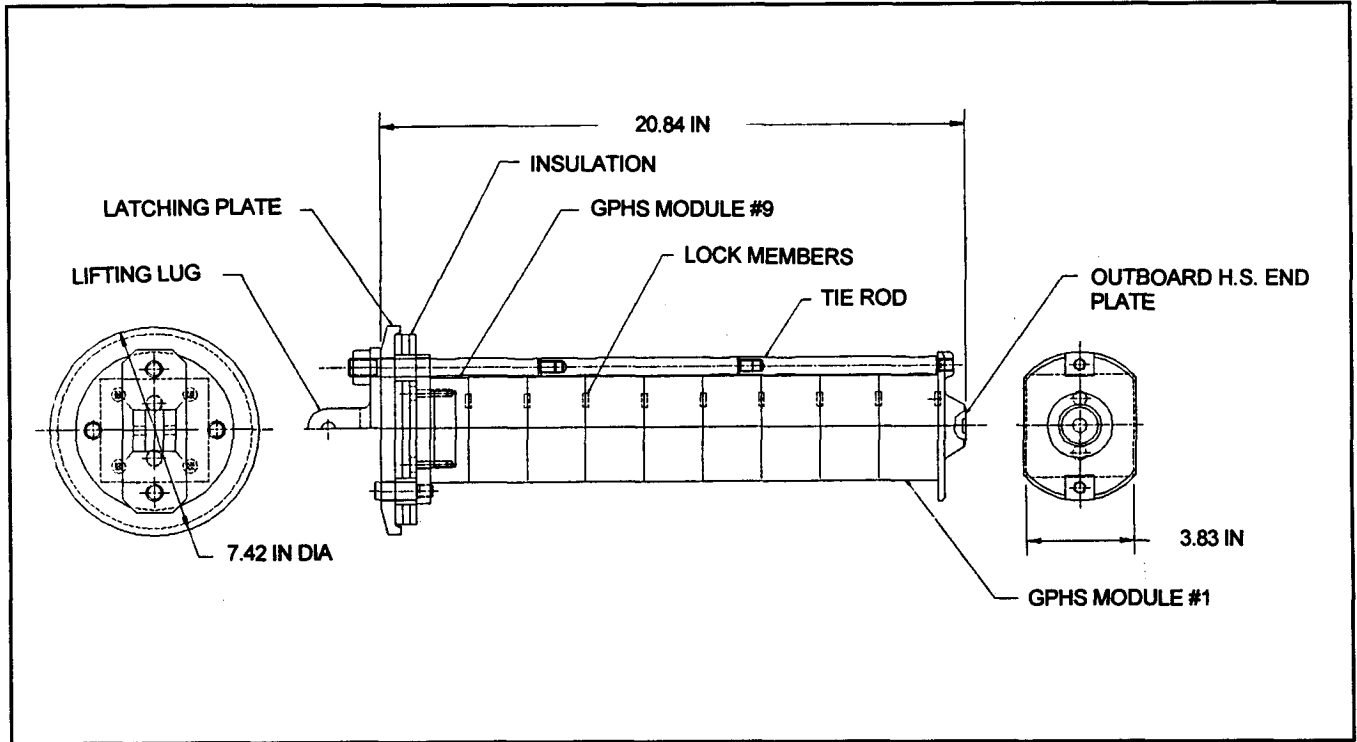
Figure 6.9-5. Heat Source Stack Configuration for RTG End-on Impact Tests
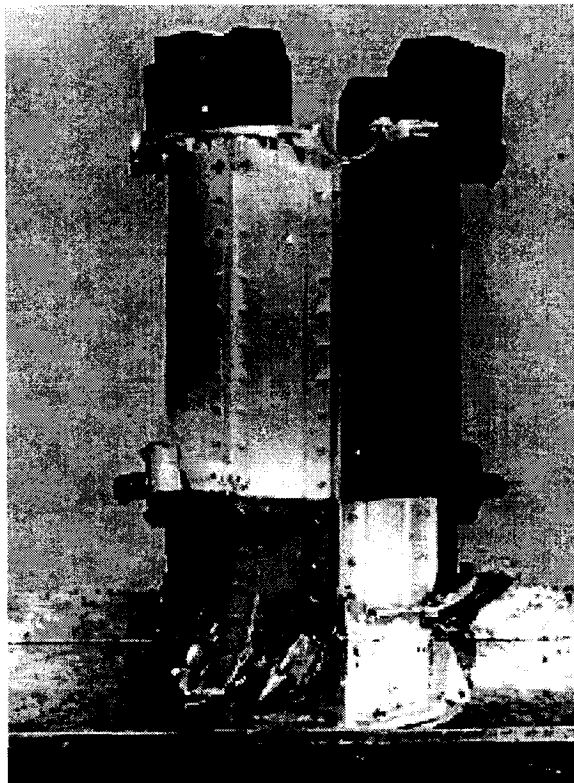
Figure 6.9-6. RTG Outer Shell Damage after 57 m/s Impact

The module #1 and #2 aeroshells and GISs were shattered into several pieces. Fueled clad deformations are listed in Table 6.9-1. The largest deformations were experienced by the fueled clads in module #1, as expected. No visible cracks or breaches were observed in any of the fueled clads. Fueled clad SC0076 was located in the blind (non-threaded) end of the A GIS in module #1. It exhibited the greatest deformation, as indicated by distortion calculations, of all the fueled clads impacted in this test (Figure 6.9-7). Despite its relatively large deformation, neither SC0076 nor any other fueled clad had breached.

Table 6.9-1. Clad Distortion after 57 m/s Impact Test (RTG-1)

		Distortion, % [1]				
			Vent Cup, Diametral		Shield Cup, Diametral	
Module	Fueled Clad ID	Axial	Max.	Min.	Max.	Min.
1	SC0077	8.30	12.60	-15.08	10.71	-4.28
1	SC0076	19.48	20.57	-17.14	15.94	-11.31
1	SC0079	5.84	9.34	-2.06	6.26	-3.77
1	SC0078	5.93	11.65	-8.65	10.37	-5.14
2	SC0081	2.12	6.34	-6.51	4.03	-1.03
2	SC0080	8.72	13.28	-7.80	8.40	-5.91
2	SC0083	4.91	4.88	-3.94	4.88	-3.34
2	SC0082	2.88	6.94	-7.88	4.71	-1.20
3	SC0085	2.29	1.63	-4.37	1.29	-0.51
3	SC0084	1.78	3.34	-3.94	2.49	-1.80
3	SC0088	1.35	1.37	-4.11	0.94	-1.80
3	SC0087	1.02	0.86	-2.40	0.94	-1.63
4	SC0065	1.61	0.51	-1.97	0.77	-1.80
4	SC0064	2.03	1.46	-4.97	1.29	-3.86
4	SC0067	1.02	0.77	-3.00	1.97	-2.40
4	SC0066	2.29	2.14	-3.08	1.89	-3.60
5	SC0069	0.00	-0.26	-0.17	0.26	0.17
5	SC0068	-0.08	-0.34	0.00	0.26	0.26
5	SC0071	-0.85	-0.34	-0.26	0.34	0.17
5	SC0070	-0.08	-0.34	-0.17	0.34	0.17

[1]   Distortion calculations based on nominal dimensions (length =1.181 in. and cup diameter = 1.167 in.).

a) Impact Face
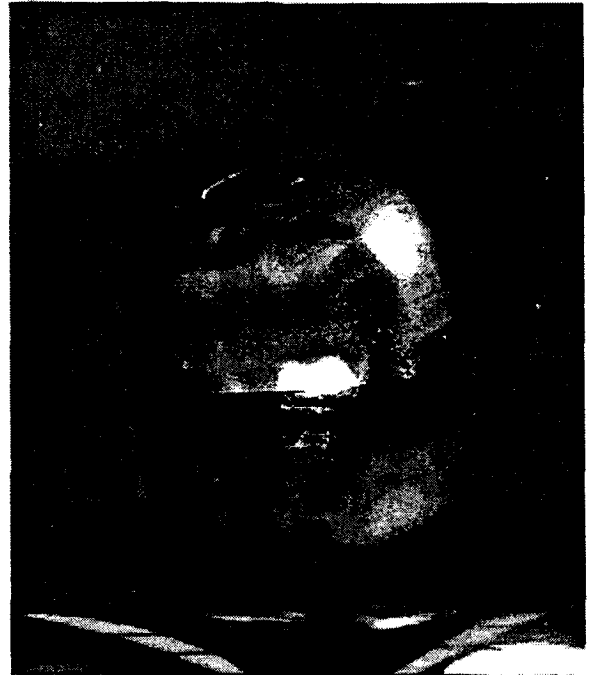
b) Profile
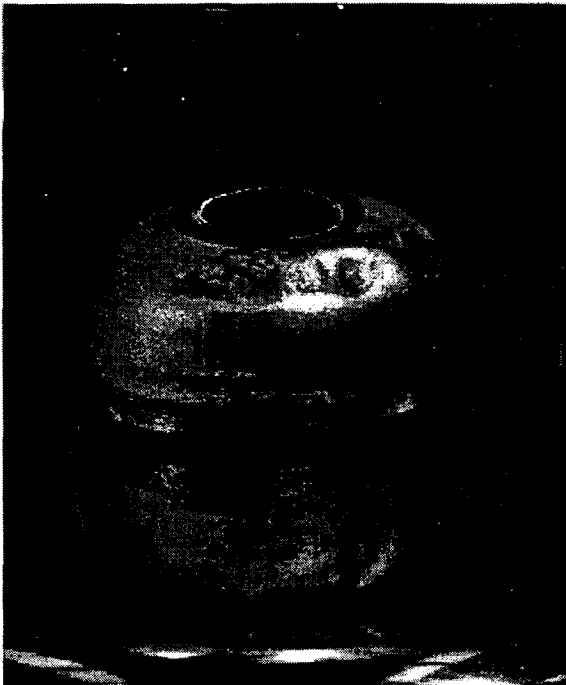
c) Trailing Face
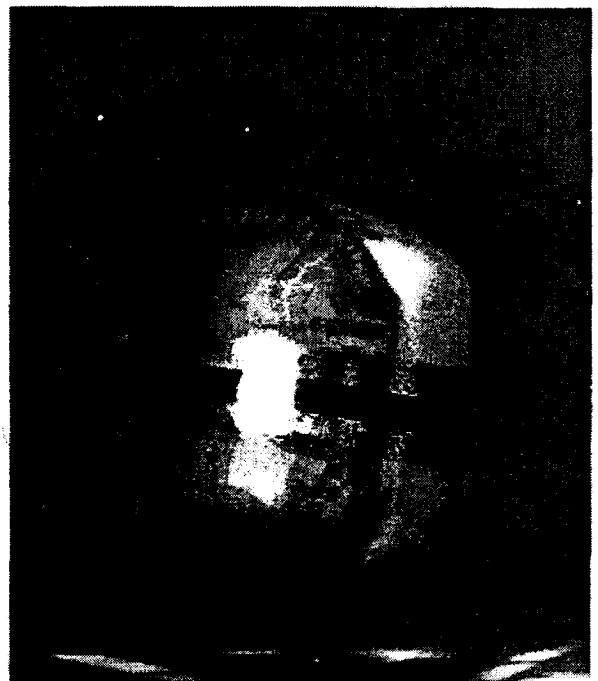
d) Opposite Profile

Figure 6.9-7. Fueled Clad SC0076 after 57 m/s Impact Test

e) Vent End

f) Blind End

6.9-7. Fueled Clad SC0076 after 57 m/s Impact Test (Cont'd)

RTG-2 Test (Impact Velocity: 77 m/s)

The RTG-2 test was conducted in May 1995 at an impact velocity of 77.1 m/s, exceeding the terminal velocity of an RTG in tumbling flight by more than one-third. Iridium fuel clad temperature, at time of impact, was $1090 \pm 5°C$.

Deformation of the RTG outer shell was significant, as shown in Figure 6.9-8. The RTG outer shell was compacted, as a result of the impact, by approximately 6 inches. The pressure dome sheared off and was found lying beside the RTG. Several of the pressure dome attachment bolts were imbedded in the concrete target. Four fueled clads were ejected from the outboard end of the RTG. They were from modules #1, #2, and #4. Four modules (#6, #7, #8, and #9) were ejected from the back (inboard end) of the RTG. Module #6 was cracked in half and contained one intact GIS. The other GIS was cracked and its fueled clads released. The other three modules were intact. A summary of the fueled clad deformations is shown in Table 6.9-2.

Three of the four fueled clads ejected from the outboard (leading) end of the RTG were breached (fueled clads SC0092, SC0096 and SC0107). A large section of iridium was missing from the vent cup of fueled clad SC0092, located in the open (threaded) end of the C GIS in module #1 (Figure 6.9-9). The impact face of the fueled clad was centered at approximately 0 degrees at the weld start. The area of this breach was measured to be 485 mm^2. Approximately 12 g of fuel simulant was released.

Breached fueled clad SC0096 was located in the open end of the C GIS in module #2. A transverse breaching crack was located in the vent cup in the impact face (0° from weld start). This crack measured approximately 10.81 mm long and had a width of approximately 1.48 mm. The widest area of the crack appears to have been pushed open by fragmentation of the simulant fuel pellet beneath the clad wall. The crack appears to have been caused by impact with a relatively sharp edge of an external component upon impact, most likely the titanium "spider" located at the outboard end of the RTG. Approximately 0.2 g of fuel simulant was released from this fueled clad.
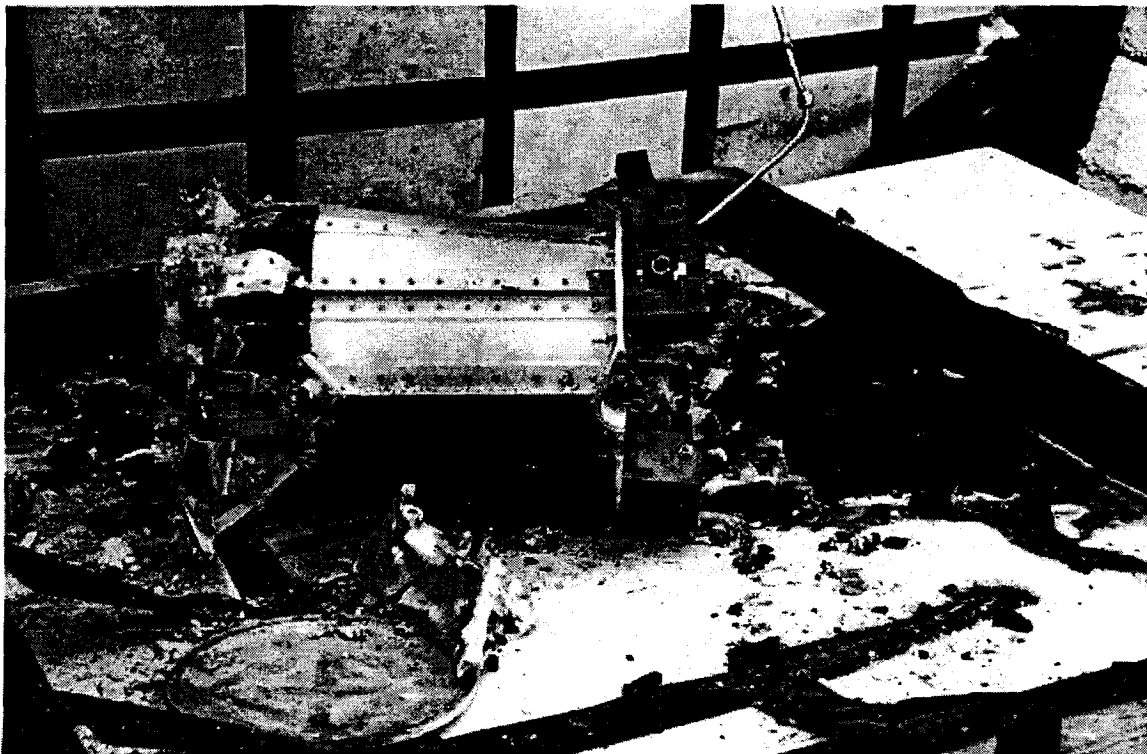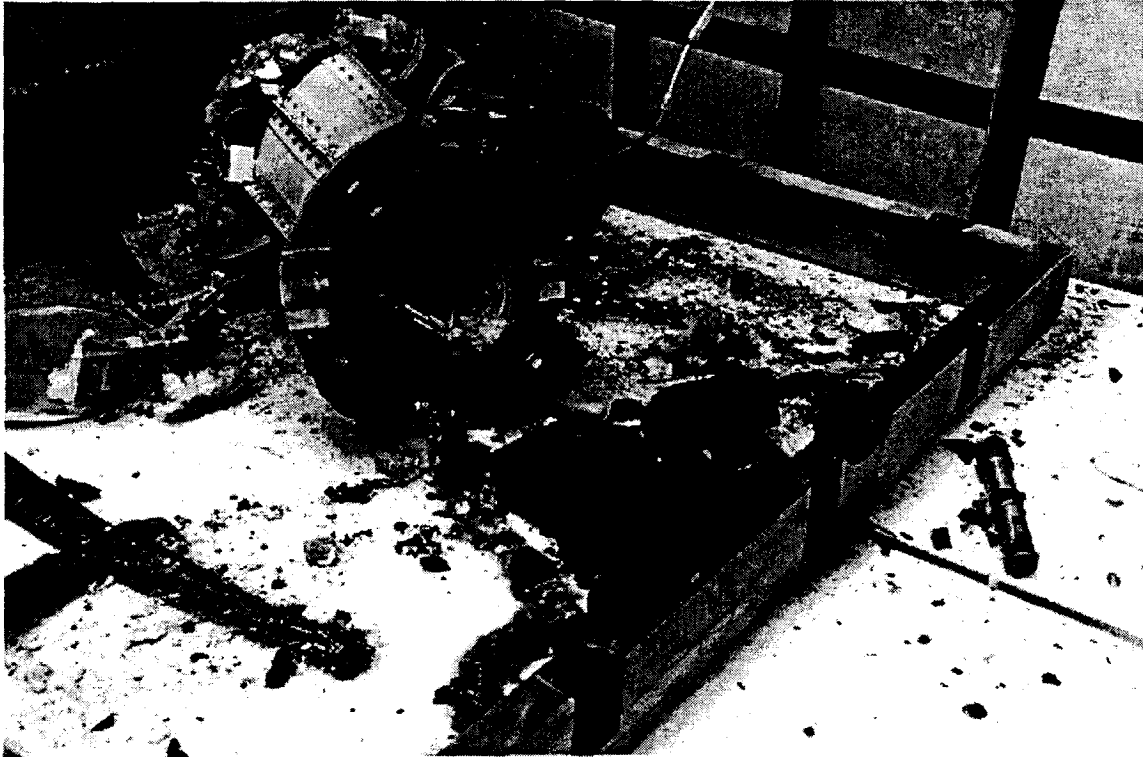
Figure 6.9-8. Simulated RTG after 77 m/s Impact Test

Table 6.9-2. Fueled Clad Distortion after 77 m/s Impact Test (RTG-2)

			Distortion, % [1]			
			Vent Cup, Diametral		Shield Cup, Diametral	
Module	Fueled Clad ID	Axial	Max.	Min.	Max.	Min.
1	SC0090	4.10	7.28	-7.03	6.77	-3.34
1	SC0089	10.65	12.51	-14.48	10.11	-8.83
1	SC0092	14.98	NM [2]	NM [2]	10.03	-4.28
1	SC0091	5.87	10.45	-12.00	5.48	-5.31
2	SC0094	2.47	4.71	-5.91	2.57	-2.31
2	SC0093	1.95	3.43	-2.48	2.48	-2.31
2	SC0096	21.48	10.37	-17.40	9.43	-11.48
2	SC0095	5.18	7.71	-11.31	6.68	-7.03
3	SC0103	2.04	2.83	-4.63	2.48	-1.37
3	SC0097	2.47	3.94	-4.20	4.03	-2.31
3	SC0105	3.90	3.00	-7.63	3.26	-5.06
3	SC0104	4.24	4.28	-6.43	4.54	-7.71
4	SC0108	1.78	0.94	-1.71	2.06	-3.00
4	SC0106	1.45	1.97	-4.46	1.54	-1.80
4	SC0107	4.16	-3.86	6.34	4.80	-6.51
4	SC0086	1.36	3.17	-4.46	3.08	-2.66
5	SC0069	0.76	1.28	-2.23	1.28	-2.06
5	SC0068	3.54	3.08	-4.54	4.28	-7.46
5	SC0071	3.15	4.46	-7.54	3.94	-5.83
5	SC0070	3.99	4.03	-3.68	2.66	-2.74
6	SC0101	0.85	0.51	-0.60	0.26	-0.17
6	SC0100	0.51	0.09	-1.28	-0.09	-0.69
6	SC0109	0.43	2.14	-3.68	1.03	-2.66
6	SC0102	2.38	1.20	-5.74	1.80	-3.60

[1] Distortion calculations based on nominal dimensions (length =1.181 in. and cup diameter = 1.167 in.).

[2] Not measurable, parts of the cup missing.

Fueled clad SC107 experienced a weld failure. This intergranular failure occurred between columnar grains located in the weld centerline. This failure appeared to be the result of fuel simulant fragment push through and resulted in a release of approximately 0.026 g of fuel simulant.

a) Impact Face

b) Profile

c) Trailing Face

d) Opposite Profile
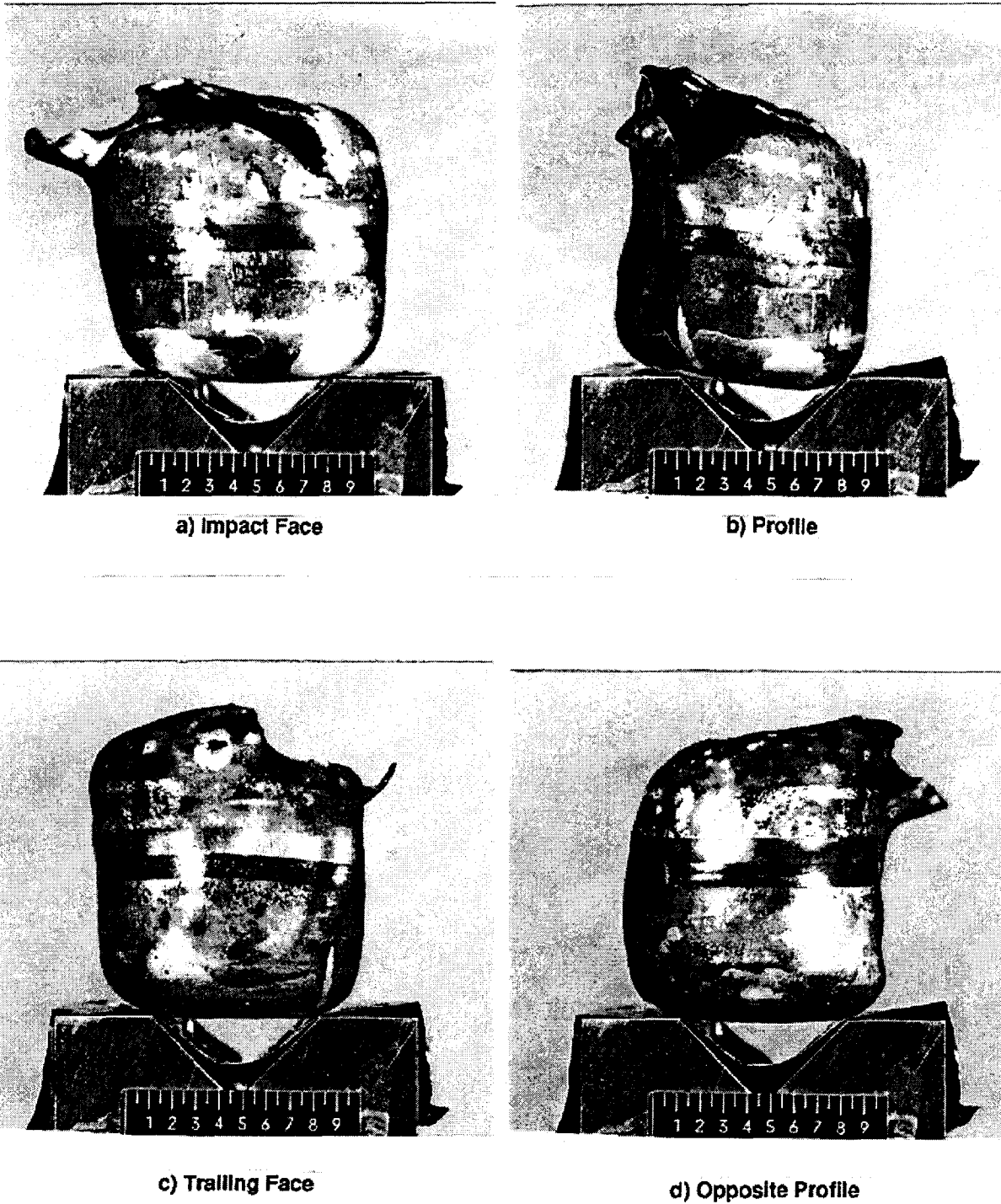
Figure 6.9-9. Fueled Clad SC0092 (Module #1) after 77 m/s Impact Test

e) Vent End

f) Blind End

Figure 6.9-9. Fueled Clad SC0092 (Module #1) after 77 m/s Impact Test (Cont'd)

6.9.2 Edge-On Fragment Test

6.9.2.1 Background

Analyses performed to estimate accident environments for the Cassini mission EIS suggested that plate fragments formed from breakup of the spacecraft propulsion module subsystem (PMS) or the Centaur propellant tank/structure during a propellant explosion may constitute a potential threat to the RTGs. The fragment test was designed to provide data on the penetrability of the RTG by plate fragments at edge-on incidence.

6.9.2.2 Test Description

Testing was conducted at the Sandia National Laboratory (SNL) Rocket Sled Test Track (Area III) and was coordinated by Los Alamos National Laboratory (LANL). The test setup is shown in Figure 6.9-10. A stack of three simulated GPHS modules was heated in a furnace with an argon atmosphere which was positioned over a simulated section of an RTG. The simulated RTG section was held in place by four rods hanging from a platform which supported the heating furnace and which allowed the rocket sled to pass underneath during the test. A motorized mechanism transferred the heat source stack into the simulated RTG. A 140 second delay allowed the heat source stack temperature to decrease from 1225°C to approximately 1090°C at the time of impact. A continuous flow of argon gas was maintained as a protective atmosphere in the furnace and in the simulated RTG.

An Al 7075-T6 simulated fragment plate was mounted in the support arms of the utility sled and the rocket sled was propelled by 15 High Velocity Aerial Rockets (HVARs). The test was designed to have the fragment hit the converter housing edge-on at a location directly in line with the long axis of the GIS in the center GPHS module (Figure 6.9-11).
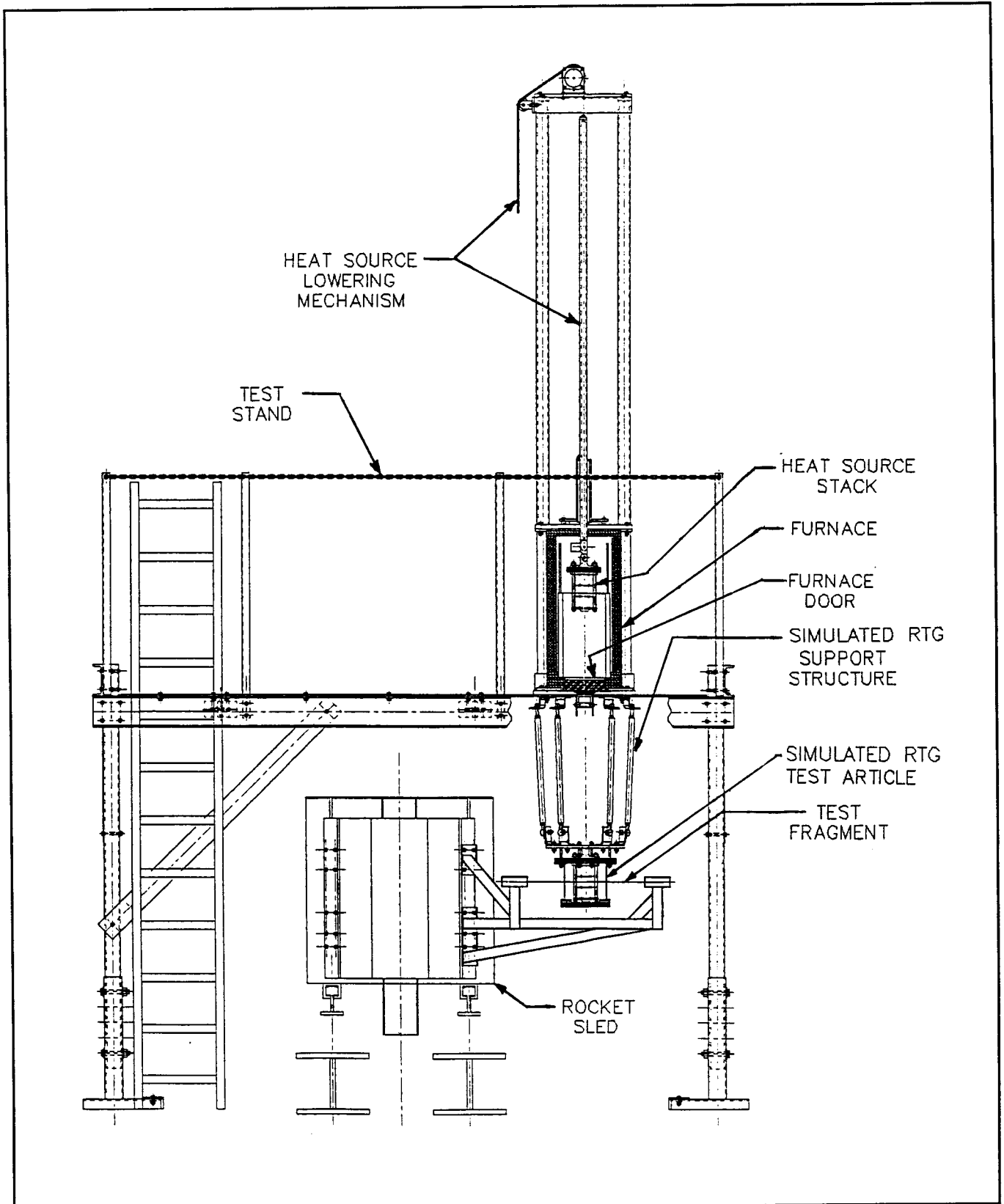
Figure 6.9-10. Edge-On Fragment Test Setup
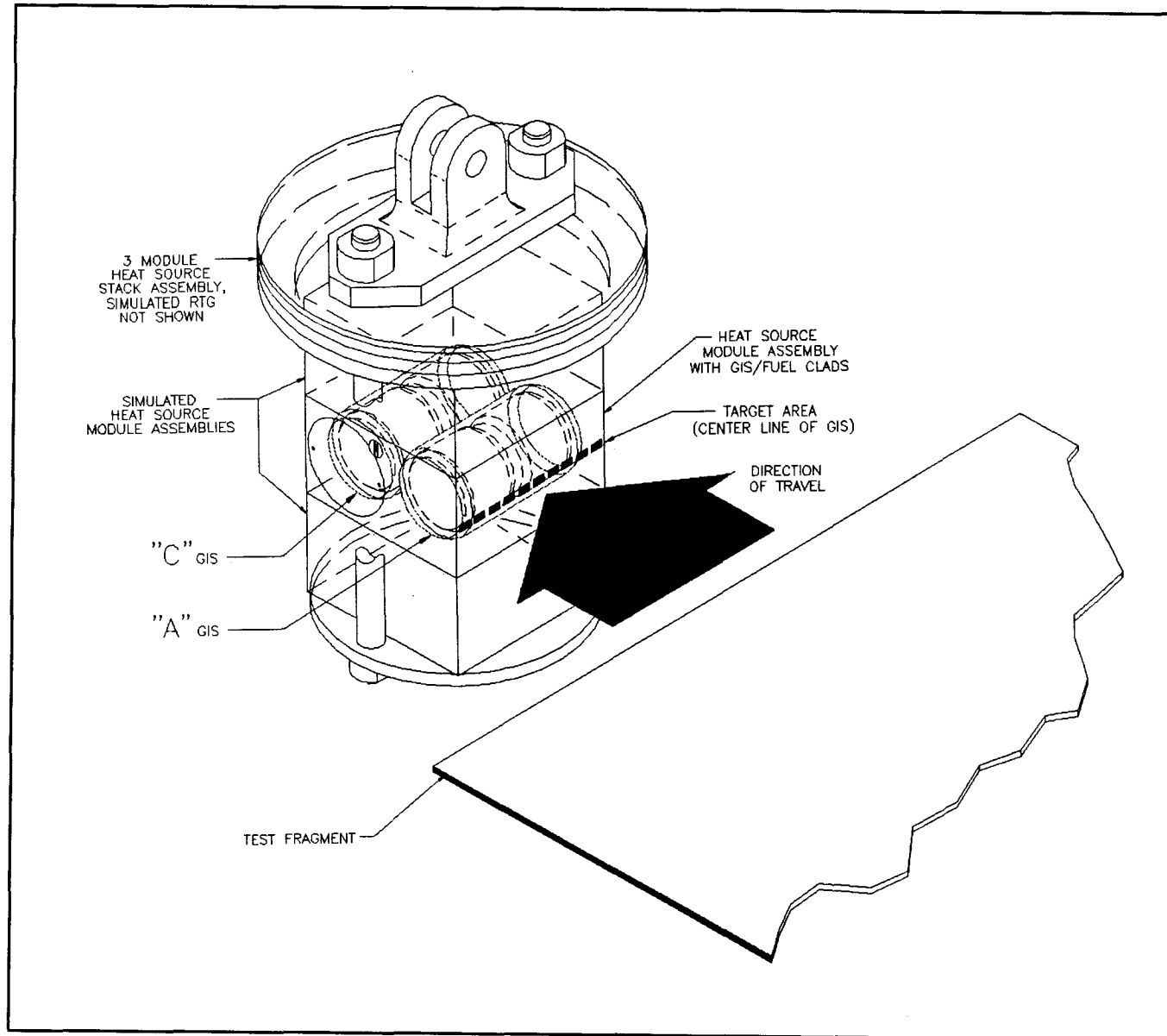
Figure 6.9-11. Heat Source/Fragment Impact Orientation

6.9.2.3 Test Hardware

The simulated RTG test article, shown in Figure 6.9-12, was prototypical of the RTG design at the point of impact with the aluminum fragment. It consisted of a section of the Al 2219 outer shell, sized to contain three GPHS modules. It contained multifoil insulation around the inner diameter, with silicon-germanium unicouples installed in the vicinity of the impact. A graphite heat source support plate was located in the base of the RTG to ensure proper heat source alignment. A purge line was provided at the base of the simulated RTG to provide an inert cover gas (argon) after heat source loading to minimize oxidation.
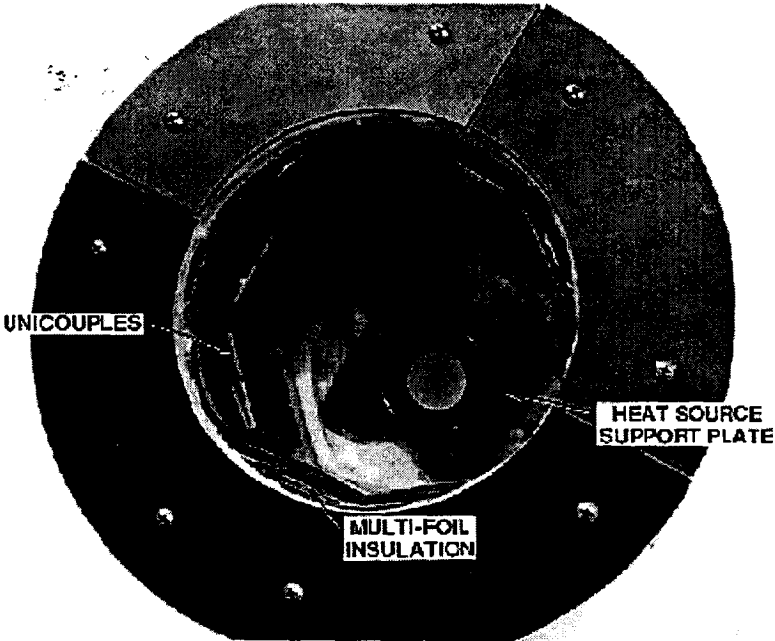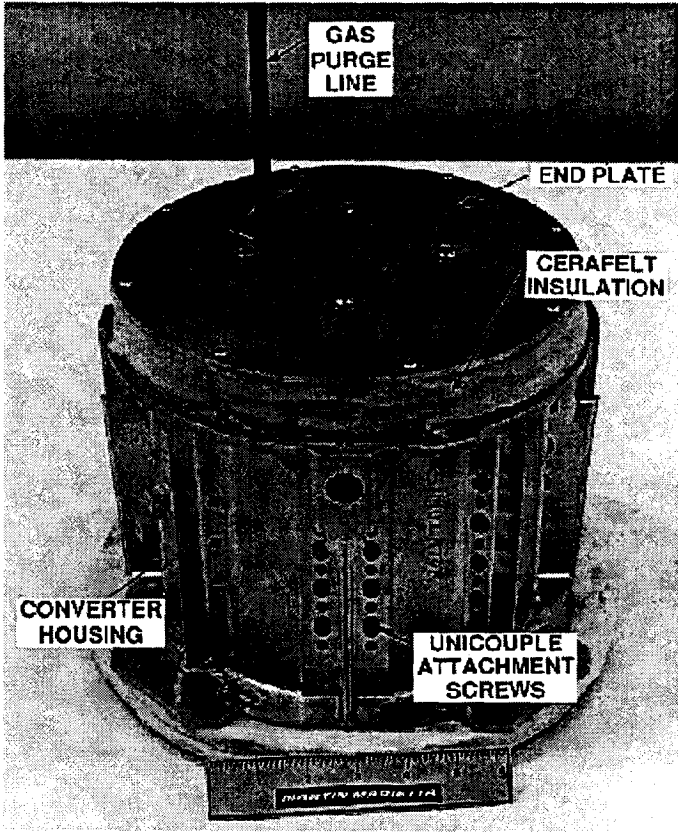
Figure 6.9-12. Simulated RTG Test Article (RTG-3) – Edge-On Fragment Impact Test

The design of the heat source stack is shown in Figure 6.9-13. The heat source test hardware was fabricated by Los Alamos National Laboratory (LANL). The heat source stack consisted of a GPHS module with flight quality graphite components and four flight quality iridium clads containing urania fuel simulant. A simulated module (POCO™ graphite aeroshell with molybdenum mass simulants) was located above and below the GPHS module to provide the correct mass simulation. The three modules were stacked using FWPF lock members and the modules held in place with POCO™ tie rods, as shown in Figure 6.9-13. A POCO™ end plate, located at the base of the stack, was used to locate the heat source in the RTG.
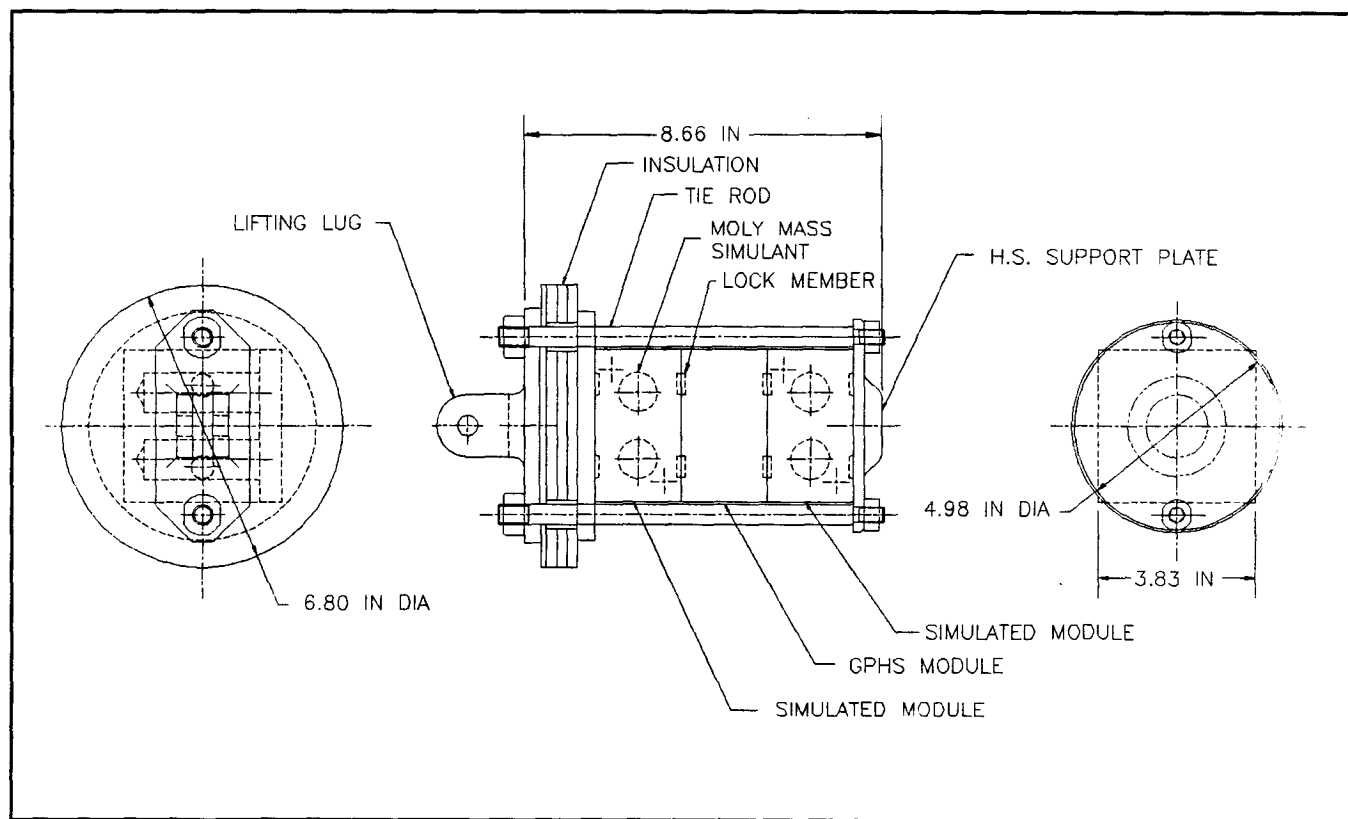
Figure 6.9-13. Heat Source Configuration for Edge-On Fragment Impact Test

6.9.2.4 Test Results

The edge-on fragment test was conducted in March 1996. The measured impact velocity was 306 ± 1.5 m/s as measured from the image motion camera. The heat source impact temperature was estimated to be 1090°C ± 10°C based on previous engineering cool-down tests.

High-speed photography of the impact indicated that the fragment leading edge impacted the converter approximately 0.63 cm above its midpoint. The fragment penetrated the converter shell to the depth of the aeroshells. The converter was cut and torn over approximately 80% of its circumference (Figure 6.9-14). The width of the gap was approximately 2 cm. The cut was clean at its upper edge but the lower edge was folded over, toward the inside of the shell. Radiological surveys of the converter outer surface and the impact vicinity, conducted immediately following the impact, indicated that no urania was released outside of the converter.
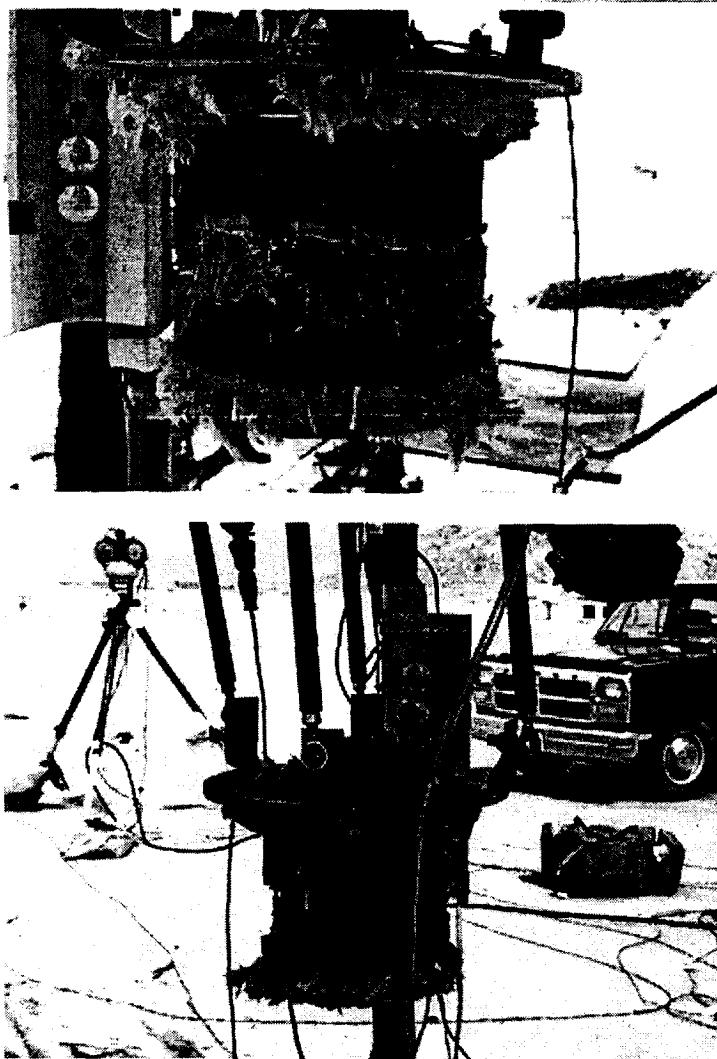
Figure 6.9-14. Simulated RTG after Fragment Impact Test

The post test dimensional inspection data for the four fueled clads are shown in Table 6.9-3.

Table 6.9-3. Fueled Clad Distortion after Edge-On Fragment Test

Fueled Clad ID	Distortion %				
	Axial	Vent Cup, Diametral Max.	Min.	Shield Cup, Diametral Max.	Min.
SC0125	0.5539	0.5044	-1.1432	0.7734	-1.1769
SC0126	3.8102	0.7066	-1.2113	1.3786	-1.1769
SC0127	0.5682	-0.5027	-0.9383	-0.1345	-0.2017
SC0128	0.7019	-0.2690	-1.0424	-0.3693	-0.8392

Fueled clad SC0126, which was located at the open end of the A GIS, had a small transverse breach (1.84 mm long, 0.40 mm wide) that was apparently caused by impact with the plate fragment (Figure 6.9-15). This breach was located approximately between 200 to 220 degrees on the shield cup radius. The estimated amount of simulant fuel released was 0.0890 g, based on the weight of the fuel retained in the fueled clad.
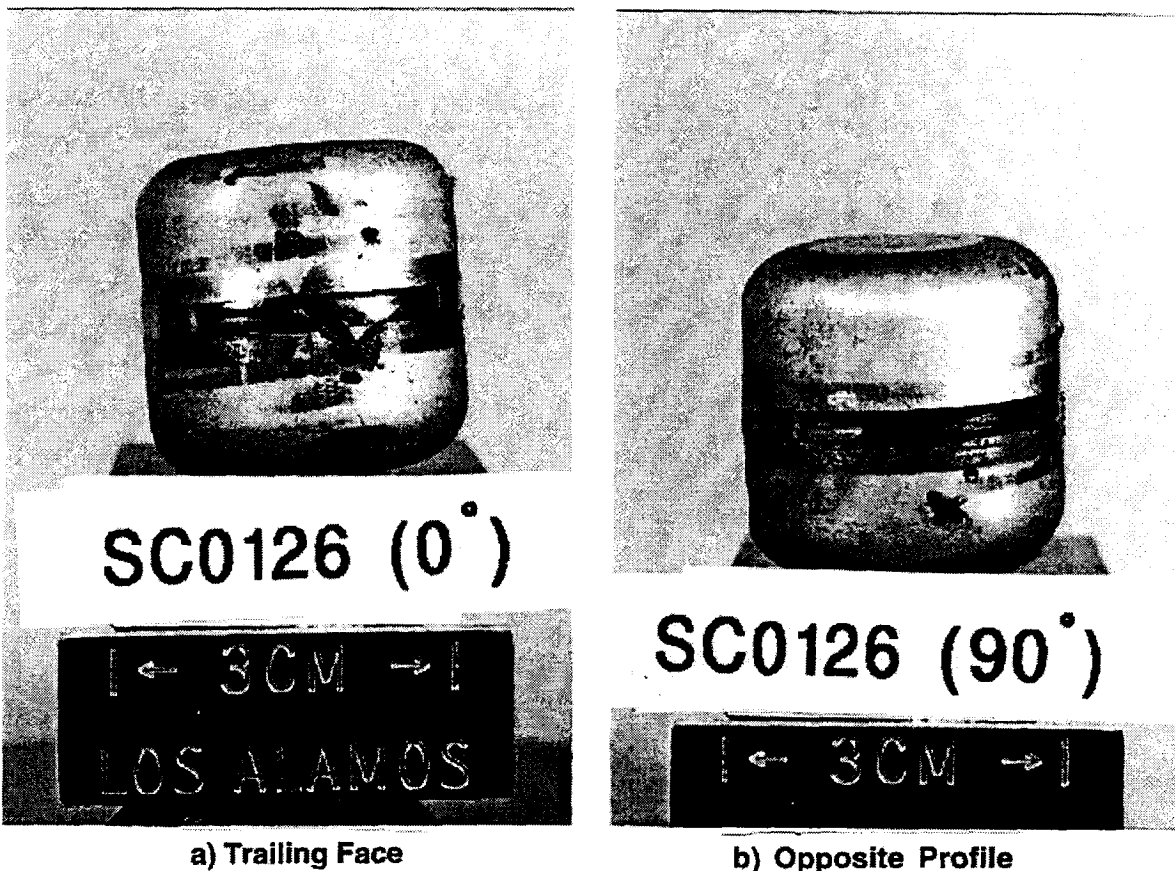
a) Trailing Face   b) Opposite Profile

Figure 6.9-15. Fueled Clad SC0126 (A GIS) after Fragment Impact Test

SC0126 (180°)

SC0126 (270°)

c) Impact Face

d) Profile

e) Blind End

f) Vent End
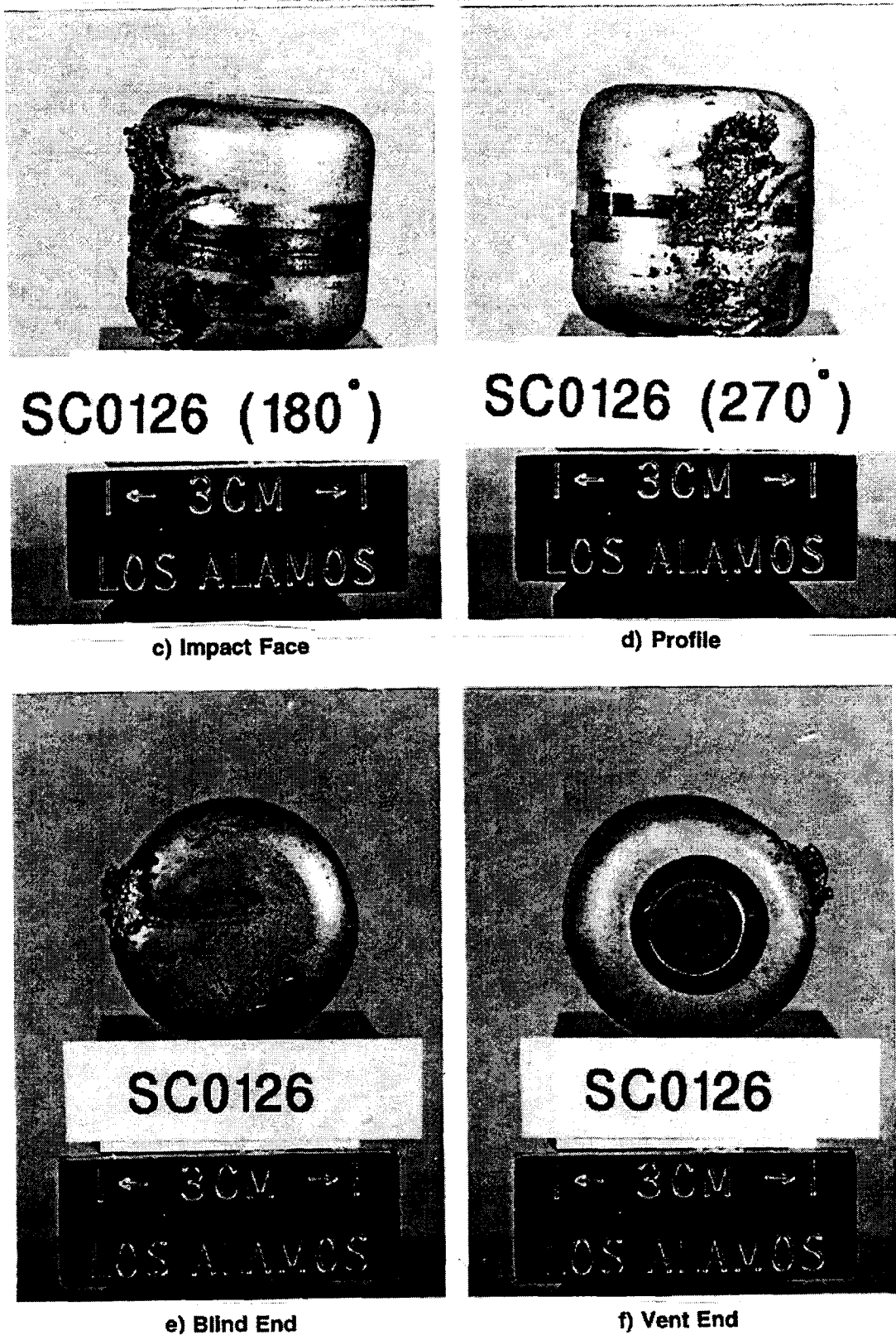
Figure 6.9-15. Fueled Clad SC0126 (A GIS) after Fragment Impact Test (Cont'd)

6.10   RTG TRANSPORTATION SYSTEM ANALYSIS

To support the development of the RTG Transportation Systems (designated USA/9904/B(U) F-85), an assessment was made of damage that might be sustained in a 30 foot drop of an RTG while in the transportation system's containment vessels and impact limiter. The assessment was made in preparation for the safety analysis required for system certification. The study had as its objective determination of the smallest heat producing component resulting from the possible break-up of the RTG. The possible size range of heat producing components begins with the RTG itself (if no break-up occurs), the next smaller size would be the aeroshell module (containing four fueled clads), followed by the GIS (containing two fueled clads), and individual fuel clad and ultimately the fuel itself. The assessment concluded in some instances the RTG case could be ruptured, thus potentially releasing heat source modules. However, no further break-down would occur and the fuel itself would not be released to the interior of the inner containment vessel.

6.10.1   Assessment Study

The assembled containment vessels, impact limiter, and RTG (termed the package and payload) are shown in Figure 6.10-1. The package is composed of two steel containment vessels, each with its own base plate. Both vessels are sealed and within them the RTG is supported by the rack assembly as shown in Figure 6.10-1. RTG attachment is made using four bolts engaging the four barrel nuts in the generator case at the inboard flange. The rack assembly in turn is attached to the nested base plate subassembly.

The packaging design contractor, PacTec, determined (based on a series of half-scale drop tests) that the RTG experiences a maximum acceleration of 300 g's when the package is dropped 30 feet. Using this acceleration load, a tabulation of RTG weights, and allowable material limits, Lockheed Martin analyzed the resulting structural margins. There were some impact orientations identified in which the heat source assembly would not be released and would not fail. Conversely, there could still be others where both might occur.

Figure 6.10-2 illustrates what is considered to be the worst case accident response since it represents the circumstance causing the most damage to the generator. The event sequence proceeds in views (a) through (d) and ends with heat source modules
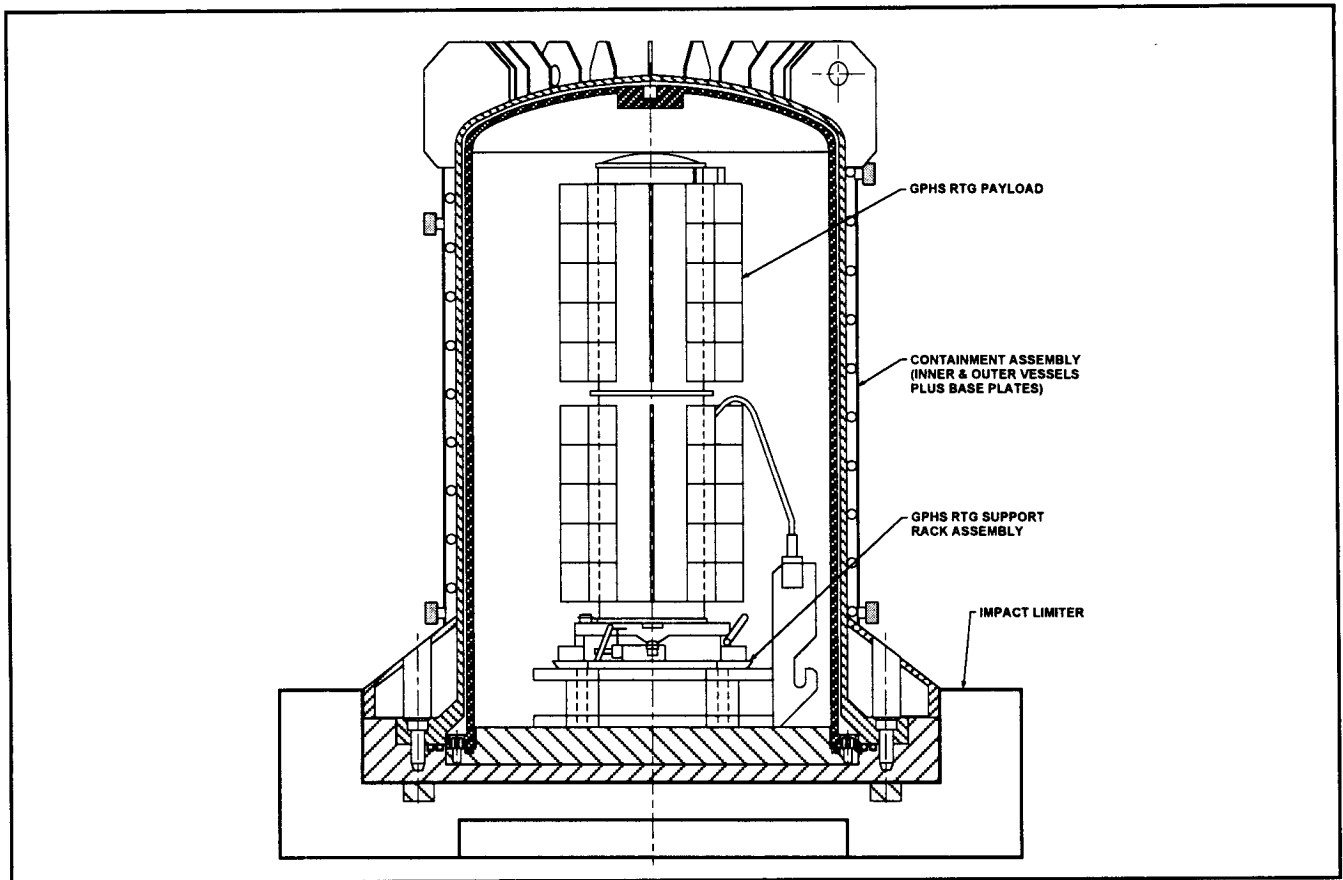
Figure 6.10-1. Shipping Container Baseline Configuration

contained within the containment vessel but released from the generator case. The post accident position, view (d) shows the package again in an upright position and represents the worst case for the container seals located at the base of the vessels. To protect the seals from overtemperature conditions if heat source components were to be released from the generator case, a baffle is used to physically separate the seals from the source of heat.

Another situation where the modules could be released from the generator case is for an inverted package impact orientation with the generator longitudinal axis nearly vertical, closely aligned with the fall line. In this orientation, heat source modules could be released from the generator case through the end dome. As indicated above, in this instance the baffle would also keep the modules from the container seals if the container came to rest in an upright position. In both the vertical orientation and the orientation shown in Figure 6.10-2 (a), all the heat source modules would remain inside the double containment vessels even though they may be released from the generator case. The impact damage to the

FIRST IMPACT (a.)

30 Foot Drop
Impact Velocity
44 ft/s

RTG Intact

CONTAINMENT VESSEL IMPACT (b.)

RTG Suffers
Multiple Failures

RTG Mounts Break

Heat Source Support
and Pressure Dome Fail
Exposing GPHS Modules

GPHS Modules Escape
From RTG Case

POST-IMPACT MOTION (c.)

Entire Package Rebounds
and Tumbles

RTG Components Impact
Shipping Container

Post Impact
Motion

Unrestrained
GPHS Modules

POST-ACCIDENT POSITION (d.)

Shipping Container
Comes to Rest Upright

Baffle Keeps
GPHS Modules
Away From Shipping
Container Seals

Seals

Figure 6.10-2. Worst Case Accident Scenario

modules upon contact with the inside of the containment vessels was analyzed by Fairchild (now OSC) and found to be very small. The Fairchild study concludes that the modules will remain intact in a 30-foot drop and therefore neither the GISs nor fueled clads will be released from the modules.

6.10.2   Conclusion

No fuel would be released under the 300 g load attributed to a 30-foot drop. Since little module damage would be experienced, the fueled clads would remain within the modules and the smallest heat producing entity will be the modules, not the GISs nor the fueled clads. The complete assessment is documented in Reference 6.10-1.

Section 6 References

6.1-1   "Cassini Titan IV/Centaur RTG Safety Databook, Rev. B," Section 2.0, Martin Marietta Technologies, Inc., a Lockheed Martin Company, Report NAS3-00031, March 1997.

6.1-2   "Final Environmental Impact Statement for the Cassini Mission," NASA, June 1995.

6.1-3   "Cassini Titan IV/Centaur RTG Safety Databook, Rev. B," Sections 3.0 and 4.0, Martin Marietta Technologies, Inc., a Lockheed Martin Company, Report NAS3-00031, March 1997.

6.1-4   "Cassini Titan IV/Centaur RTG Safety Databook, Rev. B," Section 5.0, Martin Marietta Technologies, Inc., a Lockheed Martin Company, Report NAS3-00031, March 1997.

6.2-1   JPL Interoffice Memorandum 312/04.6-759, A. McRonald to L. Reinhart, "RTG Module Release Conditions for Inadvertent Earth Reentry of the Cassini Spacecraft during the VVEJGA Earth Flyby," revised 27 May 1994; and JPL Interoffice Memorandum 312/4.6-748, A McRonald, et al., to L. Reinhart "Powered Reentry of the Centaur Vehicle Attached to the Cassini Spacecraft, Determination of Release Conditions for RTG Modules," 6 April 1994.

6.4-1   "Titan IV CRAF/Cassini EIS Databook," MCR-91-2580, Rev: Basic, Martin Marietta Space Launch Systems, Denver, CO, December 1991.

6.4-2   "Cassini Earth Swingby Plan Supplement," JPL 699-70-3-Sup, Jet Propulsion Laboratory, 19 May 1997.

6.4-3   "World Demographic Update through 1990 for Space Nuclear System Safety Analyses," Rev. 1.0, Halliburton NUS.

6.5.1-1   NASA/NASDA Joint Hydrogen/Oxygen Vertical Impact (HOVI) Test Program, NASA-WSTF, Document No. TR-800-001, 29 November 1996.

6.5.1-2   Mukunda M., "Hydrocode Analyses for the Response of the RTG to Accident Environments," FSC-ESD-217-96-550, Orbital Sciences Corporation, October 1996.

6.5.1-3   Pavone, D., LACP-86-92, Los Alamos National Laboratory, 1986.

6.5.1-4   Mukunda, M., "Response of RTG/GPHS to Solid Propellant Fallback Environments," Orbital Sciences Corporation, Letter to L. DeFillipo, 21 April 1997.

6.5.2-1   NUS Corporation, Overall Safety Manual, Volume 2, prepared for USAEC under Contract SNSO-7, June 1975.

6.5.2-2   Arya, S.P.S. "Parameterizing the Height of the Stable Atmospheric Boundary Layer," Journal of Applied Meteorology, 20, pp. 1192-1202, 1981.

6.5.2-3   Benkley, C. W. and Schulman, L. L.. "Estimating Hourly Mixing Depths from Historical Meteorological Data," Journal of Applied Meteorology, 18, pp. 772-280, 1979.

6.5.3-1   JPL Interoffice Memorandum 312/04.6-759, A. McRonald to L. Reinhart, "RTG Module Release Conditions for Inadvertent Earth Reentry of the Cassini Spacecraft during the VVEJGA Earth Flyby," revised 27 May 1994 and, JPL Interoffice Memorandum 312/4.6-748, A. McRonald, et al. to L. Reinhart, "Powered Reentry of the Centaur Vehicle Attached to the Cassini Spacecraft, Determination of Release Conditions for RTG Modules," 6 April 1994.

6.5.3-2   Lucero, E. F., JHU/APL Memo AM-96-D019, "Summary Results of Predicted GPHS Reentry Motion Resulting from a Cassini/VVEJGA Inadvertent Reentry," 20 August 1996.

6.5.3-3   Cassini GPHS-RTG Final Safety Analysis Report, Accident Model Appendices, Volume II, Book 2, Lockheed Martin Missiles & Space, (CDRL C.3), November 1996.

6.5.3-4   Blottner, F. G., "Chemically Reacting Boundary Layer with Ablation Products and Nose Bluntness Effects," General Electric Space Sciences Laboratory, TIS R67SD14, April 1967.

6.5.3-5   Nicolet, W. E. and Balakrishnan, A., "RASLE User's Manual," Accurex Corporation/Aerospace Systems Division, UM-79-10/AS, Mountain View, CA, July 1979.

6.5.3-6   Gnoffo, P. A., Gupta, R. N., and Shin, J. L., "Conservation Equations and Physical Models for Hypersonic Air Flow in Thermal and Chemical Nonequilibrium," NASA Technical Paper 2867, February 1989.

6.5.3-7   Hartung, L. C., "Predicting Radiative Heat Transfer in Thermochemical Nonequilibrium Flow Fields, Theory and User's Manual for the LORAN Code," NASA Technical Memorandum 4564, September 1994.

6.5.3-8   Bhutta, B. A., Daywitt, J. E., Rahaim, J. J., and Brant, D. N., "A New Technique for the Computation of Severe Reentry Environments," AIAA Paper 96-1861, June 1996.

6.5.3-9   Klee, P., "Background and Use of SINRAP Code, Rev. C," Lockheed Martin PIR U-Cassini-018, 29 May 1996.

6.5.3-10   "ABAQUS / Standard User's Manual, Version 5.4," Hibbitt, Karlsson & Sorensen, Inc., 1994.

6.5.3-11   Lutz, S. A. and Chan, C. C., "Ablation Response Testing of Aerospace Power Supplies," AIAA Paper 93-0381, January 1993.

6.5.3-12   Gordon, P., "Analysis of One-Dimensional Heat Conduction Computer Program," General Electric Company, SSL-MSD, TIS No. RR663D10, March 1966.

6.5.3-13   Gilbert, L., et al., "Theoretical Studies of the Reentry of Plutonium Fuel," 1967.

6.5.3-14   Eck, M. B., "Draft Final Report on Earth Flyby Reentry," Foils Engineering NASA-JPL Contract 959658, October 1993.

6.5.3-15   Bhutta, B. A., Daywitt, J.E., and Brant, D. N., "Interpretation of Enthalpies in the Energy Balance of an Ablating Graphite Surface," AeroTechnologies, Inc., Report AT-TN-96-02, May 30, 1996.

6.5.3-16   Bhutta, B. A., Daywitt, J.E., and Brant, D. N., "Comments on 'Comparison of Alternative Mass and Energy Balance Methods at an Ablating Carbon Surface'," AeroTechnologies, Inc., Report AT-TN-96-05, July 31, 1996.

6.5.3-17   Bhutta, B. A., Daywitt, J.E., and Brant, D. N., "Energy Balance at an Ablating Carbon Surface with Discontinuously Changing Species Mass Fraction," AeroTechnologies, Inc., Report AT-TN-96-06, Sept. 6, 1996.

6.5.3-18   Bhutta, B. A., Daywitt, J. E., and Brant, D. N., "Energy Balance at an Ablating Carbon Surface with Discontinuously Changing Species Mass Fraction: Supplement I," AeroTechnologies, Inc., Report AT-TN-96-07, Sept. 17,1996.

6.5.3-19   Bhutta, B. A., Daywitt, J. E., and Brant, D. N., untitled AeroTecnologies, Inc. Memo, Sept. 24,1996.

6.5.3-20   Bhutta, B. A., Daywitt, J. E., and Brant, D. N., "Supplement to Technical Note AT-TN-96-05," AeroTechnologies, Inc., Report AT-TN-96-05S, Dec. 13, 1996.

6.5.3-21   Bhutta, B. A., "Energy Equation Applied to the Infinitesimal Homogeneous Reaction Zone at the Ablating Wall," AeroTechnologies, Inc., Report AT-TN-97-02, Jan. 21, 1997.

6.5.3-22   Hobbs, R. B., "MHW-HSA Aerodynamics Performance Test Report", AEOM 9151-001, General Electric Co., August 1973.

6.6-1   U.S. Standard Atmosphere, 1976, NASA, NASA-TM-X-74336.

6.6-2   HNUS, Overall Safety Manual, Volume 2, Prepared for USAEC under Contract SNSO-7, June 1975.

6.6-3   Limits for Intakes of Radionuclides by Workers, International Commission on Radiological Protection, Publication 30. Pergamon Press, 1979.

6.6-4   1990 Recommendations of the International Commission on Radiological Protection, International Commission on Radiological Protection, Publication 60. Pergamon Press, 1991.

6.6-5   Human Respiratory Tract Model for Radiological Protection, International Commission on Radiological Protection, Publication 66. Pergamon Press, 1994.

6.6-6   Health Risks of Radon and Other Internally Deposited Alpha - Emitters. National Academy of Sciences - Committee on the Biological Effects of Ionizing Radiations. National Academy Press, Washington, DC, 1988.

6.6-7   Health Effects of Exposures to Low Levels of Ionizing Radiation. National Academy of Sciences - Committee on the Biological Effects of Ionizing Radiations. National Academy Press, Washington, DC, 1990.

6.7-1   Deane, N., "800 km EGA Flyby Analysis Using Final Updated GIS Failure and Clad Melt Probabilities," Cassini Memo No. 547A, 23 October 1997.

6.9-1   Cassini GPHS-RTG Final Safety Analysis Report, Volume II, Book 2, Appendix H, Lockheed Martin Missiles & Space, CDRL C.3, November 1996.

6.10-1   Kauffman, R. R., "Effect of Shipping Container Thirty Foot Drop Event on RTG Structural Integrity," Cassini Program PIR U-1RS1-C/C-0019, 21 April 1992.

Section 7

ETG Manufacture and Test

SECTION 7
ETG MANUFACTURE, TEST, AND QUALITY ASSURANCE

7.1 Reestablishment of Unicouple Fabrication and Process Improvements

This is a summary of the re-establishment of unicouple fabrication processes and key process improvements for Cassini unicouple and parts fabrication. For more detailed information on the issues refer to the Cassini Semi-Annual Technical Reports (Reference 7-1).

The steps taken to reestablish fabrication of unicouples at a level comparable to that on the Galileo/Ulysses program were as follows:

- Identified required materials and equipment

- Procured new materials and equipment where necessary

- Qualified new materials

- Installed and debugged new equipment

- Overhauled and checked out old equipment as required

- Upgraded Quality Control system

- Developed and carried out qualification plans with DOE concurrence

- Trained and certified manufacturing and inspection personnel as required

- Demonstrated process readiness with fabrication of Training lot hardware

- Demonstrated production readiness with fabrication of Qualification lot hardware

Problems encountered and their respective solutions during this phase of the program are listed in Appendix A.

Operator and inspector training/certification, process readiness and production readiness for unicouple production were completed by May 1993.

The final step in technology verification was demonstrated by 18 couple module performance testing, which is discussed in Section 11 of this report.

7.1.1 Equipment Upgrades

Significant upgrades and new equipment used in the fabrication of unicouples are listed below.

- Refurbished Hot Presses #2 and #3.

- Installed new temperature controllers in six heritage Brew bonding furnaces.

- Installed and qualified six new automated Brew bonding furnaces. These were initially used for second bond assemblies and later used for first bond assemblies as well. Later the heritage Brew furnaces were phased-out.

- Installed two new CVD silicon nitride coating furnaces and qualified both during the program.

- Installed a new wafering machine and slicing machine and rebuilt three grinding machines in the Parts Preparation area.

- Added new microscopes in the manufacturing, inspection, and metallography lab areas.

- Installed a new gritblaster.

New equipment was procured for processing Converter hardware and/or EHS hardware including an air furnace (L&M) and vacuum furnace for bake-out operations.

7.2 Unicouple Production

Cassini unicouple production was segregated into five builds: Qualification Lot, E-6, E-7, E-8, and Contingency. The Qualification build began in September 1991 after extensive operator training and certification, and was completed in June 1993. The E-6 build began in November 1991. The Contingency build was completed in April 1995.

The overall quantities and yields for the major unicouple assemblies and processes are shown Table 7-1. The numbers represent the combined totals for Qualification, E-6, E-7, E-8, and Contingency hardware.

Table 7-1. Cassini Unicouple Production Yields

Assembly/Process	Total Starts	Total Accepted	Yield
Vacuum Casting	292	286	97.9 %
Powder Blending	137	131	95.6 %
Hot Pressing	645	620	96.1 %
N/P Bonding	158	140	88.6 %
Pellet	15826	11878	75.1 %
Segment	16826	14269	84.8 %
Hot Shoe	6480	5438	83.9 %
First Bond	4832	4514	93.4 %
Coated First Bond	4208	3904	92.8 %
Second Bond	3649	3220	88.2 %
Nickel Plating	32419	31972	98.6 %
Couple Preassembly	3132	2729	87.1 %
Radiator	3957	3568	90.2 %
Machined Radiator	3490	3133	89.8 %
Cold Stack	3083	2745	89.0 %
Coated Spacer	3680	3247	88.2 %
Unicouple	2669	2346	87.9 %
Wrapped Unicouple	2334	2289	98.1 %

Following is a summary of the major manufacturing issues and events that occurred during unicouple production:

- Demonstration of acceptable SiMo N/P bond strength proved difficult. Low strength values were recorded during Qualification hot shoe and first bond testing. Acceptable strengths were attained with added attention to compact flatness and parallelism, by increasing hot pressing temperatures, and by boiling the polished compacts in water prior to bonding.

- During thermoelectric machining operator certification, staining of parts became a problem. The cause was discovered to be fixtures with sharp edges and coolant drying on parts. The sharp edges were removed from the fixtures and the procedures were modified to prevent coolant from drying on the parts.

- During process readiness and the qualification build for nickel plating it became necessary to use accepted residual plated hardware for subsequent processes due to delays in obtaining newly purchased unplated parts. This allowed completion of process readiness for unicouple production prior to process readiness completion for nickel plating.

- During second bond process readiness, it became necessary to more closely match the N and P segment densities due to unacceptable bonds using density mismatches of approximately 0.030 g/cm^3. This closer density matching proved to be successful.

- Successful replacement of the coolant used for thermoelectric machining was completed. The White and Bagley 1500 coolant was no longer manufactured, and was replaced by TrimClear.

- Various improvements were made during the program that yielded greater efficiencies, such as elimination of daily first bond burn-in runs, introduction of hydrogen peroxide cleaning of thermoelectric parts, and fabrication of additional thermoelectric parts from parts of compacts that previously would have been scrapped.

- Oxidation on cold stack assemblies was discovered in April 1993. The graphite fixtures used during the brazing process were baked out. After this process change was initiated, no oxidation was observed.

- Although the program had many difficult issues to resolve, many individual process yields for operator certification, the qualification build, and the production builds were significantly higher than had been anticipated.

7.3   Converter Production

Converter production consisted of two major tasks which were performed in parallel. The converter housing and heat source support assemblies were fabricated in parallel with the molybdenum foil insulation assembly. As the foil insulation lay-up was completed, the unicouple insertion and riveting was initiated. Machining of the converter housing and heat source support members was completed in time for thermopile insertion into the converter housing.

After completion of the thermopile insertion into the converter housing, the outboard heat source support frame was assembled and the EHS was prepared for insertion into the ETG. After EHS insertion, the inboard heat source assemblies were installed, and the EHS pre-loaded. The gas processing dome was installed, the ETG pressurized, and pressure decay tests were performed. The ETG was then readied for shipment for ETG processing.

During assembly of the E-6 thermopile, it was determined that the riveted unicouple electrical connector strap joints were demonstrating higher than normal resistance readings. After extensive evaluation and testing (including a new rivet design), it was determined that the cause of the resistance anomaly was an oxide film. After vacuum processing of representative samples, the resistance across the riveted jointed returned to normal.   After completing all testing and evaluations, the E-6 thermopile assembly continued without further delay.

After completing the E-7 assembly, the processing was begun. Initial testing determined that the power output of the ETG was below normal. Further investigation revealed that half the unicouples were installed backwards. The orientation and selection of each unicouple is controlled by the unicouple map generated for each ETG. This map was later found to be in error due to a software problem.

A new map was generated for E-7 and disassembly of E-7 was begun. Two hundred and eighty-six unicouples were removed from the thermopile and replaced with new, properly oriented unicouples. The total rework time amounted to a delay of five months to the delivery schedule for E-7, but did not impact the Mound fueling schedule.

In accordance with DOE contract direction, the E-8 converter was not assembled but component subassemblies were completed and placed in kits. A spare E-8 converter housing was completed and is in bonded stock. An E-8 foil insulation assembly was fabricated, assembled, and is stored on a rigid fixture protected by an inert cover gas to prevent degradation of the moly foils. In addition, a spare GMS, PRD, EHS, domes (inboard and outboard), and heat source support frames and latches for inboard and outboard ends were completed and are in stock.

7.4 ETG PROCESSING

Under the contract, two ETGs were processed. Both ETGs were prepared and processed per SI 249714. The processing prepared the units for operation as an ETG and for eventual conversion to an RTG and subsequent acceptance testing.

7.4.1 Test Sequence

Each ETG was assembled per Manufacturing planning and Quality Assurance surveillance in the Clean Room, Building B, installed into a Converter Shipping Container (CSC) and transported to Building 800. The ETG was removed from the CSC, installed into Loading and Assembly Station 2 (LAS-2) and a vacuum/thermal process cycle conducted. The outboard dome with a C-seal and the mid span caps fitted with O-rings were then installed and pressure decay tests conducted. The ETG was then removed from the LAS, weighed, ACS tests and resistance tests performed, installed into a CSC, and shipped to the Mound Facility (Miamisburg, Ohio), where RTG fueling and acceptance testing were performed.

The test sequence is shown in Figure 7-1.
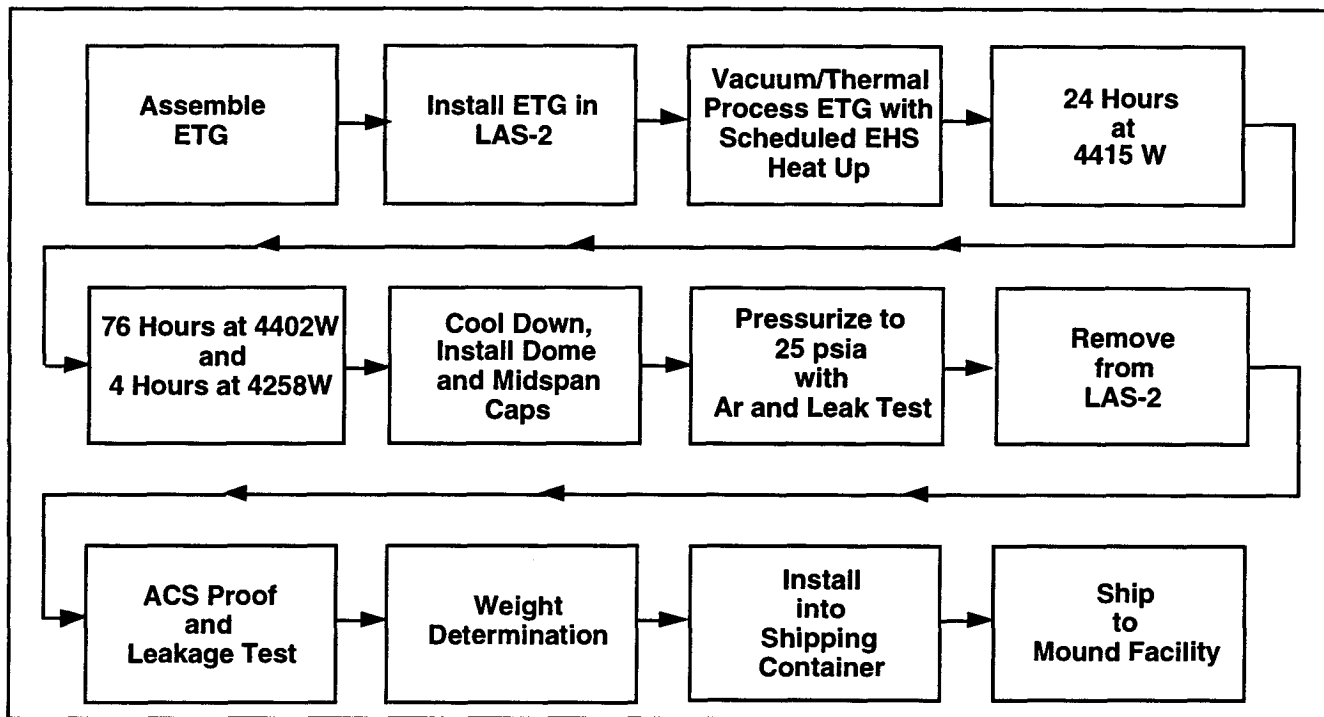
Figure 7-1. Cassini RTG Program ETG System Test Flow

7.4.2 E-6 ETG Processing and Acceptance Testing

The E-6 unit was removed from the converter shipping container (CSC), checked for proper electrical parameters and internal pressure, and placed in the Loading and Assembly Station (LAS) during the period 5-9 January, 1995. During the installation into the LAS all the cabling and gas lines were mated and verified. The Segment Readiness Review was held and approval to commence processing was granted.

The E-6 pump down was initiated on 19 January. The 24-hour soak period (ETG pressure $<1X10^{-5}$ torr) was completed on 12 January. Right after starting the heat-up, the power was decreased to zero as a result of the RGA analysis during the 24-hour soak. It showed that 50% of the gas was argon (Ar) indicating a leak. An investigation found a leak in the solenoid valve isolating the GMS from the LAS. After repairing the valve, the LAS was re-evacuated and the 24-hour soak was completed on 14 January.

Power inputs were initiated and continued until the EHS reached 400°C (19 January). EHS power inputs were then discontinued until the ETG pressure decreased to less than 7×10^{-5} torr. Later on January 19th, the power inputs were resumed.

Normal power inputs continued until 25 January when an automatic Ar backfill began. The pump isolation valves were closed and the EHS power was reduced to zero. The EHS temperature had reached approximately 600°C. The LAS was reevacuated after verifying the integrity of the LAS and the pumps.

An investigation prior to restart of the heat-up yielded that a manual valve had a small intermittent leak in its stem. New packing material was applied. During this period the cryo pump was regenerated, 12 milliliters of oil were added to the turbo-mechanical pump (TMP), and the ETG ion gage was degassed.

On 28 January, EHS power increases were resumed. The EHS reached its previous temperatures. The heat-up rate was then limited to 10 watts/hr until 2452 watts were reached. The ETG load was then switched from "start-up" to "normal" mode and the load voltage was adjusted to 17.8 volts. After allowing the ETG pressure to decrease to $<7X10^{-5}$

torr, normal power increases were made until February 4th when the ETG output was 35 volts. After adjusting the load voltage to 30 volts and achieving an ETG pressure of $<7 \times 10^{-5}$ torr (5 February), power increases were resumed.

Normal power increases continued until February 8th when the LAS pressure increased approximately one decade (to 1×10^{-5} torr). It was determined that the cryo pump needed to be regenerated. When the regeneration was complete there was still some instability in the cryo pump operation. The cryo pump compressor was then replaced. During this period, the TMP was able to hold the ETG pressures constant since no power increases were being made. Normal power inputs were resumed February 9.

Power inputs remained normal until reaching full power (4415 ± 15 watts) on 11 February. After a 24-hour soak, performance testing was initiated. The performance test data are discussed in detail in Section 5.1. For more detailed information see the E-6 ETG Processing and Test Report (Reference 7-2).

7.4.3 E-7 ETG Processing and Acceptance Testing

The E-7 ETG was installed in the converter shipping container and delivered to Building 800 on 5 July 1995. The E-7 ETG was installed into the LAS and a Test Readiness Review was completed on 26 July. EHS heating was initiated after all vacuum requirements for the LAS and ETG were satisfied. On 31 July, it was observed that the ETG voltage and current output were less than other ETGs at the equivalent heat input.

Systems Test met with Engineering and Quality Assurance on 1 August to review the ETG performance data and to outline a course of action. Based on an engineering analysis, it was determined that a shunt between the negative and positive leads of the ETG electrical circuit could cause a low ETG voltage output. To address this issue the following actions were implemented:

1. The ETG power cable between the LAS and ROC was disconnected at the LAS. The ETG voltage was then measured at the LAS connector and found to be 1.8 volts compared to an expected voltage of approximately 3 volts. This measurement verified the cause was inboard of the LAS.

2. The ETG was then cooled to room temperature and the LAS was backfilled with argon gas. This permitted disconnecting the internal LAS cable and shorting module from the ETG power circuit. This confirmed that the problem was most likely within the ETG.

3. After reviewing the thermopile assembly procedures and specifically, the unicouple insertion map, it was seen that 144 unicouples were inserted with incorrect polarity. An error in the plotting software which generated the map was the cause of the problem.

Three options for correcting the problem were considered and evaluated. The options were:

1. Rework the E-7 thermopile by repositioning the reversed polarity unicouples.

2. Rework the E-7 thermopile by replacing the reversed polarity unicouples with E-8 unicouples.

3. Remove the E-7 thermopile and replace it with the E-8 thermopile, which was yet to be completed.

These three options and their trade-offs were reviewed with DOE on 7 August in order to finalize the recovery plan. DOE provided direction to proceed with Option 2 and a Rework Plan (Reference CON #1300) and Corrective Action Plan (Reference CON #1306) were issued.

On 7 August, the ETG was prepared for removal from the LAS by installing the outboard dome and midspan caps. The ETG was pressurized with argon gas and a pressure decay test was performed to verify sealing integrity. The ETG was removed from the LAS, electrical measurements were made, and the ETG was installed into the Converter Shipping Container (CSC). The ETG/CSC was moved to Building B on 10 August in preparation for disassembly and rework.

Following the unicouple rework, the ETG was placed in the CSC and delivered to Building 800.

The E-7 unit was removed from the CSC, checked for proper electrical parameters and internal pressure, and placed in the LAS between 9 and 11 January 1996. During the installation into the LAS all the cabling and gas lines were mated and verified. The

Segment Readiness Review was then held and approval to commence processing was granted.

The E-7 pump down was initiated on 11 January. The 24-hour soak period (ETG pressure $<1 \times 10^{-5}$ torr) was completed on 13 January. The heat-up was initiated and continued nominally until the ETG reached 390 watts on 15 January. At that time an automatic Ar backfill was triggered. After verifying the integrity of the system, the LAS was re-evacuated, and the power was brought back to its pre-shutdown values. A time delay was installed on the back-fill controls to prevent any electronic noise from triggering future back-fills.

Power inputs were initiated and continued until the EHS reached 400°C (18 January). EHS power inputs were then discontinued until the ETG pressure decreased to less than 7×10^{-5} torr. Later on 18 January the power inputs were resumed.

On 19 January, the cryo hi-vac valve closed unexpectedly. Within the hour the valve was reopened. The ETG pressure remained within acceptable levels ($<7 \times 10^{-5}$ torr) during the valve closure period since the TMP remained operational. The valve closure was due to facility low air pressure.

On 19 January, EHS power increases were resumed. The heat-up continued at 10 watts/hour until 2385 watts were reached on 23 January. The ETG load was then switched from "start-up" to "normal" mode and the load voltage was adjusted to 18.5 volts. After allowing the ETG pressure to decrease to $<7 \times 10^{-5}$ torr, normal power increases were made until 27 January when the ETG output was 35 volts. After adjusting the load voltage to 30 volts and achieving an ETG pressure of $<7 \times 10^{-5}$ torr (28 January), power increases were resumed.

Power inputs remained normal until reaching full power (4415 +/- 15 watts) on 1 February. After a 24-hour soak, performance testing was initiated. Due to a higher than normal degradation of the circuit to ground resistance, the ETG power input was reduced to 2900 watts. The unit was again brought up to 4400 watts at a rate of approximately 5 watts per hour. The ETG reached full power on 17 February when a second stability test was started.

This test was terminated after 30 hours due to the further degradation of the circuit to ground resistance. The performance test data are discussed, in detail, in Section 5.1.

At JPL's request, a special capacitance test was performed on E-7. This test was performed on 19 and 20 February per SI 252256. Capacitance measurements were made with power inputs of 4100, 3800, 3500, and 3200 watts. The testing was done in the short circuit mode at all power levels and also in the open circuit mode at 3500 watts.

For more detailed information see the E-7 ETG Processing Report (Reference 7-3).

7.5 QUALITY ASSURANCE PROGRAM

A Quality Assurance Program (QAP) was designed for the Cassini program and implemented to guide all program activities to provide deliverables which were demonstrated to meet all contractual requirements. The program was guided by the Quality Assurance Program Plan (QAPP) (Reference 7-4). The plan showed how the contractual requirements defined in DOE Order 5700.6C would be met with appropriate Lockheed Martin procedures. In some cases, procedures were tailored to meet specific DOE requirements. The QAP addressed the control and acceptance of hardware, the procedures for handling defective hardware and the procedures for acceptance and delivery of hardware.

During the Cassini program, yields during unicouple production were generally at or above goals which were established for each process based on production efforts during previous programs. Yield goals ranged from 80% to 97.6% and actual yields, with few exceptions, were at those levels or above. Unicouple process performance was tracked for each process and problems were addressed when process control limits were exceeded and before specification limits were exceeded, when possible. Using this approach, the acceptance rate for each process was maximized.

Because of the limited quantities of parts and subassemblies for each process in the production of converter hardware, yields were not tracked. However, for all hardware, where defects were noted, the process was technically addressed to determine cause and corrective action, if required. During the Cassini program many process concerns were addressed using this system, and many process improvements resulted.

When hardware was determined to be defective, it was documented on a Defect Report (DR). At this level the hardware could be reworked to meet the drawing, if possible, and the process was also investigated to determined if there was a persistent problem. When hardware was not successfully addressed at this level, it was documented on a Non-Conformance Report (NR) and referred to a Materials Review Board (MRB). At the MRB level, final disposition of the hardware was made. The MRB consisted of representatives of QA, Engineering, Program Office, and DOE. Throughout the program, the quantity of

defective hardware was low enough that, even though MRB dispositions were required, production was not seriously impacted. NRs were classified as Class I or Class II, depending on the impact of the defect at that level. An NR was classified as Class I when the defect had an impact on a requirement between Lockheed Martin and an external interface. All other NRs were classified as Class II and were resolved internally by the local MRB board.

During the Cassini program only one Class I NR was issued. NR 78426 was issued because the pressure drop in the active cooling system of the E-7 shell and fin assembly exceeded specification levels. The hardware was accepted by the internal MRB board and also by the customer. A justification was provided by Lockheed Martin Engineering which included the fact that the cooling system was not required for the Cassini mission.

When a major problem exists, the MRB can initiate a Failure Review Board (FRB) to investigate the problem and recommend a solution. During the Cassini program, one such problem was referred to an FRB by the MRB. NR 79240 was issued to address low isolation resistance in the Qualification RTD cable. The problem was determined to be moisture which was trapped during the manufacturing process at the vendor, Rosemount. Corrective action was determined and all RTD assemblies were screened to determine acceptability. Four RTD assemblies were sent back for rework and the remainder were accepted. A final report of the FRB was issued (Reference 7-5).

References for Section 7

7-1   Cassini Semi-Annual Technical Reports

7-2   E-6 ETG Processing and Test Report, 19 May 1995.

7-3   E-7 ETG Processing and Test Report, 19 March 1996.

7-4   Quality Assurance Program Plan, GESP-7215, CDRL A.3, 31 January 1995.

7-5   Final Report of RTD FRB, CDRL B.3, 14 August 1995.

Section 8

GPHS Fabrication Support

SECTION 8

GENERAL PURPOSE HEAT SOURCE FABRICATION SUPPORT

Components for the General Purpose Heat Source (GPHS) were produced primarily by four DOE facilities as shown in Figure 8-1. The components were integrated at Mound into the GPHS assembly for installation in the converter provided by Lockheed Martin. Figure 3.1.1-1 shows the components of a GPHS module. A detailed discussion of the modules and GPHS assembly is provided in Reference 8-1. For the Cassini program, the fuel powder was processed by the DOE Savannah River Plant (SRP). The iridium alloy encapsulation hardware, termed the Clad Vent Set (CVS), was fabricated at DOE's facility in Oak Ridge (OR), Tennessee as was the Carbon Bonded Carbon Fiber (CBCF) insulator
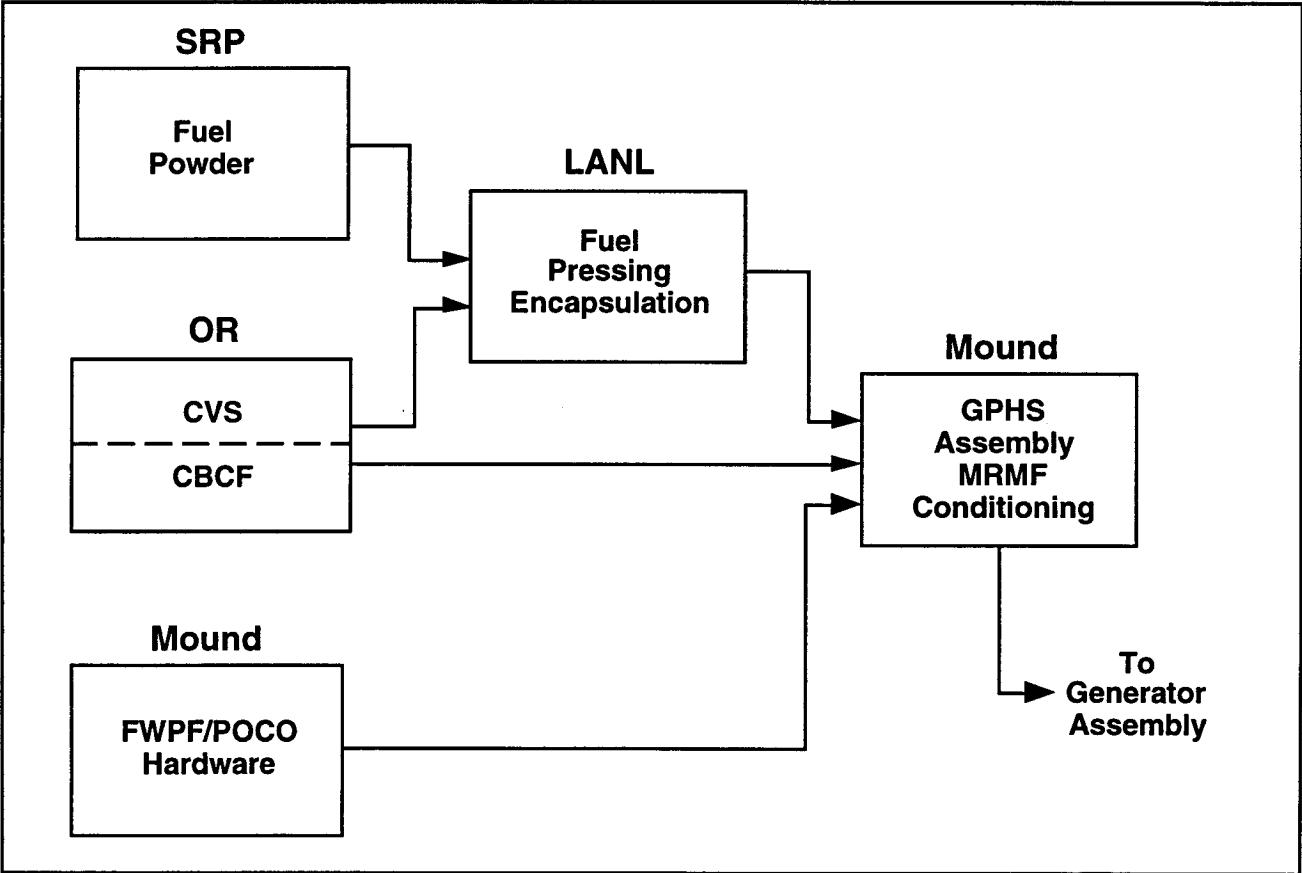
Figure 8-1. General Purpose Heat Source Hardware Suppliers

sleeve and caps. The CVS hardware was delivered to Los Alamos National Laboratory (LANL) for encapsulation of the fuel pellets which had been pressed by LANL. The fueled clads were shipped from LANL to Mound for assembly into the aeroshell modules. In addition, Mound procured Fine Weave Pierced Fabric (FWPF) billets and subcontracted for their machining into aeroshell module components. The aeroshell module graphitic hardware, including the CBCF from Oak Ridge and fueled clads from LANL were assembled into completed modules at Mound. After module assembly they were processed in the Module Reduction and Monitoring Facility (MRMF) at Mound to reduce the accumulation of carbon oxides during ground storage prior to flight vacuum operation.

The interfacing of the organizations shown in Figure 8-1 with DOE and Lockheed Martin was governed by two Interface Working Agreements approved by DOE (References 8-2 and 8-3). For the Cassini program with the GPHS design previously established (Reference 8-1) and only minor modifications implemented for Cassini (Section 4.1) Lockheed Martin activity consisted primarily of production support. Lockheed Martin personnel participated in production readiness reviews at DOE facilities producing GPHS components, made on-site visits to support problem resolution, approved GPHS related engineering change notices, as well as procedural changes and dispositioned non-conforming hardware. The latter activity was facilitated by voting membership in the Mound Material Review Board which was responsible for evaluating discrepant GPHS hardware. Table 8-1 identifies the number of Problem/Failure Reports (P/FRs) documenting discrepant Cassini GPHS hardware.

Table 8-1. Dispositioned GPHS P/FRs

Hardware	Location	No. P/FRs
CVS	Oak Ridge	105
Fuel (Powder, Pelletization Encapsulation)	Los Alamos	340
Heat Source Assembly	Mound	77

The Oak Ridge P/FRs dealt primarily with fabrication and processing problems related to the iridium alloy encapsulation hardware while the Los Alamos P/FRs, for the most part, were related to fuel impurities. Mound P/FRs involved fabrication of the graphitics, module assembly problems and/or heat source assembly concerns. In each of the P/FRs the discrepancies were reviewed and dispositioned by the MRB.

The GPHS modules designated for the three Cassini flight RTGs (F-2, F-6, and F-7) are identified in Tables 8-2, 8-3, and 8-4, respectively, along with relevant information. The position of each module in its stack is shown in the first column at the left of the table. Stack position number 1 is the inboard end of the generator nearest the spacecraft and position number 18 is at the outboard end. The first nine pack of modules is loaded into the generator at its outboard end (positions 10 through 18) while the second nine pack (positions 1 through 9) is loaded in last and is positioned at the inboard end of the generator. The module thermal wattage shown in the third column of each table is based on actual calorimetric measurements decayed out to the opening of the primary launch opportunity, 6 October 1997. (The actual launch occurred on 15 October 1997.) Individual module weight values are listed in column four. The last column in the three tables lists the four fueled clads used in each module. (For brevity, the normal FC prefix has been deleted.) The first two numbers are the fueled clads located in module cavity A, the last two are those located in cavity C. For each of the three flight generators, the module weight values and thermal inventories are consistent with specification requirements. In the case of the thermal wattages, the module-to-module variations are excellent with max-to-min ratios of less than one percent for each of the three generators. After reviewing the module stacking sequence recommended by Mound, Lockheed Martin approved the proposed module stacks.

After module assembly, Mound personnel installed the modules in MRMF cans (a can may hold two modules) and connected the cans to the MRMF manifolding. Operation of the MRMF is such that it allows periodic removal of the generated CO and CO_2 which are replaced by backfilled argon. Operation of the facility continues until at least three consecutive gas analyses (taken at no less than weekly intervals) indicate that CO partial pressure is equal to or less than 500 Pa. Prior to decanning the modules to begin fueling

operation for each of the generators, Lockheed Martin reviewed the gas analysis data provided by Mound.

Table 8-2. F-2 As-Assembled GPHS Module Data

Stack Position	Module No.	Wattage (10/6/97)	Weight (lbs)	Fueled Clads	
				Module Cavity A	Module Cavity C
1	8018	243.82	3.18	076, 120	089, 062
2	8023	243.79	3.19	073, 087	118, 095
3	8009	243.77	3.17	121, 119	140, 141
4	8001	243.75	3.17	123, 124	115, 117
5	8010	243.76	3.20	088, 083	145, 144
6	8021	243.73	3.19	104, 092	105, 093
7	8012	242.75	3.20	036, 056	156, 027
8	8024	242.76	3.18	030, 046	107, 106
9	8022	242.97	3.18	021, 023	096, 097
10	8002	241.91	3.16	094, 102	020, 025
11	8020	242.94	3.19	034, 040	111, 112
12	8025	242.95	3.18	098, 100	063, 091
13	8015	243.79	3.18	039, 054	077, 078
14	8019	243.43	3.19	048, 049	037, 041
15	8008	243.44	3.17	043, 068	109, 110
16	8016	243.45	3.18	072, 074	044, 045
17	8013	243.46	3.18	052, 064	101, 108
18	8011	243.47	3.20	079, 084	113, 114

Table 8-3. F-6 As-Assembled GPHS Module Data

Stack Position	Module No.	Wattage (10/6/97)	Weight (lbs)	Fueled Clads	
				Module Cavity A	Module Cavity C
1	8068	245.59	3.19	266, 295	305, 306
2	8067	245.43	3.19	281, 276	284, 315
3	8029	245.34	3.19	300, 302	303, 304
4	8040	245.31	3.19	299, 294	297, 298
5	8053	245.14	3.18	278, 279	293, 326
6	8060	245.12	3.19	283, 287	314, 317
7	8061	245.06	3.18	309, 310	277, 280
8	8045	244.03	3.19	321, 292	319, 320
9	8046	243.98	3.19	288, 316	311, 318
10	8041	244.22	3.19	246, 250	270, 268
11	8072	244.35	3.17	271, 272	244, 249
12	8070	244.45	3.18	190, 231	274, 275
13	8056	244.54	3.18	251, 252	267, 258
14	8047	244.60	3.18	226, 232	240, 241
15	8042	244.81	3.19	200, 269	264, 265
16	8059	244.86	3.18	237, 238	235, 245
17	8043	244.90	3.19	247, 248	257, 263
18	8063	244.91	3.17	222, 223	233, 239

Table 8-4. F-7 As-Assembled GPHS Module Data

Stack Position	Module No.	Wattage (10/6/97)	Weight (lbs)	Fueled Clads	
				Module Cavity A	Module Cavity C
1	8055	245.05	3.19	202, 225	209, 210
2	8034	244.97	3.19	220, 221	192, 205
3	8054	244.85	3.19	215, 224	207, 211
4	8051	244.60	3.18	216, 198	218, 219
5	8017	244.51	3.18	154, 155	133, 150
6	8014	244.55	3.18	051, 151	162, 160
7	8035	244.14	3.19	199, 206	228, 229
8	8026	243.76	3.18	217, 212	242, 243
9	8037	243.39	3.18	188, 197	167, 169
10	8036	244.07	3.19	163, 164	213, 214
11	8064	244.12	3.18	157, 158	194, 195
12	8069	244.12	3.20	081, 172	171, 173
13	8033	244.14	3.18	174, 182	152, 153
14	8044	244.15	3.20	170, 203	176, 179
15	8027	244.17	3.19	181, 191	122, 143
16	8050	244.21	3.19	134, 137	177, 178
17	8048	244.21	3.19	132, 138	183, 189
18	8028	244.22	3.19	146, 148	186, 196

Section 8 References

8-1   Final Report for the GPHS-RTG Program, GESP-7209, February 1991.

8-2   Interface Working Agreement for Encapsulated Plutonium-238 Fuel Form Production, Rev. 2, June 1992.

8.3   GPHS-RTG Interface Working Agreement for the Cassini RTG Program, GESP-7231, February 1996.

Section 9

Launch Site Operations

SECTION 9
LAUNCH SITE OPERATIONS

The Readiness Review for shipment of the F-2 and F-5 RTGs was convened by Mound on 17 April 1997 and the review for shipment of F-6 and F-7 was held at Mound on 1 May 1997. A LMMS representative attended and remained at Mound for RTG transportation system package assembly operations for both F-2 and F-5 as well as for F-6 and F-7. Vent plug sealing difficulties were experienced with one of the primary vessel port plugs. Mound personnel (after discussions with cognizant personnel at Hanford) reworked the vent plug threads and were successful in establishing a tight seal for all the packages. Subsequently, two convoys were used to transport all four RTGs to the Kennedy Space Center (KSC).

The first convoy delivered the F-2 and F-5 RTGs to the RTG facility at KSC on 22 April. The unloading of F-2 from the System 120 Package and installation into the BPCA base went smoothly and without problems. Difficulty was experienced when the spare F-5 RTG was removed from the transportation system package (TSP) base assembly. One of four locking pins that secure the RTG and its mid-ring assembly (MRA) to the converter support ring (CSR) was found to be incompletely retracted. Consequently, this remaining pin hindered the removal of the RTG and caused the TSP base assembly to be partially lifted with the RTG. Upon seeing one side of the base assembly approximately one half-inch off the floor, the crane operator stopped the lift, the TSP base separated from the remaining pin, and the elevated side of the base slipped back to the floor, leaving the RTG free. Subsequently, the transfer of F-5 was completed to the base and protective cover assembly (BPCA) base for storage. A small burr on one of the four MRA lugs (apparently caused by the less than fully retracted locking pin) restricted the movement of one of the MRA lugs in mating with the CSR. Eventually, the lug seated fully and the RTG was secured to the BPCA base with its CSR locking pins. Following the transfer to the BPCA base, the internal pressure of the RTG was monitored and found to be in agreement with the pre-ship value recorded by Mound. Subsequent electrical checks of F-5 also showed satisfactory values. As a result of the incident, handling procedures

were revised to include the use of a hydra-set and load cell to limit the force used to lift an RTG to a value consistent with its weight and the weight of its attached ground support equipment.

The F-6 and F-7 RTGs were delivered to KSC two weeks later on 6 May. These unloading operations went very smoothly and without difficulties. After delivery of all four RTGs to KSC, electrical measurements were performed and found to be satisfactory for each RTG. The JPL adapter rings with the power and RTD cables attached were installed on the F-6 and F-7 RTGs on 20 and 21 May. Prior to F-2 installation, electrical measurements of the cabling revealed that the outer cable covering was electrically conductive and compromised the electrical isolation of the RTG from the spacecraft at the adapter-to-RTG interface. JPL revised their cable design by including overwrapping with Sheldahl to restore electrical isolation. The F-2 adapter cabling was modified, installed on the F-2 RTG and found to be satisfactory. The F-6 and F-7 adapter/cabling assemblies were removed, modified, reinstalled and also found to be satisfactory.

Periodic electrical measurements of the RTGs were continued following the removal of the adapter rings and modification of the power and resistance temperature device cables, as noted above. Pressure measurements were also completed using the gas service carts. The measured electrical data were consistent with prior data. Both F-2 and F-5 had slight pressure increases while F-6 and F-7 had slight pressure decreases. All measurements were well within specified limits.

Argon gas exchanges were performed to remove helium produced by the decay of the Pu^{238} isotope heat source. The operation was performed to restore power output for the trial fit-up of the RTGs to the spacecraft. The exchanges were performed on a 24-hour per day basis with operations taking place on two RTGs simultaneously. F-5 and F-6 underwent nine gas exchange cycles prior to achieving maximum power; F-2 and F-7 underwent ten gas exchange cycles. The initial and final RTG power values are as shown in Table 9-1.

Table 9-1. Initial and Final RTG Output Power

RTG	Initial Power (Watts)	Final Power (Watts)
F-2	121.2	156.5
F-5	80.8	124.0
F-6	136.3	150.1
F-7	134.2	157.4

The PRDs were installed on the F-2, F-6, and F-7 RTGs on 25 June. All operations were performed per CAS 131-LM, Part 1. The safety bolt and nut were replaced with the quick release safety pin prior to PRD installation. Proper clearance between bellows and safety pin and between lance and diaphragm were verified using a videoscope. The gas flex hoses were also removed from the RTGs. The above activities were accomplished in preparation for the RTGs-to-spacecraft fit check.

Reviews of draft operational procedures continued with comments being forwarded to JPL for consideration. In addition, three LMMS individuals were trained for crane operations at PHSF to perform operations for protective cover removal and installation with the BPCA base in the PHSF air lock.

Next the RTGs were transferred to the PHSF and mated with the spacecraft. In preparation for the fit check, a Readiness Review was held on 15 July and a dress rehearsal was performed on 17 July. These operations included removal of an RTG simulator from the BPCA, transferring the RTG, and installing it onto the spacecraft at all three locations. These activities provided good training experience in handling the flight RTGs prior to their final installation on the spacecraft at the launch pad.

The fit check began 18 July when the RTGs were transferred to the PHSF and subsequently mated to the Cassini spacecraft. Upon arrival at the PHSF, the protective covers were removed and the RTGs were installed onto the spacecraft. All activities moved quickly and without difficulty. The PHSF facility crane circuit breaker activated and shut down operations for about one-half hour during removal of the BPCA protective cover for F-6. In addition, the JPL power connector's protective plastic cover touched the

RTG and left a small amount of material on the outer shell of F-6. After review in Valley Forge, the largest deposit of melted material was removed. A small amount of paint was removed at the edge of the land near one of the unicouple sealing screws. Some of the smaller deposits were not removed. A JPL Quality Engineer witnessed the removal operation and concurred with this disposition.

RTG/spacecraft electrical connections began at 1400 hours on 18 July. Spacecraft operations continued under RTG power until 0800 hours on 19 July. The electrical performance data are shown in Table 9-2.

Table 9-2. Comparison of RTG Power Following Argon Gas Flush and during Spacecraft Mating

	F-2	F-6	F-7
RTG Power - Watts			
After Gas Flush	156.6	150.1	157.4
Spacecraft Power *	149.9	141.5	150.5
* Span from Gas Flush - Days	28	30	28

Operations to remove the RTGs from the spacecraft began about 0830 hours on 19 July and by 1330 hours the RTGs were back in the RTGF. The RTG transportation system trailers were loaded without difficulty and the air conditioning system kept the inside trailer temperature below 84°F.

After the RTGs were returned to the RTGF, new flex hoses were installed on F-2, F-6, and F-7. The flex hose on F-5 was replaced with the new hose at this same time. Electrical and pressure measurements were again performed on the RTGs. F-2, F-5 and F-6 had slight pressure increases during approximately one month of storage time. F-7 had a 0.20 psia pressure decrease during the same storage period. All changes were within acceptable levels. The electrical performance data, as measured by the PTUs, were consistent with previous data prior to the spacecraft fit check.

Two Problem/Failure Reports (P/FRs) were generated by DOE Mound during RTG transport to the PHSF. One related to the set-down of the BPCA base while being lowered by the pallet truck. The other was related to the tightening of the tie-down straps

in the trailer. In both instances the load to the RTGs was minor. Inspection of the passive shock indicators showed they were not tripped and the P/FRs were dispositioned accordingly.

During their storage in the RTGF, the RTG electrical performance and pressure were monitored. All electrical data were consistent with previous measurements. Pressure checks showed that the pressure in all four RTGs continued to be satisfactory. Temperature measurements using the RTDs mounted on the RTGs were also monitored during storage. In the case of F-7 temperature variations of a few degrees were noted. An investigation led to the conclusion that these variations were related to the proximity of F-7 to one of the building's air conditioning vents. The temperature variations were not serious and no changes to the ventilation system were made.

As a contingency step, a test was performed to determine the heat-up rate of the outboard handling fixture when placed on the heater plates. Heating of the outboard handling fixtures was required if the RTGs need to be removed from the spacecraft at LC-40. Three heater plates were to be used and a heat-up time-temperature profile was established.

The final procedure for LC-40 and KSC operations was completed and submitted for approval in August. This procedure, CAS 131-LM Part 5, covered the activities for getting the spare RTG prepared for shipment to Mound and the preparation of the Ground Support Equipment (GSE) for return to Valley Forge. Photographs of F-6 were taken documenting the removal of the deposits from the electrical connector cover.

The Cassini spacecraft was moved from the PHSF to LC-40 on 27 August. The spacecraft was satisfactorily mated to the Centaur early on the following day. The Cassini spacecraft was removed from LC-40 on 7 September and returned to the PHSF, because of a concern that the Huygens Probe may have been contaminated by insulation particles due to high nitrogen purge flow. The probe was removed from the spacecraft and was cleaned, reassembled, and reattached to the spacecraft in preparation for moving to the launch pad. As a result of performing these operations, the Cassini launch was rescheduled from 6 October to 13 October.

The CAS 131-LM, Part 4 procedure for LC-40 RTG installation was red-lined for the dress rehearsal. The procedure called for the BPCA to be lifted with the RTG simulator to Level 6, the simulator removed, and lifted to Level 14 for spacecraft integration.

The LC-40 procedures were modified for lightning precautions. Once the RTG removal operation from the trailer had begun, the RTG lift would continue to level 6 under a Phase 2 warning (lightning sighted within 5 miles). If the unloading operation had not been initiated, the RTG would have remained in the trailer until the Phase 2 warning had been terminated. The responsible engineer was given the authority to return the RTG to the trailer at any time, if warranted. The RTG lift from level 6 to level 14 could not begin under a Phase 2 warning.

All hardware and procedures were in-place to perform the dress rehearsal on 27 September. LMMS personnel attended meetings with JPL, KSC, and CCAS personnel to establish roles and responsibilities for the dress rehearsal. Manloading for the RTGF, LC-40 Deck (ground level), LC-40 Level 6, and LC-40 Level 14 were established in conjunction with JPL for both the dress rehearsal and RTG installation.

The GSE was taken to LC-40 on 26 September and placed on the appropriate level. The dress rehearsal started with the BPCA being lifted from the pad deck to Level 6. The BPCA cover was removed and the RTG simulator was transferred to the JPL lifting sling. The simulator was lifted to Level 14 and mated to the spacecraft. This was the first RTG simulator installation with the payload fairing in-place. After the simulator was mounted to all three spacecraft locations, a backout operation was performed that took the RTG simulator back to Level 6, installed in the BPCA and lowered to the pad deck. This cycle lasted approximately six hours. All operations went very well and provided an excellent familiarization opportunity for the CCAS personnel. A lessons-learned review was held with all personnel.

The xenon gas exchange started on 29 September. This was a 24-hour per day activity and lasted six days. The RTGs were on open circuit for these gas exchange cycles to raise the hot side temperatures to aid in removal of the residual helium and argon gases.

The xenon gas exchange cycles were completed for F-2, F-6, and F-7. F-6 required 10 gas cycles to obtain maximum power. F-2 and F-7 required 9 gas cycles. During the gas exchange cycles the RTG open circuit voltage was monitored. When the voltage changed less than 0.1 volt between gas cycles, the cycles were terminated. Following the completion of the gas cycles, the RTGs were placed under a 30 volt load and a four hour stability test was performed. The initial open circuit voltage with argon/helium and the final open circuit voltage with xenon gas and final RTG power are shown in Table 9-3.

Table 9-3. RTG Power Following Xenon Gas Exchange

	Argon/Helium	Xenon	RTG Power
RTG-F-2	44.10 Volts	53.24 Volts	221.34 Watts
RTG-F-6	43.39 Volts	52.00 Volts	211.48 Watts
RTG-F-7	44.27 Volts	53.01 Volts	219.23 Watts
RTG-F-5	40.98 Volts	49.92 Volts	N/A

On F-5 (spare RTG) the xenon gas cycles were suspended after two gas cycles due to lack of xenon gas. The following week two hundred liters of xenon gas became available to complete the 10 gas cycles. No RTG performance test was performed on F-5 due to other activities for the flight RTGs.

On 6 October the RTGs were prepared for flight by removing the gas flex hose and other non-flight hardware and the protective covers installed onto the BPCA bases. The three flight RTGs were transferred to the launch pad on 10 October. The RTG loading began at 0400 hours and the move to LC-40 began at 0500 hours. The unloading and lift to level 6 began at approximately 0615 hours and was completed around 0830 hours. The lifts from level 6 to level 14 were completed at 1100 hours. RTG power to the spacecraft was started at 1300 hours. All operations were accomplished satisfactorily.

The Cassini spacecraft was launched on 15 October at 0443 hours from Cape Canaveral Air Station. All systems performed nominally. The RTG power was 890 watts after achieving stability, just two watts different than the 888 watts pre-launch predictions.

F-2 was 299.7 watts, F-6 was 293.1 watts, and F-7 was 297.4 watts corrected for spacecraft cable loss.

On 20 October Lockheed Martin returned to the launch pad to remove BPCAs and other GSE from level 6 and return it to the RTGF. Also on 20 October Lockheed Martin personnel initiated the exchange of the xenon gas on F-5 to argon gas. Nine gas cycles were completed on F-5 by 24 October. A PTU performance test was performed on this RTG to provide a reference for receipt at DOE Mound.

The PTU test data are shown in Table 9-4.

Table 9-4. F-5 RTG Performance Prior to Shipment to DOE Mound

Voltage	1.234 volts
Current	14.92 amps
RTD Average	158.6°C
Resistance (Internal)	2.195 ohms
Open Circuit Voltage	33.99 volts
Resistance to Case	868k ohms
RTG Pressure	23.2 psia

The RTG Shipping Package was prepared for receiving the RTG on 27 October. F-5 was installed into the package on 28 October and loaded onto the Transportation System Trailer. The convoy left KSC the following morning and arrived at DOE Mound Plant on 30 October. The Package was unloaded and F-5 removed. Pressure and electrical checks were made and found to be consistent with pre-ship data.

The ground support equipment and personal belongings were loaded on trucks on 29 and 30 October for return to Valley Forge, ending the KSC/CCAS launch support activities.

A summary of the RTG electrical data and pressure history at KSC and a few data points taken at Mound are shown in Tables 9-5 through 9-8.

Table 9-5. RTG F-2 Data

Date	RTG pressure PSIA	RTG shorted voltage VDC	RTG shorted current Amps	RTG Open Cir voltage VDC	Case Open Cir voltage VDC	Case Close Cir voltage VDC	RTD #1 temp Deg. C	RTD #2 temp Deg. C	RTD #3 temp Deg. C	RTD #4 temp Deg. C	RTD Avg temp Deg. C	RTG power Watts	RTG internal res Ohms	RTG load res Ohms	Case res 2 min. KOhms
MOUND															
4/2/97		1.281	15.10	35.21	0.343	0.017	161.7	162.7	164.4	161.1	162.5	19.3	2.247	0.085	191.2
4/2/97		1.269	15.29	35.88	0.666	0.046	164.4	165.3	166.2	163.8	164.9	19.4	2.264	0.083	134.8
4/14/97	24.60	1.271	14.91	34.99	0.348	0.019	166.2	167.1	165.3	166.5	166.3	19.0	2.262	0.085	177.8
4/14/97	23.65	1.271	14.91	34.99	0.348	0.019	166.2	167.1	165.3	166.5	166.3	19.0	2.262	0.085	177.8
KSC															
4/24/97	23.60	1.261	14.92	34.83	0.307	0.017	165.7	165.8	165.9	165.8	165.8	18.8	2.250	0.085	170.0
4/24/97	24.50														
5/13/97	24.67														
5/23/97	note 1.	1.137	16.04	38.59	0.406	0.037	NA	169.7	167.7	166.6	168.0	18.24	2.335	0.071	99.7
6/2/97	note 2.	1.066	14.72	34.59	0.377	0.018	NA	163.7	160.8	162.4	162.3	15.69	2.277	0.072	199.4
6/3/97	24.79														
RTG IN NORMAL LOAD MODE				ARGON GAS											
6/20/97	24.90	30.06	5.21	42.14	20.35	5.60	NA	159.3	157.1	158.2	158.2	156.61	2.319	5.770	263.4
7/25/97	25.03														
7/25/97	24.50	1.131	15.50	36.16	0.304	0.019	NA	163.9	162.9	163.5	163.4	17.53	2.260	0.073	150.0
8/19/97		1.117	15.26	36.00	0.3005	0.01949	NA	161.5	161.6	161.9	161.7	17.05	2.286	0.073	144.2
8/20/97	24.80														
RTG IN NORMAL LOAD				XENON GAS											
10/1/97	23.7	30.05	7.37	46.43	20.26	8.48	NA	157.7	155.3	155.4	156.1	221.34	2.224	4.081	139.1

Notes:

1 Data taken after extended period in OPEN mode, during adapter installation. Conditions were unstable.

2 Stable data taken after JPL adapter was installed.

Table 9-6. RTG F-5 Data

Date	RTG pressure PSIA	RTG shorted voltage VDC	RTG shorted current Amps	RTG Open Cir voltage VDC	Case Open Cir voltage VDC	Case Close Cir voltage VDC	RTD #1 temp Deg. C	RTD #2 temp Deg. C	RTD #3 temp Deg. C	RTD #4 temp Deg. C	RTD Avg temp Deg. C	RTG power Watts	RTG internal res Ohms	RTG load res Ohms	Case res 2 min. KOhms
MOUND															
3/25/97	24.85	1.118	12.55	30.52	0.168	0.00054	158.1	156.7	156.7	156.5	157.0	14.0	2.343	0.089	3101.1
4/8/97	24.75	1.071	12.50	30.33	0.161	0.00058	158.1	157.6	158.5	159.2	158.4	13.4	2.341	0.086	2765.9
4/14/97	24.75	1.112	12.49	30.31	0.155	0.00053	156.3	155.0	154.9	154.8	155.3	13.9	2.338	0.089	2914.5
4/14/97	23.60	1.112	12.49	30.31	0.155	0.00053	156.3	155.0	154.9	154.8	155.3	13.9	2.338	0.089	2914.5
KSC															
4/24/97	23.55	1.115	12.47	30.24	0.218	0.00052	158.0	158.5	157.8	157.6	158.0	13.90	2.336	0.089	4182.3
4/29/97	23.55														
4/29/97	24.50														
5/13/97	24.61														
6/2/97		1.086	12.48	30.16	0.189	0.00053	157	158.4	156	156.7	157.0	13.55	2.330	0.087	3556.0
6/3/97	24.81														
RTG in NORMAL OAD MODE ARGON GAS															
6/18/97	25.1	30.061	4.12	40.08	21.922	1.877	155.6	155.9	154.1	154.5	155.0	123.88	2.432	7.295	1067.9
7/25/97	24.52														
7/25/97	24.00	1.214	13.91	34.10	0.257	0.00218	154.5	155.9	155.0	153.9	154.9	16.89	2.364	0.087	1168.9
8/19/97		1.212	13.77	33.79	0.251	0.00207	155	155.6	154.1	153.4	154.4	16.69	2.366	0.088	1202.6
8/20/97	24.50														
10/24/97	23.2	1.234	14.92	33.99	0.2475	0.00282	157.1	158.5	159.1	158.1	158.6	18.41	2.195	0.083	867.7

Notes:

1   Data taken after extended period in OPEN mode, during adapter installation. Conditions were unstable.

2   Stable data taken after JPL adapter was installed.

Table 9-7. RTG F-6 Data

Date	RTG pressure PSIA	RTG shorted voltage VDC	RTG shorted current Amps	RTG Open Cir voltage VDC	Case Open Cir voltage VDC	Case Close Cir voltage VDC	RTD #1 temp Deg. C	RTD #2 temp Deg. C	RTD #3 temp Deg. C	RTD #4 temp Deg. C	RTD Avg temp Deg. C	RTG power Watts	RTG internal res Ohms	RTG load res Ohms	Case res 2 min. KOhms
MOUND															
4/16/97	24.50	1.287	15.72	35.63	0.328	0.011	167.7	170.0	169.2	168.4	168.8	20.23	2.185	0.082	288.2
4/16/97	25.20	1.287	15.72	35.63	0.328	0.011	167.7	170.0	169.2	168.4	168.8	20.23	2.185	0.082	288.2
4/28/97	22.10	1.297	15.71	35.67	0.343	0.011	161.5	158.5	160.3	161.3	160.4	20.38	2.188	0.083	301.8
4/28/97	23.60	1.297	15.71	35.67	0.343	0.011	161.5	158.5	165.3	161.3	160.4	20.38	2.188	0.083	301.8
KSC															
5/7/97		1.317	15.53	35.38	0.361	0.012	169.7	169.1	168.7	170.5	169.5	20.45	2.193	0.085	290.8
5/12/97	23.55														
5/12/97	24.46														
5/21/97	note 1.	1.112	16.77	39.44	0.470	0.035	NA	175.7	175.7	176.2	175.9	18.65	2.286	0.066	124.3
5/29/97	note 1.	1.12	17.35	40.33	0.493	0.043	NA	178.8	177.7	178.3	178.3	19.43	2.260	0.065	104.7
6/2/97	note 2.	1.049	15.53	35.00	0.412	0.014	NA	168.3	167	168.7	168.0	16.29	2.186	0.068	284.3
6/4/97	24.32														
6/4/97	24.97														
RTG IN NORMAL LOAD MODE				ARGON GAS											
6/18/97	25.04	30.00	5.00	41.24	27.85	12.44	NA	162.7	162.5	162.6	162.6	150.03	2.248	5.999	123.9
7/25/97	25.12	1.036	15.48	35.5	0.5302	0.0244	NA	165.9	165.9	165.9	165.9	16.04	2.226	0.067	207.3
8/1/97							NA	167.0	166.0	167.0	166.7				
8/4/97							NA	167.0	167.0	168.0	167.3				
8/11/97							NA	166.0	166.0	167.0	166.3				
8/19/97		1.023	15.26	35.5	0.5417	0.02431	NA	163.1	163.5	165	163.9	15.61	2.259	0.067	212.8
8/20/97	25.25														
8/20/97	24.94														
RTG IN NORMAL LOAD MODE				XENON GAS											
10/3/97	24.7	30.01	7.05	45.64	27.07	15.47	NA	161.8	161.5	161.9	161.7	211.48	2.218	4.259	750.4

Notes:

1 Data taken after extended period in OPEN mode, during adapter installation. Conditions were unstable.

2 Stable data taken after JPL adapter was installed.

Table 9-8. RTG F-7 Data

Date	RTG pressure PSIA	RTG shorted voltage VDC	RTG shorted current Amps	RTG Open Cir voltage VDC	Case Open Cir voltage VDC	Case Close Cir voltage VDC	RTD #1 temp Deg. C	RTD #2 temp Deg. C	RTD #3 temp Deg. C	RTD #4 temp Deg. C	RTD Avg temp Deg. C	RTG power Watts	RTG internal res Ohms	RTG load res Ohms	Case res 2 min. KOhms
MOUND															
3/18/97	25.20	1.434	15.60	35.93	0.468	0.014	164.6	166.7	161.7	163.7	164.2	22.37	2.211	0.092	324.3
4/1/97	24.80	1.384	15.54	35.89	0.475	0.014	163.7	169.4	164.4	162.8	165.1	21.51	2.220	0.089	329.3
4/15/97	24.50	1.397	15.42	35.76	0.449	0.014	165.5	170.3	168.8	165.5	167.5	21.54	2.228	0.091	310.7
4/29/97	24.90	1.346	15.35	35.68	0.440	0.013	166.4	166.7	165.3	165.5	166.0	20.66	2.237	0.088	328.5
4/29/97	23.60	1.346	15.35	35.68	0.440	0.013	166.4	166.7	165.3	165.5	166.0	20.66	2.237	0.088	328.5
KSC															
5/7/97		1.380	15.32	35.47	0.407	0.012	167.3	167.7	167.9	167.2	167.5	21.14	2.225	0.090	329.2
5/12/97	23.57														
5/12/97	24.45														
5/20/97	note 1.	1.259	16.83	39.88	0.599	0.042	NA	171.9	171.8	173.2	172.3	21.19	2.295	0.075	132.6
5/30/97	note 1.	1.251	17.12	40.53	0.584	0.048	NA	173.3	174.4	173.8	173.8	21.42	2.294	0.073	111.7
6/2/97	note 2.	1.122	15.29	34.96	0.473	0.012	NA	164.7	165.7	164.5	165.0	17.16	2.213	0.073	384.2
6/4/97	24.40														
6/4/97	24.99														
RTG IN NORMAL LOAD MODE				ARGON GAS											
6/20/97	24.80	30.03	5.24	41.97	27.64	11.05	NA	161.7	160.4	159	160.3	157.36	2.279	5.731	150.1
7/25/97	24.80														
7/25/97	25.00	1.151	15.7	36.14	0.522	0.0223	NA	157.0	159.2	154.0	156.7	18.07	2.229	0.073	224.1
7/25/97							NA	157.0	161.0	157.0	158.3				
8/1/97							NA	163.0	163.0	161.0	162.3				
8/4/97							NA	163.0	163.5	161.0	162.5				
8/11/97							NA	163.0	163.0	161.0	162.3				
8/19/97		1.220	15.33	36.08	0.5138	0.02127	NA	159.3	161.9	161.2	160.8	18.70	2.274	0.080	231.6
8/20/97	25.16														
8/20/97	25.02														
RTG IN NORMAL LOAD MODE				XENON GAS											
10/1/97	24.2	30.01	7.31	46.26	26.09	11.74	NA	158.4	158.3	156.8	157.8	219.23	2.225	4.106	122.2

Notes:

1 Data taken after extended period in OPEN mode, during adapter installation. Conditions were unstable.

2 Stable data taken after JPL adapter was installed.

Section 10

Material and Equipment Status

SECTION 10
MATERIALS AND EQUIPMENT STATUS

10.1 RESIDUAL CASSINI UNICOUPLE HARDWARE

Table 10-1 lists the hardware related to unicouple production, which is residual from the Cassini Program. This hardware has been packaged for long term storage per document GESP-7244, *Requirements for Long Term Packaging of Unicouple and Converter Hardware.* These items are available for future unicouple production, or any other suitable application.

Table 10-1. Cassini Residual Unicouple Hardware

Item	Drawing Number	Stock Qty	U/M
Boron Powder	M31A1	300	GM
Braze Shim	47A303830P1	5303	EA
Braze Shim	47A303831P1	7988	EA
Braze Shim	47A303832P1	16500	EA
Braze Shim	47A303833P1	2473	EA
Braze Shim	47A303834P1	8700	EA
Cold Shoe, Tumbled	47A303803P1	426	EA
Cold Shoe, Tumbled	47A303803P1-901	2660	EA
Cold Stack	47A303957G1	52	EA
Compact Less Sample, 78% n-SiGe	47A303807P1-900	2	EA
Compact Less Sample, 78% p-SiGe	47A303808P1-900	1	EA
Compact, 63.5% n-SiGe	47A303821P1	2	EA
Compact, 63.5% p-SiGe	47A303822P1	2	EA
Compact, 78% n-SiGe	47A303819P1	2	EA
Compact, 78% p-SiGe	47A303820P1	5	EA
Compact, 85% n-SiMo	47A303823P1	18	EA
Compact, 85% p-SiMo	47A303824P1	15	EA
Compact, Polished n-SiMo	47A303817P1	2	EA
Compact, Polished p-SiMo	47A303818P1	2	EA
Connector, Plated	47A303841P2	37	EA
Connector, Tumbled	47A303841P2-901	935	EA
Connector, Unplated	47A303841P2-900	3913	EA
Couple Preassembly	47A303929G1	49	EA
First Bond	47A303959G1	164	EA
First Bond, Si$_3$N$_4$ Coated	47A303962G1	121	EA
Foil, Titanium	M14B1	4	FT
Germanium	M30A1	5043	GM
Germanium, Crushed	RM1B1-901	1783	GM
Heat Shunt, Etched	47A303847P2-900	73	EA

Table 10-1. Cassini Residual Unicouple Hardware (Cont'd)

Item	Drawing Number	Stock Qty	U/M
Heat Shunt, Less Etch and Plate	47A303847P2-901	15	EA
Heat Shunt, Less Plate	47A303847P2-900	73	EA
Heat Shunt, Machined	47A303847P2-901	15	EA
Heat Shunt, Plated	47A303847P2	45	EA
Hot Shoe	47A303858P1	206	EA
Hot Shoe Spacer, As Purchased	47A303922P1-900	926	EA
Hot Shoe Spacer, Fired	47A303922P1	162	EA
Hot Shoe Spacer, Si$_3$N$_4$ Coated	47A303923P1	146	EA
Hot Shoe, H$_2$O$_2$ Cleaned	47A303959G1-900	31	EA
Insulation, Fired	M49A1	1.6	SF
Insulation, Unfired	M49A1-900	47	SF
Insulator	47A303845P1	1832	EA
Insulator, Machined	47A303844P1	198	EA
Insulator, Plated	47A303846P1	21	EA
Mo Compensator, Plated	47A303805P1	45	EA
Mo Compensator, Unplated	47A303805P1-900	932	EA
Molybdenum Powder	M8D1	16344	GM
N/P Bonded Compact	47A303956G1	3	EA
Pedestal, Plated	47A303801P1	150	EA
Pedestal, Tumbled, Unplated	47A303801P1-902	662	EA
Pellet, n-	47A303807P1	664	EA
Pellet, p-	47A303808P1	418	EA
Pellet, p-, Cleaned Random Length	47A303808P1-901	31	EA
Phosphorus	M32A1	375	GM
Powder Blend, 63.5% n-SiGe	47A303821P1-901	22	MC
Powder Blend, 63.5% p-SiGe	47A303822P1-901	8	MC
Powder Blend, 78% n-SiGe	47A303819P1-901	15	MC
Powder Blend, 78% p-SiGe	47A303820P1-901	13	MC
Powder Blend, 85% n-SiMo	47A303823P1-901	12	MC
Powder Blend, 85% p-SiMo	47A303824P1-901	1	MC
Pressure Pad, Annealed	47A303806P1-901	1211	EA
Pressure Pad, Plated	47A303806P1	73	EA
Pressure Pad, Tumbled	47A303806P1-901	1211	EA
Pressure Pad, Untumbled, w/ Burrs	47A303806P1-905	1020	EA
Radiator	47A303955G1	16	EA
Radiator, Machined	47A303852P1	38	EA
Second Bond	47A303927G1	80	EA
Segment, n-	47A303809P1	1225	EA
Segment, p-	47A303810P1	3816	EA
Shim, Titanium	47A303837P6-900	19	EA

Table 10-1. Cassini Residual Unicouple Hardware (Cont'd)

Item	Drawing Number	Stock Qty	U/M
Silicon	M29A1	135	KG
Silicon, Crushed	RM1B1-900	1850	GM
Unicouple	47A303931G1	12	EA
Unicouple, Wrapped	47A303948G1	1023	EA
Vacuum Casting, 63.5% n-SiGe	47A303821P1-900	1	EA
Vacuum Casting, 78% p-SiGe	47A303820P1-900	1	EA
W Compensator, Plated	47A303802P1	183	EA
W Compensator, Tumbled	47A303802P1-901	1268	EA
Yarn, Fired Quartz	M9D1	3	SP

Notes:
- The quantities listed include qualification and flight hardware, but not Engineering hardware.
- The quantities listed are from Cassini stockroom plant code V8D only.

10.2 DOE THERMOELECTRIC MANUFACTURING EQUIPMENT

This paragraph discusses the thermoelectric production equipment which was maintained in an operational mode following completion of the Cassini unicouple build. Per DOE direction, the thermoelectric production equipment was operated on a monthly basis from December 1995 through September 1997. The equipment operated were six small Brew bonding furnaces, two compact hot presses, two vacuum casting furnaces, two CVD Si_3N_4 coating furnaces, four Brown and Sharp grinders, one STC wafering machine, and the ITI slicer. All the vacuum equipment was operated and checked for the time required to reach operating conditions. Equipment that did not achieve acceptable vacuum levels were repaired, as required. Machine tool equipment was cleaned and drained of coolant. These were then operated monthly to cycle the equipment.

As Space Power exited Building B, most of the thermoelectric equipment was put into storage for future possible use. Two Brew bonding furnaces, three vacuum test stations, and three laminar flow benches were transferred to AMPS to support the ARPS work.

10.3 DOE LOADING AND ASSEMBLY STATION

The Loading and Assembly Station (LAS) is a unique facility used to process ETGs. Major upgrades were made to this facility during the Cassini program and are discussed in the following paragraphs. The necessity to perform the processing in such a facility is

established by the ETGs susceptibility to degradation in an oxygen atmosphere (air) while at elevated temperatures. The LAS, as shown in Figure 10-1, consists of an airtight main chamber which houses the ETG, tools, and fixtures, and provides a controlled inert environment in which work is performed through rubber/viton gloves, and an internal loadlock chamber through which large tools and fixtures can be passed while maintaining the integrity of the inert gas environment in the main chamber.

The LAS is a vertical water-jacketed cylindrical chamber with an inside height of 80 inches and a diameter of 54 inches. Both the main chamber and the loadlock chamber can be simultaneously or individually evacuated and backfilled. The LAS can be utilized as a vacuum facility or as a glove box. The Assembly Station has its own Turbo-Molecular Pump (TMP) and a Cryogenic Pump for high vacuum applications. There are four work stations located around the LAS; at 0°, 90°, 195°, and 270°. Each of the four work stations is equipped with a 17 inch viewport and a pair of penetration gloves with the 90° station having an upper and lower pair. In addition, 6 inch viewports are located between the lower pair of gloves at the 90° station and just above the loadlock at the 0° station.

The glove ports are configured such that the gloves may be removed or replaced without affecting the chamber environment. Special closures and pumpout capability from two Welch mechanical pumps are provided. A Portable Tool-lock is available that can be attached to any glove port. It also utilizes the special evacuation and backfill capabilities of the glove ports and serves as a pass-through for small tools.

The internal loadlock chamber at the 0° work station has an internal capacity 20 inches wide by 12 inches high for passing larger items into the main chamber during in-process operations without affecting the environment's purity levels. A removable internal loadlock cover provides access to the main chamber.

Hydraulic lifts are provided at the loadlock station. They are equipped with a 5 inch bore hydraulic ram to remotely raise equipment within the loadlock for transfer to the main chamber. They have a maximum elevation of 19 inches and a three-position direction control for up/down/stop. The system is operated by an electrically powered hydraulic
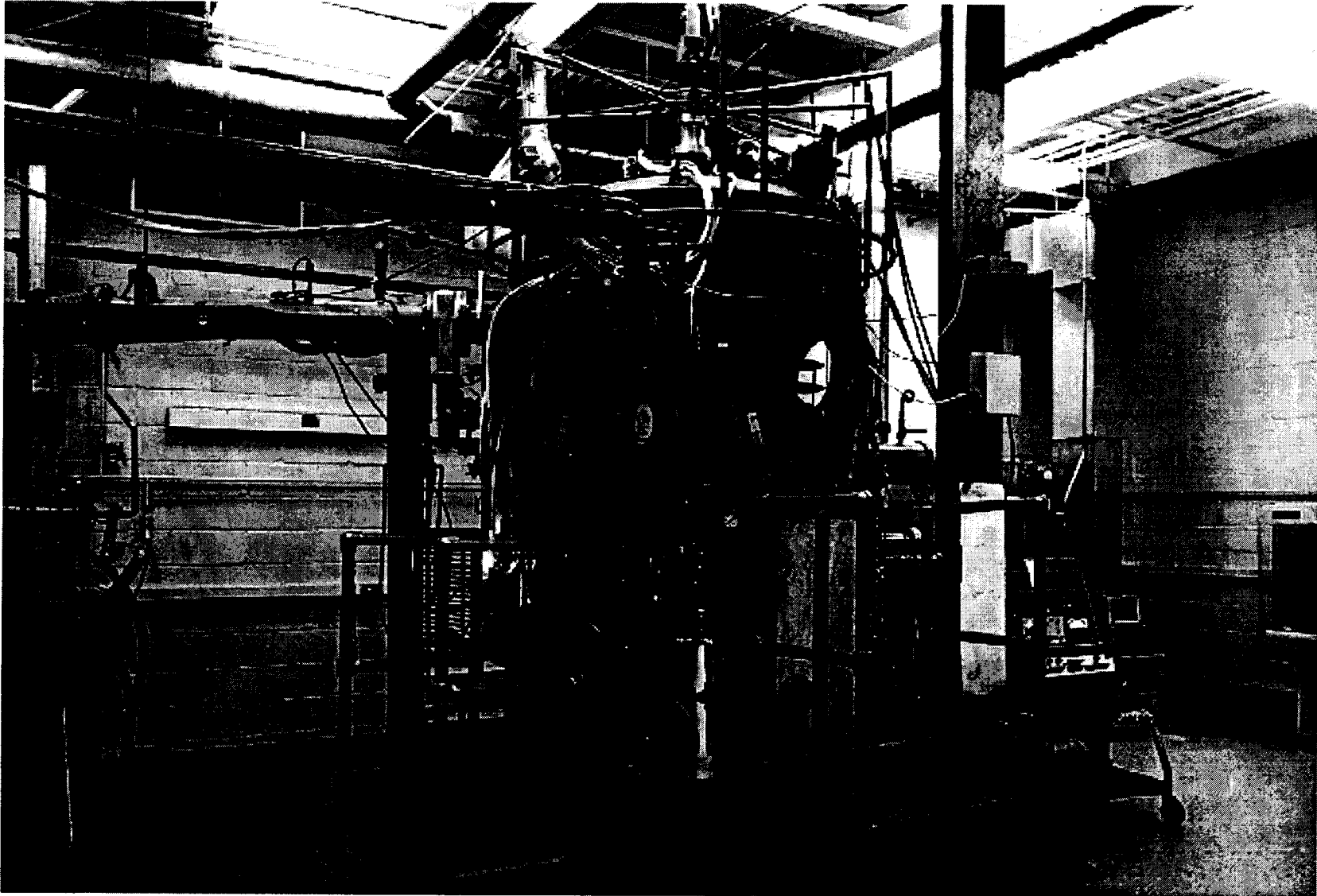
Figure 10-1. Loading and Assembly Station

pump. Also, a manually operated reciprocating pump provides a backup capability. The LAS has a second hydraulic ram at the 195° converter work station and a separate three-position controller, independent of the loadlock controller, which is activated when selected by a selector valve on the hydraulic pump. The capability to manually rotate the ETG 360° is also provided.

Internal lighting of the chamber is achieved with three 300 watt incandescent lamps with individual rheostat control of their intensity. These lamps are recessed in the top dome of the chamber and are located at approximately 15°, 120°, and 240° orientations.

The internal environment requirements of the ETGs are such that all operations must be performed in a vacuum or argon environment. Evacuation operations are accomplished utilizing a combination of mechanical roughing, TMP, and a closed cycle helium cryogenic system, which are described below. While in an argon environment, the GMS (described below) maintains a slight positive pressure (approximately +1 inch water) to ensure minimum backstreaming of air. Gas purification is accomplished and maintained by circulation through a scrubbing system that removes oxygen, nitrogen, and water vapor. The LAS is equipped with a pressure relief valve (set at 2 psi) to prevent over-pressurization due to mechanical malfunction.

10.3.1 The Pumping Subsystems

Evacuation and vacuum operations are performed by three (3) pumping subsystems which are described as follows.

Roughing Pump: The Stokes Model 1730 mechanical roughing pump is a two stage system consisting of a 150 CFM piston pump that operates from atmospheric pressure to 30 torr at which point an internal pressure switch automatically turns on the 516 CFM blower which has the pumping capacity to bring the LAS to approximately 10 microns. A 6 inch liquid nitrogen coldtrap with automatic level control completes the system.

Turbo-Molecular Pumping System: The system consists of a 1500 L/Sec TMP (TMH 1600) backed by a 13 CFM (DUO-016B) two stage rotary vane pump. Both pumps operate simultaneously from atmospheric pressure, but not independently. This pumping system was purchased for the Cassini Program.

Cryogenic Pump: A Cryogenics Technology Model 1020-10-16 cryo pump is a cryogenic array within a shroud bolted to a 16 inch gate valve. The array is cooled by a refrigeration unit on the external end plate. The refrigerator is fed compressed helium from the compressor which rests on the floor in close proximity to the LAS. The cryo pump operates by condensing and freezing the gases at the temperature of the helium refrigerant. This temperature is approximately 15K (-430°F) to 26K (-413°F) which is sufficient to remove all gases except helium, neon, and hydrogen. These gases, noncondensable by the cryo pump, are removed by the TMP. A helium compressor was purchased for the Cassini Program.

Isolation to all pumps is provided by air operated gate valves manufactured by NRC and are sized to accommodate the individual pump requirements.

10.3.2 Gas Management System (GMS)

This system was purchased for the Cassini Program. The GMS consists of a Vacuum Atmospheric gas purification system for argon gas. Because of the critical effect of gas purity and condition on the eventual ETG/RTG performance, impurity levels are continually monitored during processing operations. Visual and audible alarms are automatically activated prior to reaching any level of impurity that would adversely affect that performance. The GMS performs the following functions:

1. Scrubs the argon gas by removing oxygen, water vapor, and nitrogen.

2. Monitors impurity levels and activates alarms when preset levels are exceeded.

3. Controls chamber pressure to maintain a pressure of -5 to +5 inch water column within ± one inch.

4. Recirculates the gas within the LAS at 40 CFM.

10.3.3 The Control System

The control system for the LAS and its associated equipment described above are housed in two (2) racks. The following lists the controls, alarms, and instrumentation contained in these control racks.

1. Vacuum gages for all pumping and LAS systems

2. Vacuum valve controls

3. Vacuum pump controls

4. Vacuum interlock controls

5. Loss of vacuum alarms

6. Liquid nitrogen coldtrap controls

7. Cooling water operating indicators

8. Cooling water alarms

9. LAS illumination controls

10. Gas purification alarms

A typical ETG processing flow is shown in Figure 10-2.

Following completion of the Cassini Program, the LAS was removed from Building 800 and relocated to Building 100 of the Valley Forge complex. It is planned to reestablish the LAS to working order for processing units in support of the ARPS program.
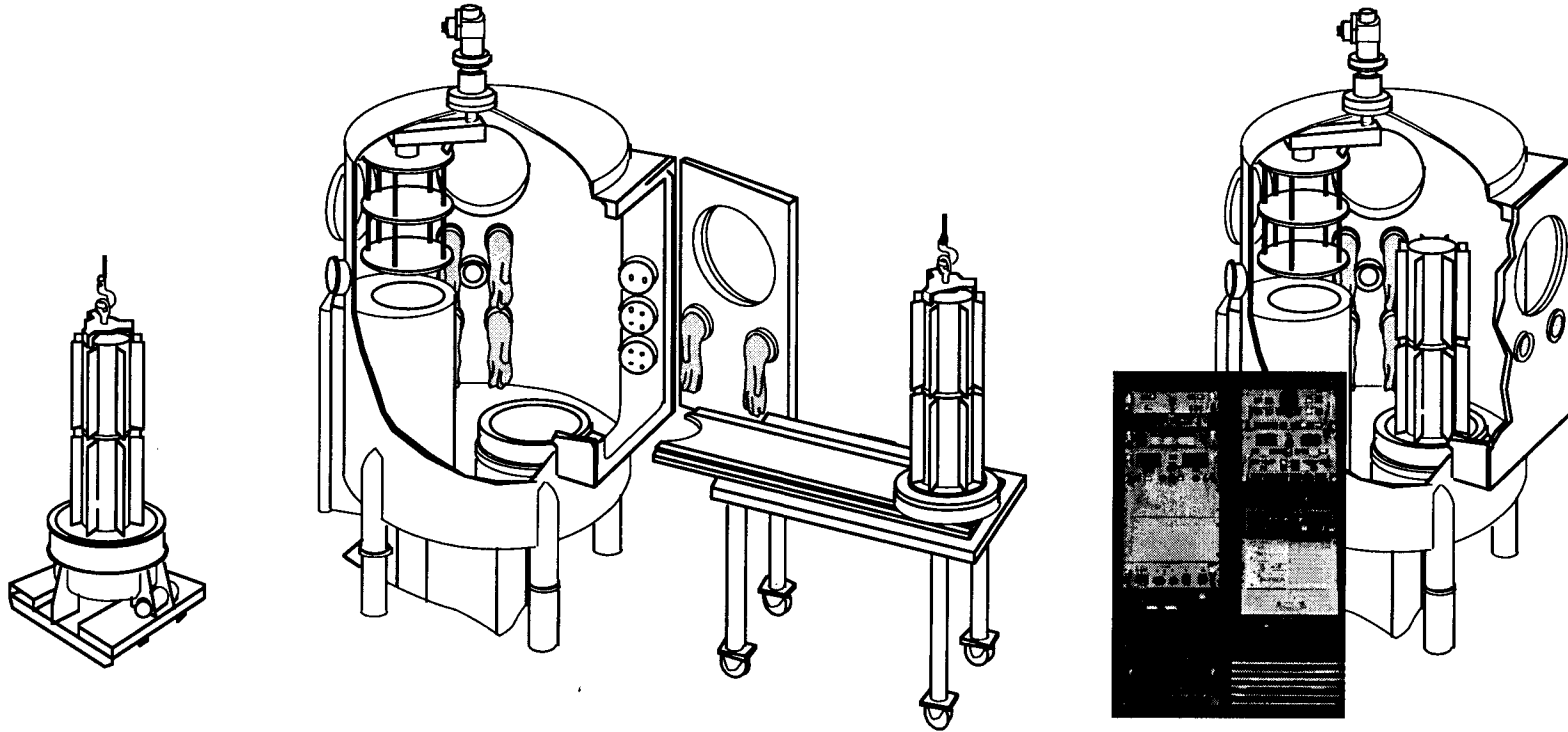
- REMOVE ETG FROM
  CONVERTER SHIPPING
  CONTAINER

- PLACE ETG ON SLIDETRAY CART

- POSITION SLIDETRAY CART AT 195° STATION

- SLIDE ETG INTO LAS AT CONVERTER STATION

- MAKE ELECTRICAL AND PNEUMATIC CONNECTIONS

- SECURE DOOR

- EVACUATE CHAMBER

- APPLY POWER FROM ROC TO PERFORM
  PROCESSING

- BACKFILL LAS AND REDOME ETG

- RUN PERFORMANCE TEST

- PERFORM PRESSURE DECAY TEST

- REMOVE FROM LAS AND RETURN ETG
  TO SHIPPING CONTAINER

VF97-0779

Figure 10-2. Typical ETG Processing Flow

Section 11

Thermoelectric Module Testing

SECTION 11
THERMOELECTRIC MODULE TESTING

11.1 EIGHTEEN COUPLE MODULES

11.1.1 Test Data/Results

Three modules were built and tested under the Cassini program. The modules were identical in design to those tested in the GPHS RTG program. Module instrumentation is shown in Figure 11.1-1. Couples 4, 5, 6 and 13, 14, 15 have hot shoe and cold strap thermocouples. (In this section, unicouples are referred to as "couples.") The latter are also used as voltage taps so that the electrical performance of these individual couples can be monitored during testing. Thermocouples are located at the end of each row to allow for monitoring of individual row (three couples) electrical performance.
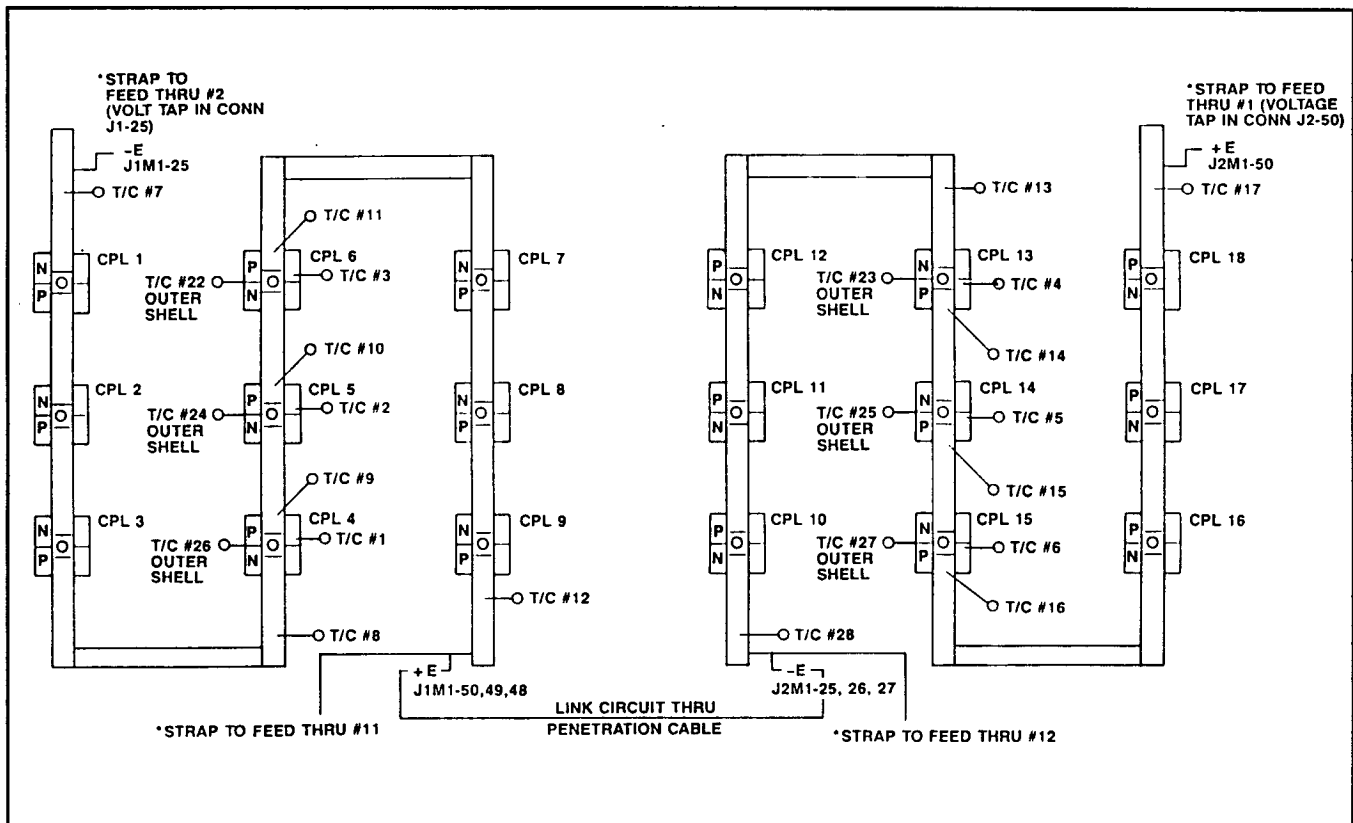
Figure 11.1-1. Eighteen Couple Module Instrumentation

The purpose of the module tests is twofold. First, an assessment of the thermoelectric performance is made at the normal hot shoe temperature of 1035°C comparing power output, internal resistance, and open circuit voltage with previously tested GPHS program

18 couple modules. Second, the effectiveness of the Si_3N_4 coating is evaluated from the trend of isolation resistance (foil to thermoelectric circuit) at an accelerated temperature of 1135°C for two of the modules and at normal temperature for the third module. A sharp decrease in the isolation resistance (indication of Si_3N_4 failure) is not expected until after 2000 hours at 1135°C, equating to 40,000 hours at normal operating temperatures (1035°C).

Table 11.1-1 summarizes the source of the couples, the test temperatures and total test hours.

Table 11.1-1. Test Temperatures and Life Test Hours

Module	Unicouple Source	Test Temperature Hot Shoe	Status as of 28 September 1997
18-10	Early Qualification Lot	1135°C	10,400 Hours Performance Normal Test Terminated October 1994
18-11	Full Qualification Lot	1135°C	30,709 Hours Performance Normal Test Terminated September 1997
18-12	Early Flight Production Lot	1035°C	26,817 Hours Performance Normal Test Terminated September 1997

Module 18-10

This module contained couples from the early qualification lot. Table 11.1-2 lists the serial number and location of each couple. Also shown is the room temperature resistance at each stage of assembly and the Si_3N_4 coating weight gain during the coating process.

Module 18-10 was brought up to operating temperature over a three week period in July 1993. It reached 1035°C on 29 July 1993. The heat-up rate was scheduled to closely match that of the GPHS program module 18-7 (operated at 1035°C). This was done to ensure a meaningful comparison of initial power output and internal resistance with previous GPHS 18 couple modules. Matching the heat-up rate produces similar dopant precipitation effects in the SiGe components of each unicouple, which affects power

Table 11.1-2. Module 18-10 Couple Room Temperature Resistance (Milliohm) and Coating Weight

Loc. Serial No.	2nd Bond	Pre-assembly	Unicouple	Wrapped	Avg of 4	Preplug	Inserted	Riveted	Coating Run	Wt. Gain, mg
1. HO148	22.90	22.60	22.80	22.80	22.78	22.70	22.80	22.80	7	7.57
2. HO149	22.90	22.70	22.80	22.80	22.80	22.70	22.80	22.80	7	7.56
3. HO150	22.80	22.50	22.60	22.70	22.65	22.60	22.65	22.60	7	7.49
4. HO250	23.20	22.80	23.00	23.10	23.03	23.20	23.05	23.05	13	7.14
5. HO256	23.10	22.70	22.90	23.00	22.93	23.10	22.95	22.95	13	7.18
6. HO172	22.80	22.80	22.80	23.20	22.90	23.50	23.35	23.20	10	7.86
7. HO044	23.00	22.30	22.40	22.40	22.53	22.30	22.40	22.35	5	7.43
8. HO145	22.50	22.20	22.40	22.30	22.35	22.30	22.35	22.30	7	7.57
9. HO113	22.50	22.30	22.50	22.50	22.40	22.40	22.45	22.40	9	7.78
10. HO103	22.60	22.40	22.60	22.60	22.55	22.50	22.55	22.50	9	7.71
11. HO184	22.80	22.40	22.40	22.75	22.59	23.00	22.85	22.70	10	7.95
12. HO146	22.70	22.40	22.60	22.60	22.58	22.50	22.60	22.58	7	7.67
13. HO125	22.30	22.00	22.30	22.20	22.20	22.40	22.25	22.20	9	7.93
14. HO290	23.10	22.20	22.60	22.60	22.62	22.90	22.65	22.70	14	8.18
15. HO201	22.50	22.10	22.30	22.30	22.30	22.50	22.30	22.35	8	7.72
16. HO176	22.60	22.10	22.60	22.50	22.45	22.60	22.50	22.50	10	7.89
17. HO129	22.50	22.20	22.50	22.50	22.43	22.40	22.45	22.45	9	8.02
18. HO215	22.60	22.00	22.40	22.50	22.38	22.30	22.40	22.40	14	8.02

Resistance in milliohms

Statistics

	2nd Bond	Pre-assembly	Unicouple	Wrapped	Avg of 4	Preplug	Inserted	Riveted	Wt. Gain, mg
Mean	22.74	22.37	22.58	22.63	22.58	22.66	22.63	22.60	7.70
Std. Dev.	0.25	0.26	0.21	0.28	0.23	0.35	0.29	0.27	0.28
Std. Err.	0.06	0.06	0.05	0.06	0.05	0.08	0.07	0.06	0.07
95% Conf.	0.13	0.13	0.10	0.14	0.11	0.17	0.14	0.14	0.14
99% Conf.	0.17	0.18	0.14	0.19	0.16	0.24	0.20	0.19	0.19
Size	18.00	18.00	18.00	18.00	18.00	18.00	18.00	18.00	18.00
Sum	409.40	402.70	406.50	407.35	406.44	407.90	407.35	406.83	138.67
Max.	23.20	22.80	23.00	23.20	23.03	23.50	23.35	23.20	8.18
Min.	22.30	22.00	22.30	22.20	22.20	22.30	22.25	22.20	7.14
Missing	0.00	0.00	0.00	0.00	0.00	0.00	0.00	0.00	0.00

Table 11.1-3. Comparison of Initial Performance of Modules 18-10 and 18-7

	Module 18-7	Module 18-10
Heat Input, Watts	162	162.6
Hot Shoe, °C Average	1035.6	1033.4
Hot Shoe Range, °C	12	7.5
Cold Strap, °C Average (8 T/Cs)	293.9	285.4
Cold Strap Range, °C (8 T/Cs)	9.7	9.0
Cold Strap Average, °C (12 T/Cs)	290.0	280.8
Cold Strap Range, °C (12 T/Cs)	21.3	19.8
Load Voltage, Volts	3.504	3.501
Link Voltage, Volts	0.164	0.163
Current, Amps	2.520	2.596
Open Circuit Voltage, Volts	6.353	6.355
Normalized Open Circuits, Volts (8T/Cs)	6.293	6.239
Normalized Open Circuits, Volts (12 T/Cs)	6.258	6.199
Average Couple Seebeck Coefficient, Volts/K (12)	499×10^{-6}	495×10^{-6}
Internal Resistance, Ohms	1.065	1.041
Internal Resistance Per Couple, Ohms (Avg.)	0.0592	0.0578
Power Measured, Watts (Load + Link)	9.246	9.485
Power Normalized, Watts (8 T/Cs)	9.072	9.142
Power Normalized, Watts (12 T/Cs)	8.970	9.027
Isolation		
Circuit to Foil, Volts	-1.55	-1.86
Circuit to Foil, Ohms	9.2K	18K

degradation rates. A comparison of the initial performance of modules 18-10 and 18-7 is given in Table 11.1-3. Comparison of the initial normalized power output and internal resistance with the average initial values of the GPHS 18 couple modules is given in Table 11.1-4. Module 18-10 performance was in excellent agreement with both 18-7 and with the average GPHS 18 couple module performance. A tabulation of the six individual row internal resistances is also shown in Table 11.1-4. All row internal resistances fell within a

Table 11.1-4. Comparison of the Initial Normalized Power Output and Internal Resistance with the Average Initial Values of the GPHS Modules

1. Test Chronology
   - Processing Started: 9 July 1993
   - Reached 1035°C: 29 July 1993
   - 2,000 Hour Milestone Reached: 26 October 1993

2. 1035°C Operation

	18-10 (t = 0)	18-10 (t = 22 Hours)	GPHS 18 Couple Modules (t = 24 Hours)
Load Voltage	3.65V	3.65V	3.65V
Normalized Power (1035°C/300°C)	9.03 W	9.06 W	9.06 W (Average) / Range 8.84 to 9.29 W / σ 0.18 W
Internal Resistance	57.8 m Ω	58.4 m Ω	58.9 m Ω (Average) / Range 57.2 to 61.0 m Ω

Individual Rows (18-10) (t = 0)

Resistance - ohms	Open Circuit Voltage - volts
1. 0.174	1.064
2. 0.175	1.059
3. 0.173	1.060
4. 0.174	1.063
5. 0.173	1.057
6. 0.173	1.062

Isolation Resistance
Module Circuit to Foil   18 k Ω   Average 12 K Ω   Range 8 K to 56 K

2% band and open circuit voltages fell within a 0.5% band. In Table 11.1-3, two values of normalized power are shown: a normalization using all 12 cold strap thermocouples and one using the 8 cold straps closest to the hot shoe instrumentation (see Figure 11.1-1). The 8 thermocouple normalization gives a more accurate average power per couple. The 12 thermocouple normalization has been calculated because much of the previously published 18 couple module data was reported on this basis. The normalization is to a 700°C ΔT (1000°C/300°C) from hot to cold junction. A 1035°C hot shoe corresponds to 1000°C hot junction. An isolation current-voltage characteristic test between the thermoelectric circuit and foil was performed. Results are plotted in Figure 11.1-2. The I-V characteristic shows the usual non-ohmic signature of the quartz yarn leg wrap. The module was held at 1035°C for approximately 100 hours and then taken up to the life test temperature of 1135°C.
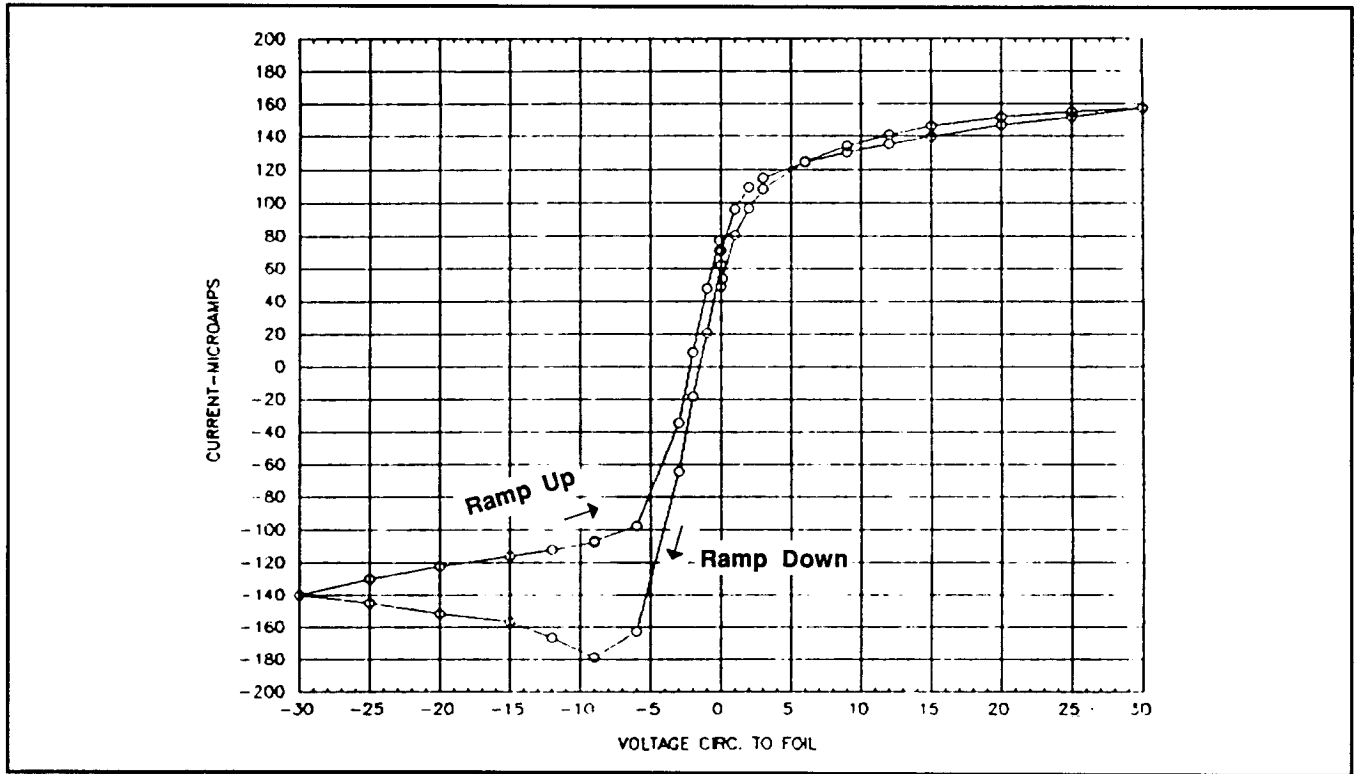
Figure 11.1-2. Circuit to Foil Isolation Characteristic at 1035°C (Module 18-10)

The module was run at the accelerated test condition for 10,400 hours. A constant heat input was maintained throughout the test. All performance parameters were normal during the life testing and the module was shut down in October 1994 to make the vacuum chamber available for testing of another module. Initial and final test data are summarized in Figure 11-1-3 and Table 11.1-5 shows the internal resistance ratio trend for the module compared to module 18-8 which was tested during the GPHS program. The ratio is the resistance at any time divided by the initial value. Figure 11.1-4 shows the power factor ratio in comparison to module 18-8. The power factor is the open circuit voltage squared divided by the internal resistance. Agreement between the GPHS and Cassini modules was excellent and provided a high degree of confidence that the GPHS unicouple manufacturing processes were successfully replicated. The performance trends of the six individual rows and the six individual couples were monitored throughout the test. Table 11.1-6 gives the initial and final internal resistance values and shows that the changes were very uniform and fell within a narrow band.
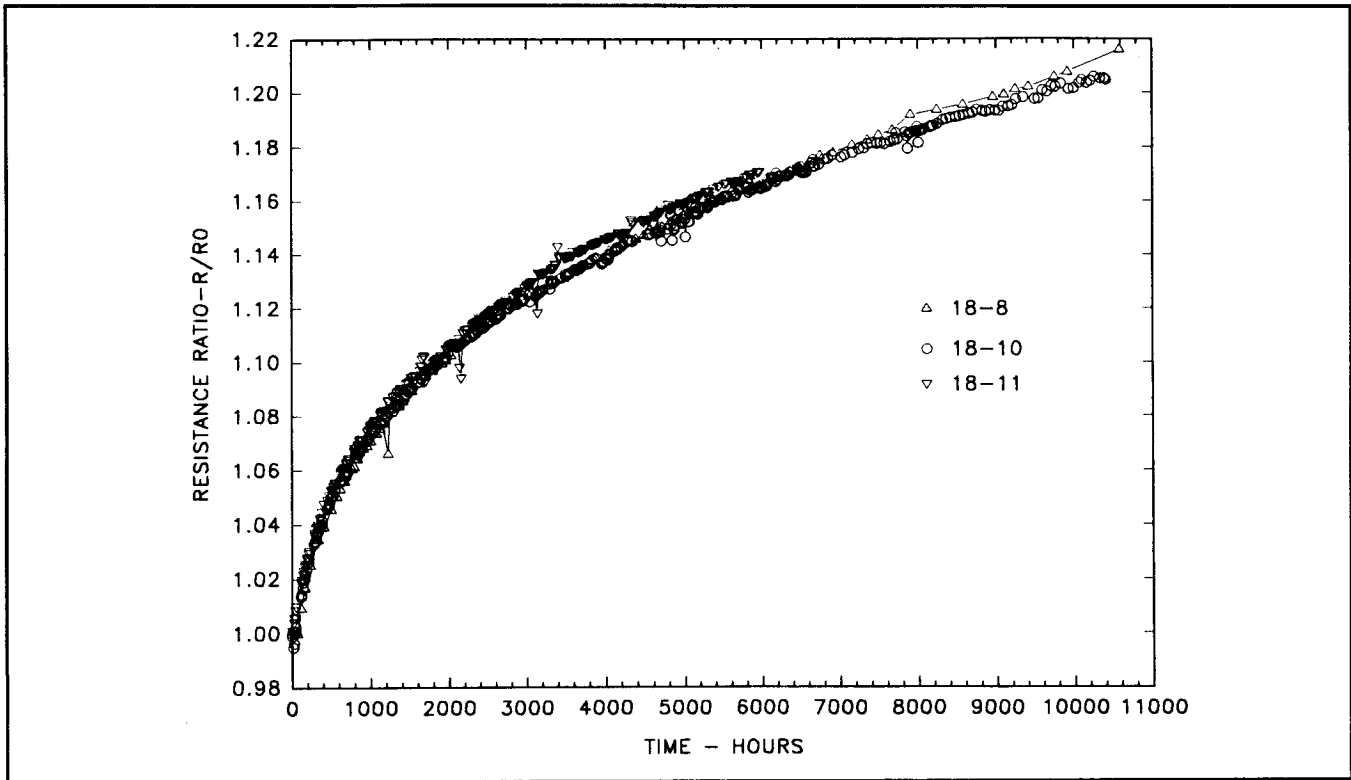
Figure 11.1-3. 18 Couple Module Internal Resistance Ratio Vs. Time (1135°C Operation)
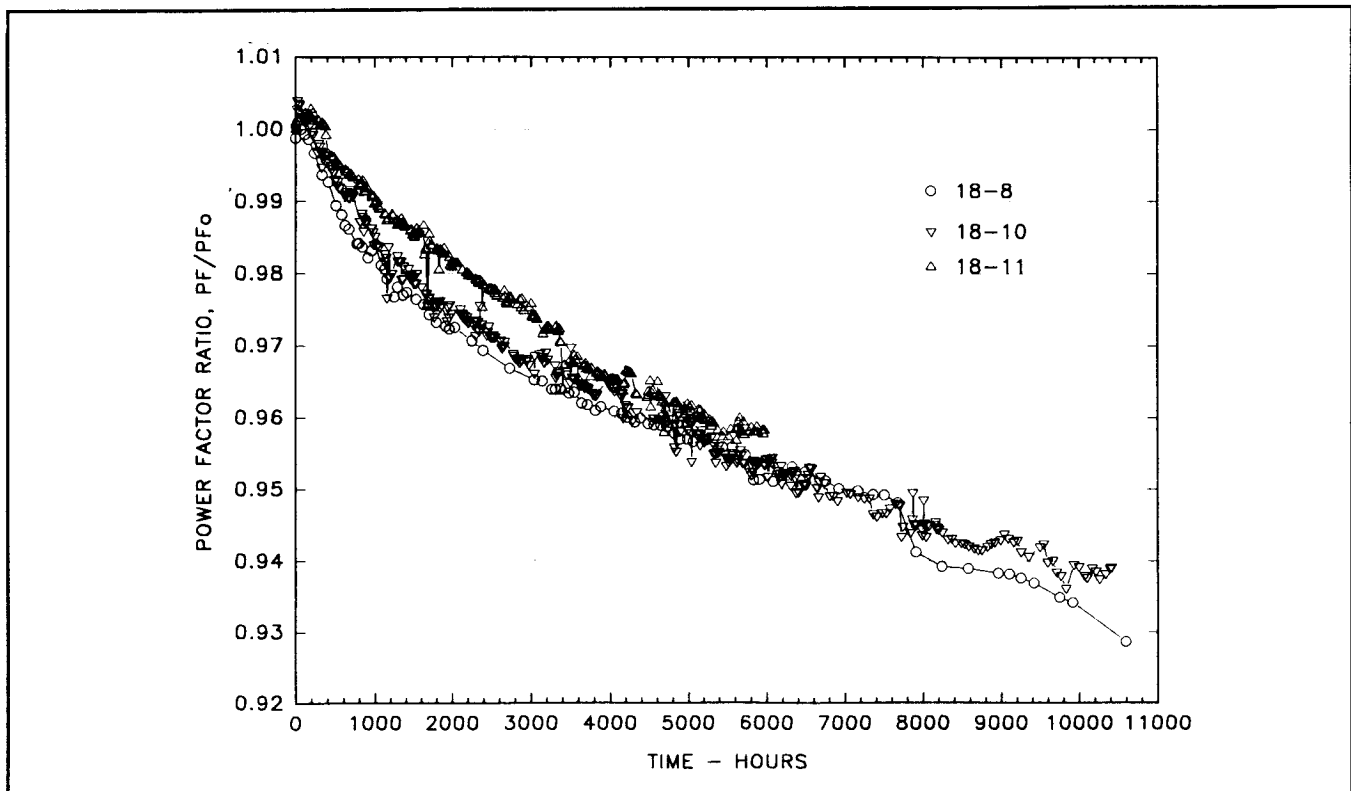
Figure 11.1-4. 18 Couple Module Power Factor Ratio Vs. Time (1135°C Operation)

Table 11.1-5. Comparison of Initial and 10,400 Hour Performance of Module 18-10 at 1135°C

	Initial 8/4/93	t = 14,400 Hours 10/19/94
Heat Input, Watts	191	191.2
Hot Shoe, °C Average	1136.2	1118.9
Hot Shoe Range, °C	3.9	7.7
Cold Strap, °C Average (8 T/Cs)	309.5	306.5
Cold Strap Range, °C (8 T/Cs)	10.8	14.0
Cold Strap Average, °C (12 T/Cs)	304.6	301.1
Cold Strap Range, °C (12 T/Cs)	22.3	22.6
Load Voltage, Volts	3.501	3.506
Link Voltage, Volts	0.189	0.172
Current, Amps	3.168	2.884
Open Circuit Voltage, Volts	7.151	7.477
Normalized Open Circuits, Volts (8T/Cs)	6.324	6.732
Normalized Open Circuits, Volts (12 T/Cs)	6.284	6.686
Average Couple Seebeck Coefficient, Volts/K (12)	499×10^{-6}	530.6×10^{-6}
Internal Resistance, Ohms	1.093	1.317
Internal Resistance Per Couple, Ohms (Avg.)	0.0607	0.0732
Power Measured, Watts (Load + Link)	11.691	10.61
Power Normalized, Watts (8 T/Cs)	9.143	8.60
Power Normalized, Watts (12 T/Cs)	9.028	8.48
Power Factor	40.987×10^{-5}	38.48×10^{-5}
Isolation		
Circuit to Foil, Volts	-1.676	-1.071
Circuit to Foil, Ohms	5.22K	1.14K

Table 11.1-6. Module 18-10 Internal Resistance Changes

Position	Serial #	2nd Bond Milliohm	Preassy Milliohm	ΔRi Milliohm	T = O Milliohm	T=1,500 Hours	ΔRi Milliohm	Percent Increase	T=10391 Hours	ΔRi Milliohm	Percent Increase
1	H0148	22.90	22.60	-0.30							
2	H0149	22.90	22.70	-0.20							
3	H0150	22.80	22.50	-0.30							
					183.00	198.70	15.70	8.60	220.4	37.4	20.4
4	H0250	23.20	22.80	-0.40	61.60	66.80	5.20	8.40	73.9	12.3	20.0
5	H0256	23.10	22.70	-0.40	61.60	67.00	5.40	8.80	74.0	12.4	20.1
6	H0172	22.80	22.80	0.00	61.20	66.90	5.70	9.30	73.9	12.7	20.8
					184.00	200.00	16.00	8.70	221.1	37.1	20.2
7	H0044	23.00	22.30	-0.70							
8	H0145	22.50	22.20	-0.30							
9	H0113	22.50	22.30	-0.20							
					181.00	197.60	16.60	9.20	218.6	37.6	20.8
10	H0103	22.60	22.40	-0.20							
11	H0184	22.80	22.40	-0.40							
12	H0146	22.70	22.40	-0.30							
					183.00	198.60	15.60	8.50	219.6	36.6	20.0
13	H0125	22.30	22.00	-0.30	60.00	65.80	5.80	9.70	72.9	12.9	21.5
14	H0290	23.10	22.20	-0.90	61.20	66.80	5.60	9.20	73.9	12.7	20.8
15	H0201	22.50	22.10	-0.40	60.90	66.70	5.80	9.50	73.8	12.9	21.2
					182.00	198.70	16.70	9.20	219.9	37.9	20.8
16	H0176	22.60	22.10	-0.50							
17	H0129	22.50	22.20	-0.30							
18	H0215	22.60	22.00	-0.60							
					182.00	198.60	16.60	9.10	219.7	37.7	20.7

The isolation resistance trend between the thermoelectric circuit and the foil is shown in Figure 11.1-5 with modules from the MHW and GPHS programs. At the accelerated temperature of 1135°C, the same amount of sublimation occurs in about 1,650 hours as would occur in a 16 year Cassini mission. This takes into account the decrease in hot junction temperature during the mission. Consequently, during the module life test about six times as much sublimation has occurred as will occur during the Cassini mission. The module isolation resistance trend fell within the GPHS data base and, therefore, confirmed the adequacy of the silicon nitride coating on the early qualification couples.

Module 18-11

Assembly of module 18-11 was completed in December 1993. This module contained unicouples selected from the qualification lot of unicouples, built prior to the E-6 converter production lot. Table 11.1-7 lists, for each couple, the location, serial number, room temperature resistances during assembly and the Si_3N_4 coating weight gain.
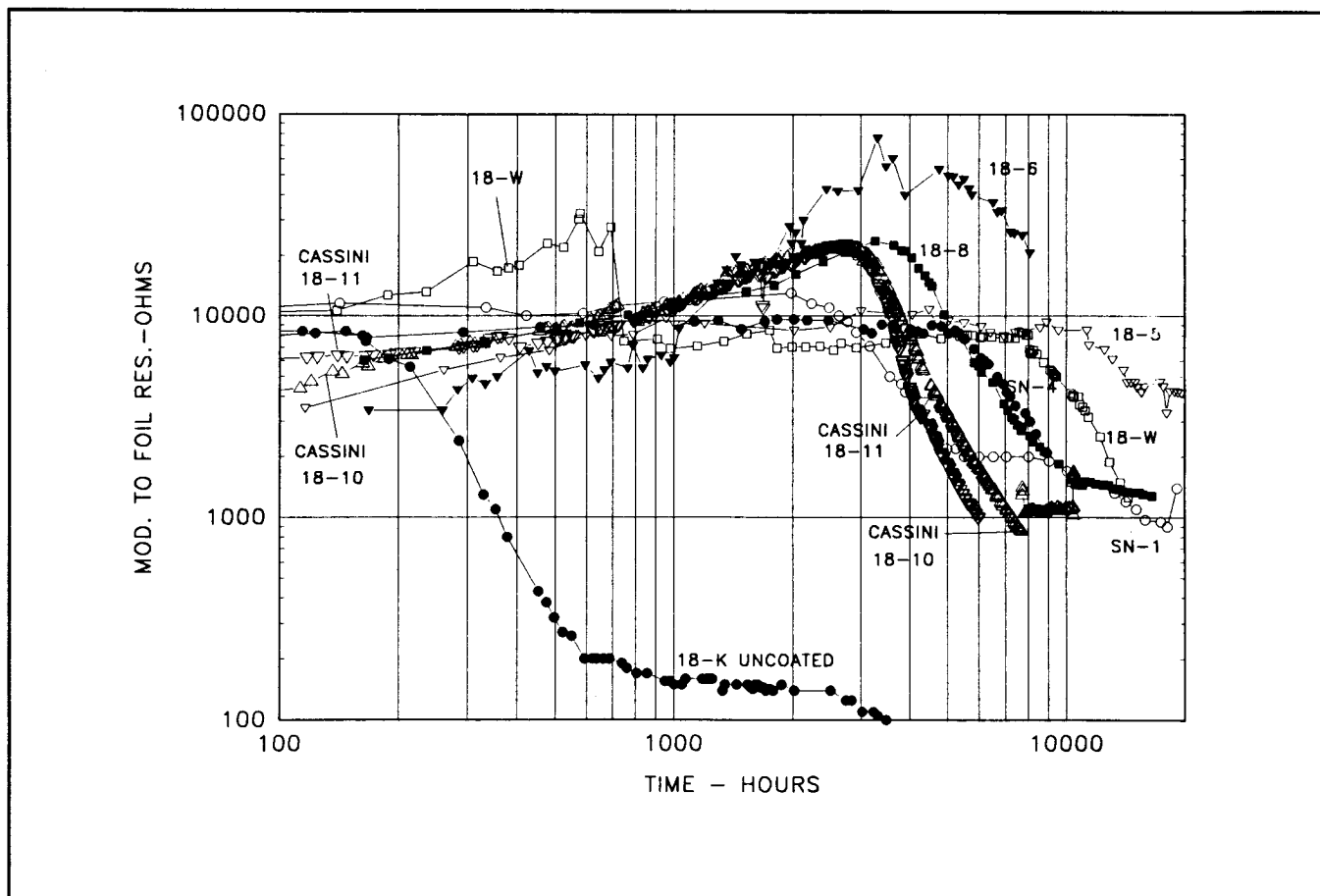
**Figure 11.1-5. Isolation Resistance - Module Circuit to Foil
(18-11, 18-10, GPHS 18-8 and MHW Modules) - 1135°C Operation**

The module was brought up to temperature in the same manner as previously described for 18-10. Data were taken at 1035°C for comparison with GPHS module 18-7 and module 18-10 as shown in Table 11.1-8. The performance parameters for all three modules fell within a very narrow band. The module was tested at 1035°C for 140 hours and then taken up to the 1135°C accelerated test condition for life testing. Life testing with constant heat input was carried out for 30,709 hours until the module was shut down in September 1997. Internal resistance and power factor trends are shown in Figures 11.1-6 and 11.1-7, respectively. Performance was in good agreement with GPHS module 18-8 and module 18-10. Initial and final performance is given in Table 11.1-9.

Table 11.1-7. Internal Resistance and Si₃N₄ Coating Weight of Couples Selected for Module 18-11

Position	Serial #	2nd Bond Milliohm	Preassembly Milliohm	Unicouple Milliohm	Wrapped Milliohm	Avg. of 4 Milliohm	Weight Gain Milligrams	Coat Run No.
1	H2006	22.50	22.10	22.30	22.60	22.38	7.17	104
2	H0507	22.40	21.90	22.40	22.30	22.25	7.24	21
3	H0512	22.70	22.20	22.70	22.60	22.55	7.28	21
4	H0439	23.20	22.70	22.40	22.20	22.38	7.65	31
5	H0587	22.50	22.40	22.70	22.70	22.58	7.41	24
6	H0657	22.70	22.50	22.60	22.80	22.65	7.49	32
7	H0585	22.90	22.70	22.60	22.70	22.68	7.48	24
8	H0459	22.50	22.10	22.50	22.70	22.45	7.53	27
9	H0562	22.70	22.30	22.60	23.00	22.65	7.57	23
10	H0248	22.70	22.30	22.80	22.70	22.63	7.78	15
11	H0163	22.90	22.40	23.00	22.90	22.80	7.96	8
12	H0282	22.70	22.40	22.70	22.40	22.55	8.07	14
13	H0328	22.90	22.30	22.90	22.80	22.73	7.48	18
14	H0326	22.60	22.00	22.60	22.70	22.48	7.57	18
15	H0232	22.60	22.00	22.60	22.30	22.38	7.82	17
16	H0590	22.60	22.40	22.60	22.70	22.58	7.73	24
17	H0393	22.60	22.10	22.40	22.70	22.45	7.71	102
18	H0496	22.50	22.30	22.50	22.70	22.55	7.67	22

Statistics

		2nd Bond Milliohm	Preassembly Milliohm	Unicouple Milliohm	Wrapped Milliohm	Avg. of 4 Milliohm	Weight Gain Milligrams	
Mean		22.68	22.28	22.61	22.64	22.54	7.59	
Std. Dev.		0.20	0.23	0.18	0.21	0.14	0.24	
Std. Err.		0.05	0.05	0.04	0.05	0.03	0.06	
95% Conf.		0.10	0.11	0.09	0.11	0.07	0.12	
99% Conf.		0.13	0.15	0.12	0.14	0.10	0.16	
Sum		408.20	401.10	406.90	407.50	405.68	136.61	
Max.		23.20	22.70	23.00	23.00	22.80	8.07	
Min.		22.40	21.90	22.30	22.20	22.25	7.17	

Table 11.1-8. Comparison of Initial Performance at 1035°C of Modules 18-7, 18-10, and 18-11

	Module 18-7	Module 18-10	Module 18-11
Heat Input, Watts	162	162.6	163.4
Hot Shoe, °C Average	1035.6	1033.4	1034.6
Hot Shoe Range, °C	12	7.5	5.7
Cold Strap, °C Average (8 T/Cs)	293.9	285.4	291.5
Cold Strap Range, °C (8 T/Cs)	9.7	9.0	1.6
Cold Strap Average, °C (12 T/Cs)	290.0	280.8	286.9
Cold Strap Range, °C (12 T/Cs)	21.3	19.8	19.1
Load Voltage, Volts	3.504	3.501	2.504
Link Voltage, Volts	0.164	0.163	0.096
Current, Amps	2.520	2.596	2.586
Open Circuit Voltage, Volts	6.353	6.355	6.381
Normalized Open Circuits, Volts (8T/Cs)	6.293	6.239	6.308
Normalized Open Circuits, Volts (12 T/Cs)	6.258	6.199	6.297
Average Couple Seebeck Coefficient, Volts/K (12)	499×10^{-6}	495×10^{-6}	497×10^{-6}
Internal Resistance, Ohms	1.065	1.041	1.075
Internal Resistance Per Couple, Ohms (Avg.)	0.0592	0.0578	0.0597
Power Measured, Watts (Load + Link)	9.246	9.485	9.311
Power Normalized, Watts (8 T/Cs)	9.072	9.142	9.099
Power Normalized, Watts (12 T/Cs)	8.970	9.027	8.981
Power Factor	41.67×10^{-5}	41.88×10^{-5}	41.42×10^{-5}
Isolation			
Circuit to Foil, Volts	-1.55	-1.86	-1.66
Circuit to Foil, Ohms	9.2K	18K	24.5K
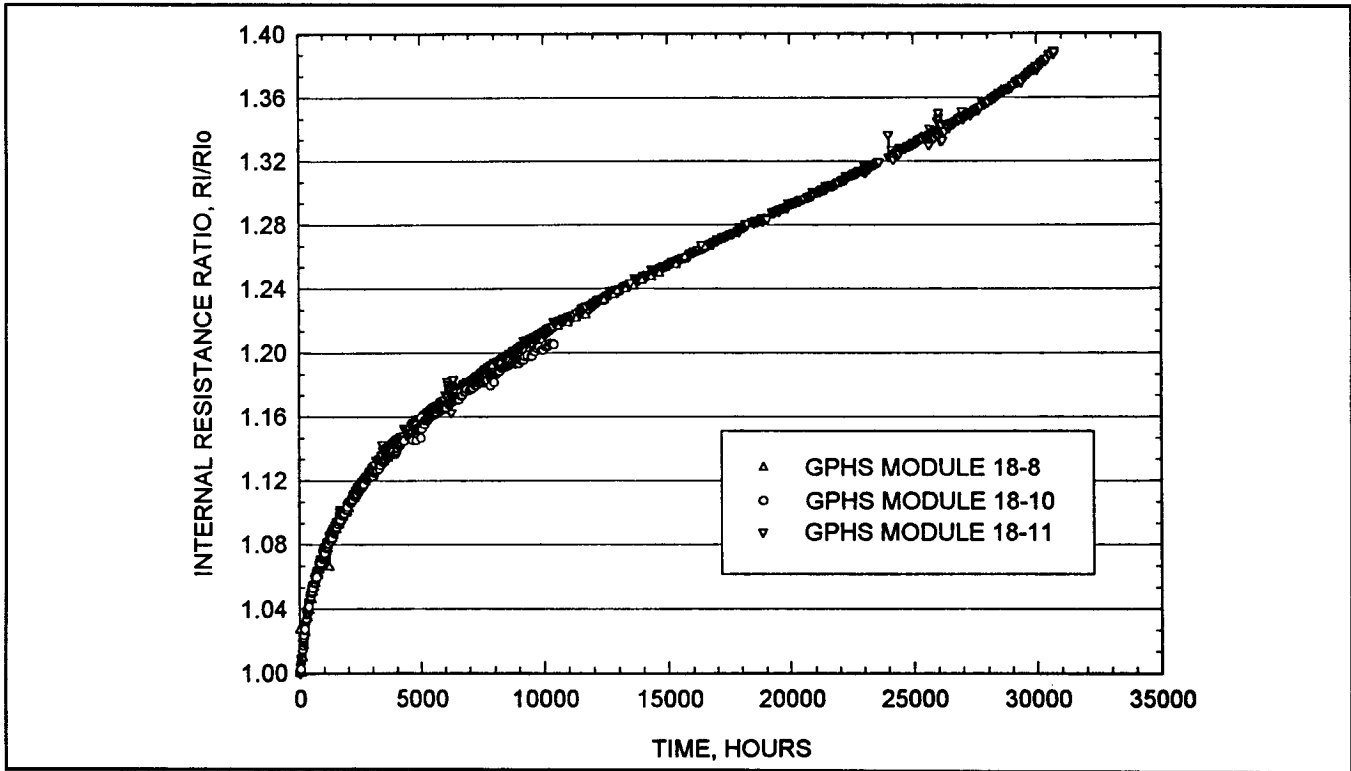
**Figure 11.1-6. Internal Resistance Ratio Vs. Time
(Modules 18-10, 18-11, GPHS Module 18-8) - 1135°C Operation**
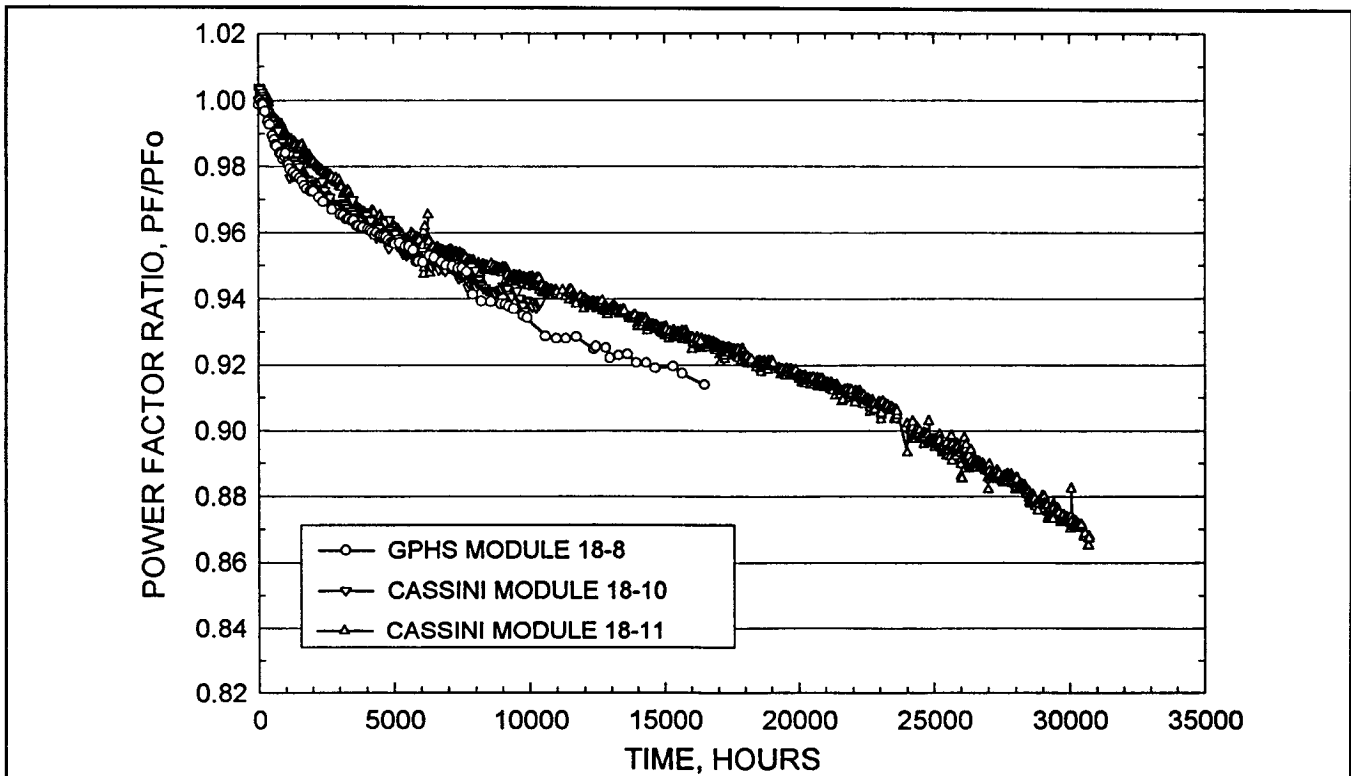
**Figure 11.1-7. Power Factor Ratio Vs. Time
(18-10, 18-11, GPHS Module 18-8) - 1135°C Operation**

Table 11.1-9. Comparison of Initial and 30,709 Hour Performance of Module 18-11 at 1135°C

	Initial 2/2/94	t = 52 Hours V_L = 3.5V 2/4/94	t = 30,709 Hours 9/10/97
Heat Input, Watts	190	192.9	193.2
Hot Shoe, °C Average	1137.8	1137.5	1106.0
Hot Shoe Range, °C	5.4	5.2	10.7
Cold Strap, °C Average (8 T/Cs)	311.9	314.3	303.6
Cold Strap Range, °C (8 T/Cs)	2.6	2.5	2.1
Cold Strap Average, °C (12 T/Cs)	306.5	308.9	298.7
Cold Strap Range, °C (12 T/Cs)	20.1	20.3	18.0
Load Voltage, Volts	3.895	3.499	3.49
Link Voltage, Volts	0.108	0.121	0.092
Current, Amps	2.842	3.174	2.619
Open Circuit Voltage, Volts	7.140	7.160	7.599
Normalized Open Circuits, Volts (8T/Cs)	6.319	6.359	6.941
Normalized Open Circuits, Volts (12 T/Cs)	6.276	6.316	6.888
Avg. Couple Seebeck Coefficient, Volts/K (12)	498 X 10^{-6}	501 X 10^{-6}	546.7 X 10^{-6}
Internal Resistance, Ohms	1.104	1.115	1.533
Internal Resistance Per Couple, Ohms (Avg.)	0.0613	0.0620	0.0852
Power Measured, Watts (Load + Link)	11.375	11.492	9.39
Power Normalized, Watts (8 T/Cs)	8.909	9.065	7.81
Power Normalized, Watts (12 T/Cs)	8.789	8.942	7.71
Power Factor	40.452 X 10^{-5}	40.557 X 10^{-5}	35.1 X 10^{-5}
Isolation			
Circuit to Foil, Volts	-1.68	-1.36	-1.71
Circuit to Foil, Ohms	6.29K	5.95K	0.318K

Module 18-11 accumulated the longest test time at accelerated temperatures of any SiGe module ever tested. Significant sublimation at the hot junction became evident from an increase in the slope of the internal resistance and power factor. The slope change which developed in the last few thousand hours was expected as a normal consequence of a reduced cross sectional area at the hot junction region. A 100°C increase in temperature provides an acceleration factor of approximately 20. Consequently, the 30,000 hour accelerated test is equivalent to approximately 600,000 hours (68 years) at a nominal 1035°C design temperature. Table 11.1-10 shows the internal resistance changes of the rows and individual couples. It is seen that the range has widened considerably, with couple number 15 showing the largest increase.

Table 11.1-10. Module 18-11 Internal Resistance Changes

Position	Serial #	2nd Bond Milliohm	Preassy Milliohm	ΔRi Milliohm	T = 0 Milliohm	T=1,509 Hours	ΔRi Milliohm	Percent Increase	T=30,709 Hours	ΔRi Milliohm	Percent Increase
1	H2006	22.50	22.10	-0.40							
2	H0507	22.40	21.90	-0.50							
3	H0512	22.7	22.20	-0.50							
					182.30	199.70	17.40	9.54	252.60	70.30	38.56
4	H0439	23.20	22.70	-0.50	62.30	67.90	5.60	8.99	86.40	24.10	38.68
5	H0587	22.50	22.40	-0.10	61.00	66.50	5.50	9.02	82.20	21.20	34.75
6	H0657	22.70	22.50	-0.20	61.40	67.30	5.90	9.61	83.60	22.20	36.16
					184.10	201.10	17.00	9.23	251.40	67.30	36.56
7	H0585	22.90	22.50	-0.40							
8	H0459	22.50	22.10	-0.40							
9	H0562	22.70	22.30	-0.40							
					185.70	203.20	17.50	9.42	265.50	79.80	42.97
10	H0248	22.70	22.30	-0.40							
11	H0163	22.90	22.40	-0.50							
12	H0282	22.70	22.40	-0.30							
					184.90	201.70	16.80	9.09	253.70	68.80	37.21
13	H0428	23.10	22.70	-0.40	62.10	67.90	5.80	9.34	85.00	22.90	36.88
14	H0326	22.60	22.00	-0.60	62.20	68.30	6.10	9.81	87.30	25.10	40.35
15	H0232	22.60	22.00	-0.60	60.90	66.60	5.70	9.36	89.70	28.80	47.29
					184.70	202.30	17.60	9.53	261.30	76.60	41.47
16	H0590	22.60	22.40	-0.20							
17	H0393	22.60	22.10	-0.50							
18	H0496	22.50	22.30	-0.20							
					184.20	201.40	17.20	9.34	250.10	66.80	36.27

The isolation resistance trend between the thermoelectric circuit and the foil is shown in Figure 11.1-8 along with modules from the MHW and GPHS programs. The isolation resistance plateaued at about 1000 ohms between 6,000 and 7,000 hours. It then started a slow decrease to 324 ohms at the end of testing. A similar plateau and gradual decline were observed in MHW module SN-1. At the accelerated temperature of 1135°C the same
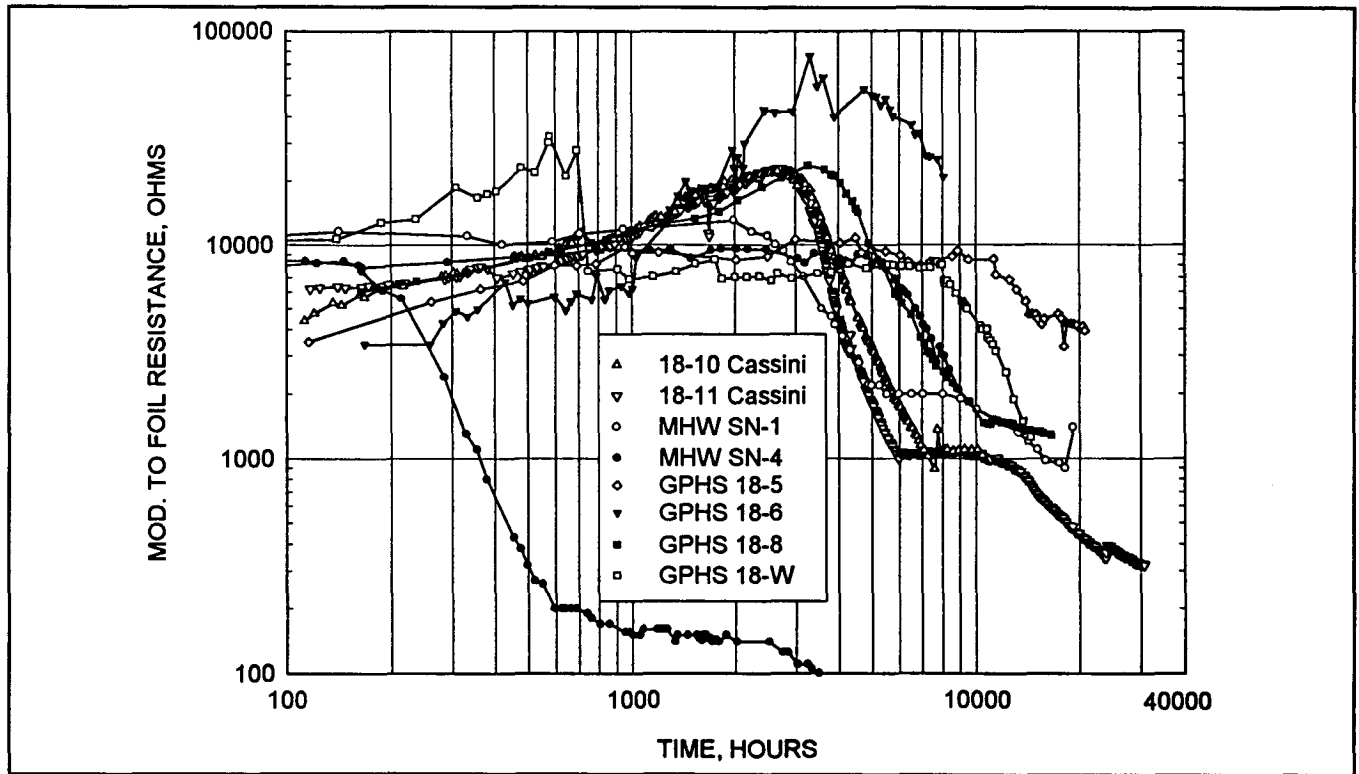
**Figure 11.1-8. Isolation Resistance - Module Circuit to Foil
(18-10, 18-11, GPHS Module 18-8) - 1135°C Operation**

amount of sublimation occurs in about 1,650 hours of testing as would occur in a 16-year Cassini mission, taking into account the drop in hot junction temperature throughout the mission.

Consequently, approximately 18.6 times as much sublimation had occurred during the test duration of module 18-11 as will occur during the Cassini mission. The module performance, therefore, confirmed the adequacy of the silicon nitride coating on the qualification unicouples.

Module 18-12

Assembly of module 18-12 was completed in May 1994 . The unicouples were selected from the flight production lots (from the balance of E-6 production units not used in the E-6 thermopile and the early E-7 production lot). Six couples were from the E-6 lot and 12 from the E-7 lot.

Table 11.1-11 lists for each couple the location, serial number, room temperature resistances during assembly and the Si_3N_4 coating weight gain.

Table 11.1-11. Module 18-12, Couple Room Temperature Resistance (Milliohm) and Coating Weight

Loc. Serial No.	2nd Bond	Pre-assembly	Unicouple	Wrapped	Avg of 4	Preplug	Inserted	Riveted	Coating Run	Wt. Gain, mg
1. 00H2594	23.80	22.90	23.40	23.30	23.35	23.40	23.36	23.35	135	7.46
2. 00H2634	22.70	22.60	22.80	22.90	22.75	22.90	22.82	22.83	139	7.50
3. 00H2606	23.50	22.40	22.90	22.80	22.90	22.84	22.82	22.81	137	7.50
4. 00H2168	22.20	21.70	22.20	22.00	22.03	22.36	22.41	22.41	111	8.07
5. 00H2151	22.40	21.90	22.00	22.30	22.15	22.37	22.35	22.34	112	7.72
6. 00H2256	22.20	21.70	22.40	22.30	22.15	22.25	22.26	22.26	114	8.36
7. 00H2597	24.40	23.20	23.90	23.80	23.83	23.80	23.79	23.78	135	7.71
8. 00H2680	22.60	23.00	23.10	23.20	22.98	23.20	23.11	23.11	141	8.01
9. 00H2658	22.70	23.00	22.90	23.00	22.90	23.03	23.03	23.04	140	7.72
10. 00H1506	23.50	23.20	23.00	23.70	23.35	23.63	23.59	23.59	81	7.58
11. 00H1392	23.80	23.00	23.30	23.80	23.48	23.65	23.60	23.60	74	7.77
12. 00H1606	23.60	22.60	22.90	23.40	23.13	23.12	23.09	23.08	85	8.29
13. 00H1344	23.60	23.50	23.90	23.60	23.65	23.73	23.76	23.76	71	8.28
14. 00H1618	23.30	24.00	23.10	23.10	23.38	23.08	23.13	23.13	85	7.86
15. 00H1262	23.70	23.30	23.90	23.80	23.68	24.03	24.05	24.06	67	7.81
16. 00H1580	23.00	23.70	22.60	23.00	23.08	22.73	22.76	22.76	86	7.77
17. 00H2127	22.80	22.10	23.40	22.80	22.78	22.78	22.77	22.77	63	7.97
18. 00H2113	22.90	22.20	23.50	22.80	22.85	22.86	22.82	22.80	111	8.26

Resistance in milliohms

Statistics

	2nd Bond	Pre-assembly	Unicouple	Wrapped	Avg of 4	Preplug	Inserted	Riveted	Wt. Gain, mg
Mean	23.1500	22.7778	23.0667	23.0889	23.0233	23.0978	23.0844	23.0822	7.8689
Std. Dev.	0.6261	0.6752	0.5562	0.5444	0.5284	0.5229	0.5189	0.5203	0.2897
Std. Err.	0.1476	0.1592	0.1311	0.1283	0.1245	0.1232	0.1223	0.1226	0.0683
95% Conf.	0.3114	0.3358	0.2766	0.2707	0.2628	0.2600	0.2581	0.2588	0.1441
99% Conf.	0.4278	0.4613	0.3800	0.3719	0.3610	0.3572	0.3545	0.3555	0.1979
Size	18.0000	18.0000	18.0000	18.0000	18.0000	18.0000	18.0000	18.0000	18.0000
Total	416.7000	410.0000	415.2000	415.6000	414.4200	415.7600	415.5200	415.4800	141.6400
Min.	22.2000	21.7000	22.0000	22.0000	22.0300	22.2500	22.2600	22.2600	7.4600
Max.	24.4000	24.000	23.9000	23.8000	23.8300	24.0300	24.0500	24.0600	8.3600
Min. Pos.	22.2000	21.7000	22.0000	22.0000	22.0300	22.2500	22.2600	22.2600	7.4600

The module was brought up to temperature in the same manner as previously described for 18-10. Data were taken at 1035°C for comparison with GPHS module 18-7 and Cassini modules 18-10 and 18-11 as shown in Table 11.1-12. The performance parameters for all four modules fell within a very narrow band. The module was life tested at a constant heat input with an initial average hot shoe temperature of 1035°C. Life testing continued for 26,817 hours until it was shut down in September 1997. Internal resistance and power factor trends are shown in Figures 11.1-9 and 11.1-10, respectively. Performance was in good agreement with GPHS module 18-8 and module 18-10. Initial and final performance are given in Table 11.1-13. The resistance changes of individual rows and couples are shown in Table 11.1-14. Figure 11.1-11 shows the resistance trends of the six individually instrumented couples. All resistances fell within a narrow band indicating excellent manufacturing reproducibility and uniform aging effects.

The isolation resistance trend between the thermoelectric circuit and the foil is shown in Figure 11.1-12 along with modules from the MHW and GPHS programs. The isolation resistance was still increasing at the end of the life test. This trend indicates the effectiveness of the Si_3N_4 coating.

11.1.2 Assembly Process

A summary follows of issues/problems which arose during fabrication and assembly of 18 couple modules 18-10, 18-11, and 18-12.

The first problem occurred early in the fabrication of molybdenum foil and Astroquartz panels. Panels for all four modules were being made simultaneously. The size and location of the six square holes were out of tolerance per drawing requirements. Existing tooling was worn out and not efficient, having to punch one hole at a time, moving from one location to another. Manufacturing Engineering opted to utilize converter tooling to punch three holes at a time, only having to move the panels one time for the other three holes. This required the following: 1) two punches were removed from the punch and die set for clearance, and 2) a set of stops were fabricated for the correct offset needed. This was directly related to where each respective panel fit in different levels of the foil insulation assembly. Panel fabrication went extremely fast with a full complement of approved panels.

Table 11.1-12. Comparison of Initial Performance at 1035°C of Modules 18-7, 18-10, 18-11, and 18-12

|	Module 18-7	Module 18-10	Module 18-11	Module 18-12
Heat Input, Watts	162	162.6	163.4	169.15
Hot Shoe, °C Average	1035.6	1033.4	1034.6	1035.9
Hot Shoe Range, °C	12	7.5	5.7	5.7
Cold Strap, °C Average (8 T/Cs)	293.9	285.4	291.5	287.1
Cold Strap Range, °C (8 T/Cs)	9.7	9.0	1.6	5.0
Cold Strap Average, °C (12 T/Cs)	290.0	280.8	286.9	282.7
Cold Strap Range, °C (12 T/Cs)	21.3	19.8	19.1	19.8
Load Voltage, Volts	3.504	3.501	2.504	3.578
Link Voltage, Volts	0.164	0.163	0.096	0.155
Current, Amps	2.520	2.596	2.586	2.548
Open Circuit Voltage, Volts	6.353	6.355	6.381	6.431
Normalized Open Circuits, Volts (8T/Cs)	6.293	6.239	6.308	6.307
Normalized Open Circuits, Volts (12 T/Cs)	6.258	6.199	6.297	6.268
Average Couple Seebeck Coefficient, Volts/K (12)	499×10^{-6}	495×10^{-6}	497×10^{-6}	497×10^{-6}
Internal Resistance, Ohms	1.065	1.041	1.075	1.053
Internal Resistance Per Couple, Ohms (Avg.)	0.0592	0.0578	0.0597	0.0588
Power Measured, Watts (Load + Link)	9.246	9.485	9.311	9.510
Power Normalized, Watts (8 T/Cs)	9.072	9.142	9.099	9.146
Power Normalized, Watts (12 T/Cs)	8.970	9.027	8.981	8.011
Power Factor	41.67×10^{-5}	41.88×10^{-5}	41.42×10^{-5}	42.06×10^{-5}
Isolation				
Circuit to Foil, Volts	-1.55	-1.86	-1.66	-1.71
Circuit to Foil, Ohms	9.2K	18K	24.5K	21.3K
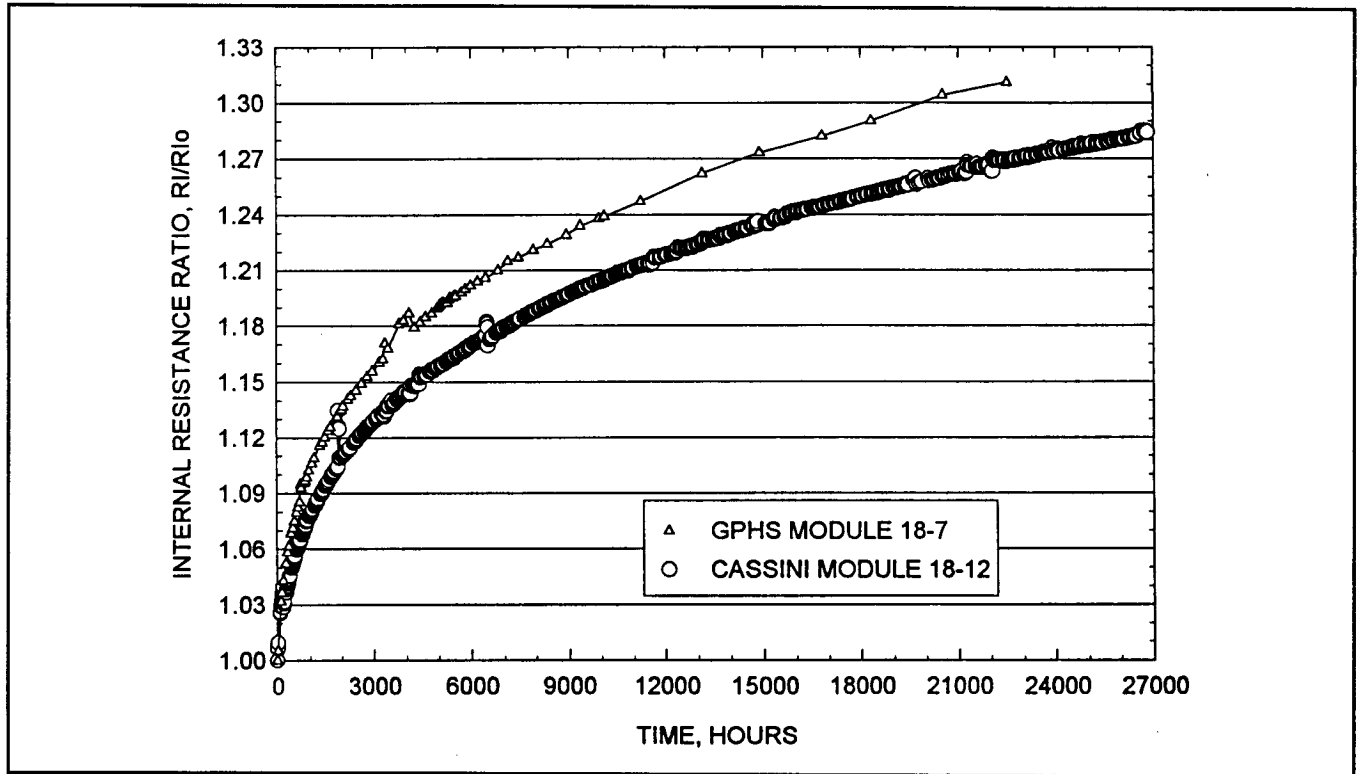
**Figure 11.1-9. Internal Resistance Ratio Vs. Time
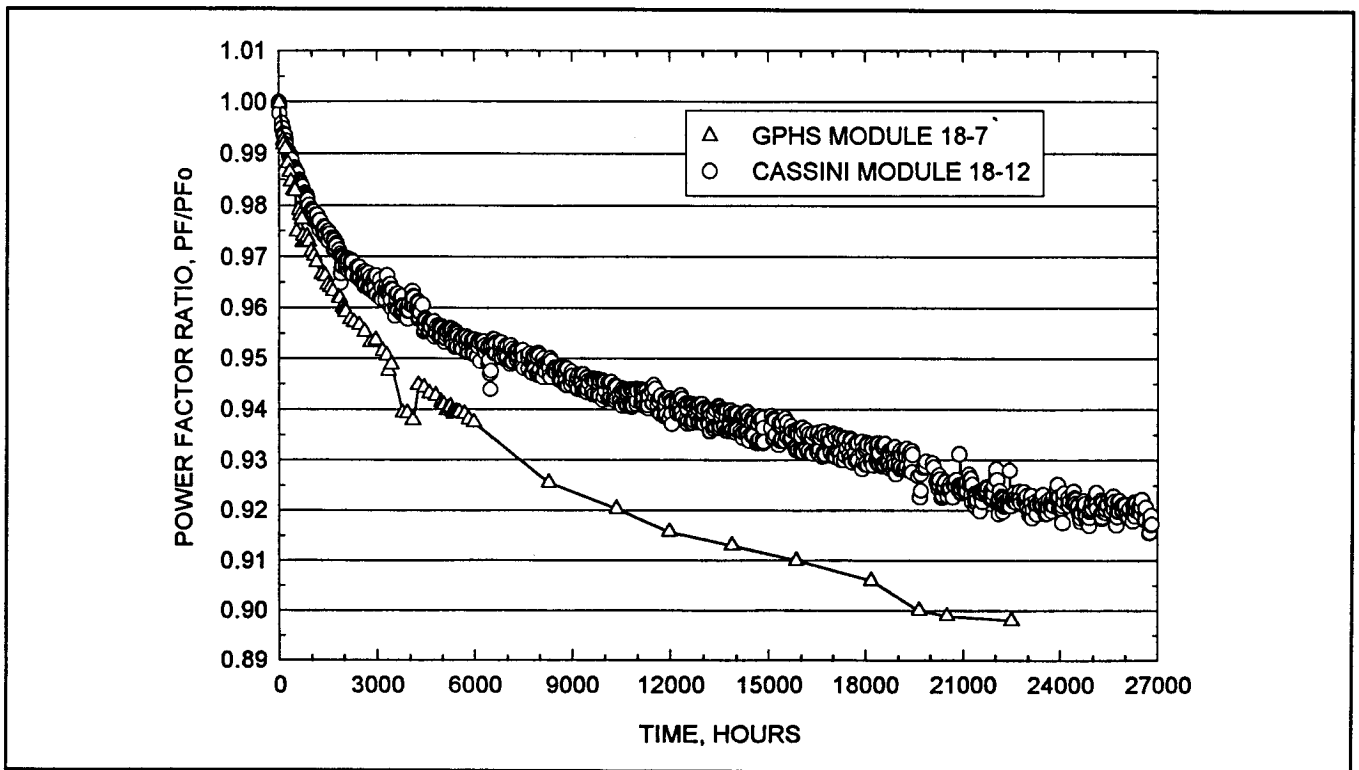(Modules 18-12 and 18-7) - 1035°C Operation**

**Figure 11.1-10. Power Factor Ratio Vs. Time at Temperature
(Modules 18-7 and 18-12) - 1035°C Operation**

Table 11.1-13. Comparison of Initial and 26,817 Hour Performance of Module 18-12 at 1135°C

	Initial 6/16/94	t = 26,817 Hours 9/11/97
Heat Input, Watts	169.15	169.1
Hot Shoe, °C Average	1035.9	1022
Hot Shoe Range, °C	5.7	4.0
Cold Strap, °C Average (8 T/Cs)	287.1	278.4
Cold Strap Range, °C (8 T/Cs)	5.0	4.7
Cold Strap Average, °C (12 T/Cs)	282.7	274.1
Cold Strap Range, °C (12 T/Cs)	19.8	19.1
Load Voltage, Volts	3.578	3.498
Link Voltage, Volts	0.155	0.152
Current, Amps	2.548	2.412
Open Circuit Voltage, Volts	6.431	6.931
Normalized Open Circuits, Volts (8T/Cs)	6.307	6.842
Normalized Open Circuits, Volts (12 T/Cs)	6.268	6.801
Average Couple Seebeck Coefficient, Volts/K (12)	497×10^{-6}	539.8×10^{-6}
Internal Resistance, Ohms	1.053	1.360
Internal Resistance Per Couple, Ohms (Avg.)	0.0588	0.0755
Power Measured, Watts (Load + Link)	9.510	8.81
Power Normalized, Watts (8 T/Cs)	9.146	8.58
Power Normalized, Watts (12 T/Cs)	9.011	8.46
Power Factor	42.06×10^{-5}	38.57×10^{-5}
Isolation		
Circuit to Foil, Volts	-1.71	-0.87
Circuit to Foil, Ohms	21.3K	188.2K

Table 11.1-14. Module 18-12 Internal Resistance Changes

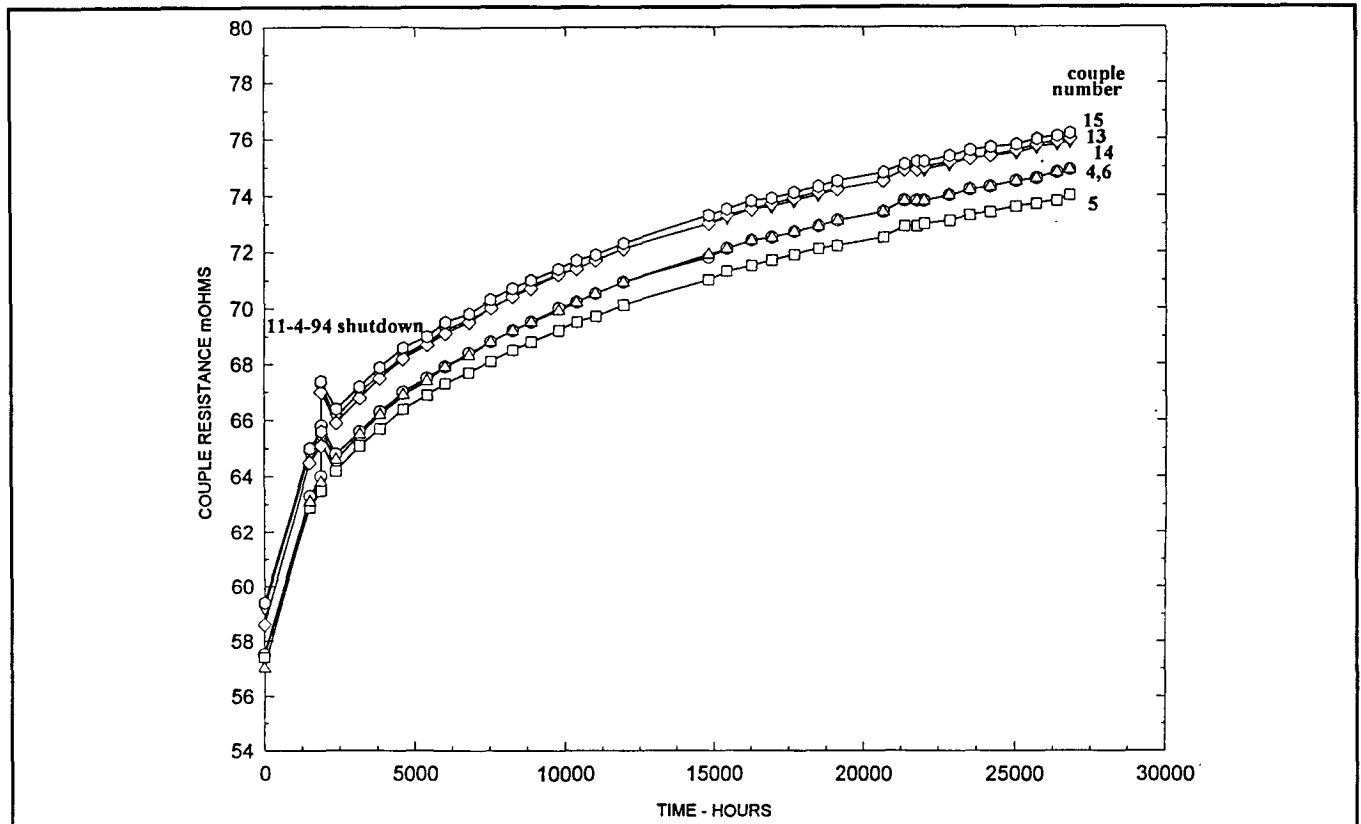| Position	Serial #	2nd Bond Milliohm	Preassy Milliohm	ΔRi Milliohm	T = 0 Milliohm	T=1,505 Hours	ΔRi Milliohm	Percent Increase	T=26,817 Hours	ΔRi Milliohm	Percent Increase
1	H2594	23.80	22.90	-0.90							
2	H2634	22.70	22.60	-0.10							
3	H2606	23.50	22.40	-1.10							
					176.80	192.10	15.30	8.65	224.60	47.80	27.04
4	H2168	22.20	21.70	-0.50	57.50	63.30	5.80	10.09	74.90	17.40	30.26
5	H2151	22.40	21.90	-0.50	57.40	62.90	5.50	9.58	74.00	16.60	28.92
6	H2256	22.20	21.70	-0.50	57.00	63.10	6.10	10.70	74.90	17.90	31.40
					171.20	188.60	17.40	10.16	222.90	51.70	30.20
7	H2597	24.40	23.20	-1.20							
8	H2680	22.60	23.00	0.40							
9	H2658	22.70	23.00	0.30							
					178.00	193.60	15.60	8.76	226.10	48.10	27.02
10	H1506	23.50	23.20	-0.30							
11	H1392	23.80	23.00	-0.80							
12	H1606	23.60	22.60	-1.00							
					176.20	193.40	17.20	9.76	227.00	50.80	28.83
13	H1344	23.60	23.50	-0.10	59.20	64.80	5.60	9.46	75.90	16.70	28.21
14	H1618	23.30	24.00	0.70	58.60	64.50	5.90	10.07	76.00	17.40	29.69
15	H1262	23.70	23.30	-0.40	59.40	65.00	5.60	9.43	76.20	16.80	28.28
					176.60	193.70	17.10	9.68	227.50	50.90	28.82
16	H1580	23.00	23.70	0.70							
17	H2127	22.80	22.10	-0.70							
18	H2113	22.90	22.20	-0.70							
					174.50	191.30	16.80	9.63	224.90	50.40	28.88

Figure 11.1-11. Individual Unicouple Internal Resistance Trends (Module 18-12)
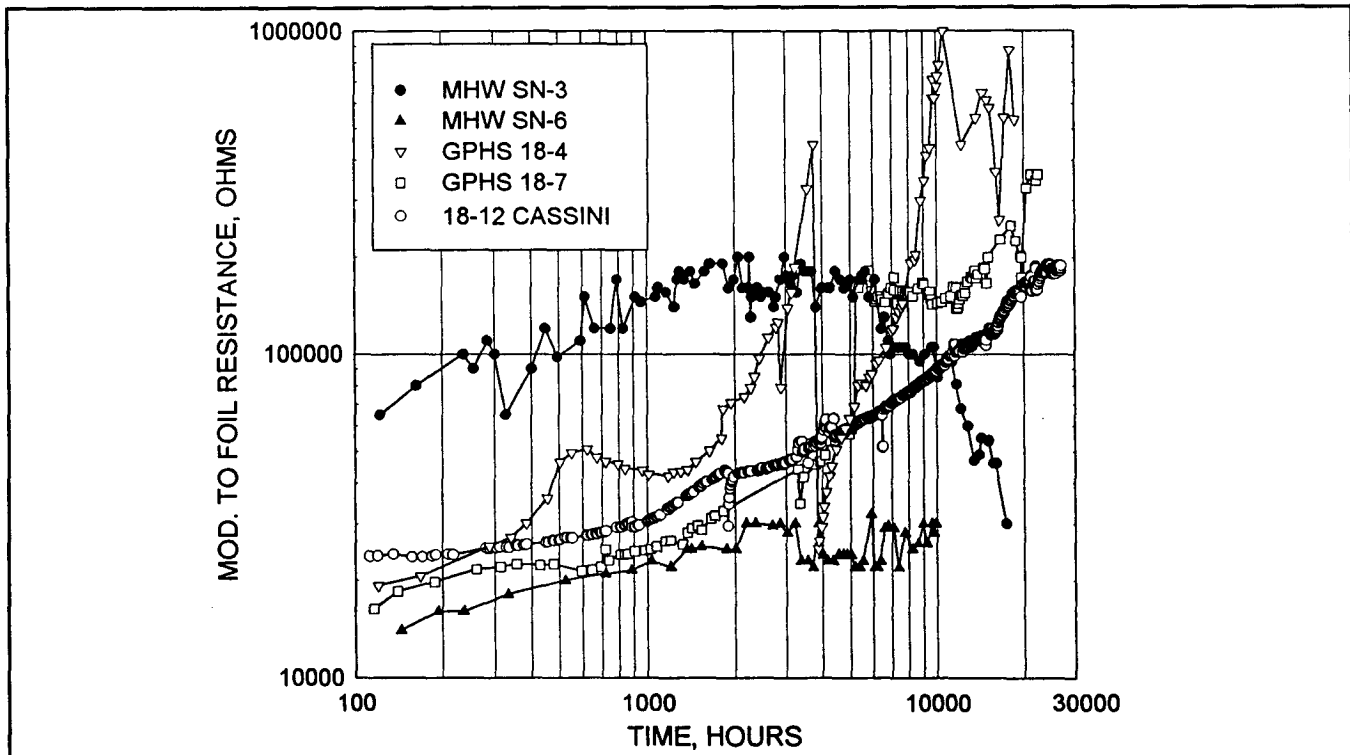
**Figure 11.1-12. Isolation Resistance - Module Circuit to Foil
(18-12, GPHS and MHW Modules) - 1035°C Operation**

Module 18-10 — During assembly of this module, it was determined that four unicouples had to be replaced. Damage to these unicouples was suspected, identified from increased unicouple resistances. After researching the rivet removal process and tooling, a decision was made to alter both. Upon approving the process change, addition of tooling, and training personnel, the unicouples were successfully removed. Evaluation of the damaged unicouples showed fractures in the N-segment in three of the four assemblies.

Investigations were conducted to determine the cause of failures. Two significant tooling modifications were made. First, a rivet gun alignment tool was added to control both rivet orientation and loading of the electrical connectors during riveting. Second, a manual tool for swaging the pop rivets was replaced by a pneumatic tool. Both of these tools had been used in the GPHS program but not identified in the 18 couple module manufacturing planning instructions. Both tools were added to the planning master.

Module 18-11—Prior to riveting operations on this module, pneumatic rivet guns were purchased and qualified. These guns eliminated the torquing motion experienced with the

electric rivet gun cycle. One hot side thermocouple, attached to the hot shoe of a unicouple, was found to be open during assembly of 18-10. At Material Review Board (MRB) direction, the opened thermocouple was not replaced as the remaining five provided adequate measurement redundancy. During potting of the module's instrumentation leads into a 50-pin connector, one of three voltage sensing leads was damaged. A jumper was installed in the vacuum test station to provide the necessary connections for the test rack.

Module 18-12—Prior to assembly of this module, a series of drawing and assembly process changes were made to correct errors encountered during fabrication of modules 18-10 and 18-11. No significant problems occurred during this assembly.

11.1.3 Improved Thermoelectric Materials and Test Results

The objective of this task was to fabricate an improved performance unicouple and to evaluate its performance in an 18 couple test module. The 18 couple module is a proven test device to determine unicouple performance relative to the database for standard coarse grain SiGe prepared for the Galileo/Ulysses and Cassini RTG programs with tests typically spanning over 10,000 hours. Details of the improved materials selection, unicouple fabrication, predicted and actual 18 couple module performance, and results of post test analyses are provided in the Cassini topical report entitled "Evaluation of an Improved Performance Unicouple" (Reference 11.1.3-1).

Improved N-type and P-type 78 atomic % SiGe thermoelectric materials were prepared at Ames Laboratory and Lockheed Martin, respectively. The N-type material was prepared by mechanical alloying Si, Ge, GaP and the P dopant followed by hot isostatic pressing. This method produced materials with a more controlled composition and microstructure. The N-type composition was $Si_{0.784}Ge_{0.196}Ga_{0.005}P_{0.015}$. The P-type material was prepared by vacuum casting Si, Ge and the B dopant and double hot pressing. Double hot pressing refers to crushing a hot pressed SiGe puck and then re-pressing to produce finer grain size and more uniform composition than standard Cassini materials. The P-type composition was $Si_{0.796}Ge_{0.199}B_{0.005}$.

The new materials and the standard coarse grain Cassini SiGe materials were characterized by room temperature Hall effect and high temperature thermoelectric properties including the Seebeck coefficient, electrical resistivity and thermal conductivity.

The figure-of-merit improvement for the N-type material was 10% and 20% for the P-type material. The improvements in the figure-of-merit over standard SiGe were primarily due to a reduction in the thermal conductivity associated with a smaller grain size.

Standard Cassini processes were used to fabricate the improved unicouples except that a two stage process was developed for bonding the improved SiGe materials to the SiMo hot shoe due to the disparity in melting temperature of the improved materials. The optimum bonding temperatures were 1321°C for the improved P-type material and 1248°C for the improved N-type material. Blisters or solidified regions of previously melted material were preferentially located near the hot end of the GaP-containing N-type leg. Prior to silicon nitride coating, these blisters were mechanically removed. Many small blisters ruptured through the silicon nitride coating during the next bonding process in which the 63.5 atomic % SiGe segments were bonded to the 78% SiGe legs. Accelerated weight loss experiments at 1150°C indicated that the sublimation rate was 2 to 3 times higher than for typical Cassini unicouples, however, within Cassini specification requirements. Two unicouples successfully passed a rivet test to verify that the bond between the segment and cold shoe would be strong enough to withstand loads introduced during 18 couple module assembly operations.

An 18 couple module, designated 18-Z, was assembled and put on ingradient life test for 2000 hours at cold side and hot side temperatures of 300°C and 1035°C, respectively, to evaluate unicouple performance. The required electric heater power input was predicted to be lower for module 18-Z compared with standard Cassini unicouples for the same reference hot side and cold side radiator temperatures. In actual performance, the electric heater power input was higher than predicted, there was no improvement in module efficiency over standard Cassini unicouples and the internal resistance and open circuit voltage increased more rapidly compared to a standard Cassini 18 couple module operating at the same hot side temperature.

The higher than predicted heater power input suggested that the reduction in thermal conductivity in the as-pressed, improved materials was not retained after unicouple fabrication. Grain growth in the P-type material and both localized melting and grain growth in the N-type material were confirmed by metallographic and SEM evaluation. These

microstructure changes were responsible for the increase in thermal conductivity and, in turn, the lack of performance improvement over standard Cassini materials.

The mechanism for the accelerated resistance and open circuit voltage increases was attributed to a loss or redistribution of dopants which increased the electrical resistivity and Seebeck coefficient. Loss of phosphorus in the N-type material through the cracks in the silicon nitride coating was confirmed. It was also suspected that the boron precipitated out of solution in the P-type material since the dopant level exceeded the solid solubility limit at the hot side test temperature.

From the results of the 18 couple module test, it was evident that a lower temperature manufacturing method, such as sputter brazing and bonding at temperatures below 1200°C, for the attachment of the N-type material to the SiMo hot shoe (as was employed for MOD-RTG multicouple assembly) would be required to eliminate incipient melting. In addition, long duration dopant precipitation studies and development of an applicable dopant precipitation model would also be necessary to more fully assess the performance of an 18 couple module composed of improved materials.

11.2 MULTICOUPLE TESTING

11.2.1 Background

Multicouples were fabricated on the MOD-RTG Program (Contract DE-AC01-83NE-32112) and life testing of these multicouples was continued on the Cassini RTG Program as part of Task 8, Subtask B. Direction was received from DOE in September 1994 (Reference 11.2-1) to terminate the multicouple life tests in a controlled manner. The direction specified that each multicouple be removed from its test station and visually examined at 40X magnification. The performance of the five multicouples placed on life test as well as the observations from the post test visual examination are presented below.

11.2.2 Multicouple Description

The multicouple design is illustrated in Figure 11.2-1 for reference. Four of the multicouples were of the Build 5 configuration and one was from the Build 3 configuration. A detailed description of each of the configurations can be found in Reference 11.2-2. The Build 5 configuration was fabricated with improvements to the hot end glass bond which would
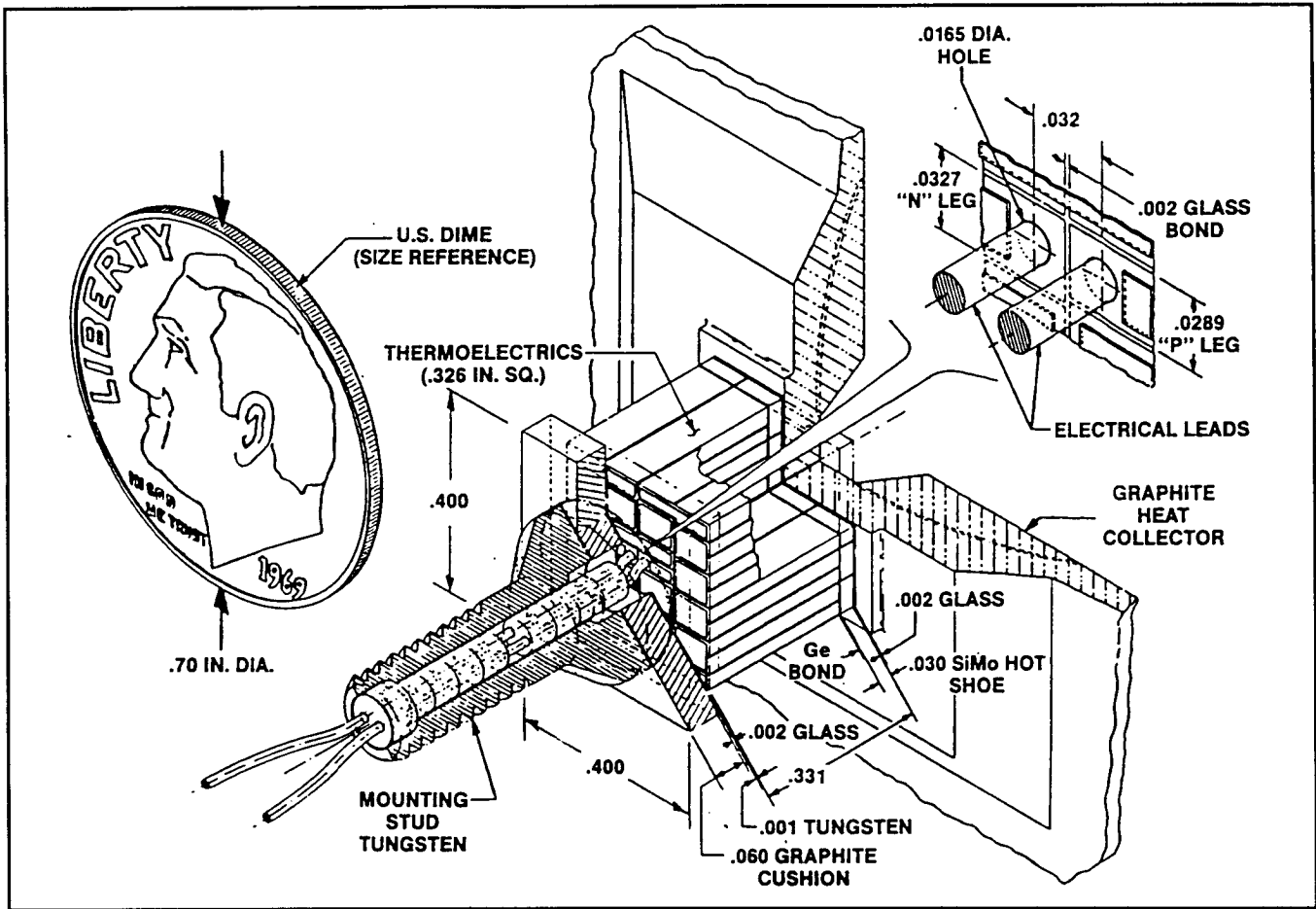
Figure 11.2-1. MOD-RTG Multicouple Design

permit testing at accelerated temperature. These improvements included the use of a silicon nitride/silicon dioxide coating applied to the hot end glass bond as well as the addition of a glass filet to the same bond to reduce thermal stresses. The Build 3 multicouple was an earlier configuration, built in 1987, which did not have the design and process improvements incorporated into the Build 5 configuration.

Four of the tested multicouples were fabricated with SiGe/GaP N-legs and SiGe P-legs and one was fabricated without GaP (i.e., with SiGe N-legs and SiGe P-legs). The five tested multicouples were identified as follows:

- Build 3 M/C 1026-8
- Build 5 M/C M042-G4
- Build 5 M/C M043-18
- Build 5 M/C N043-5 (No GaP)
- Build 5 M/C M043-19

11.2.3 Multicouple Test Results

Test stations were designed and fabricated at Lockheed Martin to measure multicouple ingradient performance. Two vacuum chambers were modified to each contain a cruciform containing four heater stations (See Figure 11.2-2). Each heater box contained a graphite heater and radiation plate and was insulated with multifoil insulation. Each multicouple was mounted to an aluminum alloy fin to simulate outer shell mounting. The fin area was sized and coated with high emissivity coating to achieve the required cold junction temperature of the multicouple. Heater power was supplied by GPHS-RTG Power Supply Consoles. A modified GPHS-RTG Readout Console (ROC) was used to monitor multicouple performance and provide automatic test shutdown in the event of an overtemperature or loss of vacuum event.

All multicouples except M043-19 were operated at normal RTG operating temperatures (1000°C hot junction; 300°C cold junction) with a -6 volt bias applied between the negative multicouple terminal and ground. Multicouple M043-19 was operated at reduced, normal and accelerated hot side temperatures as shown in Table 11.2-1. Accelerated testing of multicouple M043-19 was terminated because of unwanted reactions in the heater station which were not associated with the multicouple. It was found that reactions were occurring between the alumina insulation and graphite heater components. These reactions produced aluminum carbide which deposited on the molybdenum insulation as well as the multicouple assembly. The same reaction occurred in 8 couple test modules which were tested at Fairchild Industries (now Orbital Sciences Corporation) as discussed in more detail in Reference 11.2-2.

Table 11.2-1. Multicouple M043-19 Test History

Hot Junction Operating Temp (°C)	Time at Operating Temp (Hours).
1000	1838
1050	3753
950	11,267
Total	**16,858**

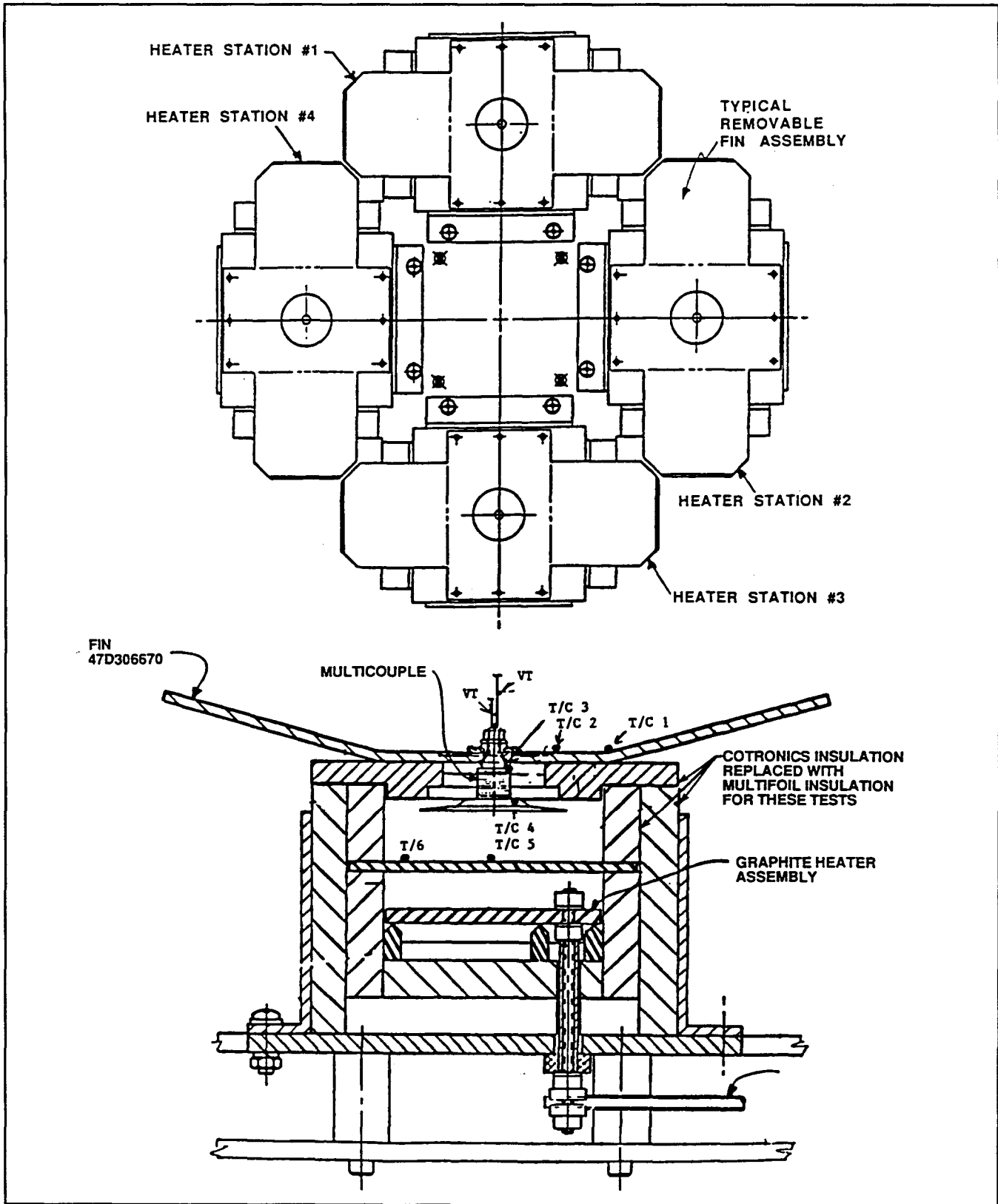**Figure 11.2-2. Lockheed Martin Multicouple Heater Boxes (Two Views)**

The life test hours accumulated by each multicouple are shown in Table 11.2-2.

Table 11.2-2. Multicouple Life Test Summary

Multicouple	Test Completion	Accumulated Test Hours
Build 3 - M/C 1026-8	8/14/94	25,012
Build 5 - M/C M042-G4	8/14/94	9,070
Build 5 - M/C M043-18	9/9/94	7,878
Build 5 - M/C N043-5 (No GaP)	8/31/94	16,406
Build 5 - M/C M043-19	8/31/94	16,858

Table 11.2-3 summarizes the performance ratios for each multicouple at the end of testing.

Table 11.2-3. P/P_0, R/R_0, E/E_0 Ratios at End of Testing

Multicouple	Test Hours	P/P_0	R/R_0	E/E_0	ΔR % / ΔE%
1026-8	25,012	0.785	1.490	1.080	6.1
M043-18	7,878	0.894	1.321	1.087	3.7
M042-G4	9,070	0.900	1.267	1.068	3.9
N043-5	16,406	0.756	1.454	1.048	9.5
M043-19	16,858	0.7705	1.473	1.065	7.28

11.2.3.1 Multicouple 1026-8 (Build 3)

This multicouple operated for 25,012 hours at normal RTG operating temperatures. This was the longest operating time achieved for any multicouple. Normalized power degradation (Figure 11.2-3) during this time was 22%, which is approximately twice that of the unicouples as measured in GPHS 18 couple modules 18-4 and 18-7. The greater power degradation is due to both a higher rate of internal resistance increase (Figure 11.2-4) and a lower rate of increase in open circuit voltage (Figure 11.2-5). The higher rate of internal resistance increase is attributed to accelerated dopant precipitation in the fine grain materials. This is discussed in more detail in Reference 11.2-3. The lower rate of increase in open circuit voltage is attributed primarily to an increase in temperature drop across the insulating glasses. The ratio of the percentage change in internal resistance to the percentage change in open circuit voltage due to dopant precipitation effects is in the range of 2.0 to 3.0 for unicouples with course grain material. Table 11.2-3 shows that this ratio is much higher for the multicouples.
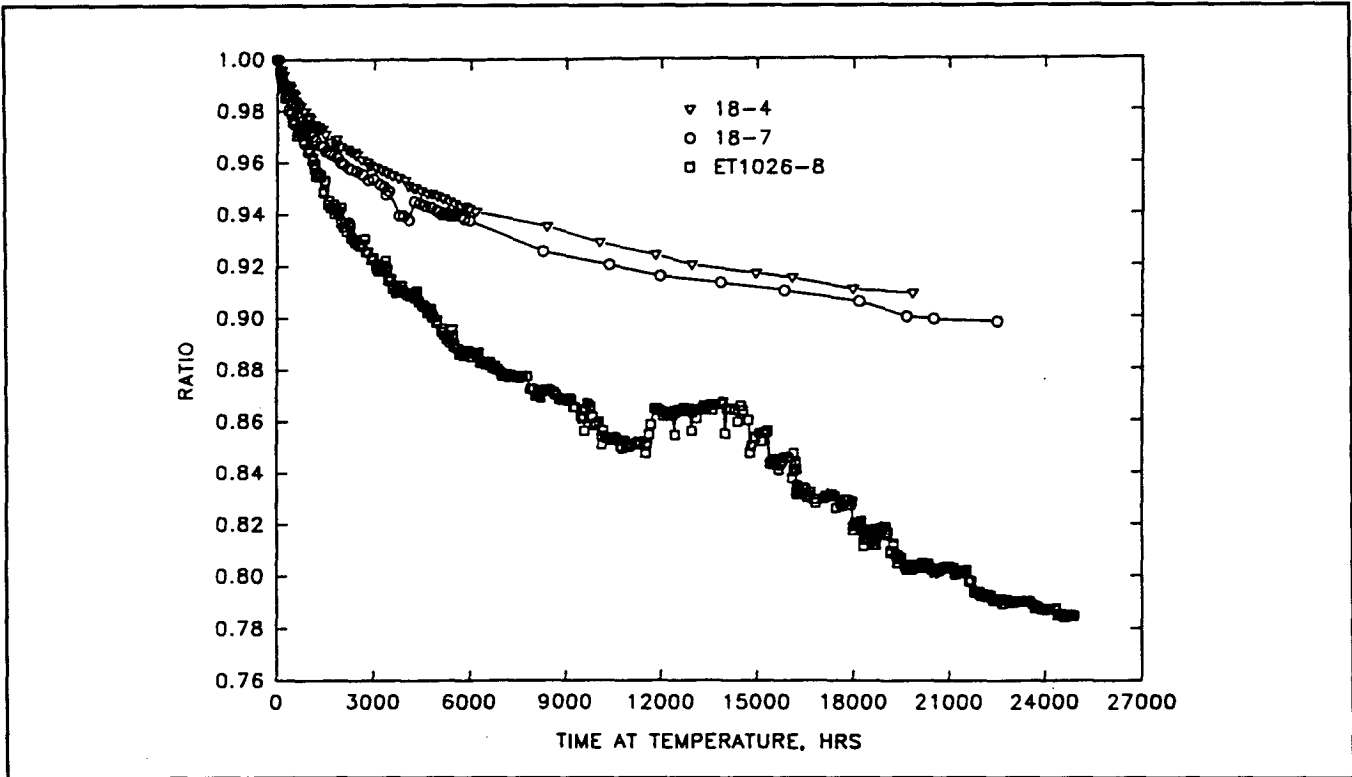
**Figure 11.2-3. ET1026-8, 18-4, 18-7 – Normalized Maximum Power/
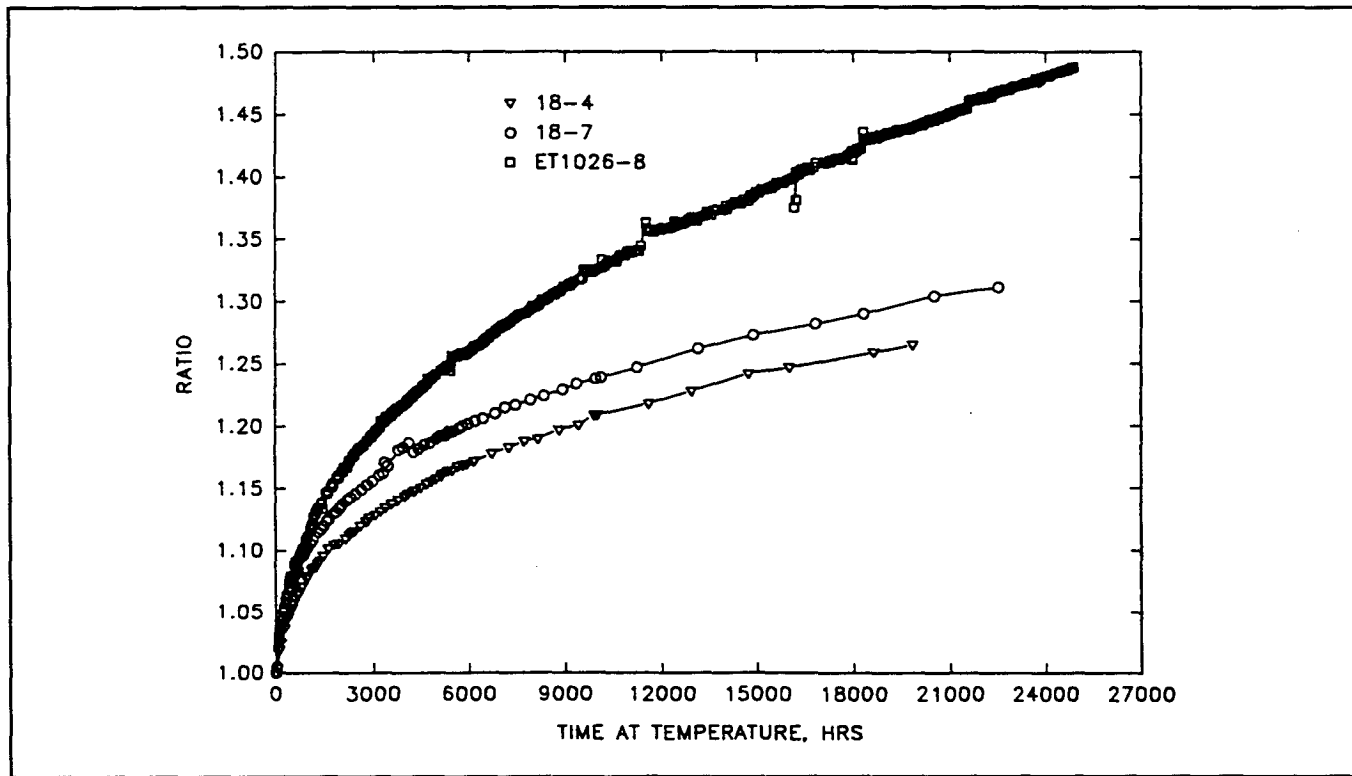Initial Value Versus Time at Temperature**

**Figure 11.2-4. ET1026-8, 18-4, 18-7 – Normalized Internal Resistance/
Initial Value Versus Time at Temperature**
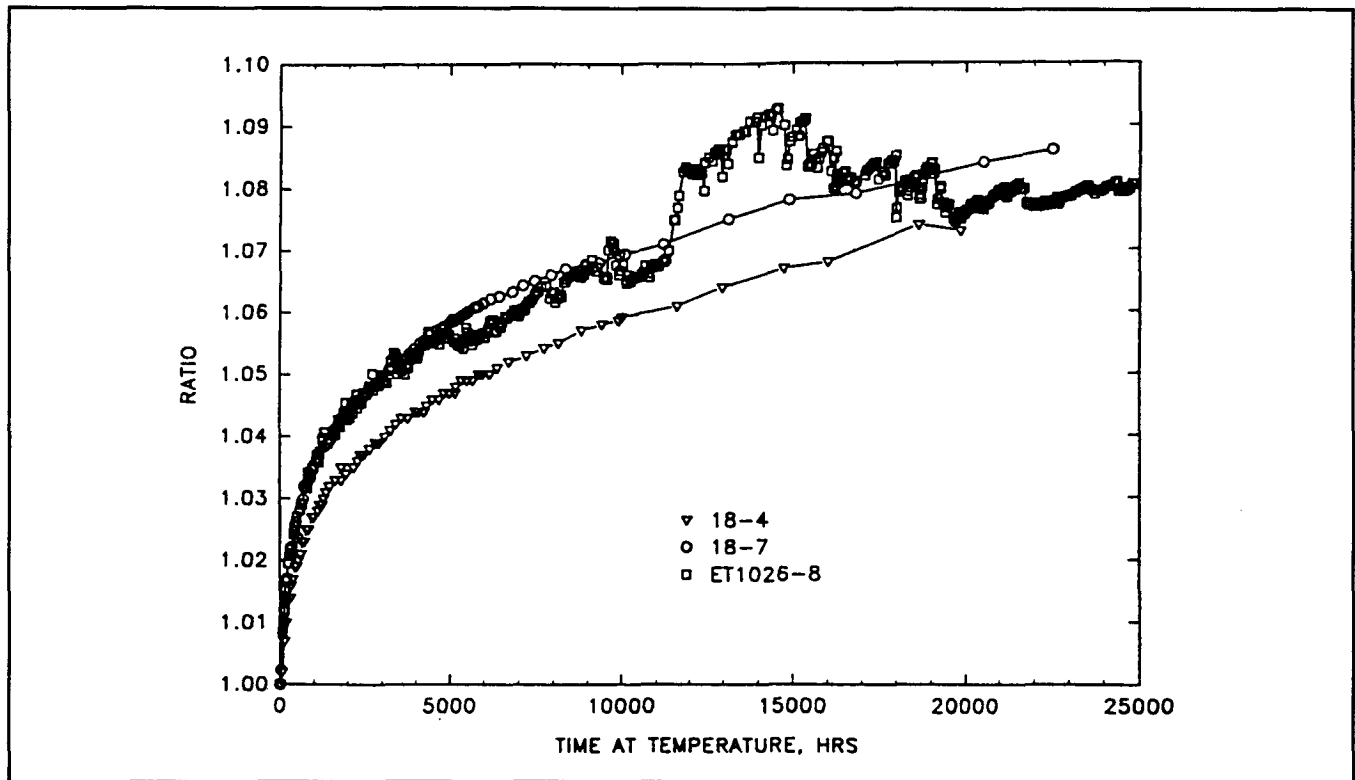
**Figure 11.2-5. ET1026-8, 18-4, 18-7 – Normalized Open Circuit Voltage/
Initial Value Versus Time at Temperature**

11.2.3.2 Multicouple M043-18 (Build 5)

This multicouple accumulated 7,878 hours of operation at normal RTG operating temperatures. Overall, its power degradation was not quite double that of unicouples. Its higher degradation appeared more due to internal resistance increase than open circuit voltage rate increase.

11.2.3.3 Multicouple M042-G4 (Build 5)

This multicouple was tested for a total of 9,070 hours at normal RTG operating temperatures which included 2,000 hours in the Fairchild (now Orbital Sciences Corporation) Build 5 test module. Its overall degradation was 10% compared to 7% for unicouples. However, there was a steep change in the degradation rate of about 1.5% between the Fairchild and Lockheed Martin tests. If this is taken into account, the degradation was about 20% greater than unicouples. Both internal resistance and open circuit voltage increased faster than unicouples indicating that accelerated dopant precipitation was the dominant degradation mechanism.

11.2.3.4   Multicouple N043-5   (Build 5 – No GaP in SiGe Alloys)

This multicouple accumulated 16,406 hours of operation at normal RTG operating temperatures. Its power degradation was approximately twice that of unicouples. Both internal resistance and open circuit behavior contributed to the higher rate of degradation. Its degradation characteristics were similar to the other multicouples, indicating that the GaP was not the cause of the more rapid degradation.

11.2.3.5   Multicouple M043-19   (Build 5)

This multicouple was tested for a total of 16,858 hours. Most of the testing was at the reduced heat collector temperature of 1015°C (950°C hot junction). The multicouple began testing at the accelerated temperature of 1115°C (1050° hot junction), but it became necessary to reduce the temperature because Residual Gas Analyzer (RGA) data showed that the partial pressure of carbon monoxide was increasing in the test chamber. This was an indication that aluminum carbide formation reactions were taking place. Its degradation was about 2.5 times that of unicouples. Both internal resistance and open circuit anomalous behavior contributed to the higher degradation rate.

11.2.4   Post Test Examinations

Table 11.2-4 lists the multicouples, test conditions and a summary of the post-test visual observations. In brief, three of the multicouples appeared to be very clean and free of unusual deposits (Multicouples ET1026-8, M042-G4, and N042-5). Two of the multicouples, however, had a heavy powdery, yellow-white coating on most of the heat collector and the exposed surface of the moly foil package (Multicouples M043-18 and M043-19). These two multicouples also had heavy blue-gray and yellow-brown crusty deposits on the quartz yarn wrapping on the thermopiles. A more detailed description of the post test examination findings may be found in Reference 11.2-4.

Table 11.2-4. Multicouple Test Conditions and Post-Test Visual Appearance

Multicouple	Build	Accum. Test Hours	Vacuum Station	Heater Station	Test Temperature	Heat Collector Appearance	Quartz Yarn Appearance	Perimeter Glass Appearance
M/C 1026-8	3	25,012	3	2	Normal	Normal: No Deposits	Normal: Slight Discoloration	Normal: Off-White with random areas of Yellow-Brown near mid-section.
M042-G4	5	9,070	3	4	Normal	Normal	Normal	Normal
N042-5 (No GaP)	5	16,406	5	3	Normal	Normal	Normal	Normal
M043-18	5	7,878	3	1	Normal	Yellow-White Powder Coating	Hot-to-Cold: Yellow-White, Blue-Gray, Yellow-Brown, Off-White	Normal
M043-19	5	16,858	5	2	Normal = 1,838 Hrs. +50° = 3,753 Hrs. -50° = 11,267 Hrs.	Yellow-White Powder Coating	Hot-to-Cold: Yellow-White, Blue-Gray, Yellow-Brown, Off-White	Normal

References for Section 11

11.1.3-1 DeFillipo, L. E., B. Franklin, C. E. Kelly, P. M. Klee and J. F. Nakahara, "Evaluation of an Improved Performance Unicouple," Cassini RTG Program Topical Report, 17 June 1996.

11.2-1 Letter from DOE (Ser-RTG-052), Promani to Waks, LMMS, 7 September 1994.

11.2-2 GESP-7230, MOD-RTG Final Technical Report, 31 December 1992.

11.2-3 Kelly, C. E., R. F. Hartman, P. M. Klee, S. Loughin, Technical Paper, "MOD-RTG Program Multicouple Life Testing," 28th IECEC, August 1993.

11.2-4 Franklin, B. R., R. F. Hartman, C. E. Kelly, P. M. Klee, Cassini RTG Program Topical Report, "Multicouple Life Test Results," 31 January 1995.

Appendix A

Issues and Solutions for Re-Establishment of Unicouple Fabrication

APPENDIX A

ISSUES AND SOLUTIONS FOR
RE-ESTABLISHMENT OF UNICOUPLE FABRICATION

This appendix lists the problems encountered during the re-establishment and flight production of unicouple fabrication during the Cassini program. The problems and their respective solutions for the major operations and processes involved are summarized.

Vacuum Casting

At the beginning of the Cassini program, it was recommended that chilled water cooled pancake style castings be made instead of the finger type castings fabricated during the Galileo/Ulysses program. The advantages were more uniform and reproducible casting characteristics. Also, the set-up and break down of the molds were simpler for the pancake style casting. A qualification plan was developed and implemented. The room temperature densities and Seebeck coefficients were similar to the Galileo/Ulysses statistical and process control data, however, the alternate process did not produce thermoelectric materials with the proper microstructure. All the vacuum castings subsequently prepared for the Cassini program were the finger style. There were no significant process problems during production.

Powder Blending

The only change implemented was the method in which molybdenum powder was added to the doped silicon powder. During the Galileo/Ulysses program the -325 mesh Mo powder was mixed directly with the Si powder. For the Cassini program the Mo powder was pre-sieved through a 325 mesh screen before mixing with Si, resulting in a reduced amount of Mo agglomeration and a more uniform SiMo material. There were no significant process problems during production.

Hot Pressing

At the beginning of the Cassini program, it was intended to hot press thicker SiGe compacts to increase the number of machined parts per compact. Initially, powders prepared from the pancake style castings were used and were later repeated using powders prepared from

finger style castings. The porosity and homogeneity could not be duplicated in the thicker compacts and it was decided to revert back to 0.5 inch thick SiGe compacts. It was later determined that a higher hot press temperature and load were required to prepare thicker SiGe compacts with the proper porosity and microstructure. All SiGe and SiMo compacts prepared for the Cassini program were 0.5 inch thick. There were no significant process problems during production.

N-P Bond/Hot Shoes

Problem	Low N-P bond joint strength.
Solution	Added a SiMo compact cleaning step (in boiling water) after polishing, duplicating the Galileo/Ulysses process.
Problem	Decreased hot shoe strength and increased resistance.
Cause	Bonding temperature needed to be optimized and flatness verified.
Solution	Completed temperature profile study in each hot press to achieve a 1285°C bond temperature.
	Determined optimum set points for both hot presses (hot press #2: 1306°C, hot press #3: 1315°C). Also verified lapping table operation to achieve flatness requirement.

Thermoelectric Parts Preparation (Machining)

During the Galileo/Ulysses program the thermoelectric elements and hot shoes were sliced oversized and ground (pellets and segments) or lapped (hot shoes) to size. The new precision machining equipment procured for the Cassini program wafered and sliced parts to size, minimizing the amount of grinding. A verification plan was developed and implemented to verify that the modified machining techniques did not adversely affect the ability of subsequent silicon nitride coatings to inhibit material vaporization at unicouple operating temperatures. Tests included dimensional inspection, first bond fabrication and silicon nitride coating, followed by second bond, couple preassembly and unicouple thermal cycling. Hot shoes were evaluated for strength, electrical resistance and bond porosity. After thermal cycling, the coated first bond was subjected to a 40 hour thermogravimetric analysis (TGA) test. The Cassini verification data matched previous Galileo/Ulysses data.

A second set of tests were also performed to determine the adherence of silicon nitride coatings on wafered and ground surfaces which may have a different surface texture. SiGe pellets and hot shoes were silicon nitride coated and heated in vacuum between 1150 and 1160°C for up to 750 hours. Sublimation performance of the Cassini silicon nitride coatings were found to be equivalent to Galileo/Ulysses coatings and were equivalent for wafered and ground surfaces. The verification test results, summarized in Cassini PIR 028, indicated that the new Cassini machining methods were acceptable.

Other Problems and Their Respective Solutions Are Summarized Below:

Problem	Staining on pellets and segments.
Cause	Fixture marks and coolant (deionized water) residue.
Solution	Removed sharp edges from fixtures and replaced coolant with that used on the Galileo/Ulysses program.

Problem	Hot shoe staining
Cause	Water spots and epoxy residue.
Solution	Prevented coolant from drying on parts and removed epoxy mechanically rather than chemically.

Problem	Variation of gray color on P-wafers and P-pellets (lacy pattern).
Solution	Completed series of studies, including process review, SEM, Auger, SIMS, first bonding, coating, TGA and methods of rework.
	Found that the subtle pattern was a harmless artifact of ultrasonic cleaning. No difference in chemistry, and the pattern was eliminated during first bonding. ECN issued to accept nonuniformity of gray color and added visual standard for inspection Reference.
Reference	Cassini Memo #135 and ECN RTG-0215

Problem	Recurring excessive chipping and staining of pellets.
Solution	Increased supervision in machining area to provide in-process checks.

Problem	Machining coolant (White and Bagley) not available, discontinued.
Solution	Tested two alternatives and switched to TrimClear coolant.
	Testing included chemical analysis, machining trials, SIMS surface analysis, Seebeck coefficient, coating, and TGA.
Reference	Cassini Memos #133, #144, #157, and ECN RTG-0223

Problem	Stains on pellets and segments.
Solution	Replaced five swabbing steps with hydrogen peroxide cleaning. This provided significantly cleaner parts with less handling.
Reference	ECN RTG-0286, and Cassini Memo #195

Issue	Increase quantity of pellets and segments machined from a compact.
Solution	Optimized machining to increase parts machined by ~35%.

First Bond Assembly

Problem	Low acceptance yield due to stains on hot shoe.
Cause	Carbonization of (non-visible) organic residues on hot shoe during first bond cycle.
Solution	Added hydrogen peroxide cleaning step to hot shoes prior to first bond assembly.

Issue	Opportunity to increase throughput by reducing furnace "burn-in" runs.
Solution	Conducted tests to require burn-in runs only if furnace was idle for more than 24 hours. Successful test results.

Silicon Nitride Coating

Problem	"White spots" on coated first bond assemblies
Cause	Chemically resistant residue on parts from Teflon tweezers tip. Excessive blister removal from first bond assemblies.
Solution	Replaced Teflon tweezers with Delrin. Reduced the amount of blister removal.

Problem	Bluish color on P-side of hot shoe coating after TGA testing.
Cause	A possible cause was the interaction between the Si-rich Si_3N_4 layer and SiO_2. Another explanation was that the Si-rich areas agglomerated or changed during thermal processing to produce a blue reflection.
Solution	Since the blue discoloration was not an indication of the quality of the Si_3N_4 coating, no process changes were instituted.
Reference	Cassini Memo #306

Second Bond Assembly

Problem	Voids at P-segment to pellet bond. Yield decreased to ~60%.
Cause	• Different lots of tungsten bonding clips not performing well. • P-segments have a higher melting point than N-segments. • Can improve on fixture design to eliminate use of clips.
Solution	• Procured and evaluated new lots of clips. • Evaluated properties of available segment lots to obtain better match. Found that best P-segment material was hot pressed at 1305°C. Produced more P-segment/compacts hot pressed at ~1305°C. These P-segments provided improved bond joints: yield ~95%. • Designed and tested new fixture type, without clips, "Second Bond Static Load Fixture". Good results were obtained. Revised specification to allow use of this alternate fixture ECN RTG-0336). Also added option to use heavier weights with fixture (ECN # RTG-0432). Fixture was used for ~15% of remaining second bond assemblies.

Tungsten Cold Shoe

Problem	Microcracks, chips and out-of-parallel condition in new EDM cut parts from vendor (Schwarzkopf and lapping vendor, Assabet).
Cause	Lapping conditions needed to be studied, controlled and optimized.
Solution	Engineering, Manufacturing, Quality (EMQ) worked closely with both vendors to remedy problems. Modifications were made to lapping methods. Lapping load was too heavy. Supplier Instructions added to drawing 47A303803P1-900. Drawing 47A303803 modified to add allowable radius (ECN RTG-0459).
Reference	Martin Marietta, Cassini Trip Reports:

9/9/94 (Hofmeister, Dadd), 10/31/94 (Franklin, Dadd),

11/21/94 (Dadd, Schreiber), 12/9/94 (Franklin, Dower, Dadd)

12/21/94 (Franklin, Dadd)

Radiator Attachment Assembly

Problem	Numerous poor workmanship issues with machining vendor (Sheffield).
Solution	Ultimately, discontinued machining at vendor. Established capability for in-house machining with good results.

Cold Stack Assembly

Problem	Oxidation (discoloration) during brazing cycle.
Cause	Outgassing from graphite brazing fixtures.
Solution	Vacuum-fired graphite fixtures and stored fixtures in nitrogen dry-box when not in use.

Problem	Braze voids at radiator to electrical insulator bond.
Cause	Radiator surface not flat.
Solution	Modified machining methods and eliminated hand sanding.

Couple Pre-Assembly

Problem	Braze defects.
Solution	Lowered allowable minimum brazing temperature and clarified steel wool scrubbing technique. ECN issued.
Reference	ECN RTG-0450

Problem	Water stains and poor braze flow.
Solution	Modified cleaning step to eliminate water spots and modified gritblasting method to protect brazing surface.
Reference	ECN RTG-0409

Unicouple Assembly

Problem	Stains appeared on unicouple during braze cycle.
Cause	Residue (non-visible) on unicouple from Teflon tweezers.
Solution	Replace Teflon tweezers with Delrin tweezers.

Problem	Foreign material in braze joint.
Cause	Carbonized residue from acrylic binder (M50A1).
Solution	Added solvent swabbing/nitrogen blow-off step to specification.

Problem	Voids in braze joint.
Solution	• Replaced binding fixture screw with better fitting screw.
	• Replaced defective nut plate fixture parts.
	• Added cold stack parallelism data sheet to in-process traveler.
Reference	Cassini Memos #312, #317, #337

Problem	Stains appearing on hot shoe spacers during braze cycle (low yields).
Cause	Residue (non-visible) on spacers prior to brazing.
Solution	Added cleaning and screening step to spacers prior to braze cycle. Also added better handling, cleaning, and storage methods.
	Handled fired parts with ceramic tipped tweezers only.
Reference	ECN RTG-0413 and Cassini Memos #290, #290A

Hot Shoe Spacer

Problem	Cracking of hot shoe spacer after unicouple assembly.
Cause	Vendor (AlSiMag) used a new laser machining process to form the spacers causing high stresses and cracking.
Solution	Replaced laser machining with die forming in the green state, as was used on GPHS.
Reference	Monthly Technical Progress Reports dated March 1993 and September 1993

Wrapped Unicouple Assembly

Problem	Specification was not consistent with past process.
Solution	Clarified specification.

Nickel Plating

Problem	Delays in procurement of parts to nickel plate.
Solution	Direct interaction with vendors by Manufacturing, Engineering, Quality and Purchasing to expedite delivery.

Problem	Blisters on plated heat shunts.
Cause	Surface defects formed on the parts during rolling at vendor.
Solution	Etched parts in a nitric acid/hydrofluoric acid solution to remove surface defects prior to plating.

Molybdenum Compensators

Problem	Gouges on plated molybdenum compensators.
Cause	Unplated parts have gouges on the surface, damaged during vendor machining. No tumbling process was used to remove flaws.
Solution	Additional inspector training to screen out gouged parts.

Tungsten Compensators

Problem   Stained after tumbling, prior to plating.

Solution
- Added step to electro-clean parts in Oakite following tumbling.
- Added process control definitions to tumbling method.

Copper Pedestals

Problem   Excessive burrs after tumbling. Additional tumbling removed burrs but caused excessive embedded particles.

Cause   Burrs formed during part fabrication by vendor.

Solution
- Improved forming method (blanking) using new tooling at vendor.
- Added process control definitions to tumbling method.

Heat Shunts

Problem   Unacceptable dimensional variations.

Solution   Worked with vendor (Carr) to improve dimensional control.

Problem   Interior plating thickness did not meet minimum requirement (0.05 mil).

Solution   Evaluated GPHS plated parts to compare with current parts.

Current parts found to be comparable. Clarified Met lab measurement methods. Revised minimum thickness requirement.

Electrical Connectors

Problem   Burrs in the hole of electrical connectors following tumbling. Additional tumbling removed burrs but caused excessive embedded particles.

Cause   Burrs formed during part fabrication by vendor.

Solution
- Deburred delivered parts by hand.
- Improved forming method (blanking) to reduce burrs at vendor.

Electrical Insulators

Problem	Low strength of new lot of insulators from vendor (Wesgo).
Solution	• Reduced metallized layer thickness.
	• Heat treated metallized parts (study showed that GPHS also applied a heat treatment to metallized parts).
	• Redefined visual standards to allow small pinholes in metallized layer (0.5 to 1.0 mil) as was found to be consistent with GPHS parts.
	• Optimized mesh size for application of metallized layer.

Problem	Vendor machined insulators have foreign material and cracks.
Solution	• Worked with vendor (Sheffield) to improve deburring procedure and made several modifications to edge grinding procedures.
	• Established alternate machining vendor (Insaco) to machine parts. Trial lot of parts received for evaluation. No orders made beyond this.

M50A1 Acrylic Binder

Problem	New batch of binder had very high viscosity. Specification lacked detail.
Cause	Wrong chemical was ordered and used in new batch.
Solution	Determined correct name of chemical. Revised material specification to clarify chemical name and revised process specification with more detail.
Reference	ECN RTG-0296 and NR 78366

New Ultrasonic Cleaners

Issue	Need to evaluate new, higher frequency, ultrasonic cleaners.
Solution	Compared new cleaners to old cleaners by the "aluminum foil erosion test." Also evaluated noise level. Found new cleaners to be equivalent to old cleaners. Built noise suppression enclosures following EHS recommendations.
Reference	• "The Ultrasonic Cleaning Process", Microcontamination (periodical), Vol. 2, No. 5, 1984.
	• ET #5157 and CRAF/Cassini Equivalent Item Approval Form signed 2/9/95
	• "Employee Noise Exposure Monitoring Report" EHS Record #A950203-1.

Rework Methods

Issue	Could streamline MRB/rework cycle if commonly used rework methods were captured in one new specification to be used as a Reference.
Solution	Studied common rework methods, created and issued a new specification.
Reference	ECN RTG-0470 and Specification 23021621

Long Term Packaging

Issue	Need to determine methods and materials to protect and inhibit corrosion of residual Cassini hardware during long term storage.
Solution	Evaluated protective packaging materials for storage and corrosion protection. Recommendations, test results and specification written.
Reference	Cassini Memos #333, #346, #355, and Specification GESP 7244.

E-7 Rework

Issue   Need to rework 144 unicouples removed from E-7 ETG.

Solution   Several engineering tests were run to optimize rework processes.

The rework method: unwrap, solvent clean, hydrogen anneal at 715°C for 10-15 minutes to restore ductility to copper connectors, resize heat shunt (if required), hot shoe spacer chem etch-clean (if required), and rewrap. The rework acceptance yield was 87.5%.

Reference   Cassini Memo #440.

Quartz Yarn Firing

Issue   Brittle quartz yarn after firing in air furnace per specification methods.

Solution   Investigated materials, process and equipment.

Found that furnace control thermocouple was not in optimum location; resulting in overtemperature situation, crystallization and brittleness of yarn.

Ran tests with thermocouple in optimum position with good results.

Modified specifications to define and clarify furnace set-up, temperature profile process, and inspection method (knot test).

Reference   ECNs RTG-0566 and RTG-0557.

Training Videos

Issue   Could expedite start-up of next unicouple build with fabrication videos.

Solution   Completed video production of 18 tapes, which document unicouple fabrication processes, to be used as training aids. Also produced 10 tapes which document converter assembly processes.